COMMONALITIES AND DIFFERENCES IN VESTIBULAR AND AUDITORY PATHWAYS

EDITED BY: Soroush G. Sadeghi and Gwenaelle S. G. Geleoc
PUBLISHED IN: Frontiers in Neuroscience and Frontiers in Neural Circuits

frontiers Research Topics

frontiers

ISSN 1664-8714
ISBN 978-2-88974-920-1
DOI 10.3389/978-2-88974-920-1

About Frontiers

Frontiers is more than just an open-access publisher of scholarly articles: it is a pioneering approach to the world of academia, radically improving the way scholarly research is managed. The grand vision of Frontiers is a world where all people have an equal opportunity to seek, share and generate knowledge. Frontiers provides immediate and permanent online open access to all its publications, but this alone is not enough to realize our grand goals.

Frontiers Journal Series

The Frontiers Journal Series is a multi-tier and interdisciplinary set of open-access, online journals, promising a paradigm shift from the current review, selection and dissemination processes in academic publishing. All Frontiers journals are driven by researchers for researchers; therefore, they constitute a service to the scholarly community. At the same time, the Frontiers Journal Series operates on a revolutionary invention, the tiered publishing system, initially addressing specific communities of scholars, and gradually climbing up to broader public understanding, thus serving the interests of the lay society, too.

Dedication to Quality

Each Frontiers article is a landmark of the highest quality, thanks to genuinely collaborative interactions between authors and review editors, who include some of the world's best academicians. Research must be certified by peers before entering a stream of knowledge that may eventually reach the public - and shape society; therefore, Frontiers only applies the most rigorous and unbiased reviews.
Frontiers revolutionizes research publishing by freely delivering the most outstanding research, evaluated with no bias from both the academic and social point of view. By applying the most advanced information technologies, Frontiers is catapulting scholarly publishing into a new generation.

What are Frontiers Research Topics?

Frontiers Research Topics are very popular trademarks of the Frontiers Journals Series: they are collections of at least ten articles, all centered on a particular subject. With their unique mix of varied contributions from Original Research to Review Articles, Frontiers Research Topics unify the most influential researchers, the latest key findings and historical advances in a hot research area! Find out more on how to host your own Frontiers Research Topic or contribute to one as an author by contacting the Frontiers Editorial Office: frontiersin.org/about/contact

COMMONALITIES AND DIFFERENCES IN VESTIBULAR AND AUDITORY PATHWAYS

Topic Editors:
Soroush G. Sadeghi, University at Buffalo, United States
Gwenaelle S. G. Geleoc, Boston Children's Hospital, Harvard Medical School, United States

Citation: Sadeghi, S. G., Geleoc, G. S. G., eds. (2022). Commonalities and Differences in Vestibular and Auditory Pathways. Lausanne: Frontiers Media SA. doi: 10.3389/978-2-88974-920-1

Table of Contents

frontiers in Neuroscience

EDITORIAL
published: 23 March 2022
doi: 10.3389/fnins.2022.876798

Editorial: Commonalities and Differences in Vestibular and Auditory Pathways

Soroush G. Sadeghi[1]* *and Gwenaëlle S. G. Géléoc*[2]*

[1] Center for Hearing and Deafness, Department of Communicative Disorders and Science, University at Buffalo, Buffalo, NY, United States, [2] Boston Children's Hospital and Harvard Medical School, Boston, MA, United States

Keywords: vestibular, auditory, hair cells, afferent innervation, efferent innervation, ototoxicity, planar polarity

Editorial on the Research Topic

Commonalities and Differences in Vestibular and Auditory Pathways

At the core of the inner ear sensory organs are hair cells capable of detecting nanometer-scale motion induced by movement of the endolymph, either by sound or head movement. Hair cells convert mechanical input into electro-chemical signals (Corey and Hudspeth, 1979) which are transmitted to and interpreted by the central nervous system. While the auditory and vestibular sensory organs in the inner ear have a common evolutionary origin and share many features, the two systems also have many differences that specializes them for appropriate coding of different sensory modalities. For example, transmembrane channel-like Tmc1 and Tmc2 are expressed in auditory and vestibular hair cells of the inner ear where they form the pore of the mechanotransduction channel (Kawashima et al., 2011; Pan et al., 2013). While Tmc2 is only transiently expressed in the developing cochlea, its expression persists in vestibular hair cells (Kawashima et al., 2011). This Research Topic highlights some of the recent advances in the auditory and vestibular fields, with both original research and review articles. One of the aims was also to provide a comparison between vestibular and auditory systems through these articles. Below is a brief review of the topics addressed by articles in this collection.

PLANAR POLARITY OF VESTIBULAR AND AUDITORY HAIR CELLS

One of the key properties, common to both cochlea and labyrinth is the organization or the planar polarity of hair cells. Deans reviews our current understanding of the developmental mechanisms underlying the generation of planar polarity in the inner ear and its functional significance for effective stimulation of hair cells by sound or motion. Tarchini discusses the similarities between mechanisms that provide orientation of hair cells in the maculae of the otolith organs and the cochlea during development. Finally, Simon et al. show the functional importance of this organization by measuring the vestibulo-ocular response in a mouse model (Celsr1 KO mice) with disorganized hair cell polarity in all vestibular end organs. They show a decrease in the gain of the vestibulo-ocular reflex (VOR) in response to stimulation of either canals or otoliths.

VESTIBULAR AND AUDITORY HAIR CELLS

Typically, depolarization of hair cells results in opening of voltage sensitive calcium channels ($Ca_V1.3$) and entrance of calcium into the cell, which then activates calcium-sensitive mechanisms of vesicular release of glutamate from the hair cell onto afferent terminals. There is also a non-quantal method of synaptic transmission present in the vestibular periphery, between type

OPEN ACCESS

Edited and reviewed by:
Rufin VanRullen,
Centre National de la Recherche Scientifique (CNRS), France

***Correspondence:**
Soroush G. Sadeghi
soroushs@buffalo.edu
Gwenaëlle S. G. Géléoc
gwenaelle.geleoc@childrens.harvard.edu

Specialty section:
This article was submitted to Perception Science, a section of the journal Frontiers in Neuroscience

Received: *15 February 2022*
Accepted: *24 February 2022*
Published: *23 March 2022*

Citation:
Sadeghi SG and Géléoc GSG (2022) Editorial: Commonalities and Differences in Vestibular and Auditory Pathways. Front. Neurosci. 16:876798. doi: 10.3389/fnins.2022.876798

I hair cells and their calyx terminals, which is due to accumulation of potassium ions and glutamate (Contini et al., 2012, 2017, 2020; Songer and Eatock, 2013; Sadeghi et al., 2014). This is in contrast to fast and large multivesicular quantal synaptic transmission between inner hair cells and afferent terminals in the cochlea (Keen and Hudspeth, 2006; Grant et al., 2010, 2011; Rutherford et al., 2012; Huang and Moser, 2018; Niwa et al., 2021). Interestingly, loss of $Ca_V1.3$ in a KO mouse model results in deafness, but no clear signs of imbalance. Using patch clamp recording from hair cells in these mice, Manca et al. show that the calcium current is about 20% of the normal value in both cochlear inner hair cells and type I and II vestibular hair cells. This suggests an abnormal vesicular transmission. However, the hair cells show a normal development of potassium channels, resulting in accumulation of potassium between type I hair cells and their calyx afferent terminals with hair cell depolarization. While these mice most likely have compensatory changes in their central vestibular pathways, the results of this study also suggest a role for the non-quantal transmission in the vestibular periphery in the lack of apparent imbalance in these mice.

VESTIBULAR AND AUDITORY AFFERENTS

Vestibular afferents have specific innervation patterns in the periphery and those with irregular resting discharges innervate the central regions of the cristae and maculae where more type I hair cells and calyx terminals are present (Goldberg et al., 1984, 1990; Baird et al., 1988; Fernandez et al., 1988, 1995; Desai et al., 2005a,b). In the mammalian vestibular periphery, calyx terminals specifically express calretinin as their calcium binding protein (Desmadryl and Dechesne, 1992; Dechesne et al., 1994; Lysakowski et al., 2011). Reichenberger et al. show that in frogs, which as anamniotes lack calyx terminals and type I hair cells, calretinin is expressed only in the ganglion cells that innervate hair cells in the auditory end organ and not in the vestibular end organ. The authors discuss the functional significance of these findings in relation to requirements for encoding different sensory modalities (i.e., movement vs. acoustic stimulation). Kalluri reports that even though auditory and vestibular afferents serve different functions, they are similar in the range of resting potentials, voltage thresholds, current thresholds, input resistances, and first-spike latencies in mice.

VESTIBULAR AND AUDITORY EFFERENT INNERVATION

Efferent inputs are required for normal function of the vestibular (Hubner et al., 2015; Raghu et al., 2019) and auditory pathways (Glowatzki and Fuchs, 2000; Maison et al., 2006; Johnson et al., 2013) and play a role in aging (Lauer et al., 2012; Zachary and Fuchs, 2015; Fuchs and Lauer, 2019; Boero et al., 2020; Vicencio-Jimenez et al., 2021). In this collection, Lorincz et al. provide a detailed map of central and peripheral projections of cholinergic vestibular efferent neurons in mice, using state of the art methods, including transgenic mice and Cre-dependent adeno-associated virus mediated expression of fluorescent reporters. Their results show a rich dendritic arborization toward the vestibular nuclei (suggesting that they receive their inputs mainly from these nuclei) and a dominant contralateral vestibular efferent innervation in this mammalian model. In another article, Lee et al. compare the effectiveness of intratympanic, intracochlear, and systemic application of different cholinergic agonists and antagonists and their effect on the resting discharge of afferents. In another article in this collection, using patch clamp recordings Meredith and Rennie study the role of dopamine, another candidate efferent neurotransmitter in both the auditory and vestibular periphery. They show that activation of D2 dopaminergic receptors decreases the amplitude of Na^+ currents in calyx terminals, with possible inhibitory effects on afferent firing. This is in contrast to the excitatory effects of activation of cholinergic (Poppi et al., 2020; Ramakrishna et al., 2021; Schneider et al., 2021) and GABA-B (Ramakrishna and Sadeghi, 2020) receptors in the calyx. Finally, a review article by Cullen and Wei provides a comparative summary of our current knowledge about vestibular efferents across different animal models, sensory/motor signals carried by efferents, and their possible function compared to auditory efferents.

DEVELOPMENT AND AGING OF THE INNER EAR

On the topic of developmental changes, Quinn et al. study the expression of Na^+ channels in the developing hair cells of the human fetal inner ear neuroepithelia. They show that the number of vestibular and auditory hair cells that express these channels decreases with age and while both TTX-sensitive and TTX-insensitive/resistant currents are present in developing hair cells, there is a differential role for TTX-sensitive Nav1.6 (SCN8A) channels in the vestibular neuroepithelium compared to Nav1.7 (SCN9A) in the cochlea. Rabbitt and Holman study another part of the peripheral circuitry, the supporting cells and show a calcium signal that can be modulated by purinergic or cholinergic inputs. This signal can play a role in the development/maturation of the vestibular end organs and pathways, similar to what has been proposed in the cochlea (Glowatzki and Fuchs, 2000).

Two articles address aging in the inner ear. Paplou et al. review and compare what we know about age-related hearing and vestibular loss. This review provides similarities and differences in the prevalence of age-related changes in the two systems, possible common underlying mechanisms (such as inflammation, oxidative stress, and genetic factors), and changes at the cellular level in the peripheral sensory organs of the two systems. Andresen et al. provide further information regarding age-related changes in expression of melanin pigmentation in the vestibular and auditory periphery in mouse and human samples. With increasing age, they find an increase in pigmentation in the stria vascularis, but little change in the vestibular end organ. Whether this change in pigmentation plays any protective role remains to be studied.

STIMULATION BY VIBRATION VS. SOUND

The vestibular system has traditionally been tested with slow sinusoidal rotations. More recent clinical tests (e.g., vestibular

evoked myogenic potentials or VEMPs) use higher frequency bone vibrations or sound for stimulating the vestibular end organs. Previous studies have shown that afferents, particularly irregular ones that innervate the otoliths or canals can be stimulated by vibration or sound (Zhu et al., 2011, 2014; Curthoys et al., 2014, 2019). In this collection, Curthoys et al. use a mix of data and modeling approaches to provide a broad overview of VEMP tests and their neural pathways, the mechanics of otolith high frequency responses or its "seismometer mode," and the phase locking of afferents during such fast movements. Finally, they compare these high frequency otolith responses to those of the auditory periphery. Chen et al. explore the response to sound at the level of the vestibular nuclei (VN), abducens, and eye movements in rats. They show that the stimulation results in activity in VN neurons that receive inputs from canals and/or otoliths. Interestingly, while the stimulation results in the activity of less than half of the recorded abducens neurons, it results in eye movements with horizontal and vertical components.

CISPLATIN OTOTOXICITY

Prayuenyong et al. review the evidence that shows cisplatin, a chemotoxic drug used for treating different cancers differentially affects the cochlea and has little effect on the labyrinth. This is evidenced by loss of hair cells in the cochlea (particularly the outer hair cells), but almost no effect on vestibular hair cells. Consistent with this pattern of peripheral damage, while a proportion of patients complain about hearing loss and tinnitus there is little evidence for any abnormal vestibular tests. The authors propose different hypotheses for this selective effect, including easier transfer through the stria vascularis into the cochlear endolymph, higher endocochlear potential that might help drive the drug into auditory hair cells, and higher concentrations of the drug in the cochlear perilymph.

CONCLUSION

Taken together, the collection of studies in this Research Topic addresses the similarities and differences between the auditory and vestibular systems at different levels. Review articles provide a summary of the current state and new research articles add to this knowledge. Hopefully, this Research Topic will motivate researchers to consider the similarities of two systems, as it brings about the potential to uncover basic mechanisms that may be conserved in evolution. On the other hand, the articles also emphasize the differences between the two systems, which shows the mechanisms developed to optimize them for their specific functions. Some of the articles also highlight the interaction between basic science findings and their clinical applications, holding promise for identifying novel testing paradigms or therapeutic approaches in the inner ear, with more targeted effects and fewer side effects.

AUTHOR CONTRIBUTIONS

Both authors contributed to this editorial and approved the submitted version.

FUNDING

SS received funding from Capita Foundation.

ACKNOWLEDGMENTS

We wish to thank the authors, reviewers, and technical staff for their invaluable contributions to this Research Topic.

REFERENCES

Baird, R. A., Desmadryl, G., Fernandez, C., and Goldberg, J. M. (1988). The vestibular nerve of the chinchilla. II. Relation between afferent response properties and peripheral innervation patterns in the semicircular canals. *J. Neurophysiol.* 60, 182–203. doi: 10.1152/jn.1988.60.1.182

Boero, L. E., Castagna, V. C., Terreros, G., Moglie, M. J., Silva, S., Maass, J. C., et al. (2020). Preventing presbycusis in mice with enhanced medial olivocochlear feedback. *Proc. Natl. Acad. Sci. U.S.A.* 117, 11811–11819. doi: 10.1073/pnas.2000760117

Contini, D., Holstein, G. R., and Art, J. J. (2020). Synaptic cleft microenvironment influences potassium permeation and synaptic transmission in hair cells surrounded by calyx afferents in the turtle. *J. Physiol.* 598, 853–889. doi: 10.1113/JP278680

Contini, D., Price, S. D., and Art, J. J. (2017). Accumulation of K(+) in the synaptic cleft modulates activity by influencing both vestibular hair cell and calyx afferent in the turtle. *J. Physiol.* 595, 777–803. doi: 10.1113/JP273060

Contini, D., Zampini, V., Tavazzani, E., Magistretti, J., Russo, G., Prigioni, I., et al. (2012). Intercellular K(+) accumulation depolarizes Type I vestibular hair cells and their associated afferent nerve calyx. *Neuroscience* 227, 232–246. doi: 10.1016/j.neuroscience.2012.09.051

Corey, D. P., and Hudspeth, A. J. (1979). Ionic basis of the receptor potential in a vertebrate hair cell. *Nature* 281, 675–677. doi: 10.1038/281675a0

Curthoys, I. S., Burgess, A. M., and Goonetilleke, S. C. (2019). Phase-locking of irregular guinea pig primary vestibular afferents to high frequency (>250Hz) sound and vibration. *Hear. Res.* 373, 59–70. doi: 10.1016/j.heares.2018.12.009

Curthoys, I. S., Vulovic, V., Burgess, A. M., Manzari, L., Sokolic, L., Pogson, J., et al. (2014). Neural basis of new clinical vestibular tests: otolithic neural responses to sound and vibration. *Clin. Exp. Pharmacol. Physiol.* 41, 371–380. doi: 10.1111/1440-1681.12222

Dechesne, C. J., Rabejac, D., and Desmadryl, G. (1994). Development of calretinin immunoreactivity in the mouse inner ear. *J. Comp. Neurol.* 346, 517–529. doi: 10.1002/cne.903460405

Desai, S. S., Ali, H., and Lysakowski, A. (2005a). Comparative morphology of rodent vestibular periphery. II. Cristae ampullares. *J. Neurophysiol.* 93, 267–280. doi: 10.1152/jn.00747.2003

Desai, S. S., Zeh, C., and Lysakowski, A. (2005b). Comparative morphology of rodent vestibular periphery. I. Saccular and utricular maculae. *J. Neurophysiol.* 93, 251–266. doi: 10.1152/jn.00746.2003

Desmadryl, G., and Dechesne, C. J. (1992). Calretinin immunoreactivity in chinchilla and guinea pig vestibular end organs characterizes the calyx unit subpopulation. *Exp. Brain Res.* 89, 105–108. doi: 10.1007/BF00229006

Fernandez, C., Baird, R. A., and Goldberg, J. M. (1988). The vestibular nerve of the chinchilla. I. Peripheral innervation patterns in the horizontal and superior semicircular canals. *J. Neurophysiol.* 60, 167–181. doi: 10.1152/jn.1988.60.1.167

Fernandez, C., Lysakowski, A., and Goldberg, J. M. (1995). Hair-cell counts and afferent innervation patterns in the cristae ampullares of the squirrel

monkey with a comparison to the chinchilla. *J. Neurophysiol.* 73, 1253–1269. doi: 10.1152/jn.1995.73.3.1253

Fuchs, P. A., and Lauer, A. M. (2019). Efferent inhibition of the cochlea. *Cold Spring Harb. Perspect. Med.* 9:a033530. doi: 10.1101/cshperspect.a033530

Glowatzki, E., and Fuchs, P. A. (2000). Cholinergic synaptic inhibition of inner hair cells in the neonatal mammalian cochlea. *Science* 288, 2366–2368. doi: 10.1126/science.288.5475.2366

Goldberg, J. M., Desmadryl, G., Baird, R. A., and Fernandez, C. (1990). The vestibular nerve of the chinchilla. V. Relation between afferent discharge properties and peripheral innervation patterns in the utricular macula. *J. Neurophysiol.* 63, 791–804. doi: 10.1152/jn.1990.63.4.791

Goldberg, J. M., Smith, C. E., and Fernandez, C. (1984). Relation between discharge regularity and responses to externally applied galvanic currents in vestibular nerve afferents of the squirrel monkey. *J. Neurophysiol.* 51, 1236–1256. doi: 10.1152/jn.1984.51.6.1236

Grant, L., Yi, E., and Glowatzki, E. (2010). Two modes of release shape the postsynaptic response at the inner hair cell ribbon synapse. *J. Neurosci.* 30, 4210–4220. doi: 10.1523/JNEUROSCI.4439-09.2010

Grant, L., Yi, E., Goutman, J. D., and Glowatzki, E. (2011). Postsynaptic recordings at afferent dendrites contacting cochlear inner hair cells: monitoring multivesicular release at a ribbon synapse. *J. Vis. Exp.* 48, 2442. doi: 10.3791/2442

Huang, C. H., and Moser, T. (2018). Ca(2+) Regulates the kinetics of synaptic vesicle fusion at the afferent inner hair cell synapse. *Front. Cell. Neurosci.* 12:364. doi: 10.3389/fncel.2018.00364

Hubner, P. P., Khan, S. I., and Migliaccio, A. A. (2015). The mammalian efferent vestibular system plays a crucial role in the high-frequency response and short-term adaptation of the vestibuloocular reflex. *J. Neurophysiol.* 114, 3154–3165. doi: 10.1152/jn.00307.2015

Johnson, S. L., Wedemeyer, C., Vetter, D. E., Adachi, R., Holley, M. C., Elgoyhen, A. B., et al. (2013). Cholinergic efferent synaptic transmission regulates the maturation of auditory hair cell ribbon synapses. *Open Biol.* 3:130163. doi: 10.1098/rsob.130163

Kawashima, Y., Geleoc, G. S., Kurima, K., Labay, V., Lelli, A., Asai, Y., et al. (2011). Mechanotransduction in mouse inner ear hair cells requires transmembrane channel-like genes. *J. Clin. Invest.* 121, 4796–4809. doi: 10.1172/JCI 60405

Keen, E. C., and Hudspeth, A. J. (2006). Transfer characteristics of the hair cell's afferent synapse. *Proc. Natl. Acad. Sci. U.S.A.* 103, 5537–5542. doi: 10.1073/pnas.0601103103

Lauer, A. M., Fuchs, P. A., Ryugo, D. K., and Francis, H. W. (2012). Efferent synapses return to inner hair cells in the aging cochlea. *Neurobiol. Aging* 33, 2892–2902. doi: 10.1016/j.neurobiolaging.2012.02.007

Lysakowski, A., Gaboyard-Niay, S., Calin-Jageman, I., Chatlani, S., Price, S. D., and Eatock, R. A. (2011). Molecular microdomains in a sensory terminal, the vestibular calyx ending. *J. Neurosci.* 31, 10101–10114. doi: 10.1523/JNEUROSCI.0521-11.2011

Maison, S. F., Rosahl, T. W., Homanics, G. E., and Liberman, M. C. (2006). Functional role of GABAergic innervation of the cochlea: phenotypic analysis of mice lacking GABA(A) receptor subunits alpha 1, alpha 2, alpha 5, alpha 6, beta 2, beta 3, or delta. *J. Neurosci.* 26, 10315–10326. doi: 10.1523/JNEUROSCI.2395-06.2006

Niwa, M., Young, E. D., Glowatzki, E., and Ricci, A. J. (2021). Functional subgroups of cochlear inner hair cell ribbon synapses differently modulate their EPSC properties in response to stimulation. *J. Neurophysiol.* 125, 2461–2479. doi: 10.1152/jn.00452.2020

Pan, B., Geleoc, G. S., Asai, Y., Horwitz, G. C., Kurima, K., Ishikawa, K., et al. (2013). TMC1 and TMC2 are components of the mechanotransduction channel in hair cells of the mammalian inner ear. *Neuron* 79, 504–515. doi: 10.1016/j.neuron.2013.06.019

Poppi, L. A., Holt, J. C., Lim, R., and Brichta, A. M. (2020). A review of efferent cholinergic synaptic transmission in the vestibular periphery and its functional implications. *J. Neurophysiol.* 123, 608–629. doi: 10.1152/jn.00053.2019

Raghu, V., Salvi, R., and Sadeghi, S. G. (2019). Efferent inputs are required for normal function of vestibular nerve afferents. *J. Neurosci.* 39, 6922–6935. doi: 10.1523/JNEUROSCI.0237-19.2019

Ramakrishna, Y., Manca, M., Glowatzki, E., and Sadeghi, S. G. (2021). Cholinergic modulation of membrane properties of calyx terminals in the vestibular periphery. *Neuroscience* 452, 98–110. doi: 10.1016/j.neuroscience.2020.10.035

Ramakrishna, Y., and Sadeghi, S. G. (2020). Activation of GABAB receptors results in excitatory modulation of calyx terminals in rat semicircular canal cristae. *J. Neurophysiol.* 124, 962–972. doi: 10.1152/jn.00243.2020

Rutherford, M. A., Chapochnikov, N. M., and Moser, T. (2012). Spike encoding of neurotransmitter release timing by spiral ganglion neurons of the cochlea. *J. Neurosci.* 32, 4773–4789. doi: 10.1523/JNEUROSCI.4511-11.2012

Sadeghi, S. G., Pyott, S. J., Yu, Z., and Glowatzki, E. (2014). Glutamatergic signaling at the vestibular hair cell calyx synapse. *J. Neurosci.* 34, 14536–14550. doi: 10.1523/JNEUROSCI.0369-13.2014

Schneider, G. T., Lee, C., Sinha, A. K., Jordan, P. M., and Holt, J. C. (2021). The mammalian efferent vestibular system utilizes cholinergic mechanisms to excite primary vestibular afferents. *Sci. Rep.* 11:1231. doi: 10.1038/s41598-020-80367-1

Songer, J. E., and Eatock, R. A. (2013). Tuning and timing in mammalian type I hair cells and calyceal synapses. *J. Neurosci.* 33, 3706–3724. doi: 10.1523/JNEUROSCI.4067-12.2013

Vicencio-Jimenez, S., Weinberg, M. M., Bucci-Mansilla, G., and Lauer, A. M. (2021). Olivocochlear changes associated with aging predominantly affect the medial olivocochlear system. *Front. Neurosci.* 15:704805. doi: 10.3389/fnins.2021.704805

Zachary, S. P., and Fuchs, P. A. (2015). Re-emergent inhibition of cochlear inner hair cells in a mouse model of hearing loss. *J. Neurosci.* 35, 9701–9706. doi: 10.1523/JNEUROSCI.0879-15.2015

Zhu, H., Tang, X., Wei, W., Maklad, A., Mustain, W., Rabbitt, R., et al. (2014). Input-output functions of vestibular afferent responses to air-conducted clicks in rats. *J. Assoc. Res. Otolaryngol.* 15, 73–86. doi: 10.1007/s10162-013-0428-6

Zhu, H., Tang, X., Wei, W., Mustain, W., Xu, Y., and Zhou, W. (2011). Click-evoked responses in vestibular afferents in rats. *J. Neurophysiol.* 106, 754–763. doi: 10.1152/jn.00003.2011

Conflict of Interest: The authors declare that the research was conducted in the absence of any commercial or financial relationships that could be construed as a potential conflict of interest.

Publisher's Note: All claims expressed in this article are solely those of the authors and do not necessarily represent those of their affiliated organizations, or those of the publisher, the editors and the reviewers. Any product that may be evaluated in this article, or claim that may be made by its manufacturer, is not guaranteed or endorsed by the publisher.

frontiers in Neuroscience

ORIGINAL RESEARCH
published: 14 May 2021
doi: 10.3389/fnins.2021.680994

Comparison of Age-Related Pigmentary Changes in the Auditory and Vestibular Systems Within Mouse and Human Temporal Bones

Nicholas S. Andresen[1], Sarah Coreas[1], Dillan F. Villavisanis[2] and Amanda M. Lauer[1,3]*

[1] Department of Otolaryngology – Head & Neck Surgery, Johns Hopkins University School of Medicine, Baltimore, MD, United States, [2] Icahn School of Medicine at Mount Sinai, New York, NY, United States, [3] Department of Neuroscience, Johns Hopkins University School of Medicine, Baltimore, MD, United States

Background: Melanin pigmentation is present within the auditory and vestibular systems of the mammalian inner ear and may play a role in maintaining auditory and vestibular function. Melanocytes within the stria vascularis (SV) are necessary for the generation of the endocochlear potential (EP) and decreased EP has been linked to age-related hearing loss. Melanocytes and pigment-containing "dark cells" are present within the vestibular system, but have a less well-defined role. African–American individuals have increased pigmentation within the SV and vestibular system, which is hypothesized to be related to lower rates of age-related hearing loss and vestibular dysfunction. It remains unclear if increased pigmentation confers lifelong protection against hearing loss and vestibular dysfunction.

Methods: Mouse temporal bones were collected from juvenile (3–4 week) and aged (20–32 months) CBA/CaJ mice. Pediatric and adult human temporal bones from Caucasian or African–American individuals were examined from the Johns Hopkins Temporal Bone Collection. Information regarding Fitzpatrick skin type were unavailable, and self-identified race/ethnicity was used as a proxy. Images were taken using light microscopy at 20× magnification. ImageJ software (v1.53) was used to measure pigment within the SV and vestibular system.

Results: In mouse temporal bones pigmentation within the SV increased with age, but pigmentation within the vestibular system did not increase with age. In human temporal bones pigmentation within the SV increased with age and pigmentation within the vestibular system increased within the wall of the utricle, but not other regions of the vestibular system. African–American individuals had higher amounts of pigment within the SV and vestibular system, among both pediatric and adult populations.

Conclusion: Stria vascularis pigmentation increases with age in mouse and human temporal bones. Pigmentation within the vestibular system did not increase with age in mouse specimens and only increased within the utricular wall with age in human specimens. Individuals who identified as African–American had higher pigment

OPEN ACCESS

Edited by:
Soroush G. Sadeghi, University at Buffalo, United States

Reviewed by:
Sarath Vijayakumar, Creighton University, United States
Nicolas Pilon, Université du Québec à Montréal, Canada

****Correspondence:***
Nicholas S. Andresen
nandres1@jhmi.edu

Specialty section:
This article was submitted to Perception Science, a section of the journal Frontiers in Neuroscience

Received: *15 March 2021*
Accepted: *22 April 2021*
Published: *14 May 2021*

Citation:
Andresen NS, Coreas S, Villavisanis DF and Lauer AM (2021) Comparison of Age-Related Pigmentary Changes in the Auditory and Vestibular Systems Within Mouse and Human Temporal Bones. Front. Neurosci. 15:680994. doi: 10.3389/fnins.2021.680994

content within the SV and vestibular system, both as children and as adults. These results highlight how similar age-related pigmentary changes occur in the auditory and vestibular systems across species and underscore the importance of racial/ethnic diversity in human temporal bone studies.

Keywords: melanin, pigmentation, cochlea, vestibular, auditory, age-related hearing loss

INTRODUCTION

Pigmentation is present within the auditory and vestibular systems of the mammalian ear. Alfonso Corti first noted the presence of inner ear pigmentation in 1851 (Corti, 1851), however, since this time little has been learned about its function. Pigmentary disorders are associated with inner ear dysfunction (Lezirovitz et al., 2006; Léger et al., 2012; Milunsky, 2017). In humans Waardenburg syndrome and Tietz syndrome cause congenital deafness and hypopigmentation of the hair, eyes, and skin (Milunsky, 2017). Pigmentary disorders have similarly been associated with congenital deafness in dogs and cats (Strain, 2004, 2017). Conversely, differential levels of pigmentation have been hypothesized to alter susceptibility to noise-induced hearing loss and presbycusis (Bunch and Raiford, 1930; Ardiç et al., 1998; Ishii and Talbott, 1998; Murillo-Cuesta et al., 2010; Lin et al., 2011, 2012; Sun et al., 2014), and potentially vestibular dysfunction (Erbele et al., 2016).

Within the cochlea, the primary pigment melanin is produced by intermediate cells (ICs) within the stria vascularis (SV). ICs are melanocyte-like, neural crest progenitor cells that are necessary for the development of the SV, production of endolymph, and development of the endocochlear potential (EP) (Steel and Barkway, 1989; Kim et al., 2013). Precise toxigenic ablation of ICs results in deafness (Kim et al., 2013). In albino mice, the absence of strial melanin is associated with increased age-related EP decline and hearing loss (Ohlemiller et al., 2009). Increased cochlear pigmentation has been observed in African–American individuals (Sun et al., 2014), which correlates with lower risk of noise-induced hearing loss and presbycusis observed in population based studies (Ishii and Talbott, 1998; Lin et al., 2012). Interestingly, in a mouse model of age-related hearing loss, pigment within the SV was observed to increase with age (Kobrina et al., 2020). Similar qualitative observations have been reported in other species (Takahashi, 1971; Keithley et al., 1992; Ohlemiller et al., 2006), raising the question of whether differences in cochlear pigmentation are simply differential responses to the aging process or whether pigmentation has a protective effect.

Less is known regarding the role of melanin in the vestibular system. Previous studies have identified melanocytes within the dark cell areas of the vestibular system (Kimura, 1969; Masuda et al., 1994, 1995). Specifically, melanin has been found with increased concentration in the utricle, dark cell region around the ampullae of the semicircular canals, and the endolymphatic duct (ED) (Kimura, 1969). Temporal bone studies have found that African–American individuals have increased pigment within the vestibular system (Erbele et al., 2016).

Few studies have quantitatively compared pigmentation within the auditory and vestibular systems of the same individuals or analyzed how pigmentation changes throughout adulthood in the mammalian inner ear. The goal of this study was to compare pigmentation within the auditory and vestibular system of mouse and human temporal bones.

MATERIALS AND METHODS

Human Temporal Bone Subjects and Imaging

Human temporal bones were obtained from the Johns Hopkins Human Temporal Bone Collection (Nager Collection). These temporal bones were collected between the years of 1940 and 1988 and contain both pediatric and adult specimens. Demographic data consisting of age, sex, and race were available for all individuals. Specimens from adults that had available audiometric data were selected for analysis. The adult temporal bones studied were the same as those used in previous studies from our institution (Sun et al., 2014; Erbele et al., 2016). The pediatric temporal bones analyzed were from the same collection. Human temporal bone specimens were prepared using standard methods that have been described elsewhere (Crowe et al., 1934). In brief, fresh specimens were fixed in formalin, decalcified in nitric acid, dehydrated in alcohol baths, and then embedded in celloidin. The specimens were sectioned in 24 μM slices in the sagittal (vertical) plane and every 10th section was mounted on a glass slide and stained with hematoxylin and eosin (H&E).

Seventy-one human temporal bones were identified for analysis, of which 25 were from pediatric patients (mean age: 3.3 years; range 0–12 years) and 46 were from adult patients (mean age: 68 years; range 38–94 years). Thirteen of the pediatric temporal bones and 16 of the adult temporal bones were from females, respectively. Fourteen of the pediatric temporal bones were from Caucasian individuals and 11 were from African–American individuals. Twenty-seven of the adult temporal bones were from Caucasian individuals and 19 were from African–American individuals. The demographics of the human temporal bone cohort are described in **Table 1**.

Mid-modiolar images of the SV were then taken at 20× magnification using a digital camera mounted on a microscope with image acquisition software (Jenoptik ProgResCF). The vestibular system was imaged at 10× magnification at the following locations: the ED as it enters the vestibule prior to the endolymphatic sinus, the posterior semicircular canal (PSCC) as the posterior ampullary nerve enters, the ampulla of the

TABLE 1 | Description of demographic data for human temporal bone specimens.

Age, years (range)	
Pediatric	3.3 (0–12)
Adult	68 (38–94)
Gender, female (%)	
Pediatric	13 (52)
Adult	16 (35)
Race, *n* (%)	
Adult	46 (65)
Caucasian	27 (38)
African–American	19 (26)
Pediatric	25 (35)
Caucasian	14 (20)
African–American	11 (15)

superior semicircular canal (SSCC) with portions of the superior vestibular nerve, and the utricular wall (**Figure 1**).

Mouse Temporal Bone Subjects and Imaging

CBA/CaJ mice were used to analyze age-related changes in pigmentation within the auditory and vestibular systems in a mouse strain that exhibits cochlear aging at a similar rate to humans when compared across the lifespan (Sergeyenko et al., 2013). Breeding pairs were originally obtained from the Jackson Laboratory and were bred in a quiet vivarium. Mice were housed individually or in groups with unrestricted access to food and water and kept on a 12:12 h day/night cycle. Some of these animals underwent auditory response brainstem (ABR) testing that has been described elsewhere (Kobrina et al., 2020). Temporal bones were harvested from mice at 3–4 weeks and 20–32 months of age. All procedures were approved by the Johns Hopkins University Animal Care and use Committee and complied with the ARRIVE guidelines and the associated NIH Guide for Care and Use of Laboratory Animals. In order to harvest temporal bones, animals were deeply anesthesized with a 0.3–0.5 mg/g intraperitoneal dose of pentobarbital, transcardially perfused with 60 mL of 4% paraformaldehyde fixative solution, and decapitated. The cochleas were reperfused with 4% paraformaldehyde through the oval and round windows, and then allowed to postfix overnight. Cochleas were then disarticulated from the skull and decalcified in 1% ethylenediaminetetraacetic acid (EDTA) for at least 1 week until spongy. Cochleas were dehydrated and embedded in Araldite and sectioned into 30 μM sections parallel to the modiolus with a rotary microtome following methods described by Schrode et al. (2018). The sections were mounted on subbed slides, stained with toluidine blue, and a coverslip was applied.

Nine juvenile (3–4 week) and 12 adult (20–32 months) CBA mice were identified for analysis. Six (66%) of the juvenile and eight (66%) of the aged mice were female. Five of the aged CBA mice were subjected to a 2 h 100 dB SPL octave band (8–16 kHz) noise exposure 3–4 months prior to tissue harvest. We included these specimens because recent work has suggested that much of the age-related degeneration reported in human temporal bone specimens is due to a history of noise exposure (Wu et al., 2020). Mouse models offer us the opportunity to look for potential additive effects of noise exposure on age-related inner ear pigmentation in a cohort of mice with otherwise similar life histories and genetic backgrounds.

Images of the SV were then taken at 20× magnification using a digital microscope mounted on a microscope with image acquisition software (Jenoptik ProgResCF). Images of the vestibular system were collected at 10× magnification in the same locations as for human temporal bones.

Image Analysis

Images were analyzed using ImageJ (Bethesda, MD, United States). The cross-sectional area of the SV was determined by manually out-lining the border of the SV and using ImageJ. The area of the SV was measured in square micrometers after calibration with a scale bar. Pigmentation in the SV was measured using color thresholding (**Figure 2**), by a blinded observer, to measure the area (μM^2) of SV containing pigment. The percentage of the SV containing pigment was then calculated for each image. The pigment content of the vestibular end organs was measured by a blind observer using

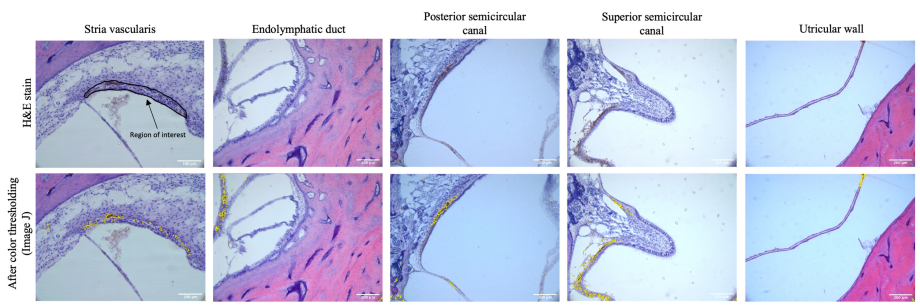

FIGURE 1 | The top row shows representative images of the stria vascularis, endolymphatic duct, posterior semicircular canal, superior semicircular canal, and utricular wall in human temporal bones taken at 10× magnification using light microscopy. The stria vascularis is outlined (region of interest) in the top left panel. For the vestibular system the entire image as pictured above was used as the region of interest to measure pigment content. The bottom rows shows the images after color thresholding on ImageJ with the pigmented areas shaded in yellow.

color thresholding to select the area (μM^2) containing pigment, which was then quantified as the area containing pigment per high power field (HPF).

Statistics

Statistical analysis was performed using Stata 16 (College Station, Texas). Between group means were compared using a student's *t*-test with a two-tailed *p*-value and a Bonferroni correction. The *p*-value for significance was set to 0.025 (0.05/2) when two comparisons were made (mouse vestibular system), 0.0125 (0.05/4) when four comparisons were made (mouse cochlea and human vestibular system), and 0.01 (0.01/5) when five comparisons were made (human cochlea). Within group tonotopic differences in SV pigmentation were tested with a one-way ANOVA test. Multivariable liner regression was performed to assess the effect of gender, age, and race on the pigment content with the SV of human temporal bones. For the human temporal bones, a comparison of the pigment content of the SV and audiometric thresholds has been performed previously and described elsewhere (Sun et al., 2014).

RESULTS

Age-Related Effects on Pigmentation Within the SV

Compared to pediatric human temporal bones, the adult temporal bones had increased pigmentation within the SV of the lower middle turn ($p = 0.008$, $t = 2.745$, 95% CI = 1.06–6.32%), upper middle turn ($p = 0.0013$, $t = 3.36$, 95% CI = 1.54–5.84%), and apex ($p = 0.012$, $t = 2.57$, 95% CI = 1.11–8.23%). The comparison of SV pigmentation in pediatric and adult human temporal bones is shown in **Figure 3A**. Among the mouse temporal bone specimens, there was increased pigmentation within the SV of aged mice, compared to juvenile mice, at the hook ($p < 0.00001$, $t = 7.66$, 95% CI = 7.39–12.67%), mid-basal

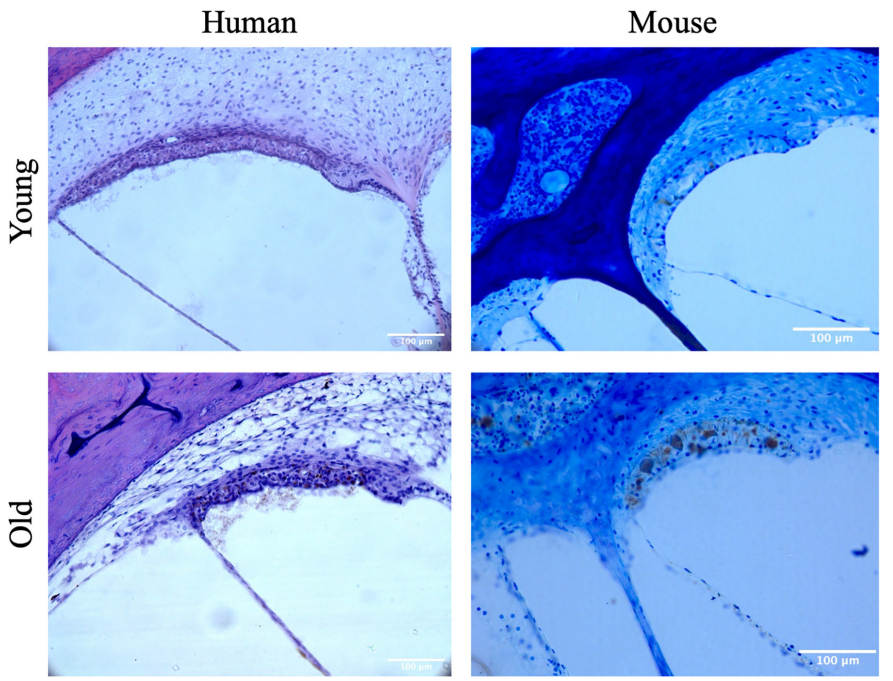

FIGURE 2 | Representative images of the stria vascularis from young and aged mice and humans.

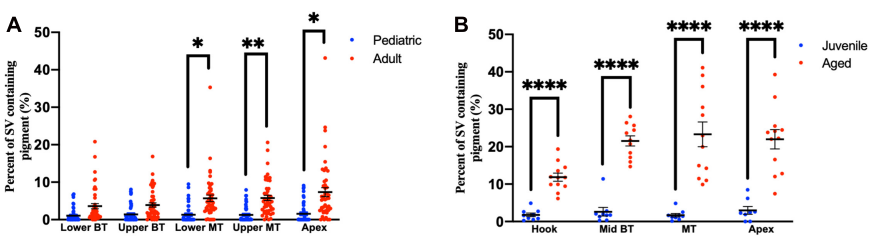

FIGURE 3 | Percentage of the stria vascularis containing pigment within human **(A)** and mouse **(B)** temporal bones. Error bars indicate standard error. Stria vascularis, SV; BT, basal turn; MT, middle turn. *Adjusted *p*-value < 0.05, **adjusted *p*-value < 0.01, and ****adjusted *p*-value < 0.0001.

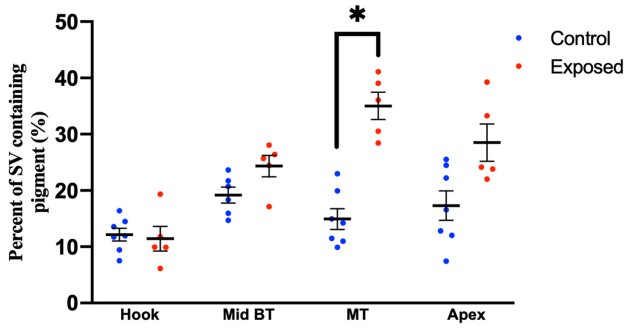

FIGURE 4 | Percentage of the stria vascularis containing pigment within adult (20–32 month) mouse temporal bone specimens with or without noise exposure. Error bars indicate standard error. *Adjusted p-value < 0.05.

turn ($p < 0.00001$, $t = 10.50$, 95% CI = 15.31–22.51%), middle turn ($p < 0.00001$, $t = 9.45$, 95% CI = 17.05–26.21%), and apex ($p < 0.00001$, $t = 6.10$, 95% CI = 12.77–25.21%). The results for SV pigmentation in juvenile and aged mice are shown in **Figure 3B**. Aged mice subjected to noise exposure had increased pigment within the SV of the middle turn ($p = 0.00005$, $t = 7.74$, 95% CI = 17.14–23.12%), but not the hook ($p = 0.89$, $t = 0.14$, 95% CI = −4.21 to 4.84%), mid-basal turn ($p = 0.04$, $t = 2.35$, 95% CI = 0.76–9.64%), or apex ($p = 0.02$, $t = 11.20$, 95% CI = 2.83–19.57%) compared to aged mice without noise exposure. The results for noise exposure are shown in **Figure 4**. One-way ANOVA test showed tonotopic differences in SV pigmentation in adult human ($p = 0.005$; $F = 3.82$) and aged mouse ($p = 0.0002$; $F = 8.37$) temporal bones, but not pediatric human ($p = 0.81$; $F = 0.39$) or juvenile mouse ($p = 0.62$; $F = 0.60$) temporal bones.

Age-Related Effects on Pigmentation Within the Vestibular System

Adult human temporal bones had increased pigmentation within the utricular wall ($p = 0.008$, $t = 2.73$, 95% CI = 145–940 μM^2/HPF), but not the ED ($p = 0.12$, $t = 1.56$, 95% CI = −229 to 1,851 μM^2/HPF), superior semicircular canal (SSCC) ($p = 0.018$, $t = 2.42$, 95% CI = 386–4,052 μM^2/HPF), or PSCC ($p = 0.09$, $t = 1.71$, 95% CI = −233 to 2,987 μM^2/HPF), compared to pediatric temporal bones. The results for the pigmentation of the human vestibular system are shown in **Figure 5A**. Aged mice did not have increased pigmentation of the superior semicircular canal (SSCC) ($p = 0.65$, $t = 0.48$, 95% CI = −737 to 1,199 μM^2/HPF) or utricular wall (UW) ($p = 0.23$, $t = 1.30$, 95% CI = 146–686 μM^2/HPF). The results for the analysis of the mouse vestibular system are shown in **Figure 5B**.

Ethnicity and Inner Ear Pigmentation

Among adult human temporal bone specimens from African–American individuals, there was increased pigmentation of the SV at the lower basal turn ($p = 0.0004$, $t = 3.84$, 95% CI = 2.19–6.96%), upper basal turn ($p = 0.003$, $t = 3.14$, 95% CI = 1.18–5.32%), lower middle turn ($p = 0.016$, $t = 2.50$, 95% CI = 0.84–7.37%), and upper middle turn ($p = 0.005$, $t = 2.97$, 95% CI = 1.32–6.46%) compared to Caucasian adults. Among pediatric human temporal bone specimens from African–American individuals, there was increased pigmentation of the SV at the lower basal turn ($p = 0.005$, $t = 3.10$, 95% CI = 0.84–3.72%), upper basal turn ($p = 0.0008$, $t = 3.83$, 95% CI = 1.59–4.95%), lower middle turn ($p = 0.0003$, $t = 4.22$, 95% CI = 2.00–5.45%), upper middle turn ($p = 0.0005$, $t = 4.04$, 95% CI = 1.59–4.61%) and apex ($p = 0.0001$, $t = 4.57$, 95%

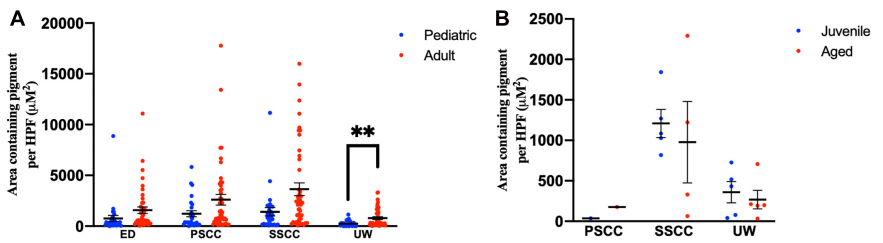

FIGURE 5 | Pigmentation within the vestibular system in human **(A)** and mouse **(B)** temporal bones. Error bars indicate standard error. ED, endolymphatic duct; PSCC, posterior semicircular canal; SCCC, superior semicircular canal; UW, utricle wall. **Adjusted p-value < 0.01.

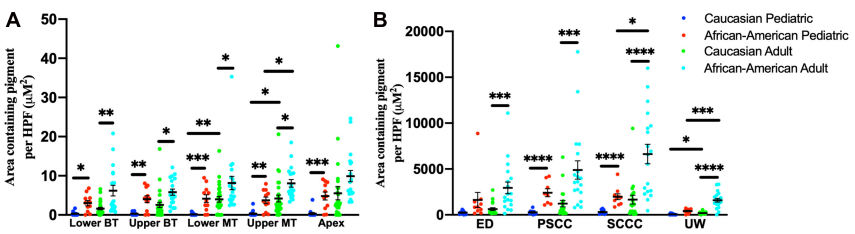

FIGURE 6 | Pigmentation within the stria vascularis **(A)** and vestibular system **(B)** of human temporal bones, broken down by age and race. Error bars indicate standard error. SV, stria vascularis, BT, basal turn; MT, middle turn; ED, endolymphatic duct; PSCC, posterior semicircular canal; SCCC, superior semicircular canal; UW, utricle wall. *Adjusted p-value < 0.05, **adjusted p-value < 0.01, ***adjusted p-value < 0.001, and ****adjusted p-value < 0.0001.

CI = 2.43–6.07%) compared to Caucasian individuals. African–American adult specimens had increased pigmentation within the SV of the upper middle turn (p = 0.004, t = 3.12, 95% CI = 1.63–7.07%), but not the lower basal turn (p = 0.10, t = 1.72, 95% CI = −0.45–6.84%), upper basal turn (p = 0.15, t = 1.47, 95% CI = −0.58 to 4.16%), lower middle turn (p = 0.10, t = 1.69, 95% CI = −0.65 to 8.61), or apex (p = 0.019, t = 2.49, 95% CI = 1.07–9.11%) compared to African–American pediatric specimens. Caucasian adult specimens had increased pigmentation within the SV of the lower middle turn (p = 0.0006, t = 3.72, 95% CI = 1.69–5.45%) and upper middle turn (p = 0.004, t = 3.06, 95% CI = 1.29–5.83%), but not the lower basal turn (p = 0.09, t = 1.71, 95% CI = −0.12 to 1.92%), upper basal turn (p = 0.06, t = 1.94, 95% CI = −0.01 to 3.63%), or apex (p = 0.029, t = 2.26, 95% CI = 0.66–9.28%) compared to Caucasian pediatric specimens. The results for pigmentation of the SV by age and race are shown in **Figure 6A**.

For temporal bone specimens from African–American adults there was increased pigmentation of the endolymphatic duct (ED) (p = 0.00009, t = 4.29, 95% CI = 1,257–3,369 μM^2/HPF), PSCC (p = 0.00008, t = 4.34, 95% CI = 2,122 to 5,622 μM^2/HPF), superior semicircular canal (SSCC) ($p < 0.00001$, t = 5.27, 95% CI = 3,255–7,109 μM^2/HPF), and utricular wall (UW) ($p < 0.00001$, t = 7.42, 95% CI = 979–1,681 μM^2/HPF) compared to Caucasian adults. Among pediatric temporal bones, there was increased pigmentation within the PSCC ($p < 0.00001$, t = 6.38, 95% CI = 1,482–2,798 μM^2/HPF), superior semicircular canal (SSCC) ($p < 0.00001$, t = 6.03, 95% CI = 1,130–2,220 μM^2/HPF) and utricular wall (UW) (p = 0.00004, t = 5.04, 95% CI = 209–475 μM^2/HPF) of African–American individuals compared to Caucasian individuals. African–American adult specimens had increased pigmentation within the superior semicircular canal (SSCC) (p = 0.0026, t = 3.30, 95% CI = 1,897–7,428 μM^2/HPF) and utricular wall (UW) (p = 0.0002, t = 4.30, 95% CI = 643–1,721 μM^2/HPF), but not the endolymphatic duct (ED) (p = 0.20, t = 1.30, 95% CI = −663 to 2,332 μM^2/HPF) or PSCC (p = 0.08, t = 1.84, 95% CI = −168 to 5,132 μM^2/HPF) compared to African–American pediatric specimens. Caucasian adult specimens had increased pigmentation within the utricular wall (UW) (p = 0.006, t = 2.87, 95% CI = 62–326 μM^2/HPF), but not the endolymphatic duct (ED) (p = 0.017, t = 2.49, 95% CI = 94–780 μM^2/HPF), PSCC (p = 0.05, t = 1.99, 95% CI = 14–1,487 μM^2/HPF), or superior semicircular canal (SSCC) (p = 0.03, t = 2.87, 95% CI = 140–2,170-μM^2/HPF) compared to Caucasian pediatric specimens. Measurements for pigmentation of the vestibular system by age and race are shown in **Figure 6B**.

Multivariable linear regression analysis for the total pigment content within the SV of human temporal bones showed that increased age ($p < 0.001$, t = 4.93, 95% CI = 0.03–0.07%) and African–American race ($p < 0.001$, t = 6.06, 95% CI = 2.78–5.51%) were associated with increased pigmentation, but pigmentation was not influenced by gender (p = 0.28, t = 1.10, 95% CI = −0.6 to 2.13%).

DISCUSSION

The present study found that pigmentation increases with age in the SV of the mammalian inner ear, but does not clearly increase with age in the vestibular system. Specifically, pigmentation within the SV of human temporal bones increased from childhood to adulthood, and these changes correlated with similar findings in a mouse model of age-related hearing loss. Amongst the mouse temporal bones noise exposure resulted in increased pigmentation with the SV of the middle turn, but not other regions of the cochlea. It was not possible to control for noise exposure amongst the human temporal bones and it is possible that some of the increased pigmentation seen with age is related to noise exposure. Pigmentation within the vestibular system increased with age in the utricular wall of human temporal bones, but this relationship was unclear in other regions of the vestibular system and did not hold true in mouse temporal bones. Skin color was also found to correlate with inner ear pigmentation in human temporal bones, both in childhood and adulthood. This association between skin color and inner ear pigmentation has previously been described (Sun et al., 2014; Erbele et al., 2016), but this study is the first to describe differences in inner ear pigmentation during childhood and the increase in pigmentation observed with age.

Pigment has long been proposed to play an important role in the function of the inner ear. In 1965 Bonaccorsi hypothesized that eye color may predict inner ear pigmentation and provide protection against noise-induced hearing loss (Bonaccorsi, 1965). However, current evidence suggests that the relationship between eye color and cochlear pigmentation is unclear (Mujica-Mota et al., 2015). Inner ear pigmentation has been hypothesized to protect against oxidative injury and maintaining calcium homeostasis by acting as a metal ion chelator (Bush and Simon, 2007; Laurell et al., 2007; Murillo-Cuesta et al., 2010; Fetoni et al., 2019). Cochlear pigmentation appears to be protective against radiation-induced sensorineural hearing loss (Mujica-Mota et al., 2015). Previous studies have reported cochlear pigmentation to be increased in African–American individuals (Sun et al., 2014) and decreased rates of hearing loss in African–American individuals on population based studies. The similar changes observed within the SV in both humans and mouse model highlight the potentially important role of pigmentation within the inner ear. Pigmentary defects are known to cause hearing loss in both humans (Lezirovitz et al., 2006; Léger et al., 2012) and animal models (Keithley et al., 1992; Ohlemiller et al., 2009), and the similar changes observed within the SV across mammalian models highlights that pigment may play a fundamental and important role in the cochlea.

Whether pigment plays a protective role against noise- or age-related hearing loss remains unclear. While individuals with darker skin have a lower incidence of hearing loss (Ishii and Talbott, 1998; Lin et al., 2012) the actual function of melanin within the SV has yet to be elucidated. Increased pigmentation in the SV from African–American pediatric temporal bones suggests that melanin is present at a young age and thus could be present to play a protective role against age-related degeneration or accrual of noise-induced hearing loss over the course of a lifetime. However, lipofuscin is also known to increase with age, and some of the increased pigmentation observed, particularly within the mouse model, may be the result of lipofuscin accumulation. The fact that pigment increases with age

and is often concurrent with presbycusis raises the possibility that pigmentation is simply a metabolic by-product that may not serve a protective role.

The observed age-related changes in pigmentation within the SV highlights the need for precise identification of the site of otologic pathology in age-related hearing-loss, which has been a subject of controversy and conflicting reports. Early temporal bone studies identified neural degeneration and outer hair cell (OHC) loss as principal components of presbycusis (Guild et al., 1931; Crowe et al., 1934). A primary role for OHC loss in presbycusis is supported by a more recent human temporal bone study that used statistical modeling and immunolabeling to more precisely measure neural degeneration (Wu et al., 2020). However, other human temporal bone studies have pointed to SV degeneration as a principal mechanism of age-related hearing loss (Schuknecht et al., 1974), and numerous animal studies have implicated the SV in age-related hearing loss (Strain, 2004, 2017; Ohlemiller et al., 2006, 2009). Part of this discrepancy may be explained by the fact that human temporal bone studies are limited to histopathologic correlations and can only measure atrophy of the SV, rather than function. However, further study is warranted given the importance of this question in the development of targeted therapies for presbycusis.

Pigmentary changes within the vestibular system are comparatively less understood. It has been over 50 years since Kimura first provided a detailed description of the distribution of dark cells and subepithelial melanocytes within the vestibular system of animal models and humans (Kimura, 1969). However, little is understood regarding the function of pigment within the vestibular system. Much of this knowledge deficit is likely related to the difficulty of studying vestibular function relative to hearing. Our findings build upon the findings of Erbele et al. (2016) by showing that race was associated with increased pigmentation of the vestibular system in childhood, as well as adulthood, and these pigmentary changes increase with age. There is some evidence that individuals with darker skin may have improved vestibular function (Agrawal et al., 2008; Li et al., 2015), but this association has been questioned when less sensitive measures of vestibular function were used (Agrawal et al., 2009). In the mouse temporal bone specimens we were unable to demonstrate a difference in pigmentation with age, which may have been the result of inadequate sample size or could mean that there is in fact no difference with age. Previous studies have shown that humans and mice have a similar distribution of pigment-containing cells within the vestibular system (Kimura, 1969; LaFerriere et al., 1974). The observed differences in age-related pigmentary changes in the cochlea and vestibular system may be related to the different origins of cochlear and vestibular melanocytes (Bonnamour et al., 2020) or that the lifelong presence of dark cells accounts for a large amount of vestibular pigmentation (Kimura, 1969). Changes in vestibular pigmentation with age, skin pigmentation, or inner-ear insults such as noise exposure are poorly understood. In particular, no data exists describing changes in pigmentation in relation to vestibular function.

This study has several limitations. First, we are limited to the use of race as a surrogate for Fitzpatrick skin type, which is both an indirect and possibly imprecise measure of skin pigmentation. There may also be differences in SV pigmentation in mice related to coat color, which was not addressed in this study due to the use of a single mouse strain. Future studies should further examine strain- and coat-related differences in SV pigmentation (Bartels et al., 2001). Further, the techniques used in this study are not capable of unambiguously differentiating between different types of pigment. Lipofuscin is known to accumulate in cells with age and may have been inadvertently measured as pigment. There are also different types of melanin, eumelanin and pheomelanin, that we were unable to differentiate among in this study. In addition to this, the cross-sectional nature of this study limits the inferences that can be made regarding the actual function of melanin in the inner ear. Future studies are needed that specifically analyze the biologic role of melanin in the aging auditory and vestibular periphery. Comparison of albino and darkly pigmented mice may provide further insight into the role of pigment in inner ear function (Murillo-Cuesta et al., 2010; Gi et al., 2018). The development of *in vivo* pharmacologic techniques to manipulate melanin concentration within the ear may allow us to better understand the role of pigment within the inner ear.

In summary, this study showed that pigmentation within the cochlea increases with age in mouse and human temporal bone specimens. Pigmentation within the vestibular system increased with age in the utricular wall of human temporal bones, but did not increase in other human vestibular end organs and did not increase with age in the mouse vestibular system. Individuals who identified as African–American had higher pigment content within the SV and vestibular epithelia, both as juveniles and as adults. These results highlight how similar age-related pigmentary changes occur in the auditory systems across species. Our findings also underscore the need for representation of participants who reflect the racial/ethnic diversity of the aging population both within temporal bone studies and within studies of inner ear function more broadly.

DATA AVAILABILITY STATEMENT

The raw data supporting the conclusions of this article will be made available by the authors, without undue reservation.

ETHICS STATEMENT

Ethical review and approval was not required for the study on human participants in accordance with the local legislation and institutional requirements. Written informed consent for participation was not required for this study in accordance with the national legislation and the institutional requirements. The animal study was reviewed and approved by the Johns Hopkins University Animal Use and Care Committee.

AUTHOR CONTRIBUTIONS

NA and AL conceptualized the project and drafted the initial manuscript. NA, SC, and DV performed the data collection and

analysis. NA, SC, DV, and AL interpreted the data. All authors contributed to the writing.

FUNDING

This study was supported in part by funding from the NIH grants R01 DC016641 to AL and T32DC000027 to NA; the David M. Rubenstein Fund for Hearing Research to AL; and the Acoustical Society of America James E. West Fellowship to DV.

ACKNOWLEDGMENTS

The authors thank Madison Weinberg and Hamad Javaid for technical assistance and Bryan Ward for comments on an earlier version of this manuscript.

REFERENCES

Agrawal, Y., Carey, J. P., Della Santina, C. C., Schubert, M. C., and Minor, L. B. (2009). Disorders of balance and vestibular function in US adults: data from the National Health and Nutrition Examination Survey, 2001-2004. *Arch. Intern. Med.* 169, 938–944. doi: 10.1001/archinternmed.2009.66

Agrawal, Y., Platz, E. A., and Niparko, J. K. (2008). Prevalence of hearing loss and differences by demographic characteristics among US adults: data from the National Health and Nutrition Examination Survey, 1999-2004. *Arch. Intern. Med.* 168, 1522–1530. doi: 10.1001/archinte.168.14.1522

Ardiç, F. N., Aktan, S., Kara, C. O., and Sanli, B. (1998). High-frequency hearing and reflex latency in patients with pigment disorder. *Am. J. Otolaryngol.* 19, 365–369. doi: 10.1016/s0196-0709(98)90038-2

Bartels, S., Ito, S., Trune, D. R., and Nuttall, A. L. (2001). Noise-induced hearing loss: the effect of melanin in the stria vascularis. *Hear. Res.* 154, 116–123. doi: 10.1016/s0378-5955(01)00213-1

Bonaccorsi, P. (1965). [The color of the iris as a "test" in the quantitative estimation, in man, of the melanin concentration in the stria vascularis]. *Ann. Laringol. Otol. Rinol. Faringol.* 64, 725–738.

Bonnamour, G., Soret, R., and Pilon, N. (2020). *Dhh*—expressing Schwann cell precursors contribute to skin and cochlear melanocytes, but not to vestibular melanocytes. *Pigment Cell Melanoma Res.* 34, 648–654. doi: 10.1111/pcmr.12938

Bunch, C. C., and Raiford, T. S. (1930). Race and sex variations in auditory acuity. *Arch. Otolaryngol.* 18, 425–434.

Bush, W. D., and Simon, J. D. (2007). Quantification of Ca(2+) binding to melanin supports the hypothesis that melanosomes serve a functional role in regulating calcium homeostasis. *Pigment Cell Res.* 20, 134–139. doi: 10.1111/j.1600-0749.2007.00362.x

Corti, A. (1851). Research on the organ of hearing in mammals. *Z. Wiss Zool.* 3, 109–169.

Crowe, S., Guild, S., and Polvogt, L. (1934). Observations on the pathology of high-tone deafness. *Bull. Johns Hopkins Hosp.* 54, 315–379.

Erbele, I. D., Lin, F. R., Agrawal, Y., Francis, H. W., Carey, J. P., and Chien, W. W. (2016). Racial differences of pigmentation in the human vestibular organs. *Otolaryngol. Head Neck Surg.* 155, 479–484. doi: 10.1177/0194599816645764

Fetoni, A. R., Paciello, F., Rolesi, R., Paludetti, G., and Troiani, D. (2019). Targeting dysregulation of redox homeostasis in noise-induced hearing loss: oxidative stress and ROS signaling. *Free Radic. Biol. Med.* 135, 46–59. doi: 10.1016/j.freeradbiomed.2019.02.022

Gi, M., Shim, D. B., Wu, L., Bok, J., Song, M. H., and Choi, J. Y. (2018). Progressive hearing loss in vitamin A-deficient mice which may be protected by the activation of cochlear melanocyte. *Sci. Rep.* 8:16415. doi: 10.1038/s41598-018-34653-8

Guild, S. R., Crowe, S. J., Bunch, C. C., and Polvogt, L. M. (1931). Correlations of differences in the density of innervation of the organ of Corti with differences in the acuity of hearing, including evidence as to the location in the human cochlea of the receptors for certain tones. *Acta Oto Laryngol.* 15, 269–308. doi: 10.3109/00016483109119096

Ishii, E. K., and Talbott, E. O. (1998). Race/ethnicity differences in the prevalence of noise-induced hearing loss in a group of metal fabricating workers. *J. Occup. Environ. Med.* 40, 661–666. doi: 10.1097/00043764-199808000-00001

Keithley, E. M., Ryan, A. F., and Feldman, M. L. (1992). Cochlear degeneration in aged rats of four strains. *Hear Res.* 59, 171–178. doi: 10.1016/0378-5955(92)90113-2

Kim, H. J., Gratton, M. A., Lee, J. H., Perez Flores, M. C., Wang, W., Doyle, K. J., et al. (2013). Precise toxigenic ablation of intermediate cells abolishes the "battery" of the cochlear duct. *J. Neurosci.* 33, 14601–14606. doi: 10.1523/JNEUROSCI.2147-13.2013

Kimura, R. S. (1969). Distribution, structure, and function of dark cells in the vestibular labyrinth. *Ann. Otol. Rhinol. Laryngol.* 78, 542–561. doi: 10.1177/000348946907800311

Kobrina, A., Schrode, K. M., Screven, L. A., Javaid, H., Weinberg, M. M., Brown, G., et al. (2020). Linking anatomical and physiological markers of auditory system degeneration with behavioral hearing assessments in a mouse (*Mus musculus*) model of age-related hearing loss. *Neurobiol. Aging* 96, 87–103. doi: 10.1016/j.neurobiolaging.2020.08.012

LaFerriere, K. A. I, Arenberg, K., Hawkins, J. E., and Johnsson, L. G. (1974). Melanocytes of the vestibular labyrinth and their relationship to the microvasculature. *Ann. Otol. Rhinol. Laryngol.* 83, 685–694. doi: 10.1177/000348947408300518

Laurell, G., Ekborn, A., Viberg, A., and Canlon, B. (2007). Effects of a single high dose of cisplatin on the melanocytes of the stria vascularis in the guinea pig. *Audiol. Neurootol.* 12, 170–178. doi: 10.1159/000099020

Léger, S., Balguerie, X., Goldenberg, A., Drouin-Garraud, V., Cabot, A., Amstutz-Montadert, I., et al. (2012). Novel and recurrent non-truncating mutations of the MITF basic domain: genotypic and phenotypic variations in Waardenburg and Tietz syndromes. *Eur. J. Hum. Genet.* 20, 584–587. doi: 10.1038/ejhg.2011.234

Lezirovitz, K., Nicastro, F. S., Pardono, E., Abreu-Silva, R. S., Batissoco, A. C., Neustein, I., et al. (2006). Is autosomal recessive deafness associated with oculocutaneous albinism a "coincidence syndrome"? *J. Hum. Genet.* 51, 716–720. doi: 10.1007/s10038-006-0003-7

Li, C., Layman, A. J., Carey, J. P., and Agrawal, Y. (2015). Epidemiology of vestibular evoked myogenic potentials: data from the baltimore longitudinal study of aging. *Clin. Neurophysiol.* 126, 2207–2215. doi: 10.1016/j.clinph.2015.01.008

Lin, F. R., Maas, P., Chien, W., Carey, J. P., Ferrucci, L., and Thorpe, R. (2012). Association of skin color, race/ethnicity, and hearing loss among adults in the USA. *J. Assoc. Res. Otolaryngol.* 13, 109–117. doi: 10.1007/s10162-011-0298-8

Lin, F. R., Thorpe, R., Gordon-Salant, S., and Ferrucci, L. (2011). Hearing loss prevalence and risk factors among older adults in the United States. *J. Gerontol. A Biol. Sci. Med. Sci.* 66, 582–590. doi: 10.1093/gerona/glr002

Masuda, M., Yamazaki, K., Kanzaki, J., and Hosoda, Y. (1994). Ultrastructure of melanocytes in the dark cell area of human vestibular organs: functional implications of gap junctions, isolated cilia, and annulate lamellae. *Anat. Rec.* 240, 481–491. doi: 10.1002/ar.1092400406

Masuda, M., Yamazaki, K., Matsunaga, T., Kanzaki, J., and Hosoda, Y. (1995). Melanocytes in the dark cell area of human vestibular organs. *Acta Otolaryngol. Suppl.* 519, 152–157. doi: 10.3109/00016489509121892

Milunsky, J. (2017). *Waardenburg Syndrome*. Danbury, CT: National Organization of Rare Diseases.

Mujica-Mota, M. A., Schermbrucker, J., and Daniel, S. J. (2015). Eye color as a risk factor for acquired sensorineural hearing loss: a review. *Hear Res.* 320, 1–10. doi: 10.1016/j.heares.2014.12.002

Murillo-Cuesta, S., Contreras, J., Zurita, E., Cediel, R., Cantero, M., Varela-Nieto, I., et al. (2010). Melanin precursors prevent premature age-related and noise-induced hearing loss in albino mice. *Pigment Cell Melanoma Res.* 23, 72–83. doi: 10.1111/j.1755-148X.2009.00646.x

Ohlemiller, K. K., Lett, J. M., and Gagnon, P. M. (2006). Cellular correlates of age-related endocochlear potential reduction in a mouse model. *Hear Res.* 220, 10–26. doi: 10.1016/j.heares.2006.06.012

Ohlemiller, K. K., Rice, M. E., Lett, J. M., and Gagnon, P. M. (2009). Absence of strial melanin coincides with age-associated marginal cell loss and endocochlear potential decline. *Hear Res.* 249, 1–14. doi: 10.1016/j.heares.2008.12.005

Schrode, K. M., Muniak, M. A., Kim, Y. H., and Lauer, A. M. (2018). Central compensation in auditory brainstem after damaging noise exposure. *eNeuro* 5:ENEURO.0250-18.2018. doi: 10.1523/ENEURO.0250-18.2018

Schuknecht, H. F., Watanuki, K., Takahashi, T., Belal, A. A. Jr., Kimura, R. S., Jones, D. D., et al. (1974). Atrophy of the stria vascularis, a common cause for hearing loss. *Laryngoscope* 84, 1777–1821. doi: 10.1288/00005537-197410000-00012

Sergeyenko, Y., Lall, K., Liberman, M. C., and Kujawa, S. G. (2013). Age-related cochlear synaptopathy: an early-onset contributor to auditory functional decline. *J. Neurosci.* 33, 13686–13694. doi: 10.1523/JNEUROSCI.1783-13.2013

Steel, K. P., and Barkway, C. (1989). Another role for melanocytes: their importance for normal stria vascularis development in the mammalian inner ear. *Development* 107, 453–463. doi: 10.1242/dev.107.3.453

Strain, G. M. (2004). Deafness prevalence and pigmentation and gender associations in dog breeds at risk. *Vet. J.* 167, 23–32. doi: 10.1016/s1090-0233(03)00104-7

Strain, G. M. (2017). Hearing disorders in cats. *J. Feline Med. Surg.* 19, 276–287. doi: 10.1177/1098612X17695062

Sun, D. Q., Zhou, X., Lin, F. R., Francis, H. W., Carey, J. P., and Chien, W. W. (2014). Racial difference in cochlear pigmentation is associated with hearing loss risk. *Otol. Neurotol.* 35, 1509–1514. doi: 10.1097/MAO.0000000000000564

Takahashi, T. (1971). The ultrastructure of the pathologic stria vascularis and spiral prominence in man. *Ann. Otol. Rhinol. Laryngol.* 80, 721–735. doi: 10.1177/000348947108000515

Wu, P. Z., O'Malley, J. T., de Gruttola, V., and Liberman, M. C. (2020). Age-related hearing loss is dominated by damage to inner ear sensory cells, not the cellular battery that powers them. *J. Neurosci.* 40, 6357–6366. doi: 10.1523/JNEUROSCI.0937-20.2020

Conflict of Interest: The authors declare that the research was conducted in the absence of any commercial or financial relationships that could be construed as a potential conflict of interest.

frontiers in Neuroscience

REVIEW
published: 23 June 2021
doi: 10.3389/fnins.2021.684800

Differences in the Structure and Function of the Vestibular Efferent System Among Vertebrates

Kathleen E. Cullen[1,2,3,4]* *and Rui-Han Wei*[1]

[1] Department of Biomedical Engineering, Johns Hopkins University, Baltimore, MD, United States, [2] Department of Otolaryngology, Johns Hopkins University School of Medicine, Baltimore, MD, United States, [3] Department of Neuroscience, Johns Hopkins University, Baltimore, MD, United States, [4] Kavli Neuroscience Discovery Institute, Johns Hopkins University, Baltimore, MD, United States

The role of the mammalian vestibular efferent system in everyday life has been a long-standing mystery. In contrast to what has been reported in lower vertebrate classes, the mammalian vestibular efferent system does not appear to relay inputs from other sensory modalities to the vestibular periphery. Furthermore, to date, the available evidence indicates that the mammalian vestibular efferent system does not relay motor-related signals to the vestibular periphery to modulate sensory coding of the voluntary self-motion generated during natural behaviors. Indeed, our recent neurophysiological studies have provided insight into how the peripheral vestibular system transmits head movement-related information to the brain in a context independent manner. The integration of vestibular and extra-vestibular information instead only occurs at next stage of the mammalian vestibular system, at the level of the vestibular nuclei. The question thus arises: what is the physiological role of the vestibular efferent system in mammals? We suggest that the mammalian vestibular efferent system does not play a significant role in short-term modulation of afferent coding, but instead plays a vital role over a longer time course, for example in calibrating and protecting the functional efficacy of vestibular circuits during development and aging in a role analogous the auditory efferent system.

Keywords: vestibular, neural coding, multimodal, visual, somatosensory, efference copy, perception, evolution

OPEN ACCESS

Edited by:
Soroush G. Sadeghi, University at Buffalo, United States

Reviewed by:
Enrique Soto, Meritorious Autonomous University of Puebla, Mexico
Stuart Johnson, The University of Sheffield, United Kingdom

***Correspondence:**
Kathleen E. Cullen
Kathleen.Cullen@jhu.edu

Specialty section:
This article was submitted to Perception Science, a section of the journal Frontiers in Neuroscience

Received: *24 March 2021*
Accepted: *13 May 2021*
Published: *23 June 2021*

Citation:
Cullen KE and Wei R-H (2021) Differences in the Structure and Function of the Vestibular Efferent System Among Vertebrates. Front. Neurosci. 15:684800. doi: 10.3389/fnins.2021.684800

INTRODUCTION

While the function of the mammalian auditory efferent system is well understood, the role of the mammalian vestibular efferent system remains a mystery. Yet the peripheral vestibular system (i.e., the sensory epithelium of the three semicircular canals and two otoliths) receives central projections from the vestibular efferent system in all vertebrate species (Meredith, 1988; Goldberg et al., 2012). Interestingly, there is considerable heterogeneity in the organization and location of the efferent cell bodies across different vertebrate classes (**Figure 1A**). In four of the five classes of vertebrates –fish, amphibians, reptiles, and birds—the efferent neurons that project to the vestibular and auditory periphery are localized in a single cell group. In aquatic vertebrates, efferent neurons within this cell group also innervate lateral line neuromasts. In such vertebrates, a single efferent neuron can innervate the sensory epithelium of both the vestibular and lateral-line systems (larval Xenopus:

Claas et al., 1981; fish: Highstein and Baker, 1986; Meredith and Roberts, 1987). In contrast to the other four vertebrate classes, the organization of the vestibular efferent system is markedly different in mammals as compared. Notably, the cell bodies of efferents innervating the mammalian vestibular and auditory periphery are located in separate nuclei; the vestibular efferent nucleus is commonly referred to as the "group-e," whereas the auditory efferent nucleus is the superior olivary complex.

In this review, we consider differences in both the structure and function of the vestibular efferent system across vertebrate classes. We focus on how the vestibular efferent systems transmit extra-vestibular sensory and motor information to the vestibular periphery in lower vertebrates (i.e., fish and amphibians). We also discuss how this extra-vestibular information influences the responses of vestibular afferents in these aquatic vertebrates. Additionally, we contrast these findings with those of studies in mammals establishing the absence of such efferent-mediated effects. Taken together, this evidence suggests an evolution in the primary role of the vestibular efferent system. We speculate that instead of playing a key role in the short-term modulation of afferent coding as it does in aquatic vertebrates, the function of the mammalian vestibular efferent system is to regulate pathway efficacy during development in a role analogous the auditory efferent system.

The Vestibular Efferent System: Organization and Embryologic Origin

Vestibular, auditory, as well as lateral line efferents are thought to have a common embryologic origin that is shared with facial and branchiomotor motoneurons (Fritzsch, 1996). Accordingly, both vestibular and auditory efferent neurons in some lower vertebrates (e.g., eels and toads) are located within or overlapping the facial nucleus. However, there is considerable heterogeneity in the specific location of vestibular efferent neurons both across vertebrate classes and across different mammalian species. For example, in reptiles and birds the efferent nucleus is distinct from the facial nucleus, and is located more dorsally (**Figure 1A**, *bottom*). While a single nucleus comprises both auditory and vestibular efferents in these vertebrates, the somas of vestibular efferents tend to be located more dorsally (reviewed in Goldberg and Cullen, 2011). In contrast, the cell bodies of the mammalian vestibular efferent system are located in the group-e nucleus, which is distinct from the auditory efferent system. The mammalian group-e nucleus is located even further from the facial nucleus, with the vestibular efferent somas situated dorsal to the genu of the facial nerve and just medial to the VI (abducens) nucleus (**Figure 1A**, *top*). There is likewise heterogeneity in the dendritic morphology of the vestibular efferent system across vertebrate classes. The dendrites of efferent neurons in fish and amphibians span a large portion of the brainstem, whereas the dendrites of group-e neurons in mammals span a far more limited area and are relatively sparse. These striking differences in the anatomy and morphology of the vestibular efferent system likely underlie differences in its functional role across vertebrate classes (detailed further below).

The Vestibular Efferent System in Mammals: A Neural Circuit for the Modulation of Motion Sensing

Across species the mammalian vestibular efferent system comprises only about 300 neurons on each side and sends bilateral projections to the peripheral vestibular system (Goldberg and Fernandez, 1980; Marco et al., 1993). The projections of an individual efferent axon can be profuse, spanning multiple vestibular organs (Purcell and Perachio, 1997), where they target type II vestibular hair cells as well as the afferents innervating both type I and II hair cells (**Figure 1B**, reviewed in Goldberg, 2000). Experiments in monkey, cat, and chinchilla have shown that electrical microstimulation of the mammalian "group-e" nucleus (**Figure 1A**) evokes comparable excitatory responses in the vestibular afferents on both sides (**Figure 1C**; Goldberg and Fernandez, 1980; Marlinski et al., 2004; McCue and Guinan, 1994). However, there are important differences in the magnitude of efferent-activated responses across individual afferents. In particular, the responses evoked in afferents with more "irregular" resting discharges are an order of magnitude greater than those evoked in their regular counterparts (**Figure 1C**).

Importantly, both canal and otolith afferent fibers can be classified based on the regularity of their resting discharge. In general, regular afferents preferentially provide bouton endings to type II hair cells, whereas irregular afferents have larger axons and either transmit information from the type I hair cells located at the center of neuroepithelium or integrate inputs from both type I and II hair cells. The firing rates of regular afferents in turn encode more information about head motion than irregular afferents (Sadeghi et al., 2007). On the other hand, more recent studies (Jamali et al., 2016, 2019) have shown that irregular afferents better discriminate between head motion stimuli through differential patterns of precise (∼6 ms) spike timing than regular afferents. These two parallel streams of sensory input provided by regular and irregular afferents are preserved and further refined in mammalian central vestibular pathways. Notably, regular and irregular afferents preferentially target vestibulo-ocular reflex (VOR) and vestibulo-spinal pathways, respectively (reviewed in Cullen, 2019). Thus, the fact that efferent-activated responses are greater for irregular than regular afferents suggests that the mammalian vestibular efferent system could potentially play a more significant role modulating vestibulo-spinal vs. vestibulo-ocular reflex) pathways.

To date, however, no study has directly recorded the responses of mammalian vestibular efferent neurons. The sparsity of the target population presents a challenge for definitively identifying efferent units. Early experiments in lower vertebrates (fish and amphibians) have established that the vestibular efferent system integrates information across multiple vestibular end organs and from both labyrinths (Gleisner and Henriksson, 1963; Schmidt, 1963; Precht et al., 1971; Blanks and Precht, 1976;

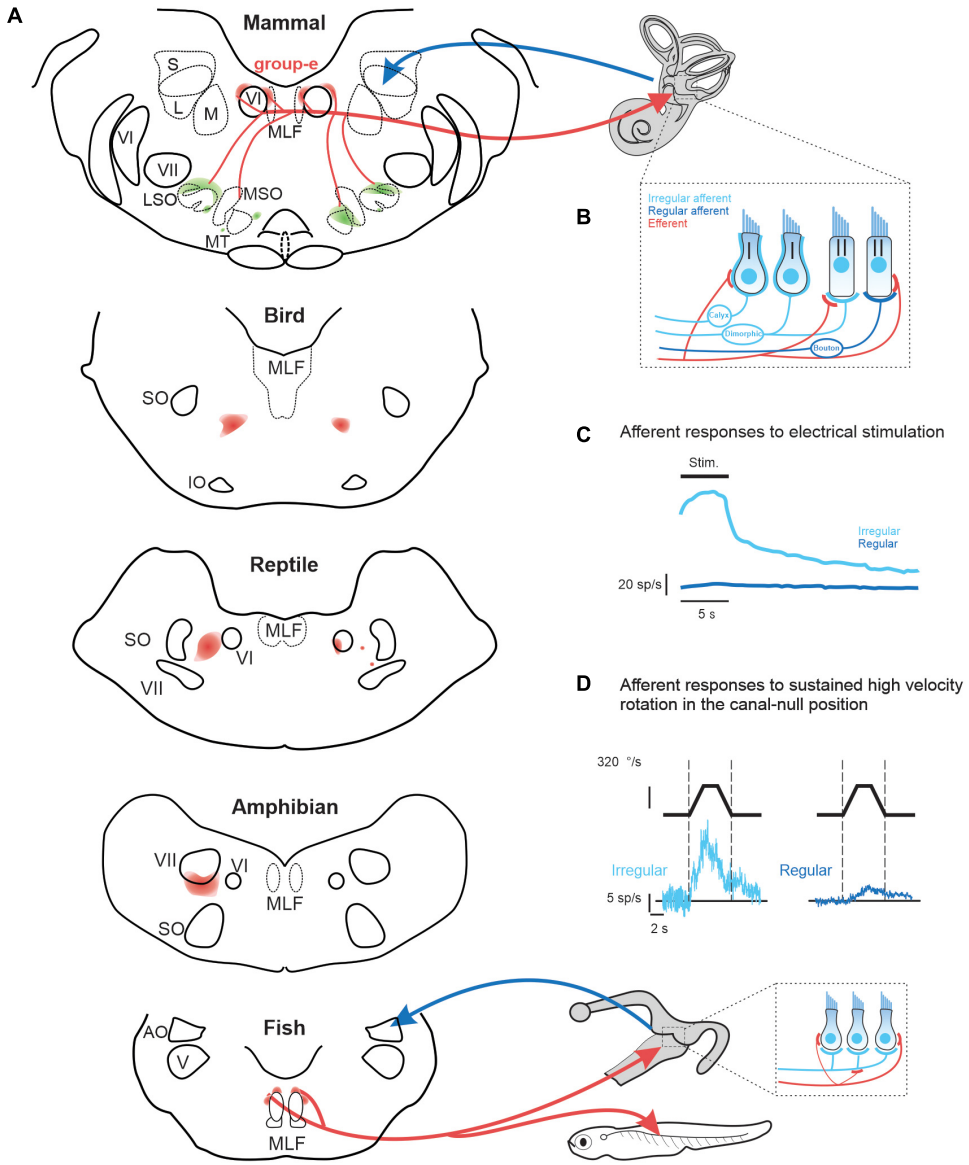

FIGURE 1 | (A) of vestibular efferent (red) and afferent (blue) projections across vertebrates including: mammals (squirrel monkey: Goldberg and Fernandez, 1980), birds (pigeon: Eden and Correia, 1981), reptile (lizard: Barbas-Henry and Lohman, 1988), amphibians (toad: Pellegrini et al., 1985), and fish (toadfish: Highstein and Baker, 1986). **(B)** In mammals, irregular afferents (light blue) typically innervate both type I and II hair cells (i.e., dimorphic afferents), while regular afferent (dark blue) more selectively innervate type II hair cells. Note that the mammalian vestibular efferent system innervates type II hair cells and their afferent bouton endings, as well as the afferent calyces of type I hair cells (Lysakowski and Goldberg, 1997, 2008). In contrast, in lower vertebrates, which do not have hair cells with calyx endings, the vestibular efferent system innervates type II hair cells and, in some species, such as the toadfish (Sans and Highstein, 1984) also their afferent bouton endings [*bottom inset*, **(A)**]. **(C)** Comparison of the population-averaged efferent-mediated responses of irregular vs. regular afferents to electrical microstimulation of central "group-e" neurons (Goldberg and Fernandez, 1980). **(D)** Efferent-mediated population responses of irregular (*left*) vs. regular (*right*) afferents to sustained high amplitude rotation in the canal-null position (Sadeghi et al., 2009). Note, in contrast to their conventional evoked by natural head motion, afferents displayed excitatory responses for stimulation in both directions—termed a type III response. AO, nucleus anterior octavus; LSO, MSO, MT, lateral and medial superior olive and medial nucleus of the trapezoid body; MLF, medial longitudinal fasciculus; IO, inferior olive; S, L, M, superior, lateral and medial superior vestibular nucleus; SO, superior olive; V, trigeminal nucleus; VI, abducens nucleus; VII, facial nucleus.

Hartmann and Klinke, 1980). Vestibular efferents target the vestibular periphery, and do not make synaptic contacts with neurons within the vestibular nuclei (reviewed in Holt et al., 2011). As such the vestibular efferent system can only modulate the afferent input to vestibular nucleus neurons by inducing significant changes in afferent responses (e.g., in contrast to the presynaptic control observed in dorsal root ganglion). Thus, subsequent studies in mammals have provided insight into the responses of vestibular efferent neurons by recording from individual vestibular afferents.

Recordings made from semicircular canal afferents during have high velocity rotations have further demonstrated that the efferent vestibular circuitry is functional in mammals. These studies used a sophisticated experimental design in which the conventional semicircular canal afferent responses to head rotation were first minimized by positioning the head in the null plane for the superior semicircular canal (Plotnik et al., 2002, 2005; Sadeghi et al., 2009). With the head in this null orientation, sustained steps of high constant-velocity rotation ($> 300\ ^{\circ}$/s) were then passively applied. In response, superior semicircular canal afferents displayed excitatory responses for both rotation directions—termed a type III response. The vestibular source of the efferent-mediated responses was then conformed by plugging the horizontal and posterior canals (Sadeghi et al., 2009). Importantly, these type III responses markedly contrast with the characteristic type I responses of afferents evoked by natural head rotations, for which rotations in the opposite directions lead to excitatory vs. inhibitory responses (**Figure 1D**). Furthermore, type III responses evoked in irregular afferents were an order of magnitude greater than those evoked in their regular counterparts (**Figure 1D**). Moreover, this high velocity rotation in the null plane (**Figure 1D**), similar to microsimulation of group-e neurons (**Figure 1D**) evoked responses in irregular afferents with comparable dynamics, which notably included a slow response component with a long time constant of 5–20 s (Goldberg and Fernandez, 1980; Sadeghi et al., 2009). Thus, artificial activation of the vestibular efferent system via both microstimulation and sustained high velocity rotation appears to predominately alter coding in irregular afferents and, in turn, the time course of this activation is relatively long relative to the head movements experienced during natural self-motion (Carriot et al., 2014, 2017).

Synaptic Physiology of the Mammalian Vestibular Efferent System: Implications for Function

Acetylcholine (ACh) is the main neurotransmitter at the vestibular efferent synapses across vertebrate classes (reviewed in Goldberg et al., 2012). Furthermore, pharmacology of the vestibular efferent synapses has additional complexity. First, the neuroactive peptide calcitonin gene-related peptide (CGRP) is widely present in the vestibular efferent neurons of mammals, fish and amphibians (Sewell and Starr, 1991; Highstein, 1992; Eybalin, 1993; Bailey and Sewell, 2000) and is co-expressed by vestibular efferent neurons and peripheral efferent terminals (Ohno et al., 1991; Luebke et al., 2014). Second, additional substances are commonly co-expressed in cholinergic neurons, including, adenosine 5′-triphosphate (ATP), dopamine (DA), GABA, and neuronal nitric oxide synthase (nNOS) have also been reported within vestibular efferent neuron terminals of the vestibular end organs (reviewed in Mathews et al., 2017).

Recent experiments in mammals (Schneider et al., 2021) have shown that muscarinic and nicotinic AChR antagonists block the slow and fast component of the excitatory responses induced in afferents by efferent microstimulation (i.e., **Figure 1C**). Furthermore, because the expression of CGRP accompanies development of the vestibular efferent system, it has been proposed that the vestibular efferent system plays a slow modulatory role in shaping the functional connectivity/efficacy of the peripheral organs during maturation (Holt et al., 2011). Consistent with this idea, CGRP null mice demonstrate a substantial reduction in the efficacy of their vestibulo-ocular refex (Luebke et al., 2014). Interestingly, as noted above, electrical microsimulation of mammalian vestibular efferent neurons generates an increase in vestibular afferent activity (see review, Holt et al., 2011). In contrast, electrical microstimulation of the auditory efferent system suppresses auditory afferent nerve activity. Given that ACh is the primary neurotransmitter released by auditory and vestibular efferent neurons and hyperpolarizes the hair cells in both sensory systems, the difference in excitation vs. inhibition of vestibular vs. auditory afferents initially difficult to reconcile. However, recent studies have established the synaptic mechanisms by which efferent-mediated hyperpolarization vestibular hair cells leads to excitation of vestibular afferent activity in mammals (reviewed in Poppi et al., 2020).

Extra-Vestibular Sensory Integration in the Vestibular Periphery: Strategies Differ Across Vertebrate Classes

The discovery that (i) microstimulation or (ii) sustained high velocity vestibular stimulation alters the responses of vestibular afferents indicates that the vestibular efferent system circuitry remains functional in mammals. This has led to the common view that the efferent neurons may modulate the activity of vestibular afferents in more natural conditions as well. However, it is important to emphasize that electrical and rotational stimuli used in these two experimental approaches are unnatural and thus not actually experienced in everyday life. Indeed, it had proven difficult to find more natural circumstances that lead to large efferent-mediated responses in the mammalian vestibular nerve, even in irregular units. Further, it must be recognized that even the responses sustained high velocity vestibular are small ($\approx$10 spikes/s) compared with those produced by conventional afferent stimulation ($>$200 spikes/s) to the same stimuli (Sadeghi et al., 2007). To date, no study has directly characterized the responses of mammalian vestibular efferent neurons during natural stimulation. Instead, prior experiments have only reported the responses of vestibular efferents in lower vertebrate classes, namely fish and amphibians. Studies in these lower vertebrates have established that individual vestibular efferents respond to extra-vestibular sensory stimulation, thus providing a substrate for the integration of vestibular and extra-vestibular inputs at the level of the vestibular periphery.

In particular, vestibular efferent neurons in fish and amphibians respond to somatosensory inputs produced by passively manipulating the limbs and applying pressure to the skin (goldfish: Hartmann and Klinke, 1980; toadfish: Highstein and Baker, 1985; frog: Schmidt, 1963; salamander: Schmidt, 1965). Additionally, there are reports that vestibular efferents can be driven by a visual or auditory stimulation in these two classes of vertebrate (visual—goldfish: Schmidt et al., 1972;

Hartmann and Klinke, 1980; frog: Caston and Bricout-Berthout, 1982; auditory—toadfish: Highstein and Baker, 1985; frog: Bricout-Berthout and Caston, 1982). The above findings in fish and amphibians raise two fundamental questions. First, how do the vestibular and extra-vestibular sensory signals carried by vestibular efferent neurons modify the responses of the **vestibular afferents** that they target in fish and amphibians? Second, is this strategy conserved across all vertebrate classes—including mammals?

Indeed, with respect to the first question, the observation that activation of the "vestibular system" can produce efferent-mediated responses in **vestibular afferents** appears to be common across vertebrates. However, the sign and magnitude of this effect does vary. For example, a neurophysiological study in birds demonstrated heterogeneity in efferent-mediated afferent responses evoked by stimulation of the horizontal semicircular canal on the contralateral side (Dickman and Correia, 1993). Both excitation and inhibition were observed across individual afferents. In contrast, as reviewed above, stimulation of the vestibular system in mammals always produces excitatory efferent-mediated responses in vestibular afferents. Specifically, high amplitude vestibular stimulation (∼300 deg/s) evoked an increase in afferent firing rate regardless of movement direction in both anesthetized chinchilla and alert rhesus monkey (**Figure 1C**; Plotnik et al., 2002; Sadeghi et al., 2009). However, it is notable that these effects were relatively less marked in alert monkeys.

However, there are marked differences across species regarding the influence of "extra-vestibular" sensory input (i.e., somatosensory, visual, and auditory) on the responses of vestibular afferents. These differences indicate distinct strategies among vertebrates (**Figure 2**). Classic studies in fish (**Figure 2A**) demonstrated that somatosensory stimulation activates individual vestibular afferents (Hartmann and Klinke, 1980; Highstein and Baker, 1985), and that visual stimulation can evoke directionally sensitive responses (Klinke, 1970). Likewise, somatosensory and visual stimulation has also been reported to alter the firing activity of individual vestibular

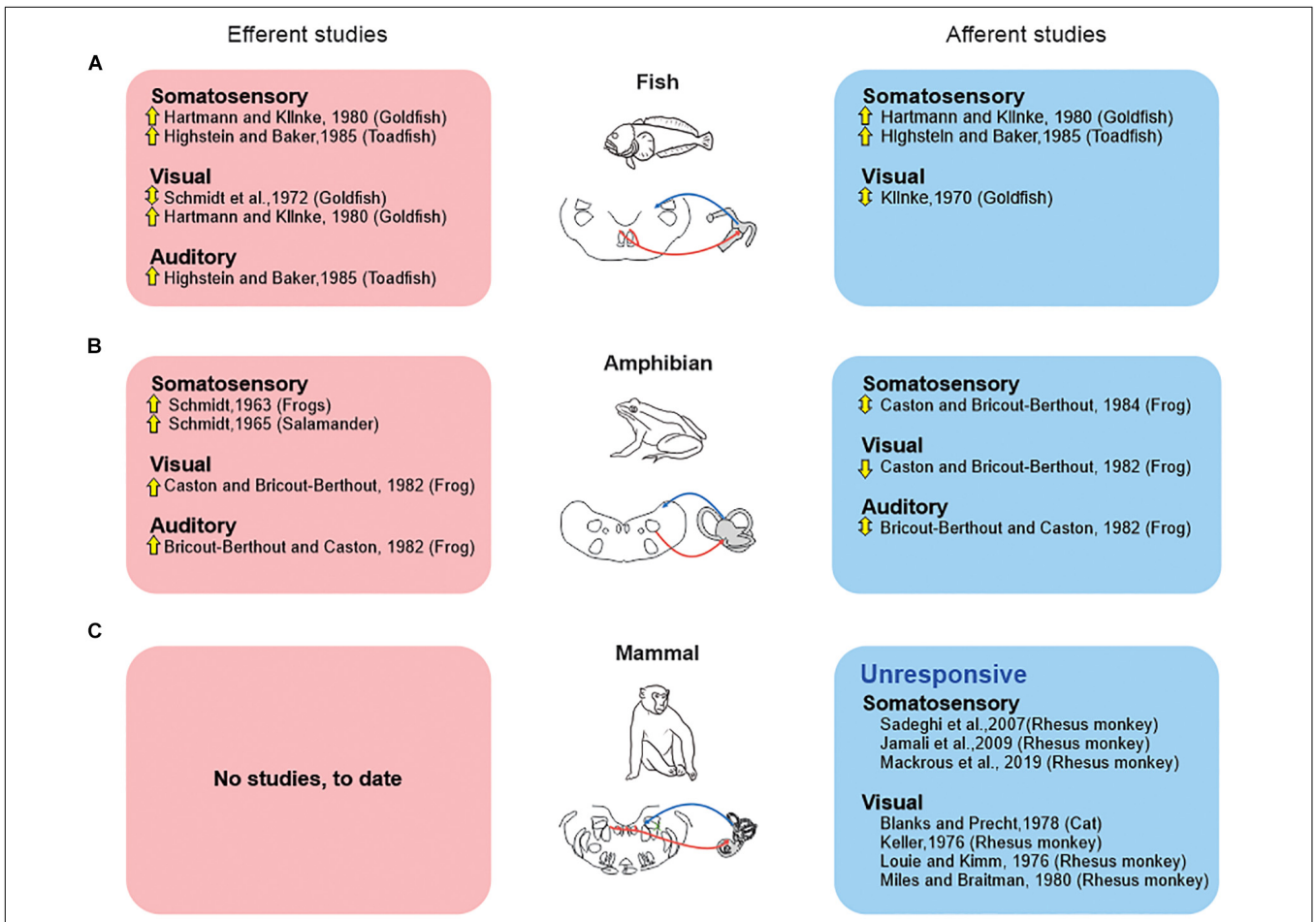

FIGURE 2 | Extra-vestibular sensory systems (somatosensory, visual, auditory) have been reported to alter peripheral vestibular processing in fish and amphibians but not in mammals. Studies that directly recorded from the vestibular efferent pathway (red boxes), vs. those that recorded efferent-mediated effects in vestibular afferents (blue boxes) are shown for studies in fish **(A)**, amphibians **(B)**, and mammals **(C)**. *Symbols*: up arrows: excitation; down arrows: inhibition; up-down arrows: both excitation and inhibition.

afferents in amphibians (**Figure 2B**; frog: Caston and Bricout-Berthout, 1982, 1984, respectively). Yet, in this latter vertebrate class, somatosensory stimulation can both inhibit and excite afferents, and thus contrasts with what is seen in fish. Likewise, auditory stimulation can evoke either excitatory or inhibitory responses in individual afferents in amphibians (**Figure 2B**; Bricout-Berthout and Caston, 1982). Thus, in answer to the first question, it is clear that both the vestibular and extra-vestibular sensory signals carried by vestibular efferent neurons modify the responses of the **vestibular afferents** that they target in fish and amphibians and that this resultant modulation is generally excitatory in fish and excitatory or bidirectional in amphibians (see **Figure 2**).

This then leads to the second question of whether this strategy is conserved across all vertebrate classes—including mammal. The evidence to date indicates that the integration of vestibular and extra-vestibular sensory signals at the level of the vestibular periphery is not a strategy that is conserved across all vertebrate classes—including mammals. Importantly, and in contrast to the above findings in fish and amphibians, experiments in rhesus monkeys (Sadeghi et al., 2007; Jamali et al., 2009; Mackrous et al., 2019) have revealed that afferents are unresponsive to related to somatosensory/proprioceptive signals (**Figure 2C**). Specifically, afferent responses are unresponsive to proprioceptive stimulation alone, and respond identically to passive whole body (i.e., vestibular-only stimulation) and passive

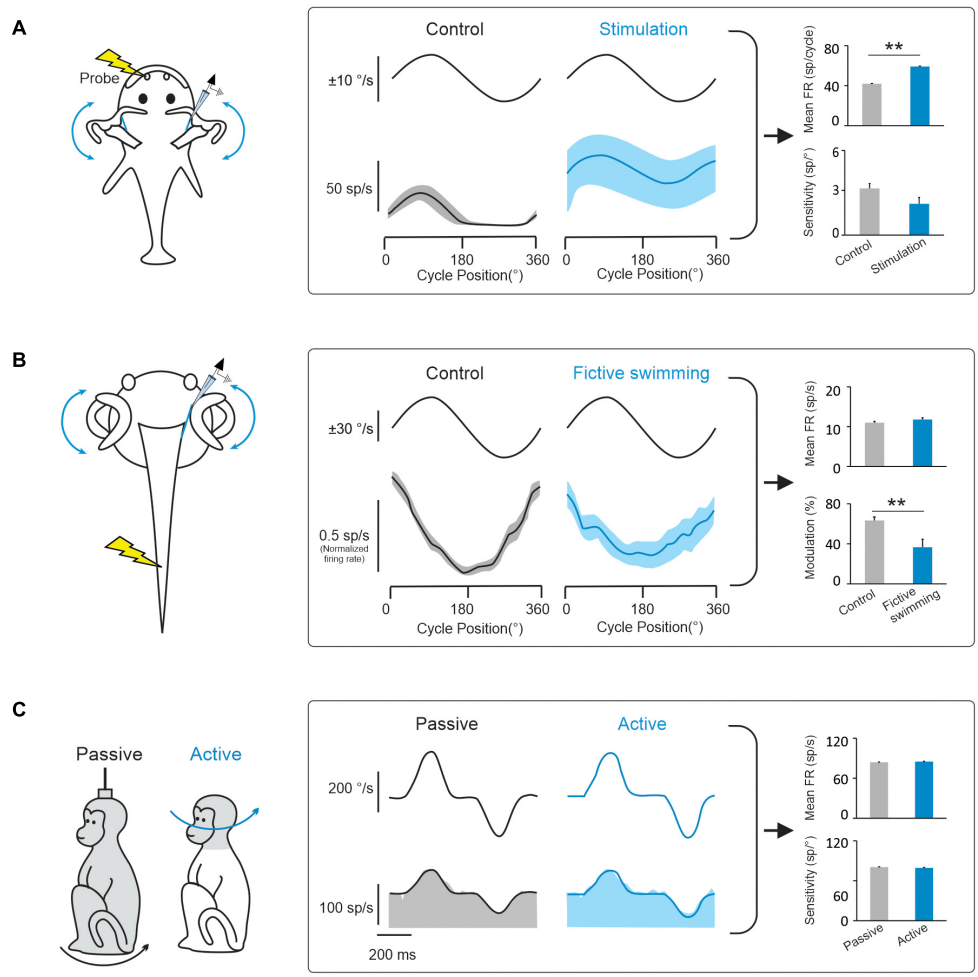

FIGURE 3 | Behaviorally-dependent efferent-mediated responses have been reported in fish and amphibians but not in mammals. **(A)** *Left:* Inducing a behavioral escape response in a head fixed toadfish activates vestibular efferent neurons. *Middle:* Behavioral activation of efferents alters vestibular afferent responses to passive whole-body rotation in the head-restrained fish. *Right:* bar plots comparing effects of electrical efferent stimulation on background and rotation-induced firing of horizontal canal afferents (data replotted from Boyle and Highstein, 1990). **(B)** *Left:* Afferent recordings made in a semi-isolated *in vitro* anaesthetized larval Xenopus preparation, during passive whole-body rotation. Responses to this passive rotation were compared before and during bouts of fictive swimming induced via applied electrical stimulation. *Middle:* The induction of fictive swimming alters vestibular afferent responses. *Right*: Bar plots compare the effects of fictive swimming on background and rotation-induced discharges of horizontal canal afferents (data replotted from Chagnaud et al., 2015). **(C)** *Left:* Afferent recordings made in rhesus monkeys during active and comparable passive head motion. *Middle:* Primate afferent responses are the same during active and comparable passive head motion (reviewed in Cullen, 2019). *Right*: Bar plots compare afferents resting rates and sensitivities in these two conditions (Cullen and Minor, 2002). Note: error bars represent SEM; $^{**}P \leq 0.001$ (Wilcoxon signed-rank test).

head-on-body movements (i.e., vestibular + proprioceptive stimulation). Likewise, visual stimulation does not alter primate vestibular afferent activity (**Figure 2C**). Vestibular afferents are further unresponsive to full-field visual motion in both cats (Blanks and Precht, 1978) and rhesus monkeys (Keller, 1976; Louie and Kimm, 1976; Miles and Braitman, 1980). Thus, to date, there is no evidence to support the proposal that extra-vestibular sensory stimulation in mammals can alter the responses of vestibular afferents.

Behaviorally/Context Independent Coding in the Vestibular Periphery of Mammals

During natural activities, vestibular information is integrated with motor signals, as well as other sensory signals (including visual and proprioceptive signals). In this context, a prevailing hypothesis has been that a key function of the vestibular efferent system is to alter peripheral motion sensing during active movements. In this view, the vestibular efferent pathway transmits motor-related signals to the vestibular periphery that modulate the responses of receptor cells within the semicircular canal and otolith sensory organs to effectively extend their head motion coding range during voluntary behaviors (reviewed in Goldberg, 2000; Mathews et al., 2017). Indeed, there is evidence for this proposal from studies of non-mammalian species (fish and tadpoles). Vestibular afferents in head-restrained toadfish display an increase in mean firing rate and a reduction in sensitivity to passive vestibular stimulation when preparing an escape response, which is thought to make them less likely to demonstrate inhibitory cut-off and/or saturation (**Figure 3A**; Boyle and Highstein, 1990; Rabbitt et al., 1995). Similarly, using a semi-isolated *in vitro* anaesthetized larval Xenopus preparation, showed that motor signals originating in the spinal locomotor circuitry are conveyed to the vestibular periphery to produce an overall reduction in afferent sensitivity to passive vestibular stimulation (**Figure 3B**; Chagnaud et al., 2015). The results of these studies have led to the common view that motor efference copies (i.e., an internal copy of the motor command) used to generate active behaviors are conveyed by the vestibular efferent system to the periphery to modulate responses in receptor cells and vestibular afferent fibers.

However, while studies in non-mammalian species provide support for the idea that the vestibular efferent system modulates peripheral sensory processing during active behaviors, this strategy does not appear to be common among all species. In particular, there is no direct evidence to date that the vestibular efferent system modulates afferent responses during active motion in mammals including primates. In rhesus monkeys, neither semicircular canal nor otolith afferent responses are altered during active orienting head movements or the generation of motor commands that activate the neck musculature (**Figure 3C**; Cullen and Minor, 2002; Sadeghi et al., 2007; Jamali et al., 2009; Mackrous et al., 2019). Furthermore, the motor pathways that control eye movements also do not alter the responses of vestibular afferents; the responses of semicircular canal and otolith afferents are insensitive to saccadic eye movements, smooth pursuit, and optokinetic nystagmus (Keller, 1976; Louie and Kimm, 1976; Miles and Braitman, 1980; Cullen and Minor, 2002; Sadeghi et al., 2007; Jamali et al., 2009). Finally, findings that afferents respond similarly in anesthetized and alert monkeys (Fernandez and Goldberg, 1971; Keller, 1976; Lisberger and Pavelko, 1986) and that afferent responses remain unchanged when animals are engaged in a vestibular heading discrimination task in which monkeys made saccades to indicate whether their perceived direction of translation was leftward or rightward relative to straight ahead (Yu et al., 2015). Thus to date, the evidence available indicates that the vestibular efferent system does not alter sensory processing by relaying behaviorally-dependent (e.g., motor commands that drive active head or eye movements) or context-dependent (e.g., alertness, feature attention) signals to vestibular periphery.

It is noteworthy that the above experiments, which found no change in in vestibular afferent responses during active orienting head movements in rhesus monkeys, included head movements that extended well into the amplitude range of other common active head movements, including those generated during locomotion (Carriot et al., 2017). Yet it is also important to note that these head movements are generated by the descending pathways to the neck musculature, rather than by the locomotor circuitry. This then raises the question of whether locomotion might preferentially alter the responses of afferents, via the vestibular efferent system, in mammals. Across species, locomotion provides us with the ability to explore our world and is critical for survival. The influential studies in aquatic vertebrates, described above (i.e., toadfish: Boyle and Highstein, 1990; larval xenopus: Chagnaud et al., 2015), are widely considered as support the idea that locomotion alters the responses of afferents via the vestibular efferent system. Importantly, however, neither of these studies actually recorded the afferent activity during voluntary active movement. Instead, the animals were head restrained and vestibular stimuli were passively applied. Accordingly, the question of whether the vestibular efferent pathway modulates peripheral coding of active head motion during locomotion remains open. We predict that it will be unlikely that such a strategy is utilized by higher vertebrates—notably primates. Instead, we speculate that coding of head motion by the vestibular periphery is context independent during natural active behaviors. This alternate strategy allows pathway-selective modulation of relationships between motor signals and the resultant vestibular feedback during active behaviors.

FUTURE DIRECTIONS AND CONCLUSION

The function of the mammalian vestibular efferent system in everyday life remains poorly understood. The finding that it can be artificially activated by electrical stimulation and/or high velocity vestibular stimulation (**Figure 1**) demonstrates that its circuitry is intact and operational in mammals, including

chinchillas and monkeys. However, in contrast to what has been reported in lower vertebrate classes, the mammalian vestibular efferent system does not relay inputs from other sensory modalities to the vestibular periphery (**Figure 2**). Instead, the integration of vestibular and extra-vestibular information occurs only at next stage of processing in the mammalian vestibular system—specifically, at the level of the first central neurons within the vestibular nuclei. For example, VOR pathways integrate gaze commands that suppress the VOR when the behavioral goal is to voluntarily redirect gaze (Roy and Cullen, 1998, 2002). Further, vestibulo-spinal and thalamocortical pathways integrate proprioceptive and voluntary head movement commands that suppress these pathways during voluntarily motion relative to space (Roy and Cullen, 2004; Brooks and Cullen, 2014; Dale and Cullen, 2019). Additionally, in further contrast to what has been observed in lower vertebrate classes, the mammalian vestibular efferent system does not function to prevent overstimulation by the voluntary movements experienced during everyday behaviors such as active head movements and locomotion (**Figure 3**; Cullen and Minor, 2002; Sadeghi et al., 2007; Jamali et al., 2009).

What then is the physiological role of this system in mammals? One possibility is that mammalian vestibular efferent system does not play a role in short-term modulation of afferent coding, but instead plays a role in modifying sensory encoding over a longer time course. In this regard, our knowledge of the function role of the auditory efferent system may provide some clues, given that the vestibular and auditory systems have a common phylogenetic origin (reviewed in Fritzsch, 1992). The auditory efferent system can induce long-term plastic changes in afferent physiology following cochlear de-efferentation (Liberman, 1990). Thus, one possibility is that the vestibular efferent system similarly plays a role in the similar role in the plasticity of the vestibular system following a similar perturbation, such as the loss of peripheral vestibular nerve input. Surprisingly, however, an experiment testing whether the vestibular efferent system plays a role in rebalancing input from the two labyrinths, after compensation to lesion of vestibular nerve on one side, found no change in afferent mean resting rates or sensitivities recorded in the *intact* nerve on the other side (i.e., the contralesional nerve; Sadeghi et al., 2007). Likewise, although the vestibular system shows remarkable plasticity in response to the altered environmental requirements induced by the wearing of visual lenses, the head velocity sensitivity or resting discharge of monkey vestibular afferents are unchanged following weeks of such visually induced plasticity (Miles and Braitman, 1980). Interestingly, in the above compensation study, Sadeghi et al. (2007) did report a small but significant increase in the proportion of irregular afferents and a decrease in the proportion of regular afferents. This result fits with the recent finding that inactivation of vestibular efferent fibers in mice preferentially influences the firing of irregular afferents (Raghu et al., 2019), and could provide insight into the role of the mammalian efferent system.

Another possibility is that a primary function of the mammalian vestibular efferent system is to calibrate pathway efficacy during development– in a role analogous to that shown for auditory efferents (Walsh et al., 1998; Lauer and May, 2011; Mishra, 2020). Indeed, as reviewed above there are some notable parallels between the synaptic physiology of the auditory and vestibular efferent pathways. More specifically, the auditory efferent system comprises the medial (MOC) and lateral olivocochlear (LOC) systems. The mechanism of synaptic transmission in the MOC pathway is similar to that in the vestibular efferent system; activation of both systems results in acetylcholine releases, which in turn hyperpolarizes receptor cells in the periphery via activation of α9/α10 nAChRs (Ballestero et al., 2011). Nevertheless, the vestibular efferent system also shares a similarity with the LOC system, namely that the neuroactive peptide calcitonin-gene related peptide (CGRP) acts at efferent synapses and their targets in both systems (Wackym et al., 1993; Maison et al., 2003; Ahn et al., 2009; Xiaocheng et al., 2013). Importantly, the efferent innervation of the cochlea occurs early in development (reviewed in Simmons, 2002). In particular, medial efferent neurons mature first and initially project to the inner hair cell region of the cochlea and then synapse on outer hair cells, while lateral efferent neurons mature later and predominately project to the inner hair cell region. Accordingly, it has been proposed that the early efferent innervation of the cochlea plays an important role in shaping the functional connectivity/efficacy of peripheral auditory signaling. Likewise, the efferent innervation of the vestibular sensory organs occurs early in development. Maturing type I and type II hair cells initially receive direct efferent contacts, which in the case of type I hair cells are displaced during development by the calyx afferent terminals (Favre and Sans, 1979) to the outer face of calyx terminal. The use of transgenic mouse models with a targeted deletion loss of CGRP *from birth* has revealed impaired functional efficacy, specifically an attenuation of auditory nerve responses (Walsh et al., 1998; Lauer and May, 2011) and, as noted above, also a marked reduction in VOR gain (Luebke et al., 2014). Thus, disrupting both the auditory LOC and vestibular efferent pathways from birth causes deficits that are consistent with the view that both efferent pathways play a vital role in calibrating pathway efficacy during development. Furthermore, lesions of the mammalian auditory efferent pathway accelerate age-related hearing loss (Liberman et al., 2014), and reduces protection against loud noise exposure (reviewed in Lauer et al., 2021). Thus, we further speculate that lesions to the mammalian vestibular efferent pathway in mammals would accelerate age-related peripheral vestibular impairment (Merchant et al., 2000; Lopez et al., 2005) and reduce protection against noise-induced damage (reviewed in Stewart et al., 2020).

SUMMARY

Overall, the evidence available to date contradicts the common wisdom that the mammalian vestibular efferent system dynamically modulates sensory coding by the vestibular periphery during natural behaviors. Specifically, neurophysiological studies have demonstrated that the mammalian vestibular efferent system does not play a significant role in short-term modulation of vestibular afferent responses. Instead, the evidence to date suggests that the

mammalian vestibular afferents encode head motion in a context-independent manner during natural behaviors, refuting an increasingly popular idea that efferent-mediated modulation of the vestibular periphery enhances postural and gaze stability during active behaviors (e.g., Jahn et al., 2000; Dietrich and Wuehr, 2019; Dietrich et al., 2020). Overall, the available evidence supports a competing hypothesis, namely that the mammalian efferent vestibular system predominantly plays a role over a longer time course, for example in calibrating vestibular pathway efficacy during neural development and/or protecting peripheral transmission during aging.

AUTHOR CONTRIBUTIONS

KC wrote the initial version of the manuscript with support from R-HW. R-HW provided critical feedback and helped shape the research arguments presented in the manuscript. Both authors contributed to the article and approved the submitted version.

FUNDING

This work was funded by the National Institute on Deafness and Other Communication Disorders at the National Institutes of Health (Grants R01-DC002390 and R01-DC013069 to KC) and Brain Initiative Grant 1UF1NS111695.

ACKNOWLEDGMENTS

We would like to thank Vanessa Chang, Aamna Lawrence, Olivia Leavitt, Robyn Mildren, Mai Rajborirug, Wagner Souza, Oliver Stanley, Yvette Tan, Pum Wiboonsaksakul, and Omid Zobeiri for critically reading the manuscript.

REFERENCES

Ahn, S. K., Khalmuratova, R., Jeon, S. Y., Kim, J. P., Park, J. J., and Hur, D. G. (2009). Colocalization of 5-HT1F receptor and calcitonin gene-related peptide in rat vestibular nuclei. *Neurosci. Lett.* 465, 151–156. doi: 10.1016/j.neulet.2009.09.008

Bailey, G. P., and Sewell, W. F. (2000). Contribution of glutamate receptors to spontaneous and stimulus-evoked discharge in afferent fibers innervating hair cells of the Xenopus lateral line organ. *Hear. Res.* 144, 8–20. doi: 10.1016/s0378-5955(00)00023-x

Ballestero, J., Zorrilla, de San Martin, J., Goutman, J., Elgoyhen, A. B., Fuchs, P. A., et al. (2011). Short-term synaptic plasticity regulates the level of olivocochlear inhibition to auditory hair cells. *J. Neurosci.* 31, 14763–14774. doi: 10.1523/jneurosci.6788-10.2011

Barbas-Henry, H. A., and Lohman, A. H. (1988). Primary projections and efferent cells of the VIIIth cranial nerve in the monitor lizard. *Varanus exanthematicus*. *J. Comp. Neurol.* 277, 234–249. doi: 10.1002/cne.902770206

Blanks, R. H., and Precht, W. (1976). Functional characterization of primary vestibular afferents in the frog. *Exp. Brain Res.* 25, 369–390.

Blanks, R. H., and Precht, W. (1978). Response properties of vestibular afferents in alert cats during optokinetic and vestibular stimulation. *Neurosci. Lett.* 10, 225–229. doi: 10.1016/0304-3940(78)90230-6

Boyle, R., and Highstein, S. M. (1990). Efferent vestibular system in the toadfish: action upon horizontal semicircular canal afferents. *J. Neurosci.* 10, 1570–1582. doi: 10.1523/jneurosci.10-05-01570.1990

Bricout-Berthout, A., and Caston, J. (1982). Responses of afferent and efferent neurons to auditory inputs in the vestibular nerve of the frog. *J. Comp. Physiol.* 147, 305–312. doi: 10.1007/bf00609664

Brooks, J. X., and Cullen, K. E. (2014). Early vestibular processing does not discriminate active from passive self-motion if there is a discrepancy between predicted and actual proprioceptive feedback. *J. Neurophysiol.* 111, 2465–2478. doi: 10.1152/jn.00600.2013

Carriot, J., Jamali, M., Chacron, M. J., and Cullen, K. E. (2014). Statistics of the vestibular input experienced during natural self-motion: implications for neural processing. *J. Neurosci.* 34, 8347–8357. doi: 10.1523/jneurosci.0692-14.2014

Carriot, J., Jamali, M., Chacron, M. J., and Cullen, K. E. (2017). The statistics of the vestibular input experienced during natural self-motion differ between rodents and primates. *J. Physiol.* 595, 2751–2766. doi: 10.1113/jp273734

Caston, J., and Bricout-Berthout, A. (1982). Responses of afferent and efferent neurons to visual inputs in the vestibular nerve of the frog. *Brain Res.* 240, 141–145. doi: 10.1016/0006-8993(82)90651-5

Caston, J., and Bricout-Berthout, A. (1984). Responses to somatosensory input by afferent and efferent neurons in the vestibular nerve of the frog. *Brain Behav. Evol.* 24, 135–143. doi: 10.1159/000121311

Chagnaud, B. P., Banchi, R., Simmers, J., and Straka, H. (2015). Spinal corollary discharge modulates motion sensing during vertebrate locomotion. *Nat. Commun.* 6:7982.

Claas, B., Fritzsch, B., and Münz, H. (1981). Common efferents to lateral line and labyrinthine hair cells in aquatic vertebrates. *Neurosci. Lett.* 27, 231–235. doi: 10.1016/0304-3940(81)90435-3

Cullen, K. E. (2019). Vestibular processing during natural self-motion: implications for perception and action. *Nat. Rev. Neurosci.* 20, 346–363. doi: 10.1038/s41583-019-0153-1

Cullen, K. E., and Minor, L. B. (2002). Semicircular canal afferents similarly encode active and passive head-on-body rotations: implications for the role of vestibular efference. *J. Neurosci.* 22:RC226.

Dale, A., and Cullen, K. E. (2019). The ventral posterior lateral thalamus preferentially encodes externally applied versus active movement: implications for self-motion perception. *Cereb. Cortex* 29, 305–318. doi: 10.1093/cercor/bhx325

Dickman, J. D., and Correia, M. J. (1993). Bilateral communication between vestibular labyrinths in pigeons. *Neuroscience* 57, 1097–1108. doi: 10.1016/0306-4522(93)90052-h

Dietrich, H., and Wuehr, M. (2019). Selective suppression of the vestibulo-ocular reflex during human locomotion. *J. Neurol.* 266, 101–107. doi: 10.1007/s00415-019-09352-7

Dietrich, H., Heidger, F., Schniepp, R., MacNeilage, P. R., Glasauer, S., and Wuehr, M. (2020). Head motion predictability explains activity-dependent suppression of vestibular balance control. *Sci. Rep.* 10:668.

Eden, A. R., and Correia, M. J. (1981). Vestibular efferent neurons and catecholamine cell groups in the reticular formation of the pigeon. *Neurosci. Lett.* 25, 239–242. doi: 10.1016/0304-3940(81)90398-0

Eybalin, M. (1993). Neurotransmitters and neuromodulators of the mammalian cochlea. *Physiol. Rev.* 73, 309–373. doi: 10.1152/physrev.1993.73.2.309

Favre, D., and Sans, A. (1979). Morphological changes in afferent vestibular hair cell synapses during the postnatal development of the cat. *J. Neurocytol.* 8, 765–775. doi: 10.1007/bf01206675

Fernandez, C., and Goldberg, J. M. (1971). Physiology of peripheral neurons innervating semicircular canals of the squirrel monkey. II. response to sinusoidal stimulation and dynamics of peripheral vestibular system. *J. Neurophysiol.* 34, 661–675. doi: 10.1152/jn.1971.34.4.661

Fritzsch, B. (1992). *The Water-to-Land Transition: Evolution of the Tetrapod Basilar Papilla, Middle Ear, and Auditory Nuclei*. New York: Springer-Verlag.

Fritzsch, B. (1996). Development of the labyrinthine efferent system. *Ann. N. Y. Acad. Sci.* 781, 21–33. doi: 10.1111/j.1749-6632.1996.tb15690.x

Gleisner, L., and Henriksson, N. G. (1963). Efferent and afferent activity pattern in the vestibular nerve of the frog. *Acta Otolaryngol. Suppl.* 192, 90–103. doi: 10.3109/00016486409134632

Goldberg, J. M. (2000). Afferent diversity and the organization of central vestibular pathways. *Exp. Brain Res.* 130, 277–297. doi: 10.1007/s002210050033

Goldberg, J. M., and Cullen, K. E. (2011). Vestibular control of the head: possible functions of the vestibulocollic reflex. *Exp. Brain Res.* 210, 331–345. doi: 10.1007/s00221-011-2611-5

Goldberg, J. M., and Fernandez, C. (1980). Efferent vestibular system in the squirrel monkey: anatomical location and influence on afferent activity. *J. Neurophysiol.* 43, 986–1025. doi: 10.1152/jn.1980.43.4.986

Goldberg, J. M., Wilson, V. J., Cullen, K. E., Angelaki, D. E., Broussard, D. M., Buttner-Ennever, J., et al. (2012). *The Vestibular System: a Sixth Sense*. Oxford: Oxford University Press.

Hartmann, R., and Klinke, R. (1980). Efferent activity in the goldfish vestibular nerve and its influence on afferent activity. *Pflugers Arch.* 388, 123–128. doi: 10.1007/bf00584117

Highstein, S. M. (1992). The efferent control of the organs of balance and equilibrium in the toadfish, *Opsanus tau*. *Ann. N. Y. Acad. Sci.* 656, 108–123. doi: 10.1111/j.1749-6632.1992.tb25203.x

Highstein, S. M., and Baker, R. (1985). Action of the efferent vestibular system on primary afferents in the toadfish, *Opsanus tau*. *J. Neurophysiol.* 54, 370–384. doi: 10.1152/jn.1985.54.2.370

Highstein, S. M., and Baker, R. (1986). Organization of the efferent vestibular nuclei and nerves of the toadfish, *Opsanus tau*. *J. Comp. Neurol.* 243, 309–325. doi: 10.1002/cne.902430303

Holt, J. C., Lysakowski, A., and Goldberg, J. M. (2011). "The Efferent Vestibular System," in *Auditory and Vestibular Efferents*, eds Ryugo, K. and Fay, R. (New York, NY: Springer), 135–186.

Jahn, K., Strupp, M., Schneider, E., Dieterich, M., and Brandt, T. (2000). Differential effects of vestibular stimulation on walking and running. *Neuroreport* 11, 1745–1748. doi: 10.1097/00001756-200006050-00029

Jamali, M., Carriot, J., Chacron, M. J., and Cullen, K. E. (2019). Coding strategies in the otolith system differ for translational head motion vs. static orientation relative to gravity. *eLife* 8:e45573.

Jamali, M., Chacron, M. J., and Cullen, K. E. (2016). Self-motion evokes precise spike timing in the primate vestibular system. *Nat. Commun.* 7:13229.

Jamali, M., Sadeghi, S. G., and Cullen, K. E. (2009). Response of vestibular nerve afferents innervating utricle and saccule during passive and active translations. *J. Neurophysiol.* 101, 141–149. doi: 10.1152/jn.91066.2008

Keller, E. L. (1976). Behavior of horizontal semicircular canal afferents in alert monkey during vestibular and optokinetic stimulation. *Exp. Brain Res.* 24, 459–471.

Klinke, R. (1970). Efferent influence on the vestibular organ during active movements of the body. *Pflugers Arch.* 318, 325–332. doi: 10.1007/bf00586972

Lauer, A. M., and May, B. J. (2011). The medial olivocochlear system attenuates the developmental impact of early noise exposure. *J. Assoc. Res. Otolaryngol.* 12, 329–343. doi: 10.1007/s10162-011-0262-7

Lauer, A. M., Jimenez, S. V., and Delano, P. H. (2021). Olivocochlear efferent effects on perception and behavior. *Hear. Res.* 108207. doi: 10.1016/j.heares.2021.108207

Liberman, M. C. (1990). Quantitative assessment of inner ear pathology following ototoxic drugs or acoustic trauma. *Toxicol. Pathol.* 18, 138–148. doi: 10.1177/019262339001800119

Liberman, M. C., Liberman, L. D., and Maison, S. F. (2014). Efferent feedback slows cochlear aging. *J. Neurosci.* 34, 4599–4607. doi: 10.1523/jneurosci.4923-13.2014

Lisberger, S. G., and Pavelko, T. A. (1986). Vestibular signals carried by pathways subserving plasticity of the vestibulo-ocular reflex in monkeys. *J. Neurosci.* 6, 346–354. doi: 10.1523/jneurosci.06-02-00346.1986

Lopez, I., Ishiyama, G., Tang, Y., Tokita, J., Baloh, R. W., and Ishiyama, A. (2005). Regional estimates of hair cells and supporting cells in the human crista ampullaris. *J. Neurosci. Res.* 82, 421–431. doi: 10.1002/jnr.20652

Louie, A. W., and Kimm, J. (1976). The response of 8th nerve fibers to horizontal sinusoidal oscillation in the alert monkey. *Exp. Brain Res.* 24, 447–457.

Luebke, A. E., Holt, J. C., Jordan, P. M., Wong, Y. S., Caldwell, J. S., and Cullen, K. E. (2014). Loss of α-calcitonin gene-related peptide (αCGRP) reduces the efficacy of the Vestibulo-ocular reflex (VOR). *J. Neurosci.* 34, 10453–10458. doi: 10.1523/jneurosci.3336-13.2014

Lysakowski, A., and Goldberg, J. M. (1997). A regional ultrastructural analysis of the cellular and synaptic architecture in the chinchilla cristae ampullares. *J. Comp. Neurol.* 389, 419–443. doi: 10.1002/(sici)1096-9861(19971222)389:3<419::aid-cne5>3.0.co;2-3

Lysakowski, A., and Goldberg, J. M. (2008). Ultrastructural analysis of the cristae ampullares in the squirrel monkey (*Saimiri sciureus*). *J. Comp. Neurol.* 511, 47–64. doi: 10.1002/cne.21827

Mackrous, I., Carriot, J., Jamali, M., and Cullen, K. E. (2019). Cerebellar prediction of the dynamic sensory consequences of gravity. *Curr. Biol.* 29, 2698–2710.e4.

Maison, S. F., Adams, J. C., and Liberman, M. C. (2003). Olivocochlear innervation in the mouse: immunocytochemical maps, crossed versus uncrossed contributions, and transmitter colocalization. *J. Comp. Neurol.* 455, 406–416. doi: 10.1002/cne.10490

Marco, J., Lee, W., Suárez, C., Hoffman, L., and Honrubia, V. (1993). Morphologic and quantitative study of the efferent vestibular system in the chinchilla: 3-D reconstruction. *Acta Otolaryngol.* 113, 229–234. doi: 10.3109/00016489309135798

Marlinski, V., Plotnik, M., and Goldberg, J. M. (2004). Efferent actions in the chinchilla vestibular labyrinth. *J. Assoc. Res. Otolaryngol.* 5, 126–143.

Mathews, M. A., Camp, A. J., and Murray, A. J. (2017). Reviewing the role of the efferent vestibular system in motor and vestibular circuits. *Front. Physiol.* 8:552.

McCue, M. P., and Guinan, J. J. (1994). Acoustically responsive fibers in the vestibular nerve of the cat. *J. Neurosci.* 14, 6058–6070. doi: 10.1523/jneurosci.14-10-06058.1994

Merchant, S. N., Velázquez-Villaseñor, L., Tsuji, K., Glynn, R. J., Wall, C., and Rauch, S. D. (2000). Temporal bone studies of the human peripheral vestibular system. normative vestibular hair cell data. *Ann. Otol. Rhinol. Laryngol. Suppl.* 181, 3–13. doi: 10.1177/00034894001090s502

Meredith, G. E. (1988). Comparative view of the central organization of afferent and efferent circuitry for the inner ear. *Acta Biol. Hung.* 39, 229–249.

Meredith, G. E., and Roberts, B. L. (1987). Distribution and morphological characteristics of efferent neurons innervating end organs in the ear and lateral line of the *European eel*. *J. Comp. Neurol.* 265, 494–506. doi: 10.1002/cne.902650404

Miles, F. A., and Braitman, D. J. (1980). Long-term adaptive changes in primate vestibuloocular reflex. II. electrophysiological observations on semicircular canal primary afferents. *J. Neurophysiol.* 43, 1426–1436. doi: 10.1152/jn.1980.43.5.1426

Mishra, S. K. (2020). The role of efferents in human auditory development: efferent inhibition predicts frequency discrimination in noise for children. *J. Neurophysiol.* 123, 2437–2448. doi: 10.1152/jn.00136.2020

Ohno, K., Takeda, N., Yamano, M., Matsunaga, T., and Tohyama, M. (1991). Coexistence of acetylcholine and calcitonin gene-related peptide in the vestibular efferent neurons in the rat. *Brain Res.* 566, 103–107. doi: 10.1016/0006-8993(91)91686-u

Pellegrini, M., Ceccotti, F., and Magherini, P. (1985). The efferent vestibular neurons in the toad (Bufo bufo L.): their location and morphology. a horseradish peroxidase study. *Brain Res.* 344, 1–8. doi: 10.1016/0006-8993(85)91183-7

Plotnik, M., Marlinski, V., and Goldberg, J. M. (2002). Reflections of efferent activity in rotational responses of chinchilla vestibular afferents. *J. Neurophysiol.* 88, 1234–1244. doi: 10.1152/jn.2002.88.3.1234

Plotnik, M., Marlinski, V., and Goldberg, J. M. (2005). Efferent-mediated fluctuations in vestibular nerve discharge: a novel, positive-feedback mechanism of efferent control. *J. Assoc. Res. Otolaryngol.* 6, 311–323. doi: 10.1007/s10162-005-0010-y

Poppi, L. A., Holt, J. C., Lim, R., and Brichta, A. M. (2020). A review of efferent cholinergic synaptic transmission in the vestibular periphery and its functional implications. *J. Neurophysiol.* 123, 608–629. doi: 10.1152/jn.00053.2019

Precht, W., Llinás, R., and Clarke, M. (1971). Physiological responses of frog vestibular fibers to horizontal angular rotation. *Exp. Brain Res.* 13, 378–407.

Purcell, I. M., and Perachio, A. A. (1997). Three-dimensional analysis of vestibular efferent neurons innervating semicircular canals of the gerbil. *J. Neurophysiol.* 78, 3234–3248. doi: 10.1152/jn.1997.78.6.3234

Rabbitt, R. D., Boyle, R., and Highstein, S. M. (1995). Mechanical indentation of the vestibular labyrinth and its relationship to head rotation in the toadfish, *Opsanus tau*. *J. Neurophysiol.* 73, 2237–2260. doi: 10.1152/jn.1995.73.6.2237

Raghu, V., Salvi, R., and Sadeghi, S. G. (2019). Efferent inputs are required for normal function of vestibular nerve afferents. *J. Neurosci.* 39, 6922–6935. doi: 10.1523/jneurosci.0237-19.2019

Roy, J. E., and Cullen, K. E. (1998). A neural correlate for vestibulo-ocular reflex suppression during voluntary eye-head gaze shifts. *Nat. Neurosci.* 1, 404–410. doi: 10.1038/1619

Roy, J. E., and Cullen, K. E. (2002). Vestibuloocular reflex signal modulation during voluntary and passive head movements. *J. Neurophysiol.* 87, 2337–2357. doi: 10.1152/jn.2002.87.5.2337

Roy, J. E., and Cullen, K. E. (2004). Dissociating self-generated from passively applied head motion: neural mechanisms in the vestibular nuclei. *J. Nurosci.* 24, 2102–2111. doi: 10.1523/jneurosci.3988-03.2004

Sadeghi, S. G., Goldberg, J. M., Minor, L. B., and Cullen, K. E. (2009). Efferent-mediated responses in vestibular nerve afferents of the alert macaque. *J. Neurophysiol.* 101, 988–1001. doi: 10.1152/jn.91112.2008

Sadeghi, S. G., Minor, L. B., and Cullen, K. E. (2007). Response of vestibular-nerve afferents to active and passive rotations under normal conditions and after unilateral labyrinthectomy. *J. Neurophysiol.* 97, 1503–1514. doi: 10.1152/jn.00829.2006

Sans, A., and Highstein, S. M. (1984). New ultrastructural features in the vestibular labyrinth of the toadfish, *Opsanus tau*. *Brain Res.* 308, 191–195. doi: 10.1016/0006-8993(84)90936-3

Schmidt, C. L., Wist, E. R., and Dichgans, J. (1972). Efferent frequency modulation in the vestibular nerve of goldfish correlated with saccadic eye movements. *Exp. Brain Res.* 15, 1–14.

Schmidt, R. S. (1963). Frog labyrinthine efferent impulses. *Acta Otolaryngol.* 56, 51–64. doi: 10.3109/00016486309127679

Schmidt, R. S. (1965). Amphibian acoustico-lateralis efferents. *J. Cell. Physiol.* 65, 155–162. doi: 10.1002/jcp.1030650204

Schneider, G. T., Lee, C., Sinha, A. K., Jordan, P. M., and Holt, J. C. (2021). The mammalian efferent vestibular system utilizes cholinergic mechanisms to excite primary vestibular afferents. *Sci. Rep.* 11:1231.

Sewell, W. F., and Starr, P. A. (1991). Effects of calcitonin gene-related peptide and efferent nerve stimulation on afferent transmission in the lateral line organ. *J. Neurophysiol.* 65, 1158–1169. doi: 10.1152/jn.1991.65.5.1158

Simmons, D. D. (2002). Development of the inner ear efferent system across vertebrate species. *J. Neurobiol.* 53, 228–250. doi: 10.1002/neu.10130

Stewart, C. E., Holt, A. G., Altschuler, R. A., Cacace, A. T., Hall, C. D., Murnane, O. D., et al. (2020). Effects of noise exposure on the vestibular system: a systematic review. *Front. Neurol.* 11:593919.

Wackym, P. A., Popper, P., and Micevych, P. E. (1993). Distribution of calcitonin gene-related peptide mRNA and immunoreactivity in the rat central and peripheral vestibular system. *Acta Otolaryngol.* 113, 601–608. doi: 10.3109/00016489309135871

Walsh, E. J., McGee, J., McFadden, S. L., and Liberman, M. C. (1998). Long-term effects of sectioning the olivocochlear bundle in neonatal cats. *J. Neurosci.* 18, 3859–3869. doi: 10.1523/jneurosci.18-10-03859.1998

Xiaocheng, W., Zhaohui, S., Ka, B., Junhui, X., Lei, Z., Feng, X., et al. (2013). The expression of calcitonin gene-related Peptide and acetylcholine in the vestibular-related nucleus population of wild-type mice and retinal degeneration fast mice after rotary stimulation. *J. Mol. Neurosci.* 51, 514–521. doi: 10.1007/s12031-013-0087-4

Yu, X. J., Dickman, J. D., DeAngelis, G. C., and Angelaki, D. E. (2015). Neuronal thresholds and choice-related activity of otolith afferent fibers during heading perception. *Proc. Natl. Acad. Sci. U.S.A.* 112, 6467–6472. doi: 10.1073/pnas.1507402112

Conflict of Interest: The authors declare that the research was conducted in the absence of any commercial or financial relationships that could be construed as a potential conflict of interest.

frontiers in Neuroscience

ORIGINAL RESEARCH
published: 07 July 2021
doi: 10.3389/fnins.2021.691962

Calretinin Immunoreactivity in the VIIIth Nerve and Inner Ear Endorgans of *Ranid* Frogs

*Ingrid Reichenberger[1], Claude J. Caussidier-Dechesne[2] and Hans Straka[1]**

[1] Department Biology II, Ludwig-Maximilians-University Munich, Planegg, Germany, [2] INSERM U254, Université de Montpellier, Montpellier, France

Calcium-binding proteins are essential for buffering intracellular calcium concentrations, which are critical for regulating cellular processes involved in neuronal computations. One such calcium-binding protein, calretinin, is present in many neurons of the central nervous system as well as those which innervate cranial sensory organs, although often with differential distributions in adjacent cellular elements. Here, we determined the presence and distribution of calretinin-immunoreactivity in the peripheral vestibular and auditory system of *ranid* frogs. Calretinin-immunoreactivity was observed in ganglion cells innervating the basilar and amphibian *papilla*, and in a subpopulation of ganglion cells innervating the saccular epithelium. In contrast, none of the ganglion cells innervating the lagena, the utricle, or the three semicircular canals were calretinin-immunopositive, suggesting that this calcium-binding protein is a marker for auditory but not vestibular afferent fibers in the frog. The absence of calretinin in vestibular ganglion cells corresponds with the lack of type I hair cells in anamniote vertebrates, many of which in amniotes are contacted by the neurites of large, calyx-forming calretinin-immunopositive ganglion cells. In the sensory epithelia of all endorgans, the majority of hair cells were strongly calretinin-immunopositive. Weakly calretinin-immunopositive hair cells were distributed in the intermediate region of the semicircular canal *cristae*, the central part of the saccular *macula*, the utricular, and lagenar striola and the medial part of the amphibian *papilla*. The differential presence of calretinin in the frog vestibular and auditory sensory periphery might reflect a biochemical feature related to firing patterns and frequency bandwidths of self-motion *versus* acoustic stimulus encoding, respectively.

Keywords: immunocytochemistry, vestibular, auditory, hair cells, calcium-binding proteins

OPEN ACCESS

Edited by:
Soroush G. Sadeghi, University at Buffalo, United States

Reviewed by:
Rebecca Lim, The University of Newcastle, Australia
Anna Lysakowski, University of Illinois at Chicago, United States

****Correspondence:***
Hans Straka
straka@lmu.de
orcid.org/0000-0003-2874-0441

Specialty section:
This article was submitted to Perception Science, a section of the journal Frontiers in Neuroscience

Received: *07 April 2021*
Accepted: *16 June 2021*
Published: *07 July 2021*

Citation:
Reichenberger I, Caussidier-Dechesne CJ and Straka H (2021) Calretinin Immunoreactivity in the VIIIth Nerve and Inner Ear Endorgans of Ranid Frogs. Front. Neurosci. 15:691962. doi: 10.3389/fnins.2021.691962

INTRODUCTION

Calcium-binding proteins regulate cellular calcium homeostasis and thus control neuronal processes, such as excitability thresholds, response dynamics, synaptic transmission mechanisms, and indirectly influence neuronal susceptibility to impairments (Baimbridge et al., 1992; Fairless et al., 2019; Schwaller, 2002). In the inner ear, calcium-binding proteins, such as calretinin (CaR),

calbindin, parvalbumin, calmodulin, oncomodulin, or the S-100 protein are present in differential, yet partly overlapping subpopulations of hair cells and afferent neurons as demonstrated in a variety of vertebrate species (Saidel et al., 1990; Demêmes et al., 1992; Kerschbaum and Hermann, 1993; Raymond et al., 1993; Roberts, 1993; Jaramillo, 1995; Pack and Slepecky, 1995; Baird et al., 1997; Kevetter and Leonard, 2002a,b; Desai et al., 2005a,b; Simmons et al., 2010; Lysakowski et al., 2011; Hoffman et al., 2018; Prins et al., 2020). The variety of proteins suggests that their different calcium-buffer capacities correlate with the dynamic properties or requirements of a particular cell type (Heizmann and Hunziker, 1991; Baimbridge et al., 1992). Accordingly, the presence of the same calcium-binding protein in different neurons might indicate similar buffer-requirements for comparable neuronal computations, which conveniently render the different proteins suitable as a tag for specific cell groups (Baimbridge et al., 1992).

Calretinin is the most-studied calcium-binding protein in the inner ear (Dechesne et al., 1991, 1993, 1994; Demêmes et al., 1992; Desmadryl and Dechesne, 1992; Raymond et al., 1993; Imamura and Adams, 1996; Edmonds et al., 2000; Kevetter and Leonard, 2002a; Desai et al., 2005a,b; Lysakowski et al., 2011; Holt et al., 2015; Jordan et al., 2015). Immunohistochemical evaluation of the rodent peripheral vestibular system indicated that CaR is present in a morpho-physiologically distinct population of afferents, the calyx fibers (Desmadryl and Dechesne, 1992; Desai et al., 2005a,b; Lysakowski et al., 2011). These calyx fibers, present in all amniote vertebrates, predominate in central epithelial areas and contact type I hair cells, whereas bouton fibers preferentially terminate in peripheral areas on type II hair cells (Goldberg, 2000). Dimorphic fibers supply both type I and type II hair cells throughout most of the epithelia with calyx and bouton endings, respectively (Goldberg, 2000). The different synaptic configurations coincide with several other, interrelated morpho-physiological parameters such as axon diameter, discharge regularity, and response dynamics (Paulin and Hoffman, 2019; Goldberg, 2000). Accordingly, larger fibers, which supply more central epithelial regions, have a more irregular resting discharge and phasic response dynamics; conversely, smaller fibers supply more peripheral regions, have a more regular resting discharge, and exhibit more tonic response properties (Goldberg, 2000).

Anamniote vertebrates lack type I hair cells and thus calyx-type synaptic terminations (Gleisner et al., 1973; Wersäll and Bagger-Sjöback, 1974). Nonetheless, vestibular afferents of, e.g., *ranid* frogs (Honrubia et al., 1981, 1989; Baird and Lewis, 1986; Baird and Schuff, 1994; Reichenberger and Dieringer, 1994; Straka and Dieringer, 2004) form a broad spectrum of fibers with correlations between resting discharge regularity, response dynamics, fiber diameter, and regional innervation of the sensory epithelium similar to the morpho-physiology of vestibular afferents in amniote vertebrates (Goldberg, 2000). This structural and functional similarity prompted us to study the distribution of CaR-immunoreactivity of inner ear neuronal elements in frogs with the hypothesis that CaR has a cell type-specific differential expression pattern.

MATERIALS AND METHODS

Tissue Preparation

Experiments were performed on 19 adult frogs of both sexes (*Rana esculenta* and *Rana temporaria*) and comply with the "Principles of animal care," publication No. 86-23, revised 1985 of the National Institutes of Health. Permission for these experiments was granted by the Regierung von Oberbayern (211-2531-31/95). In a first set of experiments, animals (*Rana esculenta*, $n = 7$; *Rana temporaria*, $n = 6$) were anesthetized with 0.1% 3-aminobenzoic acid ethyl ester (MS-222) and perfused transcardially with frog Ringer solution (75 mM NaCl, 25 mM $NaHCO_3$, 2 mM $CaCl_2$, 2 mM KCl, 0.5 mM $MgCl_2$, and 11 mM glucose; pH 7.4; 5 ml), followed by 4% paraformaldehyde in 0.1 M phosphate buffer (PB, pH 7.4). The VIIIth nerves along with the otic capsule and all inner ear organs were removed on both sides, post-fixed for 2 h, immersed in 15% sucrose and kept in 30% sucrose overnight at 4°C. The nerves and attached sensory epithelia were cut on a cryostat (10 μm) and sections were mounted directly on glass slides. In a second set of experiments, frogs (*Rana esculenta*, $n = 6$) were anesthetized and decapitated. The inner ears on both sides were quickly removed, dissected and the individual sensory epithelia immersed in 4% paraformaldehyde fixative in 0.1 M PB (pH 7.4) for 3–5 h. Subsequently, the sensory epithelia of two frogs were embedded in 4% agarose in 0.1 M phosphate-buffered saline (PBS, pH 7.4), cut on a vibratome in 50 μm sections, collected and stored in PBS. The sensory epithelia of four other frogs were stored as whole-mounts in PBS until further use.

Immunocytochemical Procedures

Consecutive cryostat sections mounted on glass slides in the first set of experiments were processed for calretinin immunocytochemistry using the avidin-biotin-complex method. Accordingly, cryostat sections were washed in PBS, pre-incubated for 1 h with PBS containing 0.3% Triton X-100 and 2% normal goat serum and incubated overnight at 4°C with polyclonal rabbit anti-calretinin antibodies (1:5,000, SWant). Thereafter, sections were rinsed in PBS, incubated for 1 h with biotinylated goat anti-rabbit IgG (1:100, Vectastain), rinsed again in PBS and incubated for 1 h in the avidin-biotin complex in PBS (1:100, Vectastain). The peroxidase-labeled avidin-biotin complex was detected by 0.05% diaminobenzidine and 0.01% H_2O_2 in 0.05 M *Tris* buffer (pH 7.6). Subsequently, sections were rinsed, dehydrated in alcohol and cover-slipped.

Vibratome sections and whole-mounts of the sensory epithelia in the second set of experiments were processed free-floating to visualize CaR immunofluorescence. Accordingly, the tissue was washed in PBS, pre-incubated for 1 h in PBS containing 0.3% Triton X-100 and 2% normal donkey serum and incubated in anti-calretinin antiserum (1:5,000, SWant). Thereafter, the tissue was washed in PBS and incubated for 3 h in a solution containing Cy3^{TM}-conjugated donkey anti-rabbit IgG (1:500, Jackson ImmunoResearch Laboratories) in darkness. After rinsing in PBS, the vibratome sections were transferred onto glass slides, the whole-mounts on depression slides and

cover-slipped with FluorSave reagent (Calbiochem). Primary and secondary antibodies were diluted in the same solution as used for the pre-incubation. No immunostaining was observed in sections processed without primary antibodies. The anti-calretinin antiserum has been characterized by Schwaller et al. (1993) and was shown to react specifically with calretinin in tissue originating from human, monkey, rat, and mouse and not to cross-react with calbindin or other calcium-binding proteins.

Confocal Microscopy

Visualization of immunofluorescent labeling with confocal microscopy allowed an overview of the different parts of the sensory epithelia in whole-mounts and thick vibratome sections and facilitated the analysis of immunolabeled cellular elements. The immunofluorescence was captured with 0.5–1.0 μm thick single optical sections of tissue using a laser scanning confocal microscope (Bio-Rad, MRC 600). Images were obtained by averaging 4–10 consecutive scans and subsequent processing with the software provided by the manufacturer (Cosmos program). The contrast of the images was optimized using the contrast stretch option. Vibratome sections of 5–26 μm thickness were reconstructed by a projection of serial optical sections.

RESULTS

Scarpa's Ganglion and VIIIth Nerve Afferent Fibers

The VIIIth nerve contains afferent fibers that connect inner ear endorgans with their target nuclei in the brainstem. In all vertebrate species, the VIIIth nerve ramifies into an anterior and a posterior branch before peripherally entering the otic capsule (a, p in **Figure 1A**; de Burlet, 1929). In *ranid* frogs, the anterior branch supplies the horizontal and anterior vertical semicircular canal, the utricle and the saccule, while the posterior branch supplies the posterior vertical semicircular canal, the lagena, the basilar and amphibian *papilla* (**Figure 1A**). The cell bodies of the afferent fibers are located at the junction of the two branches and form Scarpa's ganglion (SG in **Figure 1A**). With respect to the presence of calretinin in the VIIIth nerve, strong CaR-immunoreactivity was observed in a subset of ganglion cells and their proximal and distal neurites (**Figures 1B,C**). CaR-immunopositive cell bodies were relatively small and round with a diameter of ∼15 μm (15.3 ± 3.3 μm; mean ± SD; n = 134) and preferentially clustered in the compartment of Scarpa's ganglion that contains somata and neurites that supply endorgans through the posterior branch. CaR-immunopositive afferent fibers were also observed in the VIIIth nerve between the ganglion and the entrance of the nerve into the brainstem terminating in the dorsal hindbrain known to contain the anuran auditory nuclei (Suarez et al., 1985). However, there were other, small as well as large ganglion cells in the anterior portion of the VIIIth nerve, both of which lacked an obvious CaR-immunoreactivity. These cells, according to their position in the anterior part of the VIIIth nerve supply hair cells in the anterior vertical and horizontal semicircular canal and the utricle, suggesting that size per se does not seem to be a differentiator for CaR-immunoreactivity of the ganglion cells.

The distal neurites of CaR-immunopositive ganglion cells in the posterior branch formed two separate bundles within this branch that could be followed to two endorgans, known to represent anuran auditory organs (Frishkopf and Flock, 1974; Capranica, 1978). One CaR-immunopositive fiber bundle traversed along the posterior branch and curved medially to reach the amphibian *papilla*. The vast majority of fibers innervating this endorgan were intensely CaR-immunopositive with parent cell bodies mainly located in dorsal and lateral portions of the posterior compartment of the ganglion. The second CaR-immunopositive fiber bundle contained only few fibers, diverged from the main branch only very distally to terminate in the basilar *papilla*. In contrast to the amphibian *papilla*, all fibers innervating this auditory endorgan appeared to be CaR-immunopositive. The corresponding cell bodies of afferents innervating the basilar *papilla* were located separately from those of the amphibian *papilla* in the posterior compartment of Scarpa's ganglion, corroborating earlier observations of an endorgan-specific ganglion cell topography (Hiraoka et al., 1995).

The anterior compartment of Scarpa's ganglion was largely lacking the broad presence of CaR-immunopositive cells, except for a small set of dispersed neurons at the junction of the two ganglionic compartments (**Figure 1B**). These cells were round and similarly small in diameter as compared to those located in the posterior compartment of Scarpa's ganglion (15.7 ± 3.5 μm; mean ± SD; n = 43). The few CaR-immunopositive fibers projected distally as a small bundle in the anterior branch to reach the saccular *macula* (**Figures 1B**, **2F**). Compared to the entire population of saccular afferents, CaR-immunopositive fibers comprised ∼20–30% of all afferents supplying this endorgan. In contrast, afferent fibers innervating the three semicircular canals (**Figures 1B**, **2C**), the utricle (**Figures 1B**, **3C**), and the lagena (**Figure 3F**) consistently lacked a noticeable CaR-immunoreactivity. The size of the respective ganglion cells was rather heterogeneous with significantly larger diameters (23.3 ± 7.4 μm; mean ± SD; n = 215) as compared to those of the CaR-immunopositive ganglion cells ($p < 0.0001$; Mann-Whitney U-test). Collectively, these findings suggest that CaR-immunoreactivity was restricted to afferent fibers of inner ear endorgans involved in the detection of air-borne sound (amphibian and basilar *papilla*, saccule) while afferent fibers of typical vestibular endorgans such as the semicircular canals, utricle, and lagena (Straka and Dieringer, 2004) were devoid of a clear CaR-immunoreactivity. Such distributions thus establish CaR-immunopositivity as a differentiating marker that is able to distinguish frog vestibular and auditory afferents from each other.

Inner Ear Sensory Epithelia

Beyond afferent immunoreactivity, the sensory epithelia of the different endorgans were tested for CaR-immunoreactivity using either cryostat sections and immunoperoxidase-based antibody detection or whole-mount tissue/vibratome sections and immunofluorescence labeling. Confocal imaging of whole-mounts and vibratome sections revealed different regions of the

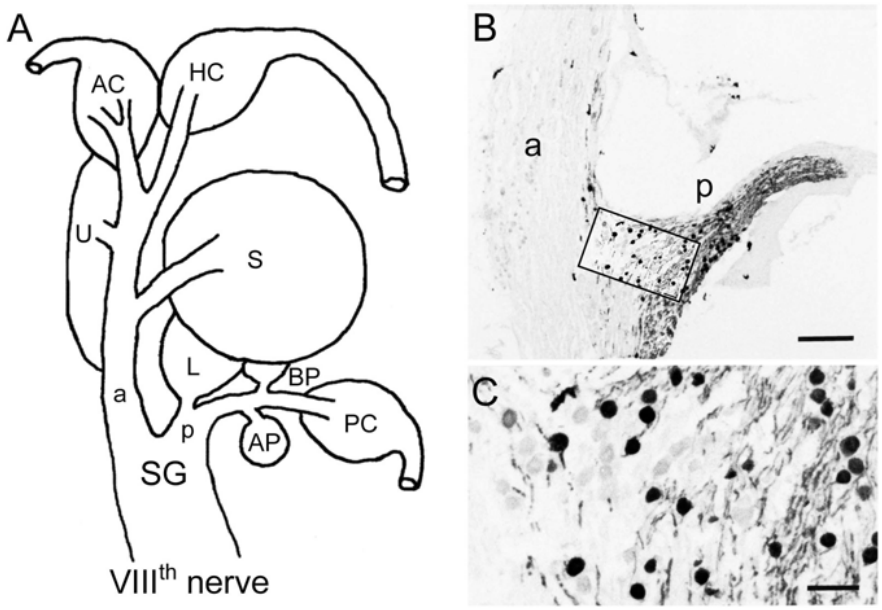

FIGURE 1 | Immunohistochemical localization of calretinin in the VIIIth nerve. **(A)** Schematic of the VIIIth nerve and inner ear endorgans. **(B,C)** Cryostat section through Scarpa's ganglion (SG) depicting calretinin (CaR)-immunopositive ganglion cells and afferent fibers (peroxidase staining), revealing many cells in the posterior (p) and only few in the anterior branch (a) of the VIIIth nerve; higher magnification **(C)** of the outlined area in panel **(B)**. AP, amphibian *papilla*; AC, HC, PC, anterior, horizontal, posterior semicircular canal; BP, basilar *papilla*; L, lagena; S, saccule; U, utricle. Scale bars are 200 μm in panel **(B)** and 50 μm in panel **(C)**.

sensory epithelia, which presented with hair cells of different morphological shape and extent of CaR-immunoreactivity (**Figure 2A**). The different intensity of CaR-immunopositive hair cells described below is likely related to different concentrations but might be also influenced by endorgan-specific aspects such as tissue thickness, confocal stack size or antibody penetration. In contrast to quantitative studies of concentration and distribution of calcium buffering proteins in the mammalian cochlea (Hackney et al., 2003, 2005), the present approach was purely descriptive and qualitative, providing a general overview of the distribution of CaR in the inner ear of frogs. The confocal images, illustrating CaR-immunofluorescence, are of high contrast rendering even the outline of presumed "CaR-immunonegative" hair cells visible. Accordingly, the presence and tentative absence of immunofluorescent labeling was denoted as strong *versus* weak CaR-immunopositivity.

Based on their shapes, hair cells were categorized into four subtypes. (1) Club-like hair cells with a narrow cytoplasmic projection to the epithelial surface and an expanded basal portion with occasional short processes. (2) Cylindrical hair cells with a relatively uniform width from the apex to the base. (3) Spherical hair cells with a larger diameter in the central region compared to the apical or basal portion of the cell body. (4) Dumbbell-shaped hair cells with a smaller diameter in the central region of the cell body than at the apical and basal end of the cell body (present only in the saccule). CaR-immunoreactivity was generally observed in all sensory epithelia (**Figures 2–4**), however, it was restricted to neurosensory structures, such as hair cells or afferent fibers. Non-neurosensory cell types, such as supporting cells intercalated between hair cells, were at best only very weakly CaR-immunopositive. Intracellularly, the staining of CaR-immunopositive hair cells was particularly strong in the cytoplasm, the cuticular plate, and the cilial bundle, but weak or absent in the nucleus and nucleolus. Given the differences in CaR-immunopositive cell morphologies across endorgans, within-endorgan CaR-immunopositive cell subtypes were further examined.

Semicircular Canal *cristae*

The epithelium of the anterior and posterior vertical semicircular canal *cristae* form a symmetric haltere-like shape with two oppositely oriented, but proportional, peripherally enlarged regions and two thin intermediate areas adjacent to a broader central region (**Figures 2A,B**). The receptor area of the horizontal semicircular canal forms half of a vertical semicircular canal *crista*. Strongly CaR-immunopositive hair cells were found in the *cristae* of all semicircular canals, although with differential regional distributions. Hair cells in central and peripheral regions expressed an intense CaR-immunoreaction, whereas a considerable fraction of hair cells in the intermediate region appeared to express at most a very weak CaR-immunoreaction (**Figure 2A**). Strongly CaR-immunopositive hair cells were mostly cylindrical (**Figure 2C**) or club-like, while weakly CaR-immunopositive hair cells in the intermediate region were large, spherical cells.

Saccular *macula*

The sensory epithelium of the saccule has the shape of a flattened kidney with the *hilus* indicating the entrance of

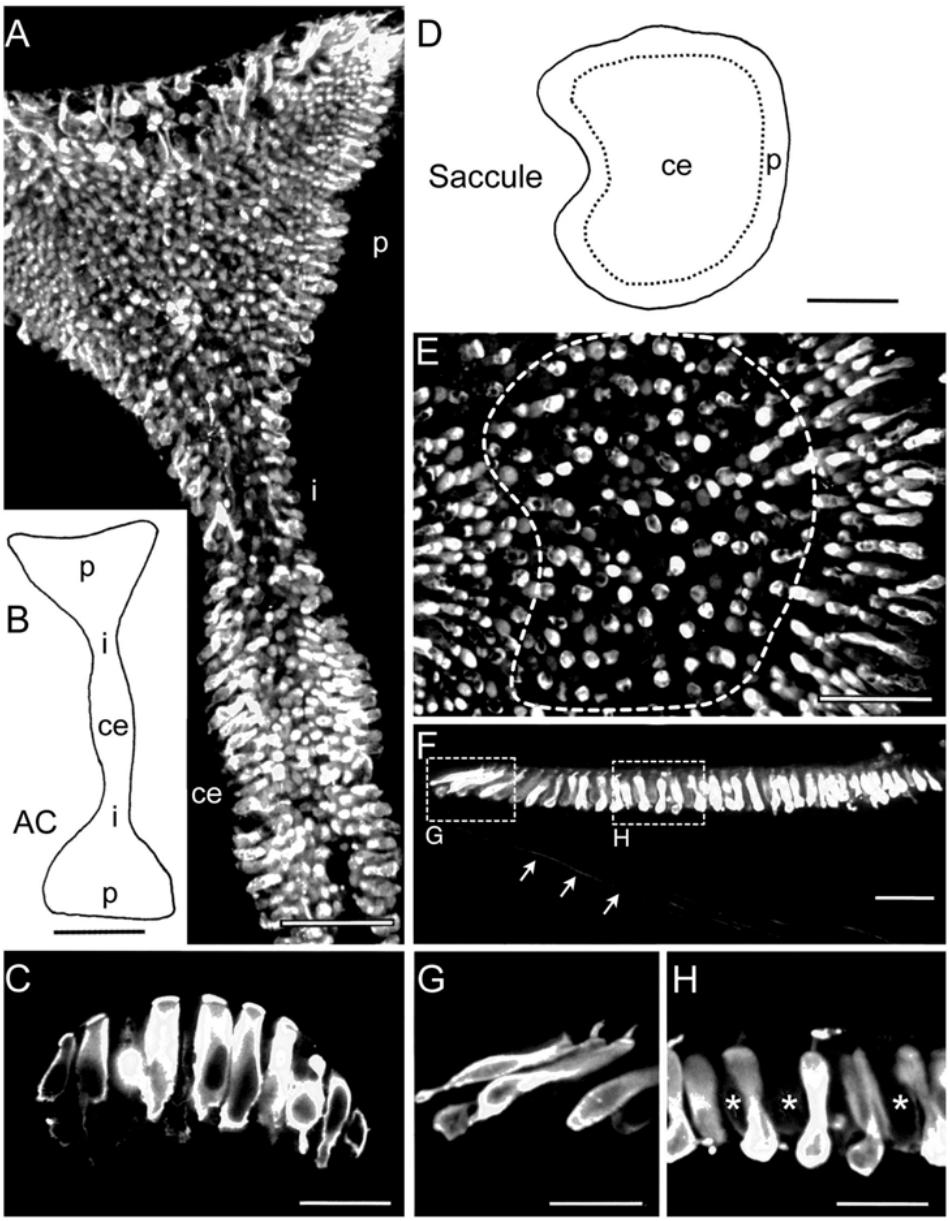

FIGURE 2 | Immunohistochemical localization of calretinin in semicircular canal and saccular sensory epithelia. **(A,B)** Microphotograph of a whole-mount anterior semicircular canal (AC) *crista* **(A)** depicting strongly CaR-immunopositive hair cells with preferential locations in central (ce) and peripheral (p) epithelial regions based on the schematic outline **(B)**. **(C)** Close-up optical reconstruction of a section through the central region of the *crista* illustrating strongly CaR-immunopositive cylindrical hair cells. **(D,E)** Schematic of the saccular *macula* indicating the tentative separation into two epithelial regions (dashed lines) and microphotograph of a whole-mount of the saccule **(E)** depicting strongly CaR-immunopositive hair cells preferentially located in the periphery rather than the center. **(F–H)** Optical reconstruction of a section through the saccule **(F)** depicting a close-up of strongly CaR-immunopositive hair cells in the periphery **(G)** and dumbbell-shaped cells in the center of the epithelium **(H)**; the center contained few interspersed hair cells that were only very weakly CaR-immunopositive (* in **H**); also note the few CaR-immunopositive afferent fibers (arrows in **F**). i, intermediate region. Scale bars are 50 μm in panels **(A,E,F)**, 200 μm in panels **(B,D)** and 25 μm in panels **(C,G,H)**.

the nerve branch into the epithelium (**Figure 2D**). Hair cells in the peripheral part of the saccular *macula* were consistently and strongly CaR-immunopositive, whereas the central part of the *macula* contained a mixture of few, strongly CaR-immunolabeled hair cells intermingled with a substantial number of weakly CaR-immunolabeled hair cells (**Figures 2E,F,H**). Strongly CaR-immunopositive hair cells in the peripheral part of the *macula* had a club-like shape (**Figure 2G**) and usually occupied the first 2–6 cell rows along the edge of the epithelium (**Figure 2D**). The majority of strongly CaR-immunopositive hair cells in the center of the saccular *macula* were dumbbell-shaped

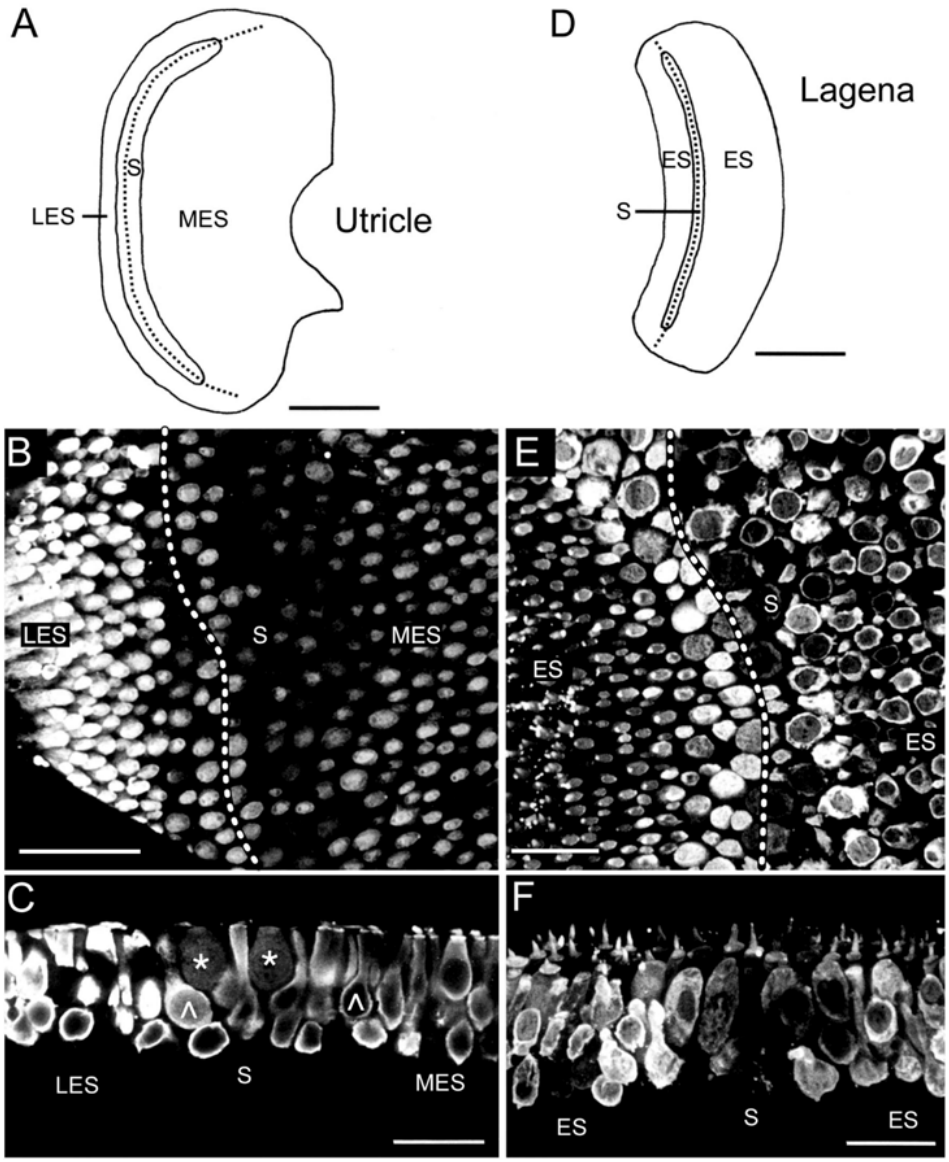

FIGURE 3 | Immunohistochemical localization of calretinin in the utricular and lagenar sensory epithelia. **(A–C)** Schematic of the utricular *macula* indicating the tentative separation into the striola (S) and lateral (LES) and medial extrastriolar (MES) regions and microphotograph of a whole-mount utricle **(B)** with strongly CaR-immunopositive hair cells in the LES and MES and many weakly CaR-immunopositive hair cells along the striola; close-up optical reconstruction of a longitudinal section **(C)** through the utricle shown in panel **(B)**, illustrating several club-like (^) or cylindrical, strongly CaR-immunopositive hair cells and two spherical, weakly CaR-immunopositive hair cells (*). **(D)** Schematic of the lagenar *macula* indicating the tentative separation into a striola (S) and extrastriolar (ES) region. **(E,F)** Optical reconstruction of a horizontal **(E)** and longitudinal section **(F)** through the lagena depicting a region-specific CaR-immunoreactivity with weakly CaR-immunopositive hair cells along the striola; note the intense cilial bundle staining and absence of noticeable CaR-immunoreactivity in supporting cells and nerve fibers. Dotted lines in panels **(A,B,D,E)** indicate the tentative reversal line of hair cell polarization. Scale bars are 200 μm in panels **(A,D)**, 50 μm in panel **(B)** and 25 μm in panels **(C,E,F)**.

with an occasional CaR-immunopositivity of the cilial bundle (**Figure 2H**).

Utricular and Lagenar *macule*

The utricle also has a kidney-shaped appearance, while the lagena forms a broad arc (**Figures 3A,D**). The *macule* of both organs are, respectively, divided into the striola, a narrow zone of distinctive morphology, and an extrastriolar region (**Figures 3A,D**). The striola was easily identifiable by a smaller density of hair cells with shorter cilial bundles as compared to those located in the extrastriolar region. The pattern of CaR-immunolabeling was similar for the utricle and the lagena. All extrastriolar and part of the striolar hair cells were strongly CaR-immunopositive (**Figures 3B,C,E,F**). Hair cells in the lateral extrastriolar region of the utricle and in the small extrastriolar region of the lagena were mostly club-shaped or cylindrical (**Figure 3C**). Strongly

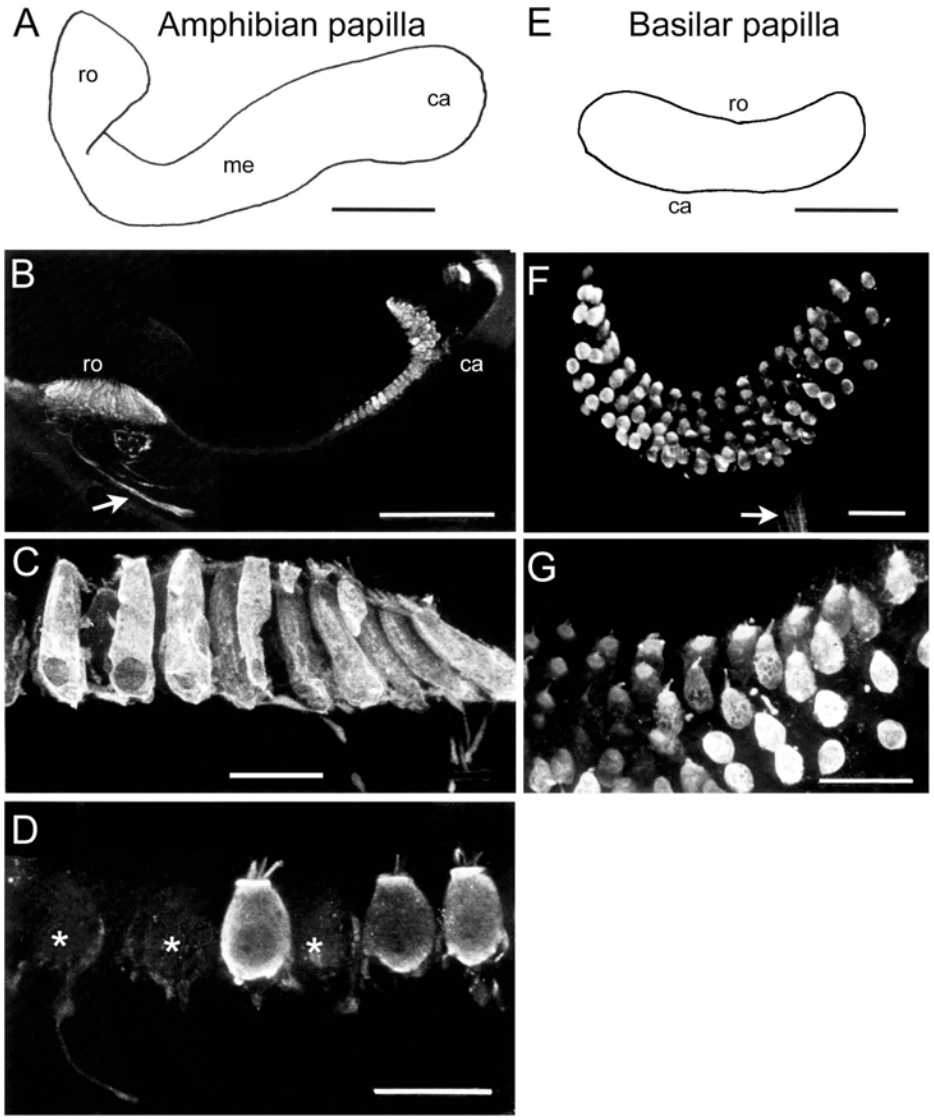

FIGURE 4 | Immunohistochemical localization of calretinin in the sensory epithelium of the amphibian and basilar *papilla*. **(A)** Schematic of the amphibian *papilla* distinguishing a rostral (ro), medial (me), and caudal (ca) region. **(B)** Optical reconstruction of a section through the rostral and caudal end of the amphibian *papilla* depicting strongly CaR-immunopositive hair cells as well as few weakly CaR-immunolabeled afferent fibers (arrow). **(C,D)** Close-up optical reconstructions of cylindrical, strongly CaR-immunopositive hair cells in the rostral region **(C)** and of spherical hair cells in the medial region of the amphibian *papilla* **(D)**, some of which were only very weakly CaR-immunopositive (*). **(E)** Schematic of the basilar *papilla* representing a small, oval-shaped epithelial area. **(F,G)** Microphotographs of a whole-mount basilar *papilla* **(F)** depicting small, spherical and strongly CaR-immunopositive hair cells **(G)** innervated by weakly CaR-immunopositive fibers [arrow in panel **(F)**]. Scale bars are 200 μm in panels **(A,B)**, 50 μm in panel **(E)** and 25 μm in panels **(C,D,F,G)**.

CaR-immunopositive hair cells along the striola were either club-shaped or cylindrical, while the weakly CaR-immunopositive hair cells were mostly spherical (**Figure 3C**). Based on the position along the striola, the latter cells potentially correspond to pear-shaped hair cells described for the fish utricle (Chang et al., 1992). Hair cells in the medial extrastriolar region of the utricle and the large extrastriolar area of the lagena decreased in size toward the edges. These latter hair cells were cylindrical, club-shaped, or spherical, and consistently expressed a relatively strong CaR-immunoreactivity (**Figures 3C,F**), matching the large population of striolar (20–40%) and extrastriolar (70–80%) type II CaR-immunopositive hair cells of rodents (Desai et al., 2005b; see also below).

Amphibian and Basilar *papilla*

The receptor area of the amphibian *papilla* forms an elongated and three-dimensionally curved epithelium (**Figure 4A**), covered by a structure that is reminiscent of a tectorial membrane. The three-dimensional complexity of this endorgan along with the relatively large volume of cartilage, encapsulating the duct lumen (Geisler et al., 1964), prevented a confocal reconstruction of the sensory epithelium. The receptor area can be separated into

three zones based on hair cell morphology (Lewis and Li, 1975; Simmons et al., 1994). All hair cells in the caudal and rostral portion of the epithelium were strongly CaR-immunopositive (**Figures 4B,C**), whereas the medial part contained a sizeable number of very weakly labeled CaR-immunopositive hair cells (**Figure 4D**). Strongly CaR-immunopositive hair cells in the rostral portion were mostly cylindrical or club-shaped (**Figure 4C**), while those in the caudal portion were spherical and noticeably smaller. The medial portion of the amphibian *papilla* formed a transitory zone with hair cells exhibiting features intermediate to those located in the adjacent rostral and caudal sections of the endorgan, a condition that was largely independent of the overall level of CaR-immunoreactivity (**Figure 4D**). In compliance with the findings on the CaR-immunoreactivity of *papillar* afferent fibers (see **Figure 1**), a more or less distinct CaR-immunofluorescent fiber bundle was encountered (arrow in **Figure 4B**). The poor visibility of the fibers is likely due to the small proportion of optical sections containing immunolabeled afferents within the entire confocal image stack. The basilar *papilla* (**Figure 4E**) represents a small, oval-shaped, and dorso-ventrally curved epithelium with ∼60 hair cells in ranid frogs (see Geisler et al., 1964). The sensory epithelium was found to consist of 5–6 parallel rows of morphologically rather homogeneous hair cells (**Figure 4F**) that were surmounted by the tectorial-like membrane. All hair cells were relatively small and of spherical shape and expressed either a strong or at least a moderate CaR-immunoreactivity (**Figures 4F,G**). Compatible with the strong CaR-immunoreactivity of *papillar* afferents illustrated in **Figure 1**, small bundles of CaR-immunofluorescent fibers were consistently encountered at the basal aspect of the epithelium (arrow in **Figure 4F**). The rather faint labeling of these afferents likely derives from an under-representation of the fiber bundle within the confocally reconstructed image stack.

DISCUSSION

Calretinin-immunohistochemistry revealed a population of small, strongly CaR-immunolabeled ganglion cells with thin axons that innervate the amphibian and basilar *papilla* and the saccular epithelium, all of which are endorgans and epithelial areas known to detect air-borne sound. In contrast, ganglion cells and associated afferents innervating typical vestibular sensory endorgans lacked an obvious CaR-immunoreactivity. In contrast to the selective labeling of afferent fibers, the majority of hair cells in all endorgans were strongly CaR-immunopositive, however, with variations related to epithelial location and cell morphology.

Morpho-Physiology of Ganglion Cells

The selective CaR-immunopositivity of all *papilla* and a subpopulation of saccular ganglion cells suggests that CaR is a marker for non-vestibular afferent fibers, which transmit sound information (Lewis et al., 1982a,b). In fact, the amphibian and basilar *papillae* represent morpho-physiologically specialized endorgans for the reception of air-borne sound with different frequency ranges, respectively (Frishkopf and Flock, 1974; Feng et al., 1975; Lewis et al., 1982a). While the amphibian *papilla* is sensitive to frequencies of 100–1,000 Hz, the basilar *papilla* detects air-borne sound with frequencies of 1,000–2,000 Hz (Lewis et al., 1982a). The encoding and transmission of these high frequency sensory stimuli (as compared to vestibular stimuli) by afferent neurons of both *papillar* organs requires physiological properties that ensure phase-locked neuronal activity during prolonged episodes of acoustic stimuli as occurring during intraspecies communication (Schwartz and Simmons, 1990). Thus, frog auditory nerve fibers from the *papilla* organs require adaptations that allow a sustenance of phase-locked afferent spikes related to the frequency of the conspecific vocalization patterns (Capranica and Moffat, 1975; Feng et al., 1975). Such a capacity critically depends on specific biochemical properties, including the endowment with calcium-binding proteins (Baimbridge et al., 1992). These calcium-buffers assist in rendering acoustic afferents dynamically capable of persistent spiking that is phase-coupled to the sound stimulus frequency (Ronken, 1991). Vocalization-related acoustic afferent activity would in fact be promoted by the presence of CaR, known to possess a relatively fast kinetics for buffering intracellular Ca^{2+}-levels as well as to facilitate efficient Ca^{2+}-clearance by a cooperative binding of Ca^{2+} (Barinka and Druga, 2010).

The presence of CaR-immunopositive saccular afferents is consistent with this interpretation given the reported sensitivity of this endorgan also for sound (Ashcroft and Hallpike, 1934; Moffat and Capranica, 1976; Koyama et al., 1982). Saccular fibers are sensitive to a relatively broad range of sound frequencies (Moffat and Capranica, 1976). These sound-sensitive fibers comprise ∼30% of all saccular afferents in toad (Moffat and Capranica, 1976) with similar discharge patterns as fibers that innervate the amphibian and basilar *papillae* (Feng et al., 1975). The fraction of these physiologically identified saccular fibers coincides in magnitude with the 20–30% CaR-immunopositive saccular afferents encountered in the present study, suggesting that the latter indeed represent sound-sensitive saccular afferents. According to this classification scheme, CaR-immunopositivity might be a suitable tag for auditory afferent fibers, consistent with their exclusive central termination in the "dorsal nucleus" of the hindbrain (not shown), known to form the auditory relay area in anurans (Feng and Lin, 1996). This immunohistochemical organization of anuran auditory afferents is consistent with the CaR-immunopositivity of most spiral ganglion cells innervating the mammalian cochlea (Dechesne et al., 1991, 1994; Imamura and Adams, 1996). Therefore, CaR might have evolved as a contributing molecular player toward a necessary physiological pre-requisite that permits encoding of persistent high-frequency acoustic stimuli.

The lack of CaR-immunoreactivity by ganglion cells and associated afferent fibers that innervate the three semicircular canals, the utricle, and the lagena complement the suggestive evidence that CaR is a marker for auditory afferents. While semicircular canals and the utricle have an exclusive vestibular function in almost all vertebrates (Straka and Dieringer, 2004), the frog lagena represents an endorgan with a dual function: detection of tilt and translation and substrate-borne vibrations (MacNaughton and McNally, 1946; Caston et al., 1977; Cortopassi and Lewis, 1996). The absence of

CaR-immunoreactivity from lagenar fibers suggests that CaR is not only absent from distinct vestibular afferents but also from seismically-sensitive fibers, which apparently separates the latter from the subgroup of air-borne sound-sensitive saccular or *papillar* afferents. This coincides with the sensitivity of most seismic afferents to lower frequencies (<100 Hz; Cortopassi and Lewis, 1996), while sound-sensitive fibers encode considerably higher frequencies (>500 Hz; Ronken, 1991), potentially rendering CaR in the latter afferents an important biochemical substrate for the transmission of respective spike rates and patterns (see above).

In contrast to the complete lack of CaR-immunoreactivity in frog vestibular afferents, a subpopulation of rather thick mammalian vestibular afferents is densely CaR-immunopositive (Dechesne et al., 1991, 1994; Demêmes et al., 1992; Desmadryl and Dechesne, 1992; Raymond et al., 1993; Kevetter and Leonard, 2002a). These latter fibers form calyces with type I hair cells located at the apex of the semicircular canal *cristae* and the striola of the utricle (Desmadryl and Dechesne, 1992; Dechesne et al., 1994). The involvement of these calyces and associated afferent fibers in the encoding and transmission of high frequency/acceleration head motion signals suggests that CaR in these afferent neurons likely ensures the faithful transmission of phase-timed sensory components (Goldberg, 2000). Although such a requirement also applies to motion detection in frogs, the corresponding population of thick anuran vestibular afferents was found to obviously lack noticeable levels of CaR. The difference between mammals and frogs with respect to CaR-immunoreactivity of vestibular afferents is the absence of type I hair cells and calyx synapses in the latter species. This correlation is supported by the progressive establishment of CaR-immunoreactivity during ontogeny in mice. In fact, the developmental appearance of CaR-immunoreactivity in mammalian vestibular afferents coincides with the functional maturation of calyces in the central zone of the semicircular canal *crista* (Dechesne et al., 1994). This apparent dissociation between hair cell and vestibular afferent CaR-immunopositivity complies with the post-mitotic immunoreactivity for CaR in hair cells but not in afferents in rodents (Zheng and Gao, 1997). The subsequent postnatal permanent loss of CaR-immunopositivity in subsets of hair cells and pure calyx afferents might form part of the electrophysiological maturation process of these vestibular elements (Dechesne et al., 1994; Zheng and Gao, 1997). Even though some aspects of mouse inner ear hair cell/afferent CaR-ontogeny are reminiscent of the pattern present in frog, a distinct recapitulation of phylogenetic principles during development is possible but likely too simplistic.

Morpho-Physiology of Hair Cells

Although frogs possess only type II hair cells, these mechanoreceptor cells form a rather diverse population with morphological differences related to epithelial location (Wersäll and Bagger-Sjöback, 1974). The differences in hair cell and cilial bundle morphology coincide with adaptations of membrane properties and response dynamics (Lewis and Li, 1975; Baird, 1994a,b; Baird and Schuff, 1994). The diversity of the dynamic tuning of hair cells is likely matched by a differential endowment with calcium-binding proteins (Saidel et al., 1990; Baird et al., 1997; Prins et al., 2020). The present results demonstrate that the CaR-immunoreactivity of hair cells might depend on the shape and regional position within the epithelium. Club-like hair cells, located mainly at the edge of the receptor area, consistently expressed strong CaR-immunopositivity. Cylindrical hair cells were also strongly CaR-immunopositive in the *cristae*, the utricle, lagena and amphibian *papilla*, but only very weakly CaR-immunopositive in the saccule. Smaller spherical hair cells were strongly CaR-immunopositive and present in the extrastriolar regions of the utricle and lagena, in the basilar *papilla* and the caudal region of the amphibian *papilla*. In contrast, larger spherical cells consistently expressed an only very weak CaR-immunoreaction and were present in the striolar region of the utricle and lagena, the intermediate region of the *cristae*, and in the medial part of the amphibian *papilla*. This apparently rather erratic and mosaic-like distribution of strong CaR-immunopositivity in hair cells makes it difficult to extract a consistent picture that might be related to physiological profile, shape, or regional location.

Despite the presence of very weakly CaR-immunopositive hair cells, the majority of frog hair cells were strongly CaR-immunopositive with extensive labeling of the cytoplasm and intense staining of the cuticular plate and cilial bundles (**Figures 2–4**). This pattern, however, differs from a previous study on the distribution of calcium-binding proteins, including calretinin, in bullfrog (*Rana catesbeiana*) otolith organs (Baird et al., 1997). This latter study demonstrated CaR-immunoreactivity exclusively in cilial bundles of saccular and utricular hair cells, but not in the cytoplasm or other subcellular structures. The CaR-immunopositive cilial bundles were homogeneously distributed across the otolithic epithelia (Baird et al., 1997), without evidence for a hair cell shape-specific presence of this calcium-binding protein. This difference with respect to the current study might be related to the employment of different antibodies or different methodological details or might simply reflect species-specific variations. After all, it is known that even rather closely related ranid species such as *Rana pipiens* (Leopard frog), *Rana esculenta* (Common water frog) and *Rana temporaria* (Grass frog) differ in vestibular hair cell morphologies (Guth et al., 1994; Gioglio et al., 1995) along with eco-physiological adaptations such as sensitivity to substrate vibration, locomotor style and proficiency or vestibulo-ocular reflex organization (Pantle and Dieringer, 1998).

The cell type-specific, strong CaR-immunopositivity in the current study allowed linking these hair cells with epithelial regions that were previously characterized by cilial bundle and/or hair cell morphology (Lewis and Li, 1975; Baird, 1994a; Guth et al., 1994; Gioglio et al., 1995). Accordingly, strongly CaR-immunopositive hair cells were located in central and posterior regions of the *cristae*, and peripheral regions of the *macule*. In the intermediate region of the *cristae* and along the striola, hair cells were only weakly labeled. These latter hair cells, most numerous in the striolar region, are characterized by membrane properties that might depend on calcium-binding proteins other than CaR (Gioglio et al., 1995; Chabbert et al., 1997). In contrast, club-like shaped strongly CaR-immunopositive hair cells along the

perimeter of the saccule might represent immature hair cells in the process of being added to the sensory epithelium (Lewis and Li, 1973). Although the epithelial region-specific hair cell morpho-physiology yields a clear correlation between structure and function, the presence of calcium-binding proteins in general and of CaR in particular appears to be less deterministic. The observed CaR distribution pattern is obviously not exclusive to a specific hair cell type but rather representative for a larger functional subgroup with physiological properties that are yet to be determined.

With respect to the CaR-immunoreactivity in the inner ear of other vertebrates, mammals also possess CaR-immunopositive hair cells, although with a differential abundance in different endorgans and hair cell types. In the mammalian cochlea, only inner hair cells were CaR-immunopositive, whereas outer hair cells were CaR-immunonegative (Dechesne et al., 1991, 1994; Pack and Slepecky, 1995; Imamura and Adams, 1996). Adult mammalian vestibular hair cells exhibit a widespread presence of CaR in all inner ear sensory organs, a feature that is only gradually acquired during embryonic development and generally maintained in post-mitotic hair cells (Zheng and Gao, 1997). The abundance of CaR in hair cells has subsequently been confirmed, although with varying distributions, in different endorgans and hair cell types (Desai et al., 2005a,b). According to the latter studies, the largest number of CaR-immunopositive hair cells comprised extrastriolar type II hair cells (70–80%), followed by ∼30% of striolar type II hair cells and <10% type I hair cells (Desai et al., 2005a,b). Along with the specific class of CaR-immunolabeled calyx afferents, CaR thus appears to represent a particular marker for inner ear cellular elements (Dechesne et al., 1991, 1994; Pack and Slepecky, 1995; Imamura and Adams, 1996; Zheng and Gao, 1997; Desai et al., 2005a,b).

DATA AVAILABILITY STATEMENT

The raw data supporting the conclusions of this article will be made available by the authors, without undue reservation.

ETHICS STATEMENT

The animal study was reviewed and approved by Regierung von Oberbayern (211-2531-31/95).

AUTHOR CONTRIBUTIONS

IR performed the experiments and analyzed all data, made the figures, and edited the manuscript. CC-D performed the experiments and edited the manuscript. HS planned the experiments and wrote the manuscript. All authors contributed to the article and approved the submitted version.

FUNDING

Financial support was provided by the German Science Foundation (CRC 462 and CRC 870, B12, reference number: 118803580).

ACKNOWLEDGMENTS

The authors thank Clayton Gordy for critically reading the manuscript.

REFERENCES

Ashcroft, D. W., and Hallpike, C. S. (1934). On the function of the saccule. *J. Laryngol.* 49, 450–460.

Baimbridge, K. G., Celio, M. R., and Rogers, J. H. (1992). Calcium-binding proteins in the nervous system. *Trends Neurosci.* 15, 303–309. doi: 10.1016/0166-2236(92)90081-i

Baird, R. A. (1994a). Comparative transduction mechanisms of hair cells in the bullfrog utriculus. I. Responses to intracellular current. *J. Neurophysiol.* 71, 666–684. doi: 10.1152/jn.1994.71.2.666

Baird, R. A. (1994b). Comparative transduction mechanisms of hair cells in the bullfrog utriculus. II. Sensitivity and response dynamics to hair bundle displacement. *J. Neurophysiol.* 71, 685–705. doi: 10.1152/jn.1994.71.2.685

Baird, R. A., and Lewis, E. R. (1986). Correspondences between afferent innervation patterns and response dynamics in the bullfrog utricle and lagena. *Brain Res.* 369, 48–64. doi: 10.1016/0006-8993(86)90512-3

Baird, R. A., and Schuff, N. R. (1994). Peripheral innervation patterns of vestibular nerve afferents in the bullfrog utriculus. *J. Comp. Neurol.* 342, 279–298. doi: 10.1002/cne.903420210

Baird, R. A., Steyger, P. S., and Schuff, N. R. (1997). Intracellular distribution and putative functions of calcium-binding proteins in the bullfrog vestibular otolith organs. *Hear. Res.* 103, 85–100. doi: 10.1016/s0378-5955(96)00167-0

Barinka, F., and Druga, R. (2010). Calretinin expression in the mammalian neocortex: a review. *Physiol. Res.* 59, 665–677. doi: 10.33549/physiolres.931930

Capranica, R. R. (1978). Auditory processing in anurans. *Fed. Proc.* 37, 2324–2328.

Capranica, R. R., and Moffat, A. J. M. (1975). Selectivity of the peripheral auditory system of spadefoot toads (*Scaphiopus couchi*) for sounds of biological significance. *J. Comp. Physiol. A* 100, 231–249. doi: 10.1007/bf00614533

Caston, J., Precht, W., and Blanks, R. H. I. (1977). Response characteristics of frog's lagena afferents to natural stimulation. *J. Comp. Physiol. A* 118, 273–289. doi: 10.1007/bf00614351

Chabbert, C., Chambard, J. M., Valmier, J., Sans, A., and Desmadryl, G. (1997). Voltage-activated sodium currents in acutely isolated mouse vestibular ganglion neurons. *Neuroreport* 8, 1253–1256. doi: 10.1097/00001756-199703240-00039

Chang, J. S., Popper, A. N., and Saidel, W. M. (1992). Heterogeneity of sensory hair cells in a fish ear. *J. Comp. Neurol.* 324, 621–640. doi: 10.1002/cne.903240413

Cortopassi, K. A., and Lewis, E. R. (1996). High-frequency tuning properties of bullfrog lagenar vestibular afferent fibers. *J. Vestib. Res.* 6, 105–119. doi: 10.3233/ves-1996-6205

de Burlet, H. M. (1929). Zur vergleichenden anatomie der labyrinthinnervation. *J. Comp. Neurol.* 47, 155–169. doi: 10.1002/cne.900470202

Dechesne, C. D., Rabejac, D., and Desmadryl, G. (1994). Development of calretinin immunoreactivity in the mouse inner ear. *J. Comp. Neurol.* 346, 517–529. doi: 10.1002/cne.903460405

Dechesne, C. D., Winsky, L., Kim, H. N., Goping, G., Vu, T. D., Wenthold, R. J., et al. (1991). Identification and ultrastructural localization of a calretinin-like calcium-binding protein (protein 10) in the guinea pig and rat inner ear. *Brain Res.* 560, 139–148. doi: 10.1016/0006-8993(91)91224-o

Dechesne, C. D., Winsky, L., Moniot, B., and Raymond, J. (1993). Localization of calretinin mRNA in rat and guinea pig inner ear by *in situ* hybridization using radioactive and non-radioactive probes. *Hear. Res.* 69, 91–97. doi: 10.1016/0378-5955(93)90096-j

Demêmes, D., Raymond, J., Atger, P., Grill, C., Winsky, L., and Dechesne, C. J. (1992). Identification of neuron subpopulations in the rat vestibular ganglion by calbindin-D 28K, calretinin and neurofilament proteins immunoreactivity. *Brain Res.* 582, 168–172. doi: 10.1016/0006-8993(92)90334-6

Desai, S. S., Ali, H., and Lysakowski, A. (2005a). Comparative morphology of rodent vestibular periphery. II. Cristae ampullares. *J. Neurophysiol.* 93, 267–280. doi: 10.1152/jn.00747.2003

Desai, S. S., Zeh, C., and Lysakowski, A. (2005b). Comparative morphology of rodent vestibular periphery. I. Saccular and utricular maculae. *J. Neurophysiol.* 93, 251–266. doi: 10.1152/jn.00746.2003

Desmadryl, G., and Dechesne, C. J. (1992). Calretinin immunoreactivity in chinchilla and guinea pig vestibular end organs characterizes the calyx unit subpopulation. *Exp. Brain Res.* 89, 105–108.

Edmonds, B., Reyes, R., Schwaller, B., and Roberts, W. M. (2000). Calretinin modifies presynaptic calcium signaling in frog saccular hair cells. *Nat. Neurosci.* 3, 786–790. doi: 10.1038/77687

Fairless, R., Williams, S. K., and Diem, R. (2019). Calcium-binding proteins as determinants of central nervous system neuronal vulnerability to disease. *Int. J. Mol. Sci.* 20:2146. doi: 10.3390/ijms20092146

Feng, A. S., and Lin, W. Y. (1996). Neural architecture of the dorsal nucleus (cochlear nucleus) of the frog, *Rana pipiens pipiens*. *J. Comp. Neurol.* 366, 320–334. doi: 10.1002/(sici)1096-9861(19960304)366:2<320::aid-cne10>3.0.co;2-t

Feng, A. S., Narins, P. M., and Capranica, R. R. (1975). Three populations of primary auditory fibers in the bullfrog (*Rana catesbeiana*): their peripheral origin and frequency sensitivities. *J. Comp. Physiol. A* 100, 221–229. doi: 10.1007/bf00614532

Frishkopf, L. S., and Flock, A. (1974). Ultrastructure of the basilar papilla, an auditory organ in the bullfrog. *Acta Otolaryngol.* 77, 176–184. doi: 10.3109/00016487409124615

Geisler, C. D., van Bergeijk, W. A., and Frishkopf, L. S. (1964). The inner ear of the bullfrog. *J. Morphol.* 114, 43–57. doi: 10.1002/jmor.1051140103

Gioglio, L., Congiu, T., Quacci, D., and Prigioni, I. (1995). Morphological features of different regions in frog crista ampullaris (*Rana esculenta*). *Arch. Histol. Cytol.* 58, 1–16. doi: 10.1679/aohc.58.1

Gleisner, L., Flock, Å, and Wersäll, J. (1973). The ultrastructure of the afferent synapse on hair cells in the frog labyrinth. *Acta Otolaryngol.* 76, 199–207. doi: 10.3109/00016487309121500

Goldberg, J. M. (2000). Afferent diversity and the organization of central vestibular pathways. *Exp. Brain Res.* 130, 277–297. doi: 10.1007/s002210050033

Guth, P. S., Fermin, C. D., Pantoja, M., Edwards, R., and Norris, C. (1994). Hair cells of different shapes and their placement along the frog crista ampullaris. *Hear. Res.* 73, 109–115. doi: 10.1016/0378-5955(94)90288-7

Hackney, C. M., Mahendrasingam, S., Jones, E. M., and Fettiplace, R. (2003). The distribution of calcium buffering proteins in the turtle cochlea. *J. Neurosci.* 23, 4577–4589. doi: 10.1523/jneurosci.23-11-04577.2003

Hackney, C. M., Mahendrasingam, S., Penn, A., and Fettiplace, R. (2005). The concentrations of calcium buffering proteins in mammalian cochlear hair cells. *J. Neurosci.* 25, 7867–7875. doi: 10.1523/jneurosci.1196-05.2005

Heizmann, C. W., and Hunziker, W. (1991). Intracellular calcium-binding proteins: more sites than insights. *Trends Biochem. Sci.* 16, 98–103. doi: 10.1016/0968-0004(91)90041-s

Hiraoka, I., Suzuki, M., Harada, V., Tagashira, N., and Takumida, M. (1995). Anatomical and physiological characteristics of the vestibular ganglion of the bull frog. *Acta Otolaryngol. Suppl.* 519, 253–256. doi: 10.3109/00016489509121917

Hoffman, L. F., Choy, K. R., Sultemeier, D. R., and Simmons, D. D. (2018). Oncomodulin expression reveals new insights into the cellular organization of the murine utricle striola. *J. Assoc. Res. Otolaryngol.* 19, 33–51. doi: 10.1007/s10162-017-0652-6

Holt, J. C., Kewin, K., Jordan, P. M., Cameron, P., Klapczynski, M., McIntosh, J. M., et al. (2015). Pharmacologically distinct nicotinic acetylcholine receptors drive efferent-mediated excitation in calyx-bearing vestibular afferents. *J. Neurosci.* 35, 3625–3643. doi: 10.1523/jneurosci.3388-14.2015

Honrubia, V., Hoffmann, L. F., Sitko, S., and Schwartz, I. R. (1989). Anatomic and physiological correlates in bullfrog vestibular nerve. *J. Neurophysiol.* 61, 688–701. doi: 10.1152/jn.1989.61.4.688

Honrubia, V., Sitko, S., Kimm, J., Betts, W., and Schwartz, I. R. (1981). Physiological and anatomical characteristics of primary vestibular afferent neurons in the bullfrog. *Int. J. Neurosci.* 15, 197–206. doi: 10.3109/00207458108985857

Imamura, S., and Adams, J. C. (1996). Immunolocalization of peptide 19 and other calcium-binding proteins in the guinea pig cochlea. *Anat. Embryol.* 194, 407–418.

Jaramillo, F. (1995). Signal transduction in hair cells and its regulation by calcium. *Neuron* 15, 1227–1230. doi: 10.1016/0896-6273(95)90003-9

Jordan, P. M., Fettis, M., and Holt, J. C. (2015). Efferent innervation of turtle semicircular canal cristae: comparisons with bird and mouse. *J. Comp. Neurol.* 523, 1258–1280. doi: 10.1002/cne.23738

Kerschbaum, H. H., and Hermann, A. (1993). Calcium-binding proteins in the inner ear of *Xenopus laevis* (Daudin). *Brain Res.* 617, 43–49. doi: 10.1016/0006-8993(93)90610-y

Kevetter, G. A., and Leonard, R. B. (2002a). Molecular probes of the vestibular nerve. I. Peripheral termination patterns of calretinin, calbindin and peripherin containing fibers. *Brain Res.* 928, 8–17. doi: 10.1016/s0006-8993(01)03268-1

Kevetter, G. A., and Leonard, R. B. (2002b). Molecular probes of the vestibular nerve. II. Characterization of neurons in Scarpa's ganglion to determine separate populations within the nerve. *Brain Res.* 928, 18–29. doi: 10.1016/s0006-8993(01)03264-4

Koyama, H., Lewis, E. R., Leverenz, E. L., and Baird, R. A. (1982). Acute seismic sensitivity in the bullfrog ear. *Brain Res.* 250, 168–172. doi: 10.1016/0006-8993(82)90964-7

Lewis, E. R., and Li, C. W. (1973). Evidence concerning the morphogenesis of saccular receptors in the bullfrog (*Rana catesbeiana*). *J. Morph.* 139, 351–362. doi: 10.1002/jmor.1051390305

Lewis, E. R., and Li, C. W. (1975). Hair cell types and distributions in the otolithic and auditory organs of the bullfrog. *Brain Res.* 83, 35–50. doi: 10.1016/0006-8993(75)90856-2

Lewis, E. R., Baird, R. A., Leverenz, E. L., and Koyama, H. (1982a). Inner ear: dye injection reveals peripheral origins of specific sensitivities. *Science* 215, 1641–1643. doi: 10.1126/science.6978525

Lewis, E. R., Leverenz, E. L., and Koyama, H. (1982b). The tonotopic organization of the bullfrog amphibian papilla, an auditory organ lacking a basilar membrane. *J. Comp. Physiol. A* 145, 437–445. doi: 10.1007/bf00612809

Lysakowski, A., Gaboyard-Niay, S., Calin-Jageman, I., Chatlani, S., Price, S. D., and Eatock, R. A. (2011). Molecular microdomains in a sensory terminal, the vestibular calyx ending. *J. Neurosci.* 31, 10101–10114. doi: 10.1523/jneurosci.0521-11.2011

MacNaughton, I. P., and McNally, W. J. (1946). Some experiments which indicate that the frog's lagena has an equilibrial function. *J. Laryngol. Otol.* 61, 204–214. doi: 10.1017/s0022215100007842

Moffat, A. J., and Capranica, R. R. (1976). Auditory sensitivity of the saccule in the American toad (*Bufo americanus*). *J. Comp. Physiol. A* 105, 1–8. doi: 10.1007/bf01380048

Pack, A. K., and Slepecky, N. B. (1995). Cytoskeletal and calcium-binding proteins in the mammalian organ of Corti: cell type-specific proteins displaying longitudinal and radial gradients. *Hear. Res.* 91, 119–135. doi: 10.1016/0378-5955(95)00173-5

Pantle, C., and Dieringer, N. (1998). Spatial transformation of semicircular canal signals into abducens motor signals. A comparison between grass frogs and water frogs. *J. Comp. Physiol. A* 182, 475–487. doi: 10.1007/s003590050195

Paulin, M. G., and Hoffman, L. F. (2019). Models of vestibular semicircular canal afferent neuron firing activity. *J. Neurophysiol.* 122, 2548–2567. doi: 10.1152/jn.00087.2019

Prins, T. J., Myers, Z. A., Saldate, J. J., and Hoffman, L. F. (2020). Calbindin expression in adult vestibular epithelia. *J. Comp. Physiol. A* 206, 623–637. doi: 10.1007/s00359-020-01418-6

Raymond, J., Dechesne, C. J., Desmadryl, G., and Demêmes, D. (1993). Different calcium-binding proteins identify subpopulations of vestibular ganglion neurons in the rat. *Acta Otolaryngol.* 503, 114–118. doi: 10.3109/00016489309128090

Reichenberger, I., and Dieringer, N. (1994). Size-related colocalization of glycine and glutamate immunoreactivity in frog and rat vestibular afferents. *J. Comp. Neurol.* 349, 603–614. doi: 10.1002/cne.903490408

Roberts, W. M. (1993). Spatial calcium buffering in saccular hair cells. *Nature* 363, 74–76. doi: 10.1038/363074a0

Ronken, D. A. (1991). Spike discharge properties that are related to the characteristic frequency of single units in the frog auditory nerve. *J. Acoust. Soc. Am.* 90, 2428–2440. doi: 10.1121/1.402047

Saidel, W. M., Presson, J. C., and Chang, J. S. (1990). S-100 immunoreactivity identifies a subset of hair cells in the utricle and saccule of a fish. *Hear. Res.* 47, 139–146. doi: 10.1016/0378-5955(90)90171-k

Schwaller, B. (2002). 'New' functions for 'old' proteins: the role of the calcium-binding proteins calbindin D-28k, calretinin and parvalbumin, in cerebellar physiology. Studies with knockout mice. *Cerebellum* 1, 241–258. doi: 10.1080/147342202320883551

Schwaller, B., Buchwald, P., Blümcke, I., Celio, M. R., and Hunziker, W. (1993). Characterization of a polyclonal antiserum against the purified human recombinant calcium-binding protein calretinin. *Cell Calcium* 14, 639–648. doi: 10.1016/0143-4160(93)90089-o

Schwartz, J. J., and Simmons, A. M. (1990). Encoding of a spectrally-complex communication sound in the bullfrog's auditory nerve. *J. Comp. Physiol. A* 166, 489–499.

Simmons, D. D., Bertolotto, C., and Narins, P. M. (1994). Morphological gradients in sensory hair cells of the amphibian papilla of the frog, *Rana pipiens pipiens*. *Hear. Res.* 80, 71–78. doi: 10.1016/0378-5955(94)90010-8

Simmons, D. D., Tong, B., Schrader, A. D., and Hawkes, A. J. (2010). Oncomodulin identifies different hair cell types in the mammalian inner ear. *J. Comp. Neurol.* 518, 3785–3802. doi: 10.1002/cne.22424

Straka, H., and Dieringer, N. (2004). Basic organization principles of the VOR: lessons from frogs. *Prog. Neurobiol.* 73, 259–309. doi: 10.1016/j.pneurobio.2004.05.003

Suarez, C., Kuruvilla, A., Sitko, S., Schwartz, I. R., and Honrubia, V. (1985). Central projections of primary vestibular fibers in the bullfrog. II. Nerve branches from individual receptors. *Laryngoscope* 95, 1238–1250.

Wersäll, J., and Bagger-Sjöback, D. (1974). "Morphology of the vestibular sense organ," in *Handbook of Sensory Physiology. Vestibular system. Basic Mechanisms*, ed. H. H. Kornhuber (New York: Springer), 123–170. doi: 10.1007/978-3-642-65942-3_4

Zheng, J. L., and Gao, W.-Q. (1997). Analysis of rat vestibular hair cell development and regeneration using calretinin as an early marker. *J. Neurosci.* 17, 8270–8282. doi: 10.1523/JNEUROSCI.17-21-08270.1997

Conflict of Interest: The authors declare that the research was conducted in the absence of any commercial or financial relationships that could be construed as a potential conflict of interest.

frontiers in Neuroscience

REVIEW
published: 26 July 2021
doi: 10.3389/fnins.2021.695268

Preferential Cochleotoxicity of Cisplatin

Pattarawadee Prayuenyong[1,2†], David M. Baguley[2,3,4†], Corné J. Kros[5†] and Peter S. Steyger[6†]*

[1] Department of Otorhinolaryngology, Head and Neck Surgery, Faculty of Medicine, Prince of Songkla University, Songkhla, Thailand, [2] Hearing Sciences, Division of Clinical Neurosciences, School of Medicine, University of Nottingham, Nottingham, United Kingdom, [3] National Institute for Health Research (NIHR) Nottingham Biomedical Research Centre, Nottingham, United Kingdom, [4] Nottingham Audiology Services, Nottingham University Hospitals NHS Trust, Nottingham, United Kingdom, [5] School of Life Sciences, University of Sussex, Brighton, United Kingdom, [6] Translational Hearing Center, Biomedical Sciences, Creighton University, Omaha, NE, United States

OPEN ACCESS

Edited by:
Gwenaelle S. G. Geleoc, Boston Children's Hospital and Harvard Medical School, United States

Reviewed by:
Hernan Lopez-Schier, Helmholtz Zentrum München, Helmholtz-Gemeinschaft Deutscher Forschungszentren (HZ), Germany
Suhrud Rajguru, University of Miami, United States

***Correspondence:**
David M. Baguley
David.baguley@nottingham.ac.uk

†ORCID:
Pattarawadee Prayuenyong
orcid.org/0000-0002-3002-0497
David M. Baguley
orcid.org/0000-0002-0767-0723
Corné J. Kros
orcid.org/0000-0003-1429-4145
Peter S. Steyger
orcid.org/0000-0002-6103-5237

Specialty section:
This article was submitted to Perception Science, a section of the journal Frontiers in Neuroscience

Received: 14 April 2021
Accepted: 06 July 2021
Published: 26 July 2021

Citation:
Prayuenyong P, Baguley DM, Kros CJ and Steyger PS (2021) Preferential Cochleotoxicity of Cisplatin. Front. Neurosci. 15:695268. doi: 10.3389/fnins.2021.695268

Cisplatin-induced ototoxicity in humans is more predominant in the cochlea than in the vestibule. Neither definite nor substantial vestibular dysfunction after cisplatin treatment has been consistently reported in the current literature. Inner ear hair cells seem to have intrinsic characteristics that make them susceptible to direct exposure to cisplatin. The existing literature suggests, however, that cisplatin might have different patterns of drug trafficking across the blood-labyrinth-barrier, or different degrees of cisplatin uptake to the hair cells in the cochlear and vestibular compartments. This review proposes an explanation for the preferential cochleotoxicity of cisplatin based on current evidence as well as the anatomy and physiology of the inner ear. The endocochlear potential, generated by the stria vascularis, acting as the driving force for hair cell mechanoelectrical transduction might also augment cisplatin entry into cochlear hair cells. Better understanding of the stria vascularis might shed new light on cochleotoxic mechanisms and inform the development of otoprotective interventions to moderate cisplatin associated ototoxicity.

Keywords: cisplatin, ototoxicity, cochlea, vestibular, cochleotoxicity, vestibulotoxicity

INTRODUCTION

Cisplatin (platinum-based chemotherapy), is the mainstay treatment for curative care of various cancers (Makovec, 2019). Ototoxicity is a common side effect of cisplatin which can limit its usage and dosage (Qi et al., 2019). Ototoxicity refers to drug-induced damage affecting the inner ear structures and related neural tissues, causing cochlear dysfunction (such as hearing loss or tinnitus) and/or vestibular dysfunction (such as vertigo, dizziness, or imbalance) or both (Lanvers-Kaminsky et al., 2017). The damage can manifest in cellular degeneration and/or functional impairment. Unlike other side effects of cisplatin (such as nephrotoxicity), ototoxicity can cause irreversible injury to the inner ear as human inner ear sensory hair cells generally cannot regenerate (Rubel et al., 2013). Furthermore, no known effective protective or curative strategies are presently available for cisplatin-induced ototoxicity although clinical trial data is emerging (Mukherjea et al., 2020).

This review gleans the current evidence of cisplatin-induced ototoxicity and the mechanisms in the light of existing literature and data. Possible mechanisms are suggested as to why

cisplatin predominantly affects the cochlea while relatively sparing the vestibular counterpart based on available preclinical and clinical data.

SIMILARITIES AND DIFFERENCES OF COCHLEAR AND VESTIBULAR ORGANS

The cochlear (responsible for hearing) and vestibular (responsible for balance) parts of the inner ear have a very close anatomical relationship, and share a common source of blood and fluid supplies (Flint et al., 2014). These two components have replete similarities in anatomy, cellular and molecular components. The perilymph and endolymph of both structures have similar electrolyte compositions—the perilymph containing low potassium (K^+) and high sodium (Na^+) concentrations, and the endolymph containing high K^+ and low Na^+ concentrations. Specific cells and structures are required to maintain the electrolyte concentrations and homeostasis of the inner ear fluid (Koppl et al., 2018). Active transport mechanisms and essential structures for cation transport (e.g., Na^+/K^+-ATPase, Na^+-K^+-$2Cl^-$ cotransporter and mitochondria) are needed to maintain a very high K^+ concentration and recycling of electrolytes into endolymph (Wangemann, 1995; Ciuman, 2009). Vestibular and cochlear sensory hair cells, responsible for mechanosensation, are comparable in many respects including shape, morphology and the arrangement of stereocilia at the apical membrane.

However, a major physiological difference of both structures is the endolymphatic potential. The endolymphatic potential is a K^+ equilibrium diffusion potential, in the cochlea across the apical membranes of the intermediate cells in the stria vascularis (Wangemann, 2002). Considering the inner ear as an electrical field, the endolymphatic potential is the quantity that determines the energy of charge. The endocochlear potential is as high as +80–100 mV (relative to perilymph) while the endovestibular potential is only up to + 10 mV. Mammals have an extremely high endocochlear potential compared to other animal species (Koppl et al., 2018). It is suggested that positive extracellular potentials around the hair cells augment the electrical gradient that is the major driving force for K^+ and Ca^{2+} (calcium) influx during sensory transduction and subsequently enhance the neurotransmission of sounds (Hibino and Kurachi, 2006; Koppl et al., 2018). In contrast, the vestibular compartment demands lower endolymphatic potentials for its proper function, and equivalently has an endolymphatic potential of less than +10–15 mV among different species (fish, amphibia, reptiles, birds, and mammals) (Koppl et al., 2018). Lee and Jones (2018) demonstrated the functional discrepancy of both compartments after the disruption of K^+ concentration causing acute reductions in the endolymphatic potentials in mice. While the cochlear response was significantly reduced as it requires a large transepithelial electrical potential for appropriate function, the vestibular response was unaffected as it is relatively insensitive to changes in the endolymphatic potentials.

The marginal cells of the cochlea, and the dark cells of the vestibule are responsible for endolymph production and homeostasis in maintaining the high K^+ concentration (Takeuchi et al., 2000; Ciuman, 2009). Despite the morphological and functional similarities of both cells, the marginal cells are part of the multi-layered stria vascularis, while the vestibular dark cells form a single-layered epithelium (Ciuman, 2009). The complex structure of the stria vascularis at the lateral wall of the endolymphatic space of the cochlea - consisting of marginal, intermediate and basal cell layers—seems to underlie the high endocochlear potential. Intermediate cells and basal cells of the stria vascularis, and fibrocytes in the adjacent spiral ligament are responsible for the generation of the endocochlear potential (Takeuchi et al., 2000; Marcus et al., 2002). On the other hand, there is no analogous structure in the vestibular organ. Cochlear and vestibular structures and supporting cells are illustrated in **Figure 1**.

PRECLINICAL DATA OF CISPLATIN OTOTOXICITY

Cisplatin is a cell-cycle non-specific agent that can kill a cell during any phase of the cell cycle, and so can act on both proliferating and non-proliferating cells (Mills et al., 2018). The neutral cisplatin is activated when it enters human cells, in that one or both of the chloride ions can rapidly be substituted by water (aquation) resulting in monovalent or divalent cations (Makovec, 2019).

The cytotoxic effects of cisplatin may occur via at least two major mechanisms. One mechanism is the formation of DNA (deoxyribonucleic acid) adducts, leading to DNA denaturation which blocks cell division processes (Makovec, 2019). Another mechanism of action involves the increased formation of reactive oxygen species and oxidative stress (Rybak et al., 2019). The intracellular pathway remains unclear but it seems to be related to apoptosis (programmed cell death) and necroptosis (programmed necrosis or inflammatory cell death) pathways (Callejo et al., 2015; Ruhl et al., 2019). These mechanisms ultimately lead to cell death via apoptosis (Mitra et al., 2017).

Preclinical Data of Cochleotoxicity

The suggested pathway of cisplatin trafficking from the bloodstream into the cochlea is displayed in **Figure 2**. To cause ototoxic damage, cisplatin must first cross the blood-labyrinth barrier, a specialized structure consisting of tight junction-coupled inner ear endothelial cells, which separates the inner ear tissues from the blood stream. The small size of the cisplatin molecule allows it to enter the inner ear via the blood-labyrinth barrier at the stria vascularis (Karasawa and Steyger, 2015; Chu et al., 2016; Breglio et al., 2017). Cisplatin then enters the endolymph in the scala media, potentially via the organic cation transporter 2 (OCT2) and/or copper transporter 1 (CTR1) in the marginal cells. Drug clearance from the stria vascularis into the endolymph seems to be a major contributing factor for ototoxicity among platinum-based chemotherapy (Ding et al., 2012; Gersten et al., 2020). From the endolymph, cisplatin can enter the cochlear hair cells via a variety of cation transporters, *via* the mechanoelectrical transduction

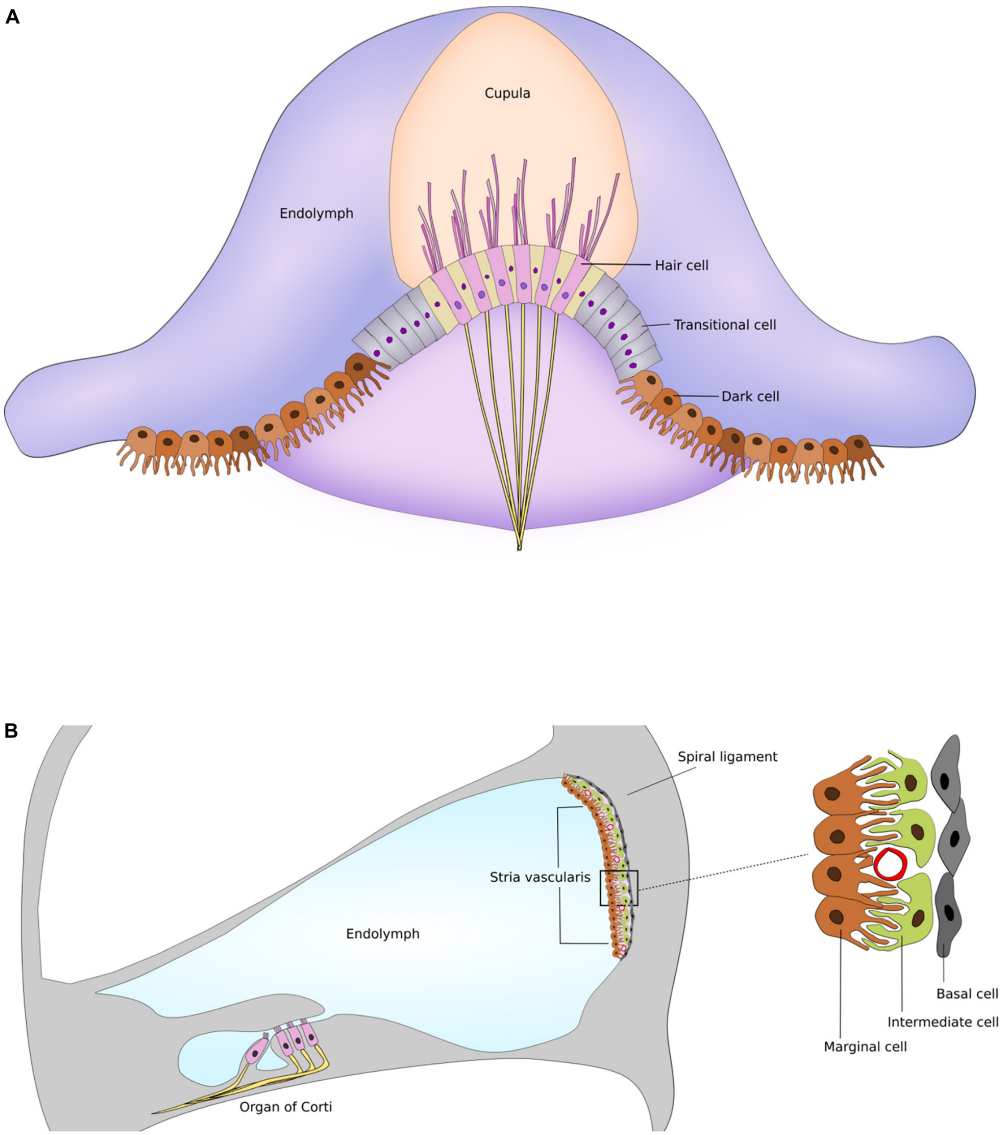

FIGURE 1 | Supporting cells and structures of the inner ear. **(A)** Schematic drawing of dark cells and transitional cells in the semicircular canal. **(B)** Schematic drawing of stria vascularis within the cochlea illustrating the marginal, intermediate and basal cell layers. Figures are not drawn to scale.

channel pore, transmembrane channel-like protein 1 (TMC1), or by passive diffusion at apical membranes (Pabla et al., 2009; Ding et al., 2012; Waissbluth and Daniel, 2013; Kros and Steyger, 2018). Furthermore, platinum is retained in the human cochlea for many months to years after cisplatin treatment, while it is eliminated over the following days to weeks in other organs (Breglio et al., 2017). The hyper-deposition of cisplatin in the human cochlea appears to be a unique important mechanism of progressive and delayed-onset cisplatin-induced cochleotoxicity. It is suggested that cochlear cells are susceptible to cisplatin because of high drug uptake, high metabolic rate of these cells, and long-term retention of the drug (Schacht et al., 2012; Breglio et al., 2017).

The mechanisms of cisplatin-induced cochlear dysfunction are associated with cellular damage as well as disruption of cochlear homeostasis. After cisplatin administration, cellular degeneration was observed in outer hair cells of the organ of Corti, marginal cells of the stria vascularis, spiral ganglion cells, and synaptopathy between inner hair cells and spiral ganglion neurons (Brock et al., 2012; Chen et al., 2021).

Marginal cells of the stria vascularis could be the earliest targets of cisplatin ototoxicity (Thomas et al., 2006). Damage of the stria vascularis triggers functional alterations and apoptotic damage resulting in a reduced generation of the endocochlear potential and a disturbance in the electrolyte composition of endolymph, both of which are required for optimal auditory function (Laurell et al., 2007). A temporary reduction and recovery of endocochlear potential after cisplatin administration has been reported (Klis et al., 2002; Sluyter et al., 2003; Breglio et al., 2017). This occurrence could be primarily responsible

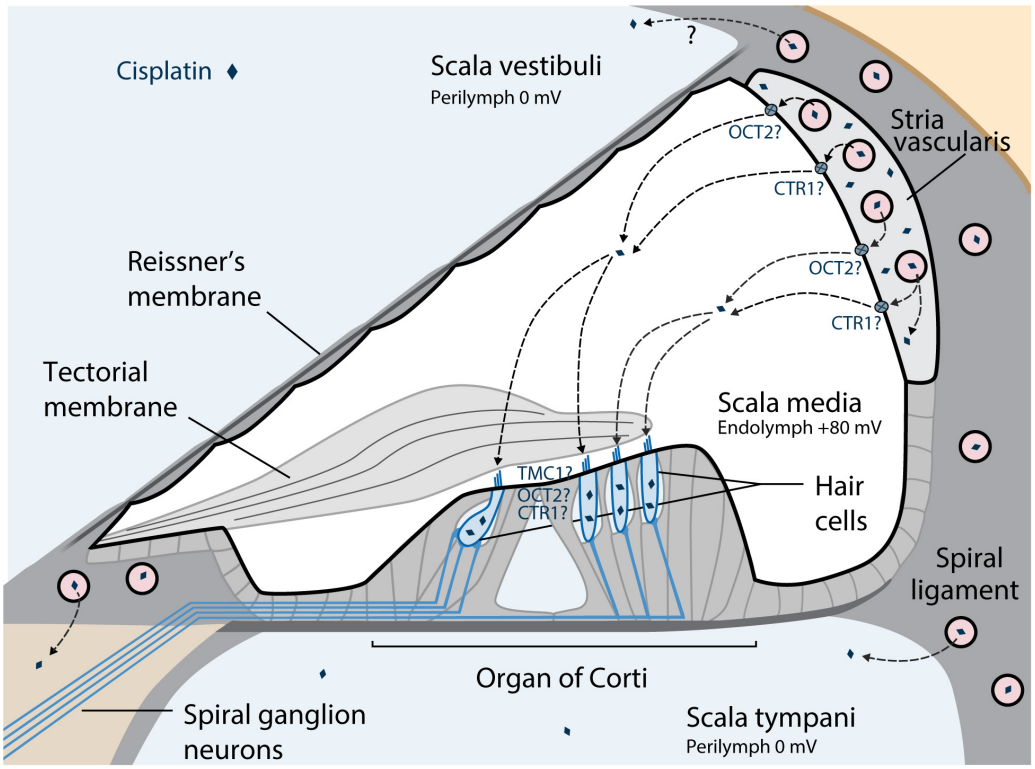

FIGURE 2 | Suggested pathways of cisplatin trafficking in the cochlea. The major entry route for cisplatin entry into the cochlea is via the blood-strial barrier into the stria vascularis, and clearance into the endolymph from the stria vascularis prior to entry into hair cells across their apical membrane. Reproduced with modifications from Kros and Steyger (2018) with permission of Cold Spring Harbor Laboratory Press. OCT2, Organic cation transporter; CTR1, Copper transporter 1; TMC1, Transmembrane channel-like protein 1.

for very early short-term reversible hearing loss after cisplatin exposure when a very slight degeneration of cochlear hair cells was reported (Tsukasaki et al., 2000; Klis et al., 2002). Cochlear function then recovers in parallel with the restoration of the endocochlear potential as long as the hair cells remain intact.

Cochlear outer hair cells showed the most prominent damage after cisplatin treatment, suggesting that they are more susceptible to injury and have a limited capacity for recovery (Callejo et al., 2015). Permanent hair cell loss is thought to be responsible for long-term irreversible hearing loss (Tsukasaki et al., 2000; Klis et al., 2002). Hair cell apoptosis could be caused by either direct injury after cisplatin entrance, or an indirect effect related to the disruption of cochlear fluid homeostasis.

Preclinical Data of Vestibulotoxicity

There are fewer reports in the literature about cisplatin vestibulotoxicity than about cochleotoxicity. After topical cisplatin administration, degeneration of vestibular hair cells in utricular macula and cochlear outer hair cells was similar (Zhang et al., 2003; Cunningham and Brandon, 2006; Schmitt et al., 2009). Likewise, a parallel degree of vestibular and cochlear hair cells loss was reported after trans-tympanic cisplatin administration in the rat (Callejo et al., 2017). These results indicate that cisplatin, by local administration, seems to have a similar effect on hair cells of both compartments. However, the direct cisplatin exposure routes in these studies are not standard methods of cisplatin treatment in humans and so they lack the potential to evaluate physiological pharmacokinetics, especially vascularity and blood-labyrinth barrier function.

Conversely, minimal or no impact upon vestibular hair cells was reported after systemic cisplatin administration in guinea pigs, whereas there was a substantial loss of cochlear outer hair cells within the same setting (Schweitzer et al., 1986; Laurell and Bagger-Sjoback, 1991; Sergi et al., 2003). A minor loss of hair bundles after cisplatin exposure was also described (Nakayama et al., 1996; Ding et al., 1997). Overall, no study demonstrated extensive histological deterioration of vestibular organs after systemic cisplatin exposure as in analogous cochlear studies.

In animal models, some functional vestibular loss has been identified after cisplatin administration in semicircular canals (Sergi et al., 2003; Cheng et al., 2006; Takimoto et al., 2016), and otolith organs (Lo et al., 2015). The fact that morphological vestibular damage was not found at an early stage suggests that functional vestibular impairment may not be associated with sensory hair cell damage but other biochemical factors that cannot be seen in histological results (e.g., electrolyte or electropotential disturbance).

Currently, there is no study of cisplatin trafficking, uptake, and disruption of intracellular physiological pathways in the vestibular organs. It is possible that it involves the vestibular

equivalent of the stria vascularis (dark cells and/or the transitional cells surrounding vestibular sensory epithelia, that are responsible for endolymph production and homeostasis) which has been demonstrated for aminoglycoside antibiotics (Liu et al., 2015; Kros and Steyger, 2018).

CLINICAL DATA OF CISPLATIN OTOTOXICITY

Clinical Data of Cochleotoxicity

Hearing loss to variable degrees has been reported in 40–80% of patients treated with cisplatin depending on patient characteristics, drug dosage, and differences in tools and grading system (Landier et al., 2014; Frisina et al., 2016). The typical characteristics of cisplatin-induced hearing loss are irreversible, bilateral symmetrical sensorineural hearing loss affecting higher frequencies initially, then followed by lower frequencies (Rybak et al., 2019). Hearing loss often occurs in a dose-related and cumulative fashion (Landier, 2016; Paken et al., 2016). Forty percent of testicular cancer survivors who received cisplatin also complained of tinnitus which was significantly correlated with reduced hearing (Frisina et al., 2016). Therefore, monitoring of cochleotoxic effects of cisplatin is advised and implemented in clinical practice (Brooks and Knight, 2017; Clemens et al., 2019; Sprouse and Gozdecki, 2019). Age- and sex-adjusted audiometry is also suggested in long-term follow-up of adult cancer survivors to minimize the effects of age-related hearing loss (Skalleberg et al., 2020).

The phenomenon of cochlear dead regions involves loss of inner hair cells whilst outer hair cells are intact, can lead to difficulty understanding speech in noisy environments. This situation has been reported in a small cohort of adults who had undergone cisplatin chemotherapy (Schultz et al., 2019) but this result has not yet been corroborated by other studies.

Clinical Data of Vestibulotoxicity

The clinical evidence regarding the potential of cisplatin vestibulotoxicity is limited in the published literature. The reported rate of abnormal caloric or rotational tests associated with cisplatin varied considerably from 0 to 50% (Prayuenyong et al., 2018). Some limitations of published studies include small numbers of patients, and different methods of evaluation and of criteria for abnormality.

Recently, we reported that all of a group of 65 adult survivors of cancer who had completed cisplatin treatment had normal video Head Impulse Test (vHIT) results (Prayuenyong et al., 2021). On the other hand, 14% of patients complained of hearing change after cisplatin treatment, 44% had new-onset or worsening tinnitus, and 29% had abnormal audiogram results which are in line with current literature in cancer survivors receiving standard dosage of cisplatin (100–400 mg/m^2). The normal vHIT results indicate that the vestibulo-ocular reflex (VOR) activity is unaffected after cisplatin treatment. No evidence of corrective saccades was found, indicating that there was no subclinical vestibular impairment. The vHIT has the major advantage of specificity but at the expense of sensitivity (Halmagyi et al., 2017). This means that a positive finding of abnormality on vHIT can strongly rule in vestibular disorder, but that a negative result may not be relied upon to exclude vestibular pathology. However, the vHIT assesses VOR function in the high frequency where it is physiologically most relevant. Additionally, benign paroxysmal positional vertigo (BPPV) was relatively prevalent in this group of patients (9.2%). This figure is higher than the life-time prevalence of BPPV (2%) (von Brevern et al., 2007), and vertigo (7%) (Neuhauser et al., 2005) in the adult general population.

To date, there is no study of patients treated with cisplatin that incorporates the caloric test, rotational chair test, and vHIT to evaluate the VOR across different frequency ranges in the same setting. In case of aminoglycoside ototoxicity, vestibular function in low-mid frequency ranges was selectively affected but high frequency function was spared (Walther, 2017). It is thus possible that the caloric and rotational chair tests are more sensitive tools to detect vestibular impairment after ototoxic medication treatment (American Academy of Audiology, 2009).

PROPOSED HYPOTHESIS OF PREFERENTIAL COCHLEOTOXICITY OF CISPLATIN

In general, cisplatin affects both cochlear structure and function, yet has a much lower likelihood to do so in the vestibular organ. One plausible explanation is that cisplatin does affect vestibular end organs, yet only a relatively low occurrence of vestibular symptoms is reported due to bilateral effects, insidious onset, and effective compensation mechanisms (Lacour et al., 2016). However, the current evidence does not support this notion and rather suggests that cisplatin does not cause vestibular insult or does so to a very limited extent. This raises the question why the cochlea is more vulnerable while the vestibule is generally preserved after cisplatin treatment.

The observations regarding morphological, biochemical, and functional changes after cisplatin exposure might shed some lights on the mechanisms of ototoxicity. The distinct patterns of hair cell loss after topical and systemic cisplatin administration could be explained by different drug trafficking across the blood-labyrinth-barrier or different degrees of cisplatin entry into sensory hair cells in the cochlear and vestibular compartments. Different endolymphatic potential status and supporting structures of the cochlear and the vestibular labyrinth might explain this phenomenon. The high electrochemical driving force of the endocochlear potential at 80–100 mV might strongly drive cisplatin, provided it is in its aquated, positively charged forms, to enter the hair cells (Koppl et al., 2018; Kros and Steyger, 2018). This is boosted by the −40 to −70 mV resting membrane potential of cochlear hair cells to generate a substantial electrical gradient of 120–170 mV across the apical membrane of the hair cells (Kros and Steyger, 2018). The vestibular endolymph has a smaller endolymphatic potential of 0–10 mV; thus, cisplatin might be less likely to enter vestibular hair cells (Koppl et al., 2018). Note, however, that cisplatin is predominantly neutral in a chloride-rich

solution (which includes endolymph) and there is no study of cisplatin trafficking and concentration in the inner ear to support this assumption. Further studies are needed to tackle the issue of drug trafficking and uptake in the vestibular organs. Better understanding of the stria vascularis might shed further insight into the ototoxic mechanisms of cisplatin and otoprotective strategies to preserve hearing during systemic cisplatin treatment.

Cisplatin initially damages the outer hair cells at the basal turn of the cochlea, resulting in hearing loss at higher frequencies. There are at least two possible explanations for the sensitivity to cochleotoxic damage of cisplatin along the cochlear spiral. The first one relates to different drug distribution along the base-to-apex in the cochlea that facilitates greater cisplatin uptake in the basal part. Cisplatin signal intensity was highest in the cochlear base, and it generally decreased with progression toward the apex (Breglio et al., 2017). The concentration of cisplatin in scala tympani perilymph was fourfold higher in the basal turn of the cochlea than in the apex at 10 min after the administration (Hellberg et al., 2013). A second explanation concerns a greater intrinsic susceptibility of basal cochlear hair cells to cisplatin. Sha et al. (2001) showed that the base-to-apex vulnerability of hair cells remained when all parts of *ex vivo*, organotypic cultures of the cochlea were exposed to cisplatin. Also, they found a significant lower level of the antioxidant glutathione in basal outer hair cells compared with apical outer hair cells, suggesting that basal outer hair cells are more vulnerable to free-radical damage than apical ones. On the other hand, the preferential frequency of cisplatin vestibulotoxicity is unclear. It is possible that vestibular impairment is not homogenous across the frequency range. Unlike the cochlea, which has a well-structured tonotopic arrangement, the motion- and vibration-sensitive arrangement of the vestibular organs is not well structured.

A recent finding of the relatively high prevalence of BPPV after cisplatin treatment is of interest in this regard (Prayuenyong et al., 2021). The pathophysiology of BPPV involves displaced otoconia (extracellular calcium crystalline structures) from the utricular macula into the semicircular canal (Lee and Kim, 2010). It is associated with biochemical disruption of inner ear fluid, particularly Ca^{2+} metabolism, which is not necessarily correlated with hair cell injury. Cisplatin could cause electrochemical alteration of Ca^{2+} homeostasis in the vestibular compartment rather than hair cell damage (Scott et al., 1995). The reduction of Ca^{2+} concentration in endolymph induces the release of Ca^{2+} from otoconia and otoconial detachment from the otolithic membranes. Alternatively, limited physical activities due to general fatigue of cancer patients could also underlie the relatively high rate of BPPV in this sample (Pollak et al., 2011). These observations warrant further investigation, especially the effect of cisplatin in disrupting ionic hemostasis in the inner ear.

CONCLUSION

In general, cisplatin ototoxicity appears to target cochlear structures resulting in hearing loss and/or tinnitus. Definite vestibular dysfunction after cisplatin treatment has not been consistently reported in the current literature. Cisplatin might have different pattern of drug trafficking across the blood-labyrinth-barrier or varying degrees of entry into hair cells in the cochlear and vestibular compartments. The endocochlear potential might also increase uptake of aquated cisplatin into the cochlear hair cells through cation transporters or the mechanoelectrical transduction channels. Although the VOR was generally unaffected, other vestibular effects of cisplatin such as biochemical disruption are possible. Further investigations are warranted for greater insight into the mechanisms of cisplatin trafficking, cellular uptake kinetics, and electrochemical disruptions. Better understanding of the stria vascularis might shed new light on ototoxic mechanisms and inform the development of otoprotective interventions to moderate cisplatin-induced ototoxicity.

AUTHOR CONTRIBUTIONS

PP wrote, revised, and edited the manuscript. DB wrote, reviewed, revised, and edited the manuscript. CK and PS reviewed and edited the manuscript. All authors contributed to the article and approved the submitted version.

FUNDING

DB was supported by the UK National Institute for Health Research (NIHR), but his views are his own and do not represent those of the NIHR, nor the UK Department of Health and Social Care. CK was supported by the Royal National Institute for Deaf People (RNID). PS was funded by NIDCD R01 DC004555, NIDCD R01 DC016880 and NIGMS P20 GM139762, and by Creighton University.

REFERENCES

American Academy of Audiology (2009). *American Academy of Audiology Position Statement and guidelines: Ototoxicity monitoring.* Reston, VA: American Academy of Audiology. Available online at: https://audiologyweb.s3.amazonaws.com/migrated/OtoMonGuidelines.pdf_539974c40999c1.58842217.pdf

Breglio, A. M., Rusheen, A. E., Shide, E. D., Fernandez, K. A., Spielbauer, K. K., McLachlin, K. M., et al. (2017). Cisplatin is retained in the cochlea indefinitely following chemotherapy. *Nat. Commun.* 8:1654. doi: 10.1038/s41467-017-01837-1

Brock, P. R., Knight, K. R., Freyer, D. R., Campbell, K. C., Steyger, P. S., Blakley, B. W., et al. (2012). Platinum-induced ototoxicity in children: a consensus review on mechanisms, predisposition, and protection, including a new International Society of Pediatric Oncology Boston ototoxicity scale. *J Clin. Oncol.* 30, 2408–2417. doi: 10.1200/JCO.2011.39.1110

Brooks, B., and Knight, K. (2017). Ototoxicity monitoring in children treated with platinum chemotherapy. *Int. J. Audiol.* 57, S34–S40. doi: 10.1080/14992027.2017.1355570

Callejo, A., Durochat, A., Bressieux, S., Saleur, A., Chabbert, C., Domenech Juan, I., et al. (2017). Dose-dependent cochlear and vestibular toxicity of trans-tympanic cisplatin in the rat. *Neurotoxicology* 60, 1–9. doi: 10.1016/j.neuro.2017.02.007

Callejo, A., Sedo-Cabezon, L., Juan, I. D., and Llorens, J. (2015). Cisplatin-Induced ototoxicity: effects, mechanisms and protection strategies. *Toxics* 3, 268–293. doi: 10.3390/toxics3030268

Chen, Y., Bielefeld, E. C., Mellott, J. G., Wang, W., Mafi, A. M., Yamoah, E. N., et al. (2021). Early physiological and cellular indicators of cisplatin-induced ototoxicity. *J. Assoc. Res. Otolaryngol.* 22, 107–126. doi: 10.1007/s10162-020-00782-z

Cheng, P. W., Liu, S. H., Young, Y. H., and Lin-Shiau, S. Y. (2006). D-Methionine attenuated cisplatin-induced vestibulotoxicity through altering ATPase activities and oxidative stress in guinea pigs. *Toxicol. Appl. Pharmacol.* 215, 228–236. doi: 10.1016/j.taap.2006.02.014

Chu, Y. H., Sibrian-Vazquez, M., Escobedo, J. O., Phillips, A. R., Dickey, D. T., Wang, Q., et al. (2016). Systemic delivery and biodistribution of cisplatin in vivo. *Mol. Pharm.* 13, 2677–2682. doi: 10.1021/acs.molpharmaceut.6b00240

Ciuman, R. R. (2009). Stria vascularis and vestibular dark cells: characterisation of main structures responsible for inner-ear homeostasis, and their pathophysiological relations. *J. Laryngol. Otol.* 123, 151–162. doi: 10.1017/s0022215108002624

Clemens, E., van den Heuvel-Eibrink, M. M., Mulder, R. L., Kremer, L. C. M., Hudson, M. M., Skinner, R., et al. (2019). Recommendations for ototoxicity surveillance for childhood, adolescent, and young adult cancer survivors: a report from the International Late Effects of Childhood Cancer Guideline Harmonization Group in collaboration with the PanCare Consortium. *Lancet Oncol.* 20, e29–e41. doi: 10.1016/s1470-2045(18)30858-1

Cunningham, L. L., and Brandon, C. S. (2006). Heat shock inhibits both aminoglycoside- and cisplatin-induced sensory hair cell death. *J. Assoc. Res. Otolaryngol.* 7, 299–307.

Ding, D., Allman, B. L., and Salvi, R. (2012). Review: ototoxic characteristics of platinum antitumor drugs. *Anat. Rec. (Hoboken)* 295, 1851–1867. doi: 10.1002/ar.22577

Ding, D., Wang, J., and Salvi, R. J. (1997). Early damage in the chinchilla vestibular sensory epithelium from carboplatin. *Audiol. Neurootol.* 2, 155–167.

Flint, P. W., Haughey, B. H., Robbins, K. T., Thomas, J. R., Niparko, J. K., Lund, V. J., et al. (2014). *Cummings Otolaryngology - Head and Neck Surgery E-Book*. Amsterdam: Elsevier Health Sciences.

Frisina, R. D., Wheeler, H. E., Fossa, S. D., Kerns, S. L., Fung, C., Sesso, H. D., et al. (2016). Comprehensive audiometric analysis of hearing impairment and tinnitus after cisplatin-based chemotherapy in survivors of adult-onset cancer. *J. Clin. Oncol.* 34, 2712–2720. doi: 10.1200/JCO.2016.66.8822

Gersten, B. K., Fitzgerald, T. S., Fernandez, K. A., and Cunningham, L. L. (2020). Ototoxicity and platinum uptake following cyclic administration of platinum-based chemotherapeutic agents. *J. Assoc. Res. Otolaryngol.* 21, 303–321. doi: 10.1007/s10162-020-00759-y

Halmagyi, G. M., Chen, L., MacDougall, H. G., Weber, K. P., McGarvie, L. A., and Curthoys, I. S. (2017). The video head impulse test. *Front. Neurol.* 8:258. doi: 10.3389/fneur.2017.00258

Hellberg, V., Wallin, I., Ehrsson, H., and Laurell, G. (2013). Cochlear pharmacokinetics of cisplatin: an in vivo study in the guinea pig. *Laryngoscope* 123, 3172–3177. doi: 10.1002/lary.24235

Hibino, H., and Kurachi, Y. (2006). Molecular and physiological bases of the K+ circulation in the mammalian inner ear. *Physiology (Bethesda)* 21, 336–345.

Karasawa, T., and Steyger, P. S. (2015). An integrated view of cisplatin-induced nephrotoxicity and ototoxicity. *Toxicol. Lett.* 237, 219–227. doi: 10.1016/j.toxlet.2015.06.012

Klis, S. F., O'Leary, S. J., Wijbenga, J., de Groot, J. C., Hamers, F. P., and Smoorenburg, G. F. (2002). Partial recovery of cisplatin-induced hearing loss in the albino guinea pig in relation to cisplatin dose. *Hear. Res.* 164, 138–146. doi: 10.1016/s0378-5955(01)00425-7

Koppl, C., Wilms, V., Russell, I. J., and Nothwang, H. G. (2018). Evolution of endolymph secretion and endolymphatic potential generation in the vertebrate inner ear. *Brain Behav. Evol.* 92, 1–31. doi: 10.1159/000494050

Kros, C. J., and Steyger, P. S. (2018). Aminoglycoside- and cisplatin-induced ototoxicity: mechanisms and otoprotective strategies. *Cold Spring Harb. Perspect. Med.* 9:a033548. doi: 10.1101/cshperspect.a033548

Lacour, M., Helmchen, C., and Vidal, P. P. (2016). Vestibular compensation: the neuro-otologist's best friend. *J. Neurol.* 263(Suppl. 1), S54–S64. doi: 10.1007/s00415-015-7903-4

Landier, W. (2016). Ototoxicity and cancer therapy. *Cancer* 122, 1647–1658. doi: 10.1002/cncr.29779

Landier, W., Knight, K., Wong, F. L., Lee, J., Thomas, O., Kim, H., et al. (2014). Ototoxicity in children with high-risk neuroblastoma: prevalence, risk factors, and concordance of grading scales–a report from the Children's Oncology Group. *J. Clin. Oncol.* 32, 527–534. doi: 10.1200/jco.2013.51.2038

Lanvers-Kaminsky, C., Zehnhoff-Dinnesen, A. A., Parfitt, R., and Ciarimboli, G. (2017). Drug-induced ototoxicity: mechanisms, Pharmacogenetics, and protective strategies. *Clin. Pharmacol. Ther.* 101, 491–500. doi: 10.1002/cpt.603

Laurell, G., and Bagger-Sjoback, D. (1991). Dose-dependent inner ear changes after i.v. administration of cisplatin. *J. Otolaryngol.* 20, 158–167.

Laurell, G., Ekborn, A., Viberg, A., and Canlon, B. (2007). Effects of a single high dose of cisplatin on the melanocytes of the stria vascularis in the guinea pig. *Audiol. Neurootol.* 12, 170–178.

Lee, C., and Jones, T. A. (2018). Acute blockade of inner ear marginal and dark cell K(+) secretion: effects on gravity receptor function. *Hear. Res.* 361, 152–156. doi: 10.1016/j.heares.2018.02.002

Lee, S.-H., and Kim, J. S. (2010). Benign paroxysmal positional vertigo. *J. Clin. Neurol. (Seoul Korea)* 6, 51–63. doi: 10.3988/jcn.2010.6.2.51

Liu, J., Kachelmeier, A., Dai, C., Li, H., and Steyger, P. S. (2015). Uptake of fluorescent gentamicin by peripheral vestibular cells after systemic administration. *PLoS One* 10:e0120612. doi: 10.1371/journal.pone.0120612

Lo, W. C., Chang, C. M., Liao, L. J., Wang, C. T., Young, Y. H., Chang, Y. L., et al. (2015). Assessment of D-methionine protecting cisplatin-induced otolith toxicity by vestibular-evoked myogenic potential tests, ATPase activities and oxidative state in guinea pigs. *Neurotoxicol. Teratol.* 51, 12–20. doi: 10.1016/j.ntt.2015.07.004

Makovec, T. (2019). Cisplatin and beyond: molecular mechanisms of action and drug resistance development in cancer chemotherapy. *Radiol. Oncol.* 53, 148–158. doi: 10.2478/raon-2019-0018

Marcus, D. C., Wu, T., Wangemann, P., and Kofuji, P. (2002). KCNJ10 (Kir4.1) potassium channel knockout abolishes endocochlear potential. *Am. J. Physiol. Cell Physiol.* 282, C403–C407.

Mills, C. C., Kolb, E. A., and Sampson, V. B. (2018). Development of chemotherapy with cell-cycle inhibitors for adult and pediatric cancer therapy. *Cancer Res.* 78, 320–325. doi: 10.1158/0008-5472.CAN-17-2782

Mitra, R., Goddard, R., and Porschke, K. R. (2017). 9,9-Difluorobispidine analogues of cisplatin, Carboplatin, and Oxaliplatin. *Inorg. Chem.* 56, 6712–6724. doi: 10.1021/acs.inorgchem.7b00836

Mukherjea, D., Dhukhwa, A., Sapra, A., Bhandari, P., Woolford, K., Franke, J., et al. (2020). Strategies to reduce the risk of platinum containing antineoplastic drug-induced ototoxicity. *Expert Opin. Drug Metab. Toxicol.* 16, 965–982. doi: 10.1080/17425255.2020.1806235

Nakayama, M., Riggs, L. C., and Matz, G. J. (1996). Quantitative study of vestibulotoxicity induced by gentamicin or cisplatin in the guinea pig. *Laryngoscope* 106(2 Pt 1), 162–167.

Neuhauser, H. K., von Brevern, M., Radtke, A., Lezius, F., Feldmann, M., Ziese, T., et al. (2005). Epidemiology of vestibular vertigo: a neurotologic survey of the general population. *Neurology* 65, 898–904. doi: 10.1212/01.wnl.0000175987.59991.3d

Pabla, N., Murphy, R. F., Liu, K., and Dong, Z. (2009). The copper transporter Ctr1 contributes to cisplatin uptake by renal tubular cells during cisplatin nephrotoxicity. *Am. J. Physiol. Renal Physiol.* 296, F505–F511.

Paken, J., Govender, C. D., Pillay, M., and Sewram, V. (2016). Cisplatin-Associated ototoxicity: a review for the health professional. *J. Toxicol.* 2016:1809394. doi: 10.1155/2016/1809394

Pollak, L., Kushnir, M., and Goldberg, H. S. (2011). Physical inactivity as a contributing factor for onset of idiopathic benign paroxysmal positional vertigo. *Acta Otolaryngol.* 131, 624–627. doi: 10.3109/00016489.2011.552524

Prayuenyong, P., Kasbekar, A. V., Hall, D. A., Hennig, I., Anand, A., and Baguley, D. M. (2021). Imbalance associated with cisplatin chemotherapy in adult cancer survivors: a clinical study. *Otol. Neurotol.* 42, e730–e734. doi: 10.1097/mao.0000000000003079

Prayuenyong, P., Taylor, J. A., Pearson, S. E., Gomez, R., Patel, P. M., Hall, D. A., et al. (2018). Vestibulotoxicity associated with platinum-based chemotherapy in survivors of cancer: a scoping review. *Front. Oncol.* 8:363. doi: 10.3389/fonc.2018.00363

Qi, L., Luo, Q., Zhang, Y., Jia, F., Zhao, Y., and Wang, F. (2019). Advances in toxicological research of the anticancer drug cisplatin. *Chem. Res. Toxicol.* 32, 1469–1486. doi: 10.1021/acs.chemrestox.9b00204

Rubel, E. W., Furrer, S. A., and Stone, J. S. (2013). A brief history of hair cell regeneration research and speculations on the future. *Hear. Res.* 297, 42–51. doi: 10.1016/j.heares.2012.12.014

Ruhl, D., Du, T.-T., Wagner, E. L., Choi, J. H., Li, S., Reed, R., et al. (2019). Necroptosis and apoptosis contribute to cisplatin and aminoglycoside ototoxicity. *J. Neurosci.* 39, 2951–2964. doi: 10.1523/JNEUROSCI.1384-18.2019

Rybak, L. P., Mukherjea, D., and Ramkumar, V. (2019). Mechanisms of cisplatin-induced ototoxicity and prevention. *Semin. Hear.* 40, 197–204. doi: 10.1055/s-0039-1684048

Schacht, J., Talaska, A. E., and Rybak, L. P. (2012). Cisplatin and aminoglycoside antibiotics: hearing loss and its prevention. *Anat. Rec. (Hoboken)* 295, 1837–1850. doi: 10.1002/ar.22578

Schmitt, N. C., Rubel, E. W., and Nathanson, N. M. (2009). Cisplatin-induced hair cell death requires STAT1 and is attenuated by epigallocatechin gallate. *J. Neurosci.* 29, 3843–3851. doi: 10.1523/jneurosci.5842-08.2009

Schultz, C., Pecora Liberman, P. H., and Schmidt Goffi-Gomez, M. V. (2019). Are there cochlear dead regions involved in hearing loss after cisplatin ototoxicity? *Audiol. Neurootol.* 24, 253–257. doi: 10.1159/000502250

Schweitzer, V. G., Rarey, K. E., Dolan, D. F., Abrams, G. E., and Sheridan, C. (1986). Vestibular morphological analysis of the effects of cisplatin vs. platinum analogs, CBDCA (JM-8) and CHIP (JM-9). *Laryngoscope* 96(9 Pt 1), 959–974.

Scott, R. H., Woods, A. J., Lacey, M. J., Fernando, D., Crawford, J. H., and Andrews, P. L. (1995). An electrophysiological investigation of the effects of cisplatin and the protective actions of dexamethasone on cultured dorsal root ganglion neurones from neonatal rats. *Naunyn Schmiedebergs Arch. Pharmacol.* 352, 247–255. doi: 10.1007/bf00168554

Sergi, B., Ferraresi, A., Troiani, D., Paludetti, G., and Fetoni, A. R. (2003). Cisplatin ototoxicity in the guinea pig: vestibular and cochlear damage. *Hear. Res.* 182, 56–64. doi: 10.1016/s0378-5955(03)00142-4

Sha, S. H., Taylor, R., Forge, A., and Schacht, J. (2001). Differential vulnerability of basal and apical hair cells is based on intrinsic susceptibility to free radicals. *Hear. Res.* 155, 1–8.

Skalleberg, J., Småstuen, M. C., Oldenburg, J., Osnes, T., Fosså, S. D., and Bunne, M. (2020). The relationship between cisplatin-related and age-related hearing loss during an extended follow-up. *Laryngoscope* 130, E515–E521. doi: 10.1002/lary.28543

Sluyter, S., Klis, S. F., de Groot, J. C., and Smoorenburg, G. F. (2003). Alterations in the stria vascularis in relation to cisplatin ototoxicity and recovery. *Hear. Res.* 185, 49–56.

Sprouse, B., and Gozdecki, M. K. (2019). Audiological management of pediatric oncology patients. *Hear. J.* 72, 16–18. doi: 10.1097/01.HJ.0000579572.29927.bc

Takeuchi, S., Ando, M., and Kakigi, A. (2000). Mechanism generating endocochlear potential: role played by intermediate cells in stria vascularis. *Biophys. J.* 79, 2572–2582.

Takimoto, Y., Imai, T., Kondo, M., Hanada, Y., Uno, A., Ishida, Y., et al. (2016). Cisplatin-induced toxicity decreases the mouse vestibulo-ocular reflex. *Toxicol. Lett.* 262, 49–54. doi: 10.1016/j.toxlet.2016.09.009

Thomas, J. P., Lautermann, J., Liedert, B., Seiler, F., and Thomale, J. (2006). High accumulation of platinum-DNA adducts in strial marginal cells of the cochlea is an early event in cisplatin but not carboplatin ototoxicity. *Mol. Pharmacol.* 70, 23–29.

Tsukasaki, N., Whitworth, C. A., and Rybak, L. P. (2000). Acute changes in cochlear potentials due to cisplatin. *Hear. Res.* 149, 189–198. doi: 10.1016/s0378-5955(00)00182-9

von Brevern, M., Radtke, A., Lezius, F., Feldmann, M., Ziese, T., Lempert, T., et al. (2007). Epidemiology of benign paroxysmal positional vertigo: a population based study. *J. Neurol. Neurosurg. Psychiatry* 78, 710–715. doi: 10.1136/jnnp.2006.100420

Waissbluth, S., and Daniel, S. J. (2013). Cisplatin-induced ototoxicity: transporters playing a role in cisplatin toxicity. *Hear. Res.* 299, 37–45. doi: 10.1016/j.heares.2013.02.002

Walther, L. E. (2017). Current diagnostic procedures for diagnosing vertigo and dizziness. *GMS Curr. Top. Otorhinolaryngol. Head Neck Surg.* 16, Doc02–Doc02. doi: 10.3205/cto000141

Wangemann, P. (1995). Comparison of ion transport mechanisms between vestibular dark cells and strial marginal cells. *Hear. Res.* 90, 149–157.

Wangemann, P. (2002). K+ cycling and the endocochlear potential. *Hear. Res.* 165, 1–9.

Zhang, M., Liu, W., Ding, D., and Salvi, R. (2003). Pifithrin-alpha suppresses p53 and protects cochlear and vestibular hair cells from cisplatin-induced apoptosis. *Neuroscience* 120, 191–205

Conflict of Interest: The authors declare that the research was conducted in the absence of any commercial or financial relationships that could be construed as a potential conflict of interest.

Publisher's Note: All claims expressed in this article are solely those of the authors and do not necessarily represent those of their affiliated organizations, or those of the publisher, the editors and the reviewers. Any product that may be evaluated in this article, or claim that may be made by its manufacturer, is not guaranteed or endorsed by the publisher.

frontiers in Neuroscience

REVIEW
published: 12 August 2021
doi: 10.3389/fnins.2021.695179

Similarities and Differences Between Vestibular and Cochlear Systems – A Review of Clinical and Physiological Evidence

Ian S. Curthoys[1], John Wally Grant[2], Christopher J. Pastras[3], Laura Fröhlich[4] and Daniel J. Brown[5]*

[1] Vestibular Research Laboratory, School of Psychology, The University of Sydney, Sydney, NSW, Australia, [2] Department of Biomedical Engineering and Mechanics, Virginia Tech, Blacksburg, VA, United States, [3] The Menière's Research Laboratory, Sydney Medical School, The University of Sydney, Sydney, NSW, Australia, [4] Department of Otorhinolaryngology, Head and Neck Surgery, Martin Luther University Halle-Wittenberg, Halle, Germany, [5] School of Pharmacy and Biomedical Sciences, Curtin University, Bentley, WA, Australia

OPEN ACCESS

Edited by:
Soroush G. Sadeghi, University at Buffalo, United States

Reviewed by:
Robert Burkard, University at Buffalo, United States
Devin McCaslin, University of Michigan, United States
Herman Kingma, Maastricht University, Netherlands

***Correspondence:**
Ian S. Curthoys
ian.curthoys@sydney.edu.au

Specialty section:
This article was submitted to Perception Science, a section of the journal Frontiers in Neuroscience

Received: *14 April 2021*
Accepted: *12 July 2021*
Published: *12 August 2021*

Citation:
Curthoys IS, Grant JW, Pastras CJ, Fröhlich L and Brown DJ (2021) Similarities and Differences Between Vestibular and Cochlear Systems – A Review of Clinical and Physiological Evidence. Front. Neurosci. 15:695179. doi: 10.3389/fnins.2021.695179

The evoked response to repeated brief stimuli, such as clicks or short tone bursts, is used for clinical evaluation of the function of both the auditory and vestibular systems. One auditory response is a neural potential — the Auditory Brainstem Response (ABR) — recorded by surface electrodes on the head. The clinical analogue for testing the otolithic response to abrupt sounds and vibration is the myogenic potential recorded from tensed muscles — the vestibular evoked myogenic potential (VEMP). VEMPs have provided clinicians with a long sought-after tool — a simple, clinically realistic indicator of the function of each of the 4 otolithic sensory regions. We review the basic neural evidence for VEMPs and discuss the similarities and differences between otolithic and cochlear receptors and afferents. VEMPs are probably initiated by sound or vibration selectively activating afferent neurons with irregular resting discharge originating from the unique type I receptors at a specialized region of the otolithic maculae (the striola). We review how changes in VEMP responses indicate the functional state of peripheral vestibular function and the likely transduction mechanisms allowing otolithic receptors and afferents to trigger such very short latency responses. In section "ELECTROPHYSIOLOGY" we show how cochlear and vestibular receptors and afferents have many similar electrophysiological characteristics [e.g., both generate microphonics, summating potentials, and compound action potentials (the vestibular evoked potential, VsEP)]. Recent electrophysiological evidence shows that the hydrodynamic changes in the labyrinth caused by increased fluid volume (endolymphatic hydrops), change the responses of utricular receptors and afferents in a way which mimics the changes in vestibular function attributed to endolymphatic hydrops in human patients. In section "MECHANICS OF OTOLITHS IN VEMPS TESTING" we show how the major VEMP results (latency and frequency response) follow from modeling the physical characteristics of the macula (dimensions, stiffness etc.). In particular, the

structure and mechanical operation of the utricular macula explains the very fast response of the type I receptors and irregular afferents which is the very basis of VEMPs and these structural changes of the macula in Menière's Disease (MD) predict the upward shift of VEMP tuning in these patients.

Keywords: vestibular, otolith, labyrinth, vemp, semicircular canal, saccular, utricular

INTRODUCTION

Similar goals have driven both auditory and vestibular research – the need for clinical tests to identify disorders of the sensory system. For an excellent reference for much of the basic vestibular neurophysiology discussed here see Goldberg et al. (2012). In the case of hearing, the audiogram has been a key test and vestibular research started, similarly, with a strong emphasis on a "vestibulogram" or "cupulogram"- measuring vestibular thresholds. This was mainly from investigators in the Netherlands around 1950 e.g. Groen and Jongkees (1948). Paralleling the results of those threshold studies were basic science studies such as the development and elaboration of the Steinhausen torsion pendulum model of semicircular canal operation (Van Egmond et al., 1949; Groen, 1957; Straka et al., 2021), measurement of neural responses and modeling of the peripheral semicircular canal (and otolith) mechanisms determining the thresholds (von Bekesy, 1955) and the first mechanical model of otolith function (de Vries, 1950). However, the use of psychophysical thresholds to vestibular stimulation did not prove to be as useful in clinical assessment of vestibular function as it has been for audition. Vestibular thresholds are difficult to measure, of limited reliability and it is costly and clinically impractical to deliver angular and linear accelerations safely to a whole person to determine their thresholds. So vestibular threshold studies have largely remained in the lab (Clark, 1967; Karmali et al., 2016; Kobel et al., 2021) although they have contributed to models of vestibular mechanics.

Clinical auditory testing progressively turned to objective tests – where clicks or short tone bursts elicit the auditory brainstem response (ABR) which is a neural response recorded by surface electrodes on the head and is used to evaluate dysfunction in the auditory system (Rowe, 1981; Eggermont, 2017; Drexl et al., 2018). The ABR is a short-latency response generated by neural structures in the ascending hearing pathway of the auditory brainstem, including a post-stimulus interval of 1 to 12 ms. The evaluation of latencies and amplitudes of peaks in the ABR waveform allows for the assessment of dysfunction in the auditory system. In parallel fashion vestibular investigators have turned to measuring objective vestibular tests – vestibular evoked responses—with the prime evoked response being the vestibular evoked myogenic potential (VEMP). This is a short latency myogenic potential evoked by air-conducted sound (ACS) or bone-conducted vibration (BCV) (mainly clicks or short (7 ms) tone bursts of 500 Hz) either in tensed sternocleidomastoid (SCM) neck muscles [the cervical VEMP (cVEMP) or in stretched inferior oblique (IO) eye muscles (the ocular VEMP (oVEMP)]. For a history of VEMPs see Colebatch and Halmagyi (1992), Colebatch et al. (1994), Curthoys et al. (2018), Rosengren and Colebatch (2018) (see **Figure 1**). The amplitude of the oVEMP is largest for short rise time stimuli (Burgess et al., 2013) as analogous to the wave I of the ABR (Finneran et al., 2018)– pointing to the synchronous activation of primary vestibular afferents in this case as having a major role in the generation of the evoked response (Goldstein and Kiang, 1958).

The VEMP

As we discuss in detail below an abrupt sound or vibration stimulus activates, within one millisecond, a small subgroup of otolithic receptors and afferents with irregular resting discharge – originating from the central striolar area of the otolithic sensory regions (Curthoys et al., 2006; Curthoys and Vulovic, 2011). The afferents from the utricular macula project via the vestibular nuclei and oculomotor nuclei to the contralateral IO (Suzuki et al., 1969) causing short latency (7 ms) myogenic potentials in these ocular muscles which can be recorded by surface electrodes above the IO eye muscles as the patient looks up (**Figure 2**). This response is identified as the ocular VEMP (oVEMP) and is predominantly of utricular origin (Curthoys, 2010). The anatomical projections from the vestibular nuclei to the eye muscles are partially known (Uchino and Kushiro, 2011) but recordings from single motor units in human eye muscles conclusively show that clicks generate short latency excitation in inferior oblique eye muscles (Rosengren et al., 2011; Weber et al., 2012). Afferents from the saccular macula project to the ipsilateral sternocleidomastoid (SCM) causing short latency inhibitory myogenic potentials in these muscles, again recordable by surface electrodes above the tensed SCM. This response is predominantly saccular and is identified as the cervical VEMP (cVEMP). There are similar short latency inhibitory single motor unit responses in human cervical muscle units (Rosengren et al., 2015) in response to BCV.

These data serve as the physiological basis for the clinical use of VEMPs to indicate the functional status of the peripheral otolithic receptors in each labyrinth. So, the one stimulus generates responses which probe the function of both the utricular and the saccular maculae (Curthoys, 2010) and

Abbreviations: ACS, air conducted sound; ANN, auditory nerve neurophonic; ABR, auditory brainstem response; BCV, bone-conducted vibration; CF, characteristic frequency; CFL, column filament layer; CM, cochlear microphonic; CAP, compound action potential; ECochG, electrocochleography; GL, gel layer; HC, hair cell; HCB, hair cell bundles; IHC, inner hair cell; IO, inferior oblique eye muscle; K+, potassium ion; MD, Menière's Disease; MET, mechanoelectrical transduction channels; NEL, neuroepithelial layer; OAE, otoacoustic emission; OHC outer hair cell; OL, otoconial layer; OM, otolithic membrane; pN, picoNewtons; RMP resting membrane potential; SCM, sternocleidomastoid muscle; SL, shear layer; SCD, semicircular canal dehiscence; SP summating potential; UDNF undamped natural frequency; UM, utricular microphonic; VM vestibular microphonic; VEMP, vestibular evoked myogenic potential.; oVEMP, ocular vestibular evoked myogenic potential; cVEMP, cervical vestibular evoked myogenic potential; VsEP, vestibular evoked potential.

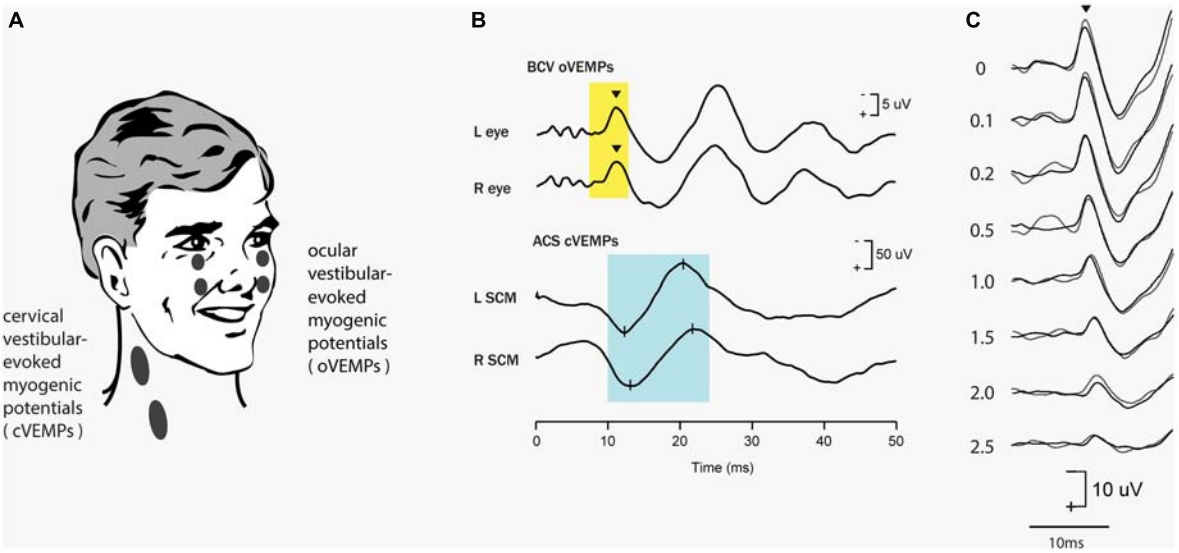

FIGURE 1 | Vestibular evoked myogenic potentials (VEMPs). There are a host of VEMPs since vestibular input projects indirectly to many muscle groups. The two VEMPs which have received the most attention are cervical VEMPs (cVEMPs) and ocular VEMPs (oVEMPs). cVEMPs are recorded by surface EMG electrodes over the tensed sternocleidomastoid muscles (SCM) (Colebatch and Halmagyi, 1992; Colebatch et al., 1994; Adams et al., 2010). The cVEMP consists of a short-latency (13 ms from onset to peak) positive (i.e., inhibitory) EMG potential in response to high-intensity ACS or BCV (Halmagyi et al., 1995). Ocular VEMPs (oVEMPs) consist of a small (5–10 μV) negative (i.e., excitatory) potentials recorded by surface electrodes on the skin beneath the eyes from the inferior oblique in response to BCV or ACS (Rosengren et al., 2005; Iwasaki et al., 2007). To record the oVEMP the subject must be looking up. **(A)** Electrode placement for oVEMPs and cVEMPs; the ground electrode (not shown) is typically on the chin or sternum. **(B)** Typical oVEMP and cVEMP records for a healthy subject in response to bilaterally equal amplitude stimuli: the magnitude of the n10 response is approximately equal beneath both eyes for the oVEMP, and, similarly, the magnitude of the p13-n23 response is approximately equal in both SCMs for the cVEMP. **(C)** For stimuli in the one subject, increasing the rise time of the 500 Hz stimulus reduces the amplitude of the oVEMP (Burgess et al., 2013). The number next to each record shows the rise time in milliseconds. Reproduced from Frontiers.

unilateral otolithic loss shows the reduced myogenic response from the affected ear (**Figure 2B**). Reviews give extensive information about the history, the detailed physiology and how to perform these VEMP tests clinically (MacDougall et al., 2015; Dlugaiczyk, 2017; Rosengren and Colebatch, 2018; van de Berg et al., 2018; Rosengren et al., 2019). VEMPs are now being used as a routine indicator of the operation of otolithic receptors in patients with probable vestibular neuritis or even with intracochlear schwannoma (Frohlich et al., 2020) and also to pinpoint probable central neural deficits (Oh et al., 2016). Hence, just as the ABR is used to assess peripheral (and central) auditory dysfunction, the VEMP is being used clinically to probe peripheral (and central) vestibular function.

Clicks or short tone bursts of sound or vibration are used to assess the function of both the vestibular and the auditory system because physiological evidence has shown that some vestibular receptors and afferents are activated at very short latency by these stimuli (Curthoys et al., 2006, 2014; Curthoys and Vulovic, 2011; Pastras et al., 2018). There has been debate whether VEMPs contain an auditory contribution in human patients. However, a wealth of clinical and physiological evidence conclusively shows the vestibular (and specifically otolithic) origin of VEMPs (for reviews see Rosengren and Colebatch, 2005; Iwasaki et al., 2008; Curthoys et al., 2011a; Curthoys, 2020; Curthoys and Dlugaiczyk, 2020).

The major clinical VEMP results are: (1) unilateral vestibular loss (due to surgery for vestibular schwannoma removal or vestibular neuritis) causes loss of ipsilateral cVEMPs and contralateral oVEMPs corresponding to the neural projection pattern shown in **Figure 2** (Colebatch and Halmagyi, 1992; Iwasaki et al., 2007; **Figure 2**). (2) Thinning of the bony wall of the anterior semicircular canal [known as semicircular canal dehiscence (SCD)] changes the mechanical operation of the labyrinth and affects both cochlear and vestibular receptors (Rosowski et al., 2004; Curthoys, 2017; Iversen and Rabbitt, 2017; Iversen et al., 2018; Dlugaiczyk et al., 2019; Rabbitt, 2019). SCD enhances the neural response of otolith neurons and activates previously unresponsive semicircular canal neurons with irregular resting discharge to sound and vibration and so causes enhanced VEMP responses (Colebatch et al., 1998; Manzari et al., 2013; Curthoys, 2017; Dlugaiczyk et al., 2019).

The cause of that enhanced response was demonstrated in guinea pigs where single canal or otolith neurons were recorded continuously while the dehiscence was carried out, and it was found that after SCD, ACS and BCV enhanced the activation of the irregular otolithic afferents, but also activated irregular semicircular canal neurons, which had been unresponsive to these stimuli prior to the SCD (**Figure 3**). Both canal and otolith neurons showed phase locking up to very high stimulus frequencies (even beyond 3000 Hz). The contribution of canal neurons was shown by the fact that canal neurons which were activated after SCD (which had been unresponsive prior to the SCD) (**Figure 3**) again became unresponsive after the SCD was resealed. After SCD otolith neurons showed a lower threshold

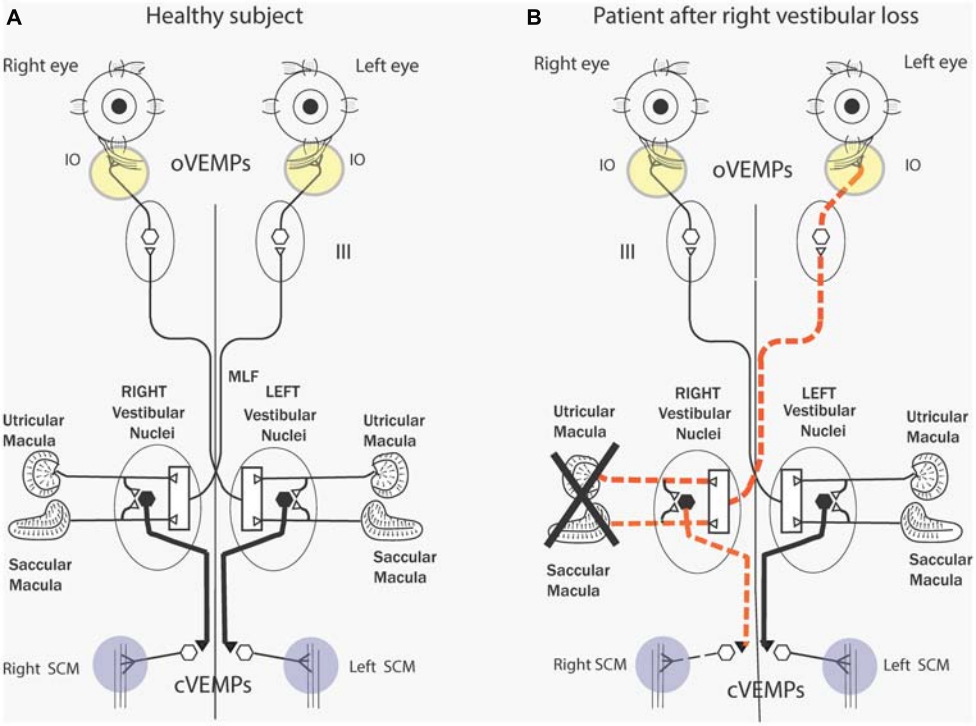

FIGURE 2 | (A) Simplified schematic diagram of some of the known neural vestibulo-ocular and vestibulo-collic projections that underlie the oVEMP and cVEMP myogenic responses. The Figure is based on known anatomical projections (Uchino and Kushiro, 2011) and on physiological results that high-frequency electrical stimulation of the utricular nerve results in the activation of the contralateral inferior oblique (IO) (Suzuki et al., 1969). Electrodes beneath the eyes record the oVEMP as the person looks up. Afferents from the saccular and utricular macula project to the vestibular nuclei, but the exact termination of these afferents with the nucleus is still unclear so this figure represents the present uncertainty about the exact neural connections of these afferents within the nuclei as an open box. The projections of the saccular macula in the inferior vestibular nerve, synapsing on an inhibitory neuron in the vestibular nucleus (*thick black lines*), projecting to spinal motoneurons controlling the sternocleidomastoid muscle (SCM), are established (Uchino and Kushiro, 2011). Electrodes over contracted SCM muscles record the cVEMP. Unilateral vestibular loss **(B)** has been shown to result in reduced or absent contralateral oVEMP n10 and a reduced or absent ipsilateral cVEMP. Reproduced from Curthoys et al. (2011a) with permission from Wiley.

and enhanced response to higher frequencies in contrast to their more limited high frequency response prior to SCD (Curthoys et al., 2006; Curthoys and Vulovic, 2011; Curthoys, 2017; Curthoys and Dlugaiczyk, 2020). In corresponding fashion human patients with SCD show enhanced amplitude VEMPs to 500 Hz stimuli but also show clearVEMPs to very high frequency "vestibular" stimuli (4000 Hz) whereas healthy subjects do not have VEMPs to such high vestibular frequencies, thus making the VEMP response to 4000 Hz an excellent, simple, specific indicator of human SCD (Manzari et al., 2013; Curthoys and Manzari, 2020; Noij and Rauch, 2020). Note, that "high frequency" with regards to vestibular stimulation (and the VEMP) refers to frequencies greater than about 500 Hz, which is much lower than what is considered high frequency in the cochlea.

Sound and Vibration in the Cochlea and Otoliths

Prior to discussing the various sensitivities of the cochlea and vestibular system to ACS or BCV stimuli of various frequencies, it is worth noting that it is not a straightforward task to compare a system's sensitivity to these different modes of stimulation. That is, whilst colloquially we may state that the vestibular system is more sensitive to vibration than sound, and the cochlea more sensitive to sound than vibration, in isolation we cannot make this comparison. That is, ACS and BCV level are usually measured in completely different, non-comparable units. The level of an ACS stimulus is relatively straightforward to calibrate, being the sound level in the ear canal, in units of dB SPL (or dB nHL for stimuli of short duration with reference to hearing levels). Calibrating the level of a BCV stimulus requires significantly more consideration, as it should ideally be provided in units of acceleration of the skull (or some permutation of such, e.g., vibratory force level dB VFL, as it is done for audiometric applications). The measurement depends upon where the BCV stimulator is placed, and where the acceleration is measured (Govender et al., 2015; Govender and Colebatch, 2017; Govender and Colebatch, 2018) (not to mention a likely large variability in physical properties of the skull across individuals which will influence the vibration in the otoliths, particularly for transient stimuli).

That said, in the clinical setting, for evoking responses such as the VEMP or ABR, the BCV device is likely to be something like a RadioEar B81 (or B71) audiometry grade transducer, placed

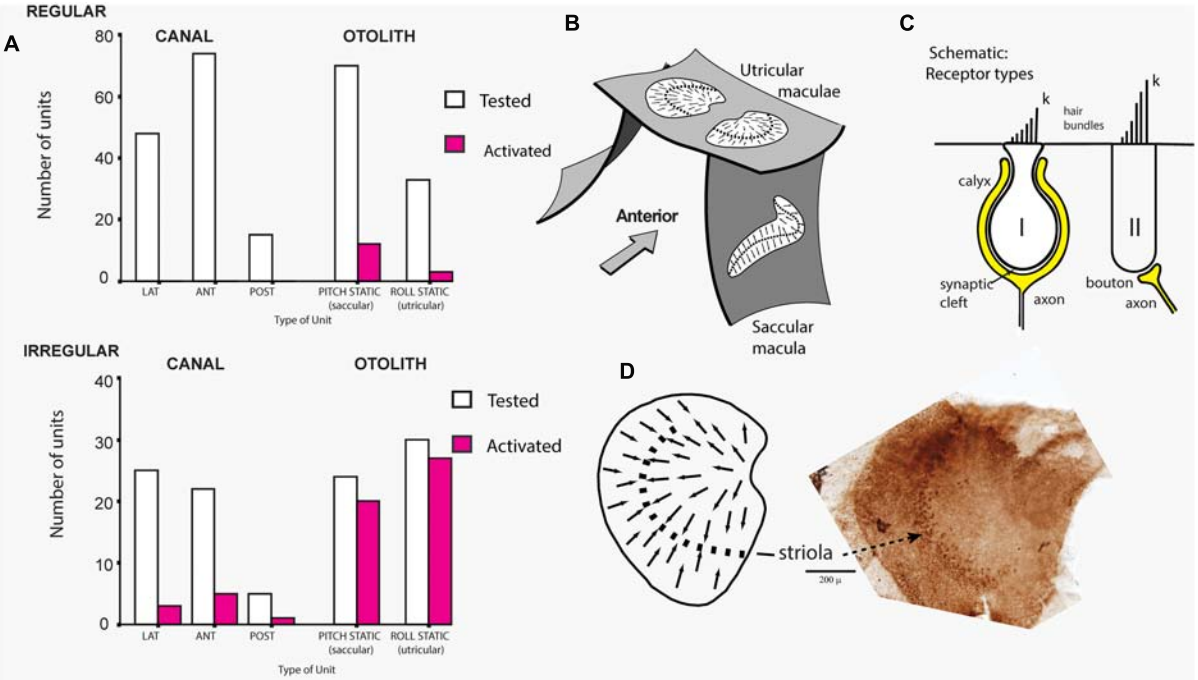

FIGURE 3 | (A) Proportions of primary vestibular afferent neurons tested (open bars) and activated (filled bars) by bone-conducted vibration (BCV) stimuli from each vestibular sensory region. Top chart - Regular neurons, bottom chart irregular neurons. Lat, horizontal canal; Ant, anterior canal; Post, posterior canal. The otolith neurons are divided into Pitch static and Roll static. The results show that only a very small proportion of semicircular canal neurons, or regular otolithic neurons, were activated. However, a large proportion of otolithic irregular neurons were activated. Reproduced, from Curthoys et al. (2006) with permission of Springer. **(B)** Schematic representation of the plates of otolithic receptors (the utricular and saccular maculae) of the inner ear. The arrows show the preferred polarizations of hair cell receptors across the maculae. The dashed lines are lines of polarity reversal, where the preferred polarizations of receptors reverse. The striola refers to a thin band of receptors on either side of the line of polarity reversal. **(C)** Schematic representation of type I and type II receptor hair cells and their calyx and bouton afferent terminals. The longest cilium, the kinocilium (k), defines the preferred direction of cell polarization (shown by small arrows in **B** and **D**). The type I receptor is enveloped by the calyx afferent ending. **(D)** Schematic representation of a dorsal view of the whole guinea pig utricular macula. Adjacent to this schematic is a dorsal view of a guinea pig utricular macula treated by calretinin—the band of cells comprising the striola is clearly visible. Reproduced from Curthoys et al. (2012), with permission from Elsevier.

over the mastoid bone. Whilst there is unlikely to be any effort to measure the acceleration of the skull, if the same "voltage source" (i.e., from the audiometer device) is used to drive both the calibrated headphones (or earphones) for ACS stimulation, and the BCV transducer, then the clinician may be tempted to draw some approximations about the "relative" sensitivity of responses such as the ABR and VEMP to BCV or ACS in units of dB SPL, dB VFL, or dB nHL. But even then, it must be understood that comparing the voltage drive to a headphone or bone-conductor required to evoke an ABR (or VEMP) at threshold, does not tell you about the relative sensitivity of the cochlea (or vestibular system) to ACS or BCV. It merely tells you about the relative efficiency of that headphone or bone conductor to produce stimulation within the ear, for a given voltage drive. However, we can compare the relative sensitivity of the cochlea vs. otoliths to a given stimulus (either a BCV or an ACS stimulus). To evoke a VEMP at threshold, using say a 500 Hz ACS stimulus, requires roughly 60 to 70 dB higher sound level than that which is required to evoke an ABR using the same stimulus (Gorga et al., 1993; Rosengren and Colebatch, 2018). Conversely, to evoke a VEMP using say a 500 Hz BCV stimulus (a B81 bone conductor placed on the mastoid), requires approximately 40 to 60 dB higher vibratory force level compared to evoking an ABR (Hakansson et al., 2018; Mueller et al., 2020; Frohlich et al., 2021). If we reference BCV level relative to ABR thresholds (or hearing thresholds), in terms of dB nHL, it could potentially be argued that the vestibular system is about 20 to 30 dB more sensitive to BCV than ACS, for this setup, using these devices (Groen and Jongkees, 1948). This does not suggest that the otolith is 20 to 30 dB more sensitive for BCV than ACS, as this will depend upon the specifics of the BCV stimulus and the comparison is based on terms of hearing levels (dB nHL), i.e., audiometric units specifying sensitivity relative to the cochlea.

VEMPs Frequency Response and Tuning Shift

In healthy subjects the optimum frequency for evoking VEMPs to short tone burst stimuli with a 2 ms rise time (either ACS or BCV) is around 500 Hz, with usually a clear decrease in VEMP amplitude in healthy subjects in response to 1000 Hz (Lin et al., 2006; Timmer et al., 2006; Piker et al., 2013; Singh and Barman, 2016a,b; Singh and Firdose, 2018; Noij et al., 2019). The VEMP frequency response depends

on many factors but of major importance are the physical characteristics of the macula (thickness, stiffness etc.) and the attachment of the otolithic receptors to the overlying otolithic membrane. The receptors at the specialized region of the macula, the striola (see **Figures 3B,C**), have short stiff hair bundles (Spoon and Grant, 2011, 2013) with tenuous attachment to the overlying otolithic membrane (Lindeman, 1969) and so are similar to cochlear inner hair cells which have minimal tenuous attachment to the tectorial membrane (Dallos, 1992; Hakizimana and Fridberger, 2021). In contrast the receptor hair cells of the extrastriolar regions of the otolithic maculae have long hair bundles which extend far up into the otolithic membrane and appear to have much tighter attachment to the otolithic membrane than the striolar receptors (Spoon et al., 2011).

In patients with Menière's Disease (MD) the optimum stimulus frequency for VEMPs is around 1000 Hz with a smaller response to 500 Hz. This is the opposite of the response preference in healthy subjects where 500 Hz causes a larger response than 1000 Hz. So, the ratio of VEMP amplitude at 500 Hz to VEMP amplitude at 1000 Hz is becoming recognized as an indicator of Menière's Disease – the "upward shift" of tuning in MD patients (Lin et al., 2006; Timmer et al., 2006; Piker et al., 2013; Noij et al., 2019). The major question is why patients with MD show this upward tuning shift and below (Section "MECHANICS OF OTOLITHS IN VEMPS TESTING") we show how the change in the thickness of the otolithic membrane (and so its stiffness) during MD (Calzada et al., 2012; Ishiyama et al., 2015) changes the mechanical tuning of the otolithic macula and predicts such an upward tuning shift of VEMPs.

Cochlear and Vestibular Hair Cells and Afferents

Both the cochlea and vestibular systems have two distinct types of receptor hair cells which play unique roles in mechanoelectrical transduction and sensory processing. The cochlea hosts inner hair cells (IHCs) and outer hair cells (OHCs), whereas the vestibular sensory regions exhibit a similar dichotomy in the type I and type II hair cells (see Goldberg, 2000; Eatock and Songer, 2011; Goldberg et al., 2012) for full details (**Figure 3**). These cochlear and vestibular receptor cells are broadly similar in structure and function and modulate gating current via displacements of their stretch sensitive tip-links at the apices of the hair bundles. In the cochlea, OHCs are biological 'motors' which actively vibrate to overcome negative damping, likely driven by the electromotile protein, prestin. By contrast, IHCs are primarily 'sensors' which relay auditory information to the CNS, via spiral ganglion fibres ∼95% of which contact IHCs and only about ∼5% contact OHCs. Cochlear afferent fibres exhibit a range of characteristics, with essentially two sub-types: (1) those with a high spontaneous firing and low threshold (to sound); and (2) those with a low spontaneous rate and high threshold (Heil and Peterson, 2015, 2017). In the vestibular system, there is no motor vs sensor dichotomy comparable to the cochlear OHCs vs IHCs, but rather different receptor-afferent systems with distinct sensitivities. Type II hair cells have a considerably depolarized Resting Membrane Potential (RMP), at around −50 mV, determined by several inwardly and outwardly rectifying K+ currents (Holt and Eatock, 1995; Eatock and Songer, 2011). Type II hair cells synapse on bouton afferent fibres, which have tonic response dynamics, high thresholds, and low sensitivity to linear or angular forces. By contrast, type I hair cells have a relatively hyperpolarized RMP at −80 mV, dominated by a large, slowly activating K+ current ($I_{K,L}$) (Correia and Lang, 1990), that synapse on calyx afferent fibres, which have phasic response dynamics, low thresholds and high sensitivity to linear and angular forces (Eatock and Songer, 2011). Interestingly, dimorphic afferent fibres terminate on both types of hair cells, and generally have response properties akin to calyx units (Fernandez et al., 1990; Goldberg et al., 1990).

Vestibular Primary Afferent Neurons – Spontaneous Activity

Given the gross anatomical similarity of vestibular receptor hair cells and cochlear hair cells, it is surprising that the resting activity of afferent neurons in the two systems is so different (Walsh et al., 1972; McCue and Guinan, 1995; Heil et al., 2007; Heil and Peterson, 2015; Curthoys et al., 2016). Cochlear afferents, almost all of which arise from IHCs, have resting discharge which is irregular (Heil and Peterson, 2015, 2017). In contrast the regularity of resting discharge of primary vestibular afferents is a continuum (Goldberg, 2000) which, partly for convenience, has been divided into two main categories - some with very regular resting rates which have been shown to originate from extrastriolar dimorphic and bouton afferents synapsing on type II receptors (Fernandez et al., 1990). Other neurons with irregular resting discharge, have been shown to originate predominantly from calyx endings on type I receptors at the striola (Fernandez et al., 1990; Curthoys et al., 2012). In the vestibular system the regularity of resting discharge is associated with functional differences: recordings of single primary otolithic afferent neurons in guinea pigs, cats, squirrel monkeys have shown that sounds and vibrations are effective in activating the otolithic afferents with irregular resting discharge whereas these same stimuli are ineffective at activating afferents with regular resting discharge (see **Figures 4**, **5**), So the ACS and BCV stimuli used to generate VEMPs in patients in the clinic, selectively activate irregular dimorphic and calyx afferents synapsing on receptors at the striola of the otolithic macula where the afferents form unique calyx synapses on the amphora shaped type I receptors (Curthoys and Vulovic, 2011; Curthoys et al., 2012, 2019a; Curthoys, 2017).

Eatock and Kalluri suggest that the different resting discharge patterns of vestibular afferents probably reflect differences in the operation of channels on the cell membrane (Eatock et al., 2008; Kalluri et al., 2010). A recent study in the guinea pig confirmed that many irregular vestibular afferents have very low (or even zero) resting discharge (Yagi et al., 1977; Curthoys et al., 2016), which is comparatively rare in auditory afferent neurons (Walsh et al., 1972). The very low resting rate of some irregular vestibular afferents likely reflects the unique physiology of the vestibular

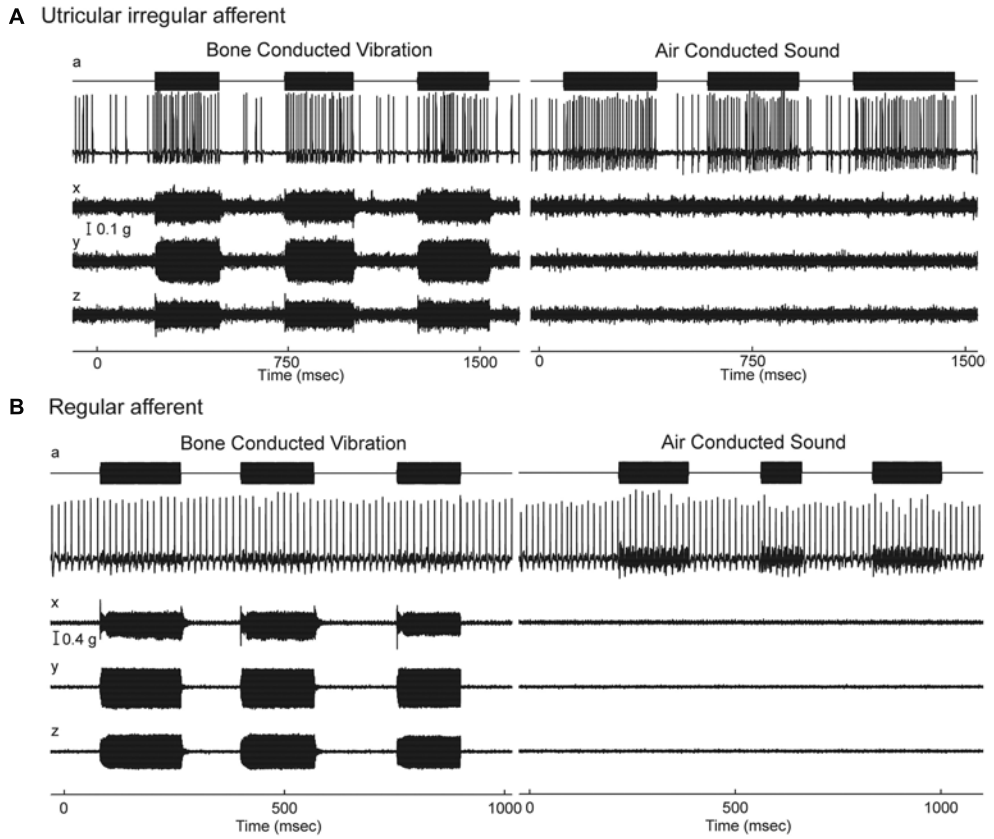

FIGURE 4 | Resting discharge pattern and response to stimulation of an irregular and a regular afferent. **(A)** Time series of the one irregular otolith neuron during stimulation by 500 Hz bone-conducted vibration (BCV) and air-conducted sound (ACS). The top trace (a) shows the command voltage, indicating when the stimulus is on. The second trace shows the action potentials by extracellular recording. The three bottom traces (*x, y, z*) show the triaxial accelerometer recording of the stimulus. The neuron is clearly activated by both BCV and ACS. **(B)** Time series of a regular semicircular canal neuron during stimulation by 500 Hz BCV and ACS as above. The regular discharge is seen before the stimulus onset. The stimuli have a far greater amplitude than in panel **(A)**, but there is no evidence of activation of this regular neuron by these strong stimuli. Reproduced from Curthoys and Vulovic (2011) with permission of Springer.

calyx synapse on type I receptors at the striola (Lysakowski et al., 2011; Lim et al., 2011; Contini et al., 2017; Contini et al., 2020).

Vestibular Primary Afferent Neurons – Sustained and Transient Systems

In summary: the otoliths (and even the semicircular canals) can be thought of as having two co-existing receptor and afferent systems. One is a relatively low frequency system with optimal sensitivity for accelerations but it is relatively insensitive to sinusoidal accelerations above 50 Hz. It is conveyed by neurons with regular resting discharge. These afferents mainly from otolithic receptors in the extrastriolar sensory regions, have a relatively poor response to sound and vibration (**Figure 4**). The other receptor-afferent system is a transient system (i.e., it is relatively more sensitive to rapid changes in acceleration) conveyed by neurons with typically low irregular resting discharge, conveyed by large diameter fast afferents (Goldberg and Fernandez, 1977; Yagi et al., 1977) and with low threshold and very sensitive responses to sound and vibration) originating from striolar receptors (**Figure 4**). The important conclusion from physiology is that it is the fast transient system from striola otolithic receptors which is responsible for triggering VEMPs. This sustained/transient division of neural processing in the vestibular system parallels sustained/transient processing in other sensory systems – vision (Cleland et al., 1971; Cleland et al., 1973; Breitmeyer and Ganz, 1976), somatosensory (Hu et al., 2015) and hearing (Andermann et al., 2020).

Ross (1936) originally showed that vestibular afferents were activated by vibration and later (Mikaelian, 1964) and (Young et al., 1977) and others (Wit et al., 1984; McCue and Guinan, 1994; Murofushi et al., 1995) demonstrated that single mammalian and avian vestibular afferents have phase locked activation to sound or vibration, similar to the phase locked activation of primary auditory afferents. Irregular primary otolithic afferents have very short latency to sound and vibration. **Figure 5** shows the responses of three single saccular afferents evoked by an air conducted click with a latency to the foot of the action potential of only 0.5 ms – even before the N1 cochlear action potential response to the click (Murofushi et al., 1995) (for reviews see McCue and Guinan, 1997; Curthoys, 2017). However, it must be stated that the latency of the compound action potential (CAP)

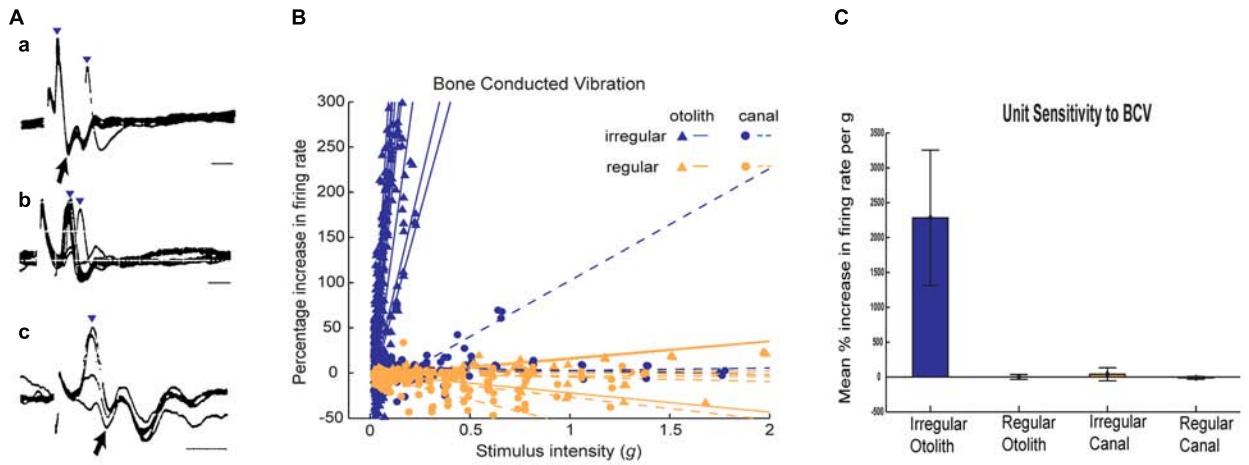

FIGURE 5 | (A) Irregular otolithic primary afferents are evoked by air conducted clicks at very short latencies (from Murofushi et al., 1995). Three examples of air conducted click-evoked action potentials (identified by inverted triangles) in three primary otolithic neurons. Superimposed recordings of responses to 5–10 clicks. Latencies from the onset of the click to the foot of the action potential were 0.5 ms (a,c) and 1.0 ms (b). b and c show responses at threshold-straddling intensities, so the action potential is not evoked on every presentation. Note that these action potentials (a, c) occur at such short latencies they precede the N1 wave of the acoustically evoked cochlear action potential (arrows). Time scales 1 ms. Reproduced from Murofushi et al. (1995) with Permission of Springer **(B)** Examples of sensitivity plots of neurons to BCV showing the high sensitivity of irregular neurons to increasing BCV stimulus strength as opposed to regular afferents. Each point shows the increase in firing rate as the percentage of baseline firing rate during a single stimulus presentation. Each *line* is the best fit calculation of the responses for one neuron (triangles - otolith neurons, circles-semicircular canal neurons; irregular afferents are blue and regular afferents are orange. The stimulus intensity is calculated in *g*, and is the root mean square of three axes as recorded by the skull-mounted triaxial accelerometer. Canal neurons and regular otolithic afferents are not activated by high stimulus levels. In contrast irregular otolithic afferents are activated at very low intensities and have a very steep increase in firing as intensity is increased. **(C)** Average sensitivities for neurons to BCV. The slopes of the best fitting lines in **(B)** are averaged for each class of neuron, and the average slope and 95% confidence intervals. The unit of sensitivity in this plot is per cent increase in firing rate per *g* above the resting discharge rate. The high sensitivity of otolith irregular neurons and the absence of response of otolith regular and semicircular canal neurons is clear. Reproduced from Curthoys and Vulovic (2011) with permission of Springer.

or wave I of the ABR is influenced by both active and passive components such as the electromotility of the OHCs and mass, stiffness and damping, which adds delays to the auditory system. By contrast, for intense acoustic vestibular stimulation, there is no active filter, and the excitation wave travels relatively quickly and so the latency is short.

Otolithic afferents with irregular resting discharge have poor response to what is regarded as the usual otolithic stimulus – maintained tilts or low-frequency linear accelerations (<50 Hz)—but instead are exquisitely responsive to time rate of change of linear acceleration (jerk) such as occur in vibration. **Figure 5** shows how irregular otolithic neurons (blue triangles) have low threshold and steep increase in firing rate to 500 Hz BCV stimuli as the amplitude of the vibration stimulus is increased. In sharp contrast, afferents with regular resting activity either otolithic (orange triangles) or canal (orange circles) simply are not activated even at very high intensities. Regular afferents originate from the extrastriolar region and have sensitive responses to low frequency (<50 Hz) linear accelerations but are not activated by sound or vibration up to high intensities (Curthoys et al., 2006; Curthoys et al., 2014; **Figure 5**). In summary afferents with regular resting discharge, originating mainly in the extrastriolar region (Goldberg et al., 1990) constitute the low frequency sustained system, whereas afferents with irregular resting activity originating mainly from receptors at the striola constitute the high frequency transient system (Curthoys and Vulovic, 2011; Curthoys et al., 2012) and it is the transient system which is activated by sound and vibration and so is responsible for VEMPs.

Relating the Neural Responses to the Mechanical Operation of the Otoliths

The high frequency transient otolithic system can be reconciled with the low frequency sustained otolithic system because it is our contention (Grant and Curthoys, 2017) that otolithic receptors function as accelerometers at low frequencies and as seismometers at high frequencies (**Figure 6**; Grant and Curthoys, 2017) (This matter is discussed in more detail in section "MECHANICS OF OTOLITHS IN VEMPS TESTING"). At low frequencies, we contend that the neuroepithelial layer (NEL) of the macula is in motion and the otoconia layer (OL) lags behind this movement due to its inertia (the accelerometer mode), whereas at high frequencies the NEL is in a vibratory motion and the OL tends to remain at rest again due to the inertia of the otoconia (the seismometer mode) (**Figures 6G,H**). Thus the OL has relative motion with respect to the head. At high frequencies in seismometer mode, the NEL has a small vibratory displacement (x), and the OL remains at rest due to its inertia (**Figure 6I**), again resulting in relative displacement between the NEL and OL and thus receptor hair cell deflection (Grant and Curthoys, 2017). In other words there is a relative displacement between the two otolithic layers at both low and

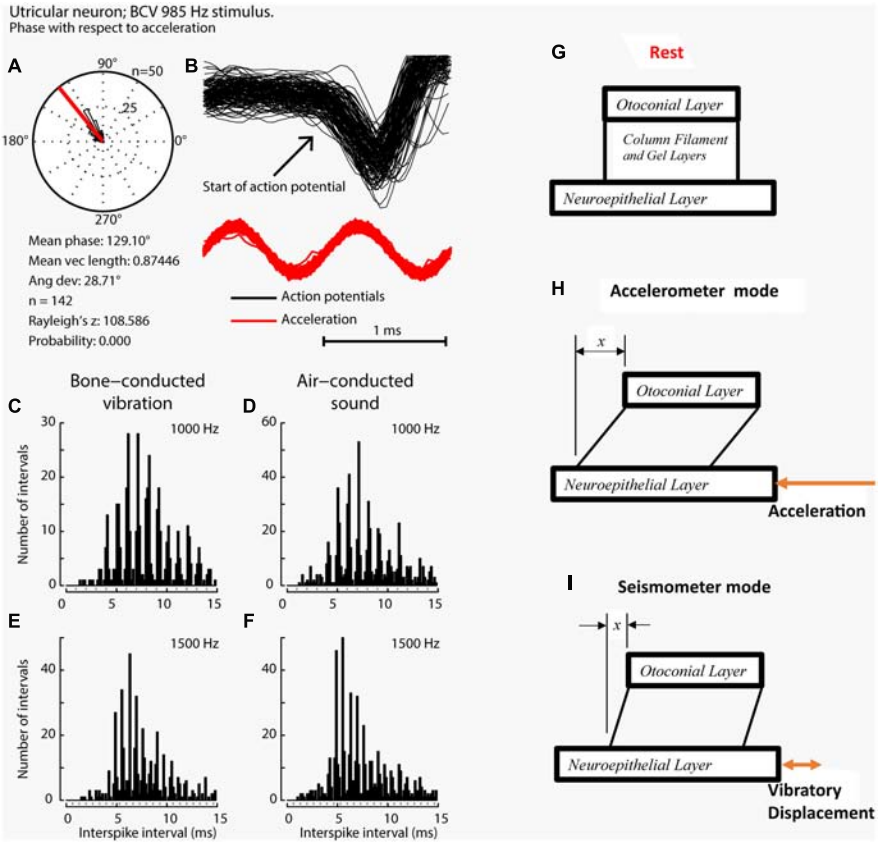

FIGURE 6 | Phase locking of a single primary utricular neuron. **(A,B)** Time series of successive action potentials of the neuron to bone-conducted vibration (BCV) at 985 Hz. Panel **(B)** shows 142 action potentials superimposed and the onset of each successive action potential is shown by the arrow. The red trace shows the *x* channel of the 3D linear accelerometer. The neuron is locked to a narrow phase band of this stimulus. Panel **(A)** shows the circular histogram of the phases of the action potentials clustered around a mean of 129.1°, with angular deviation 28.7°. The test of circular uniformity (Rayleigh's *z*), is highly significant showing the probability of a uniform phase distribution is <0.001. The neuron misses some cycles, but when it fires is locked to the stimulus waveform. Reproduced from Curthoys et al. (2019a) with permission of Elsevier. **(C–F)** Histograms of interspike intervals to show phase locking in the same utricular afferent neuron in guinea pig at two high frequencies of BCV **(C,E)** and air- conducted sound (ACS) stimuli **(D,F)**. The bin width is 0.16 ms. The dots below each histogram show integral multiples of the period for the given stimulus frequency. The clustering around these integral multiples demonstrates phase locking at both frequencies. Reproduced from Grant and Curthoys (2017) with permission of Elsevier. **(G–I)** To show the differences in otolithic stimulation between the accelerometer and seismometer modes. **(G)** Show the gross schematic. **(H)** and **(I)** Show the otolithic macula in motion in relation to an inertial reference. In the low frequency accelerometer mode, not only is neuroepithelial layer (NEL) in motion, the otoconial layer (OL) s also in motion lagging behind the NEL due to its inertia, resulting in relative displacement between the two layers. This is also true for the otolith in the seismometer mode **(I)**, where it is the NEL that is in motion with the OL remaining at rest or only slightly in motion, again due to its inertia **(I)**.

high frequencies. This relative displacement is proportional to the magnitude of the acceleration in accelerometer mode and proportional to the NEL displacement in seismometer mode. For both low and high frequencies, the hair bundles of the receptor are deflected, and the deflection mode is identical at both frequencies (Grant and Curthoys, 2017). The high sensitivity of the type I hair cell bundles in the striolar region pick up the small relative displacements that are imparted in the seismometer mode, whereas the extrastriolar hair cell bundles do not have sufficient sensitivity to pick up these small displacements.

It is unlikely that stimulation causes any deformation of the otoconial layer (OL), but it is possible. Detailed Finite Element Analysis (FEA) models were constructed of the turtle utricular macula and in this analysis there was no indication of deformation of the OL (Davis et al., 2007; Davis and Grant, 2014). These models utilized actual dimensions and shapes of real utricles developed through painstaking anatomical studies from live tissue. These models produce what is called Modal Analysis which shows deformations at various frequencies from motions of the overall OL and sections and parts of OL. This Modal Analysis did not show any deformation of the OL itself below 3 kHz.

Vestibular Primary Afferent Neurons – Phase Locking of Primary Afferents

When activated by ACS or BCV at frequencies of 250 Hz and above, guinea pig otolithic neurons with irregular resting discharge do not usually generate an action potential on every single cycle (Curthoys et al., 2019a), but the moment when they

fire in a cycle is locked to a narrow phase band of the stimulus waveform (**Figures 6A–C**), in a manner similar to the phase-locking of action potentials in single cochlear afferents to ACS (Rose et al., 1967; Palmer and Russell, 1986; Heil and Peterson, 2017). Phase-locking shows that every single cycle of the stimulus is a physiologically adequate stimulus for primary vestibular afferents, just as it is for cochlear afferents. In any vestibular neuron an action potential may not occur on every single cycle, especially for high-frequency stimuli (>250 Hz), for a number of reasons, such as neuronal refractory period. However the exact moment when the otolithic neuron fires an action potential is tightly locked to a narrow phase band of the imposed stimulus. This is true for both cochlear and vestibular afferent neurons.

For phase locking of the primary vestibular afferent to occur, the hair bundle of the receptor(s) must be deflected and activated once per cycle (at frequencies at or even above 3000 Hz) (Curthoys et al., 2019a). The evidence that this cycle-by-cycle receptor activation does occur is recordings of the cochlear microphonic and more recently the utricular microphonic (UM) – the extracellular hair cell potential caused by otolithic hair bundle deflection (Brown et al., 2017; Pastras et al., 2017a) (see section "ELECTROPHYSIOLOGY"). This important result conclusively shows that high-frequency 'vestibular' stimuli (>250 Hz) cause otolithic hair cells to generate potentials in response to these ACS and BCV stimuli (Pastras et al., 2017a; Pastras et al., 2018).

A particularly surprising result is the *precision* of phase locking of primary otolithic neurons (Curthoys et al., 2019a). Irregular vestibular afferents in guinea pigs have a measured phase locking precision to sound and vibration (Curthoys et al., 2019a) which is equal to or even superior to the precision of phase locking of guinea pig cochlear afferents to sound (Palmer and Russell, 1986). Furthermore, this high precision of phase locking of vestibular neurons extends to higher frequencies than reported for cochlear afferents. To appreciate the precision: for a 2000 Hz stimulus, the whole cycle is complete within 0.5 ms, yet the evidence shows that action potentials in some irregular primary otolithic neurons can be locked to a narrow phase band of around 20 deg within that extremely short interval – corresponding to a time window of around 50 microseconds. In short, irregular otolithic afferents have a phase precision in the microsecond time domain. The mechanism for such precision appears to lie in the unique calyx-type I receptor physiology where a very fast process, resistive coupling, may act to confer this very tight phase locking (Contini et al., 2017, 2020).

It is worth noting here that the exact mechanism by which ACS stimulates the otoliths (particularly the saccule), is not entirely clear. In the cochlea, hair cells are displaced due to a pressure gradient across the cochlear partition. In the utricle, it's possible that ACS induced pressure waves within the vestibule (which is not a fully closed system), also cause pressure gradients across the macula, and thus displacement. For the saccule, which is somewhat anchored to bone, the mechanism is less clear, however we have hypothesized that fluid pressure waves cause a direct displacement of the stereocilia.

When activated by ACS or BCV the action potentials of irregular (transient) afferents show clustering at the integral multiple of the period of the stimulus (**Figure 6C**). In the example shown, the neuron demonstrated phase-locking up to 1500 Hz for both BCV and ACS. Exactly how hair cell activation occurs is unclear at present. The hair bundles of receptors at the striola project into holes in the otolithic membrane but have tenuous attachment to that membrane. One possibility is that on each cycle the macula movement (i.e., the movement of the NEL) results in endolymph being displaced within the holes in the OL. Because of the dominant viscous flow of the endolymph at these very small dimensions, the hair bundles may track the endolymph displacement almost exactly, resulting in the motion of the hair bundle being directly coupled to the wall motion of the fluid-filled space (the hole) within the OL. Another possibility is that ACS and BCV cause displacement of the macula and that the hair bundles are deflected because they are viscously coupled to the endolymph and OL, and thus there is a differential motion of the hair cell and the hair bundle (Dallos, 1992; Cheatham and Dallos, 1999; Guinan, 2012; Guinan and Nam, 2018; Obrist, 2019; Peterson and Heil, 2020). The implications of these modes of hair cell stimulation are considered in section "MECHANICS OF OTOLITHS IN VEMPS TESTING".

A New Clinical Parallel: Auditory Neuropathy and Vestibular Neuropathy

Both the ABR and VEMP depend on synchronous activation of primary afferents and phenomena which interfere with such synchronous activation affect the evoked response. In patients, such an auditory deficit is referred to as auditory neuropathy where, although the cochlear receptors are functioning (and audiograms can appear normal), but the neural response to an abrupt onset stimulus is disturbed as shown by greatly reduced ABR responses to click stimuli (Starr et al., 1996; Michalewski et al., 2005; Kaga, 2016; Moser and Starr, 2016). There is an analogous neuropathy in VEMPs– apparently a vestibular neuropathy—where patients show poor or absent VEMPs (Hu et al., 2020) to repeated clicks or tone bursts. Some of these patients also have auditory neuropathy. The location of the auditory dysfunction was shown by recordings of electrophysiological potentials and the following Section explains the origin of these cochlear and the corresponding vestibular potentials.

The clinical and neural evidence shows that sound and vibration are effective stimuli for (some) vestibular as well as cochlear receptors and neurons. In turn that raises the question of exactly how vestibular receptors are activated by these stimuli and the extent to which vestibular receptor mechanisms have communalities with cochlear receptor mechanisms. The following section explores these similarities and differences in detail.

ELECTROPHYSIOLOGY

Background

Over the last 90 years inner ear researchers have developed an array of evoked responses to objectively examine cochlear hair cell (HC) and nerve function, and to a lesser extent vestibular

HC and nerve function *in vivo*. Although the first of these evoked potentials, the *microphonic*, was recorded around the same period for both the cochlea (1930) (Wever and Bray, 1930) and the vestibular system (1934) (Ashcroft and Hallpike, 1934), the development and uptake of subsequent tools has been vastly different across the two fields. In the auditory field, there has been steady development and use of electrophysiological potentials to investigate cochlear HC and nerve function (**Figure 7A**). Such potentials include the Cochlear Microphonic (CM), the Summating Potential (SP), the auditory nerve Compound Action Potential (CAP), the Auditory Nerve Neurophonic (ANN) and the Auditory Brainstem Response (ABR). These measures have been used to clarify cochlear operation in experimental animal research, and importantly have progressed to the clinic to diagnose human hearing disorders objectively. Clinical measures include Electrocochleography (ECochG), the ABR, and Otoacoustic Emissions (OAEs).

By comparison, vestibular research has had very few measures available to examine the electrophysiology of peripheral vestibular function, *in vivo*. Primarily, researchers have relied on single neuron recordings, or recordings of the Vestibular short-latency Evoked Potential (VsEP Jones, 1992; Jones and Jones, 1999). Several new experimental measures have recently been recorded from the utricular macula of anaesthetized guinea pigs, including the Utricular Microphonic (UM) (**Figure 7B**) (Pastras et al., 2017a), Utricular Summating Potential (Pastras et al., 2021), and the Vestibular Nerve Neurophonic. Importantly, these measures provide a first-order, physiological assessment of utricular function related to the clinical indicator, the VEMP. What follows is a direct comparison of *in vivo* evoked HC and neural responses in the cochlea and vestibular system, and how they relate to clinical response measures.

The Microphonic

In 1930, Wever and Bray documented that sound generated alternating electrical activity from the cat's cochlear nerve trunk, which closely mirrored the sinusoidal acoustic stimulus (Wever and Bray, 1930). Although initially believed to be action potentials from the cochlear afferents, it was later shown to be due to hair cell activity and so this work was the first recording of the (CM) (Hallpike and Rawdon-Smith, 1934). It only took 4 years to record the analogous potential in the vestibular system (Ashcroft and Hallpike, 1934). Even at this early stage, there were clear differences in response characteristics between measurements in the two sensory systems. Wever and Bray's ACS CM was sinusoidal between 5 Hz and 12 kHz, whereas, Ashcroft and Hallpike's non-mammalian 'VM', evoked by a tuning fork (and thus a BCV stimulus), was highly complex with double-frequency (*2f*) components and response cancellations, between 50 Hz and 1 kHz (Ashcroft and Hallpike, 1934).

In experimental animals, the CM is routinely recorded via a round window electrode following a simple dorsolateral surgery whereas the VM requires much more complex surgical exposure of the vestibular end organ and ablation of the cochlea to eliminate any cochlea contribution to putative vestibular potentials. This latter point is especially important since in identifying purely vestibular potentials it is mandatory that there can be no possible contribution from cochlear receptors. The majority of VM recordings have been from isolated *in vitro* preparations, which avoid these problems altogether (Corey and Hudspeth, 1979; Corey and Hudspeth, 1983). By comparison, the CM has been recorded in many species, such as the guinea pig (Patuzzi et al., 1989; Patuzzi and Moleirinho, 1998), chinchilla (Drescher and Eldredge, 1974), gerbil (Schmiedt and Zwislocki, 1977), rat (Brown, 1973; Uziel et al., 1981), mouse (Brown, 1973; Cheatham et al., 2004, 2011), and cat (Allen et al., 1971). These mammalian models share similarities with the human cochlea, providing a translational link for understanding human hearing disorders. Results indicate that when recorded at relatively low frequencies, the CM is a passive response primarily generated by the OHCs in the basal turn of the cochlea in close proximity to the recording electrode (Patuzzi et al., 1989).

In 2017, Pastras et al. developed a novel technique to record localized Utricular Microphonics (UMs) from the surface of the utricular macula, of anaesthetized guinea pigs (after cochlea ablation) during BCV and ACS (Pastras et al., 2017a, 2018). This technique is comparable to the CM recording as it provides a localized measure of HC function in the anaesthetized guinea pig, independently of cochlear contribution (**Figures 7A,B**). There are several important differences between the CM and UM.

Firstly, the hair bundles of the cochlea have uniform polarization, whereas the hair bundles of the utricle have opposite polarities on either side of the striola and face inwards at the striola (**Figures 3B,C**). For the cochlea, this means that a sinusoidal tone will activate stereocilia in phase and produce receptor currents which sum, resulting in an additive CM response which is large when recorded from 'near-field' locations such as the perilymph, and which is also measurable when recorded from 'far-field' locations using surface electrodes (Sohmer and Pratt, 1976). For the utricle, a sinusoidal stimulus will activate stereocilia with opposite polarities on either side of the "line of polarity reversal" at the striola, which can result in a complex, semi-cancelled UM. This is especially true when recording from the striola region where the hair bundles 'switch' polarity or at 'far-field' recording locations, such as the facial nerve canal, where anti-phase UMs sum over a large distance (Brown et al., 2017; Pastras et al., 2017a).

Despite this, a localized UM response can still be recorded in close proximity to the utricular hair bundles at the macula, away from the line of polarity reversal at the striola (Pastras et al., 2017a; Pastras et al., 2020). Like the CM, the 'near-field' UM can be used to probe localized changes in otolithic HC function and Mechanoelectrical Transduction (MET) channel gating. Here the localized UM is proportional to the summed current through a local subset of utricular HCs and the extracellular resistance between the current source and the recording electrode. For both cochlear and vestibular HCs, the relationship between MET transducer current and hair bundle displacement follows a Boltzmann activation (sigmoidal) function, and the opening probability of the hair bundle MET channels, or the transducer Operating Point (OP) can be modulated by varying the degree of stereocilia displacement. This has been demonstrated experimentally using a low-frequency biasing technique (**Figures 7D,F**; Salt et al., 2009; Pastras et al., 2020).

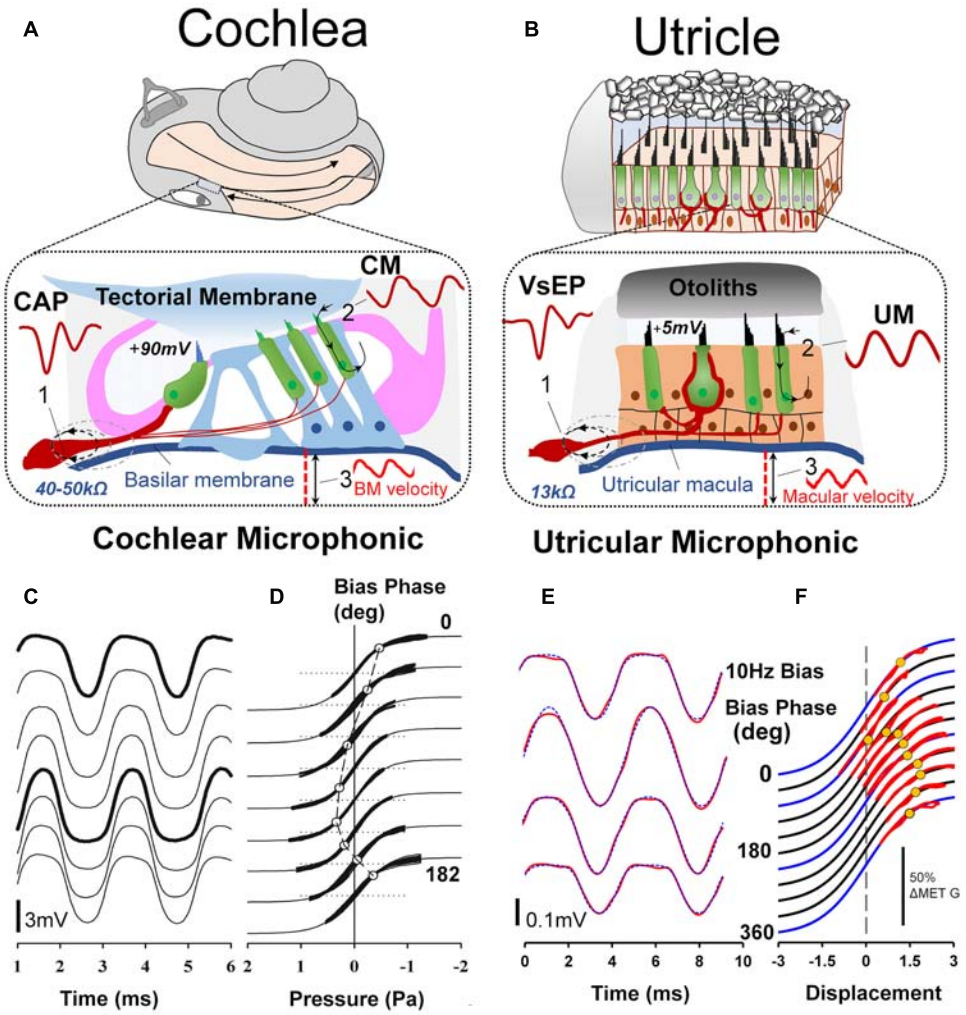

FIGURE 7 | (A) For decades auditory researchers have used objective measures of cochlear nerve, hair cell and mechanical function in the CAP, CM, and basilar membrane vibration to comprehensively investigate the cellular basis of hearing and associated disorders. **(B)** Analogous tools have recently been developed and characterized from the utricle, in the VsEP, UM and macular vibration to differentially assess peripheral vestibular function, *in vivo*. Reproduced (adapted) from Assessment of utricular nerve, hair cell and mechanical function, *in vivo*. Pg. 10. Doctoral Thesis. The University of Sydney. Christopher Pastras. 2018. With permission from Copyright owner Christopher Pastras. **(C)** Low-frequency (4.8 Hz) biased cochlear microphonic (CM) waveforms recorded from scala media of the basal turn in response to a 500 Hz, 90 dB SPL probe stimulus after injection of 0.5 μL Healon gel, used to mimic endolymphatic hydrops in the cochlear apex. **(D)** Lissajous figures show the same CM waveforms (heavy lines) plotted against a sinusoidal input, displaced to best fit the transducer curve (thinner line). The open circle indicates the displacement, which corresponds to the operating point at that point on the bias cycle. Reproduced from Salt et al. (2009) Copyright Elsevier (Hearing Research). **(E)** 220Hz Utricular microphonic (UM) waveforms during a 10 Hz hydrodynamic bias of the utricular macula. **(F)** UMs plotted on a Boltzmann Lissajous curve representing MET channel gating, using the approximated macular displacement, which includes an estimate of the operating point with displacement (gray circles).Reproduced from Pastras et al. (2020) Copyright Springer (Journal of the Association for Research in Otolaryngology).

Here a slow-dynamic displacement of the basilar membrane or utricular macula, modulates the degree to which cochlear or utricular hair bundles are biased opened (or closed), resulting in changes to cochlear and utricular hair cell sensitivity, and the CM and UM waveshape and saturation (**Figures 7C,E**).

Although the CM and UM both saturate non-linearly (**Figures 7C,E**), and a follow a first order Boltzmann function (Patuzzi and Moleirinho, 1998; Pastras et al., 2020), the CM and UM responses have different amplitudes. That is, when recorded from scala tympani, the CM is approximately 1–2 mV, or when recorded from scala media, the CM is several millivolts larger (**Figure 7C**). By comparison, the amplitude of the UM is about an order of magnitude smaller, and within the 50–500 μV range (**Figure 7E**). There are several reasons for this difference. Firstly, the differential polarization of the stereocilia in the cochlea or the utricular macula means extracellular receptor currents either sum or partially cancel (Pastras et al., 2017b). The localized UM from the macula is the result of a localized subset of utricular HCs, whereas the CM from the round window measures a much larger population of cochlear HC currents, which sum (in-phase). Secondly, the endolymphatic potential driving the HCs is approximately 20 times larger in the cochlea compared to the

utricle (+90 mV vs ∼ 4–5 mV), and surrounding membranes dividing the cochlea scalae have resistances more than twice that of the membranes of the utricular macula (∼45k Ω vs 13k Ω), producing a comparably larger electrical potential for cochlear versus utricular HC stimulation.

Cochlear HCs are also more 'sensitive' than vestibular HCs, in the sense they have lower activation thresholds to ACS (and BCV) stimulation. That is, the threshold to obtain a CM response from the round window to sound is approximately 60 dB (i.e., x1000) lower than the sound pressure level needed to obtain a UM to the same stimulus from the utricular macula. Another difference between cochlear and utricular HCs is the difference in their frequency range or bandwidth. Recordings using Laser Doppler Vibrometry (LDV) to measure utricular macula movement in the guinea pig have demonstrated that the UM is most 'sensitive' to low-frequency BCV and ACS, between 100 and 200 Hz (Pastras et al., 2018). So, the UM and CM are both sensitive to 'low-frequency' stimuli but differ greatly in their bandwidth and dynamic range. The state of the labyrinth during recordings is very different for CM and UM. For the CM, the bony labyrinth generally remains intact, and measurements are taken via non-invasive round window recordings (Brown et al., 2013). This is ideal, as it provides a robust measure of mammalian cochlear HC function with an intact membranous labyrinth, analogous to the physiological state of the labyrinth in the clinic. For the UM, a much more invasive surgical procedure is needed in which the cochlea is ablated via a ventral approach. This eliminates any cochlear contribution to the recorded potential and provides access to the basal surface of the macula in close proximity to the utricular HCs (Pastras et al., 2017a, 2018) and so allows localized UM recording. However it leaves the labyrinth in a dehiscent state, which changes the mechanical operation of the labyrinth (Rosowski et al., 2004) and so modifies the sensitivity of the utricular HCs (Pastras et al., 2018) and afferents (Curthoys, 2017).

The Summating Potential

The Summating Potential (SP) is used as an objective measure of cochlear HC function in both basic science (Durrant and Dallos, 1974) and clinical research (Gibson, 2009). More specifically, the SP is a stimulus-related DC potential primarily produced by the asymmetry of the gating mechanism on the MET channels of the stereocilia of the HCs, when stimulated by alternating stimuli, which mediates generation of the CM (Choi et al., 2004). Hence, many of the features unique to the CM, are also unique to the SP. For example, the amplitude of the SP is dependent on the size, and specifically the level asymmetry of the CM.

Although the SP has been recorded for 70 years in auditory research it has not been previously recorded in the vestibular system. This is likely due to the difficulty in recording pure vestibular HCs responses *in vivo*, independent of any cochlear contribution. We have recently developed a novel method to record localized utricular SPs from the surface of the utricular macula (Pastras et al., 2021; **Figures 8B,C**). A vestibular SP is expected since vestibular HCs also obey a similar Boltzmann activation function to that of cochlear HCs (Géléoc et al., 1997), where transduction currents saturate nonlinearly for large displacements of the stereocilia bundle (Salt et al., 2009; Pastras et al., 2020). The utricular SP has several common features with the cochlear SP. For example, the generation of the utricular SP also requires moderate to intense levels of ACS and BCV stimulation, where the hair bundles are driven into saturation (**Figure 8A** vs. **Figure 8C**). This can be modeled by increasing the stimulation level (and resultant stereocilia displacement) and extent to which the MET transducer current is modulated into asymmetrical ('high-slope') regions of the transfer function

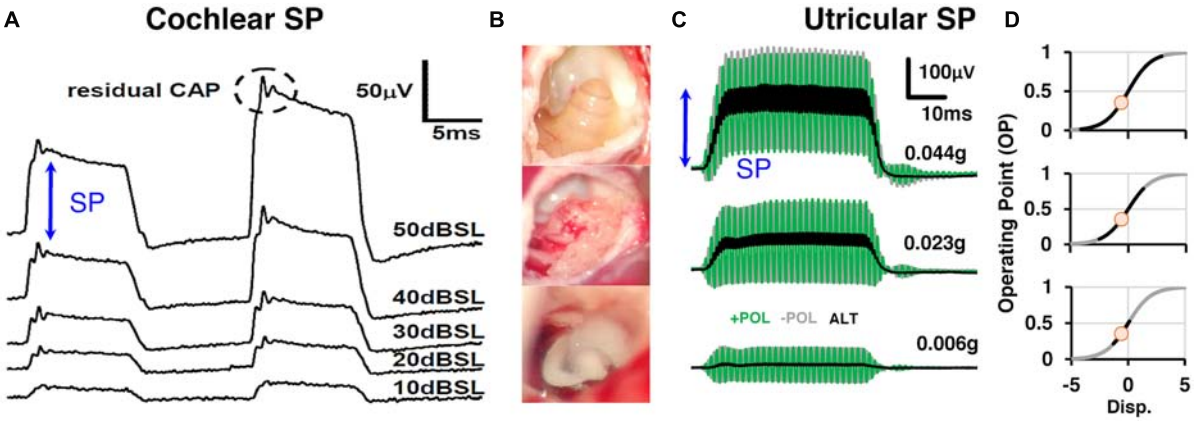

FIGURE 8 | (A) Sound-evoked responses recorded simultaneously from scala tympani and scala vestibuli subtracted from one-another to produce differential (DIFF) responses, which is an approximation of the cochlear Summating Potential. DIFF waveforms were evoked by 18 kHz and 20 kHz tone-bursts at a range of sound levels (10–50 dB SPL). Reproduced (adapted) from 'Origins and use of the stochastic and sound-evoked extracellular activity of the auditory nerve'. Pg. 162. Doctoral Thesis. The University of Western Australia. Daniel Brown. 2006. With permission from Copyright owner Daniel Brown. **(B)** In order to record utricular SPs, a ventral surgical approach is needed to surgically ablate the cochlea and expose the utricular macula for localized recordings on the macular surface. **(C)** Utricular SPs were evoked by alternating BCV stimuli at moderate to intense levels of BCV (0.023 – 0.044 g). **(D)** The generation of SPs were modeled by modulating the MET transducer current into asymmetric (high-slope) regions of the gating profile (first-order Boltzmann function). Reproduced (adapted) from Pastras et al. (2021). Copyright Elsevier (Hearing Research).

(**Figure 8D**). Because the CM and UM input-output curve is not a simple linear function, and is rather sigmoidal, an SP can be produced by large displacements of the HC, which moves the HC I/O function into 'non-linear' regions of the S-shaped curve.

Also, like cochlear hair cell responses, the AC:DC ratio of the UM declines with increasing frequency (Russell and Sellick, 1978). This is relevant, because the size of the DC component of the receptor potential (relative to the AC component) dictates the size of the SP. And where there is no DC component, and only an AC component, the response is purely microphonic. Hence, at low-frequencies (e.g., 50–200 Hz), UMs from the macula are relatively more symmetrical compared to higher frequencies (e.g. >300–2000 Hz) Pastras et al., 2021). This result parallels intracellular recordings from the cochlea, in which the AC:DC ratio is largest at low-frequency (100–300 Hz) and declines thereafter with increasing frequencies (Russell and Sellick, 1978). The reduction in AC:DC ratio with increasing frequency is also importantly correlated with the precision of phase locking of primary afferent neurons, where AC receptor potentials are needed for high-precision phase-locking of cochlear afferent neurons or the "Rate code" (Palmer and Russell, 1986). Interestingly (Curthoys et al., 2019a) recently demonstrated that utricular afferents have phase locking at least as precise as cochlear afferents suggesting that the generation of AC receptor potentials are probably relatively similar in both the utricle and cochlea.

The cochlear SP is modulated during mechanical manipulations of the organ of Corti, believed to be largely because to the HC contributions from displacement sensitive OHCs (Pappa et al., 2019). However, recently it was shown the IHCs are also likely embedded into the overlying tectorial membrane (Hakizimana and Fridberger, 2021). This makes the cochlear SP a useful tool to probe mechanical pathologies such as endolymphatic hydrops in MD (using electrocochleography – see below), which shifts the position of the basilar membrane and modulates the sensitivity of these displacement sensitive HCs. Interestingly, the utricular SP is also sensitive to static displacements of the utricular macula (Pastras et al., 2021), meaning that, like the cochlear SP, the utricular SP can also be used to assess mechanical (and morphological) changes in the labyrinth to assess vestibular health and disease.

Neural Function. The Compound Action Potential

The auditory nerve Compound Action Potential (CAP) was first recorded in the 1950s (Tasaki, 1954; Pestalozza and Davis, 1956; Goldstein and Kiang, 1958) and represents the potential caused by synchronous firing of auditory nerve fibres to the onset (or offset) of a stimulus. It has been used extensively in animal models to investigate gross cochlear nerve function and in the clinic in electrocochleography (ECochG) (Eggermont, 1976a,b) and the ABR (Eggermont, 2019) to probe hearing loss. The CAP waveform is comprised of a series of negative and positive peaks, namely the N1, P1, N2, and P2, which resemble a damped 1 kHz sinusoid (**Figure 9A**) (Brown and Patuzzi, 2010). The cellular origins of these peaks are due to the influx and efflux of sodium and potassium currents through various voltage gated ion channels along the auditory pathway. The longer latency peaks in the ABR response, such as N2, P2, etc., arise from neural activity in the central relays of the auditory pathway such as the cochlear and olivary nuclei, the lateral lemniscus, inferior colliculi (Møller and Jannetta, 1985).

Unlike the low-frequency CM (<500 Hz), which originates 'locally' from basal turn hair cells, operating well below their characteristic frequency (CF) and is mostly passive, the CAP has both passive and active elements, depending on stimulus frequency and level. For example, the low-to-moderate suprathreshold, high-frequency (>1 kHz) evoked CAP in the healthy cochlea is generated by HCs operating at the CF and is thus active. This 'sharp tuning', boosts cochlear gain by ∼ 60 dB (x1000) and is the result of prestin-mediated somatic electromotility of the OHCs (Cheatham et al., 2004). It is known as the cochlear amplifier, and it effectively negates viscous damping in the cochlea at high frequencies. However, the cochlear amplifier has stable metabolic requirements, which is why the CAP tuning curve loses its sharpness and becomes 'passive' following experimental manipulations such as hypoxia and drainage of perilymph (Sellick et al., 1982). This also partly explains hearing loss associated with pathologies such as presbycusis and age-related hearing loss (Ohlemiller, 2002).

The Vestibular short-latency Evoked Potential (VsEP) is the vestibular analogue of the cochlear CAP (**Figure 9B**) and was arguably first recorded in 1979 by Cazals et al. to ACS in the guinea pig following ototoxic ablation of cochlear HCs (Cazals et al., 1979, 1980; Didier and Cazals, 1989). Following this, the response was recorded in an array of setups and animal models, with early examples including the pigeon (Wit et al., 1981) and the rat (Elidan et al., 1982). The term 'VsEP' can be attributed to Josef Elidan and his laboratory, who first described the vestibular compound action potential evoked by abrupt angular acceleration stimuli (∼5000°/s^2), initially described as the 'short-latency vestibular evoked response (VsER) (Elidan et al., 1986, 1987a,b) and thereafter as the 'short latency vestibular evoked potential (VsEP) (Elidan et al., 1991). Since this time the VsEP has been mostly associated with the work of Jones et al. (Jones and Pedersen, 1989; Jones, 1992; Jones et al., 1998; Jones and Jones, 1999) who have recorded VsEPs from the scalp in various animal models using linear up-and-down 'jerk' stimulus pulses of short (∼ 2 ms) duration. Other notable techniques have recorded the VsEP to linear acceleration pulses using BCV from the bony facial nerve, producing a more localized field potential (Bohmer, 1995). For a more detailed overview of the VsEP, including its history, stimulation parameters, measurement details (peripheral vs central), interpretation, and techniques to reduce artifacts and cochlear contributions, see Brown et al. (2017).

Like the CAP, the VsEP also represents the synchronous firing of vestibular neurons in response to the onset of the stimulus (**Figures 9A,B**). And like the CAP, which arises from myelinated primary afferents innervating the IHCs (Brown and Patuzzi, 2010), the VsEP has been shown to arise from irregular primary vestibular afferents, which mostly innervate type I HCs at the striola. This has been inferred through single unit recordings, in which it is the irregular calyx/dimorphic

afferents which respond to transient stimuli such as BCV and ACS (see section "INTRODUCTION" above) (Curthoys et al., 2016), unlike regular bouton afferents, which respond to 'low-frequency' sustained stimuli, but not to sounds or vibration. More specifically, the VsEP has been shown to be sensitive to kinematic jerk (Jones et al., 2011)of the animal's head frame (**Figures 9C,D**). Kinematic jerk is the time rate of change of linear acceleration. It is still not clear how the HC generators of the VsEP are activated during stimulation. In the cochlea, there are several distinct micromechanical activation modes of receptor HCs, where displacement sensitive OHCs are activated by reticular lamina-tectorial membrane shearing, and the IHCs are stimulated by longitudinal and radial flow, which also become entrained with partition displacement at higher frequencies via viscous drag. However, recently it has been revealed that IHCs are likely embedded in the tectorial membrane, and may be displacement sensitive like OHCs (Hakizimana and Fridberger, 2021). Ultimately, the CAP is produced by both HC subtypes synergistically working together, where displacement sensitive OHCs amplify basilar membrane vibration and increase the input drive to the IHCs, which directly branch to myelinated spiral ganglion afferents, which generate the CAP response.

In terms of the micromechanical activation of vestibular HCs responsible for generating the VsEP, it is possible that their stereocilia are viscously coupled. That is, recent immunohistochemistry studies in the mouse utricle have shown that striolar hair bundles are short and stiff, and not physically attached to the OL, whereas the extrastriolar bundles are longer and appear to be embedded in the membrane (Li et al., 2008). This suggests that HCs responsible for generating the VsEP (i.e., striolar, type I HCs) may be viscously activated, similar to IHCs in the cochlea. Furthermore, a recent study which modulated the macromechanics of the macula using low-frequency hydrodynamic biasing (<20 Hz), required 10 times less macular displacement to modulate the sensitivity of the UM, compared to the VsEP response (**Figures 9E–I**; Pastras et al., 2020). This suggests that the UM is more likely displacement sensitive, whereas the VsEP is likely velocity sensitive. This aligns with previous work, where the UM scales with macular displacement across frequency (Pastras et al., 2018; Pastras, 2018), and not velocity - the saturation of the UM (and amplitude of the utricular SP) are modulated following static displacements of the utricular macula (Pastras et al., 2021). Taken together, these results demonstrate that the UM and VsEP can potentially be used to differentially assess distinct cellular substrates of utricular pathology, similar to how the CM and CAP are used to assess different regions of the cochlea frequency tuning curve (e.g., tail vs CF).

There is no conflict between velocity sensitivity at the micromechanical level and the jerk sensitivity of the VsEP that Jones et al. showed (Jones et al., 2011). They reported that the effective stimulus at the level of the skull is jerk, but due to the micromechanical operation at the level of the utricular macula, that jerk stimulus at the skull results in velocity of the stereocilia probably being the effective stimulus for the receptor hair cell.

Recently, dual patch recordings of the type I hair cell and calyx afferent have implicated 3 distinct modes of synaptic transmission at this unique synapse: glutamatergic quantal transmission, K+ accumulation, and resistive coupling (in the microsecond time domain). These 3 modes of synaptic transmission may explain some features of the VsEP, such asrapid response kinetics, relative insensitivity to forward-masking, unlike the cochlear CAP (i.e., the VsEP can be recorded at high stimulation rates such as 125 Hz or 8 ms between pulses, whereas the CAP is largely attenuated at these rates). Hence, there may be no need for a somatic-electromotility in the vestibular system, which in the viscous environment of the cochlea is suited to counteracting damping, especially at 'high-frequencies'. At the very least, what is needed in the otoliths are highly sensitive linear accelerometers, which operate over a physiological relevant bandwidth, from gravity to several kilohertz (see section "MECHANICS OF OTOLITHS IN VEMPS TESTING"). Displacement and velocity sensitive vestibular HCs, coupled with multiple synaptic modes of transmission, with top-down feedback from the efferents can in theory, provide this.

The VsEP can be recorded via an electrode in the facial nerve canal, near the superior branch of the vestibular nerve. This technique provides a greater electrical pick up from the primary afferent neurons and a relatively large evoked potential (∼30–50 μV). However, this response is evoked using BCV and ACS, which also stimulates the cochlea. Hence, in order to record VsEPs uncontaminated by cochlear potentials with the labyrinth intact, the cochlea must be silenced whilst also being kept structurally intact. Masking noise has been used previously to minimize cochlear contribution, and although this does a good job at disrupting the synchronized afferent activity from cochlear neurons, it does not fully eliminate receptor potentials such as the CM and SP (Deatherage et al., 1957; Marsh et al., 1972). Hence, a more reliable method is to chemically silence the cochlea using slow perfusion of KCl, whilst sparing vestibular function, as recently demonstrated in Pastras et al. (2020). Using this technique, VsEPs can be recorded from the facial nerve canal with the cochlea structurally intact, yet functionally inactive.

Electrocochleography vs. Electrovestibulography

When a combination of HC and neural field potentials are recorded together in response to ACS or BCV bursts, the technique is called Electrocochleography (ECochG) in the cochlea, or Electrovestibulography (EVestG) in the vestibular system. For the reasons listed above, ECochG is relatively straightforward to record in experimental animal models at locations such as the round window, where there is a large electrical pickup from both cochlear HCs and neurons. Moreover, ECochG has also been used for several decades in the clinic to differentially assess HC vs nerve dysfunction associated with hearing loss. However, more reliable and robust measures such as the ABR and Otoacoustic Emissions (OAEs) are taking its place.

Depending on the stimulus, ECochG will contain varying levels of an onset CAP, an Auditory Nerve Neurophonic (ANN),

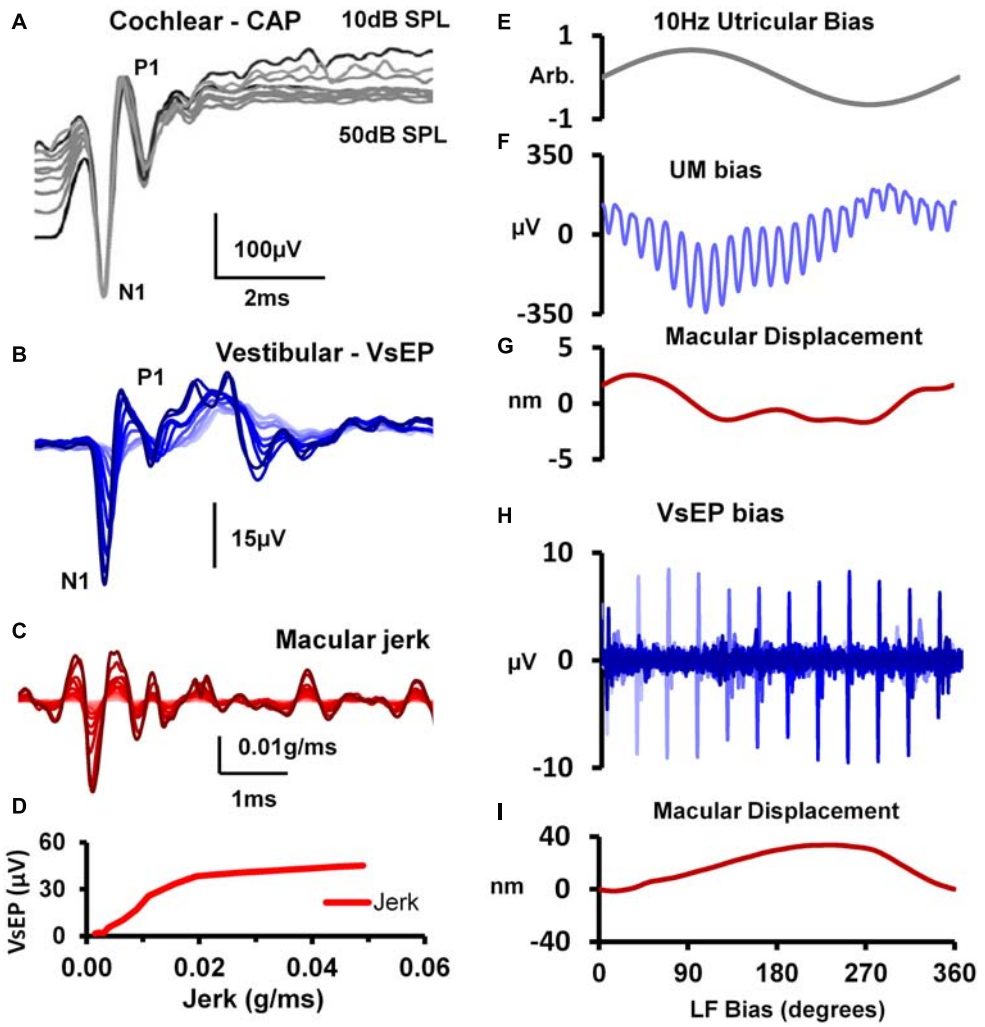

FIGURE 9 | (A) Cochlear nerve CAPs evoked by an 18 kHz, 10 ms tone-burst over a 50 dB sound level range above the CAP detection threshold (in 5 dB steps), showing that the amplitude of the N1 potential is unchanged despite such a large change in stimulus intensity. Reproduced (adapted) from 'Origins and use of the stochastic and sound-evoked extracellular activity of the auditory nerve'. Pg. 153. Doctoral Thesis. The University of Western Australia. Daniel Brown. 2006. With permission from Copyright owner Daniel Brown. **(B)** VsEPs evoked by a 0.6ms BCV pulse (0.3ms rise-fall time) over a 25 dB attenuation range. **(C)** Simultaneous measures of utricular macular jerk (integrated from LDV measures of macular velocity). **(D)** Input-output function for VsEP N1-P1 amplitude against peak-peak macular jerk. Reproduced (adapted) from Pastras et al. (2018) Copyright Elsevier (Hearing Research). 10x more macular displacement is required to modulate the sensitivity of the VsEP compared to the UM. **(E)** 10 Hz hydrodynamic bias of the utricular macula delivered via a fluid-filled pipette sealed into the horizontal semicircular canal (hSCC). **(F)** Cyclic modulation of the UM amplitude evoked by 220 Hz BCV over 1 cycle of the 10 Hz bias (100 ms), and **(G)** the corresponding level of macular displacement. **(H)** Cyclic modulation of the VsEP evoked by a 1ms BCV pulse over 1 cycle of the 10 Hz bias, and **(I)** the associated macular displacement. Adapted from Pastras et al. (2020) Copyright Springer.

SP and CM. For example, if the acoustic stimulus is well beyond the HC corner frequency, such as in **Figure 10A** with an 18 kHz tone, the CM will be largely filtered, leaving behind the SP and CAP. Moreover, if the tone exceeds the frequency for cochlear nerve synchronicity (i.e., beyond 1–2 kHz), the ANN will be non-existent. That is the reason why in **Figure 10A** only the onset CAP and SP can be detected at 18 kHz. Likewise, if the acoustic stimulus is alternated, the fundamental frequency of the CM will be largely cancelled, leaving behind the CAP, ANN, SP and any higher-order harmonic components. Additionally, the presence of the onset CAP is dependent on the rise-time of the tone burst, where a long rise-time (and highly smoothed stimulus envelope) can smear the synchronous activation of afferents and greatly diminish the onset (or offset) CAP. This helps to explain the clinical observation that VEMPs are largest to stimuli with very short rise times (Burgess et al., 2013), and that VEMPs can be activated by a multitude of transient stimuli such as tone-bursts, chirps, clicks, taps and pulses. The EVestG has been shown to contain a combination neural and HC components, which include the onset VsEP, Vestibular Nerve Neurophonic, Vestibular Microphonic and Vestibular Summating Potential.

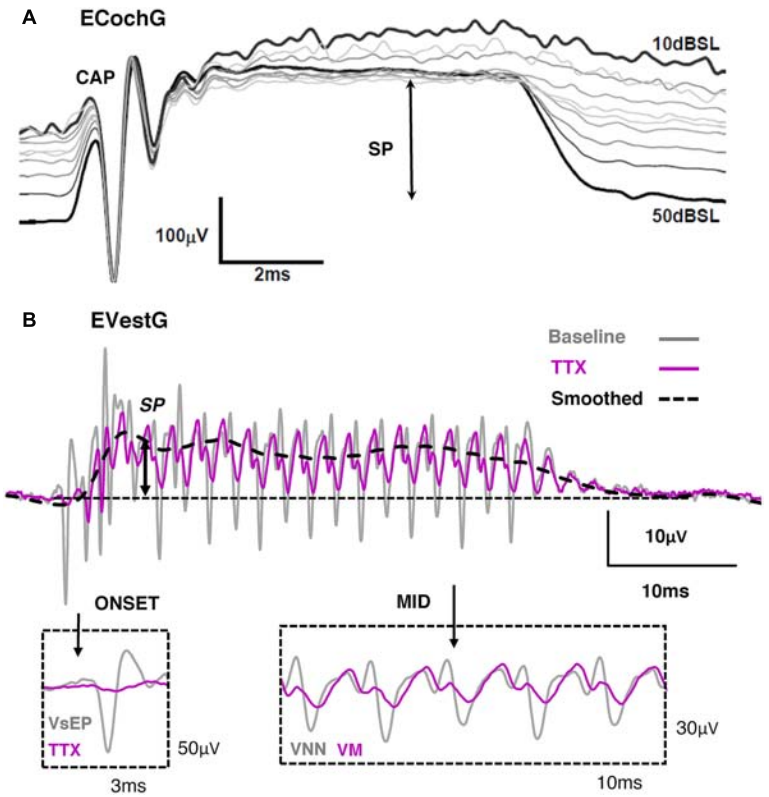

FIGURE 10 | (A) Electrocochleography (ECochG) response recorded from the round window of the guinea pig during an 18 kHz, 10ms tone burst of varying intensity. Reproduced (adapted) from 'Origins and use of the stochastic and sound-evoked extracellular activity of the auditory nerve'. Pg. 153. Doctoral Thesis. The University of Western Australia. Daniel Brown. 2006. With permission from Copyright owner Daniel Brown. **(B)** Electrovestibulography (EVestG) response taken from the facial nerve canal of the guinea pig to 507 Hz, 40 ms BCV train burst. Tetrodotoxin (TTX) abolished the onset VsEP (gray) and the mid response VNN (gray), leaving behind the VM and SP. Reproduced (adapted) from Pastras et al. (2021) Copyright Elsevier (Hearing Research).

Peripheral Electrophysiology in Experimental Animal Models and Their Link to Clinical Recordings

Clinical vestibular researchers have used an 'indirect' measure of peripheral otolith function in the VEMP (see section "INTRODUCTION"). The VEMP can be thought of as the clinical myogenic correlate of the VsEP, which is, similarly, driven by irregular primary afferents at the striola (Curthoys et al., 2019b). Hence, many of the features which apply to the VsEP (such as transient response activation), should also apply to sensory receptors generating the VEMP at the striola.

Moreover, it is possible to understand how otolithic HCs operate in the VEMP recording, from measurements of the otolithic microphonic during BCV and ACS. That is, by looking at the sensitivity and frequency range of otolithic microphonics from the macula, one can begin to understand the cellular correlates of the VEMP. Results indicate that otolithic HCs are active up to 5 kHz BCV and ACS (Pastras et al., 2018). Hence, it is no surprise that 'high-frequency' VEMPs can be recorded for stimulus frequencies beyond a kilohertz, and very clearly in patients after an SCD (Manzari et al., 2013; Curthoys and Manzari, 2020).

Recent results using simultaneous LDV recordings of macular velocity and the UM indicate that the utricular HCs have different macromechanical activation modes for BCV and ACS (Pastras et al., 2018). Hence, it is possible that the sensory activation of receptors during the VEMP is different for BCV compared to ACS (Govender et al., 2016) and some clinical evidence supports this difference (Govender et al., 2016). This may have clinical implications for the future diagnosis of vestibular disorders, such as endolymphatic hydrops in MD, where the tuning of VEMP shifts upwards to 1 kHz (see also sections "INTRODUCTION" and "MECHANICS OF OTOLITHS IN VEMPS TESTING"). For example, if the macromechanical activation pathways of the VEMP are different for sound and vibration, then the change in tuning may also be different for both stimulation modes, depending on pathology and the mechanical (or morphological) change.

In summary, basic physiological measures from the utricular macula, can be used to differentially assess utricular nerve and hair cell function, and additionally, be utilised to investigate the response characteristics of the VEMP as a means to understand vestibular health and disease.

BOX 1 | Undamped Natural Frequency – Non-Mathematical Description.

The undamped natural frequency (UDNF) of otoliths defines their dynamic behavior when it is excited by a high frequency stimulus in VEMPs testing (Curthoys and Manzari, 2020; Manzari et al., 2013; Noij and Rauch, 2020). Note, that "high frequency" with regards to vestibular stimulation (and the VEMP) is >500 Hz, which is much lower than what is considered high frequency in the cochlea.

The UDNF is defined as the square root of shear stiffness of the gel-column filament layer, divided by the mass of the otoconial layer (OL). When these two quantities, shear stiffness and OL mass, are numerically evaluated they are both functions of the utricle surface area (area defined by its perimeter), and because the stiffness is divided by the mass, the area divides out. The resulting expression for the UDNF is then the square root of the shear stiffness defined by the shear modulus of the gel-column filament layer which is divided by the product of the OL density, the thickness of this layer, and the thickness of the gel-column filament layer.

The thickness of the two layers, OL and gel-column filament layer, primarily define the UDNF of the system. The other two variables, gel-column filament layer shear modulus and OL density, are less variable and appear to remain somewhat constant. The result is that for a healthy young adult the UDNF is predicted to be 400 Hz. This frequency is dependent on the parameter values under the square root, and these parameters are difficult to measure experimentally.

The excitation frequencies for VEMP testing results in the utricle behavior as a seismometer, as opposed to an accelerometer at lower excitation frequencies (Grant and Curthoys, 2017). In seismometer mode, the OL essentially remains at rest due to its inertia, while the neural-epithelial layer is in motion, shearing the gel-column filament layer. This relative shear displacement is proportional to the head displacement imposed by the high frequency VEMP stimulus. It is this shear displacement that deflects hair cell bundles, either by their attachment to the OL and/or the bundles being dragged and forced through their surrounding endolymph, opening ion-channels and initiating neural signals.

Using the UDNF and the fact that the utricle system is underdamped (Dunlap and Grant, 2014) a curve predicting the relative shear displacement between the two layers, otoconial and neural-epithelial, relative to a unit neural-epithelial layer displacement, can be constructed as a function of stimulus frequency. This curve is called a Frequency Response Curve or Transfer Function Plot and is shown in **Figure 12**. This curve remains flat at zero displacement until the excitation frequency near the UDNF. The curve then rises rapidly as the excitation frequency increases and passes through the UDNF, continues to rise, and then flattens out with increasing excitation frequency. Because the system is underdamped, the curve has a slight upward trend or upward bulge, before it begins to flatten out beyond the UDNF. The highest point on this part of the response curve is defined as the best test frequency or just best frequency. This exact point in the response curve would be difficult to detect in VEMP testing.

MECHANICS OF OTOLITHS IN VEMPS TESTING

Undamped Natural Frequencies

The following shows how knowledge of the characteristics of the layers of the utricular macula (thickness, stiffness etc.) can be used to predict the response of receptors and afferents to stimuli of varying frequency [For a non-mathematical description of Undamped Natural Frequency (UDNF), see **Box 1** text]. The layers of the macula have been simplified to the otoconial layer (OL) and neuroepithelial layer (NEL) and between them is the shear layer comprised of the Gel layer and the column filament layer (CFL) (see **Figures 6G–I** for a simplified schematic).

The UDNF ω_n can be predicted from the Shear Layer (SL) stiffness k_{SL}, and the Otoconial Layer (OL) mass m_{OL}, using the standard expression for UDNF

$$\omega_n = \sqrt{\frac{k_{SL}}{m_{OL}}} \tag{1}$$

Note that this is a shear oscillatory frequency which results in the OL moving parallel to the Neural-Epithelial Layer (NEL).

The shear layer includes the Gel Layer (GL) which lies next to the OL, the Column Filament Layer (CFL) which rests on the NEL, and Hair Cell Bundles (HCB) which reside in both layers. The shear layer stiffness used here is an effective stiffness that includes both the GL, CFL, and the HCB stiffness collectively, and includes the entire thickness of both layers. The GL is relatively thin compared to CFL and most of the effective stiffness is contributed by the CFL and HCB. The stiffness of this effective shear layer is expressed as

$$k_{SL} = \frac{F}{\delta} \tag{2}$$

where: F = a shear force acting on the surface between the SL and OL, and δ = the relative displacement between the NEL and OL produced by the force F. The force F is hypothetical here, in an actual stimulus it is the NEL that is moving due to head motion, and the OL remains at rest due to its inertia. This force F is the resultant of a shear stress τ acting over the entire surface between the OL and SL, designating this area A, which defines the force in terms of shear stress and area $F = \tau A$. The shear stress can be defined in terms of the shear modulus G which is defined as

$$G = \frac{\tau}{\gamma} \tag{3}$$

where: g = the shear strain, which is δ = deflection divided by shear layer thickness t_{SL}, $\gamma = \frac{\tau}{t_{SL}}$

Combining these expressions, the SL stiffness expression becomes

$$k_{SL} = \frac{F}{\delta} = \frac{G\gamma A}{\gamma t_{SL}} = \frac{GA}{t_{SL}} \tag{4}$$

The shear modulus G represents a material property of the effective shear layer and can be related to Young's modulus.

The OL mass $m_{OL}$is the product of the density of the OL, ρ_{OL} and the volume of the OL, $V_{OL} = t_{OL}A$
where: t_{OL} = the thickness of the OL, and the mass then is

$$m_{OL} = \rho_{OL} A t_{OL} \tag{5}$$

The UDNF becomes

$$\omega_n = \sqrt{\frac{k_{SL}}{m_{OL}}} = \sqrt{\frac{\frac{GA}{t_{SL}}}{\rho_{OL} A t_{OL}}} = \sqrt{\frac{G}{\rho_{OL} t_{OL} t_{SL}}} \tag{6}$$

and the area divides out. The utricle and saccule area are probably larger to incorporate more HC and thus more neural input for the vestibular system. With numerical values for the parameter under the square root sign a prediction of the UDNF of an otolith can be made.

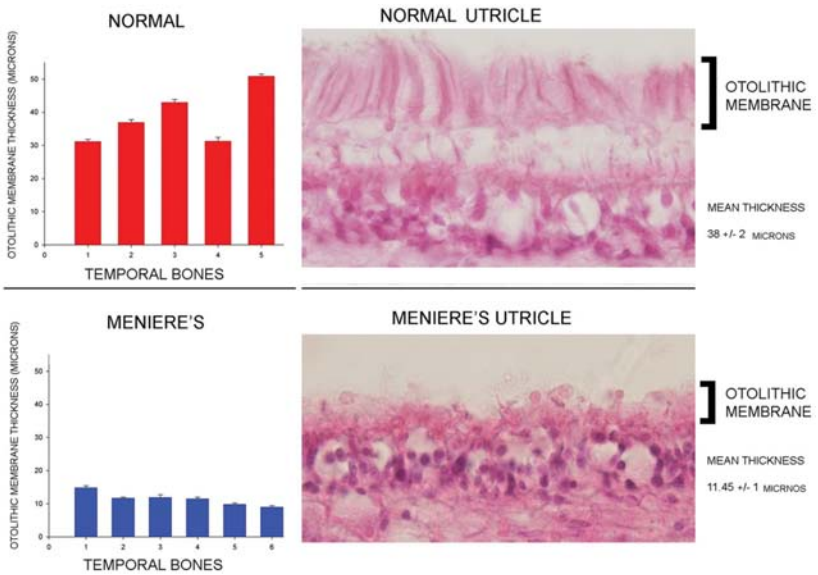

FIGURE 11 | Thickness of the human Otoconial Layer. The Normal Utricle photomicrograph shows otoconial layer thickness values from five specimens; The lower Menière's utricle showing diseased macula with a much thinner otoconial layer, photomicrograph and OL thickness for six specimens. Reproduced by permission from Ishiyama et al. (2015).

Numerical parameter values for predicting the human UDNF, those under the square root sign of Eqn. 6, will be evaluated. Most of the parameter values in Eqn. 6 have been evaluated in animals and in some humans. Thickness of the shear layer t_{SL} has not been studied in any animal or human.

Shear Modulus - G

The shear modulus has never been measured directly in any animal, including humans, but evaluations have been made using indirect experimental measures. The best experimental measurement was done in the turtle (Dunlap and Grant, 2014) where the shear modulus was 9.42 Pa (with 95% confidence interval of 8.36 – 10.49) in the medial-lateral direction, and 11.31 Pa (10.21 – 12.41) in the anterior-posterior direction. An overall mean value of 10 Pa (9.3 – 11.5) will be used here. Other researchers are in approximate agreement with these values. Shear Modulus values measured by others, converted from Young's modulus using an incompressible material, are all for the canal cupula except one and they are: G = 7 Pa in zebra fish (McHenry and van Netten, 2007); G = 11.53 Pa in pike fish (ten Kate, 1969), a human cupula model estimates of G = 3.3 Pa (Selva et al., 2009), and a human otolith model estimate of the order G = 3.3 Pa (Kondrachuk, 2001).

Otoconial Layer Density - ρ_{OL}

The OL density is based on a 4:1 calcite crystals (ρ = 2710 kg/m^3) to gel ratio (ρ = 1003 kg/m) for this layer (Pote et al., 1993). The otoconial crystals in the OL are in the calcite crystal form, and these crystals are bound together by the same protein gel material from the GL. When the five parts (4 parts crystals and 1 part gel) of the OL are considered, the density is ρ_{OL} = 2368 kg/m^3

Otoconial Layer Thickness - t_{OL}

Value for human thicknesses that will be utilized here is: t_{OL} = 38 ±2 μm (Ishiyama et al., 2015), which is the most accurate available. This thickness is shown in the **Figure 11** photomicrograph along with the five temporal bone values used for the mean.

Shear Layer Thickness - t_{SL}

Human shear layer thickness has not been measured or reported in any published research. The value has been evaluated from two photomicrographs of human specimen obtained from Ulf Rosenhall (1972). The mean of multiple scaled values from the photomicrographs with a 10% allowance for tissue processing shrinkage was t_{SL} = 17.5 μm. The shrinkage allowance may not be sufficient for this type of gel tissue; however, it is the standard value currently in use. Also scaling from the photomicrograph histological section shown in **Figure 11** with a 10% shrinkage allowance was a tenth of a micron larger. The value of t_{SL} = 17.5 μm will be used here.

Using the above mean values, the UDNF is

$$\omega_n = 401\ Hz \tag{7}$$

Using the 95% confidence interval values for G and the two values on either side of the mean for OL thickness results in the following spread in the value above using the means

$$\omega_n = 377\ Hz\ and\ 441\ Hz \tag{8}$$

The parameter values utilized are the best that can be found from current literature. A value for the human UDNF of ω_n = 400 Hz will be used here for further analysis.

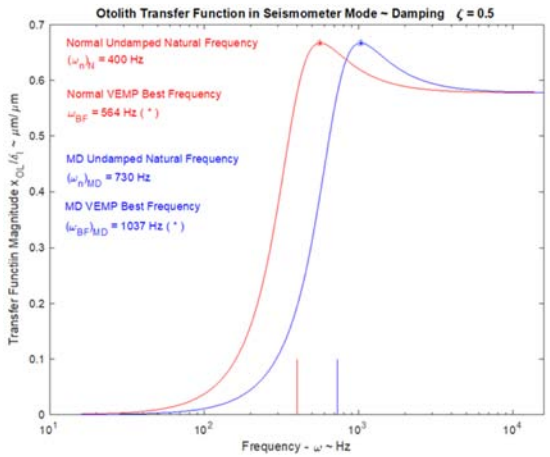

FIGURE 12 | Utricle frequency response (Bode Plot) in Seismometer Mode (shown in red) using estimated UDNF of 400 Hz (shown as vertical red line) and damping ratio of ζ = 0.5 (Dunlap and Grant, 2014). The best test frequency is 564 Hz, shown as red asterisk (*). The frequency response curve for Menière's Disease (shown in blue) using and estimated UDNF of 730 Hz and with a best frequency of 1037 Hz shown as blue asterisk (*).

Otolith Seismic Mode Transfer Function and Frequency Response

A transfer function of Neural Epithelial Layer (NEL) motion, with the utricle in seismometer mode induced by a Bone Conducted Vibration (BCV) stimulus will show the best frequency for maximizing output for clinical testing. Using the mean value for UDNF of $\omega_n =$ 400 Hz and a damping ratio of $\zeta =$ 0.5 (Dunlap and Grant, 2014) for an underdamped system, both estimates for humans, will be used.

The transfer function is developed from the basic linear differential equation that describes the relative displacement motion x between the NEL and the OL. That basic equation is

$$m\ddot{x} + c\dot{x} + kx = \left(1 - \frac{\rho_e}{\rho_{OL}}\right) mA_{GI} \tag{9}$$

where: x = relative displacement between OL and NEL, the over dots represent differentiation with time, m = OL mass, c = SL damping coefficient, k = SL stiffness coefficient, ρ_e = endolymph density, ρ_{OL} = OL density, B = $\left(1 - \frac{\rho_e}{\rho_{OL}}\right)$ = buoyancy term, and A_{GI} = gravitoinertial acceleration (sum of NEL acceleration and gravity) (Grant and Curthoys, 2017). Dividing by the OL mass the basic equation is reduced to two parameters and a buoyancy term

$$\ddot{x} + \frac{c}{m}\dot{x} + \frac{k}{m}x = BA_{GI} \tag{10}$$

This governing equation of motion for the OL relative to the NEL is converted using nomenclature for standard dynamic system parameters: Damping ratio $\zeta = \frac{c}{c_o c}$, where: c_o = critical damping, and $z < 1$ is an underdamped system, $\omega_n = \sqrt{\frac{k}{m}}$ (the UDNF as introduced above), and Eqn. 10 becomes

$$\ddot{x} + (2\zeta\omega_n)\dot{x} + \left(\omega_n^2\right)x = BA_{GI} \tag{11}$$

The above is converted into a transfer function for an utricle operating in seismometer mode:

$$\frac{x}{D_{NEL}} = B\left(\frac{\omega^2}{\left(\omega_n^2 - \omega^2\right) + j\left(2\zeta\omega_n\right)}\right) \tag{12}$$

where: D_{NEL} = displacement of the NEL relative to an inertial frame of reference, x = relative displacement between NEL and OL, $j = \sqrt{-1}$ = imaginary number, and ω = the excitation or stimulus frequency [for details of this derivation see Grant and Curthoys (2017)].

Constructing a frequency response diagram using Eqn. 12 for the otolith in seismometer mode, will have the utricle measuring the displacement of the NEL's motion. The frequency response diagram is shown in **Figure 12** (red curve) for an utricle operating above its UDNF. The **Figure 12** plot, with gain $\frac{x}{D_{NEL}}$ vs stimulus frequency ω, was done using an UNDF $\omega_n =$ 400 Hz (human value estimated above), and a damping ratio $\zeta =$ 0.5 [value measured in the turtle (Dunlap and Grant, 2014)]. The seismometer transfer functions peaks at its best frequency for use in VEMPs testing. This best test frequency is defined as the one which produces the greatest gain on the transfer function curve. This greatest gain displacement would give hair cell bundles their greatest displacement for a given stimulus displacement magnitude, producing the best neural stimulus. The best test frequency is $\omega_{BF} =$ 564 Hz, as seen in **Figure 12**, and this value is very near the most commonly used in VEMPs testing frequency of 500 Hz. Also seen in the figure is that the range of best frequency is broad from 500 to 600 Hz. There is such a modest increase in gain over this stimulus frequency range, that it would be improbable to detect the best test frequency with an VEMP test.

Menière's Transfer Function - Otolith in Seismic Mode

Recent published research shows that aging patients with Menière's Disease (MD) have decreased OL thickness and thus decreased mass, resulting in higher UDNFs (Ishiyama et al., 2015). This deficiency has been identified using higher stimulus frequencies for VEMPs to produce larger responses in aging subjects (Rosengren et al., 2019). These results are explained by the decreased OL thickness shown in postmortem evaluation of patients with Menière's Disease (Ishiyama et al., 2015). Importantly, this thickness change is likely to be related to the chronic/sustained dysfunction of hearing and balance in MD sufferers, and is unlikely to be involved in the fluctuation of symptoms (e.g., hearing fluctuation).

Using the MD decrease in OL thickness from 30 down to 11.45 μm shown in **Figure 11**, and leaving all other parameters unchanged, the UDNF increased from 401 to 730 Hz. Using this MD UDNF for a frequency response plot moves the whole curve to the right resulting in a higher frequency response as seen by the blue curve in **Figure 12**. This moves the best frequency point for normal individuals of 564 up to 1037 Hz for MD patients. From this exercise it is clearly seen that it is this change in OL thickness, decreasing the OL mass, that is probably causing the larger VEMP response at increased stimulus frequency. This loss of mass in the

OL is a change in the peripheral mechanics, and this change is seen in the neural response to a VEMPs stimulus. A fundamental principle involved here, and for any sensory system (biological, mechanical, electronic, etc.), the system cannot obtain any information that is not contained in the primary signal of the system sensor. In this case the system sensor is the otolith which has two modes: accelerometer and seismometer. In the case of MD examined here, a fundamental change in the system UDNF changes the whole system frequency response. It remains to be seen if the upward shift of VEMP tuning in MD patients is related to their low frequency hearing loss.

Transient Behavior of Otoliths in VEMPs Testing

It should be recognized that Frequency Response Diagrams as addressed in the previous section represent the steady state response to a stimulus, and any transient response to a stimulus is not reflected in these diagrams. This steady state response is by definition and by design in frequency response diagrams. Transient behavior is not represented or depicted in any way in these diagrams. The utility and mathematics for Frequency Response Diagrams or Bode Diagrams (sometimes called Bode Plots) were worked out back in the 1930s by WH Bode at Bell Labs. These diagrams were intended for use in electronic circuits and transmission line losses, as well as in control systems design and behavior work, where transient behavior was not an issue. The transient response in VEMPs testing is significant and is addressed in this section.

Solving Eqn. 11, which describes the dynamic behavior of relative displacement between NEL and OL of otoliths in its seismic mode, was integrated numerically in time using MATLAB for these solutions. The NEL stimulus used in this simulation was a sinusoidal displacement of NEL, with maximum displacement of 50 nm, and with various stimulus frequencies ω. The response shows a significant displacement at initiation of NEL motion stimulus with stimulus frequencies well above the UDNF. These results are shown in **Figure 13**, using the following parameters: UDNF ω_n = 400 Hz (human value estimated above), and a damping ratio ζ = 0.5 (value measured in the turtle Dunlap and Grant, 2014).

These results indicate that it is more advantageous to use 1000 Hz stimulus with zero rise time rather than the 500 Hz with a 2ms rise time that is in customary use for VEMPs testing. A significant transient displacement occurs in less than 5 ms, with

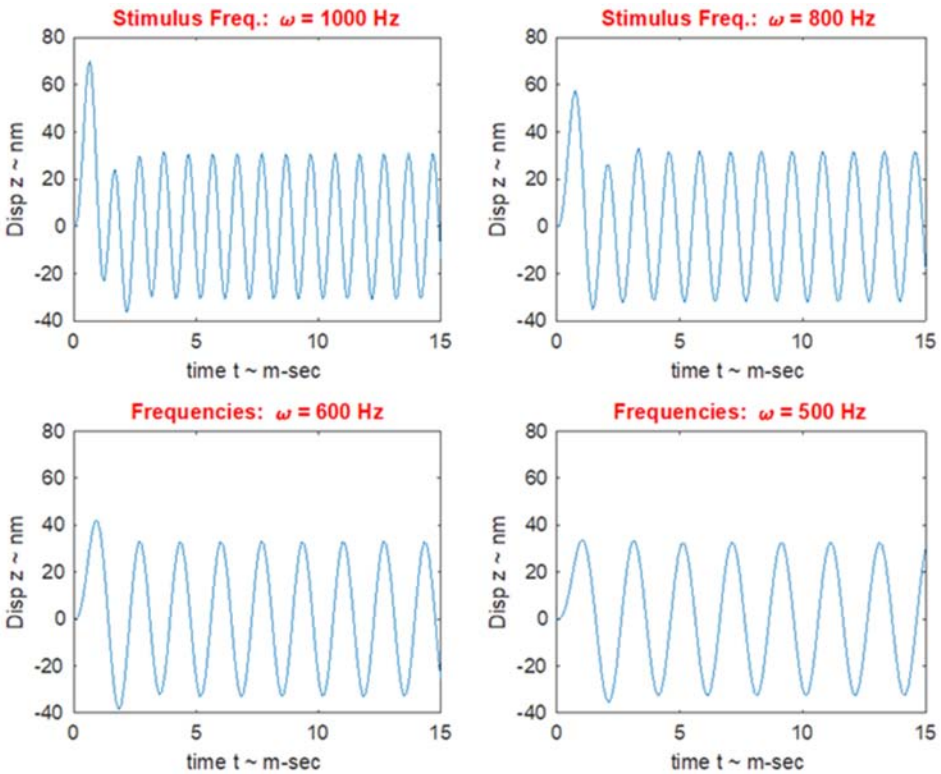

FIGURE 13 | Relative Displacement *z* vs. time *t* response curves, for solutions of Eqn. 11, the equations of motion for relative displacement between OL and NEL. Parameter for this solution: UDNF of 400 Hz (human estimate from above), damping ratio of 0.5 (value measured in the turtle; Dunlap and Grant, 2014), and with a NEL maximum displacement of 50 nm (estimate for a VEMP stimulus; Grant and Curthoys, 2017). The solutions were obtained numerically using MATLAB and show significant transient displacement response at the onset of the response when the stimulus frequency ω, indicated in red above each curve, is well above the UDNF. As can be seen in the 1000 and 800 Hz curves, the transient displacement is above the maximum stimulus value of 50 nm. The transient is present with a 600 Hz stimulus, and almost absent at 500 Hz.

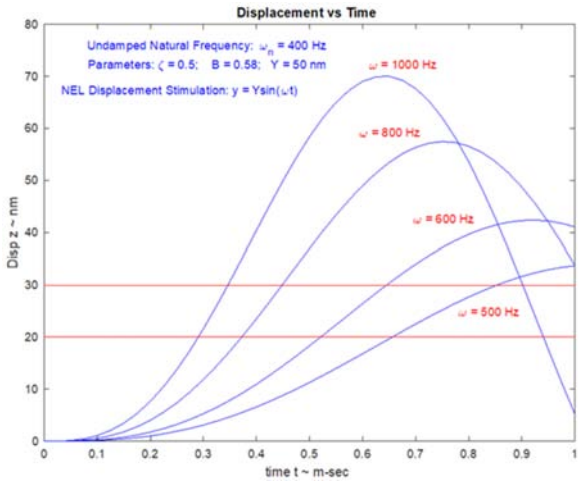

FIGURE 14 | Relative displacement *z* vs. time *t*, over 1 ms, for various stimulus frequencies. Suspected threshold range of 20–30 nm is shown in red (Grant and Curthoys, 2017). The two higher frequencies reach the threshold range before 0.5 ms, while the lower two reach this range in in a time frame greater than 0.5 ms. This figure shows a better illustration of the maximum or peak values for the transient behavior.

amplitude that is 1.4 times the NEL displacement stimulus. This transient stimulus has settled down to a steady state displacement after 0.5 ms time. Most VEMPs testing today incorporates a ramping up to the maximum displacement used for the stimulus, and these ramp times are generally in the 2–5 ms range. It is also seen that this ramp up to maximum stimulus magnitude should also be avoided to capture this transient behavior. By doubling the customary frequency of 500 Hz and eliminating the ramp up to maximum stimulus frequency, significant deflection stimulus to striolar hair cell bundles could be achieved. The significant contribution of rise time to oVEMP amplitude is shown in **Figure 1C**.

Threshold Displacement

Stimulus frequency also influences the time before relative displacement has reached the threshold displacement of hair cell bundles. Using the same simulation for stimulus frequency in the previous section (ω_n= 400 Hz, ζ = 0.5, and D_{NEL} = 50 nm) and examining the transient response over a shorter time period, shows that for higher frequencies there is shorter time to reach the range of suspected threshold deflection for striolar hair cell bundles. This is shown in **Figure 14**.

The suspected threshold for bundle displacement is expected to be in the 20 – 30 nm range (Grant and Curthoys, 2017). Evaluation of this range of NEL displacements utilizing the model, indicates that the higher this NEL stimulus displacement the higher the threshold maximum displacement value. The ratio of maximum threshold displacement to maximum stimulus displacement remains constant at 1.4 over the frequency ranges examined here.

Striolar Hair Cell Bundle Stimulus

Inner hair cells in hearing are deflected by the relative motion between their base and the surrounding endolymph fluid (Freeman and Weiss, 1990a,b). In a similar manner, type I hair bundles in the striolar region of the utricle are also deflected by

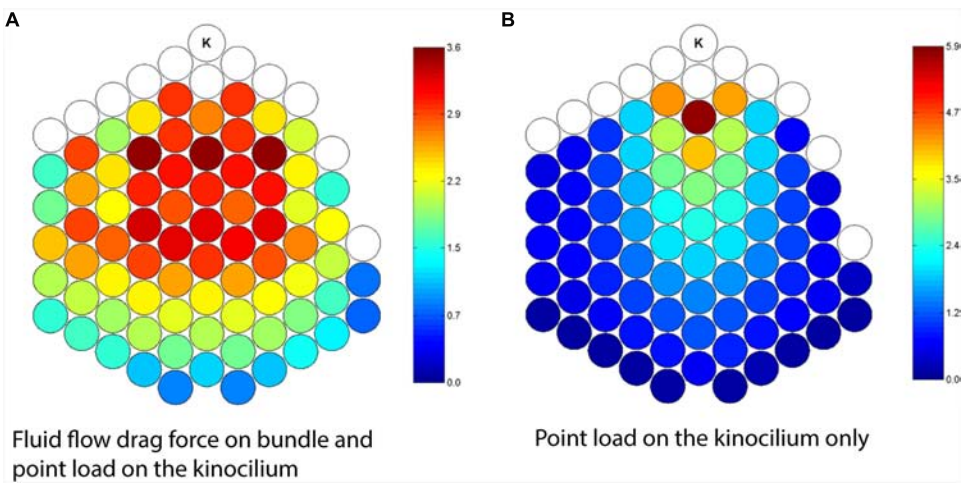

FIGURE 15 | Striolar Type I hair cell bundle viewed from above with different deflection loadings. In these diagrams, each circle represents a stereocilium or kinocilium (designated K), with stereocilia without a tip-link are in white. Tip-link tension color-scales are shown to the right of each figure in terms of pN (piconewtons) force above a resting tension of 20 pN. The resting tension is produced by the molecular motors that hold the tension at a value just below channel open probability with the bundle at rest. Any stereocilium with an increased tip-link tension of 1.0 pN above resting is considered at 50% open probability. The Bundle to the left **(A)** is loaded with both fluid flow producing a drag force on the bundle and a point load on top of the kinocilium. All tip-links in this bundle are well above the 50% open probability tension and are considered open. The bundle to the right **(B)** is only loaded with a point force load on the kinocilium top, and with no fluid flow drag force loading. A large fraction of the tip-links around the periphery are well below the 50% open probability range. Those at the bottom are not tensioned at all. Only the central portion of the bundle has well opened tip-link channels. Tip-link tensions are shown after a full dynamic loading time period of 1 ms (Nam et al., 2005).

the relative motion between their base and the surrounding fluid, as well as being somewhat or loosely attached to the OL. The term relative motion here refers to the fact that in both cases it is the base that is in motion in relation to an inertial reference. For the otolith, in accelerometer mode, not only is neuroepithelial layer (NEL) in motion, the OL is also in motion lagging behind due to its inertia, resulting in relative displacement between the two layers. This is also true for the otolith in the seismometer mode, where it is the NEL that is in motion with the OL remaining at rest or only slightly in motion, again due to its inertia. In all cases, auditory inner hair cells, utricle striolar hair cells in acceleration mode and seismometer mode, it is the relative motion of endolymph fluid flowing over hair cell bundles, producing a drag force on the bundle causing them to deflect and so activating the tip-links as shown in **Figure 15**. This has been termed the shear force due to viscous coupling or viscous drag.

Utricle striolar bundles, are structurally stiff and are large bundles with large numbers of stereocilia. These bundles appear to be weakly attached to the OL, and they are likely deflected by the relative motion of endolymph flow drag. Finite element modeling shows that with only attachment to the OL, only a central section of these bundles activated their tip-link channels. With the relative motion and relative flow of endolymph over the bundle, all the tip-link channels are opened, providing a robust stimulus to these cells (Nam et al., 2005). The two extremes of stimulus are shown schematically in **Figure 15**: A. both OL displacement and fluid forcing and B. OL displacement alone.

The next steps in the unfolding VEMPs story will hopefully elaborate on the different tip-link patterns for different stimuli.

SUMMARY AND CONCLUSION

We have given a broad overview of the clinical vestibular (otolithic) response – the vestibular evoked myogenic potential (VEMP) – to sound or vibration. We summarized the neural projections responsible for VEMPs and the neurophysiological results from *in vivo* extracellular recordings of single mammalian primary otolithic afferent neurons which provide the evidence that the VEMP is generated from a small subset of otolithic afferents with irregular resting discharge originating from receptors at the striola of the otolithic maculae. These afferents have a sensitive response to sound and vibration and show precise phase locking. Other otolithic afferents with regular resting discharge originating from extrastriolar receptors, are not activated by sound and vibration even at high intensities but show sensitive response to low frequency linear acceleration (<50 Hz). So, the otolithic maculae, like the retina, have two co-existing afferent neural systems – the transient system from the striolar afferents and the sustained system from the extrastriolar afferents.

A major objective of this publication was to communicate the contribution of the high frequency seismometer mode of otolithic response for understanding the measurement of VEMPs. For this seismometer mode of otolithic responding we addressed its mechanical origin, neural pathway, high sensitivity, phase locking capability, and overall behavior and compared this mode to auditory transduction. The significance of this high frequency mode of vestibular operation was not addressed. In daily life it may operate in two ways:

(1) As an initial signal to alert and to prepare muscles for a coming signal for contraction. This process is utilized in order to speed up the neural reflex, minimizing response time from stimulus until a muscle corrective action through contraction is taken. This can be applied to not only the vestibulo-ocular response during rapid head movements, but also is used for rapid response of the musculoskeletal system in situations such as slips or potential falls.
(2) It may also be used as a sound receptor for signals in the 0.5–3 kHz range. More than likely, this is an evolutionary remnant from fish which used this system for sea water hearing. However, it is still functioning in humans, and more than likely mammals have evolved to use this capability for rapid locomotion response to falls or other activities that require fast muscular response and rapid visual acuity in time of rapid head motion. The vestibulo ocular response is recognized as probably the fastest human reflex.

Section "ELECTROPHYSIOLOGY" addresses the main question – how is it that otolithic receptor cells are activated by sound and vibration. We summarize recent electrophysiological recordings from *in vivo* recording of mammalian utricular receptors showing that during stimulation by sound or vibration the otolithic maculae have similar electrophysiological potentials as cochlear receptors indicating receptor activation – both show microphonics, summating potentials, and gross evoked neural potentials. These electrophysiological results show that the VEMP can be thought of as the clinical myogenic correlate of the vestibular short-latency evoked potential (the VsEP) which is the vestibular correlate of wave I of the ABR. In these experiments any cochlear contribution was eliminated because the cochlea had been ablated so the potentials were purely vestibular. The similarity between the cochlear and vestibular system is to be expected since otolithic receptors are the evolutionary precursors of cochlear receptors and afferents (Straka et al., 2014).

"MECHANICS OF OTOLITHS IN VEMP TESTING" section uses mathematical modeling to show how the otolithic maculae with its layer of dense otoconia can allow the generation of hair cell and afferent response to such high frequencies. The modeling shows that the physical characteristics of the otolithic macula allow the system to respond to both very low frequency stimuli (accelerometer mode) and very high frequency stimuli (seismometer mode). The high frequency response has been especially puzzling because of the dense layer of otoconia overlying the receptors. But receptors at the striola are likely activated by fluid displacement around the hair bundle stereocilia which are tenuously attached to the otoconial membrane. The modeling not only predicts that the peak macula frequency response occurs at about 500 Hz but also that the peak frequency response shows an upward shift (to 1000 Hz) in patients with Menière's Disease.

In summary we have shown the receptor, the neurophysiological and the mechanical basis of VEMPs to sound and vibration and the similarities between vestibular and cochlear receptor electrophysiology. Of course, major questions remain: (1) a detailed time series analysis of the macula movement which will explain the extremely fast response of primary otolithic afferents; and (2) what causes the differences between sound and vibration in clinical responses; and (3) what is the exact stereociliary mechanism triggering the intracellular receptor changes in striolar receptors.

AUTHOR CONTRIBUTIONS

IC wrote the manuscript. JG wrote the section "Mechanics of Otoliths in VEMP Testing" about the accelerometer-seismometer model evidence. CP and DB wrote the section titled "Electrophysiology" about *in vivo* evoked potentials such as the microphonic and compound action potential. IC and LF wrote the section about clinical evidence. All authors reviewed and approved the text of the final manuscript.

FUNDING

CP and DB were in receipt of funding from the Garnett Passe and Rodney Williams Memorial Foundation. The authors wish to thank the Department of Biomedical Engineering and Mechanics at VA Tech, and the School of Psychology at University of Sydney for their support. The work presented here was the outcome of research collaboration sponsored by the Toni Haid scholarship of the Working Group of German-Speaking Audiologists, Neurotologists and Otologists (ADANO) to LF.

ACKNOWLEDGMENTS

Much of the work reported here has been supported by the Garnett Passe and Rodney Williams Memorial Foundation, and we are very grateful for their continued support, and also for the support of the National Health and Medical Research Council of Australia. The input of Jong-Hoon Nam is gratefully acknowledged. We are especially grateful for the expert help (again) of Ann Burgess.

REFERENCES

Adams, M. E., Heidenreich, K. D., and Kileny, P. R. (2010). Audiovestibular testing in patients with Meniere's disease. *Otolaryngol. Clin. North Am.* 43, 995–1009.

Allen, G. W., Dallos, P., Sakamoto, S., and Homma, T. (1971). Cochlear microphonic potential in cats: effects of perilymphatic pressure. *Arch. Otolaryngol.* 93, 388–396.

Andermann, M., Patterson, R. D., and Rupp, A. (2020). Transient and sustained processing of musical consonance in auditory cortex and the effect of musicality. *J. Neurophysiol.* 123, 1320–1331. doi: 10.1152/jn.00876.2018

Ashcroft, D., and Hallpike, C. (1934). On the function of the saccule. *J. Laryngol. Otol.* 49, 450–460.

Bohmer, A. (1995). Short-latency vestibular evoked-responses to linear acceleration stimuli in small mammals – masking effects and experimental applications. *Acta Otolaryngol. (Stockh)* 520 Pt 1, 120–123.

Breitmeyer, B. G., and Ganz, L. (1976). Implications of sustained and transient channels for theories of visual-pattern masking, saccadic suppression, and information-processing. *Psychol. Rev.* 83, 1–36. doi: 10.1037/0033-295x.83.1.1

Brown, A. M. (1973). High frequency peaks in the cochlear microphonic response of rodents. *J. Comp. Physiol.* 83, 377–392.

Brown, D. J., and Patuzzi, R. B. (2010). Evidence that the compound action potential (CAP) from the auditory nerve is a stationary potential generated across dura mater. *Hear Res.* 267, 12–26. doi: 10.1016/j.heares.2010.03.091

Brown, D. J., Chihara, Y., Curthoys, I. S., Wang, Y., and Bos, M. (2013). Changes in cochlear function during acute endolymphatic hydrops development in guinea pigs. *Hear. Res.* 296, 96–106. doi: 10.1016/j.heares.2012.12.004

Brown, D. J., Pastras, C. J., and Curthoys, I. S. (2017). Electrophysiological measurements of peripheral vestibular function-a review of electrovestibulography. *Front. Syst. Neurosci.* 11:34. doi: 10.3389/fnsys.2017.00034

Burgess, A. M., Mezey, L. E., Manzari, L., Macdougall, H. G., McGarvie, L. A., and Curthoys, I. S. (2013). Effect of stimulus rise-time on the ocular vestibular-evoked myogenic potential to bone-conducted vibration. *Ear. Hear.* 34, 799–805. doi: 10.1097/AUD.0b013e318294e3d2

Calzada, A. P., Lopez, I. A., Ishiyama, G., and Ishiyama, A. (2012). Otolithic membrane damage in patients with endolymphatic hydrops and drop attacks. *Otol. Neurotol.* 33, 1593–1598. doi: 10.1097/MAO.0b013e318271c48b

Cazals, Y., Aran, J. M., Erre, J. P., and Guilhaume, A. (1980). Acoustic responses after total destruction of the cochlear receptor – brain-stem and auditory-cortex. *Science* 210, 83–86. doi: 10.1126/science.6968092

Cazals, Y., Aran, J. M., Erre, J. P., Guilhaume, A., and Hawkins, J. E. (1979). Neural responses to acoustic stimulation after destruction of cochlear hair-cells. *Arch. Otorhinolaryngol.* 224, 61–70. doi: 10.1007/bf00455225

Cheatham, M. A., and Dallos, P. (1999). Response phase: a view from the inner hair cell. *J. Acoust. Soc. Am.* 105, 799–810. doi: 10.1121/1.426269

Cheatham, M. A., Naik, K., and Dallos, P. (2011). Using the cochlear microphonic as a tool to evaluate cochlear function in mouse models of hearing. *J. Assoc. Res. Otolaryngol.* 12, 113–125.

Cheatham, M., Huynh, K., Gao, J., Zuo, J., and Dallos, P. (2004). Cochlear function in Prestin knockout mice. *J. Physiol.* 560, 821–830.

Choi, C.-H., Chertoff, M. E., Bian, L., and Lerner, D. (2004). Constructing a cochlear transducer function from the summating potential using a low-frequency bias tone. *J. Acoust. Soc. Am.* 116, 2996–3007.

Clark, B. (1967). Thresholds for perception of angular acceleration in man. *Aerosp. Med.* 38, 443–450.

Cleland, B. G., Dubin, M. W., and Levick, W. R. (1971). Sustained and transient neurones in the cat's retina and lateral geniculate nucleus. *J. Physiol. Lond.* 217, 473–496. doi: 10.1113/jphysiol.1971.sp009581

Cleland, B. G., Levick, W. R., and Sanderson, K. J. (1973). Properties of sustained and transient ganglion-cells in cat retina. *J. Physiol. Lond.* 228, 649–680. doi: 10.1113/jphysiol.1973.sp010105

Colebatch, J. G., and Halmagyi, G. M. (1992). Vestibular evoked potentials in human neck muscles before and after unilateral vestibular deafferentation. *Neurology* 42, 1635–1636.

Colebatch, J. G., Day, B. L., Bronstein, A. M., Davies, R. A., Gresty, M. A., Luxon, L. M., et al. (1998). Vestibular hypersensitivity to clicks is characteristic of the Tullio phenomenon. *J. Neurol. Neurosurg. Psychiatry* 65, 670–678.

Colebatch, J. G., Halmagyi, G. M., and Skuse, N. F. (1994). Myogenic potentials generated by a click-evoked vestibulocollic reflex. *J. Neurol. Neurosurg. Psychiatry* 57, 190–197.

Contini, D., Holstein, G. R., and Art, J. J. (2020). Synaptic cleft microenvironment influences potassium permeation and synaptic transmission in hair cells surrounded by calyx afferents in the turtle. *J. Physiol. Lond.* 598, 853–889. doi: 10.1113/jp278680

Contini, D., Price, S. D., and Art, J. J. (2017). Accumulation of K+ in the synaptic cleft modulates activity by influencing both vestibular hair cell and calyx afferent in the turtle. *J. Physiol. Lond.* 595, 777–803. doi: 10.1113/jp273060

Corey, D. P., and Hudspeth, A. J. (1979). Response latency of vertebrate hair cells. *Biophys. J.* 26, 499–506. doi: 10.1016/S0006-3495(79)85267-4

Corey, D., and Hudspeth, A. (1983). Kinetics of the receptor current in bullfrog saccular hair cells. *J. Neurosci.* 3, 962–976. doi: 10.1523/jneurosci.03-05-00962.1983

Correia, M. J., and Lang, D. G. (1990). An electrophysiological comparison of solitary type I and type II vestibular hair-cellS. *Neurosci. Lett.* 116, 106–111. doi: 10.1016/0304-3940(90)90394-o

Curthoys, I. S. (2010). A critical review of the neurophysiological evidence underlying clinical vestibular testing using sound, vibration and galvanic stimuli. *Clin. Neurophysiol.* 121, 132–144. doi: 10.1016/j.clinph.2009.09.027

Curthoys, I. S. (2017). The new vestibular stimuli: sound and vibration-anatomical, physiological and clinical evidence. *Exp. Brain Res.* 235, 957–972. doi: 10.1007/s00221-017-4874-y

Curthoys, I. S. (2020). The anatomical and physiological basis of clinical tests of otolith function. A tribute to Yoshio Uchino. *Front. Neurol.* 11:566895.

Curthoys, I. S., and Dlugaiczyk, J. (2020). Physiology, clinical evidence and diagnostic relevance of sound-induced and vibration-induced vestibular stimulation. *Curr. Opin. Neurol.* 33, 126–135. doi: 10.1097/wco.0000000000000770

Curthoys, I. S., and Manzari, L. (2020). A simple specific functional test for SCD: VEMPs to high frequency (4,000Hz) stimuli-their origin and explanation. *Front. Neurol.* 11:612075. doi: 10.3389/fneur.2020.612075

Curthoys, I. S., and Vulovic, V. (2011). Vestibular primary afferent responses to sound and vibration in the guinea pig. *Exp. Brain Res.* 210, 347–352. doi: 10.1007/s00221-010-2499-5

Curthoys, I. S., Burgess, A. M., and Goonetilleke, S. C. (2019a). Phase-locking of irregular guinea pig primary vestibular afferents to high frequency (> 250 Hz) sound and vibration. *Hear. Res.* 373, 59–70. doi: 10.1016/j.heares.2018.12.009

Curthoys, I. S., Grant, J. W., Burgess, A. M., Pastras, C. J., Brown, D. J., and Manzari, L. (2018). Otolithic receptor mechanisms for vestibular-evoked myogenic potentials: a review. *Front. Neurol.* 9:366. doi: 10.3389/fneur.2018.00366

Curthoys, I. S., Grant, J. W., Pastras, C. J., Brown, D. J., Burgess, A. M., Brichta, A. M., et al. (2019b). A review of mechanical and synaptic processes in otolith transduction of sound and vibration for clinical VEMP testing. *J. Neurophysiol.* 122, 259–276. doi: 10.1152/jn.00031.2019

Curthoys, I. S., Iwasaki, S., Chihara, Y., Ushio, M., McGarvie, L. A., Burgess, A. M., and Burgess, A. M. (2011b). Probability and the weight of evidence. Reply to Xie: "Comment on the ocular vestibular-evoked myogenic potential to air-conducted sound; probable superior vestibular nerve origin". *Clin. Neurophysiol.* 122, 1269–1270. doi: 10.1016/j.clinph.2010.10.047

Curthoys, I. S., Kim, J., McPhedran, S. K., and Camp, A. J. (2006). Bone conducted vibration selectively activates irregular primary otolithic vestibular neurons in the guinea pig. *Exp. Brain Res.* 175, 256–267. doi: 10.1007/s00221-006-0544-1

Curthoys, I. S., Vulovic, V., Burgess, A. M., Cornell, E. D., Mezey, L. E., Macdougall, H. G., et al. (2011a). The basis for using bone-conducted vibration or air-conducted sound to test otolithic function. *Ann. N. Y. Acad. Sci.* 1233, 231–241. doi: 10.1111/j.1749-6632.2011.06147.x

Curthoys, I. S., Vulovic, V., Burgess, A. M., Manzari, L., Sokolic, L., Pogson, J., et al. (2014). Neural basis of new clinical vestibular tests: otolithic neural responses to sound and vibration. *Clin. Exp. Pharmacol. Physiol.* 41, 371–380. doi: 10.1111/1440-1681.12222

Curthoys, I. S., Vulovic, V., Burgess, A. M., Sokolic, L., and Goonetilleke, S. C. (2016). The response of guinea pig primary utricular and saccular irregular neurons to bone-conducted vibration (BCV) and air-conducted, sound (ACS). *Hear. Res.* 331, 131–143. doi: 10.1016/j.heares.2015.10.019

Curthoys, I. S., Vulovic, V., Sokolic, L., Pogson, J., and Burgess, A. M. (2012). Irregular primary otolith afferents from the guinea pig utricular and saccular maculae respond to both bone conducted vibration and to air conducted sound. *Brain Res. Bull.* 89, 16–21. doi: 10.1016/j.brainresbull.2012.07.007

Dallos, P. (1992). The active cochlea. *J. Neurosci.* 12, 4575–4585.

Davis, J. L., and Grant, J. W. (2014). Turtle utricle dynamic behavior using a combined anatomically accurate model and experimentally measured hair bundle stiffness. *Hear. Res.* 318, 37–44. doi: 10.1016/j.heares.2014.10.010

Davis, J. L., Xue, J., Peterson, E. H., and Grant, J. W. (2007). Layer thickness and curvature effects on otoconial membrane deformation in the utricle of the red-ear slider turtle: static and modal analysis. *J. Vestib. Res.* 17, 145–162.

de Vries, H. (1950). The mechanics of the labyrinth otoliths. *Acta Oto. Laryngol.* 38, 262–273. doi: 10.3109/00016485009118384

Deatherage, B. H., Davis, H., and Eldredge, D. H. (1957). Physiological evidence for the masking of low frequencies by high. *J. Acoust. Soc. Am.* 29, 132–137. doi: 10.1121/1.1908641

Didier, A., and Cazals, Y. (1989). Acoustic responses recorded from the saccular bundle on the 8th nerve of the guinea-pig. *Hear. Res.* 37, 123–127. doi: 10.1016/0378-5955(89)90034-8

Dlugaiczyk, J. (2017). Ocular vestibular evoked myogenic potentials: where are we Now? *Otol. Neurotol.* 38, E513–E521. doi: 10.1097/mao.0000000000001478

Dlugaiczyk, J., Burgess, A. M., Goonetilleke, S. C., Sokolic, L., and Curthoys, I. S. (2019). Superior canal dehiscence syndrome: relating clinical findings with vestibular neural responses from a guinea pig model. *Otol. Neurotol.* 40, e406–e414. doi: 10.1097/mao.0000000000001940

Drescher, D. G., and Eldredge, D. H. (1974). Species differences in cochlear fatigue related to acoustics of outer and middle ears of guinea pig and chinchilla. *J. Acoust. Soc. Am.* 56, 929–934.

Drexl, M., Krause, E., and Gurkov, R. (2018). A comparison of distortion product otoacoustic emission properties in Meniere's disease patients and normal-hearing participants. *Ear. Hear.* 39, 42–47. doi: 10.1097/aud.0000000000000461

Dunlap, M. D., and Grant, J. W. (2014). Experimental measurement of utricle system dynamic response to inertial stimulus. *JARO J. Assoc. Res. Otolaryngol.* 15, 511–528. doi: 10.1007/s10162-014-0456-x

Durrant, J. D., and Dallos, P. (1974). Modification of DIF summating potential components by stimulus biasing. *J. Acoust. Soc. Am.* 56, 562–570.

Eatock, R. A., and Songer, J. E. (2011). Vestibular hair cells and afferents: two channels for head motion signals. *Annu. Rev. Neurosci.* 34, 501–534. doi: 10.1146/annurev-neuro-061010-113710

Eatock, R. A., Xue, J., and Kalluri, R. (2008). Ion channels in mammalian vestibular afferents may set regularity of firing. *J. Exp. Biol.* 211, 1764–1774. doi: 10.1242/jeb.017350

Eggermont, J. J. (1976a). Analysis of compound action potential responses to tone bursts in the human and guinea pig cochlea. *J. Acoust. Soc. Am.* 60, 1132–1139. doi: 10.1121/1.381214

Eggermont, J. J. (1976b). *Electrocochleography. Auditory System*. Berlin: Springer, 625–705.

Eggermont, J. J. (2017). Ups and Downs in 75 Years of Electrocochleography. *Front. Syst. Neurosci.* 11:2. doi: 10.3389/fnsys.2017.00002

Eggermont, J. J. (2019). "Auditory brainstem response," in *Auditory System. Handbook of Sensory Physiology*, Vol. 513, eds W. D. Keidel and W. D. Neff, 451–464. doi: 10.1016/b978-0-444-64032-1.00030-8

Elidan, J., Langhofer, L., and Honrubia, V. (1987a). Recording of short-latency vestibular evoked-potentials induced by acceleration impulses in experimental-animals - current status of the method and its applications. *Electroencephalogr. Clin. Neurophysiol.* 68, 58–69. doi: 10.1016/0168-5597(87)90070-0

Elidan, J., Langhofer, L., and Honrubia, V. (1987b). The neural generators of the vestibular evoked-response. *Brain Res.* 423, 385–390. doi: 10.1016/0006-8993(87)90868-7

Elidan, J., Leibner, E., Freeman, S., Sela, M., Nitzan, M., and Sohmer, H. (1991). Short and middle latency vestibular evoked-responses to acceleration in man. *Electroencephalogr. Clin. Neurophysiol.* 80, 140–145. doi: 10.1016/0168-5597(91)90151-m

Elidan, J., Lin, J., and Honrubia, V. (1986). The effect of loop diuretics on the vestibular system - assessment by recording the vestibular evoked-response. *Arch. Otol. Head Neck Surg.* 112, 836–839.

Elidan, J., Sohmer, H., and Nizan, M. (1982). Recording of short latency vestibular evoked-potentials to acceleration in rats by means of skin electrodes. *Electroencephalogr. Clin. Neurophysiol.* 53, 501–505. doi: 10.1016/0013-4694(82)90062-1

Fernandez, C., Goldberg, J. M., and Baird, R. A. (1990). The vestibular nerve of the chinchilla. III. Peripheral innervation patterns in the utricular macula. *J. Neurophysiol.* 63, 767–780.

Finneran, J. J., Mulsow, J., Houser, D. S., and Burkard, R. F. (2018). Effects of noise burst rise time and level on bottlenose dolphin (*Tursiops truncatus*) auditory brainstem responses. *J. Acoust. Soc. Am.* 143, 2914–2921. doi: 10.1121/1.5037586

Freeman, D. M., and Weiss, T. F. (1990a). Hydrodynamic-forces on hair bundles at high-frequencies. *Hear. Res.* 48, 31–36. doi: 10.1016/0378-5955(90)90197-w

Freeman, D. M., and Weiss, T. F. (1990b). Superposition of hydrodynamic-forces on a hair bundle. *Hear. Res.* 48, 1–15. doi: 10.1016/0378-5955(90)90195-u

Frohlich, L., Curthoys, I. S., Kosling, S., Obrist, D., Rahne, T., and Plontke, S. K. (2020). Cervical and ocular vestibular-evoked myogenic potentials in patients with intracochlear schwannomas. *Front. Neurol.* 11:549817. doi: 10.3389/fneur.2020.549817

Frohlich, L., Wilke, M., Plontke, S. K., and Rahne, T. (2021). Influence of bone conduction transducer type and placement on ocular and cervical vestibular evoked myogenic potentials. *Sci. Rep.* 11:8500. doi: 10.1038/s41598-021-87682-1

Géléoc, G., Lennan, G., Richardson, G., and Kros, C. (1997). A quantitative comparison of mechanoelectrical transduction in vestibular and auditory hair cells of neonatal mice. *Proc. R. Soc. Lond. B Biol. Sci.* 264, 611–621.

Gibson, W. P. (2009). A comparison of two methods of using transtympanic electrocochleography for the diagnosis of Meniere's disease: click summating potential/action potential ratio measurements and tone burst summating potential measurements. *Acta Otolaryngol. (Stockh)* 129, 38–42.

Goldberg, J. M. (2000). Afferent diversity and the organization of central vestibular pathways. *Exp. Brain Res.* 130, 277–297.

Goldberg, J. M., and Fernandez, C. (1977). Conduction times and background discharge of vestibular afferents. *Brain Res* .122, 545–550. doi: 10.1016/0006-8993(77)90465-6

Goldberg, J. M., Desmadryl, G., Baird, R. A., and Fernandez, C. (1990). The vestibular nerve of the chinchilla. V. Relation between afferent discharge properties and peripheral innervation patterns in the utricular macula. *J. Neurophysiol.* 63, 791–804.

Goldberg, J. M., Wilson, V. J., and Cullen, K. E. (2012). *The Vestibular System: A Sixth Sense*. New York, NY: Oxford University Press.

Goldstein, M. H., and Kiang, N. Y. S. (1958). Synchrony of neural activity in electric responses evoked by transient acoustic stimuli. *J. Acoust. Soc. Am.* 30, 107–114. doi: 10.1121/1.1909497

Gorga, M. P., Kaminski, J. R., Beauchaine, K. L., and Bergman, B. M. (1993). A comparison of auditory brain-stem response thresholds and latencies elicited by air-conducted and bone-conducted stimuli. *Ear. Hear.* 14, 85–94. doi: 10.1097/00003446-199304000-00003

Govender, S., and Colebatch, J. G. (2017). Effects of midline sagittal location on bone-conducted cervical and ocular vestibular evoked myogenic potentials. *J. Appl. Physiol.* 122, 1470–1484. doi: 10.1152/japplphysiol.01069.2016

Govender, S., and Colebatch, J. G. (2018). Location and phase effects for ocular and cervical vestibular-evoked myogenic potentials evoked by bone-conducted stimuli at midline skull sites. *J. Neurophysiol.* 119, 1045–1056. doi: 10.1152/jn.00695.2017

Govender, S., Dennis, D. L., and Colebatch, J. G. (2015). Vestibular evoked myogenic potentials (VEMPs) evoked by air- and bone-conducted stimuli in vestibular neuritis. *Clin. Neurophysiol.* 126, 2004–2013. doi: 10.1016/j.clinph.2014.12.029

Govender, S., Rosengren, S. M., Dennis, D. L., Lim, L. J. Z., and Colebatch, J. G. (2016). Contrasting phase effects on vestibular evoked myogenic potentials (VEMPs) produced by air- and bone-conducted stimuli. *Exp. Brain Res.* 234, 141–149. doi: 10.1007/s00221-015-4441-3

Grant, W., and Curthoys, I. (2017). Otoliths – Accelerometer and seismometer. Implications in Vestibular Evoked Myogenic Potential (VEMP). *Hear. Res.* 353, 26–35. doi: 10.1016/j.heares.2017.07.012

Groen, J. J. (1957). The semicircular canal system of the organs of equilibrium .2. *Phys. Med. Biol.* 1, 225–242. doi: 10.1088/0031-9155/1/3/302

Groen, J. J., and Jongkees, L. B. W. (1948). The threshold of angular acceleration perception. *J. Physiol. Lond.* 107, 1–7.

Guinan, J. J. (2012). How are inner hair cells stimulated? Evidence for multiple mechanical drives. *Hear. Res.* 292, 35–50. doi: 10.1016/j.heares.2012.08.005

Guinan, J. J., and Nam, H. (2018). Auditory-nerve phenomena relevant to cochlear mechanics. *AIP Confer. Proc.* 1965:120005.

Hakansson, B., Jansson, K. J. F., Tengstrand, T., Johannsen, L., Eeg-Olofsson, M., Rigato, C., et al. (2018). VEMP using a new low-frequency bone conduction transducer. *Med. Devices Evidence Res.* 11, 301–312. doi: 10.2147/mder.s171369

Hakizimana, P., and Fridberger, A. (2021). Inner hair cell stereocilia are embedded in the tectorial membrane. *Nat. Commun.* 12:2604. doi: 10.1038/s41467-021-22870-1

Hallpike, C., and Rawdon-Smith, A. (1934). The 'Wever and Bray phenomenon.' A study of the electrical response in the cochlea with especial reference to its origin. *J. Physiol.* 81, 395–408.

Halmagyi, G. M., Yavor, R. A., and Colebatch, J. G. (1995). Tapping the head activates the vestibular system: a new use for the clinical reflex hammer. *Neurology* 45, 1927–1929.

Heil, P., and Peterson, A. J. (2015). Basic response properties of auditory nerve fibers: a review. *Cell Tissue Res.* 361, 129–158. doi: 10.1007/s00441-015-2177-9

Heil, P., and Peterson, A. J. (2017). Spike timing in auditory-nerve fibers during spontaneous activity and phase locking. *Synapse* 71, 5–36. doi: 10.1002/syn.21925

Heil, P., Neubauer, H., Irvine, D. R. F., and Brown, M. (2007). Spontaneous activity of auditory-nerve fibers: insights into Stochastic processes at ribbon synapses. *J. Neurosci.* 27, 8457–8474. doi: 10.1523/jneurosci.1512-07.2007

Holt, J. R., and Eatock, R. A. (1995). Inwardly rectifying currents of saccular hair cells from the leopard frog. *J. Neurophysiol.* 73, 1484–1502. doi: 10.1152/jn.1995.73.4.1484

Hu, J., Chen, Z. C., Zhang, Y. Z., Xu, Y., Ma, W. J., Zhang, Y., et al. (2020). Vestibular dysfunction in patients with auditory neuropathy detected by vestibular evoked myogenic potentials. *Clin. Neurophysiol.* 131, 1664–1671. doi: 10.1016/j.clinph.2020.02.002

Hu, L., Zhang, L., Chen, R., Yu, H. B., Li, H., and Mouraux, A. (2015). The primary somatosensory cortex and the insula contribute differently to the processing of transient and sustained nociceptive and non-nociceptive somatosensory inputs. *Hum. Brain Mapp.* 36, 4346–4360. doi: 10.1002/hbm.22922

Ishiyama, G., Lopez, I. A., Sepahdari, A. R., and Ishiyama, A. (2015). Meniere's disease: histopathology, cytochemistry, and imaging. *Ann. N. Y. Acad. Sci.* 1343, 49–57.

Iversen, M. M., and Rabbitt, R. D. (2017). Wave mechanics of the vestibular semicircular canals. *Biophys. J.* 113, 1133–1149. doi: 10.1016/j.bpj.2017.08.001

Iversen, M. M., Zhu, H., Zhou, W., Della Santina, C. C., Carey, J. P., and Rabbitt, R. D. (2018). Sound abnormally stimulates the vestibular system in canal dehiscence syndrome by generating pathological fluid-mechanical waves. *Sci. Rep.* 8:10257. doi: 10.1038/s41598-018-28592-7

Iwasaki, S., McGarvie, L. A., Halmagyi, G. M., Burgess, A. M., Kim, J., Colebatch, J. G., et al. (2007). Head taps evoke a crossed vestibulo-ocular reflex. *Neurology* 68, 1227–1229.

Iwasaki, S., Smulders, Y. E., Burgess, A. M., McGarvie, L. A., MacDougall, H. G., Halmagyi, G. M., et al. (2008). Ocular vestibular evoked myogenic potentials to bone conducted vibration of the midline forehead at Fz in healthy subjects. *Clin .Neurophysiol.* 119, 2135–2147.

Jones, T. A. (1992). Vestibular short latency responses to pulsed linear acceleration in unanesthetized animals. *Electroencephalogr. Clin. Neurophysiol.* 82, 377–386. doi: 10.1016/0013-4694(92)90007-5

Jones, T. A., and Jones, S. M. (1999). Short latency compound action potentials from mammalian gravity receptor organs. *Hear. Res.* 136, 75–85. doi: 10.1016/s0378-5955(99)00110-0

Jones, T. A., and Pedersen, T. L. (1989). Short latency vestibular responses to pulsed linear acceleration. *Am. J. Otolaryngol.* 10, 327–335. doi: 10.1016/0196-0709(89)90108-7

Jones, T. A., Jones, S. M., and Colbert, S. (1998). The adequate stimulus for avian short latency vestibular responses to linear translation. *J. Vestib. Res.* 8, 253–272.

Jones, T. A., Jones, S. M., Vijayakumar, S., Brugeaud, A., Bothwell, M., and Chabbert, C. (2011). The adequate stimulus for mammalian linear vestibular evoked potentials (VsEPs). *Hear. Res.* 280, 133–140. doi: 10.1016/j.heares.2011.05.005

Kaga, K. (2016). Auditory nerve disease and auditory neuropathy spectrum disorders. *Auris. Nasus. Larynx* 43, 10–20. doi: 10.1016/j.anl.2015.06.008

Kalluri, R., Xue, J., and Eatock, R. A. (2010). Ion channels set spike timing regularity of mammalian vestibular afferent neurons. *J. Neurophysiol.* 104, 2034–2051. doi: 10.1152/jn.00396.2010

Karmali, F., Chaudhuri, S. E., Yi, Y. W., and Merfeld, D. M. (2016). Determining thresholds using adaptive procedures and psychometric fits: evaluating

efficiency using theory, simulations, and human experiments. *Exp. Brain Res.* 234, 773–789. doi: 10.1007/s00221-015-4501-8

Kobel, M. J., Wagner, A. R., Merfeld, D. M., and Mattingly, J. K. (2021). Vestibular thresholds: a review of advances and challenges in clinical applications. *Front. Neurol.* 12:643634. doi: 10.3389/fneur.2021.643634

Kondrachuk, A. V. (2001). Models of the dynamics of otolithic membrane and hair cell bundle mechanics. *J. Vestib. Res.* 11, 33–42.

Li, A., Xue, J., and Peterson, E. H. (2008). Architecture of the mouse utricle: macular organization and hair bundle heights. *J. Neurophysiol.* 99, 718–733. doi: 10.1152/jn.00831.2007

Lim, R., Kindig, A. E., Donne, S. W., Callister, R. J., and Brichta, A. M. (2011). Potassium accumulation between type I hair cells and calyx terminals in mouse crista. *Exp. Brain Res.* 210, 607–621. doi: 10.1007/s00221-011-2592-4

Lin, M. Y., Timmer, F. C. A., Oriel, B. S., Zhou, G. W., Guinan, J. J., Kujawa, S. G., et al. (2006). Vestibular evoked myogenic potentials (VEMP) can detect asymptomatic saccular hydrops. *Laryngoscope* 116, 987–992. doi: 10.1097/01.mlg.0000216815.75512.03

Lindeman, H. H. (1969). Studies on the morphology of the sensory regions of the vestibular apparatus with 45 figures. *Ergeb. Anat. Entwicklungsgesch.* 42, 1–113.

Lysakowski, A., Gaboyard-Niay, S., Calin-Jageman, I., Chatlani, S., Price, S. D., and Eatock, R. A. (2011). Molecular microdomains in a sensory terminal, the vestibular calyx ending. *J. Neurosci.* 31, 10101–10114. doi: 10.1523/jneurosci.0521-11.2011

MacDougall, H. G., McGarvie, L. A., Halmagyi, G. M., Rogers, S. J., Manzari, L., Burgess, A. M., et al. (2015). Anti-compensatory saccades as an indicator of peripheral vestibular function in a new complementary video head impulse test paradigm. *Eur. J. Neurol.* 22:53.

Manzari, L., Burgess, A. M., McGarvie, L. A., and Curthoys, I. S. (2013). An indicator of probable semicircular canal dehiscence: ocular vestibular evoked myogenic potentials to high frequencies. *Otolaryngol. Head Neck Surg.* 149, 142–145. doi: 10.1177/0194599813489494

Marsh, J. T., Smith, J. C., and Worden, F. G. (1972). Receptor and neural responses in auditory masking of low frequency tones. *Electroencephalogr. Clin. Neurophysiol.* 32, 63–74. doi: 10.1016/0013-4694(72)90228-3

McCue, M. P., and Guinan, J. J. Jr. (1994). Acoustically responsive fibers in the vestibular nerve of the cat. *J. Neurosci.* 14, 6058–6070.

McCue, M. P., and Guinan, J. J. Jr. (1995). Spontaneous activity and frequency selectivity of acoustically responsive vestibular afferents in the cat. *J. Neurophysiol.* 74, 1563–1572.

McCue, M. P., and Guinan, J. J. Jr. (1997). Sound-evoked activity in primary afferent neurons of a mammalian vestibular system. *Am. J. Otol.* 18, 355–360.

McHenry, M. J., and van Netten, S. M. (2007). The flexural stiffness of superficial neuromasts in the zebrafish (Danio rerio) lateral line. *J. Exp. Biol.* 210, 4244–4253. doi: 10.1242/jeb.009290

Michalewski, H. J., Starr, A., Nguyen, T. T., Kong, Y. Y., and Zeng, F. G. (2005). Auditory temporal processes in normal-hearing individuals and in patients with auditory neuropathy. *Clin. Neurophysiol.* 116, 669–680. doi: 10.1016/j.clinph.2004.09.027

Mikaelian, D. (1964). Vestibular response to sound: single unit recording from the vestibular nerve in fenestrated deaf mice (Df/Df). *Acta Otolaryngol.* 58, 409–422.

Møller, A. R., and Jannetta, P. (1985). "Neural generators of the auditory brainstem response," in *The Auditory Brainstem Response: The Auditory Brainstem Response*, ed. J. T. Jacobson (San Diego, CA: College Hall), 13–31.

Moser, T., and Starr, A. (2016). Auditory neuropathy - neural and synaptic mechanisms. *Nat. Rev. Neurol.* 12, 135–149. doi: 10.1038/nrneurol.2016.10

Mueller, A. L., Liebmann, L. B., Petrak, M. R., Bahner, C. M., Weberling, L. M., Weiss, A. D., et al. (2020). Evaluation of the utricular function with the virtual-subject visual vertical system: comparison with ocular vestibular-evoked myogenic potentials. *Acta Otolaryngol. (Stockh)* 140, 366–372. doi: 10.1080/00016489.2020.1718202

Murofushi, T., Curthoys, I. S., Topple, A. N., Colebatch, J. G., and Halmagyi, G. M. (1995). Responses of guinea pig primary vestibular neurons to clicks. *Exp. Brain Res.* 103, 174–178.

Nam, J. H., Cotton, J. R., and Grant, J. W. (2005). Effect of fluid forcing on vestibular hair bundles. *J. Vestib. Res.* 15, 263–278.

Noij, K. S., and Rauch, S. D. (2020). Vestibular Evoked Myogenic Potential (VEMP) testing for diagnosis of superior semicircular canal dehiscence. *Front. Neurol.* 11:695. doi: 10.3389/fneur.2020.00695

Noij, K. S., Herrmann, B. S., Guinan, J. J., and Rauch, S. D. (2019). Cervical vestibular evoked myogenic potentials in Meniere's disease: a comparison of response metrics. *Otol. Neurotol.* 40, E215–E224. doi: 10.1097/mao.0000000000002092

Obrist, D. (2019). Flow phenomena in the inner ear. *Ann. Rev. Fluid Mech.* 51, 487–510.

Oh, S. Y., Kim, H. J., and Kim, J. S. (2016). Vestibular-evoked myogenic potentials in central vestibular disorders. *J. Neurol.* 263, 210–220. doi: 10.1007/s00415-015-7860-y

Ohlemiller, K. K. (2002). Reduction in sharpness of frequency tuning but not endocochlear potential in aging and noise-exposed BALB/cJ Mice. *J. Assoc. Res. Otolaryngol.* 3, 444–456. doi: 10.1007/s10162-002-2041-y

Palmer, A. R., and Russell, I. J. (1986). Phase-locking in the cochlear nerve of the guinea-pig and its relation to the receptor potential of inner hair-cells. *Hear. Res.* 24, 1–15. doi: 10.1016/0378-5955(86)90002-x

Pappa, A. K., Hutson, K. A., Scott, W. C., Wilson, J. D., Fox, K. E., Masood, M. M., et al. (2019). Hair cell and neural contributions to the cochlear summating potential. *J. Neurophysiol.* 121, 2163–2180.

Pastras, C. J. (2018). *Assessment of Utricular Nerve, Hair Cell and Mechanical Function, in vivo*. Ph D. Thesis *University of Sydney*. Sydney, NSW: The University of Sydney.

Pastras, C. J., Curthoys, I. S., and Brown, D. J. (2017a). In vivo recording of the vestibular microphonic in mammals. *Hear. Res.* 354, 38–47. doi: 10.1016/j.heares.2017.07.015

Pastras, C. J., Curthoys, I. S., and Brown, D. J. (2018). Dynamic response to sound and vibration of the guinea pig utricular macula, measured in vivo using laser doppler vibrometry. *Hear. Res.* 370, 232–237. doi: 10.1016/j.heares.2018.08.005

Pastras, C. J., Stefani, S. P., Camp, A. J., Curthoys, I. S., and Brown, D. J. (2021). Summating potentials from the utricular macula of anaesthetised guinea pigs. *Hear. Res.* 406:108259.

Pastras, C. J., Stefani, S. P., Curthoys, I. S., Camp, A. C., and Brown, D. B. (2020). Utricular sensitivity during hydrodynamic displacements of the macula. *J. Assoc. Res. Otolaryngol.* 21, 409–423.

Pastras, C., Curthoys, I., and Brown, D. (2017b). In vivo recording of the vestibular microphonic in mammals. *Hear. Res.* 354, 38–47.

Patuzzi, R. B., Yates, G. K., and Johnstone, B. M. (1989). The origin of the low-frequency microphonic in the first cochlear turn of guinea-pig. *Hear. Res.* 39, 177–188. doi: 10.1016/0378-5955(89)90089-0

Patuzzi, R., and Moleirinho, A. (1998). Automatic monitoring of mechano-electrical transduction in the guinea pig cochlea. *Hear. Res.* 125, 1–16. doi: 10.1016/s0378-5955(98)00125-7

Pestalozza, G., and Davis, H. (1956). Electric responses of the guinea pig ear to high audio frequencies. *Am. J. Physiol.* 185, 595–600.

Peterson, A. J., and Heil, P. (2020). Phase locking of auditory nerve fibers: the role of lowpass filtering by hair cells. *J. Neurosci.* 40, 4700–4714. doi: 10.1523/jneurosci.2269-19.2020

Piker, E. G., Jacobson, G. P., Burkard, R. F., McCaslin, D. L., and Hood, L. J. (2013). Effects of age on the tuning of the cVEMP and oVEMP. *Ear. Hear.* 34, e65–e73. doi: 10.1097/AUD.0b013e31828fc9f2

Pote, K. G., Weber, C. H., and Kretsinger, R. H. (1993). Inferred protein-content and distribution from density-measurements of calcitic and aragonitic otoconia. *Hear. Res.* 66, 225–232. doi: 10.1016/0378-5955(93)90142-n

Rabbitt, R. D. (2019). Semicircular canal biomechanics in health and disease. *J. Neurophysiol.* 121, 732–755. doi: 10.1152/jn.00708.2018

Rose, J. E., Brugge, J. F., Anderson, D. J., and Hind, J. E. (1967). Phase-locked response to low-frequency tones in single auditory nerve fibers of the squirrel monkey. *J. Neurophysiol.* 30, 769–793.

Rosengren, S. M., and Colebatch, J. G. (2005). Vestibular evoked potentials (VsEPs) in patients with severe to profound bilateral hearing loss. *J. Neurol. Sci.* 238:S338.

Rosengren, S. M., and Colebatch, J. G. (2018). The contributions of vestibular evoked myogenic potentials and acoustic vestibular stimulation to our

understanding of the vestibular system. *Front. Neurol.* 9:481. doi: 10.3389/fneur.2018.00481

Rosengren, S. M., Colebatch, J. G., Straumann, D., and Weber, K. P. (2015). Single motor unit responses underlying cervical vestibular evoked myogenic potentials produced by bone-conducted stimuli. *Clin. Neurophysiol.* 126, 1234–1245. doi: 10.1016/j.clinph.2014.07.037

Rosengren, S. M., Colebatch, J. G., Young, A. S., Govender, S., and Welgampola, M. S. (2019). Vestibular evoked myogenic potentials in practice: methods, pitfalls and clinical applications. *Clin. Neurophysiol. Pract.* 4, 47–68. doi: 10.1016/j.cnp.2019.01.005

Rosengren, S. M., McAngus Todd, N. P., and Colebatch, J. G. (2005). Vestibular-evoked extraocular potentials produced by stimulation with bone-conducted sound. *Clin. Neurophysiol.* 116, 1938–1948.

Rosengren, S. M., Weber, K. P., Michels, R., Sturm, V., Landau, K., and Straumann, D. (2011). Single motor unit recordings of ocular vestibular evoked myogenic potentials in human extraocular muscles. *J. Neurol.* 258:39.

Rosenhall, U. (1972). Vestibular macular mapping in man. *Ann. Otol. Rhinol. Laryngol.* 81, 339–351. doi: 10.1177/000348947208100305

Rosowski, J. J., Songer, J. E., Nakajima, H. H., Brinsko, K. M., and Merchant, S. N. (2004). Clinical, experimental, and theoretical investigations of the effect of superior semicircular canal dehiscence on hearing mechanisms. *Otol. Neurotol.* 25, 323–332. doi: 10.1097/00129492-200405000-00021

Ross, D. S. (1936). Electrical studies on the frog's labyrinth. *J. Physiol. Lond.* 86, 117–146. doi: 10.1113/jphysiol.1936.sp003348

Rowe, M. J. (1981). The brain-stem auditory evoked-response in neurological disease - a review. *Ear. Hear.* 2, 41–51. doi: 10.1097/00003446-198101000-00008

Russell, I., and Sellick, P. (1978). Intracellular studies of hair cells in the mammalian cochlea. *J. Physiol.* 284, 261–290.

Salt, A. N., Brown, D. J., Hartsock, J. J., and Plontke, S. K. (2009). Displacements of the organ of Corti by gel injections into the cochlear apex. *Hear, Res.* 250, 63–75.

Schmiedt, R., and Zwislocki, J. (1977). Comparison of sound-transmission and cochlear-microphonic characteristics in *Mongolian gerbil* and guinea pig. *J. Acoust. Soc. Am.* 61, 133–149.

Sellick, P. M., Patuzzi, R., and Johnstone, B. M. (1982). Measurement of basilar membrane motion in the guinea pig using the Mössbauer technique. *J. Acoust. Soc. Am.* 72, 131–141. doi: 10.1121/1.387996

Selva, P., Oman, C. M., and Stone, H. A. (2009). Mechanical properties and motion of the cupula of the human semicircular canal. *J. Vestib. Res.* 19, 95–110. doi: 10.3233/ves-2009-0359

Singh, N. K., and Barman, A. (2016a). Frequency-amplitude ratio of ocular vestibular-evoked myogenic potentials for detecting Meniere's disease: a preliminary investigation. *Ear. Hear.* 37, 365–373. doi: 10.1097/aud.0000000000000263

Singh, N. K., and Barman, A. (2016b). Utility of the frequency tuning measure of oVEMP in differentiating Meniere's disease from BPPV. *J. Am. Acad. Audiol.* 27, 764–777. doi: 10.3766/jaaa.15141

Singh, N. K., and Firdose, H. (2018). Characterizing the age and stimulus frequency interaction for ocular vestibular-evoked myogenic potentials. *Ear. Hear.* 39, 251–259. doi: 10.1097/aud.0000000000000482

Sohmer, H., and Pratt, H. (1976). Recording of the cochlear microphonic potential with surface electrodes. *Electroencephalogr. Clin. Neurophysiol.* 40, 253–260. doi: 10.1016/0013-4694(76)90149-8

Spoon, C., and Grant, W. (2011). Biomechanics of hair cell kinocilia: experimental measurement of kinocilium shaft stiffness and base rotational stiffness with Euler-Bernoulli and Timoshenko beam analysis. *J. Exp. Biol.* 214, 862–870. doi: 10.1242/jeb.051151

Spoon, C., and Grant, W. (2013). Biomechanical measurement of kinocilium. *Methods Enzymol.* 525, 21–43. doi: 10.1016/b978-0-12-397944-5.00002-x

Spoon, C., Moravec, W. J., Rowe, M. H., Grant, J. W., and Peterson, E. H. (2011). Steady-state stiffness of utricular hair cells depends on macular location and hair bundle structure. *J. Neurophysiol.* 106, 2950–2963. doi: 10.1152/jn.00469.2011

Starr, A., Picton, T. W., Sininger, Y., Hood, L. J., and Berlin, C. I. (1996). Auditory neuropathy. *Brain* 119, 741–753. doi: 10.1093/brain/119.3.741

Straka, H., Fritzsch, B., and Glover, J. C. (2014). Connecting ears to eye muscles: evolution of a 'Simple' reflex arc. *Brain Behav. Evol.* 83, 162–175. doi: 10.1159/000357833

Straka, H., Paulin, M. G., and Hoffman, L. F. (2021). Translations of Steinhaisen's publications provide insight into their contributions to peripheral vestibular neuroscience. *Front. Neurol.* 12:676723. doi: 10.3389/fneur.2021.676723

Suzuki, J. I., Tokumasu, K., and Goto, K. (1969). Eye movements from single utricular nerve stimulation in the cat. *Acta Otolaryngol.* 68, 350–362.

Tasaki, I. (1954). Nerve impulses in individual auditory nerve fibers of guinea pig. *J Neurophysiol* 17, 97–122.

ten Kate, J. H. (1969). *The Oculo-Vestibular Reflex of the Growing Pike. A Biophysical Study.* Ph.D. Thesis, *University of Groningen*. Netherlands: University of Groningen.

Timmer, F. C. A., Zhou, G. W., Guinan, J. J., Kujawa, S. G., Herrmann, B. S., and Rauch, S. D. (2006). Vestibular evoked myogenic potential (VEMP) in patients with Meniere's disease with drop attacks. *Laryngoscope* 116, 776–779. doi: 10.1097/01.mlg.0000205129.78600.27

Uchino, Y., and Kushiro, K. (2011). Differences between otolith- and semicircular canal-activated neural circuitry in the vestibular system. *Neurosci. Res.* 71, 315–327. doi: 10.1016/j.neures.2011.09.001

Uziel, A., Romand, R., and Marot, M. (1981). Development of cochlear potentials in rats. *Audiology* 20, 89–100.

van de Berg, R., Rosengren, S., and Kingma, H. (2018). Laboratory examinations for the vestibular system. *Curr. Opin. Neurol.* 31, 111–116. doi: 10.1097/wco.0000000000000526

Van Egmond, A. A. J., Groen, J. J., and Jongkees, L. B. W. (1949). The mechanics of the semicircular canal. *J. Physiol. Lond.* 110, 1–17.

von Bekesy, G. (1955). Subjective cupulometry – threshold, adaptation, and sensation intensity of the vestibular organ for rotations in the horizontal plane. *Arch Otolaryngol* 61, 16–28.

Walsh, B. T., Kiang, N. Y. S., Miller, J. B., and Gacek, R. R. (1972). Spontaneous activity in the eighth cranial nerve of the cat. *Int. J. Neurosci.* 3, 221–235. doi: 10.3109/00207457209147026

Weber, K. P., Rosengren, S. M., Michels, R., Sturm, V., Straumann, D., and Landau, K. (2012). Single motor unit activity in human extraocular muscles during the vestibulo-ocular reflex. *J. Physiol. Lond.* 590, 3091–3101. doi: 10.1113/jphysiol.2011.226225

Wever, E. G., and Bray, C. W. (1930). Action currents in the auditory nerve in response to acoustical stimulation. *Proc. Natl. Acad. Sci. U.S.A.* 16, 344–350. doi: 10.1073/pnas.16.5.344

Wit, H. P., Bleeker, J. D., and Mulder, H. H. (1984). Responses of pigeon vestibular nerve-fibers to sound and vibration with audiofrequencies. *J. Acoust. Soc. Am.* 75, 202–208. doi: 10.1121/1.390396

Wit, H. P., Bleeker, J. D., and Segenhout, J. H. (1981). Vestibular and cochlear responses to acoustic transients - some properties of whole-nerve action-potentials in pigeons. *Acta Otolaryngol. (Stockh)* 92, 409–422. doi: 10.3109/00016488109133280

Yagi, T., Markham, C. H., and Simpson, N. E. (1977). Relationship of conduction-velocity to other physiological properties of cats horizontal canal neurons. *Exp. Brain Res.* 30, 587–600.

Young, E. D., Fernandez, C., and Goldberg, J. M. (1977). Responses of squirrel monkey vestibular neurons to audio-frequency sound and head vibration. *Acta Otolaryngol.* 84, 352–360.

Conflict of Interest: The authors declare that the research was conducted in the absence of any commercial or financial relationships that could be construed as a potential conflict of interest.

Publisher's Note: All claims expressed in this article are solely those of the authors and do not necessarily represent those of their affiliated organizations, or those of the publisher, the editors and the reviewers. Any product that may be evaluated in this article, or claim that may be made by its manufacturer, is not guaranteed or endorsed by the publisher.

frontiers in Neuroscience

REVIEW
published: 03 September 2021
doi: 10.3389/fnins.2021.680856

Age-Related Changes in the Cochlea and Vestibule: Shared Patterns and Processes

Vasiliki Paplou[1], *Nick M. A. Schubert*[1,2] *and Sonja J. Pyott*[1,2]*

[1] Department of Otorhinolaryngology and Head/Neck Surgery, University of Groningen, University Medical Center Groningen, Groningen, Netherlands, [2] Research School of Behavioural and Cognitive Neurosciences, Graduate School of Medical Sciences, University of Groningen, Groningen, Netherlands

Both age-related hearing loss (ARHL) and age-related loss in vestibular function (ARVL) are prevalent conditions with deleterious consequences on the health and quality of life. Age-related changes in the inner ear are key contributors to both conditions. The auditory and vestibular systems rely on a shared sensory organ – the inner ear – and, like other sensory organs, the inner ear is susceptible to the effects of aging. Despite involvement of the same sensory structure, ARHL and ARVL are often considered separately. Insight essential for the development of improved diagnostics and treatments for both ARHL and ARVL can be gained by careful examination of their shared and unique pathophysiology in the auditory and vestibular end organs of the inner ear. To this end, this review begins by comparing the prevalence patterns of ARHL and ARVL. Next, the normal and age-related changes in the structure and function of the auditory and vestibular end organs are compared. Then, the contributions of various molecular mechanisms, notably inflammaging, oxidative stress, and genetic factors, are evaluated as possible common culprits that interrelate pathophysiology in the cochlea and vestibular end organs as part of ARHL and ARVL. A careful comparison of these changes reveals that the patterns of pathophysiology show similarities but also differences both between the cochlea and vestibular end organs and among the vestibular end organs. Future progress will depend on the development and application of new research strategies and the integrated investigation of ARHL and ARVL using both clinical and animal models.

Keywords: auditory – visual perception, vestibular, inner ear, presbycusis or age-induced hearing loss, balance disorders, aging, inflammation, oxidative stress

OPEN ACCESS

Edited by:
Soroush G. Sadeghi,
University at Buffalo, United States

Reviewed by:
Robert Burkard,
University at Buffalo, United States
Carey David Balaban,
University of Pittsburgh, United States

***Correspondence:**
Sonja J. Pyott
s.pyott@umcg.nl

Specialty section:
This article was submitted to Perception Science, a section of the journal Frontiers in Neuroscience

Received: *15 March 2021*
Accepted: *20 July 2021*
Published: *03 September 2021*

Citation:
Paplou V, Schubert NMA and Pyott SJ (2021) Age-Related Changes in the Cochlea and Vestibule: Shared Patterns and Processes Front. Neurosci. 15:680856. doi: 10.3389/fnins.2021.680856

INTRODUCTION

Aging causes the function of multiple organ systems to decline (Khan et al., 2017), and, like other sensory organs, the inner ear is also susceptible to the effects of aging. The inner ear is comprised of two sensory structures: the cochlea, which is responsible for the sense of hearing, and the vestibular end organs, which are responsible for the sense of balance (along with vision, proprioception, and motor systems). Both structures show age-related changes in structure and function, and both age-related hearing loss (ARHL), or presbycusis, and age-related loss of vestibular function (ARVL), also called presbyastasis or presbyequilibrium, are common among the older population. The personal, societal, and economic burden of ARHL and ARVL are substantial, whereas the prevention and

treatment strategies are still quite limited. Moreover, both ARHL and ARVL can directly and indirectly exacerbate other effects of aging.

The cochlea provides the brain with acoustic information, which is essential for communication and personal safety. ARHL is typified by progressive, bilateral, symmetric hearing loss, especially in the high frequencies, and accompanied with difficulty understanding speech, especially in noise. ARHL is the most prevalent sensory deficit in the elderly (Bowl and Dawson, 2019) and is associated with an increased odds of social isolation (Mick et al., 2014), an increased odds of reported falling (Lin and Ferrucci, 2012), accelerated cognitive decline and incident cognitive impairment (Lin et al., 2013), and an increased risk of dementia (Lin et al., 2011a). Moreover, hearing aid use is associated with reduced odds of depression (Mener et al., 2013). Importantly, these studies indicate links but do not distinguish common from causal mechanisms. In addition to significant health burden and reduction in the quality of life (Ciorba et al., 2012), ARHL results in substantial economic burden in both direct medical costs and costs attributable to lost productivity (Stucky et al., 2010). Unlike conductive hearing loss, which can often be treated, restoration of hearing in cases of sensorineural hearing loss, by far the most common cause of ARHL, is not possible. Hearing aids that amplify sounds and cochlear implants, which bypass the sensory transduction machinery of the inner ear and directly stimulate the auditory nerve, can be used to mitigate symptoms but do not fully restore auditory input.

The end organs of the vestibular system provide the brain with information necessary for detection of self-motion, spatial orientation, and postural control (Liston et al., 2014). ARVL can present as dizziness but vestibular hypofunction can also go undetected (van de Berg et al., 2015). Regardless of presentation, dizziness, imbalance, or even simply feeling unsteady diminishes the quality of life of older adults (Agrawal et al., 2018). The declining ability to perform daily tasks, the loss of independence, and the fear of falling can lead to anxiety and depression. ARVL contributes to the increased likelihood and severity of falls (Herdman et al., 2000), which are the leading cause of fatal and trauma-related injuries among older adults (Scuffham et al., 2003; Stevens et al., 2006). Moreover, balance disorders were recently associated with all causes of mortality in older adults (Cao et al., 2021). Finally, recent work indicates that ARVL is associated with the increased likelihood and rate of cognitive decline in the aging (Semenov et al., 2016; Dobbels et al., 2019). These studies indicate links between balance disorders, which involve multiple sensory and motor systems, and do not identify shared or causal mechanisms. Not surprisingly, the estimated economic burden of vestibular disorders is enormous (Sun et al., 2014; Kovacs et al., 2019). Unfortunately, both the clinical detection and management of ARVL is limited (Anson and Jeka, 2015; Arshad and Seemungal, 2016; Renga, 2019).

Like other multifactorial conditions, ARHL and ARVL show substantial individual variation and result from a combination of both intrinsic factors, such as genetics, as well as external factors, like environmental conditions (e.g., noise exposure), lifestyle factors (e.g., smoking), medications (e.g., ototoxic drugs), and other comorbidities (e.g., cardiovascular disease). ARHL (recently reviewed in Bowl and Dawson, 2019; Fischer et al., 2020; Keithley, 2020; Tawfik et al., 2020; Wang and Puel, 2020) and ARVL (reviewed in Sturnieks et al., 2008; Anson and Jeka, 2015; Fernandez et al., 2015; Iwasaki and Yamasoba, 2015; Arshad and Seemungal, 2016; Brosel et al., 2016; Ji and Zhai, 2018; Brosel and Strupp, 2019; Jahn, 2019) are often investigated separately even though both conditions rely on age-related changes in the same sensory structure. Therefore, insight essential for the development of treatments for ARHL and ARVL can be gained by careful examination of their shared and unique pathophysiology in the inner ear. To this end, the review begins by comparing the prevalence patterns of ARHL and ARVL. Next, the normal structure and function of the auditory and vestibular end organs and their age-related changes are compared. Then, the contributions of various molecular mechanisms, notably inflammaging, oxidative stress, and genetic factors, are evaluated as possible common culprits that interrelate age-related pathology in the cochlea and vestibule as part of ARHL and ARVL. The links between age-related changes in the peripheral and central auditory and vestibular systems are then highlighted. Finally, future directions to advance investigation of ARHL and ARVL are offered.

PREVALENCE OF ARHL AND ARVL

Estimates of the prevalence of ARHL and associated risk factors have been conducted using large cohorts. Prevalence is the number of individuals with a given condition in a given population at a specific point in time. Although the patterns of ARHL vary, several studies have used well-defined criteria, and a summary of the prevalence numbers from these studies is shown in **Figure 1**. Epidemiological studies also identified the risk factors associated with ARHL (reviewed in Yamasoba et al., 2013). Males are more likely to have ARHL. Modifiable risk factors associated with the increased likelihood of ARHL include greater exposure to noise, smoking, and comorbidities of hypertension and cardiovascular disease, cerebrovascular disease, and diabetes. In contrast to ARHL, the prevalence of ARVL has been less investigated. An often-cited study using the modified Romberg Test of Standing Balance on Firm and Compliant Support Surfaces reported an overall prevalence of vestibular dysfunction in just over one-third of adults aged 40 years and older in the United States (Agrawal et al., 2009). In this study and a recent follow up study (Cao et al., 2021), the odds of vestibular dysfunction were higher in individuals with lower educational status, lower physical activity, and with diabetes or cardiovascular disease. In this study, the odds of vestibular dysfunction were lower in individuals with greater education and higher in those with diabetes. Other studies have assessed the prevalence of ARVL using the occurrence of symptoms such as vertigo, dizziness, and dysequilibrium (Colledge et al., 1994; Jönsson et al., 2004). A few, smaller sized studies have used clinical assessments of both auditory and vestibular function (Zuniga et al., 2012; Tan et al., 2016). A summary of the prevalence numbers from most of these studies investigating ARVL is also shown in **Figure 1**.

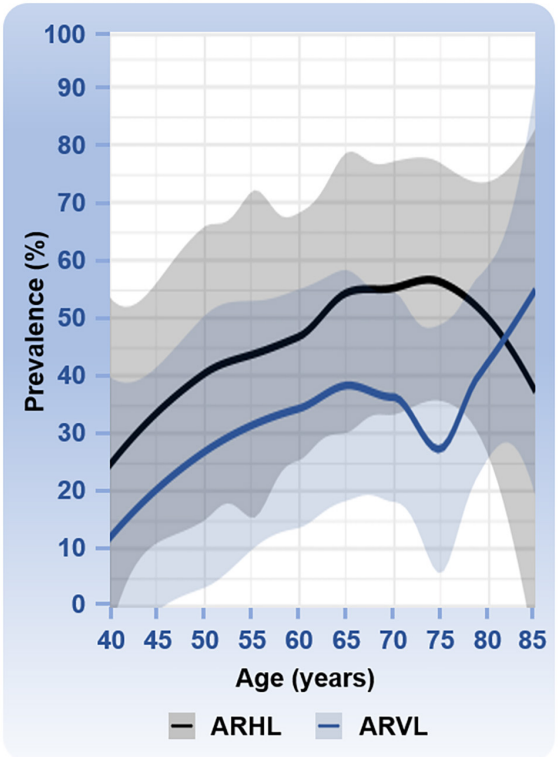

FIGURE 1 | Prevalence of age-related hearing loss (ARHL) and age-related vestibular loss (ARVL). Prevalence numbers (age range from 40 to 85 years) are based on six studies with various sample sizes for ARHL: *N* = 654,113 (Hogan et al., 2009), *N* = 3,831 (Hoffman et al., 2017), *N* = 3,184 (Feder et al., 2015), *N* = 4,357 (Gong et al., 2018), *N* = 5,742 (Agrawal et al., 2008), and *N* = 7,490, (Lin et al., 2011b); and four studies with various sample sizes for ARVL: *N* = 3,197 (Jönsson et al., 2004), *N* = 6,785 (Agrawal et al., 2009), *N* = 216 (Tan et al., 2016), and *N* = 1,000 (Colledge et al., 1994). Mean percentages with the 95% confidence intervals are shown. ARHL was defined as followed in the different studies: a hearing disability associated with communication difficulty and/or use of hearing aids (Hogan et al., 2009); high-frequency hearing loss (Hoffman et al., 2017); combined mild, moderate, or worse hearing loss in high frequencies (Feder et al., 2015); hearing loss ≥25 dB HL (Gong et al., 2018); high frequency hearing loss overall (Agrawal et al., 2008); and bilateral hearing loss ≥25 dB HL (Lin et al., 2011b). ARVL was determined based on reported overall occurrence of balance symptoms (Jönsson et al., 2004), the Romberg testing and difficulty with balance or falling in the past 12 months (Agrawal et al., 2009), the clinical test for sensory interaction on balance (Tan et al., 2016), and a dizziness questionnaire (Colledge et al., 1994). The clinical test of sensory interaction and balance provides information about the ability to stand upright under six sensory conditions: (1) quiet standing on the floor, looking straight ahead; (2) quiet standing on the floor with eyes closed; (3) quiet standing on the floor wearing the conflict dome; (4) quiet standing on the foam, with eyes open; (5) quiet standing on the foam, with eyes close; and (6) quiet standing on the foam wearing the conflict dome (Cohen et al., 1993). One study reported an especially low prevalence of ARVL at 75 years of age (Tan et al., 2016). One study cited in the text was not used in this analysis because the study included only two age categories, 70 to 80 years and >80 years (Zuniga et al., 2012).

When comparing the prevalence patterns between ARHL and ARVL (**Figure 1**), both rise most steeply between the ages of 40 and 60 to 70 years of age. Interestingly the prevalence of ARHL decreases slightly after the age of 75 years whereas ARVL continues to increase with age. The apparent dip in prevalence of ARVL at 75 years of age arises from one study that reported a considerably lower prevalence at this age (Tan et al., 2016) compared to other studies. This dip in ARVL prevalence around 75 years of age should be interpreted cautiously considering that studies included were cross-sectional, assessed vestibular dysfunction with different methods (e.g., questionnaires versus balance testing), and utilized different age inclusion criteria such that not all studies cover the complete age range. Longitudinal studies would be necessary to examine trends over time. Moreover, the various ways in which vestibular dysfunction is measured in these studies complicates interpretation and likely underestimates the overall prevalence of ARVL. Specifically, hypofunction of the vestibular end organs is not always associated with dizziness (van de Berg et al., 2015) and, therefore, could have been missed in some of these studies. Importantly, the incidence, or occurrence of new cases within a given period of time, of ARHL and ARVL is also expected to increase due to the rapidly increasing aging population. ARHL is estimated to affect 60 million Americans above the age of 64 by the year 2025, an increase in prevalence from 9.3% in 2007 to 19% of the total population in 2025 (Liu and Yan, 2007), and ARVL is expected to increase from 12.9% in 2015 to 23.7% in 2050 (Zalewski, 2015).

ANATOMY AND FUNCTIONAL ASSESSMENT OF THE COCHLEA AND VESTIBULAR END ORGANS

The inner ear consists of both the auditory and vestibular end organs (**Figure 2**). The auditory and vestibular structures of the inner ear share the same embryonic origin (Morsli et al., 1998) and utilize similar yet distinct sensorineural structures and mechanisms of transduction. The auditory end organ consists of a coiled tube called the cochlea. Projections from the primary sensory neurons, with cell bodies housed in the spiral ganglion, are relayed first to the cochlear nucleus in the brainstem and ultimately reach the primary auditory cortex for the conscious perception of sound (reviewed in Pickles, 2015). The vestibular end organs consist of two otolithic organs – the utricle and saccule, which detect linear acceleration in the horizontal and vertical planes, respectively, – and the horizontal, anterior, and posterior semicircular canals, which detect head angular accelerations around the vertical, sagittal, and frontal axes. The otolithic structures are so named because of the otoconia, calcium carbonate structures, that lie above the hair cells. Sensory signals from the vestibular end organs are relayed via the primary vestibular neurons, with cell bodies housed in Scarpa's ganglion, to the vestibular nuclei in the brainstem as well as the cerebellum. Projections then connect to the reticular formation, the spinal cord, and the thalamus. Vestibular signals contribute to spatial perception and orientation as well as automatic reflexes and motor coordination (reviewed in Kingma and van de Berg, 2016).

The sensory hair cells and peripheral dendrites of the primary sensory neurons are housed within the neuroepithelia that are, in turn, housed in the bony encasements of these end organs.

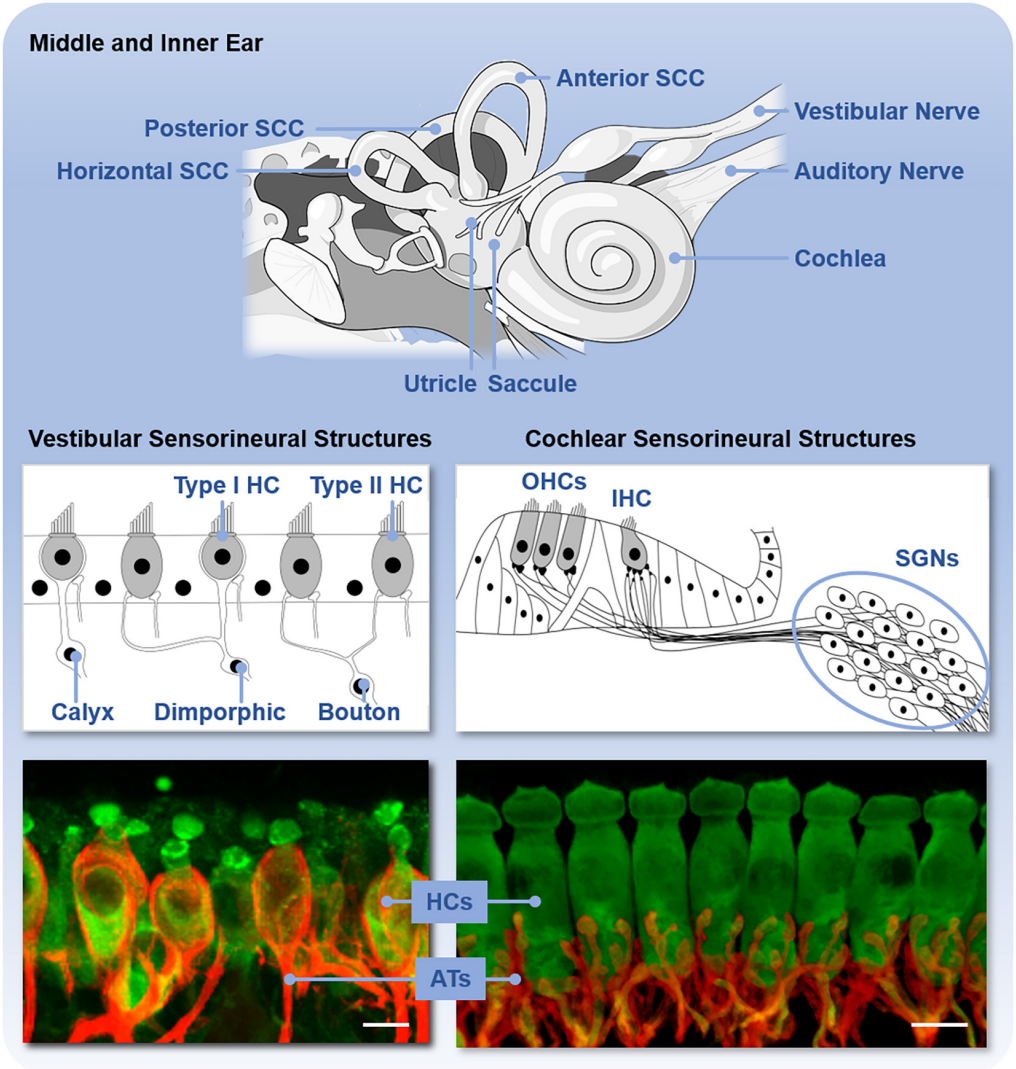

FIGURE 2 | Anatomy of the inner ear and sensorineural structures. The upper panel shows the inner ear with vestibular end organs (including the utricle, saccule, and three semicircular canals, SCC) and cochlea labeled. The middle panel shows the schematic organization and types of sensory hair cells (HC) and primary neurons in the vestibular end organs and cochlea. The vestibular end organs contain type I and type II hair cells (HC) and vestibular neurons with either calyx, dimorphic, or bouton afferent terminals. The cochlea contains outer hair cells (OHCs) and inner hair cells (IHCs) and spiral ganglion neurons (SGNs). The bottom panel shows these sensorineural structures isolated from C57BL/6 mice and immunofluorescently labeled to reveal the hair cells (HCs, green) and primary afferent terminals (ATs, red). Scale bar is 10 μm.

The classes of sensory hair cells and primary neurons and their arrangements in the sensory epithelium vary between the end organs (**Figure 2**). In the cochlea, there are two types of sensory auditory hair cells – inner and outer hair cells – and two types of primary auditory neurons – type I and II spiral ganglion neurons. These hair cells are arranged tonotopically along the length of the neuroepithelium, called the organ of Corti. Vestibular end organs contain two types of hair cells – type I and II hair cells – and three types of primary vestibular neurons – calyx, dimorphic, and bouton neurons – distinguished by the morphology of their afferent terminals. The distribution and relative abundance of the distinct types of hair cells and vestibular neurons varies spatially across the vestibular neuroepithelia. Moreover, within the vestibular neuroepithelia, there are zonal differences in the spike generation patterns – regular and irregular – of the vestibular neurons (Goldberg, 2000). Both the organ of Corti and vestibular neuroepithelia also receive efferent innervation from the brain that modifies afferent input in yet incompletely understood ways. In the mature organ of Corti, medial olivocochlear efferents originate in the medial superior olive and synapse directly on the outer hair cells. Lateral olivocochlear efferents originate in the lateral superior olive and terminate on the dendrites of type I auditory nerve afferent fibers beneath inner hair cells (Lopez-Poveda, 2018). Within vestibular neuroepithelia, efferent innervation arises from the parvocellular reticular nucleus (Warr, 1975) and synapses onto type II hair cells

as well as both calyx and bouton afferent terminals (Lysakowski and Goldberg, 1997, 2008; Jordan et al., 2015). Regardless of hair cell type, deflection of the hair bundle, due to either sound or head movement, opens mechanotransduction channels in the hair bundles that leads to depolarization of the hair cells, release of neurotransmitter, and activation of the primary auditory or vestibular neurons. These mechanisms have been comprehensively reviewed elsewhere (e.g., Fettiplace, 2017).

The hair cells in both the cochlear and vestibular end organs are bathed in endolymph, which, in contrast to many other extracellular fluids, has a relatively high concentration of potassium ions (K^+) and low concentration of sodium ions (Na^+). This concentration gradient means that influx of K^+ is depolarizing (reviewed in Hibino and Kurachi, 2006; Ciuman, 2009; Nin et al., 2016; Köppl et al., 2018). The ionic composition of the endolymph gives rise to the endolymphatic potential, which provides the driving force for hair cell mechanotransduction. In the cochlea, the endolymph is generated by the stria vascularis in the lateral wall. Much less is known about the endolymph-generating structures in the vestibular end organs, although there are probably distinct structures in each of the five end organs. Measurements indicate that the endolymphatic potential is substantially higher in the cochlea (+80 to +120 mV) than the vestibular end organs (+1 to +11 mV), but accurate measurements of the EP, especially in the microenvironment bathing the hair cells, is difficult. Direct measurement of endolymphatic potential is possible in animal models but not possible in healthy humans.

A variety of clinical assessments of peripheral auditory function in humans are available and include more commonly pure tone audiometry (PTA) and less commonly measurements of auditory brainstem responses (ABRs) (Hoth and Baljic, 2017). Similar assessments to assess cochlear function are available in animal models, although, in contrast to humans, measurement of ABRs (e.g., Willott, 2006) are more easily and, therefore, more commonly performed compared to behaviorally measured audiograms (e.g., Heffner et al., 2001). Importantly these two measures produce different absolute thresholds, with behaviorally measured thresholds often lower than electrophysiologically measured thresholds but estimations of induced hearing loss (absolute threshold shifts) being comparable in animal models (e.g., Borg and Engstrom, 1983). Objective clinical assessments of peripheral vestibular function most commonly include (van de Berg et al., 2018): (1) measurement of the cervical vestibular evoked myogenic potentials (cVEMP), which indicates the status of the saccule; (2) the ocular VEMP (oVEMP), which indicate the status of the utricle; (3) the caloric test, which indicates status of the horizontal semicircular canal; and (4) the head impulse test (HIT), which indicates status of the horizontal or anterior and posterior semicircular canals. The HIT involves an abrupt, high-acceleration, small amplitude rotation of the head by the examiner while the subject looks at a target straight ahead (Agrawal et al., 2014). To maintain gaze stability, the normal vestibulo-ocular reflex (VOR) produces an eye movement nearly equal in velocity and only slightly delayed in time in the opposite direction of head movement. The VOR response elicited by the HIT can be measured using video oculography (vHIT). Because of practical limitations imposed by video oculography, vHIT requires the examiner to apply head impulses to the subject from the back of the head and used to measure function of the horizontal canals only (Macdougall et al., 2013). Compared with HIT, vHIT has a higher sensitivity and specificity and can help differentiate between central and peripheral vertigo in patients with acute vestibular syndrome (Bartl et al., 2009; MacDougall et al., 2009). In addition to the cVEMP, oVEMP, and HIT, a variety of other screening tests are also available (reviewed in Cohen, 2019).

In animal models, peripheral vestibular function is often assessed by examination of reflex responses (e.g., Martins-Lopes et al., 2019) or measurements of vestibular evoked potentials (VsEPs), an electrophysiologic response to a change in linear acceleration (i.e., jerk) of the head that can be performed in animals with relatively small heads, such as rodents and birds (e.g., Jones et al., 2011). Moreover, in both humans and animal models, measurements of peripheral vestibular function are difficult owing to the small electrical potentials generated by the end organs and the widespread and diffuse innervation of the primary neurons in the brain. As a result, methods of assessment are often indirect and detect or are influenced by myogenic, proprioceptive, or visual responses (reviewed in Llorens et al., 2018). For example, cVEMPs are inhibitory potentials and depend on the magnitude of the contraction of the sternocleidomastoid muscles measured by electromyography (EMG). Thus, age-related loss of muscle mass and strength (sarcopenia) can also reduce the magnitude of cVEMP responses and complicate interpretation of age-related changes in vestibular function specifically. In comparison to peripheral auditory function, analogous assessments of peripheral vestibular function in humans and animal models are more limited. The development of analogous and robust assessments of peripheral vestibular function in humans and animal models is sorely needed to progress vestibular research.

AGE-RELATED CHANGES IN THE ANATOMY AND FUNCTION OF THE COCHLEA AND VESTIBULAR END ORGANS

Various studies have used functional assessments to characterize ARHL and ARVL (**Figure 3**). These studies have shown that age-related hearing loss assessed by pure-tone audiograms begins at 40 years of age and progresses bilaterally from high to low frequencies (summarized in Parthasarathy et al., 2020). The rate of hearing decline with age is highly variable (Gates and Cooper, 1991). Although there are fewer studies quantitatively assessing ARVL, patterns are beginning to emerge (reviewed in Zalewski, 2015; Ji and Zhai, 2018). Decrease in saccular function (indicated by cVEMP amplitudes) begins around the age of 50 to 60 years. A decrease in utricular function (indicated by oVEMP amplitudes) has also been reported after the age of 60 to 80 years. Thus, age-related decline in saccular and utricular function is consistently reported. In contrast, inconsistent findings are

reported for horizontal canal function (indicated by the caloric test), with some studies reporting loss of function after the age of 66 years (Maes et al., 2010) and others reporting no age-related changes in function (Mallinson and Longridge, 2004; Zapala et al., 2008). Assessments of the semicircular canals by vHIT indicated age-related decreases in function do not begin until 80 years of age (reviewed in Ji and Zhai, 2018). Collectively, these findings indicate that the otolithic structures in comparison to the semicircular canals are more vulnerable to aging. Again, these assessments, are potentially confounded by the contribution of central compensation and/or aging of the motor and sensory pathways rather than or in addition to the vestibular end organs. Moreover, there is considerable individual variation, reflected in the large age-related normative values in these measures (Zalewski, 2015). Finally, a combination of various tests, which provide complementary rather than redundant information, are necessary for completely assessing ARVL (Krager, 2018).

Together and despite the caveats highlighted above, the functional studies available indicate that in humans ARHL precedes ARVL. In many regards, studies directly comparing peripheral ARHL and ARVL using equivalent assessments of evoked potentials (ABR and VsEP) in various strains of inbred mice show similar findings to observations in humans. Specifically, age-related decline in cochlear function generally precedes decline of vestibular function (Jones et al., 2006), and there is considerable variation in the age-related decline in both cochlear (Zheng et al., 1999) and peripheral vestibular (Jones et al., 2006) function among individuals of the same strain and across strains. Given the differences in the dynamic range when comparing ABR- and VsEP-based assessments of the cochlea and vestibular end organ function (approximately 60 dB for ABR and 15 dB for VsEP), direct comparisons in these measurements and interpretation of their changes with age should be made cautiously. There is limited investigation of the correlation between clinical assessments of age-related decline of auditory and vestibular function within the same subjects. One study reported a significant correlation between ARHL (assessed with PTA) and reduced saccular function (assessed by cVEMP amplitudes) but not utricular function (assessed with oVEMP amplitudes) (Zuniga et al., 2012). Another association study reported no correlation between ARHL and ARVL (assessed using a clinical test of sensory interaction on balance) (Tan et al., 2016). More comparisons using direct and analogous assessments of inner ear function in the same individuals are necessary, especially given the large range of normative values of these measures.

Turning attention to age-related structural changes in the in the inner ear (**Figure 3**), a variety of human histological studies documented age-related hair cell loss, spiral ganglion neuron loss, and atrophy of the stria vascularis (reviewed in Merchant and Nadol, 2010). The various forms of histopathology have been linked to patterns of hearing loss indicated by audiometric testing (PTA) and led Schuknecht and colleagues to classify four main types of presbycusis: sensory, neural, metabolic or strial, and cochlear conductive (Schuknecht, 1964; Schuknecht and Gacek, 1993). More recent human histological studies documented the loss of afferent fibers and synapses between the inner hair cells and type I afferent fibers (Viana et al., 2015; Wu et al., 2019). The most recent study examined normally aging ears and used quantitative microscopic analysis and subsequent statistical modeling to relate loss of hair cells and auditory nerve fibers as well as atrophy of strial tissues to ARHL indicated by the audiogram (Wu P. Z. et al., 2020). In contrast to previous predictions based on histopathological findings, this study indicates that ARHL is well predicted by outer and then inner hair cell loss and that, perhaps unexpectedly, strial atrophy (although commonly observed) and nerve fiber loss contribute inconsequentially to ARHL. This recent study included cochleae examined previously (Schuknecht and Gacek, 1993). Thus, differences in this most recent study arise from the (1) larger number of specimens investigated, (2) quantification of fractional (and not complete) hair cell loss, and (3) statistical methodology employed. When linking structural and functional pathology, this study suggests that loss of cochlear amplification is the key contributor to ARHL in humans. Importantly, the effects of noise-induced hearing loss, which may be substantial, cannot be disentangled from the effects of ARHL. Moreover, the histological methods used do not reveal structural or functional pathology completely. For example, decline in strial function probably occurs before quantifiable strial atrophy. A variety of animal models have been used to identify histopathological changes associated with loss of cochlear function as part ARHL (reviewed in Kujawa and Liberman, 2019). Depending on the model, ARHL has been correlated with either hair cell loss, strial degeneration, or afferent synapse/fiber loss. Thus, across animal models there does not seem to be a single histopathology underlying ARHL. In these studies, animals are raised in controlled environments, and, unlike humans, show ARHL that has been largely spared from exposure to noise (but see Lauer et al., 2009) or other ototoxins. Thus, differences across animal models may better reflect different genetically determined patterns in the histopathology underlying ARHL.

Structural changes to the vestibular system with increasing age have been investigated in various human histological studies (reviewed in Zalewski, 2015; Ji and Zhai, 2018) but their relation to ARVL is not defined. When considering the sensory hair cells, some studies detected a decrease in the number of both type I and type II hair cells in different regions of the five vestibular end organs in subjects with a mean age of 84 and 94 years (Merchant et al., 2000; Rauch et al., 2001; Lopez et al., 2005; Walther and Westhofen, 2007). In contrast, another study showed no age-related loss of hair cells in the utricles of subjects with a mean age of 82 years (Gopen et al., 2003). When considering the afferent neurons, separate studies showed that the number of cells in Scarpa's ganglion steadily decreases after the age of 30 years (Velazquez-Villasenor et al., 2000; Park et al., 2001). Another earlier study showed that, while there was no decline in the number of afferent fibers during aging, deposition of amyloid bodies could be detected (Gopen et al., 2003). Loss of synapses between the hair cells and afferent fibers has not been investigated in human vestibular end organs, although recent work in FVB/N mice documented age-related loss of afferent synapses in discrete regions of the utricle (specifically calyceal innervations in the utricular extrastriolar region) (Wan et al., 2019). Direct

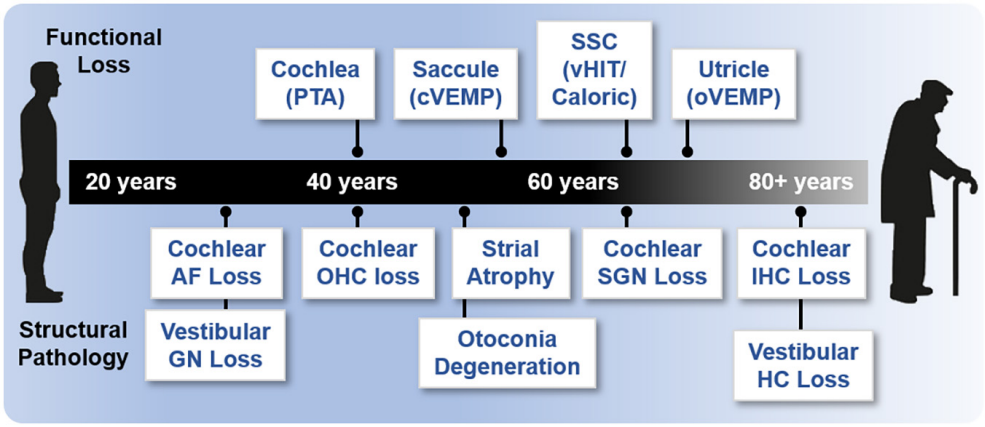

FIGURE 3 | Onset of age-related functional and structural changes in the inner ear. Age of onset of functional loss in humans is based on various methodologies and references. Loss of cochlear function is based on pure tone audiometry (PTA; 40 years) (Parthasarathy et al., 2020). Saccular function (55 years) is based on cVEMP; semicircular canal (SSC) and horizontal canal (HC) function (65 years) are based on vHIT and caloric measurements; and utricular function (70 years) is based on oVEMP (Zapala et al., 2008; Maes et al., 2010; Ji and Zhai, 2018). Various references were used to assess structural histopathology. Loss of cochlear auditory nerve (AN) fibers (>20% loss, 30 years), loss of cochlear outer hair cells (OHCs, >20% loss, 40 years), and loss of cochlear inner hair cells (IHCs, >20% loss, 80 years) are derived from Wu et al. (2019). Loss of cochlear spiral ganglion neurons (SGN, >20% loss, 35 years) are derived from the regression in Makary et al. (2011). Cochlear strial atrophy (>20% loss in apical turns) is derived from Suzuki et al. (2006). Loss of vestibular ganglion neurons (GN, age of onset, 30 years) is reviewed in two studies (Zalewski, 2015; Ji and Zhai, 2018). Otoconia degeneration (50 years) is reviewed previously (Walther and Westhofen, 2007). Loss of vestibular hair cells (HC, all structures, age of onset) is reviewed in two studies (Zalewski, 2015; Ji and Zhai, 2018) but there is a large discrepancy (see also Merchant et al., 2000; Walther and Westhofen, 2007).

comparison of peripheral (cholinergic) efferent innervation in the gerbil revealed significant loss of olivocochlear (OC) neurons but no change in efferent neurons of the vestibular system in aged compared to young adult animals (Radtke-Schuller et al., 2015). Finally, otoconia in both the otolithic structures show decreases in numbers and volumes (Igarashi et al., 1993; Walther and Westhofen, 2007; Walther et al., 2014), with otoconia in the saccule showing worse age-related loss in volume (Igarashi et al., 1993).

Importantly, direct comparison of structural pathology with vestibular function is not available from these studies. Nevertheless, a decline in the number or morphology of vestibular ganglion cells is consistent with decreased neurotransmission and declining vestibular function. Greater loss of otoconia in the saccule compared to utricle is consistent with earlier declining function of the saccule compared to utricle. In general, loss of otoconia may explain the earlier decline in function of the otolithic structures compared to the semicircular canals. Finally, no studies have investigated the age-related integrity of afferent synapses in the human vestibular end organs. However, intriguing earlier work showed that asymptomatic vestibular disorders (revealed by abnormal caloric test results) are common in patients with auditory neuropathy when a peripheral neuropathy is also present (Fujikawa and Starr, 2000). The link between age-related structural and functional changes in the vestibular end organs is also still unclear from animal models. In C57BL/6 mice, vestibular hair cells in the lateral semicircular canals were significantly reduced in 24-week-old mice whereas VOR gain (a measure of semicircular canal function) was significantly reduced only in the oldest (60-week-old) mice (Shiga et al., 2005). In contrast, another study reported age-related elevations in VsEP thresholds that were correlated with the loss of utricular ribbon synapses but not hair cells or neurons (Wan et al., 2019). These studies indicate the potential confounds of central compensation when examining vestibular function in animal models (e.g., Cassel et al., 2019) and the need to examine multiple structures and use sensitive functional assessments. Moreover, experiments utilizing C57BL/6 mice must always be interpreted cautiously considering this strain shows accelerated age-related hearing loss (Zheng et al., 1999).

MECHANISMS UNDERLYING AGE-RELATED PATHOLOGY IN THE COCHLEA AND VESTIBULAR END ORGANS AS PART OF ARHL AND ARVL

Inflammaging

Inflammation is a hallmark of aging, and other coexisting comorbidities linked to aging, such as cardiovascular disease, type 2 diabetes, and Alzheimer's (Blasko et al., 2004; Ferrucci and Fabbri, 2018). Inflammation is also associated with ARHL (Fujioka et al., 2014). Inflammaging, a portmanteau of inflammation and aging, is defined as chronic, low-grade inflammation that worsens with age and contributes to the pathogenesis of various age-related pathologies (reviewed in Baylis et al., 2013; Franceschi et al., 2018). Inflammaging arises from immunosenescence or cellular senescence of the immune system (reviewed in Muller et al., 2019). As immune system function diminishes with age, there is decreased

ability to control or down-regulate the production of pro-inflammatory proteins. This slow and continuous build-up of pro-inflammatory proteins disrupts normal function of multiple systems. Thus, inflammaging seems to promotes inflammation, immunosenescence, and cellular senescence (Rodrigues et al., 2021). Importantly, inflammaging may not necessarily be a normal or inevitable part of the aging process but rather indicative of accelerated aging (Franceschi et al., 2018), suggesting that monitoring and mitigating inflammaging may have diagnostic and treatment value.

Although inflammatory and immune responses have been characterized in various forms of acquired hearing loss (Hu B. H. et al., 2018), attention has more recently focused on the role of inflammaging in ARHL (Watson et al., 2017). In humans, Verschuur and colleagues documented a significant association between four systemic markers of inflammation, white blood cell count, neutrophil count, interleukin 6 (IL-6), and C-reactive protein, and decreased hearing thresholds (Verschuur et al., 2012). These same researchers confirmed increased white blood cell counts with presbycusis in an independent population (Verschuur et al., 2014). Supporting a role for inflammaging, or at least aberrant immune cell activity, examination of human cochlear tissue using immunohistochemistry with confocal and super-resolution imaging revealed age-related changes in both the number and morphology of macrophages (Noble et al., 2019). Activated macrophages were more abundant in basal turns and in older cochleae and found in the lateral wall and auditory nerve. Evidence supporting a role of inflammaging in ARHL also comes from animal studies. Resident macrophages present in the basilar membrane from the basal region of the cochlea of C57BL/6J mice show morphological signs consistent with activation in cochleae from aging mice (up to 10 to 12 months old) (Frye et al., 2017). Recent transcriptomic investigation of young (6-week-old) and old (one-year-old) C57BL/6 mice, showed increased enrichment of genes associated with immune responses and inflammatory pathways in older cochleae (Su et al., 2020). Finally, the cochlea – although once believed to be immune privileged – is likely susceptible to systemic inflammation (Kampfe Nordstrom et al., 2018).

The involvement of inflammaging in ARVL has not been investigated. Nevertheless, the molecular players required for inflammaging are present in the vestibular end organs, although their association with ARVL requires further investigation. Macrophages and microglia have been identified immunohistologically in the tissue underlying the saccule, utricle, and all three ampullae of the semicircular canals, among Scarpa's ganglion cells, and within the endolymphatic duct and sac in human adults with no history of hearing or balance disorders (O'Malley et al., 2016). Studies in adult C57BL/6J mice (aged 4 to 6 weeks) showed that local induction of inflammation caused significantly increased permeability and leakage of the blood-labyrinth barrier due to activation of perivascular-resident macrophage-like melanocytes (PVM/M) (Zhang et al., 2013). A similar role of PVM/M-mediated leakage of the blood-labyrinth barrier was linked to elevated high frequency hearing thresholds in this same strain of mice (Neng et al., 2015). Thus, increased permeability of the blood-labyrinth barrier may increase the susceptibility of the inner ear to systemic inflammatory processes.

More work is needed to investigate the role of inflammaging in the cochlea and especially vestibular end organs (**Figure 4**). Because inflammaging appears to involve similar molecular players and mechanisms across diseases (Michaud et al., 2013), priority should be given to investigating the relationship of specific pro-inflammatory markers, such as IL-6, IL-1, CRP, and TNF-α, to morphological and functional measures of ARHL and ARVL. For these investigations, animal models are especially tractable. Likewise, age-related associations between systemic markers of inflammaging and vestibular function should be assessed in humans. Finally, a careful comparison of the patterns of inflammaging between inner ear end organs is necessary to reveal similarities and differences in mechanisms.

Age-Related Oxidative Stress

Oxidative stress is implicated in various age-related conditions, such as cardiovascular diseases, chronic obstructive pulmonary disease, chronic kidney disease, neurodegenerative diseases, and cancer (reviewed in Liguori et al., 2018), including ARHL (reviewed in Seidman et al., 2004; Henderson et al., 2006; Prasad and Bondy, 2020) and ARVL (see Iwasaki and Yamasoba, 2015; Brosel et al., 2016). In this model (reviewed in Luo et al., 2020), age-related damage results from accumulated oxidative damage caused by free radicals known as reactive oxygen species (ROS). ROS are a natural byproduct of cellular respiration occurring in the mitochondria and play important roles in cell signaling and homeostasis (Zorov et al., 2014). Environmental stressors can also result in abnormal ROS production (Pizzino et al., 2017). Commonly defined ROS include superoxide radicals, hydrogen peroxide, hydroxyl radicals, and singlet oxygen (Valko et al., 2007). ROS may act either as free radicals directly or are readily capable of generating free radicals. ROS and free radicals can damage DNA, break down lipid and protein molecules, and trigger cell death, all of which contribute to damage to cochlear structures, specifically hair cells. Various antioxidant systems are in place to clear ROS (Valko et al., 2007). These include enzymes involved in glutathione (GSH) metabolism, such as glutathione S-transferase (GST), glutathione peroxidase (GPX), and glutathione reductase (GSR). Furthermore, enzymes involved in superoxide anion and hydrogen peroxide breakdown, catalase (CAT) and superoxide dismutase (SOD), respectively, are also crucial for the clearance of ROS. Another enzyme, methionine sulfoxide reductase (MSR), is important in reducing methionine residues that have been oxidized by ROS. Oxidative stress results from the dysregulation of redox homeostasis, with a relative increase in ROS and decrease in antioxidant capacity.

In humans, several studies identified significant associations between ARHL and polymorphisms in enzymes that have antioxidant-related roles in the cochlea, including CYP1A1, NAT2, GSTM1 and the GSTT1, UCP2 (Unal et al., 2005; Van Eyken et al., 2007; Bared et al., 2010; Angeli et al., 2012; Manche et al., 2016; Karimian et al., 2020). The link between oxidative stress and ARHL has prompted multiple investigations into the effectiveness of antioxidants in the prevention of ARHL, but the findings are inconclusive (reviewed

in Tavanai and Mohammadkhani, 2017). Much less work has been done to examine the contribution of oxidative stress to ARVL, but a recent study showed that biomarkers of oxidative stress are significantly elevated in patients with chronic subjective dizziness (Fang et al., 2020).

In animal models, several studies implicate oxidative stress in the initiation and progression of damage to the inner ear due to various insults. Although fewer studies have examined the contribution of oxidative stress to both ARHL and ARVL, the existing work suggests that the cochlea and vestibular end organs utilize overlapping but also distinct antioxidant enzymes and that these structures show differences in the age-related changes in these antioxidant enzymes. In rat, reverse transcription PCR and immunohistochemical staining revealed distinct expression of specific members of the MSR family of proteins between the cochlea and vestibular end organs as well as among cell types within the vestibular end organs (Kwon et al., 2014). Different patterns in age-related changes in antioxidant enzymes have also been documented in rat (Coling et al., 2009). In this study, a significant increase in CAT activity was observed in vestibular end organs but not the cochlea in old (24-month-old) compared to young (3-month-old) rats. In contrast, age-related increase in GPX activity was observed in the cochlea but not the vestibular end organs. Finally, redox state (measured by the ratio of reduced compared to oxidized glutathione) was increased in vestibular end organs but decreased in the cochlea tissue. In separate studies, mice lacking superoxide dismutase 1 (SOD1) show accelerated age-related loss of cochlear hair cells (Keithley et al., 2005) but not vestibular hair cells (Johnson et al., 2010), but these results may be confounded by the background strain of mice, which shows substantial ARHL with minimal ARVL (see Mock et al., 2016).

Together these results indicate that oxidative stress likely plays a role in both ARHL and ARVL (**Figure 4**), although different antioxidant systems may be involved. Speculatively, these results suggest increased involvement of GPX and SOD in ARHL compared to increased involvement of catalase in ARVL, but more work is necessary. Unfortunately, the various mouse models that exist to examine age-related oxidative stress (reviewed in Hamilton et al., 2012) have not been leveraged to examine the contribution of oxidative stress to either ARHL or ARVL. The link between ARHL and other forms of acquired hearing loss (Yang et al., 2015) suggests the examination of models known to show increased susceptibility to other forms of acquired hearing loss to better understand ARHL. For example, GPX1 knockout mice (on a mixed C57BL/6 and 129/SVJ background) show increased susceptibility to noise-induced hearing loss (Ohlemiller et al., 2000), and, therefore, should be prioritized for investigation to identify the role of oxidative stress in ARHL and ARVL.

Genetic Contributions

As multifactorial conditions, both ARHL and ARVL have underlying genetic contributions (**Figure 4**). Indeed, twin and family studies suggest that 25 to 75% of the risk for ARHL is due to heritable causes (see Yamasoba et al., 2013; Momi et al., 2015). Several genome-wide association studies (GWAS) and candidate gene studies have been performed to identify the specific genes contributing to ARHL (reviewed in Ahmadmehrabi et al., 2021). Recent work combining GWAS with other approaches (Nagtegaal et al., 2019; Wells et al., 2019; Kalra et al., 2020), including gene set enrichment analyses, transcriptomic and epigenomic data from the mouse cochlea, as well as immunohistochemistry in the mouse cochlea, implicate a role of at least some of these genes in metabolic, sensory, and neuronal functioning of the cochlea. The genetic contribution to most vestibular disorders, and specifically ARVL, remains largely unknown (Frejo et al., 2016; Gallego-Martinez et al., 2018), and GWAS have not yet been performed to identify the genetic mechanisms contributing to ARVL. Nevertheless, replicated candidate genes identified by GWAS of ARHL are expressed in the mouse utricle based on the SHIELD database (Shen et al., 2015), including (but not necessarily limited to) ILDR1 (Nagtegaal et al., 2019), a cell surface marker; ZNF318, a cell signaling molecule; NID2 a cell adhesion molecule; and ARHGEF28, a guanine nucleotide exchange factor with various functions. Additional prospective candidates for ARVL may be identified by applying a similar approach that used exome sequencing from individuals with ARHL to identify pathogenic variants in known (non-syndromic) deafness genes (Lewis et al., 2018; Boucher et al., 2020; de Bruijn et al., 2020). Finally, identification of the non-coding genetic elements (approximately 98% of the total human genome) contributing to ARHL and ARVL has only just begun despite the well-recognized contribution of non-coding genetic information to other diseases (reviewed in Esteller, 2011). Initial findings suggest overlapping candidates in both the cochlea and vestibular end organs (Schrauwen et al., 2016; Ushakov et al., 2017; Zhao et al., 2020). MicroRNAs (miRNAs), short non-coding RNA molecules that can specifically regulate gene expression by binding to complementary mRNA molecules, have been studied in the context of ARHL and show to regulate important biological processes in the aging cochlea (reviewed in Hu W. et al., 2018). These miRNAs are very stable and can be utilized as biomarkers and therapeutic targets (Pang et al., 2016; Hu W. et al., 2018).

Overlapping and Interacting Mechanisms

The mechanisms highlighted above are closely linked and also interact with each other and other mechanisms associated with aging (**Figure 4**). Unchecked oxidative damage initiates inflammation that, in turn, produces ototoxic ROS and pro-inflammatory elements. Both oxidative stress and inflammation are linked to autophagy, mitophagy, and apoptosis as part of ARHL (reviewed in Wu J. et al., 2020). Oxidative stress is linked to accelerated senescence in a senescence mouse model (Hosokawa, 2002). Moreover, with aging, protein homeostasis – dubbed proteostasis – becomes less effective, so protein translation, chaperone-assisted protein folding, and protein degradation pathways become less accurate (reviewed in Kaushik and Cuervo, 2015). Along with faulty protein production and modification, inefficient removal of cellular waste products activates inflammatory pathways and results in cellular damage (Pizzino et al., 2017). Proteostasis is essential during cochlear development (Freeman et al., 2019) and is worthy of further

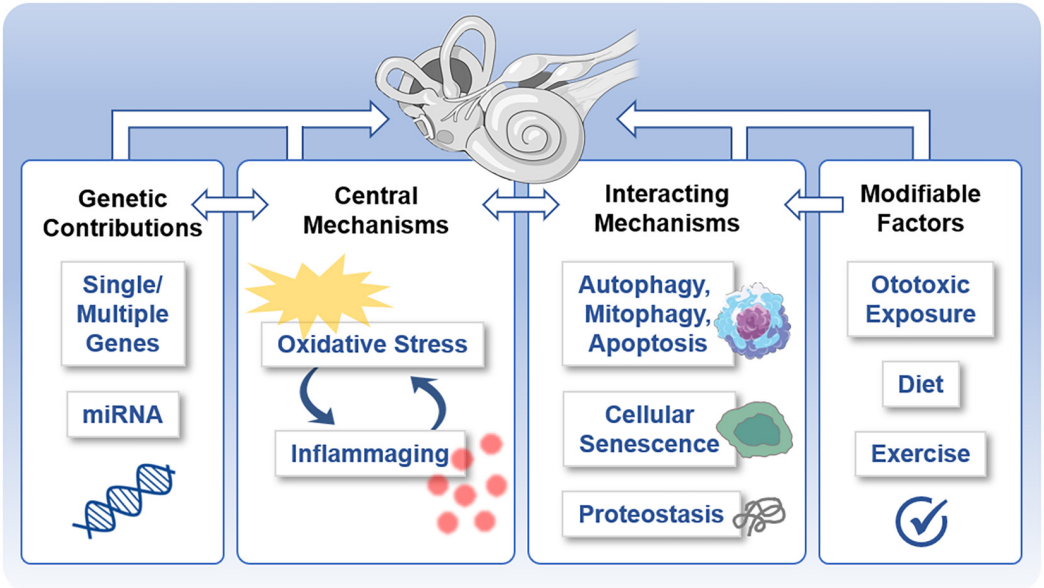

FIGURE 4 | Potentially shared mechanisms underlying both age-related hearing loss (ARHL) and age-related vestibular loss (ARVL). Various molecular mechanisms underlie and interrelate age-related damage to the inner ear that gives rise to ARHL and ARVL. These include the central mechanisms of oxidative stress and inflammation, genetic contributions, interacting mechanisms, and potentially modifiable factors.

investigation as a contributing factor to ARHL and ARVL. Dysregulation of proteostasis may give rise to altered ion and water homeostatic mechanisms, which have been indicated in dysfunction of the inner ear generally (Trune, 2010) and ARHL specifically (Peixoto Pinheiro et al., 2020). Intriguing work examining ARHL in the fruit fly indicates that the manipulation of evolutionary conserved transcription-factor homeostatic master regulators in the fly's auditory neurons altered (accelerated or protected) the ARHL phenotype (Keder et al., 2020). Allelic variants of various genes can influence both the susceptibility to dysregulation of these various pathways as well as the susceptibility to functional and structural damage exerted by these pathways. Finally, potentially modifiable factors can also influence these mechanisms. Diet (Someya et al., 2010) and exercise (Han et al., 2016) influence ARHL, and exposure to ototoxins (Yang et al., 2015) and noise (Stewart et al., 2020) influence both acquired hearing loss and vestibular dysfunction (**Figure 4**).

Mechanisms, like cellular senescence, and structures, like mitochondria, may serves as common points of intersection or even central regulators in these interacting mechanisms. A senescence-accelerated mouse model (SAMP8 mice) shows accelerated ARHL associated with indicators of oxidative stress, inflammation, altered proteostasis, and apoptosis (Menardo et al., 2012), consistent with a role for cellular senescence as an overarching regulator of ARHL. Mitochondria, which are important for metabolism, redox homeostasis, signaling, and regulation of programmed cell death, are known to be involved in ARHL (Crawley and Keithley, 2011; Fujimoto and Yamasoba, 2014). Since comparatively less is known about the molecular mechanisms involved in ARVL, these common points of intersection may be especially fruitful avenues of investigation to identify mechanisms underlying ARVL. Interaction of multiple mechanisms may be good news for strategies to diagnosis and mitigate the effects of ARHL and ARVL, providing multiple biomarkers relevant for improved diagnosis and allowing multiple points of intervention to mitigate the effects of ARHL and ARVL.

Finally, additional insights into the mechanisms interrelating age-related pathology in the cochlea and vestibular end organs come from the long-recognized oto- and nephrotoxicity of some drugs, especially aminoglycoside antibiotics but also chemotherapeutics like cisplatin (Kros and Steyger, 2019). Like both ARHL and ARVL, ototoxicity is associated with cochlear and vestibular hair cell and synapse loss that progresses from high frequency and central/strial regions to low frequency and peripheral/extrastriolar regions of the inner ear sensory epithelia (e.g., Greguske et al., 2021). The link between oto- and nephrotoxicity appears to result from similarities between epithelial transport in the inner ear and kidney (Torban and Goodyer, 2009). Focusing on the inner ear, aminoglycosides quickly accumulate in the endolymph, presumably via capillaries of the stria vascularis. Various suspected routes, including endocytosis and transport through ion channels, lead to accumulation of aminoglycosides in the hair cells (Huth et al., 2011). Once in the hair cells, aminoglycosides lead to the formation of ROS and ultimately trigger apoptosis (Selimoglu, 2007). Various factors increase the risk of aminoglycoside ototoxicity, but genetic predisposition is one of the main determinants of susceptibility (Huth et al., 2011). These genetic mutations appear to affect mitochondrial function and to exacerbate cochleotoxicity

preferentially. Together these and other findings suggest that genetic susceptibility to aminoglycoside ototoxicity arises from reduced mitochondrial function and, consequently, reduced strial function. There are still many discrepancies in the current understanding of aminoglycoside ototoxicity and the links shared with nephrotoxicity. Nevertheless, current insights suggest that altered transport mechanisms, oxidative stress, and genetic mutations, especially those affecting mitochondrial function, may be mechanisms underlying both ototoxicity and ARHL and ARVL and may be the mechanistic links connecting ARHL, ARVL and other comorbidities. More insights into these specific mechanisms are worthy of further investigation.

MECHANISMS UNDERLYING AGE-RELATED NEURODEGENERATION INFORM AGE-RELATED PATHOLOGY IN THE COCHLEA AND VESTIBULAR END ORGANS

The central auditory and vestibular systems also show changes associated with age-related decline in hearing and balance perception that may occur as part of brain aging and/or be driven by age-related changes in the cochlea and vestibular end organs. These changes include both anatomical and functional alterations of the brain (reviewed in Arshad and Seemungal, 2016; Sardone et al., 2019; Slade et al., 2020) and are briefly summarized here. Anatomically, ARHL has been associated with shrinking of the total brain volume (Lin et al., 2014) as well as reduced gray matter volume specifically in the auditory cortex (Eckert et al., 2012) and right temporal lobe (Lin et al., 2014). Brain imaging using functional magnetic resonance imaging (fMRI) has shown that ARHL is associated with functional changes in auditory and non-auditory brain regions as well as functional connectivity in networks important for auditory perception (reviewed in Slade et al., 2020). The landmark cross-sectional study of Lin and colleagues revealed a higher risk of dementia with ARHL (Lin et al., 2011a). Subsequent cross-sectional and a few longitudinal studies confirm an association between ARHL and cognitive impairment and dementia (Livingston et al., 2017; Loughrey et al., 2018). However, more recent work indicates that the association between hearing loss and accelerated cognitive decline was non-significant after additionally adjusting for faster cognitive decline at older ages, which was not done in previous studies (Croll et al., 2021). More evidence is necessary to substantiate the role of hearing loss as a modifiable risk factor for cognitive decline.

Various age-related anatomical and functional alterations have been reported in the central vestibular system. An age-related decrease in volume (Lopez et al., 1997) and neuronal density (Lopez et al., 1997; Tang et al., 2001) and increase in neurons with lipofuscin deposits (Lopez et al., 1997; Alvarez et al., 2000) have been reported in the vestibular nuclear complex. Various age-related changes in the cerebellum have also been reported, including reduced volume of the cerebellar vermis (Torvik et al., 1986; Luft et al., 1999) and reduced global white matter of the cerebellum (Andersen et al., 2003). Age-related decline in functional connectivity of the vestibular cortical network has also been observed using galvanic vestibular stimulation (GVS), which bypasses the peripheral vestibular system and directly stimulates the vestibular nerve. An inverse U-shape in vestibular functional response, measured by torsional eye movements in response to GVS, was found (Jahn et al., 2003). In this study, the authors speculate that central processing compensates for the reduction in vestibular hair cells and other peripheral changes by becoming hypersensitive, but, after the sixth decade, becomes insufficient. Recent work indicates that ARVL, like ARHL, is associated with the increased likelihood and rate of cognitive decline in the aging (Semenov et al., 2016; Dobbels et al., 2019).

How ARHL and ARVL are linked to cognitive impairment is not revealed in association studies, but several conceptual models have been proposed and evaluated for ARHL (e.g., Davis et al., 2016; Chern and Golub, 2019; Griffiths et al., 2020; Slade et al., 2020; Nadhimi and Llano, 2021) and are useful when considering ARVL (Smith, 2021). One possibility is that there are common mechanisms, such as vascular and/or neural pathology, that independently give rise to ARHL/ARVL and cognitive impairment. Another possibility is that ARHL/ARVL indeed causes cognitive impairment. The underlying mechanism is not known but reduced input from the cochlea and vestibular end organs may lead to (1) an impoverished or distorted sensory environment (which may contribute to or be exacerbated by social isolation), (2) reallocation of cognitive resources for listening tasks that reduces resources available for other cognitive tasks, and (3) functional and anatomical changes in the brain. While these underlying mechanisms have been specifically proposed for ARHL, loss of peripheral vestibular input would also be expected to have enormous consequences for cognition given the vast network in the cerebral cortex activated by vestibular stimulation (Lobel et al., 1998; Brandt and Dieterich, 1999; Lopez et al., 2012). Importantly, these underlying mechanisms may interact with one another in complex ways (Johnson et al., 2020), and recent works suggest that distinct mechanisms may be responsible, with different types of dementia associated with different patterns of hearing loss (Jung et al., 2021).

Various neurodegenerative disorders associated with cognitive decline and dementia frequently present not only with alterations in the central auditory and vestibular pathways but also with and peripheral auditory and/or vestibular impairment (Hardy et al., 2016; Cronin et al., 2017). Thus, the mechanisms underlying these disorders provide insights into potentially shared mechanisms underlying age-related auditory and vestibular end organ dysfunction. Among the most common neurodegenerative disorders associated with age-related dementia concomitant with auditory and vestibular impairment are Alzheimer's and Parkinson's diseases. Huntington's disease is an inherited neurodegenerative disease that presents in middle age and is also associated with hearing impairment.

Alzheimer's disease is the most common cause of dementia in the elderly and is frequently associated with ARHL

(Shen et al., 2018). Inflammation-associated neurovascular decline in the blood-brain barrier and blood-labyrinth barrier has been offered as the common cause of both Alzheimer's disease and ARHL (Shityakov et al., 2021). Moreover, cochlear pathology, including loss of auditory spiral ganglion neurons and sensory hair cells, abnormal deposition of amyloid β protein, and overexpression of tau protein in cochlea hair cells have been reported in mouse models of Alzheimer's disease and implicated in loss of cochlear function (reviewed in Shen et al., 2018). Examination of peripheral vestibular pathology in mouse models of Alzheimer's disease remains to be done. In humans, the link between Alzheimer's disease and peripheral vestibular dysfunction is unclear, with some studies identifying a link (e.g., Harun et al., 2016) and others finding no association. A recent systematic review examining the association between either Alzheimer's disease and mild cognitive impairment found no correlation between cognitive decline and semicircular canal function using vHIT, rotatory chair testing, and caloric irrigation (Bosmans et al., 2021). However, the authors of this study suggest cautious interpretation of these findings given the limited number of available studies (seven studies with a combined total of 235 subjects with impaired cognition) and the large heterogeneity in outcome measures. Nevertheless, these results tentatively implicate a role for neurovascular decline and amyloid beta aggregation, which results in oxidative stress, inflammation, and ultimately neuronal cell death (Querfurth and LaFerla, 2010; Heneka et al., 2015), as mechanisms interrelating peripheral and central dysfunction associated with Alzheimer's disease.

Like Alzheimer's disease, Parkinson's disease and the related Lewy body disease are also associated with cognitive impairment in middle to late life and both peripheral auditory and vestibular impairment (Hardy et al., 2016; Jafari et al., 2020; Johnson et al., 2020). Multiple studies report increased audiometric hearing thresholds (after adjustment for the effect of ARHL) in patients with Parkinson's disease and reduced otoacoustic emission (OAE) amplitudes (reviewed in Jafari et al., 2020; De Groote et al., 2021). Even asymptomatic hearing impairment frequently occurs in early-onset Parkinson's Disease (Shetty et al., 2019). The link between Parkinson's disease and peripheral vestibular impairment is less clear but has been documented using both caloric tests and VEMPs (Smith, 2018). Previous work in mice found reduced α-synuclein and synaptophysin expression in the cochlea, and especially medial olivocochlear efferent terminals contacting the outer hair cells, in C57 mice (which show accelerated age-related hearing loss) compared to CBA mice (which show little age-related hearing loss), suggesting a link between α-synuclein and susceptibility to age-related cochlear pathology (Park et al., 2011). α-synuclein is a neuronal protein that regulates synaptic vesicle trafficking and neurotransmitter release (Burre et al., 2018). Insoluble fibrils of α-synuclein aggregates are characteristically seen in Parkinson's disease and other neurodegenerative disorders such as dementia with Lewy bodies, but the mechanisms by which α-synuclein acts in neurodegeneration, as well as its normal cellular function, are unknown. The combination of findings described here tentatively suggest that Parkinson's disease and peripheral auditory impairment may result from altered synaptic transmission due to altered α-synuclein expression both centrally and peripherally. In addition to altered synaptic transmission, mitochondrial dysfunction has also been proposed to interrelate Parkinson's disease and at least ARHL (Jafari et al., 2020).

Huntington's disease is associated with cognitive decline and at least central auditory impairment (Hardy et al., 2016). The link between Huntington's disease and peripheral auditory impairment is less clear. One study found that patients with Huntington's disease had elevated auditory thresholds (based on PTA and ABR) compared to healthy controls (Lin et al., 2011c). This study also reported elevated auditory thresholds (based on ABR) in a mouse model of Huntington's disease. Additional findings from this study implicated mutant huntingtin protein expression in the organ of Corti and reduced expression of brain creatine kinase in the cochlea of this mouse model of Huntington's disease. Another study, however, found central but not peripheral auditory impairment in patients with Huntington's disease (Profant et al., 2017). Vestibular impairment has not been directly investigated in patients with Huntington's disease or mouse models of Huntington's disease. Although the exact pathophysiology underlying Huntington's disease is not known, aggregates of mutant huntingtin, which form inclusion bodies, may disrupt neuronal homeostasis (Jimenez-Sanchez et al., 2017) and, in this way, disrupt function of both the brain and cochlea.

More generally, markers of inflammation are associated with a variety of neurodegenerative disorders (Kinney et al., 2018) and linked to peripheral auditory impairment, including Neuro-Behçet's syndrome, antiphospholipid syndrome, multiple sclerosis, and neurological sarcoidosis (Hardy et al., 2016). Each of these neurodegenerative disorders has also been linked to vestibular impairment (e.g., Gemignani et al., 1991; Colvin, 2006; Girasoli et al., 2018; MacMahon and El Refaie, 2021). Thus, inflammation likely interrelates age-related cognitive and peripheral auditory and vestibular impairment.

Identifying the complex interactions between age-related changes in the auditory and vestibular end organs, central auditory and vestibular pathways, and cognitive impairment is critical to discovering the most effective strategies to prevent, stall, and perhaps even reverse ARHL, ARVL, and related comorbidities. Loss of peripheral auditory (and likely also vestibular) input is itself and regardless of aging a potent trigger of changes in brain structure and function and involves various synaptic mechanisms, ascending and descending auditory pathways, and neuromodulatory circuits (Persic et al., 2020). Thus, age-related loss of cochlea and vestibular end organ function may be the primary drivers of changes in the central auditory and vestibular pathways and various brain regions involved in age-related comorbidities, including cognitive decline. Thus, proactive treatment of ARHL and ARVL targeted at peripheral restoration is especially strategic and also associated with low risk and added health benefits (Ferguson et al., 2017). Moreover, understanding the peripheral

pathology underlying ARHL and ARVL is crucial regardless of whether there is a common, causal, or even unique mechanisms linking ARHL/ARVL and various comorbidities. Insights will allow identification of the key common pathologies and/or lead to the development of methods that better preserve or more fully restore peripheral auditory and vestibular input, which may ultimately be necessary to prevent the host of comorbidities associated with age-related decline of the cochlea and vestibular end organs.

CONCLUSION

Both ARHL and ARVL are prevalent conditions associated with changes in the structure and function of the cochlea and vestibular end organs. A careful comparison of these changes reveals that the patterns of pathophysiology show similarities but also differences both between the cochlea and vestibular end organs and among the vestibular end organs. This review uncovers gaps in the current research landscape and identifies specific, high impact research objectives that should be prioritized. Specifically:

- Assessments of inner ear function in both humans and animal models using a combination of tests, which provide complementary rather than redundant information, are needed to identify and examine correlations between ARHL and ARVL.
- Epidemiological studies of the prevalence of ARVL and associated risk factors, including genetic risk factors, for ARVL that utilize standardized, quantitative, clinical assessments of vestibular end organ function are needed.
- Analogous and robust assessments of peripheral vestibular function in humans and animal models need to be developed and applied.
- Animal models, which have been developed to examine other age-related conditions, should be better leveraged to identify the mechanisms contributing to ARHL and especially ARVL. The background strain of mouse models should be considered carefully since there is considerable strain-dependent variation in the susceptibility to age-related hearing loss and audiogenic seizures.
- The relationship between age-related changes in the peripheral and central auditory and vestibular systems need to be examined, especially when considering the complex, multisystem complications, like falls, depression, and cognitive decline, shared by these conditions.

Addressing these gaps will require integrated investigation of the auditory and vestibular structures of the inner ear using both clinical and animal models. Ultimately, because both ARHL and ARVL are associated with and likely mechanistically linked to other age-related conditions, treatments to prevent ARHL and ARVL are essential to strategies promoting healthy aging overall.

AUTHOR CONTRIBUTIONS

All authors contributed to data collection, analysis and interpretation of data, manuscript preparation, reviewed, and approved the final version of the manuscript.

FUNDING

This study was supported by funds from the Heinsius Houbolt Foundation to SP. NS has been funded by an M.D./Ph.D. scholarship (number 16–59) from the Junior Scientific Masterclass (Graduate School of Medical Sciences, University of Groningen, University Medical Center Groningen, Groningen, Netherlands).

ACKNOWLEDGMENTS

The authors gratefully acknowledge critical feedback from J. E. C. Wiersinga-Post.

REFERENCES

Agrawal, Y., Carey, J. P., Della Santina, C. C., Schubert, M. C., and Minor, L. B. (2009). Disorders of balance and vestibular function in US adults: data from the National health and nutrition examination survey, 2001-2004. *Arch. Intern. Med.* 169, 938–944. doi: 10.1001/archinternmed.2009.66

Agrawal, Y., Pineault, K. G., and Semenov, Y. R. (2018). Health-related quality of life and economic burden of vestibular loss in older adults. *Laryngoscope Investig. Otolaryngol.* 3, 8–15. doi: 10.1002/lio2.129

Agrawal, Y., Platz, E. A., and Niparko, J. K. (2008). Prevalence of hearing loss and differences by demographic characteristics among US adults: data from the National health and nutrition examination survey, 1999-2004. *Arch. Intern. Med.* 168, 1522–1530. doi: 10.1001/archinte.168.14.1522

Agrawal, Y., Schubert, M. C., Migliaccio, A. A., Zee, D. S., Schneider, E., Lehnen, N., et al. (2014). Evaluation of quantitative head impulse testing using search coils versus video-oculography in older individuals. *Otol. Neurotol.* 35, 283–288. doi: 10.1097/mao.0b013e3182995227

Ahmadmehrabi, S., Brant, J., Epstein, D. J., Ruckenstein, M. J., and Rader, D. J. (2021). Genetics of postlingual sensorineural hearing loss. *Laryngoscope* 131, 401–409. doi: 10.1002/lary.28646

Alvarez, J. C., Diaz, C., Suarez, C., Fernandez, J. A., Gonzalez Del Rey, C., Navarro, A., et al. (2000). Aging and the human vestibular nuclei: morphometric analysis. *Mech. Ageing Dev.* 114, 149–172. doi: 10.1016/s0047-6374(00)00098-1

Andersen, B. B., Gundersen, H. J., and Pakkenberg, B. (2003). Aging of the human cerebellum: a stereological study. *J. Comp. Neurol.* 466, 356–365. doi: 10.1002/cne.10884

Angeli, S. I., Bared, A., Ouyang, X., Du, L. L., Yan, D., and Zhong Liu, X. (2012). Audioprofiles and antioxidant enzyme genotypes in presbycusis. *Laryngoscope* 122, 2539–2542. doi: 10.1002/lary.23577

Anson, E., and Jeka, J. (2015). Perspectives on aging vestibular function. *Front. Neurol.* 6:269. doi: 10.3389/fneur.2015.00269

Arshad, Q., and Seemungal, B. M. (2016). Age-related vestibular loss: current understanding and future research directions. *Front. Neurol.* 7:231. doi: 10.3389/fneur.2016.00231

Bared, A., Ouyang, X., Angeli, S., Du, L. L., Hoang, K., Yan, D., et al. (2010). Antioxidant enzymes, presbycusis, and ethnic variability. *Otolaryngol. Head Neck Surg.* 143, 263–268. doi: 10.1016/j.otohns.2010.03.024

Bartl, K., Lehnen, N., Kohlbecher, S., and Schneider, E. (2009). Head impulse testing using video-oculography. *Ann. N. Y. Acad. Sci.* 1164, 331–333. doi: 10.1111/j.1749-6632.2009.03850.x

Baylis, D., Bartlett, D. B., Patel, H. P., and Roberts, H. C. (2013). Understanding how we age: insights into inflammaging. *Longev. Healthspan* 2:8.

Blasko, I., Stampfer-Kountchev, M., Robatscher, P., Veerhuis, R., Eikelenboom, P., and Grubeck-Loebenstein, B. (2004). How chronic inflammation can affect the brain and support the development of Alzheimer's disease in old age: the role of microglia and astrocytes. *Aging Cell* 3, 169–176. doi: 10.1111/j.1474-9728.2004.00101.x

Borg, E., and Engstrom, B. (1983). Hearing thresholds in the rabbit. A behavioral and electrophysiological study. *Acta Otolaryngol.* 95, 19–26. doi: 10.3109/00016488309130911

Bosmans, J., Jorissen, C., Gilles, A., Mertens, G., Engelborghs, S., Cras, P., et al. (2021). Vestibular function in older adults with cognitive impairment: a systematic review. *Ear Hear.* doi: 10.1097/AUD.0000000000001040 [Epub ahead of print].

Boucher, S., Tai, F. W. J., Delmaghani, S., Lelli, A., Singh-Estivalet, A., Dupont, T., et al. (2020). Ultrarare heterozygous pathogenic variants of genes causing dominant forms of early-onset deafness underlie severe presbycusis. *Proc. Natl. Acad. Sci. U.S.A.* 117, 31278–31289. doi: 10.1073/pnas.2010782117

Bowl, M. R., and Dawson, S. J. (2019). Age-related hearing loss. *Cold Spring Harb. Perspect. Med.* 9:a033217.

Brandt, T., and Dieterich, M. (1999). The vestibular cortex. Its locations, functions, and disorders. *Ann. N. Y. Acad. Sci.* 871, 293–312. doi: 10.1111/j.1749-6632.1999.tb09193.x

Brosel, S., and Strupp, M. (2019). The vestibular system and ageing. *Subcell. Biochem.* 91, 195–225. doi: 10.1007/978-981-13-3681-2_8

Brosel, S., Laub, C., Averdam, A., Bender, A., and Elstner, M. (2016). Molecular aging of the mammalian vestibular system. *Ageing Res. Rev.* 26, 72–80. doi: 10.1016/j.arr.2015.12.007

Burre, J., Sharma, M., and Sudhof, T. C. (2018). Cell biology and pathophysiology of alpha-synuclein. *Cold Spring Harb. Perspect. Med.* 8:a024091.

Cao, C., Cade, W. T., Li, S., Mcmillan, J., Friedenreich, C., and Yang, L. (2021). Association of balance function with all-cause and cause-specific mortality among US adults. *JAMA Otolaryngol. Head Neck Surg.* 147, 460–468. doi: 10.1001/jamaoto.2021.0057

Cassel, R., Bordiga, P., Carcaud, J., Simon, F., Beraneck, M., Le Gall, A., et al. (2019). Morphological and functional correlates of vestibular synaptic deafferentation and repair in a mouse model of acute-onset vertigo. *Dis. Model. Mech.* 12:dmm039115.

Chern, A., and Golub, J. S. (2019). Age-related hearing loss and dementia. *Alzheimer Dis. Assoc. Disord.* 33, 285–290. doi: 10.1097/wad.0000000000000325

Ciorba, A., Bianchini, C., Pelucchi, S., and Pastore, A. (2012). The impact of hearing loss on the quality of life of elderly adults. *Clin. Interv. Aging* 7, 159–163. doi: 10.2147/cia.s26059

Ciuman, R. R. (2009). Stria vascularis and vestibular dark cells: characterisation of main structures responsible for inner-ear homeostasis, and their pathophysiological relations. *J. Laryngol. Otol.* 123, 151–162. doi: 10.1017/s0022215108002624

Cohen, H. S. (2019). A review on screening tests for vestibular disorders. *J. Neurophysiol.* 122, 81–92. doi: 10.1152/jn.00819.2018

Cohen, H., Blatchly, C. A., and Gombash, L. L. (1993). A study of the clinical test of sensory interaction and balance. *Phys. Ther.* 73, 346–351; discussion 351–344.

Coling, D., Chen, S., Chi, L. H., Jamesdaniel, S., and Henderson, D. (2009). Age-related changes in antioxidant enzymes related to hydrogen peroxide metabolism in rat inner ear. *Neurosci. Lett.* 464, 22–25. doi: 10.1016/j.neulet.2009.08.015

Colledge, N. R., Wilson, J. A., Macintyre, C. C., and Maclennan, W. J. (1994). The prevalence and characteristics of dizziness in an elderly community. *Age Ageing* 23, 117–120. doi: 10.1093/ageing/23.2.117

Colvin, I. B. (2006). Audiovestibular manifestations of sarcoidosis: a review of the literature. *Laryngoscope* 116, 75–82. doi: 10.1097/01.mlg.0000184580.52723.9f

Crawley, B. K., and Keithley, E. M. (2011). Effects of mitochondrial mutations on hearing and cochlear pathology with age. *Hear. Res.* 280, 201–208. doi: 10.1016/j.heares.2011.05.015

Croll, P. H., Vinke, E. J., Armstrong, N. M., Licher, S., Vernooij, M. W., Baatenburg De Jong, R. J., et al. (2021). Hearing loss and cognitive decline in the general population: a prospective cohort study. *J. Neurol.* 268, 860–871. doi: 10.1007/s00415-020-10208-8

Cronin, T., Arshad, Q., and Seemungal, B. M. (2017). Vestibular deficits in neurodegenerative disorders: balance, dizziness, and spatial disorientation. *Front. Neurol.* 8:538. doi: 10.3389/fneur.2017.00538

Davis, A., Mcmahon, C. M., Pichora-Fuller, K. M., Russ, S., Lin, F., Olusanya, B. O., et al. (2016). Aging and hearing health: the life-course approach. *Gerontologist* 56(Suppl. 2), S256–S267.

de Bruijn, S. E., Smits, J. J., Liu, C., Lanting, C. P., Beynon, A. J., Blankevoort, J., et al. (2020). A RIPOR2 in-frame deletion is a frequent and highly penetrant cause of adult-onset hearing loss. *J. Med. Genet.* 58, 96–104.

De Groote, E., Bockstael, A., Botteldooren, D., Santens, P., and De Letter, M. (2021). The effect of Parkinson's disease on otoacoustic emissions and efferent suppression of transient evoked otoacoustic emissions. *J. Speech Lang. Hear. Res.* 64, 1354–1368. doi: 10.1044/2020_jslhr-20-00594

Dobbels, B., Mertens, G., Gilles, A., Claes, A., Moyaert, J., Van De Berg, R., et al. (2019). Cognitive function in acquired bilateral vestibulopathy: a cross-sectional study on cognition, hearing, and vestibular loss. *Front. Neurosci.* 13:340. doi: 10.3389/fnins.2019.00340

Eckert, M. A., Cute, S. L., Vaden, K. I. Jr., Kuchinsky, S. E., and Dubno, J. R. (2012). Auditory cortex signs of age-related hearing loss. *J. Assoc. Res. Otolaryngol.* 13, 703–713. doi: 10.1007/s10162-012-0332-5

Esteller, M. (2011). Non-coding RNAs in human disease. *Nat. Rev. Genet.* 12, 861–874.

Fang, Z., Huang, K., Gil, C. H., Jeong, J. W., Yoo, H. R., and Kim, H. G. (2020). Biomarkers of oxidative stress and endogenous antioxidants for patients with chronic subjective dizziness. *Sci. Rep.* 10:1478.

Feder, K., Michaud, D., Ramage-Morin, P., Mcnamee, J., and Beauregard, Y. (2015). Prevalence of hearing loss among Canadians aged 20 to 79: audiometric results from the 2012/2013 Canadian health measures survey. *Health Rep.* 26, 18–25.

Ferguson, M. A., Kitterick, P. T., Chong, L. Y., Edmondson-Jones, M., Barker, F., and Hoare, D. J. (2017). Hearing aids for mild to moderate hearing loss in adults. *Cochrane Database Syst. Rev.* 9:CD012023.

Fernandez, L., Breinbauer, H. A., and Delano, P. H. (2015). Vertigo and dizziness in the elderly. *Front. Neurol.* 6:144. doi: 10.3389/fneur.2015.00144

Ferrucci, L., and Fabbri, E. (2018). Inflammageing: chronic inflammation in ageing, cardiovascular disease, and frailty. *Nat. Rev. Cardiol.* 15, 505–522. doi: 10.1038/s41569-018-0064-2

Fettiplace, R. (2017). Hair cell transduction, tuning, and synaptic transmission in the mammalian cochlea. *Compr. Physiol.* 7, 1197–1227. doi: 10.1002/cphy.c160049

Fischer, N., Johnson Chacko, L., Glueckert, R., and Schrott-Fischer, A. (2020). Age-dependent changes in the cochlea. *Gerontology* 66, 33–39.

Franceschi, C., Garagnani, P., Parini, P., Giuliani, C., and Santoro, A. (2018). Inflammaging: a new immune-metabolic viewpoint for age-related diseases. *Nat. Rev. Endocrinol.* 14, 576–590. doi: 10.1038/s41574-018-0059-4

Freeman, S., Mateo Sanchez, S., Pouyo, R., Van Lerberghe, P. B., Hanon, K., Thelen, N., et al. (2019). Proteostasis is essential during cochlear development for neuron survival and hair cell polarity. *EMBO Rep.* 20:e47097.

Frejo, L., Giegling, I., Teggi, R., Lopez-Escamez, J. A., and Rujescu, D. (2016). Genetics of vestibular disorders: pathophysiological insights. *J. Neurol.* 263(Suppl. 1), S45–S53.

Frye, M. D., Yang, W., Zhang, C., Xiong, B., and Hu, B. H. (2017). Dynamic activation of basilar membrane macrophages in response to chronic sensory cell degeneration in aging mouse cochleae. *Hear. Res.* 344, 125–134. doi: 10.1016/j.heares.2016.11.003

Fujikawa, S., and Starr, A. (2000). Vestibular neuropathy accompanying auditory and peripheral neuropathies. *Arch. Otolaryngol. Head Neck Surg.* 126, 1453–1456. doi: 10.1001/archotol.126.12.1453

Fujimoto, C., and Yamasoba, T. (2014). Oxidative stresses and mitochondrial dysfunction in age-related hearing loss. *Oxid. Med. Cell. Longev.* 2014:582849.

Fujioka, M., Okano, H., and Ogawa, K. (2014). Inflammatory and immune responses in the cochlea: potential therapeutic targets for sensorineural hearing loss. *Front. Pharmacol.* 5:287. doi: 10.3389/fphar.2014.00287

Gallego-Martinez, A., Espinosa-Sanchez, J. M., and Lopez-Escamez, J. A. (2018). Genetic contribution to vestibular diseases. *J. Neurol.* 265, 29–34. doi: 10.1007/s00415-018-8842-7

Gates, G. A., and Cooper, J. C. (1991). Incidence of hearing decline in the elderly. *Acta Otolaryngol.* 111, 240–248. doi: 10.3109/00016489109137382

Gemignani, G., Berrettini, S., Bruschini, P., Sellari-Franceschini, S., Fusari, P., Piragine, F., et al. (1991). Hearing and vestibular disturbances in Behcet's syndrome. *Ann. Otol. Rhinol. Laryngol.* 100, 459–463.

Girasoli, L., Cazzador, D., Padoan, R., Nardello, E., Felicetti, M., Zanoletti, E., et al. (2018). Update on vertigo in autoimmune disorders, from diagnosis to treatment. *J. Immunol. Res.* 2018:5072582.

Goldberg, J. M. (2000). Afferent diversity and the organization of central vestibular pathways. *Exp. Brain Res.* 130, 277–297. doi: 10.1007/s002210050033

Gong, R., Hu, X., Gong, C., Long, M., Han, R., Zhou, L., et al. (2018). Hearing loss prevalence and risk factors among older adults in China. *Int. J. Audiol.* 57, 354–359. doi: 10.1080/14992027.2017.1423404

Gopen, Q., Lopez, I., Ishiyama, G., Baloh, R. W., and Ishiyama, A. (2003). Unbiased stereologic type I and type II hair cell counts in human utricular macula. *Laryngoscope* 113, 1132–1138. doi: 10.1097/00005537-200307000-00007

Greguske, E. A., Llorens, J., and Pyott, S. J. (2021). Assessment of cochlear toxicity in response to chronic 3,3'-iminodipropionitrile in mice reveals early and reversible functional loss that precedes overt histopathology. *Arch. Toxicol.* 95, 1003–1021. doi: 10.1007/s00204-020-02962-5

Griffiths, T. D., Lad, M., Kumar, S., Holmes, E., Mcmurray, B., Maguire, E. A., et al. (2020). How can hearing loss cause dementia? *Neuron* 108, 401–412. doi: 10.1016/j.neuron.2020.08.003

Hamilton, R. T., Walsh, M. E., and Van Remmen, H. (2012). Mouse models of oxidative stress indicate a role for modulating healthy aging. *J. Clin. Exp. Pathol.* Suppl. 4:005.

Han, C., Ding, D., Lopez, M. C., Manohar, S., Zhang, Y., Kim, M. J., et al. (2016). Effects of Long-term exercise on age-related hearing loss in mice. *J. Neurosci.* 36, 11308–11319. doi: 10.1523/jneurosci.2493-16.2016

Hardy, C. J. D., Marshall, C. R., Golden, H. L., Clark, C. N., Mummery, C. J., Griffiths, T. D., et al. (2016). Hearing and dementia. *J. Neurol.* 263, 2339–2354.

Harun, A., Oh, E. S., Bigelow, R. T., Studenski, S., and Agrawal, Y. (2016). Vestibular impairment in dementia. *Otol. Neurotol.* 37, 1137–1142. doi: 10.1097/mao.0000000000001157

Heffner, R. S., Koay, G., and Heffner, H. E. (2001). Audiograms of five species of rodents: implications for the evolution of hearing and the perception of pitch. *Hear. Res.* 157, 138–152. doi: 10.1016/s0378-5955(01)00298-2

Henderson, D., Bielefeld, E. C., Harris, K. C., and Hu, B. H. (2006). The role of oxidative stress in noise-induced hearing loss. *Ear Hear.* 27, 1–19. doi: 10.1097/01.aud.0000191942.36672.f3

Heneka, M. T., Carson, M. J., El Khoury, J., Landreth, G. E., Brosseron, F., Feinstein, D. L., et al. (2015). Neuroinflammation in Alzheimer's disease. *Lancet Neurol.* 14, 388–405.

Herdman, S. J., Blatt, P., Schubert, M. C., and Tusa, R. J. (2000). Falls in patients with vestibular deficits. *Am. J. Otol.* 21, 847–851.

Hibino, H., and Kurachi, Y. (2006). Molecular and physiological bases of the K+ circulation in the mammalian inner ear. *Physiology* 21, 336–345. doi: 10.1152/physiol.00023.2006

Hoffman, H. J., Dobie, R. A., Losonczy, K. G., Themann, C. L., and Flamme, G. A. (2017). Declining prevalence of hearing loss in US adults aged 20 to 69 years. *JAMA Otolaryngol. Head Neck Surg.* 143, 274–285. doi: 10.1001/jamaoto.2016.3527

Hogan, A., O'loughlin, K., Miller, P., and Kendig, H. (2009). The health impact of a hearing disability on older people in Australia. *J. Aging Health* 21, 1098–1111. doi: 10.1177/0898264309347821

Hosokawa, M. (2002). A higher oxidative status accelerates senescence and aggravates age-dependent disorders in SAMP strains of mice. *Mech. Ageing Dev.* 123, 1553–1561. doi: 10.1016/s0047-6374(02)00091-x

Hoth, S., and Baljic, I. (2017). Current audiological diagnostics. *GMS Curr. Top. Otorhinolaryngol. Head Neck Surg.* 16:Doc09.

Hu, B. H., Zhang, C., and Frye, M. D. (2018). Immune cells and non-immune cells with immune function in mammalian cochleae. *Hear. Res.* 362, 14–24. doi: 10.1016/j.heares.2017.12.009

Hu, W., Wu, J., Jiang, W., and Tang, J. (2018). MicroRNAs and presbycusis. *Aging Dis.* 9, 133–142. doi: 10.14336/ad.2017.0119

Huth, M. E., Ricci, A. J., and Cheng, A. G. (2011). Mechanisms of aminoglycoside ototoxicity and targets of hair cell protection. *Int. J. Otolaryngol.* 2011:937861.

Igarashi, M., Saito, R., Mizukoshi, K., and Alford, B. R. (1993). Otoconia in young and elderly persons: a temporal bone study. *Acta Otolaryngol. Suppl.* 504, 26–29. doi: 10.3109/00016489309128117

Iwasaki, S., and Yamasoba, T. (2015). Dizziness and imbalance in the elderly: age-related decline in the vestibular system. *Aging Dis.* 6, 38–47. doi: 10.14336/ad.2014.0128

Jafari, Z., Kolb, B. E., and Mohajerani, M. H. (2020). Auditory dysfunction in Parkinson's disease. *Mov. Disord.* 35, 537–550.

Jahn, K. (2019). The aging vestibular system: dizziness and imbalance in the elderly. *Adv. Otorhinolaryngol.* 82, 143–149. doi: 10.1159/000490283

Jahn, K., Naessl, A., Schneider, E., Strupp, M., Brandt, T., and Dieterich, M. (2003). Inverse U-shaped curve for age dependency of torsional eye movement responses to galvanic vestibular stimulation. *Brain* 126, 1579–1589. doi: 10.1093/brain/awg163

Ji, L., and Zhai, S. (2018). Aging and the peripheral vestibular system. *J. Otol.* 13, 138–140. doi: 10.1016/j.joto.2018.11.006

Jimenez-Sanchez, M., Licitra, F., Underwood, B. R., and Rubinsztein, D. C. (2017). Huntington's disease: mechanisms of pathogenesis and therapeutic strategies. *Cold Spring Harb. Perspect. Med.* 7:a024240.

Johnson, J. C. S., Marshall, C. R., Weil, R. S., Bamiou, D.-E., Hardy, C. J. D., and Warren, J. D. (2020). Hearing and dementia: from ears to brain. *Brain* 144, 391–401. doi: 10.1093/brain/awaa429

Johnson, K. R., Yu, H., Ding, D., Jiang, H., Gagnon, L. H., and Salvi, R. J. (2010). Separate and combined effects of Sod1 and Cdh23 mutations on age-related hearing loss and cochlear pathology in C57BL/6J mice. *Hear. Res.* 268, 85–92. doi: 10.1016/j.heares.2010.05.002

Jones, S. M., Jones, T. A., Johnson, K. R., Yu, H., Erway, L. C., and Zheng, Q. Y. (2006). A comparison of vestibular and auditory phenotypes in inbred mouse strains. *Brain Res.* 1091, 40–46. doi: 10.1016/j.brainres.2006.01.066

Jones, T. A., Jones, S. M., Vijayakumar, S., Brugeaud, A., Bothwell, M., and Chabbert, C. (2011). The adequate stimulus for mammalian linear vestibular evoked potentials (VsEPs). *Hear. Res.* 280, 133–140. doi: 10.1016/j.heares.2011.05.005

Jönsson, R., Sixt, E., Landahl, S., and Rosenhall, U. (2004). Prevalence of dizziness and vertigo in an urban elderly population. *J. Vestib. Res.* 14, 47–52.

Jordan, P. M., Fettis, M., and Holt, J. C. (2015). Efferent innervation of turtle semicircular canal cristae: comparisons with bird and mouse. *J. Comp. Neurol.* 523, 1258–1280. doi: 10.1002/cne.23738

Jung, J., Bae, S. H., Han, J. H., Kwak, S. H., Nam, G. S., Lee, P. H., et al. (2021). Relationship between hearing loss and dementia differs according to the underlying mechanism. *J. Clin. Neurol.* 17, 290–299. doi: 10.3988/jcn.2021.17.2.290

Kalra, G., Milon, B., Casella, A. M., Herb, B. R., Humphries, E., Song, Y., et al. (2020). Biological insights from multi-omic analysis of 31 genomic risk loci for adult hearing difficulty. *PLoS Genet.* 16:e1009025. doi: 10.1371/journal.pgen.1009025

Kampfe Nordstrom, C., Danckwardt-Lilliestrom, N., Laurell, G., Liu, W., and Rask-Andersen, H. (2018). The human endolymphatic sac and inner ear immunity: macrophage interaction and molecular expression. *Front. Immunol.* 9:3181. doi: 10.3389/fimmu.2018.03181

Karimian, M., Behjati, M., Barati, E., Ehteram, T., and Karimian, A. (2020). CYP1A1 and GSTs common gene variations and presbycusis risk: a genetic association analysis and a bioinformatics approach. *Environ. Sci. Pollut. Res. Int.* 27, 42600–42610. doi: 10.1007/s11356-020-10144-0

Kaushik, S., and Cuervo, A. M. (2015). Proteostasis and aging. *Nat. Med.* 21, 1406–1415.

Keder, A., Tardieu, C., Malong, L., Filia, A., Kashkenbayeva, A., Newton, F., et al. (2020). Homeostatic maintenance and age-related functional decline in the *Drosophila* ear. *Sci. Rep.* 10:7431.

Keithley, E. M. (2020). Pathology and mechanisms of cochlear aging. *J. Neurosci. Res.* 98, 1674–1684. doi: 10.1002/jnr.24439

Keithley, E. M., Canto, C., Zheng, Q. Y., Wang, X., Fischel-Ghodsian, N., and Johnson, K. R. (2005). Cu/Zn superoxide dismutase and age-related hearing loss. *Hear. Res.* 209, 76–85. doi: 10.1016/j.heares.2005.06.009

Khan, S. S., Singer, B. D., and Vaughan, D. E. (2017). Molecular and physiological manifestations and measurement of aging in humans. *Aging Cell* 16, 624–633. doi: 10.1111/acel.12601

Kingma, H., and van de Berg, R. (2016). Anatomy, physiology, and physics of the peripheral vestibular system. *Handb. Clin. Neurol.* 137, 1–16. doi: 10.1007/0-387-21567-0_1

Kinney, J. W., Bemiller, S. M., Murtishaw, A. S., Leisgang, A. M., Salazar, A. M., and Lamb, B. T. (2018). Inflammation as a central mechanism in Alzheimer's disease. *Alzheimers Dement.* 4, 575–590.

Köppl, C., Wilms, V., Russell, I. J., and Nothwang, H. G. (2018). Evolution of endolymph secretion and endolymphatic potential generation in the vertebrate inner ear. *Brain Behav. Evol.* 92, 1–31. doi: 10.1159/000494050

Kovacs, E., Wang, X., and Grill, E. (2019). Economic burden of vertigo: a systematic review. *Health Econ. Rev.* 9:37.

Krager, R. (2018). Assessment of vestibular function in elderly patients. *Curr. Opin. Otolaryngol. Head Neck Surg.* 26, 302–306. doi: 10.1097/moo.0000000000000476

Kros, C. J., and Steyger, P. S. (2019). Aminoglycoside- and cisplatin-induced ototoxicity: mechanisms and otoprotective strategies. *Cold Spring Harb. Perspect. Med.* 9:a033548. doi: 10.1101/cshperspect.a033548

Kujawa, S. G., and Liberman, M. C. (2019). Translating animal models to human therapeutics in noise-induced and age-related hearing loss. *Hear. Res.* 377, 44–52. doi: 10.1016/j.heares.2019.03.003

Kwon, T. J., Oh, S. K., Kim, Y. R., Kim, M. A., Lee, B., Choi, K. S., et al. (2014). Methionine sulfoxide reductase A, B1 and B2 are likely to be involved in the protection against oxidative stress in the inner ear. *Cells Tissues Organs* 199, 294–300. doi: 10.1159/000368893

Lauer, A. M., May, B. J., Hao, Z. J., and Watson, J. (2009). Analysis of environmental sound levels in modern rodent housing rooms. *Lab. Anim.* 38, 154–160. doi: 10.1038/laban0509-154

Lewis, M. A., Nolan, L. S., Cadge, B. A., Matthews, L. J., Schulte, B. A., Dubno, J. R., et al. (2018). Whole exome sequencing in adult-onset hearing loss reveals a high load of predicted pathogenic variants in known deafness-associated genes and identifies new candidate genes. *BMC Med. Genomics* 11:77. doi: 10.1186/s12920-018-0395-1

Liguori, I., Russo, G., Curcio, F., Bulli, G., Aran, L., Della-Morte, D., et al. (2018). Oxidative stress, aging, and diseases. *Clin. Interv. Aging* 13, 757–772.

Lin, F. R., and Ferrucci, L. (2012). Hearing loss and falls among older adults in the United States. *Arch. Intern. Med.* 172, 369–371. doi: 10.1001/archinternmed.2011.728

Lin, F. R., Ferrucci, L., An, Y., Goh, J. O., Doshi, J., Metter, E. J., et al. (2014). Association of hearing impairment with brain volume changes in older adults. *Neuroimage* 90, 84–92. doi: 10.1016/j.neuroimage.2013.12.059

Lin, F. R., Metter, E. J., O'brien, R. J., Resnick, S. M., Zonderman, A. B., and Ferrucci, L. (2011a). Hearing loss and incident dementia. *Arch. Neurol.* 68, 214–220.

Lin, F. R., Niparko, J. K., and Ferrucci, L. (2011b). Hearing loss prevalence in the United States. *Arch. Intern. Med.* 171, 1851–1852. doi: 10.1001/archinternmed.2011.506

Lin, F. R., Yaffe, K., Xia, J., Xue, Q. L., Harris, T. B., Purchase-Helzner, E., et al. (2013). Hearing loss and cognitive decline in older adults. *JAMA Intern. Med.* 173, 293–299.

Lin, Y. S., Chen, C. M., Soong, B. W., Wu, Y. R., Chen, H. M., Yeh, W. Y., et al. (2011c). Dysregulated brain creatine kinase is associated with hearing impairment in mouse models of Huntington disease. *J. Clin. Invest.* 121, 1519–1523. doi: 10.1172/jci43220

Liston, M. B., Bamiou, D. E., Martin, F., Hopper, A., Koohi, N., Luxon, L., et al. (2014). Peripheral vestibular dysfunction is prevalent in older adults experiencing multiple non-syncopal falls versus age-matched non-fallers: a pilot study. *Age Ageing* 43, 38–43. doi: 10.1093/ageing/aft129

Liu, X. Z., and Yan, D. (2007). Ageing and hearing loss. *J. Pathol.* 211, 188–197.

Livingston, G., Sommerlad, A., Orgeta, V., Costafreda, S. G., Huntley, J., Ames, D., et al. (2017). Dementia prevention, intervention, and care. *Lancet* 390, 2673–2734.

Llorens, J., Callejo, A., Greguske, E. A., Maroto, A. F., Cutillas, B., and Martins-Lopes, V. (2018). Physiological assesment of vestibular function and toxicity in humans and animals. *Neurotoxicology* 66, 204–212. doi: 10.1016/j.neuro.2018.02.003

Lobel, E., Kleine, J. F., Bihan, D. L., Leroy-Willig, A., and Berthoz, A. (1998). Functional MRI of galvanic vestibular stimulation. *J. Neurophysiol.* 80, 2699–2709. doi: 10.1152/jn.1998.80.5.2699

Lopez, C., Blanke, O., and Mast, F. W. (2012). The human vestibular cortex revealed by coordinate-based activation likelihood estimation meta-analysis. *Neuroscience* 212, 159–179. doi: 10.1016/j.neuroscience.2012.03.028

Lopez, I., Honrubia, V., and Baloh, R. W. (1997). Aging and the human vestibular nucleus. *J. Vestib. Res.* 7, 77–85. doi: 10.3233/ves-1997-7107

Lopez, I., Ishiyama, G., Tang, Y., Tokita, J., Baloh, R. W., and Ishiyama, A. (2005). Regional estimates of hair cells and supporting cells in the human crista ampullaris. *J. Neurosci. Res.* 82, 421–431. doi: 10.1002/jnr.20652

Lopez-Poveda, E. A. (2018). Olivocochlear efferents in animals and humans: from anatomy to clinical relevance. *Front. Neurol.* 9:197. doi: 10.3389/fneur.2018.00197

Loughrey, D. G., Kelly, M. E., Kelley, G. A., Brennan, S., and Lawlor, B. A. (2018). Association of age-related hearing loss with cognitive function, cognitive impairment, and dementia: a systematic review and meta-analysis. *JAMA Otolaryngol. Head Neck Surg.* 144, 115–126. doi: 10.1001/jamaoto.2017.2513

Luft, A. R., Skalej, M., Schulz, J. B., Welte, D., Kolb, R., Burk, K., et al. (1999). Patterns of age-related shrinkage in cerebellum and brainstem observed in vivo using three-dimensional MRI volumetry. *Cereb. Cortex* 9, 712–721. doi: 10.1093/cercor/9.7.712

Luo, J., Mills, K., Le Cessie, S., Noordam, R., and Van Heemst, D. (2020). Ageing, age-related diseases and oxidative stress: what to do next? *Ageing Res. Rev.* 57:100982. doi: 10.1016/j.arr.2019.100982

Lysakowski, A., and Goldberg, J. M. (1997). A regional ultrastructural analysis of the cellular and synaptic architecture in the chinchilla cristae ampullares. *J. Comp. Neurol.* 389, 419–443. doi: 10.1002/(sici)1096-9861(19971222)389:3<419::aid-cne5>3.0.co;2-3

Lysakowski, A., and Goldberg, J. M. (2008). Ultrastructural analysis of the cristae ampullares in the squirrel monkey (*Saimiri sciureus*). *J. Comp. Neurol.* 511, 47–64. doi: 10.1002/cne.21827

Macdougall, H. G., Mcgarvie, L. A., Halmagyi, G. M., Curthoys, I. S., and Weber, K. P. (2013). The video Head Impulse Test (vHIT) detects vertical semicircular canal dysfunction. *PLoS One* 8:e61488. doi: 10.1371/journal.pone.0061488

MacDougall, H. G., Weber, K. P., Mcgarvie, L. A., Halmagyi, G. M., and Curthoys, I. S. (2009). The video head impulse test: diagnostic accuracy in peripheral vestibulopathy. *Neurology* 73, 1134–1141. doi: 10.1212/wnl.0b013e3181bacf85

MacMahon, H., and El Refaie, A. (2021). The audiovestibular manifestations as early symptoms of multiple sclerosis: a scoping review of the literature. *Ir. J. Med. Sci.* doi: 10.1007/s11845-021-02508-3

Maes, L., Dhooge, I., D'haenens, W., Bockstael, A., Keppler, H., Philips, B., et al. (2010). The effect of age on the sinusoidal harmonic acceleration test, pseudorandom rotation test, velocity step test, caloric test, and vestibular-evoked myogenic potential test. *Ear Hear.* 31, 84–94. doi: 10.1097/aud.0b013e3181b9640e

Makary, C. A., Shin, J., Kujawa, S. G., Liberman, M. C., and Merchant, S. N. (2011). Age-related primary cochlear neuronal degeneration in human temporal bones. *J. Assoc. Res. Otolaryngol.* 12, 711–717. doi: 10.1007/s10162-011-0283-2

Mallinson, A. I., and Longridge, N. S. (2004). Caloric response does not decline with age. *J. Vestib. Res.* 14, 393–396.

Manche, S. K., Jangala, M., Putta, P., Koralla, R. M., and Akka, J. (2016). Association of oxidative stress gene polymorphisms with presbycusis. *Gene* 593, 277–283. doi: 10.1016/j.gene.2016.08.029

Martins-Lopes, V., Bellmunt, A., Greguske, E. A., Maroto, A. F., Boadas-Vaello, P., and Llorens, J. (2019). Quantitative assessment of anti-gravity reflexes to evaluate vestibular dysfunction in rats. *J. Assoc. Res. Otolaryngol.* 20, 553–563. doi: 10.1007/s10162-019-00730-6

Menardo, J., Tang, Y., Ladrech, S., Lenoir, M., Casas, F., Michel, C., et al. (2012). Oxidative stress, inflammation, and autophagic stress as the key mechanisms of premature age-related hearing loss in SAMP8 mouse Cochlea. *Antioxid. Redox Signal.* 16, 263–274. doi: 10.1089/ars.2011.4037

Mener, D. J., Betz, J., Genther, D. J., Chen, D., and Lin, F. R. (2013). Hearing loss and depression in older adults. *J. Am. Geriatr. Soc.* 61, 1627–1629. doi: 10.1111/jgs.12429

Merchant, S. N., and Nadol, J. B. Jr. (2010). *Schuknecht's Pathology of the Ear*. Beijing: People's Medical Publishing House.

Merchant, S. N., Velazquez-Villasenor, L., Tsuji, K., Glynn, R. J., Wall, C. III, and Rauch, S. D. (2000). Temporal bone studies of the human peripheral vestibular system. Normative vestibular hair cell data. *Ann. Otol. Rhinol. Laryngol. Suppl.* 181, 3–13. doi: 10.1177/00034894001090s502

Michaud, M., Balardy, L., Moulis, G., Gaudin, C., Peyrot, C., Vellas, B., et al. (2013). Proinflammatory cytokines, aging, and age-related diseases. *J. Am. Med. Dir. Assoc.* 14, 877–882.

Mick, P., Kawachi, I., and Lin, F. R. (2014). The association between hearing loss and social isolation in older adults. *Otolaryngol. Head Neck Surg.* 150, 378–384. doi: 10.1177/0194599813518021

Mock, B. E., Vijayakumar, S., Pierce, J., Jones, T. A., and Jones, S. M. (2016). Differential effects of Cdh23(753A) on auditory and vestibular functional aging in C57BL/6J mice. *Neurobiol. Aging* 43, 13–22. doi: 10.1016/j.neurobiolaging.2016.03.013

Momi, S. K., Wolber, L. E., Fabiane, S. M., Macgregor, A. J., and Williams, F. M. (2015). Genetic and environmental factors in age-related hearing impairment. *Twin Res. Hum. Genet.* 18, 383–392.

Morsli, H., Choo, D., Ryan, A., Johnson, R., and Wu, D. K. (1998). Development of the mouse inner ear and origin of its sensory organs. *J. Neurosci.* 18, 3327–3335. doi: 10.1523/jneurosci.18-09-03327.1998

Muller, L., Di Benedetto, S., and Pawelec, G. (2019). The immune system and its dysregulation with aging. *Subcell. Biochem.* 91, 21–43. doi: 10.1007/978-981-13-3681-2_2

Nadhimi, Y., and Llano, D. A. (2021). Does hearing loss lead to dementia? A review of the literature. *Hear. Res.* 402:108038. doi: 10.1016/j.heares.2020.108038

Nagtegaal, A. P., Broer, L., Zilhao, N. R., Jakobsdottir, J., Bishop, C. E., Brumat, M., et al. (2019). Genome-wide association meta-analysis identifies five novel loci for age-related hearing impairment. *Sci. Rep.* 9:15192.

Neng, L., Zhang, J., Yang, J., Zhang, F., Lopez, I. A., Dong, M., et al. (2015). Structural changes in thestrial blood-labyrinth barrier of aged C57BL/6 mice. *Cell Tissue Res.* 361, 685–696. doi: 10.1007/s00441-015-2147-2

Nin, F., Yoshida, T., Sawamura, S., Ogata, G., Ota, T., Higuchi, T., et al. (2016). The unique electrical properties in an extracellular fluid of the mammalian cochlea; their functional roles, homeostatic processes, and pathological significance. *Pflugers Arch.* 468, 1637–1649. doi: 10.1007/s00424-016-1871-0

Noble, K. V., Liu, T., Matthews, L. J., Schulte, B. A., and Lang, H. (2019). Age-related changes in immune cells of the human cochlea. *Front Neurol* 10:895. doi: 10.3389/fneur.2019.00895

Ohlemiller, K. K., Mcfadden, S. L., Ding, D. L., Lear, P. M., and Ho, Y. S. (2000). Targeted mutation of the gene for cellular glutathione peroxidase (Gpx1) increases noise-induced hearing loss in mice. *J. Assoc. Res. Otolaryngol.* 1, 243–254. doi: 10.1007/s101620010043

O'Malley, J. T., Nadol, J. B. Jr., and Mckenna, M. J. (2016). Anti CD163+, Iba1+, and CD68+ cells in the adult human inner ear: normal distribution of an unappreciated class of macrophages/microglia and implications for inflammatory otopathology in humans. *Otol. Neurotol.* 37, 99–108. doi: 10.1097/mao.0000000000000879

Pang, J., Xiong, H., Yang, H., Ou, Y., Xu, Y., Huang, Q., et al. (2016). Circulating miR-34a levels correlate with age-related hearing loss in mice and humans. *Exp. Gerontol.* 76, 58–67. doi: 10.1016/j.exger.2016.01.009

Park, J. J., Tang, Y., Lopez, I., and Ishiyama, A. (2001). Age-related change in the number of neurons in the human vestibular ganglion. *J. Comp. Neurol.* 431, 437–443. doi: 10.1002/1096-9861(20010319)431:4<437::aid-cne1081>3.0.co;2-p

Park, S. N., Back, S. A., Choung, Y. H., Kim, H. L., Akil, O., Lustig, L. R., et al. (2011). alpha-Synuclein deficiency and efferent nerve degeneration in the mouse cochlea: a possible cause of early-onset presbycusis. *Neurosci. Res.* 71, 303–310. doi: 10.1016/j.neures.2011.07.1835

Parthasarathy, A., Romero Pinto, S., Lewis, R. M., Goedicke, W., and Polley, D. B. (2020). Data-driven segmentation of audiometric phenotypes across a large clinical cohort. *Sci. Rep.* 10:6704.

Peixoto Pinheiro, B., Vona, B., Lowenheim, H., Ruttiger, L., Knipper, M., and Adel, Y. (2020). Age-related hearing loss pertaining to potassium ion channels in the cochlea and auditory pathway. *Pflugers Arch.* 473, 823–840. doi: 10.1007/s00424-020-02496-w

Persic, D., Thomas, M. E., Pelekanos, V., Ryugo, D. K., Takesian, A. E., Krumbholz, K., et al. (2020). Regulation of auditory plasticity during critical periods and following hearing loss. *Hear. Res.* 397:107976. doi: 10.1016/j.heares.2020.107976

Pickles, J. O. (2015). Auditory pathways: anatomy and physiology. *Handb. Clin. Neurol.* 129, 3–25.

Pizzino, G., Irrera, N., Cucinotta, M., Pallio, G., Mannino, F., Arcoraci, V., et al. (2017). Oxidative stress: harms and benefits for human health. *Oxid. Med. Cell. Longev.* 2017:8416763.

Prasad, K. N., and Bondy, S. C. (2020). Increased oxidative stress, inflammation, and glutamate: potential preventive and therapeutic targets for hearing disorders. *Mech. Ageing Dev.* 185:111191. doi: 10.1016/j.mad.2019.111191

Profant, O., Roth, J., Bures, Z., Balogova, Z., Liskova, I., Betka, J., et al. (2017). Auditory dysfunction in patients with Huntington's disease. *Clin. Neurophysiol.* 128, 1946–1953.

Querfurth, H. W., and LaFerla, F. M. (2010). Alzheimer's disease. *N. Engl. J. Med.* 362, 329–344.

Radtke-Schuller, S., Seeler, S., and Grothe, B. (2015). Restricted loss of olivocochlear but not vestibular efferent neurons in the senescent gerbil (*Meriones unguiculatus*). *Front. Aging Neurosci.* 7:4. doi: 10.3389/fnagi.2015.00004

Rauch, S. D., Velazquez-Villasenor, L., Dimitri, P. S., and Merchant, S. N. (2001). Decreasing hair cell counts in aging humans. *Ann. N. Y. Acad. Sci.* 942, 220–227. doi: 10.1111/j.1749-6632.2001.tb03748.x

Renga, V. (2019). Clinical evaluation of patients with vestibular dysfunction. *Neurol. Res. Int.* 2019:3931548.

Rodrigues, L. P., Teixeira, V. R., Alencar-Silva, T., Simonassi-Paiva, B., Pereira, R. W., Pogue, R., et al. (2021). Hallmarks of aging and immunosenescence: connecting the dots. *Cytokine Growth Factor Rev.* 59, 9–21. doi: 10.1016/j.cytogfr.2021.01.006

Sardone, R., Battista, P., Panza, F., Lozupone, M., Griseta, C., Castellana, F., et al. (2019). The age-related central auditory processing disorder: silent impairment of the cognitive ear. *Front. Neurosci.* 13:619. doi: 10.3389/fnins.2019.00619

Schrauwen, I., Hasin-Brumshtein, Y., Corneveaux, J. J., Ohmen, J., White, C., Allen, A. N., et al. (2016). A comprehensive catalogue of the coding and non-coding transcripts of the human inner ear. *Hear. Res.* 333, 266–274. doi: 10.1016/j.heares.2015.08.013

Schuknecht, H. F. (1964). Further observations on the pathology of presbycusis. *Arch. Otolaryngol.* 80, 369–382. doi: 10.1001/archotol.1964.00750040381003

Schuknecht, H. F., and Gacek, M. R. (1993). Cochlear pathology in presbycusis. *Ann. Otol. Rhinol. Laryngol.* 102, 1–16. doi: 10.1177/00034894931020s101

Scuffham, P., Chaplin, S., and Legood, R. (2003). Incidence and costs of unintentional falls in older people in the United Kingdom. *J. Epidemiol. Commun. Health* 57, 740–744. doi: 10.1136/jech.57.9.740

Seidman, M. D., Ahmad, N., Joshi, D., Seidman, J., Thawani, S., and Quirk, W. S. (2004). Age-related hearing loss and its association with reactive oxygen species and mitochondrial DNA damage. *Acta Otolaryngol. Suppl.* 124, 16–24. doi: 10.1080/03655230410017823

Selimoglu, E. (2007). Aminoglycoside-induced ototoxicity. *Curr. Pharm. Des.* 13, 119–126. doi: 10.2174/138161207779313731

Semenov, Y. R., Bigelow, R. T., Xue, Q. L., Du Lac, S., and Agrawal, Y. (2016). Association between vestibular and cognitive function in U.S. adults: data from the national health and nutrition examination survey. *J. Gerontol. A Biol. Sci. Med. Sci.* 71, 243–250. doi: 10.1093/gerona/glv069

Shen, J., Scheffer, D. I., Kwan, K. Y., and Corey, D. P. (2015). SHIELD: an integrative gene expression database for inner ear research. *Database* 2015:bav071. doi: 10.1093/database/bav071

Shen, Y., Ye, B., Chen, P., Wang, Q., Fan, C., Shu, Y., et al. (2018). Cognitive decline, dementia, Alzheimer's disease and presbycusis: examination of the possible molecular mechanism. *Front. Neurosci.* 12:394. doi: 10.3389/fnins.2018.00394

Shetty, K., Krishnan, S., Thulaseedharan, J. V., Mohan, M., and Kishore, A. (2019). Asymptomatic hearing impairment frequently occurs in early-onset Parkinson's disease. *J. Mov. Disord.* 12, 84–90. doi: 10.14802/jmd.18048

Shiga, A., Nakagawa, T., Nakayama, M., Endo, T., Iguchi, F., Kim, T. S., et al. (2005). Aging effects on vestibulo-ocular responses in C57BL/6 mice: comparison with alteration in auditory function. *Audiol. Neurootol.* 10, 97–104. doi: 10.1159/000083365

Shityakov, S., Hayashi, K., Stork, S., Scheper, V., Lenarz, T., and Forster, C. Y. (2021). The conspicuous link between ear, brain and heart-could neurotrophin-treatment of age-related hearing loss help prevent Alzheimer's disease and associated amyloid cardiomyopathy? *Biomolecules* 11:900. doi: 10.3390/biom11060900

Slade, K., Plack, C. J., and Nuttall, H. E. (2020). The effects of age-related hearing loss on the brain and cognitive function. *Trends Neurosci.* 43, 810–821. doi: 10.1016/j.tins.2020.07.005

Smith, P. F. (2018). Vestibular functions and Parkinson's disease. *Front. Neurol.* 9:1085. doi: 10.3389/fneur.2018.01085

Smith, P. F. (2021). Hearing loss versus vestibular loss as contributors to cognitive dysfunction. *J. Neurol.*

Someya, S., Tanokura, M., Weindruch, R., Prolla, T. A., and Yamasoba, T. (2010). Effects of caloric restriction on age-related hearing loss in rodents and rhesus monkeys. *Curr. Aging Sci.* 3, 20–25. doi: 10.2174/1874609811003010020

Stevens, J. A., Corso, P. S., Finkelstein, E. A., and Miller, T. R. (2006). The costs of fatal and non-fatal falls among older adults. *Inj. Prev.* 12, 290–295. doi: 10.1136/ip.2005.011015

Stewart, C. E., Holt, A. G., Altschuler, R. A., Cacace, A. T., Hall, C. D., Murnane, O. D., et al. (2020). Effects of noise exposure on the vestibular system: a systematic review. *Front. Neurol.* 11:593919. doi: 10.3389/fneur.2020.593919

Stucky, S. R., Wolf, K. E., and Kuo, T. (2010). The economic effect of age-related hearing loss: national, state, and local estimates, 2002 and 2030. *J. Am. Geriatr. Soc.* 58, 618–619. doi: 10.1111/j.1532-5415.2010.02746.x

Sturnieks, D. L., St George, R., and Lord, S. R. (2008). Balance disorders in the elderly. *Neurophysiol. Clin.* 38, 467–478.

Su, Z., Xiong, H., Liu, Y., Pang, J., Lin, H., Zhang, W., et al. (2020). Transcriptomic analysis highlights cochlear inflammation associated with age-related hearing loss in C57BL/6 mice using next generation sequencing. *PeerJ* 8:e9737. doi: 10.7717/peerj.9737

Sun, D. Q., Ward, B. K., Semenov, Y. R., Carey, J. P., and Della Santina, C. C. (2014). Bilateral vestibular deficiency: quality of life and economic implications. *JAMA Otolaryngol. Head Neck Surg.* 140, 527–534. doi: 10.1001/jamaoto.2014.490

Suzuki, T., Nomoto, Y., Nakagawa, T., Kuwahata, N., Ogawa, H., Suzuki, Y., et al. (2006). Age-dependent degeneration of the stria vascularis in human cochleae. *Laryngoscope* 116, 1846–1850. doi: 10.1097/01.mlg.0000234940.33569.39

Tan, J. L., Tang, J., Lo, S., and Yeak, S. (2016). Investigating the risk factors of vestibular dysfunction and the relationship with presbyacusis in Singapore. *J. Laryngol. Otol.* 130, 816–821. doi: 10.1017/s0022215116008495

Tang, Y., Lopez, I., and Baloh, R. W. (2001). Age-related change of the neuronal number in the human medial vestibular nucleus: a stereological investigation. *J. Vestib. Res.* 11, 357–363.

Tavanai, E., and Mohammadkhani, G. (2017). Role of antioxidants in prevention of age-related hearing loss: a review of literature. *Eur. Arch. Otorhinolaryngol.* 274, 1821–1834. doi: 10.1007/s00405-016-4378-6

Tawfik, K. O., Klepper, K., Saliba, J., and Friedman, R. A. (2020). Advances in understanding of presbycusis. *J. Neurosci. Res.* 98, 1685–1697. doi: 10.1002/jnr.24426

Torban, E., and Goodyer, P. (2009). The kidney and ear: emerging parallel functions. *Annu. Rev. Med.* 60, 339–353. doi: 10.1146/annurev.med.60.052307.120752

Torvik, A., Torp, S., and Lindboe, C. F. (1986). Atrophy of the cerebellar vermis in ageing. A morphometric and histologic study. *J. Neurol. Sci.* 76, 283–294. doi: 10.1016/0022-510x(86)90176-0

Trune, D. R. (2010). Ion homeostasis in the ear: mechanisms, maladies, and management. *Curr. Opin. Otolaryngol. Head Neck Surg.* 18, 413–419. doi: 10.1097/moo.0b013e32833d9597

Unal, M., Tamer, L., Dogruer, Z. N., Yildirim, H., Vayisoglu, Y., and Camdeviren, H. (2005). N-acetyltransferase 2 gene polymorphism and presbycusis. *Laryngoscope* 115, 2238–2241. doi: 10.1097/01.mlg.0000183694.10583.12

Ushakov, K., Koffler-Brill, T., Rom, A., Perl, K., Ulitsky, I., and Avraham, K. B. (2017). Genome-wide identification and expression profiling of long non-coding RNAs in auditory and vestibular systems. *Sci. Rep.* 7:8637.

Valko, M., Leibfritz, D., Moncol, J., Cronin, M. T., Mazur, M., and Telser, J. (2007). Free radicals and antioxidants in normal physiological functions and human disease. *Int. J. Biochem. Cell Biol.* 39, 44–84. doi: 10.1016/j.biocel.2006.07.001

van de Berg, R., Rosengren, S., and Kingma, H. (2018). Laboratory examinations for the vestibular system. *Curr. Opin. Neurol.* 31, 111–116. doi: 10.1097/wco.0000000000000526

van de Berg, R., Van Tilburg, M., and Kingma, H. (2015). Bilateral vestibular hypofunction: challenges in establishing the diagnosis in adults. *ORL J. Otorhinolaryngol. Relat. Spec.* 77, 197–218. doi: 10.1159/000433549

Van Eyken, E., Van Camp, G., Fransen, E., Topsakal, V., Hendrickx, J. J., Demeester, K., et al. (2007). Contribution of the N-acetyltransferase 2 polymorphism NAT2*6A to age-related hearing impairment. *J. Med. Genet.* 44, 570–578. doi: 10.1136/jmg.2007.049205

Velazquez-Villasenor, L., Merchant, S. N., Tsuji, K., Glynn, R. J., Wall, C. III, and Rauch, S. D. (2000). Temporal bone studies of the human peripheral vestibular system. Normative Scarpa's ganglion cell data. *Ann. Otol. Rhinol. Laryngol. Suppl.* 181, 14–19. doi: 10.1177/00034894001090s503

Verschuur, C. A., Dowell, A., Syddall, H. E., Ntani, G., Simmonds, S. J., Baylis, D., et al. (2012). Markers of inflammatory status are associated with hearing threshold in older people: findings from the Hertfordshire ageing study. *Age Ageing* 41, 92–97. doi: 10.1093/ageing/afr140

Verschuur, C., Agyemang-Prempeh, A., and Newman, T. A. (2014). Inflammation is associated with a worsening of presbycusis: evidence from the MRC national study of hearing. *Int. J. Audiol.* 53, 469–475. doi: 10.3109/14992027.2014.891057

Viana, L. M., O'malley, J. T., Burgess, B. J., Jones, D. D., Oliveira, C. A., Santos, F., et al. (2015). Cochlear neuropathy in human presbycusis: confocal analysis of hidden hearing loss in post-mortem tissue. *Hear. Res.* 327, 78–88. doi: 10.1016/j.heares.2015.04.014

Walther, L. E., and Westhofen, M. (2007). Presbyvertigo-aging of otoconia and vestibular sensory cells. *J. Vestib. Res.* 17, 89–92.

Walther, L. E., Wenzel, A., Buder, J., Bloching, M. B., Kniep, R., and Blodow, A. (2014). Detection of human utricular otoconia degeneration in vital specimen and implications for benign paroxysmal positional vertigo. *Eur. Arch. Otorhinolaryngol.* 271, 3133–3138. doi: 10.1007/s00405-013-2784-6

Wan, G., Ji, L., Schrepfer, T., Gong, S., Wang, G. P., and Corfas, G. (2019). Synaptopathy as a mechanism for age-related vestibular dysfunction in mice. *Front. Aging Neurosci.* 11:156. doi: 10.3389/fnagi.2019.00156

Wang, J., and Puel, J. L. (2020). Presbycusis: an update on cochlear mechanisms and therapies. *J. Clin. Med.* 9:218. doi: 10.3390/jcm9010218

Warr, W. B. (1975). Olivocochlear and vestibular efferent neurons of the feline brain stem: their location, morphology and number determined by retrograde axonal transport and acetylcholinesterase histochemistry. *J. Comp. Neurol.* 161, 159–181. doi: 10.1002/cne.901610203

Watson, N., Ding, B., Zhu, X., and Frisina, R. D. (2017). Chronic inflammation – inflammaging - in the ageing cochlea: a novel target for future presbycusis therapy. *Ageing Res. Rev.* 40, 142–148. doi: 10.1016/j.arr.2017.10.002

Wells, H. R. R., Freidin, M. B., Zainul Abidin, F. N., Payton, A., Dawes, P., Munro, K. J., et al. (2019). GWAS identifies 44 independent associated genomic loci for self-reported adult hearing difficulty in UK biobank. *Am. J. Hum. Genet.* 105, 788–802. doi: 10.1016/j.ajhg.2019.09.008

Willott, J. F. (2006). Overview of methods for assessing the mouse auditory system. *Curr. Protoc. Neurosci.* Chapter 8:Unit8.21A.

Wu, J., Ye, J., Kong, W., Zhang, S., and Zheng, Y. (2020). Programmed cell death pathways in hearing loss: a review of apoptosis, autophagy and programmed necrosis. *Cell Prolif.* 53:e12915.

Wu, P. Z., Liberman, L. D., Bennett, K., De Gruttola, V., O'malley, J. T., and Liberman, M. C. (2019). Primary neural degeneration in the human cochlea: evidence for hidden hearing loss in the aging ear. *Neuroscience* 407, 8–20. doi: 10.1016/j.neuroscience.2018.07.053

Wu, P. Z., O'malley, J. T., De Gruttola, V., and Liberman, M. C. (2020). Age-related hearing loss is dominated by damage to inner ear sensory cells, not the cellular battery that powers them. *J. Neurosci.* 40, 6357–6366. doi: 10.1523/jneurosci.0937-20.2020

Yamasoba, T., Lin, F. R., Someya, S., Kashio, A., Sakamoto, T., and Kondo, K. (2013). Current concepts in age-related hearing loss: epidemiology and mechanistic pathways. *Hear. Res.* 303, 30–38. doi: 10.1016/j.heares.2013.01.021

Yang, C. H., Schrepfer, T., and Schacht, J. (2015). Age-related hearing impairment and the triad of acquired hearing loss. *Front. Cell. Neurosci.* 9:276. doi: 10.3389/fncel.2015.00276

Zalewski, C. K. (2015). Aging of the human vestibular system. *Semin. Hear.* 36, 175–196. doi: 10.1055/s-0035-1555120

Zapala, D. A., Olsholt, K. F., and Lundy, L. B. (2008). A comparison of water and air caloric responses and their ability to distinguish between patients with normal and impaired ears. *Ear Hear.* 29, 585–600. doi: 10.1097/aud.0b013e3181734ed0

Zhang, F., Zhang, J., Neng, L., and Shi, X. (2013). Characterization and inflammatory response of perivascular-resident macrophage-like melanocytes in the vestibular system. *J. Assoc. Res. Otolaryngol.* 14, 635–643. doi: 10.1007/s10162-013-0403-2

Zhao, T., Liu, X., Sun, Z., Zhang, J., Zhang, X., Wang, C., et al. (2020). RNA-seq analysis of potential lncRNAs for age-related hearing loss in a mouse model. *Aging* 12, 7491–7510. doi: 10.18632/aging.103103

Zheng, Q. Y., Johnson, K. R., and Erway, L. C. (1999). Assessment of hearing in 80 inbred strains of mice by ABR threshold analyses. *Hear. Res.* 130, 94–107. doi: 10.1016/s0378-5955(99)00003-9

Zorov, D. B., Juhaszova, M., and Sollott, S. J. (2014). Mitochondrial reactive oxygen species (ROS) and ROS-induced ROS release. *Physiol. Rev.* 94, 909–950. doi: 10.1152/physrev.00026.2013

Zuniga, M. G., Dinkes, R. E., Davalos-Bichara, M., Carey, J. P., Schubert, M. C., King, W. M., et al. (2012). Association between hearing loss and saccular dysfunction in older individuals. *Otol. Neurotol.* 33, 1586–1592. 10.1097/mao.0b013e31826bedbc

Conflict of Interest: The authors declare that the research was conducted in the absence of any commercial or financial relationships that could be construed as a potential conflict of interest.

Publisher's Note: All claims expressed in this article are solely those of the authors and do not necessarily represent those of their affiliated organizations, or those of the publisher, the editors and the reviewers. Any product that may be evaluated in this article, or claim that may be made by its manufacturer, is not guaranteed or endorsed by the publisher.

frontiers in Neuroscience

ORIGINAL RESEARCH
published: 08 September 2021
doi: 10.3389/fnins.2021.710076

ATP and ACh Evoked Calcium Transients in the Neonatal Mouse Cochlear and Vestibular Sensory Epithelia

Richard D. Rabbitt[1,2,3] *and Holly A. Holman*[1]*

[1] Department of Biomedical Engineering, University of Utah, Salt Lake City, UT, United States, [2] Graduate Program in Neuroscience, University of Utah, Salt Lake City, UT, United States, [3] Department of Otolaryngology-Head and Neck Surgery, University of Utah, Salt Lake City, UT, United States

Hair cells in the mammalian inner ear sensory epithelia are surrounded by supporting cells which are essential for function of cochlear and vestibular systems. In mice, support cells exhibit spontaneous intracellular Ca^{2+} transients in both auditory and vestibular organs during the first postnatal week before the onset of hearing. We recorded long lasting (>200 ms) Ca^{2+} transients in cochlear and vestibular support cells in neonatal mice using the genetic calcium indicator GCaMP5. Both cochlear and vestibular support cells exhibited spontaneous intracellular Ca^{2+} transients (GCaMP5 $\Delta F/F$), in some cases propagating as waves from the apical (endolymph facing) to the basolateral surface with a speed of ~25 μm per second, consistent with inositol trisphosphate dependent calcium induced calcium release (CICR). Acetylcholine evoked Ca^{2+} transients were observed in both inner border cells in the cochlea and vestibular support cells, with a larger change in GCaMP5 fluorescence in the vestibular support cells. Adenosine triphosphate evoked robust Ca^{2+} transients predominantly in the cochlear support cells that included Hensen's cells, Deiters' cells, inner hair cells, inner phalangeal cells and inner border cells. A Ca^{2+} event initiated in one inner border cells propagated in some instances longitudinally to neighboring inner border cells with an intercellular speed of ~2 μm per second, and decayed after propagating along ~3 cells. Similar intercellular propagation was not observed in the radial direction from inner border cell to inner sulcus cells, and was not observed between adjacent vestibular support cells.

Keywords: development, supporting cell, hair cell, purinergic, cholinergic, sensory cell

OPEN ACCESS

Edited by:
Gwenaelle S. G. Geleoc, Boston Children's Hospital and Harvard Medical School, United States

Reviewed by:
Paul Albert Fuchs, Johns Hopkins University, United States
Alan Martin Brichta, The University of Newcastle, Australia

***Correspondence:**
Holly A. Holman
holly.holman@utah.edu

Specialty section:
This article was submitted to Perception Science, a section of the journal Frontiers in Neuroscience

Received: *15 May 2021*
Accepted: *18 August 2021*
Published: *08 September 2021*

Citation:
Rabbitt RD and Holman HA (2021) ATP and ACh Evoked Calcium Transients in the Neonatal Mouse Cochlear and Vestibular Sensory Epithelia. Front. Neurosci. 15:710076. doi: 10.3389/fnins.2021.710076

INTRODUCTION

Functional hearing and balance rely on mature sensory hair cells and precise organization of support cell networks. These sensory hair cells and non-sensory supporting cells coordinate signaling that starts in development and continues throughout adulthood. The release of calcium (Ca^{2+}) from internal stores is critical for maturation and activity. Ca^{2+} transients appear to occur

spontaneously at rest and can also be evoked by the activation of purinergic and cholinergic receptor binding in different cell populations throughout development. ACh and/or ATP can trigger inositol triphosphate (IP_3) dependent calcium induced calcium release (CICR) in inner ear non-sensory support cells. Previous studies have shown in the cochlea that binding of extracellular ATP to G-protein coupled P2Y2 and P2Y4 receptors, expressed on the endolymphatic surface of the developing sensory epithelium, activates phospholipase-C dependent generation of IP_3 (Gale et al., 2004; Beltramello et al., 2005; Piazza et al., 2007; Ceriani et al., 2019). Additionally, muscarinic ACh receptors in the vestibular epithelium triggers IP_3 dependent CICR in specific vestibular hair cells (Holman et al., 2019, 2020). In some cases, gap junctions between adjacent support cells can lead to relatively slow propagation of intercellular Ca^{2+} waves. In addition, the probability of connexin hemichannel opening is a function of cytosolic free Ca^{2+} peaking at ∼500 nM (De Vuyst et al., 2006) which facilitates the propagation of regenerative and coordinated intercellular Ca^{2+} waves, with peak amplitude of ∼500 nM, sustained by ATP-induced ATP-release (Gale et al., 2004; Beltramello et al., 2005; Mammano et al., 2007; Piazza et al., 2007; Anselmi et al., 2008; Majumder et al., 2010).

In mouse non-sensory cells of the lesser epithelial ridge (LER), purinergic Ca^{2+} transients from intracellular Ca^{2+} wave propagation is sustained by extracellular ATP (Anselmi et al., 2008). In non-sensory cells of the greater epithelial ridge (GER), ATP evokes Ca^{2+} transients with rhythmic bursts (Hinojosa, 1977; Kamiya et al., 2001; for a list of abbreviations see **Table 1**). The frequency of spontaneous Ca^{2+} transients is reduced by purinergic antagonists. The propagation of intracellular Ca^{2+} waves in the LER and the frequency of spontaneous Ca^{2+} transients in the GER increase with decreasing the extracellular Ca^{2+} concentration (Tritsch et al., 2007; Anselmi et al., 2008; Tritsch et al., 2010), which increases the open probability of connexin hemichannels (Müller et al., 2002; Gómez-Hernández et al., 2003; Sáez et al., 2005; González et al., 2007). Intracellular Ca^{2+} modulation has been suggested to play an important role in regulation of differentiation, cell fate and circuit formation in the cochlea, crista and macula. The present report is focused on comparing and contrasting relatively slow Ca^{2+} transients in the mouse cochlear and vestibular sensory epithelium during the first postnatal week.

In the present study the genetic calcium indicator GCaMP5G was used to record Ca^{2+} transients in non-sensory and sensory cells in the organ of Corti, crista ampullaris and utricular macula. We observed spontaneous and evoked Ca^{2+} transients in semi-intact organs during the first postnatal week. The GCaMP5G indicator is suitable for events lasting > 200 ms including G protein dependent CICR but is not capable of tracking fast Ca^{2+} events. We report diverse Ca^{2+} transients evoked by cholinergic and purinergic puff application in non-sensory Hensen's and Deiters' cells in the LER and inner border cells (IBCs) and inner phalangeal cells (IPhCs) in the GER. Sensory inner hair cell (IHCs) also responded to ACh and ATP with Ca^{2+} transients during the first week. ATP and ACh evoked Ca^{2+} bursts in Hensen's cells were similar in range to the ΔF/F rates observed in the eminentia cruciata supporting cells, clino2 and clinocytes and the clino2 cells are a population of progenitor-like cells first identified by immunomorphological characteristics and location in the eminentia cruciata of anterior and posterior canals (Holman et al., 2020). This study demonstrates the robust signaling these and other supporting cells have in the vestibular epithelia along with unique Ca^{2+} transients in multiple supporting cell populations in the cochlear epithelia of the same animal throughout different stages of postnatal development in the mouse.

TABLE 1 | List of abbreviations and/or acronyms.

Term cell type	Definition
CSC	Cochlear support cell
VSC	Vestibular support cell
IBC	Inner border cell
HC	Hensen's cell
DC	Deiters' cell
ISC	Inner sulcus cell
IPhC	Inner phalangeal cell
IHC	Inner hair cell
OHC	Outer hair cell
LER	Lesser epithelial ridge
GER	Greater epithelial ridge
Clino2 (C2)	Clino2 cell
CT	Clinocyte
VSC-Type A	Vestibular support cell type A
VSC-Type B	Vestibular support cell type B
Physiology	
Ca^{2+}	Calcium
CICR	Calcium induced calcium release
GCaMP5	Genetically encoded calcium indicator 5
ACh	Acetylcholine
ATP	Adenosine triphosphate
IP_3	Inositol trisphosphate
ABR	Auditory brainstem response
DPOAE	Distortion product otoacoustic emissions
Calcium imaging	
ΔF/F	Change in fluorescence divided by baseline fluorescence
AU	Arbitrary unit
ROI	Region of interest
Gene/Protein	
Gad2/GAD2	Glutamate decarboxylase

*Statistical significance of differences in GCaMP5G ΔF/F means reported in **Figure 5**.*

MATERIALS AND METHODS

Bioethics Statement

Experiments were conducted in accordance with the NIH Guide for the Care and Use of Laboratory Animals and the National Research Council (US) Committee. All mouse procedures were in accordance with animal welfare protocols

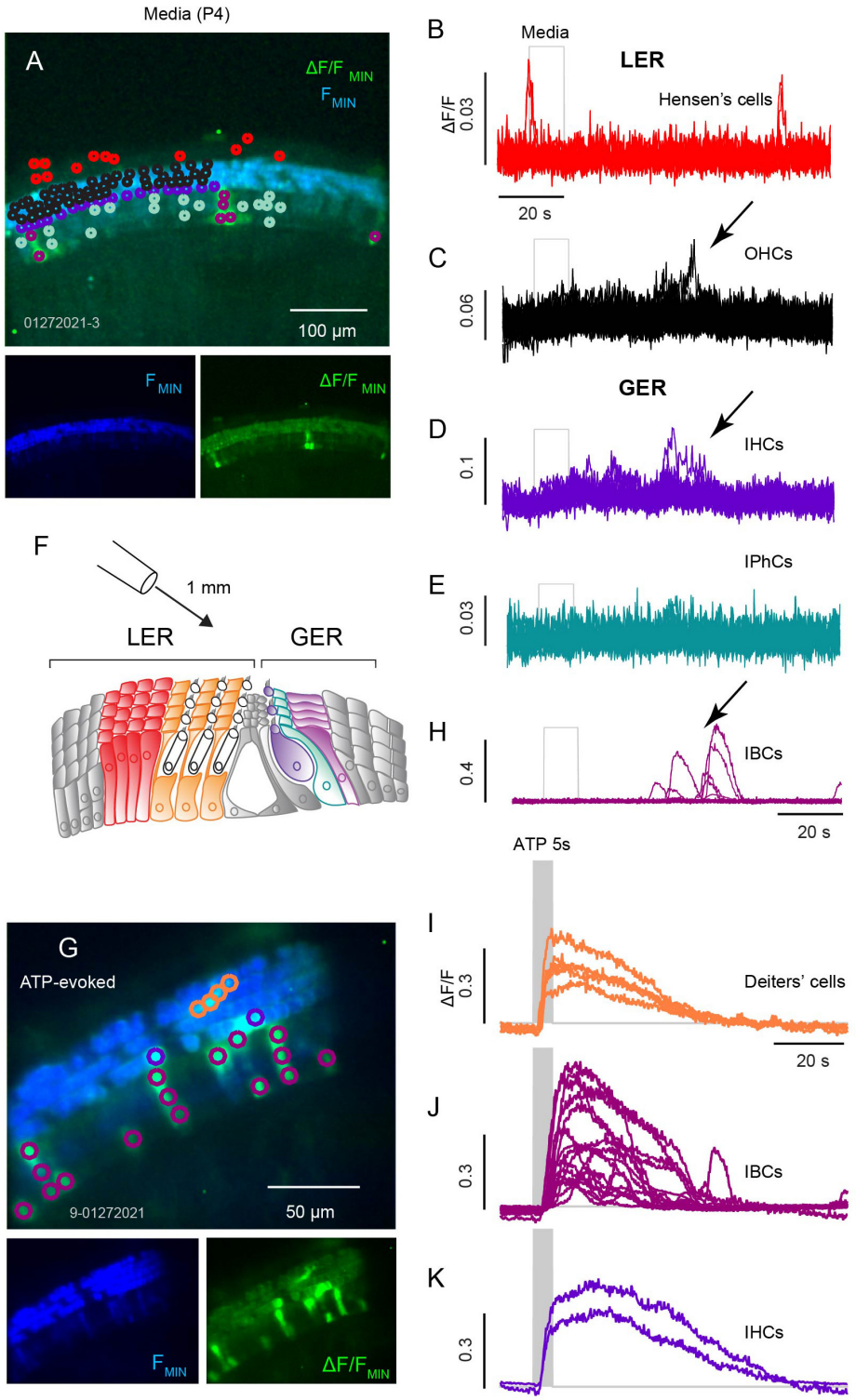

FIGURE 1 | Spontaneous and ATP evoked Ca^{2+} transients across sensory and non-sensory cells in the organ of Corti. **(A)** Confocal image of spontaneous Ca^{2+} transients in an apical turn with baseline GCaMP5G fluorescence (blue) overlaid with $\Delta F/F_{MIN}$ (green) with Ca^{2+} transients during a 100 s recording. Traces from ROIs overlying Hensen's cells **(B)**, OHCs **(C)**, IHCs **(D)**, IPhCs **(E)**, and IBCs **(F)**. **(G)** Illustration of a cochlear section with Hensen's cells (red) and Deiters' cells (orange) of the lesser epithelial ridge (LER), IHCs (purple), IPhCs (cyan), and IBCs (fuchsia) in the greater epithelial ridge (GER). (H) Image with a 40x obj. following a 10 s ATP (100 μM) puff positioned ~1 mm from the semi-intact cochlea. Ca^{2+} transients in Deiters' cells, IHCs, and IBCs. **(H,I)** Traces from ROIs overlying Deiters' cells with ATP evoked Ca^{2+} transient **(I)**; traces from ROIs overlying IBCs **(J)**; and traces from ROIs overlying IHCs **(K)** (see **Supplementary Video 1**).

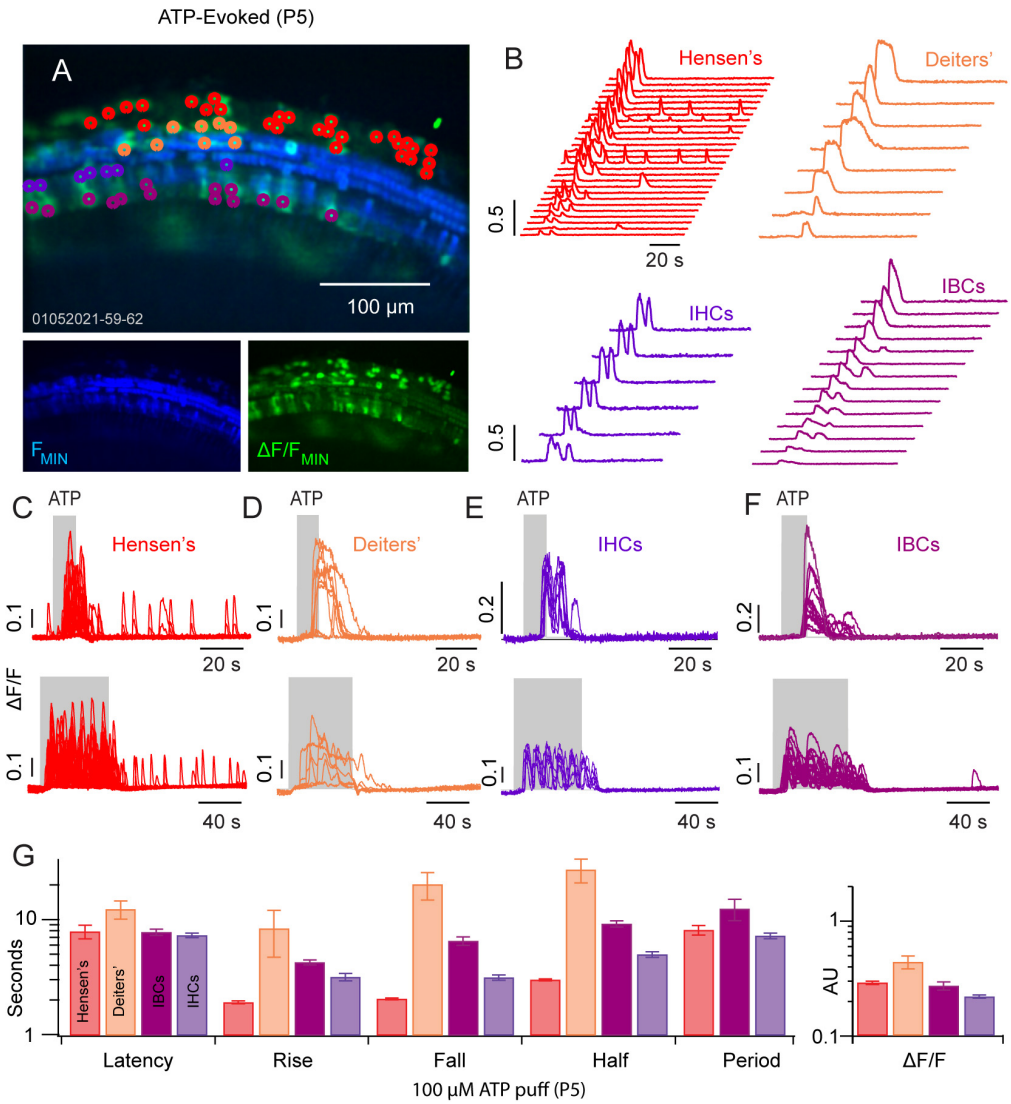

FIGURE 2 | ATP evoked Ca^{2+} transients propagate across the GER and LER. **(A)** Image of ATP evoked Ca^{2+} transients in a P5 cochlea mid-turn region. **(B)** Waterfall plots with traces from ROIs overlying Hensen's cells (red), Deiters' cells (orange), IHCs (purple) and IBCs (fuchsia). **(C–F)** Illustrate the timing of evoked transients for a 10 s (top panels) and for 50 s ATP (100 µM) puff application. **(G)** Statistics showing latency to first evoked transient, rise time, fall time, half width, period, and peak ΔF/F in each cell type (see **Supplementary Video 2**).

approved by the University of Utah's Institutional Animal Care and Use Committee.

Genotyping of Transgenic Mice

Transgenic mice expressing GCaMP5G on the C57BL/6 background strain were utilized for calcium imaging [$Polr2a^{Tn(pb-CAG-GCaMP5g,-tdTomato)Tvrd}$; Stock No: 024477] and crossed with mice homozygous for Gad2-Cre [$Gad2^{tm2(cre)Zjh/J}$; Stock No: 010802; this strain is also known as PC-G5-tdT]. Gad2-Cre drives expression in hair cells and supporting cells, thereby allowing simultaneous observation of calcium transients in multiple cell types. Homozygous transgenic mice obtained from The Jackson Laboratory were crossed to generate $Gad2^{+/GCaMP5G}$ heterozygous first-generation transgenic mice used in this study. Gad2-Cre; PC-G5-tdT mice were genotyped by standard RT-PCR using primers specific to GCaMP5G and Cre (Transnetyx). Seven Gad2-Cre; PC-G5-tdT mice aged P1-P6 provided physiology data. Male Gad2-Cre; PC-G5-tdT mice aged P44 (n = 5) and P94 (n = 5) provided auditory brain stem response (ABR) and distortion product otoacoustic emissions (DPOAE) data.

Auditory Brainstem Responses

ABRs were conducted on Gad2-Cre; PC-G5-tdT heterozygous mice F_1 generation from two age groups to test auditory function. In brief, mice were anesthetized by intraperitoneal injection with ketamine (100 mg/kg body weight) and xylazine (10 mg/kg). For adults and older mice, a small incision was

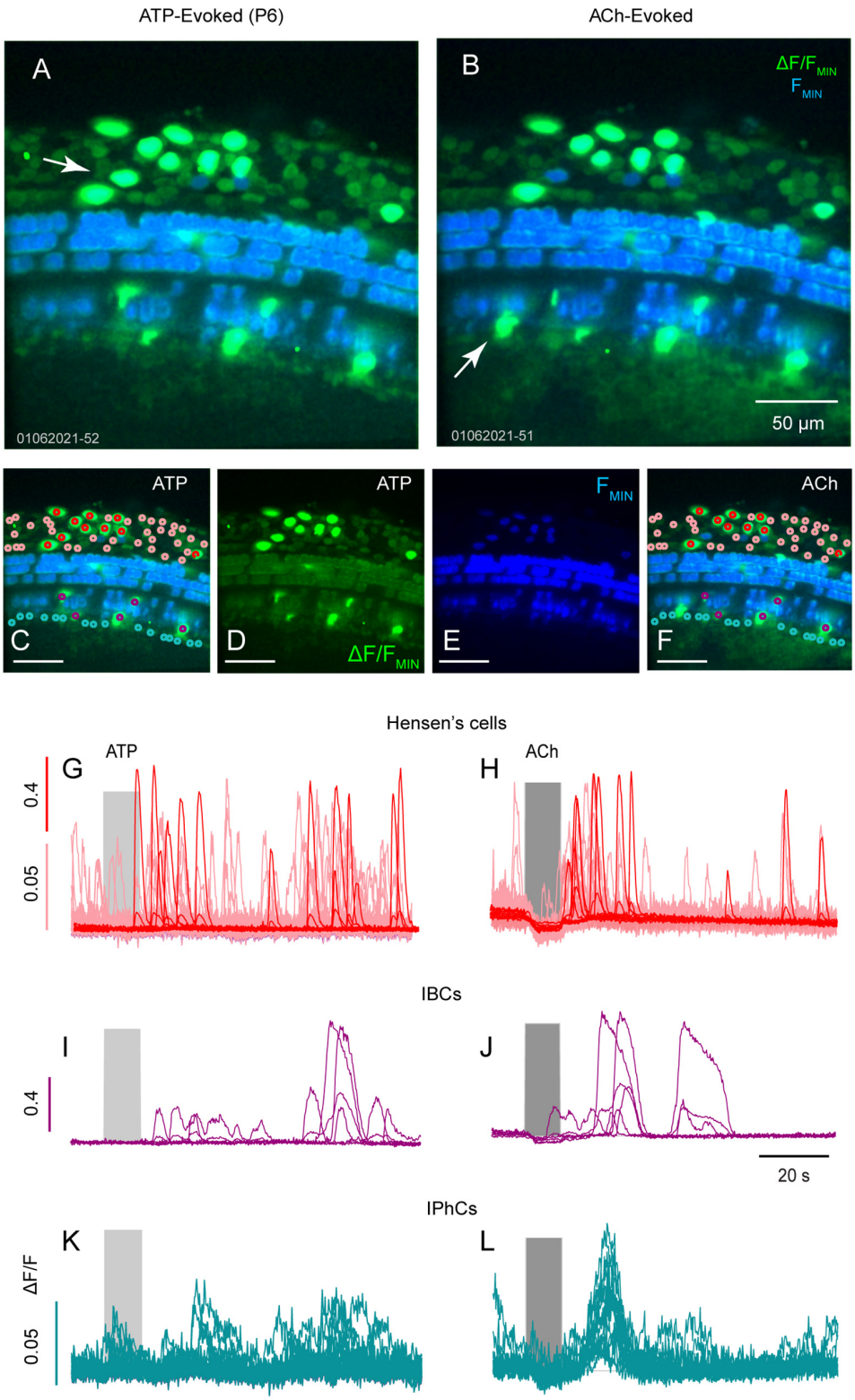

FIGURE 3 | ATP and ACh evoked Ca^{2+} transients in Hensens's cells, IBCs and IPhCs. Confocal images of ATP **(A,C,D)** and ACh **(B,E,F)** with baseline GCaMP5G fluorescence (blue) overlaid with $\Delta F/F_{MIN}$ (green) from a mid-turn cochlea age P6. Maximum $\Delta F/F_{MIN}$ evoked by ATP and ACh in ROIs overlying Hensen's cells (**G,H**; red and pink), overlying IBCs (**I,J**; cyan) and overlying IPhCs (**K,L**; fuchsia).

made at the tragus to allow direct access to the ear canal. Body temperature was maintained at ∼37°C via a heating lamp. ABR and DPOAE recordings were made in a double-walled sound chamber (IAC, Bronx, NY). Evoked potentials were measured by placing needle electrodes over the pinna and vertex in a vertex/mastoid configuration. A ground electrode was inserted subcutaneously near the tail. ABR thresholds were obtained to tone pips at 8, 12, 16, 22, 32, 4 kHz. Stimuli were presented over a 15–90 dB SPL range of intensity in 5 or 10 dB steps. ABR signals were amplified (TDT RA4), filtered 100 Hz to 3 Hz, and averaged (1024 sweeps; TDT RA16BA controlled by BioSigRP software; Tucker-Davis Technology). Threshold responses were determined by visual inspection of ABR waveforms. The cochlea was considered to be non-responsive if no signal was recorded at 90 dB SPL. Auditory phenotypes in two age groups young (P44; ∼1 month) and adult (P94; ∼3 months) male Gad2-Cre; PC-G5-tdT transgenic mice were tested.

Distortion Product Otoacoustic Emissions

Otoacoustic emission (OAEs) were measured using a microphone coupled with two speakers (ER-10B+ and 2xEC1 Etymotic Research, Elk Grove, IL). Stimuli of two primary tones, f_1 and f_2, with $f_2/f_1 = 1.2$ and f_2 level 10 dB $< f_1$ level were recorded. Primary tones were stepped from 30 to 80 dB SPL (for f_1) in 10 dB increments and swept in octave steps at 8, 22, 32 kHz. The ear canal acoustic emissions were amplified and digitized. Signals at f_1, f_2, $2f_1$–f_2, were determined by FFT after spectral averaging from 50 waveform traces, each corresponding to 84 ms of digitized ear canal sound pressure waveform. Statistical analysis of ABR and DPOAE data was performed, and data are shown in standard error of the mean ± SEM.

Tissue Preparation

Semi-intact vestibular preparations or apical and mid-turn sections of the cochlea from Gad2-Cre; PC-G5-tdT mice of either sex were studied from acutely dissected bony labyrinths in 4°C extracellular buffer [EB (mM): 5.8 KCl, 155 NaCl, 0.9 $MgCl_2$, 1.3 $CaCl_2$, 0.7 $NaHPO_4$, 5,6 glucose, 10 HEPES, 1 Na pyruvate, pH 7.4; osmolality ∼308 mmol kg^{-1}] (Holman et al., 2019). Dissected tissue from postnatal days 4–7 (P4-P7; day of birth is P0) were transferred to a recording chamber and immobilized with a nylon harp (Warner Instrument, RC-22C), and continuously perfused with EB at room temperature (21–23°C). Live cell calcium imaging was recorded up to a maximum 4 h post dissection.

Calcium Imaging

Swept field confocal microscopy (Bruker, United States) was used for live cell calcium recordings. Fluorescent confocal images were formed using water immersion objective 40X/N.A.0.8 or 20X/0.5W (Olympus, Tokyo, Japan) controlled by Prairie View (Bruker). Confocal images were collected using a 35 μm slit aperture in linear galvanometer mode, and a 512 × 512 detector (Photometrics, RoleraMGi Plus EMCCD) with in-plane single pixel size for the 40 × objective of 0.27 × 0.27 μm. For GCaMP5G fluorescence excitation was limited to a 488 nm diode laser and the detection filter was a band pass filter (525/50–25, Semrock/IDEX Health and Science, LLC, Rochester, NY).

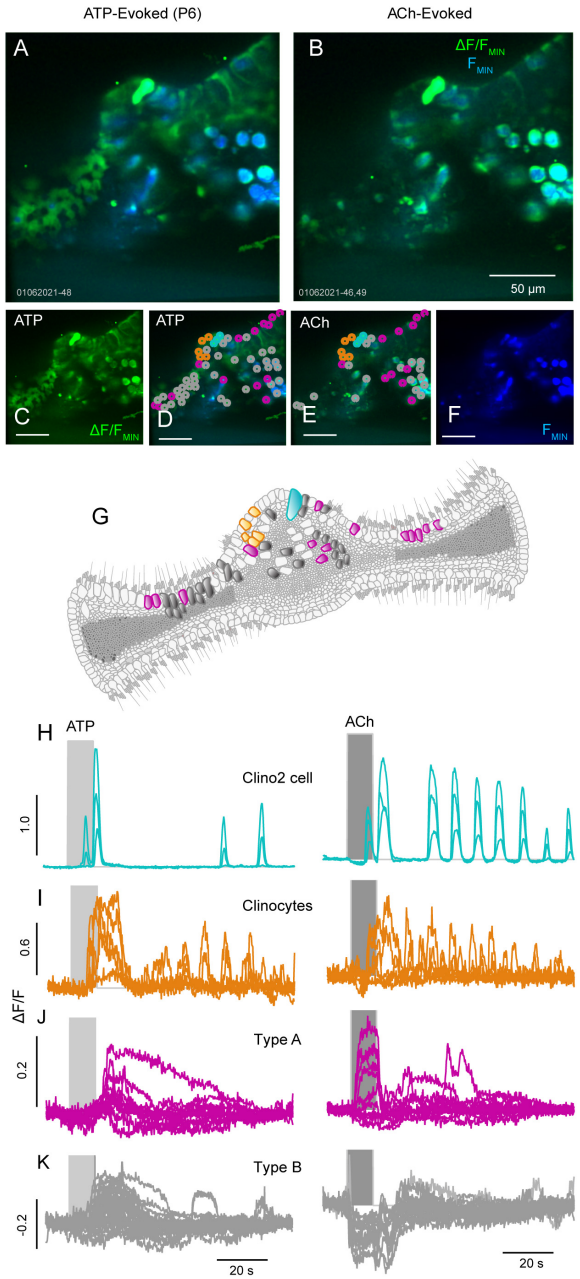

FIGURE 4 | ATP and ACh evoked Ca^{2+} transients in the crista. Confocal images of an anterior canal crista with baseline GCaMP5G fluorescence (blue) overlaid with $\Delta F/F_{MIN}$ (green) transients evoked by 100 μM ATP **(A,C,D)** or ACh **(B,E,F)** in a P6 mouse. **(G)** Illustration of the anterior canal crista mapping the color-coded supporting and sensory hair cells (not drawn to scale). The clino2 cell (**H**; teal) and clinocytes (**I**; orange) respond to ATP and ACh with evoked Ca^{2+} transients. Two other cell groups denoted type A (fuchsia) and type B (grey) also respond to ATP and ACh with evoked Ca^{2+} transients **(J,K)** but with distinctly different time courses (see **Supplementary Videos 3, 4**).

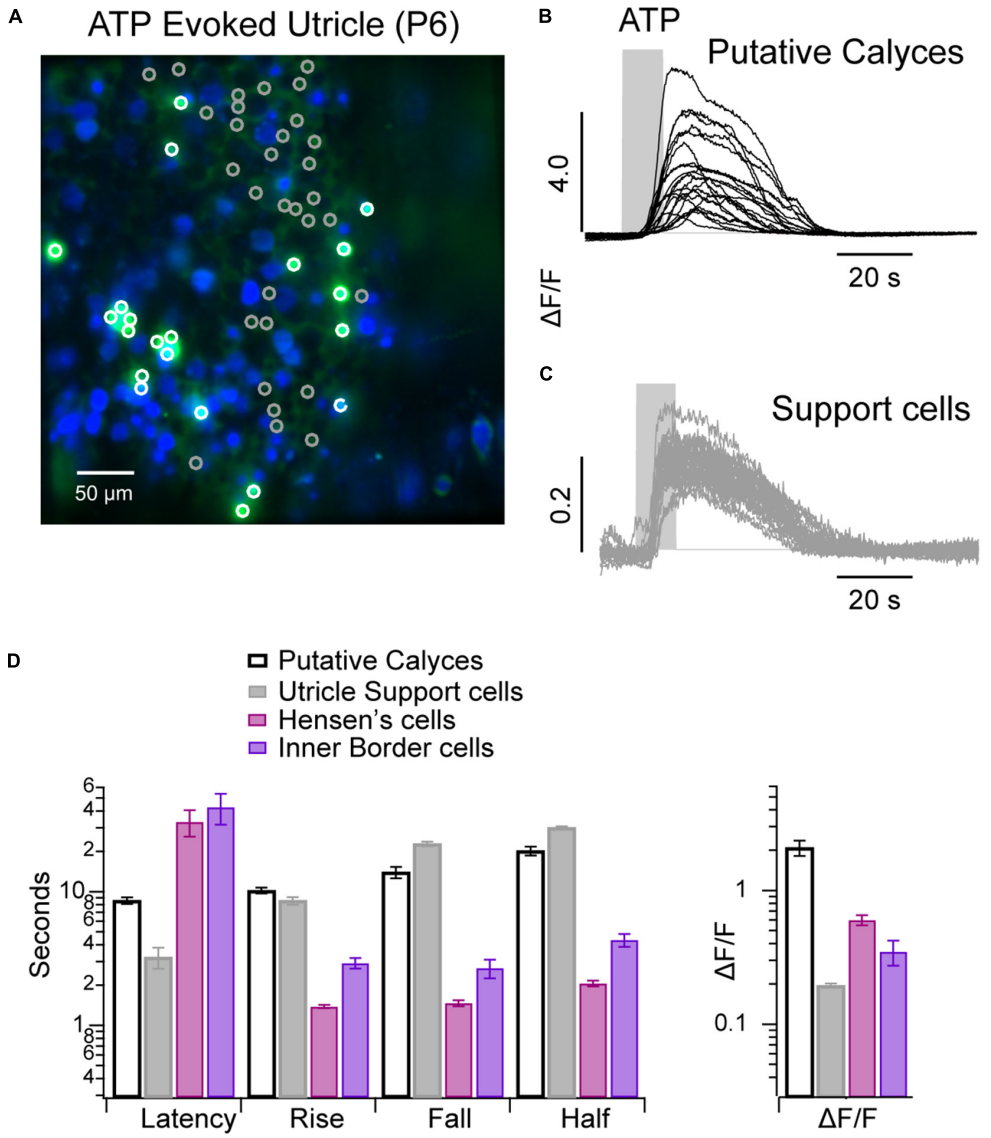

FIGURE 5 | ATP evoked Ca^{2+} transients in the utricular macula. **(A)** Confocal image of a P6 utricular maculae with ATP evoked Ca^{2+} transients $\Delta F/F_{MIN}$ (green) overlaid with baseline GCaMP5G fluorescence (green). **(B)** Ca^{2+} transients in calyces (white ROIs/black traces). **(C)** Ca^{2+} transients in support cells (gray ROIs/traces). **(D)** Bar chart summarizing ATP evoked Ca^{2+} transients in non-sensory cells from cochlea and utricle of same P6 mouse (see **Supplementary Video 5**).

For each record, 1,000–2,000 GCaMP5G fluorescence images were captured at 5 frames-s^{-1}. In a subset of recordings, ACh or ATP were applied 10 s into the record for a duration of 0.1–5 s using a pressure driven micro-manifold with a ∼100 µm tip located ∼1 mm from the tissue (ALA Scientific, QMM). Concentration in the manifold was 100 µM leading to < 100 µM (∼50 µM) at the location of the tissue. Each xy image was smoothed in space with a 3 pixel Gaussian filter (WaveMetrics, Igor). To minimize motion artifact, images were registered in space (Holman et al., 2019) over time using manually selected regions of interest. GCaMP5G fluorescence modulation was determined pixel-by-pixel using $\Delta F/F_{MIN}$, (or, $\Delta F/F$) where $\Delta F = F(t) - F_{MIN}$ and F_{MIN} was the minimum fluorescence intensity in the pixel over the entire time sequence of images. GCaMP5G has a K_D of 0.41 µM and a decay time of $t_{1/2}$ 154 ms (Sun et al., 2013).

ΔF/F Transients and Statistical Analysis

Unless otherwise noted, ΔF/F was determined as a function of time within 10 µm diameter regions of interest (ROI) identified with specific cells. Multiple ROIs were analyzed for each image sequence as indicated in individual figures. ΔF/F curves reported in the figures show the peak $f(t) = max(\Delta F/F)$ within each ROI as functions of time "t" (or frame number). The onset time of a Ca^{2+} transient relative to the stimulus was determined by the time when $f(t)$ emerged above the average noise in the ROI.

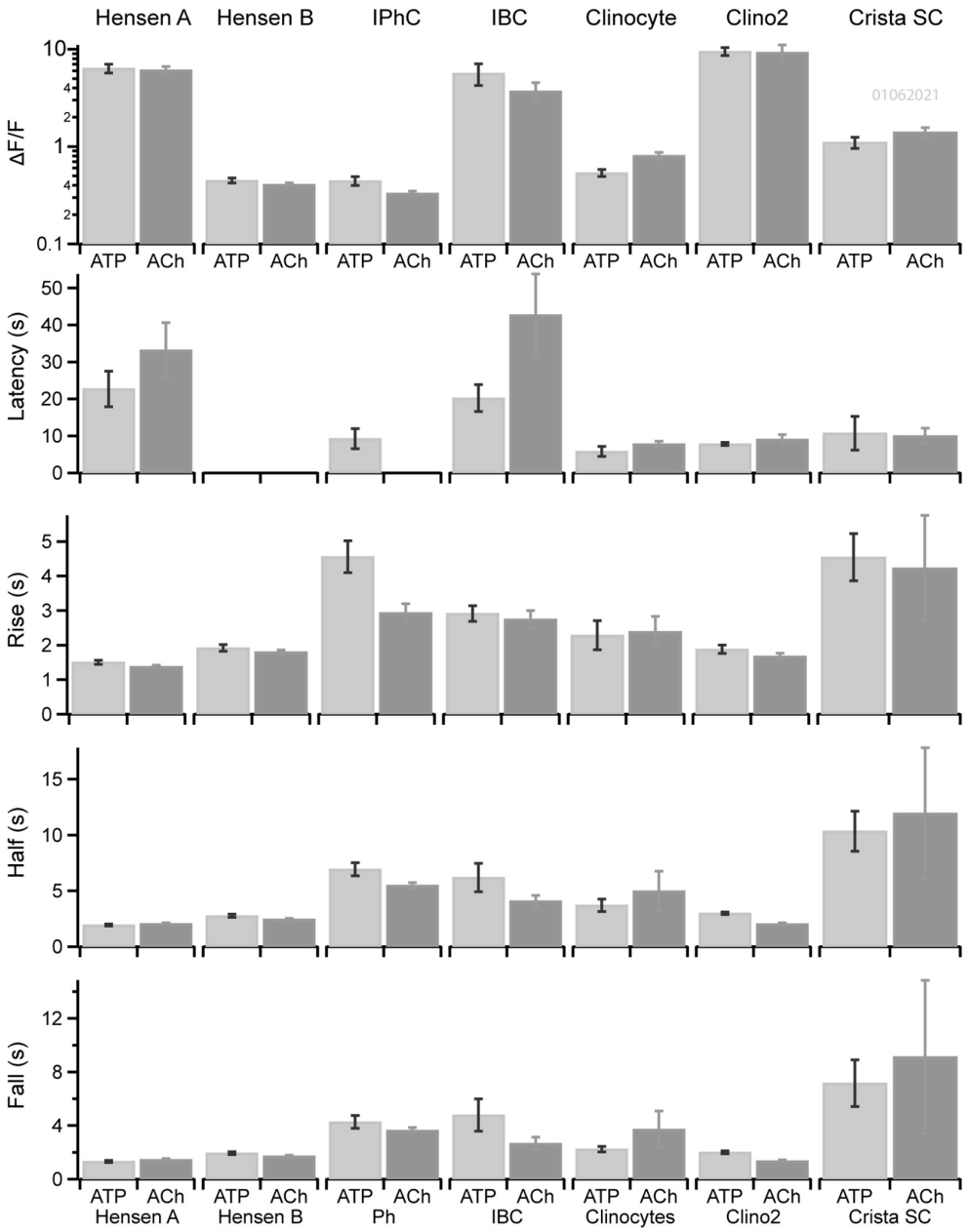

FIGURE 6 | Kinetics of Ca^{2+} transients in non-sensory cells in cochlea and crista. Kinetics of ATP (dark gray) or ACh (light gray) evoked Ca^{2+} transients in ROIs overlying Hensen's cells (type A), Hensen's cells (type B), IPhCs, clinocytes, the clino2 cell, and crista supporting cells across multiple cells of the same type in a P6 mouse. Bars show the mean and standard error of peak ΔF/F, latency to the first evoked transient relative to the stimulus onset, rise time of the transient, width at half peak amplitude and fall time.

Each transient was analyzed to find the onset time, peak ΔF/F, rise time, half width and fall time. For evoked transients, the latency was defined as the onset time of the first transient minus the onset time of the stimulus. If multiple repetitive transients occurred in a single ROI the average time between onsets was determined and reported as the period (or rate = 1/period). Mean values were determined for each statistic (peak, rise, half, fall, rate), grouped by cell type (e.g., Hensen's, Deiters'…). Error bars denote ± SEM (standard error of the mean). Transients in different cell types were compared pairwise using Student's *t*-test. *i*-values (P) where < 0.05 was the criterion for statistical significance. The experiments were not blinded during the experiment or analysis.

Data Availability

Data generated and analyzed for this study are included in this publication. Datasets generated during the study are available from the corresponding author upon request.

TABLE 2 | ΔF/F: "Y" indicates difference was significant with $P < 0.5$.

			A	B	C	D	E	F	G	H	I	J	K	L	M	N
Crista support cell	ACh	A		Y	Y	Y	Y		Y		Y	Y		Y		Y
Clino2 cell	ACh	B	Y		Y											
Clinocyte	ACh	C	Y	Y												
Inner border cell (IBC)	ACh	D	Y				Y		Y		Y	Y		Y		Y
Inner phalangeal cell (IPhC)	ACh	E	Y			Y					Y	Y		Y		
Hensen's cell A	ACh	F							Y	Y	Y	Y		Y		Y
Hensen's cell B	ACh	G	Y			Y		Y			Y	Y		Y		
Crista support cell	ATP	H						Y			Y	Y		Y		Y
Clino2 cell	ATP	I	Y			Y	Y	Y	Y	Y						
Clinocyte	ATP	J	Y			Y	Y	Y	Y	Y						
Inner border cell (IBC)	ATP	K												Y		Y
Inner phalangeal cell (IPhC)	ATP	L	Y			Y	Y	Y	Y	Y			Y			
Hensen's cell A	ATP	M														Y
Hensen's cell B	ATP	N	Y			Y		Y		Y			Y		Y	

TABLE 3 | Latency: "Y" indicates difference was significant with $P < 0.5$.

			A	B	C	D	E	F	G	H	I	J	K	L	M	N
Crista support cell	ACh	A					Y		Y			Y		Y	Y	Y
Clino2 cell	ACh	B														
Clinocyte	ACh	C														
IBC	ACh	D					Y	Y	Y	Y		Y	Y	Y	Y	Y
IPhC	ACh	E	Y			Y										
Hensen's cell A	ACh	F				Y										
Hensen's cell B	ACh	G	Y			Y										
Crista support cell	ATP	H				Y						Y		Y	Y	Y
Clino2 cell	ATP	I														
Clinocyte	ATP	J	Y			Y				Y						
IBC	ATP	K				Y								Y	Y	
IPhC	ATP	L	Y			Y				Y			Y			
Hensen's cell A	ATP	M	Y			Y				Y			Y			
Hensen's cell B	ATP	N	Y			Y				Y						

TABLE 4 | Rise time: "Y" indicates difference was significant with $P < 0.5$.

			A	B	C	D	E	F	G	H	I	J	K	L	M	N
Crista support cell	ACh	A														
Clino2 cell	ACh	B								Y						
Clinocyte	ACh	C						Y		Y	Y				Y	
IBC	ACh	D						Y		Y	Y				Y	
IPhC	ACh	E								Y						
Hensen's cell A	ACh	F			Y	Y										
Hensen's cell B	ACh	G								Y	Y				Y	
Crista support cell	ATP	H		Y	Y	Y	Y		Y							
Clino2 cell	ATP	I			Y	Y			Y							
Clinocyte	ATP	J											Y	Y	Y	
IBC	ATP	K										Y			Y	
IPhC	ATP	L										Y				
Hensen's cell A	ATP	M			Y	Y			Y			Y	Y			
Hensen's cell B	ATP	N														

TABLE 5 | Half width: "Y" indicates difference was significant with $P < 0.5$.

			A	B	C	D	E	F	G	H	I	J	K	L	M	N
Crista support cell	ACh	A														
Clino2 cell	ACh	B								Y						
Clinocyte	ACh	C				Y		Y		Y	Y			Y	Y	
IBC	ACh	D			Y			Y		Y	Y				Y	
IPhC	ACh	E						Y		Y	Y				Y	
Hensen's cell A	ACh	F			Y	Y	Y									
Hensen's cell B	ACh	G								Y	Y			Y	Y	
Crista support cell	ATP	H		Y	Y	Y	Y		Y							
Clino2 cell	ATP	I			Y	Y	Y		Y							
Clinocyte	ATP	J												Y	Y	
IBC	ATP	K												Y	Y	
IPhC	ATP	L			Y				Y			Y	Y			
Hensen's cell A	ATP	M			Y	Y	Y		Y			Y	Y			
Hensen's cell B	ATP	N														

RESULTS

Spontaneous and ATP Evoked Ca^{2+} Transients in Cochlear GER and LER Cells

During development Ca^{2+} activity in the sensory epithelia of the cochlea, semicircular canals and otolith organs facilitate mapping in the central nervous system laying the foundation for auditory and vestibular function. To measure this activity, we recorded Ca^{2+} transients in ROIs overlying cells of the GER and lower epithelial ridge (LER) from *ex vivo* cochlear preparations of apical and mid turn sections. Spontaneous $\Delta F/F$ transients for ROIs outlined in **Figures 1A–H** for tissue from a P4 mouse. Colors in **Figures 1A–H** denote ROIs overlying specific cell types in the LER and GER (**Figure 1B**, Hensen's: red, $n = 12$; **Figure 1C**, OHCs: black, $n = 46$; **Figure 1D**, IHCs: purple, $n = 20$; **Figure 1**, IPhCs: cyan, $n = 17$; **Figure 1F**, IBCs: magenta, $n = 7$). IBC ROIs (**Figure 1F**) exhibited the most intense spontaneous transients with $\Delta F/F > 0.5$ and duration often lasting longer than 10 s, while IPhCs did not exhibit detectable transients above the noise in this P4 mouse. To note, small transients in ROIs overlying IHCs and OHCs corresponded in time with large spontaneous transients in IBCs (arrows: **Figures 1C,D,F**), suggesting these events are causally related. It is difficult to completely isolate a single cell using a 20x water immersion objective, and it is likely that small signals in ROIs overlying IHCs (**Figure 1D**) and OHCs (**Figure 1C**) was fluorescence from adjacent Deiters' cells or IBCs (note temporal correspondence in **Figures 1C,D,F**: arrows). Consistent with this interpretation, large Ca^{2+} transients can be evoked in IHCs and in Deiters' cells at this age, but not in OHCs. In a subset of records, Ca^{2+} transients in IBCs appeared sequentially in adjacent cells with an apparent intercellular propagation speed of approximately 2 $\mu m\text{-}s^{-1}$ and subsiding after a distance of 1–3 cells. Hensen's cells also exhibit spontaneous Ca^{2+} activity but occurring at times uncoordinated with transients in other support cells. In this same P4 tissue, 100 μM ATP evoked large Ca^{2+} transients in IHCs, IBCs and Deiters' cells. Transients were synchronized to the onset of the ATP puff as shown in **Figures 1G–K**. IBCs responded to ATP with the highest $\Delta F/F$ intensity, with Ca^{2+} transients initiating at the apical end of the cells, propagating with an intracellular speed of ~ 25 $\mu m\text{-}s^{-1}$ (also see Supp. Video 1), consistent with typical speed of intracellular CICR waves in other cell types.

ATP Evoked Ca^{2+} Transients in the Developing Cochlea

We next examined ATP evoked Ca^{2+} transients in a P5 mouse following two different ATP exposures: 10 and 50 s puff of ATP (100 μM). Hensen's cells (**Figures 2A–C**: red ROIs and traces, $n = 32$) responded to a 10 s ATP puff with a short burst of 2–4 Ca^{2+} transients (**Figures 2A,B**; $n = 32$ cells). Prolonged exposure to ATP (50 s) gave an increased number of Ca^{2+} transients within each burst (**Figure 2C**). Smaller Ca^{2+} transient activity remained in Hensen's cells following the ATP puff with reduced $\Delta F/F$ (~ 0.1 AU). ATP evoked Ca^{2+} transients in Deiters' cells (**Figures 2A,B,D**: orange, $n = 8$) appeared as a single pulse during the ATP exposure without a clearly discernable bursting. IHCs (**Figures 2A,B,E**: purple, $n = 6$) and IBCs (**Figures 2A,B,F**: magenta, $n = 14$) also responded to ATP with a burst of Ca^{2+} transients (**Figures 2C–F**; see **Supplementary Video 1**). The onset latency, rise time, fall time, half width, burst period, and $\Delta F/F$ magnitude are shown in **Figure 2G**. Onset latencies were similar in all 4 cell types, but the stereotypical shape and rate of ATP evoked transients differed between cell types. Together, these results suggest that non-sensory and sensory cells spanning the LER and GER have a coordinated Ca^{2+} response to ATP at P5 prior to the maturation of hearing.

ATP vs. ACh Evoked Ca^{2+} Transients in the Developing Cochlea

We examined Hensen's cells, IPhCs and IBCs for Ca^{2+} transients evoked by ATP and ACh in a P6 mouse (**Figures 3A–C**). At

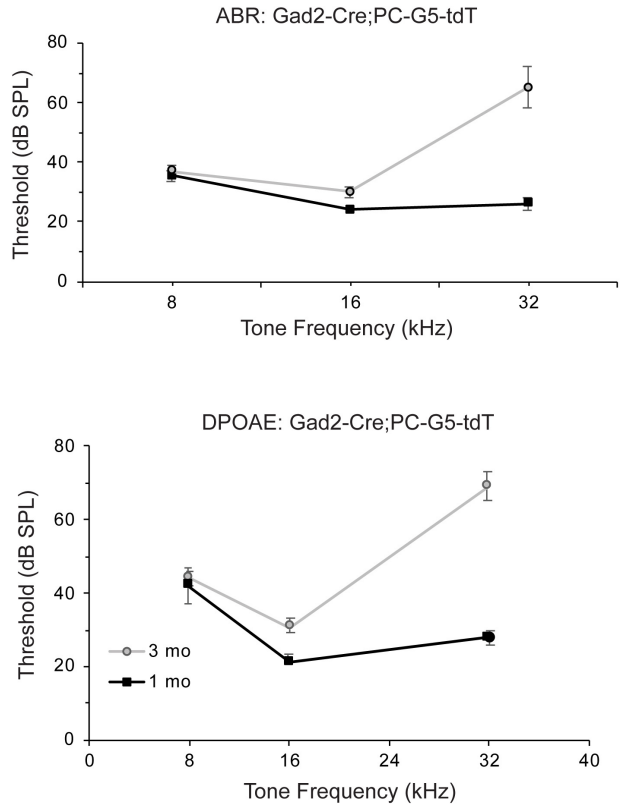

FIGURE 7 | Auditory function of Gad2-Cre; PC-G5-tdT transgenic mice declines in young adults. Auditory function auditory brain stem (ABR) and distortion product otoacoustic emissions (DPOAEs) of Gad2-Cre; PC-G5-tdT were tested for two age groups [young (1 month; n = 5 mice) and adult (3 months; n = 5 mice)]. Young mice have normal thresholds for ABR and DPOAE tests. Adult mice have elevated amplitudes for ABR and DPOAE. Error bars represent mean ± SEM.

P6, Hensen's cells (**Figures 3A–H**: red and pink), responded with Ca^{2+} bursts following 100 μM ATP (**Figure 3G**) and ACh (**Figure 3H**). Ca^{2+} transients in Hensen's cells fell into two response groups at P6; cells with large ΔF/F∼1 (**Figures 3G,H**: red) and cells with small ΔF/F∼0.1 (**Figures 3G,H**: pink). Small Ca^{2+} transients (pink) were not evoked in Hensen's cells by ATP or ACh, while large transients (red) were evoked by either compound (**Figures 3H,J,L**: The baseline depression during ACh application is motion artifact). Evoked Ca^{2+} transients in IBCs (**Figures 3A–F,I,J**: cyan) were similar in shape for ATP (**Figure 3I**) and ACh (**Figure 3J**) but the latency was increased in response to ATP relative to ACh. The delayed ATP Ca^{2+} transients in non-sensory cells reported by others suggest this may involve ATP- and inositol 1,4,5-triphiosphate (IP3) cytosolic free Ca^{2+} oscillations (Ceriani et al., 2019). In IPhCs, ATP did not evoke Ca^{2+} transients above the small spontaneous events, while ACh evoked larger highly synchronized transients (also see **Supplementary Video 2**). The present report does not examine the origin of differences between ATP vs. ACh evoked responses in these cells.

ATP and ACh Evoke Ca^{2+} Transients in Supporting Cells of the Crista Ampullaris

Previous studies from our lab have shown supporting cells in the non-sensory region of the crista have spontaneous and acetylcholine (ACh) evoked Ca^{2+} transients during early development (Holman et al., 2019, 2020). Here, we extend those studies to examine purinergic and cholinergic Ca^{2+} signaling in support cells during postnatal day 6 (**Figures 4A–G**, also see **Supplementary Videos 3, 4**). In the anterior and posterior semicircular canals, supporting cells in the peripheral zone of the crista and recently identified supporting cells, clino2 and clinocytes (Holman et al., 2020), in the eminentia cruciata (EC) have distinct ATP and ACh evoked Ca^{2+} transients (**Figure 4**). In clino2 (**Figures 4D,E,G,H**: cyan), 100 μM ATP (**Figure 4H**, left) and ACh (**Figure 4H**, right) both evoke bursts of Ca^{2+} transients. A single one clino2 cell is present in **Figure 4**, with multiple traces showing different ROIs within a single cell (**Figure 4H**). Evoked Ca^{2+} transients in the clino2 cell start at the apex facing endolymph and propagate down the cell as a wave consistent with previous studies (Holman et al., 2020). While the rise time for Ca^{2+} transients in the clino2 cell are similar when evoked by 100 μM ATP vs. ACh, the number of Ca^{2+} events in clino2 were larger following ACh for the 100 μM dose. Clinocytes also respond to both ATP and ACh with bursts of Ca^{2+} transients. However, the temporal envelope differed between the two compounds with markedly different Ca^{2+} transients in the clino2 cell and clinocytes. Although the present report did not examine the specific receptors involved, it has been shown previously that ACh responses in clino2 and clinocytes are muscarinic and sensitive to compounds blocking IP_3-dependent CICR (Holman et al., 2020).

It is difficult to precisely identify specific cell types in the sensory region of the crista from GCaMP5G images, therefore other cell types were divided into two groups (**Figures 2J,K**) based on Ca^{2+} responses to ACh (Excite: A, Other: B). Both type A (magenta) and type B (gray) cells responded to ATP with small excitatory Ca^{2+} transients following a 10 s puff application (**Figures 2J,K**), but responses during the puff itself differed between cells. The most notable difference was the short latency ΔF/F during the ACh pulse. Cell type A responded to ACh with a positive ΔF/F during the pulse that returned to zero immediately upon wash, at the maximum speed of the GCaMP5G indicator. Responses to ACh (**Figure 4J**) are consistent with activation of a nicotinic receptor, but the present study did not distinguish receptors or cell types. Similar responses were not observed in cochlear cells examined in the present study.

Purinergic Signaling in Support Cells in the Utricular Macula

Spontaneous and ACh evoked Ca^{2+} transients in utricular hair cells and supporting cells have been reported previously during the first postnatal week, but ATP evoked transients were not observed (Holman et al., 2019, 2020). Here, we report the presence of long-lasting Ca^{2+} transients evoked

by 100 μM ATP (**Figure 5**). A subset of cells responded to ATP with intense ($\Delta F/F > 5$ AU) long lasting (>20 s) Ca^{2+} transients (**Figure 5A**: white ROIs, **Figure 5B**: black traces; **Figure 5D**), while the remaining cells responded over a similar time course with much smaller Ca^{2+} transients ($\Delta F/F < 0.4$). The difference in $\Delta F/F$ identifies these as two different cell types. Background fluorescence and morphology implies cells with large $\Delta F/F$ transients are likely to be calyces (labeled "putative calyces," **Figure 4B**). A subset of utricular hair cells in this transgenic mouse line express high levels of calcium bound GCaMP5, which generate continuous background fluorescence (**Figure 5A**, blue). Based on morphology, these hair cells are type I (Holman et al., 2020). Cells with large ATP-evoked $\Delta F/F$ transients always enveloped a highly expressing cell with type I morphology, suggesting they are likely to be calyces. This feature is most easily seen in the video where the large $\Delta F/F$ transients (green) develop around and envelope another cell of smaller diameter (blue) (see **Supplementary Video 5**). Gray ROIs (**Figure 5A**) all exhibited small ATP-evoked $\Delta F/F$ transients with nearly identical latencies and duration. Based on their spatial pattern and between hair cells these cells are most likely support cells, and are labeled as such in **Figure 5C**. The onset latencies were significantly shorter in utricular vs. cochlear supporting cells (**Figure 5D**), while the kinetics were significantly slower in utricular supporting cells in a P6 mouse.

Kinetics of ACh vs. ATP Evoked Ca^{2+} Transients in Non-sensory Cells in the Organ of Corti and the Anterior Canal Crista

The kinetics of ATP and ACh evoked GCaMP5G $\Delta F/F$ transients differed between support cell types in the cochlea and vestibular sensory epithelium (e.g., **Figures 1–5**). A direct comparison between Ca^{2+} transients in supporting cell types in the organ of Corti and the crista is provided in **Figure 6** for tissue in a single ear during one experimental session. Statistics shown are: Peak $\Delta F/F$ magnitude, latency of the first evoked transient relative to the onset of the stimulus, rise time from the onset to the peak, half-width at half amplitude, and fall time from the peak to baseline. Results are shown for Hensen's cells with $\Delta F/F > 1$, Hensen's cells with $\Delta F/F < 1$, IPhCs, IBCs, clinocytes, clino2, and unnamed crista support cells. Significance of pairwise differences in means are provided in **Tables 2–5** with "Y" indicating $p < 0.05$ (Fall time statistical significance is the same as half width). The two non-sensory cells with similarly large $\Delta F/F$ are Hensen's cells and IBCs in the organ of Corti, and clino2 in the eminentia cruciatum. Although differences in peak $\Delta F/F$ exceeded an order of magnitude between cell types, differences between peak $\Delta F/F$ evoked by ATP vs. ACh within a cell type were small. There were, however, significant differences in onset latency and rise time between ACh and ATP in numerous cell types. These data suggest both stimuli are likely to trigger the same IP3 dependent CICR but, *via* unique receptor signaling pathways.

Gad2-Cre; PC-G5-tdT: Auditory Brainstem Response and Distortion Product Otoacoustic Emissions

ABRs and DPOAEs were recorded in young and adult Gad2-Cre; PC-G5-tdT mice to show this hearing is unaffected by transgenic breeding. Auditory phenotypes were tested in two age groups; 1 and 3 months old male mice were tested at 8, 16, and 32 kHz. The ABR and DPOAE testing for 1 months old transgenic mice were within normal ranges (**Figure 7**). Threshold shifts for transgenic mice 3 months old were observed at 16 kHz and more pronounced at 32 kHz. These increases in thresholds are consistent with age relating hearing loss in the parental strains (C57BLKS/J, 129/SvEMS, C57BL/6J; Zheng et al., 1999).

DISCUSSION

Calcium transients in non-sensory and sensory cells play an essential role in the maturation of auditory and vestibular organs (Wang et al., 2015; Babola et al., 2018, 2020; Eckrich et al., 2018; Holman et al., 2020). In this study, we used acute cochlear vestibular explants from GCaMP5G expressing transgenic mice to record spontaneous, purinergic and cholinergic Ca^{2+} transients across sensory and non-sensory cells in the postnatal developing cochlea, semicircular crista and utricle. GCaMP5G is a relatively slow indicator most suitable for monitoring CICR and other changes in intracellular Ca^{2+} concentration lasting longer than 200 ms. This extends previous studies utilizing the Gad2 loci with a tdTomato-GCaMP5G reporter knock-in generating the Gad2-Cre; PC-G5-tdT transgenic mouse (Holman et al., 2019, 2020). Implications of a role for Gad2 in the sensory epithelia are not known at present and were not examined herein. However, the reproducible dual reporter expression from the Gad2 loci throughout sensory epithelia, especially in hair cells and support cells during development, provided a robust system to examine spontaneous and evoked Ca^{2+} transients throughout inner ear organs in a single animal.

In the neonatal mouse cochlea, ATP evoked Ca^{2+} transients in Hensen's cells Deiters' cells, IBCs, IPhCs, and IHCs were observed by postnatal day 4. Hensen's cells responded with bursts of evoked Ca^{2+} transients following a puff application of ATP on postnatal days 5 and 6. Similar to other cells, we hypothesize that exogenous application of ATP activated purinergic receptors and triggered IP_3 receptor–dependent CICR in non-sensory cells including Hensen's and Deiters' cells of the LER and IPhCs and IBCs of the GER. In vestibular organs in the same mice, ATP evoked Ca^{2+} transients primarily in supporting cells located in eminentia cruciatum (clinocytes, clino2) and two additional cell types labeled herein type A and B. The most intense $\Delta F/F$ Ca^{2+} transients observed in this study evoked by ATP occurred in the P6 utricle. These cells are most likely calyces, based on their morphology enveloping cells with type I hair cell shape. In the crista, clino2 cells responded with the highest intensity, and in the cochlea Hensen's cells and IBCs responded with the highest intensity.

Purinergic and Cholinergic Signaling in Neonatal Auditory and Vestibular Epithelia

In the mouse, spontaneous release of ATP occurs during cochlear development and ceases upon the maturation of hearing (Sugasawa et al., 1996; Lagostena and Mammano, 2001; Tritsch et al., 2007). Purinoceptors signaling regulates auditory neurotransmission (Housley et al., 1999; Järlebark et al., 2000; Lee and Marcus, 2008; Ito and Dulon, 2010), and contributes to tonotopy during development. ATP is likely released from IBCs through connexin hemichannels, thus modulating IHC activity (Zhao et al., 2005; Majumder et al., 2010; Tritsch et al., 2010; Dayaratne et al., 2014), while ACh released from olivocochlear efferent synaptic contacts might inhibit IHC activity (Glowatzki and Fuchs, 2000; Vetter et al., 2007; Maison et al., 2010; Johnson et al., 2011, 2013). An interplay between IHCs and IBCs is consistent with release of ATP by IBCs driving IHCs to release glutamate and excite spiral ganglion neurons during development (Zhao et al., 2005; Anselmi et al., 2008). Present results demonstrate large intracellular Ca^{2+} transients in response to ACh, revealing a potential mechanism to close the loop between spontaneous centripetal inputs to the CNS and cholinergic centrifugal feedback to the cochlea during development of tonotopy. Ca^{2+} transients in IBCs propagated between adjacent cells at a speed of approximately 2 $\mu m\text{-}s^{-1}$, with the $\Delta F/F$ amplitude decreasing in the adjacent cell and decaying to zero after $\sim$3 cells. Results are consistent with intercellular communication *via* connexin gap junctions (Zhao et al., 2005; Anselmi et al., 2008; Zhu and Zhao, 2012; Dayaratne et al., 2014). In contrast to the cochlea, modest intercellular propagation of Ca^{2+} transients between adjacent VSCs indicate a similar developmental role might not be present in vestibular organs during the first postnatal week but it remains possible that a similar process takes place embryonically. Nevertheless, results suggest that supporting cell connexins might have a weaker role in vestibular epithelia relative to the cochlea during neonatal development. The fact that some connexin mutations cause severe hearing loss without vestibular impairment further supports this notion.

There are several limitations of the study worthy of note. First, results are comparative and observational in nature. Although previous work has established IP_3 dependent CICR, as well as several cholinergic and purinergic receptors in the inner ear, the present study did not examine the molecular underpinnings of differences in Ca^{2+} transients or waves. Another limitation is the small sample size at each age, which prevents examination of precise timing of developmental changes occurring during the first postnatal week. Another consideration is the GCaMP5G transgenic line, which is derived from a parental strain (C57BL/6J) known to have age related hearing loss. A potential strength is the large number of cells and cell types with GCaMP5G examined within individual animals.

DATA AVAILABILITY STATEMENT

The raw data supporting the conclusions of this article will be made available by the authors, without undue reservation.

ETHICS STATEMENT

The animal study was reviewed and approved by the University of Utah's Institutional Animal Care and Use Committee.

AUTHOR CONTRIBUTIONS

HH and RR designed the study, conducted the experiments, analyzed the data, made the figures, and edited the manuscript. HH drafted the manuscript. Both authors contributed to the article and approved the submitted version.

FUNDING

This work was supported by a grant to RR from the NIH: R01DC006685.

ACKNOWLEDGMENTS

We thank our colleague Albert Park and Yong Wang for assistance with ABR and DPOAE testing and Micah Frerck for the swept field confocal microscope build. We also thank the animal husbandry for their oversight.

SUPPLEMENTARY MATERIAL

The Supplementary Material for this article can be found online at: https://www.frontiersin.org/articles/10.3389/fnins.2021.710076/full#supplementary-material

REFERENCES

Anselmi, F., Hernandez, V. H., Crispino, G., Seydel, A., Ortolano, S., Roper, S. D., et al. (2008). ATP release through connexin hemichannels and gap junction transfer of second messengers propagate Ca2+ signals across the inner ear. *Proc. Natl. Acad. Sci. U.S.A.* 105, 18770–18775. doi: 10.1073/pnas.0800793105

Babola, T. A., Kersbergen, C. J., Wang, H. C., and Bergles, D. E. (2020). Purinergic signaling in cochlear supporting cells reduces hair cell excitability by increasing the extracellular space. *Elife* 9:e52160. doi: 10.7554/eLife.52160

Babola, T. A., Li, S., Gribizis, A., Lee, B. J., Issa, J. B., Wang, H. C., et al. (2018). Homeostatic control of spontaneous activity in the developing auditory system. *Neuron* 9, 511.e–524.e. doi: 10.1016/j.neuron.2018.07.004

Beltramello, M., Piazza, V., Bukauskas, F. F., Pozzan, T., and Mammano, F. (2005). Impaired permeability to Ins(1,4,5)P3 in a mutant connexin underlies recessive hereditary deafness. *Nat. Cell Biol.* 7, 63–69. doi: 10.1038/ncb1205

Ceriani, F., Hendry, A., Jeng, J., Johnson, S. L., Stephani, F., Olt, J., et al. (2019). Coordinated calcium signaling in cochlear sensory and non-sensory cells refines afferent innervation of outer hair cells. *EMBO J.* 38:e99389.

Dayaratne, M. W., Vlajkovic, S. M., Lipski, J., and Thorne, P. R. (2014). Kölliker's organ and the development of spontaneous activity in the auditory system: implications for hearing dysfunction. *Biomed. Res. Int.* 2014:367939. doi: 10.1155/2014/367939

De Vuyst, E., Decrock, E., Cabooter, L., Dubyak, G. R., Naus, C. C., Evans, W. H., et al. (2006). Intracellular calcium changes trigger connexin 32 hemichannel opening. *EMBO J.* 25, 34–44. doi: 10.1038/sj.emboj.7600908

Eckrich, T., Blum, K., Milenkovic, I., and Engel, J. (2018). Fast Ca^{2+} transients of inner hair cells arise coupled and uncoupled to Ca^{2+} waves of inner supporting cells in the developing mouse cochlea. *Front. Mol. Neurosci.* 30:264. doi: 10.3389/fnmol.2018.00264

Gale, J. E., Piazza, V., Ciubotaru, C. D., and Mammano, F. (2004). A mechanism for sensing noise damage in the inner ear. *Curr. Biol.* 1, 526–529. doi: 10.1016/j.cub.2004.03.002

Glowatzki, E., and Fuchs, P. A. (2000). Cholinergic synaptic inhibition of inner hair cells in the neonatal mammalian cochlea. *Science* 288, 2366–2368. doi: 10.1126/science.288.5475.2366

Gómez-Hernández, J. M., de Miguel, M., Larrosa, B., González, D., and Barrio, L. C. (2003). Molecular basis of calcium regulation in connexin-32 hemichannels. *Proc. Natl. Acad. Sci. U.S.A.* 100, 16030–16035. doi: 10.1073/pnas.2530348100

González, D., Gómez-Hernández, J. M., and Barrio, L. C. (2007). Molecular basis of voltage dependence of connexin channels: an integrative appraisal. *Prog. Biophys. Mol. Biol.* 94, 66–106. doi: 10.1016/j.pbiomolbio.2007.03.007

Hinojosa, R. (1977). A note on development of Corti's organ. *Acta Otolaryngol.* 84, 238–251. doi: 10.3109/00016487709123963

Holman, H. A., Poppi, L. A., Frerck, M., and Rabbitt, R. D. (2019). Spontaneous and acetylcholine evoked calcium transients in the developing mouse utricle. *Front. Cell. Neurosci.* 7:186. doi: 10.3389/fncel.2019.00186

Holman, H. A., Wan, Y., and Rabbitt, R. D. (2020). Developmental GAD2 expression reveals progenitor-like cells with calcium waves in mammalian crista ampullaris. *iScience* 23:101407. doi: 10.1016/j.isci.2020.101407

Housley, G. D., Kanjhan, R., Raybould, N. P., Greenwood, D., Salih, S. G., Järlebark, L., et al. (1999). Expression of the P2X(2) receptor subunit of the ATP-gated ion channel in the cochlea: implications for sound transduction and auditory neurotransmission. *J. Neurosci.* 19, 8377–8388. doi: 10.1523/JNEUROSCI.19-19-08377.1999

Ito, K., and Dulon, D. (2010). Purinergic signaling in cochleovestibular hair cells and afferent neurons. *Purinergic Signal.* 6, 201–209. doi: 10.1007/s11302-010-9183-x

Järlebark, L. E., Housley, G. D., and Thorne, P. R. (2000). Immunohistochemical localization of adenosine 5′-triphosphate-gated ion channel P2X(2) receptor subunits in adult and developing rat cochlea. *J. Comp. Neurol.* 421, 289–301. doi: 10.1002/(sici)1096-9861(20000605)421:3<289::aid-cne1<3.0.co;2-0

Johnson, S. L., Beurg, M., Marcotti, W., and Fettiplace, R. (2011). Prestin-driven cochlear amplification is not limited by the outer hair cell membrane time constant. *Neuron* 70, 1143–1154. doi: 10.1016/j.neuron.2011.04.024

Johnson, S. L., Wedemeyer, C., Vetter, D. E., Adachi, R., Holley, M. C., Elgoyhen, A. B., et al. (2013). Cholinergic efferent synaptic transmission regulates the maturation of auditory hair cell ribbon synapses. *Open Biol.* 3:130163. doi: 10.1098/rsob.130163

Kamiya, K., Takahashi, K., Kitamura, K., Momoi, T., and Yoshikawa, Y. (2001). Mitosis and apoptosis in postnatal auditory system of the C3H/He strain. *Brain Res.* 901, 296–302. doi: 10.1016/s0006-8993(01)02300-9

Lagostena, L., and Mammano, F. (2001). Intracellular calcium dynamics and membrane conductance changes evoked by Deiters' cell purinoceptor activation in the organ of Corti. *Cell Calcium* 29, 191–198. doi: 10.1054/ceca.2000.0183

Lee, J. H., and Marcus, D. C. (2008). Purinergic signaling in the inner ear. *Hear. Res.* 235, 1–7. doi: 10.1016/j.heares.2007.09.006

Maison, S. F., Liu, X. P., Vetter, D. E., Eatock, R. A., Nathanson, N. M., Wess, J., et al. (2010). Muscarinic signaling in the cochlea: presynaptic and postsynaptic effects on efferent feedback and afferent excitability. *J. Neurosci.* 3, 6751–6762. doi: 10.1523/JNEUROSCI.5080-09.2010

Majumder, P., Crispino, G., Rodriguez, L., Ciubotaru, C. D., Anselmi, F., Piazza, V., et al. (2010). ATP-mediated cell-cell signaling in the organ of Corti: the role of connexin channels. *Purinergic Signal.* 6, 167–187. doi: 10.1007/s11302-010-9192-9

Mammano, F., Bortolozzi, M., Ortolano, S., and Anselmi, F. (2007). Ca2+ signaling in the inner ear. *Physiology (Bethesda)* 2, 131–144. doi: 10.1152/physiol.00040.2006

Müller, D. J., Hand, G. M., Engel, A., and Sosinsky, G. E. (2002). Conformational changes in surface structures of isolated connexin 26 gap junctions. *EMBO J.* 2, 3598–3607. doi: 10.1093/emboj/cdf365

Piazza, V., Ciubotaru, C. D., Gale, J. E., and Mammano, F. (2007). Purinergic signalling and intercellular Ca2+ wave propagation in the organ of Corti. *Cell Calcium* 41, 77–86. doi: 10.1016/j.ceca.2006.05.005

Sáez, J. C., Retamal, M. A., Basilio, D., Bukauskas, F. F., and Bennett, M. V. (2005). Connexin-based gap junction hemichannels: gating mechanisms. *Biochim. Biophys. Acta* 1711, 215–224. doi: 10.1016/j.bbamem.2005.01.014

Sugasawa, M., Erostegui, C., Blanchet, C., and Dulon, D. (1996). ATP activates non-selective cation channels and calcium release in inner hair cells of the guinea-pig cochlea. *J. Physiol.* 49, 707–718. doi: 10.1113/jphysiol.1996.sp021251

Sun, X. R., Badura, A., Pacheco, D. A., Lynch, L. A., Schneider, E. R., Taylor, M. P., et al. (2013). Fast GCaMPs for improved tracking of neuronal activity. *Nat. Commun.* 4:2170. doi: 10.1038/ncomms3170

Tritsch, N. X., Rodríguez-Contreras, A., Crins, T. T., Wang, H. C., Borst, J. G., and Bergles, D. E. (2010). Calcium action potentials in hair cells pattern auditory neuron activity before hearing onset. *Nat. Neurosci.* 13, 1050–1052. doi: 10.1038/nn.2604

Tritsch, N. X., Yi, E., Gale, J. E., Glowatzki, E., and Bergles, D. E. (2007). The origin of spontaneous activity in the developing auditory system. *Nature* 450, 50–55. doi: 10.1038/nature06233

Vetter, D. E., Katz, E., Maison, S. F., Taranda, J., Turcan, S., Ballestero, J., et al. (2007). The alpha10 nicotinic acetylcholine receptor subunit is required for normal synaptic function and integrity of the olivocochlear system. *Proc. Natl. Acad. Sci. U.S.A.* 10, 20594–20599. doi: 10.1073/pnas.0708545105

Wang, Q., Zhu, G. H., Xie, D. H., Wu, W. J., and Hu, P. (2015). Taurine enhances excitability of mouse cochlear neural stem cells by selectively promoting differentiation of glutamatergic neurons over GABAergic neurons. *Neurochem. Res.* 40, 924–931. doi: 10.1007/s11064-015-1546-9

Zhao, H. B., Yu, N., and Fleming, C. R. (2005). Gap junctional hemichannel-mediated ATP release and hearing controls in the inner ear. *Proc. Natl. Acad. Sci. U.S.A.* 102, 18724–18729. doi: 10.1073/pnas.0506481102

Zheng, Q. Y., Johnson, K. R., and Erway, L. C. (1999). Assessment of hearing in 80 inbred strains of mice by ABR threshold analyses. *Hear. Res.* 130, 94–107. doi: 10.1016/s0378-5955(99)00003-9

Zhu, Y., and Zhao, H. B. (2012). ATP activates P2X receptors to mediate gap junctional coupling in the cochlea. *Biochem. Biophys. Res. Commun.* 426, 528–532. doi: 10.1016/j.bbrc.2012.08.119

Conflict of Interest: The authors declare that the research was conducted in the absence of any commercial or financial relationships that could be construed as a potential conflict of interest.

Publisher's Note: All claims expressed in this article are solely those of the authors and do not necessarily represent those of their affiliated organizations, or those of the publisher, the editors and the reviewers. Any product that may be evaluated in this article, or claim that may be made by its manufacturer, is not guaranteed or endorsed by the publisher.

frontiers in Neuroscience

ORIGINAL RESEARCH
published: 09 September 2021
doi: 10.3389/fnins.2021.710321

Dopaminergic Inhibition of Na^+ Currents in Vestibular Inner Ear Afferents

Frances L. Meredith[1] *and Katherine J. Rennie*[1,2]*

[1] Department of Otolaryngology – Head & Neck Surgery, School of Medicine, University of Colorado, Aurora, CO, United States, [2] Department of Physiology & Biophysics, School of Medicine, University of Colorado, Aurora, CO, United States

Inner ear hair cells form synapses with afferent terminals and afferent neurons carry signals as action potentials to the central nervous system. Efferent neurons have their origins in the brainstem and some make synaptic contact with afferent dendrites beneath hair cells. Several neurotransmitters have been identified that may be released from efferent terminals to modulate afferent activity. Dopamine is a candidate efferent neurotransmitter in both the vestibular and auditory systems. Within the cochlea, activation of dopamine receptors may reduce excitotoxicity at the inner hair cell synapse via a direct effect of dopamine on afferent terminals. Here we investigated the effect of dopamine on sodium currents in acutely dissociated vestibular afferent calyces to determine if dopaminergic signaling could also modulate vestibular responses. Calyx terminals were isolated along with their accompanying type I hair cells from the cristae of gerbils (P15-33) and whole cell patch clamp recordings performed. Large transient sodium currents were present in all isolated calyces; compared to data from crista slices, resurgent Na^+ currents were rare. Perfusion of dopamine (100 μM) in the extracellular solution significantly reduced peak transient Na^+ currents by approximately 20% of control. A decrease in Na^+ current amplitude was also seen with extracellular application of the D2 dopamine receptor agonist quinpirole, whereas the D2 receptor antagonist eticlopride largely abolished the response to dopamine. Inclusion of the phosphatase inhibitor okadaic acid in the patch electrode solution occluded the response to dopamine. The reduction in calyx sodium current in response to dopamine suggests efferent signaling through D2 dopaminergic receptors may occur via common mechanisms to decrease excitability in inner ear afferents.

Keywords: calyx, semicircular canal, crista, hair cell, sodium channel

OPEN ACCESS

Edited by:
Soroush G. Sadeghi, University at Buffalo, United States

Reviewed by:
Ruth Anne Eatock, University of Chicago, United States
Elisabeth Glowatzki, Johns Hopkins University, United States
Selina Baeza-Loya, University of Chicago, United States, in collaboration with reviewer RE

***Correspondence:**
Katherine J. Rennie
katie.rennie@cuanschutz.edu

Specialty section:
This article was submitted to Perception Science, a section of the journal Frontiers in Neuroscience

Received: *15 May 2021*
Accepted: *10 August 2021*
Published: *09 September 2021*

Citation:
Meredith FL and Rennie KJ (2021) Dopaminergic Inhibition of Na^+ Currents in Vestibular Inner Ear Afferents. Front. Neurosci. 15:710321. doi: 10.3389/fnins.2021.710321

INTRODUCTION

The inner ear houses the cochlea and vestibular system where signals relevant to auditory and vestibular perception are processed by hair cells and carried to the brain by their companion afferent nerve fibers. In mammals outer and inner hair cells are found in the cochlea, whereas type I and type II hair cells populate the sensory epithelia of the vestibular organs. Although each hair cell type is tailored toward its specific sensory purpose, all vertebrate hair cells transduce displacement of their mechanosensitive apical hair bundles into a receptor potential which regulates release of the neurotransmitter glutamate onto unmyelinated afferent terminals. Auditory and

vestibular signals are conveyed in the VIIIth nerve to the brain as action potentials in afferent neurons which have diverse properties in terms of their spontaneous action potential firing rates, thresholds and frequency responses (Goldberg, 2000; Eatock and Songer, 2011). The cochlea and vestibular organs also receive substantial efferent innervation from the brain. In the mature cochlea, medial olivocochlear efferents terminate on outer hair cells and lateral olivocochlear neurons make synapses with afferent nerve fibers beneath inner hair cells (Warr and GuinanJr., 1979). In mature vestibular epithelia, efferent fibers emanate from the brainstem to make synapses with type II hair cells and with afferent dendrites including the outer aspects of large calyx terminals surrounding type I hair cells (Wersall, 1956). The location of efferent synapses on afferent dendrites postsynaptic to hair cells supports a role for efferent modulation of glutamatergic transmission. For efferent terminals that synapse directly with type II hair cells and outer hair cells, acetylcholine acts via α9-containing nicotinic receptors to activate small conductance calcium-activated K^+ (SK) channels and hyperpolarize the membrane thus serving an inhibitory role (Fuchs and Lauer, 2019; Poppi et al., 2020). In turtle crista, efferent release of acetylcholine can also produce excitation through the muscarinic inhibition of K^+ currents mediated by KCNQ channels in calyx-bearing afferents (Holt et al., 2017; Lee et al., 2017).

Although acetylcholine is considered to be a major efferent transmitter in both the cochlea and vestibular periphery (Fuchs and Lauer, 2019; Poppi et al., 2020), other transmitters, including dopamine, may also function as neuromodulators in hair cell systems. Previous work has provided evidence for dopamine receptors in hair cell organs including frog crista, fish lateral line and saccule and rodent cochlea and vestibular otolith organs (Drescher et al., 2010; Maison et al., 2012; Toro et al., 2015; Perelmuter et al., 2019). In frog semicircular canal afferents, application of dopamine and dopaminergic agonists decreased the firing rate of action potentials (Andrianov et al., 2009). Similarly, dopamine reduced action potential firing rate in auditory afferents of guinea pig and rat cochlea (Oestreicher et al., 1997; Ruel et al., 2006; Wu et al., 2020). Sound exposure increased dopamine production in efferent neurons of mice suggesting a neuroprotective role (Maison et al., 2012; Wu et al., 2020). Together these studies support a role for dopaminergic signaling in diverse hair cell systems either through direct synaptic action or via paracrine signals.

The role of efferents in the peripheral vestibular system is poorly understood. To date, direct effects of dopamine on afferent neurons in mammalian vestibular epithelia have not been ascertained. To address this we isolated calyx terminals from semicircular canal organs of gerbils and tested the effects of dopamine on their Na^+ and K^+ currents. After finding a reduction in transient Na^+ currents in response to dopamine we further investigated underlying receptors and possible signaling pathways. We demonstrate a reduction in transient Na^+ currents in response to dopamine that appears to be mediated by D2 receptors, suggesting that efferent-mediated dopamine release may lead to decreased firing in vestibular afferents.

MATERIALS AND METHODS

Tissue Preparation

Mongolian gerbils (*Meriones unguiculatus*) of both sexes were used at postnatal days (P)13 to P33. Intraperitoneal injections of ketamine (70 mg/kg) and xylazine (3 mg/kg) in sterile saline were used to induce anesthesia with supplemental doses given when necessary. Following decapitation the cristae of the semicircular canals were dissected out and immersed in Leibovitz's L-15 medium (pH 7.4–7.45, osmolality 300–305 mosmol/kg H_2O solution). Procedures were in accordance with NIH guidelines and protocols approved by the University of Colorado's Institutional Animal Care and Use Committee.

Hair cells and calyces were mechanically separated from cristae with procedures similar to those described previously (Rennie and Streeter, 2006; Dhawan et al., 2010). Briefly the mechanical dissociation involved drawing a fine probe across the crista which was immersed in extracellular solution in the recording dish. For slice recordings (**Figure 4B**) ampullae were embedded in a low gelling temperature agarose and transverse slices (100 μm) cut through the end organ on a vibrating blade microtome (Leica VT1200 S, Leica Biosystems) (Meredith and Rennie, 2018, 2020). The cell recordings obtained for slice data in **Figure 4B** were reported previously (Meredith and Rennie, 2020).

Electrophysiological Recordings

Cells were visualized in the recording dish with a water immersion objective (X40) and differential interference contrast (DIC) optics on an Olympus microscope (BX51). Isolated cell pairs of single type I hair cells enveloped by calyx terminals or calyces within slices were selected for recordings. Electrodes were pulled from electrode glass (PG165T, Warner Instruments, Hamden, CT, United States) on a multistep horizontal puller (P-97 Sutter Instruments, San Rafael, CA, United States) and electrode tips were polished by heat using a Narishige MF 830 microforge (Narishige International United States, East Meadow, NY, United States). SYLGARD 18 (Dow Corning, Midland, MI, United States) was applied close to the tip of each electrode to reduce stray capacitance.

Calyx terminals express several different types of voltage-gated conductances including Na^+ currents (Meredith and Rennie, 2016). For experiments investigating the effect of dopamine on K^+ currents the electrode solution contained (in mM): KF (115), KCl (10), NaCl (2), HEPES (10), D-glucose (3), $MgCl_2$ (2), EGTA (10), pH 7.4 adjusted with KOH (27 mM). For all other experiments the electrode solution contained (in mM): CsF (120), CsCl (10), NaCl (2), HEPES (10), D-glucose (3), $MgCl_2$ (2), EGTA (10), pH 7.4 adjusted with CsOH (24 mM). To further isolate Na^+ currents from other conductances, recordings for investigating resurgent currents (I_{NaR}) were obtained in an extracellular solution containing in: (mM): NaCl (120), CsCl (5.4), $MgCl_2$ (2.5), tetraethylammonium Cl (30), $CaCl_2$ (1.3), glucose (10), HEPES (5). For all other experiments the external solution was Leibovitz's L-15 medium.

Electrode resistance was 2.3–5 MΩ prior to seal formation on calyces. Recordings were made at room temperature (21 – 24°C)

with voltage protocols designed to probe for transient (I_{NaT}) and resurgent (I_{NaR}) Na^+ currents. Data were acquired using pCLAMP 10 software with a patch amplifier (Axopatch 200B, Molecular Devices, Sunnyvale, CA, United States) connected to a PC via an AD converter (Digidata 1440A, Molecular Devices, Sunnyvale, CA, United States). Signals were low-pass filtered online at 5 or 10 kHz and sampled at 20–50 kHz. Correction for liquid junction potentials was made in the analysis.

Dopamine was dissolved in deionized water or L-15 on each experimental day to make a 10 mM stock solution which was then added to L-15 for a final concentration of 100 μM. In experiments with Cs^+-based electrode solutions dopamine solutions also contained 100 μM ascorbate. Most chemicals including dopamine hydrochloride were obtained from Sigma Aldrich. Okadaic acid, ascorbic acid, quinpirole hydrochloride and eticlopride were from Tocris Bioscience. The external solution was perfused using a peristaltic pump (Gilson) at a flow rate of 0.5-1.0 ml/min. Drugs were typically perfused for a minimum of 4-9 min before measurements of drug effects on Na^+ currents were taken. The length of the wash (return to control solution) was between 6 and 10 min.

Data Analysis

Clampfit 10 (Molecular Devices) and Sigmaplot 11 (Systat Software, San Jose, CA, United States) were used to analyze voltage clamp data. Mean values ± SD are reported and values were compared with paired *t*-tests.

RESULTS

Dopamine Reduces Na^+ Currents but Not K^+ Currents in Isolated Calyx Terminals

Voltage-dependent Na^+ channels are a target for neuromodulation in many cell types. In cochlear afferent neurons transient Na^+ currents are decreased by the application of dopamine (Sun and Salvi, 2001; Valdes-Baizabal et al., 2015). Dopamine may be released from cochlear efferent fibers that terminate on afferent terminals close to inner hair cell synapses (Oestreicher et al., 1997; Ruel et al., 2006). Since dopamine is also a candidate efferent transmitter in the vestibular system (Drescher et al., 2010; Lee and Jones, 2017), we tested its effect on voltage-gated currents in calyces isolated from cristae. **Figure 1A** shows a series of whole cell currents in response to depolarizing voltage steps before, during and after dopamine application in a P24 calyx. The electrode solution was K^+-based and therefore both transient Na^+ currents and outward K^+ currents were evoked at potentials above ∼ –60 mV. Na^+ currents were notably reduced during extracellular perfusion of 100 μM dopamine and recovered following return to control extracellular solution. Peak I_{NaT} in this cell was decreased during dopamine application at most voltage steps and recovered following washout as shown in the current-voltage plot (**Figure 1B**).

To test if dopamine affected voltage-dependent outward K^+ currents in isolated calyces, the potassium current (I_K) was measured during perfusion of 100 μM dopamine in a P21 isolated calyx (**Figure 1C**). The standard voltage protocol was applied at intervals throughout. Dopamine was applied following stabilization of currents in control conditions, since we previously observed that Na^+ currents in calyces often increase in size, or run up, during the first few seconds after membrane break through to whole cell recordings (Meredith et al., 2011; Meredith and Rennie, 2018). The peak I_{NaT} was measured at steps to –40 mV (black circles) and decreased markedly in the presence of dopamine shortly after the perfusion onset. K^+ current amplitude was measured at the end of 40 ms voltage steps to +20 mV and remained relatively unchanged throughout the course of dopamine application. In a group of calyces (ages P21-27) mean I_K was 2,161 ± 1,501 pA in control conditions, which was not significantly different from the mean value of 1,976 ± 1,454 pA in dopamine (mean ± SD, $n = 6$, paired *t*-test, $P = 0.066$). These experiments suggest that the effect of dopamine is specific to Na^+ currents in calyx terminals.

Having confirmed that K^+ currents were not significantly affected by dopamine, we performed additional experiments using Cs^+ in the patch electrode solution to inhibit voltage-dependent K^+ currents. In the experiments with internal Cs^+ outward currents were greatly reduced (mean 518.5 ± 241.3 pA at + 20mV, n = 11 cells). The effect of dopamine was tested in four calyces and perfusion with 100 μM dopamine reversibly reduced peak I_{NaT} at the test step of –40 mV as shown for one cell in **Figure 2A**. The effect on Na^+ current amplitude following dopamine exposure and subsequent washout is shown for cells with either K^+ or Cs^+ as the major cation in the patch electrode solution in **Figure 2B**. Peak Na^+ currents were measured at –40 mV and averaged –2,151 ± 1,685 pA in control; following dopamine perfusion mean peak current was reduced to –1,732 ± 1,718 pA ($n = 9$ cells). The decrease in amplitude was significant and a partial or complete washout was observed in all but two cells on return to normal extracellular solution (**Figure 2B**).

Mechanisms Underlying Na^+ Current Response to Dopamine

We next investigated the possible involvement of dopamine receptor subtypes. Dopamine receptors are G-protein-coupled receptors (GPCRs) and five receptor subtypes (D1-D5) have been described (Missale et al., 1998). Based on the effects on adenylyl cyclase activity, receptor subtypes fall into two classes: the D1-like receptor group includes D1 and D5 and D2-like receptors include D2, D3, and D4. Type I spiral ganglion neurons have been shown to express D1, D2, D4, and D5 receptor subtypes (Karadaghy et al., 1997; Inoue et al., 2006; Maison et al., 2012). Immunohistochemical work has provided evidence for D1 and D2 receptors in vestibular epithelia with D2-like immunoreactivity associated with calyx terminals in rat saccule (Drescher et al., 2010). We therefore tested for the presence of dopamine-receptor mediated responses in calyx afferents using quinpirole, an agonist selective for D2 receptors. We found that perfusion with extracellular solution containing 1 μM quinpirole produced a mean reduction of Na^+ current of 14.2 ± 6.3% ($n = 6$,

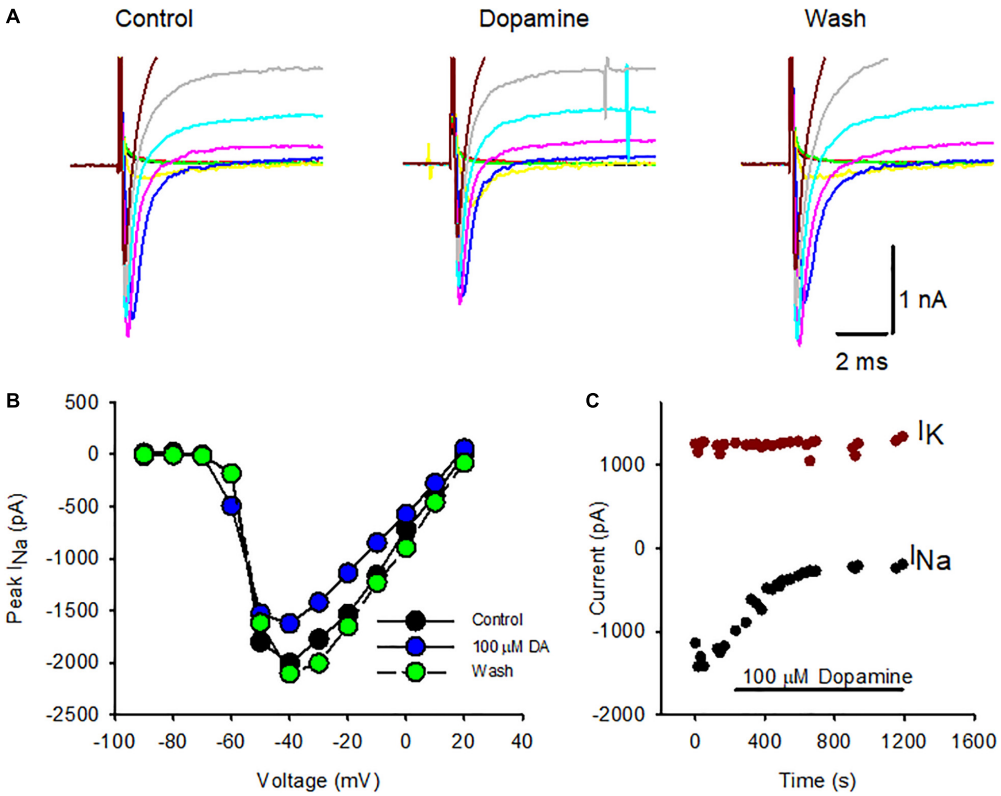

FIGURE 1 | Effect of dopamine on Na^+ and K^+ currents in isolated calyx terminals. **(A)** Whole cell currents in an isolated calyx in response to a series of voltage steps from –90 to –10 mV following a prepulse to –130 mV. Transient Na^+ currents were reduced in response to application of 100 µM dopamine and recovered following washout. **(B)** Current-voltage plot comparing peak I_{NaT} at each voltage step in control conditions (black circles), during dopamine (DA) perfusion (blue circles, 6 min of perfusion) and following washout (green circles, 10 min of perfusion). P24 calyx, female. **(C)** I_{NaT} and steady state potassium current (I_K) were measured during perfusion of 100 µM dopamine to an isolated calyx. Peak I_{NaT} was measured at successive voltage steps to –40 mV following a prepulse to –130 mV to remove Na^+ channel inactivation (black circles) and showed a sustained decrease with dopamine application. I_K was measured at the end of 40 ms for the voltage step to +20 mV (dark red circles) and remained constant throughout dopamine perfusion. P21 calyx, male. Electrode solution contained K^+ and the external solution was L-15.

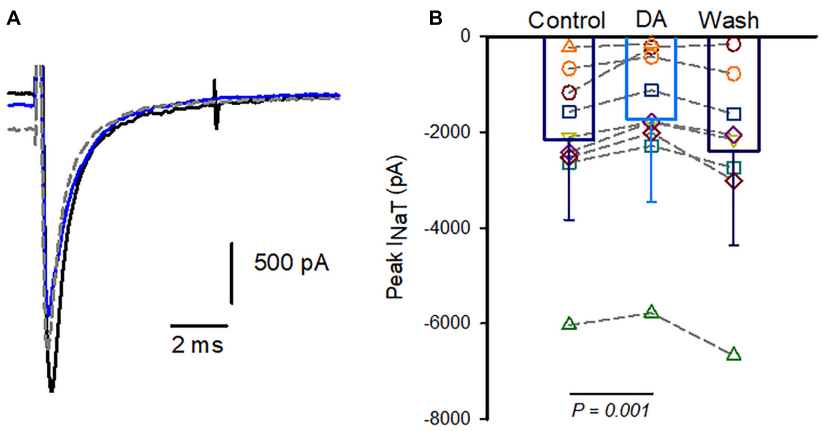

FIGURE 2 | Dopamine reversibly reduces I_{NaT} in isolated calyx terminals. **(A)** Whole cell currents in an isolated calyx in response to a voltage step from –90 to –40 mV following a prepulse to –130 mV. Control Na^+ current (black), current in 100 µM dopamine (blue) and current during washout (gray dashed line) are shown. P22 calyx, female. **(B)** Pooled data show peak currents in individual cells and bars indicate mean I_{NaT} in control, in response to 100 µM dopamine (DA) and during washes. Peak currents were measured at voltage steps to –40 mV and averaged –2,151 ± 1,685 pA in control; and –1,732 ± 1,718 pA (mean ± SD, *n* = 9 cells) in dopamine. Recovery during wash was measured in 8 cells since 1 cell was lost prior to wash (P21-27 calyces, 5 K^+-filled cells and 4 Cs^+-filled cells).

Figure 3A). Although quinpirole decreased I_{NaT} amplitude, we noted that compared to dopamine the effect of quinpirole was smaller and typically required several minutes of perfusion before the reduction in peak Na^+ current occurred. To further test for D2-like receptor involvement, we used the D2 receptor antagonist eticlopride and assessed its effect on responses to dopamine (**Figure 3B**). Eticlopride (1 μM) was first applied to cells followed by co-application of 1 μM eticlopride and dopamine (100 μM). There was no significant difference in peak I_{NaT} between the two different conditions, suggesting that antagonism of D2 receptors by eticlopride prevented D2 receptor activation by dopamine.

Based on known actions of dopamine on the phosphorylation state of Nav channels in other cell types (Cantrell and Catterall, 2001), we hypothesized that dopamine may modulate Na^+ current through a change in the phosphorylation state of Na^+ channels and inhibition of phosphatase might be expected to produce an inhibition of Na^+ currents analogous to activation of dopamine receptors. We therefore tested the effect of okadaic acid, a known inhibitor of phosphatase 1 and 2A, by perfusing cells with extracellular 100 nM okadaic acid. However, we saw no consistent change in amplitude of I_{Na} in 3 cells tested with external perfusion of okadaic acid. Next we studied the effect of including 100 nM okadaic acid in the patch electrode solution followed by extracellular dopamine perfusion (**Figure 3C**). We measured peak I_{NaT} several minutes following membrane breakthrough into the whole cell mode and subsequently began perfusion of dopamine. In these conditions only a small non-significant change in Na^+ current amplitude occurred following application of 100 μM dopamine (**Figure 3C**), strongly suggesting that intracellular okadaic acid prevented the action of dopamine on Na^+ channel activity.

I_{NaR} Is Prevalent in Calyces in Slices, but Is Rarely Observed in Isolated Calyces

In previous recordings from mature calyces in crista slices we found that transient sodium currents (I_{NaT}) were abolished by tetrodotoxin (TTX) (Meredith and Rennie, 2018). We subsequently identified resurgent (I_{NaR}) and persistent currents (I_{NaP}), which occurred frequently, but contributed much smaller components of the TTX-sensitive Na^+ current than I_{NaT} (Meredith and Rennie, 2020). Dopamine was reported to modulate only the transient Na^+ current component in pyramidal neurons (Maurice et al., 2001), but we wondered if dopamine might influence resurgent currents in vestibular calyces. I_{NaR} is a distinctive current evoked by transient membrane depolarizations and arises from an open channel block state in certain types of Nav channel (Lewis and Raman, 2014). Calyces dissociated from vestibular epithelia also express TTX-sensitive I_{NaT} (Rennie and Streeter, 2006; Meredith et al., 2011), but I_{NaR} has not been reported previously in isolated calyces. Given that resurgent current (I_{NaR}) was observed in greater than half of calyces studied in crista slices at ages P13 and older (Meredith and Rennie, 2020), we tested for the presence of I_{NaR} in solitary calyces using voltage protocols designed to maximize I_{NaR}. The membrane was stepped briefly from −130 to −10 mV to produce activation and inactivation of I_{NaT} and then to a series of potentials to repolarize the membrane and evoke I_{NaR} (**Figure 4A**). We discovered that although I_{NaT} was present in all isolated calyces tested at ages P15-33 (n = 15), I_{NaR} was only detected in 2 out of 15 isolated calyces (**Figure 4B**). Peak I_{NaR} in the 2 isolated calyces was small and did not exceed 80 pA in amplitude. This contrasts with our data from calyces in crista slices, where I_{NaR} was seen in the majority of calyces and mean peak amplitude exceeded 125 pA at the start of the third postnatal week (Meredith and Rennie, 2020). Nav1.6 channels can underlie transient and resurgent Na^+ currents and a selective Nav1.6 channel blocker, 4,9 anhydro-TTX, reduced I_{NaT} and I_{NaR} in both cochlear and vestibular afferents (Browne et al., 2017; Meredith and Rennie, 2020). It remains to be determined whether dopamine can modulate resurgent currents in inner ear primary afferents.

DISCUSSION

Dopaminergic Modulation of I_{NaT} in Calyx Terminals

In this paper we show for the first time that transient Na^+ currents in rodent vestibular afferents are modulated by dopamine. Dopamine significantly and reversibly reduced transient Na^+ currents in acutely isolated calyces. The effect of dopamine was mimicked by quinpirole and inhibited by eticlopride suggesting the presence of D2-like dopamine receptors on calyx-bearing afferents. In contrast, outward K^+ currents in calyces were not affected by dopamine application.

Dopaminergic Signaling in the Inner Ear

Dopamine receptors have been classified as either D1-like and D2-like groups based on their biochemical and pharmacological profiles (Missale et al., 1998). Both types are GPCRs and cloning studies have demonstrated five dopamine receptor subtypes (D1–D5). In the cochlea the presence of D1, D2, D4, and D5 receptor subtypes have been reported in type I spiral ganglion neurons (Karadaghy et al., 1997; Inoue et al., 2006; Maison et al., 2012). In cellular studies on isolated and cultured cochlear afferents, dopamine reduced I_{NaT} in spiral ganglion neurons of the rat cochlea (Valdes-Baizabal et al., 2015). Na^+ channels can be modulated through phosphorylation by cAMP-dependent protein kinase A or by protein kinase C (Cantrell and Catterall, 2001). In spiral ganglion neurons both D1- and D2-like receptor subtypes were implicated in dopaminergic modulation of Na^+ currents. The inhibitory effect of dopamine on I_{NaT} was mediated via two separate GPCR pathways, the D1 receptor pathway involved adenylyl cyclase/cAMP/protein kinase A and the D2 receptor pathway was dependent on protein kinase C (Valdes-Baizabal et al., 2015).

In vestibular calyces we found that application of the D2 agonist quinpirole reduced I_{NaT} and the D2 antagonist eticlopride blocked the response of calyces to dopamine, strongly suggesting that dopamine modulation occurs via D2 receptors. Phosphatase inhibition by okadaic acid also prevented the effect of dopamine on I_{NaT} suggesting phosphorylation involvement.

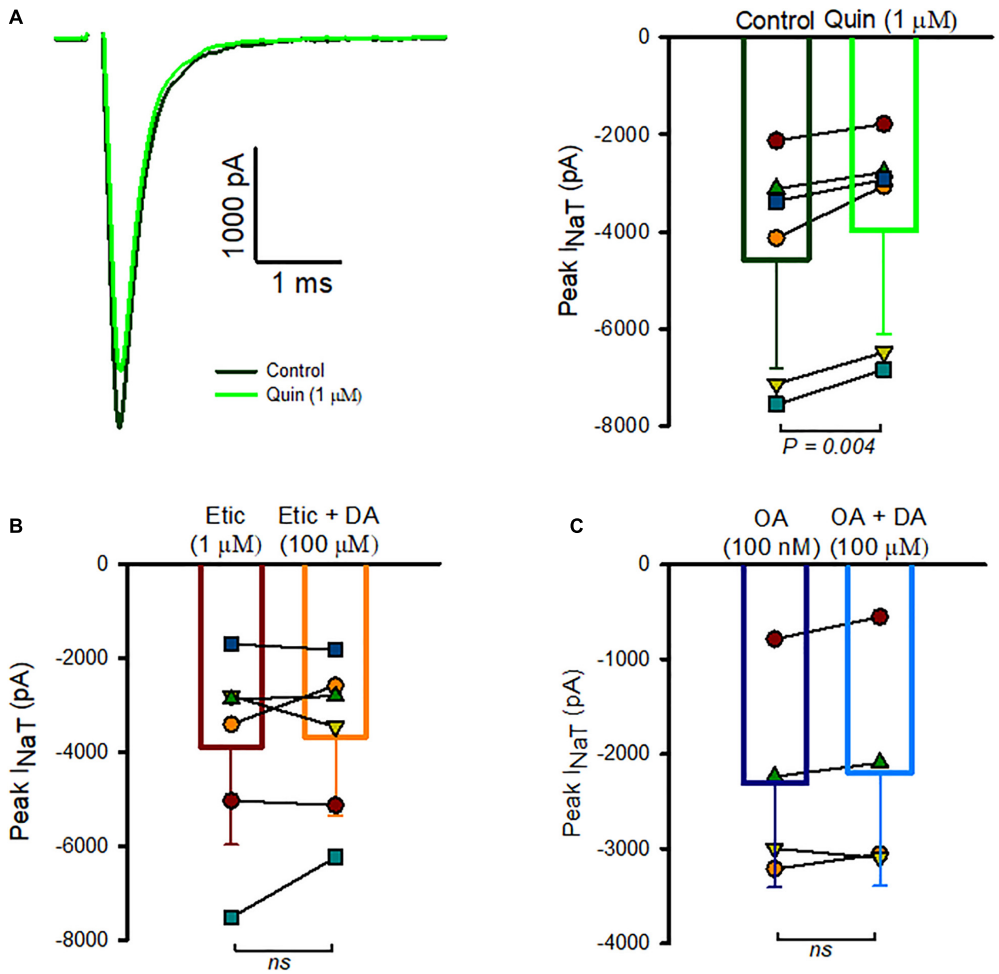

FIGURE 3 | Role of D2-like receptors in I_{NaT} inhibition. **(A)** Whole cell currents in an isolated calyx in control (black trace) and following quinpirole perfusion (green trace) are shown in response to a voltage step to –40 mV (left panel). P23 calyx, male. Box plot indicates the response of 6 calyces to quinpirole (right panel). Mean I_{NaT} control was –4,573 ± 2,247 pA, mean I_{NaT} in quinpirole was –3,978 ± 2,132 pA, n = 6, ages P19-28, P = 0.004). **(B)** Na^+ currents were measured in the presence of 1 μM eticlopride, followed by perfusion of 1 μM eticlopride and 100 μM dopamine. Peak Na^+ currents averaged –3,895 ± 2,083 pA in eticlopride which was not significantly different from peak currents in eticlopride and dopamine (–3,680.2 ± 1,679 pA, n = 6, P = 0.985). **(C)** Summary of the effect of okadaic acid (OA) in reducing the response of I_{NaT} to DA. Mean peak current measured at voltage steps to –40 mV was –2,268 ± 1,170 pA in the presence of internal OA and –2,270 ± 1,061 pA following dopamine perfusion (n = 4 cells, all P23). In 1 cell, the initial dopamine perfusion resulted in a reduction of I_{NaT}, but following a wash and return to control the cell no longer responded to dopamine application. Data from the second perfusion were used in this case.

However, a potential role for D1 receptors at the calyx synapse has not yet been ruled out. D1 and D2-like immunoreactivity was reported in vestibular epithelia at the level of vestibular hair cells and afferents in fish and rodent otolith organs and D2 receptors were associated with calyx terminals (Drescher et al., 2010). In multiunit recordings from frog semicircular canal vestibular afferents, dopamine decreased background action potential firing rate and the effect was mimicked by application of both D1 and D2 agonists (Andrianov et al., 2009). More recently dopamine signaling has also been linked to seasonal variations in midshipman fish saccule (Perelmuter et al., 2019). In the cochlea dopamine may have a direct effect on afferent terminals (Sun and Salvi, 2001; Valdes-Baizabal et al., 2015) and also an indirect effect on inner hair cells through inhibition of hair cell glutamate release at the afferent synapse (Wu et al., 2020). Through a decrease in Na^+ current amplitude and action potential firing rate, the activation of dopamine receptors may reduce excitotoxicity at inner hair cell synapses. Whether dopamine within efferent neurons could undergo dynamic regulation and also serve a neuroprotective role in the vestibular system remains to be determined.

Dopaminergic Modulation of Other Conductances in Vestibular Afferents

Voltage-dependent K^+ currents in calyces were not increased or decreased by dopamine application in this study. However, the second messenger cAMP modulates the mixed cation hyperpolarization-activated current (I_h) in auditory and vestibular afferents, where it acts to shift the activation to more

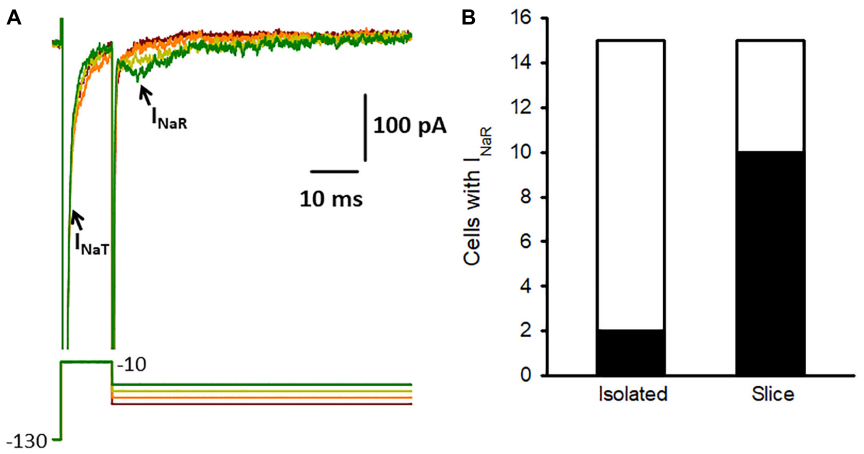

FIGURE 4 | Na^+ current characteristics in isolated calyces. **(A)** Na^+ currents (upper) recorded from an isolated P17 calyx using the voltage protocol shown below. From a holding potential of –90 mV the membrane was stepped to –130 mV for 10 ms and then stepped for 10 ms to –10 mV (complete duration of protocol not shown). The protocol resulted in large transient currents (I_{NaT}, truncated for clarity) at –10 mV, which activated and inactivated rapidly. The membrane was then repolarized to potentials between –75 and –45 mV (10 mV increments shown). Small resurging inward currents (arrow) with characteristics of I_{NaR} were seen following repolarizing steps to –35 mV and –45 mV and strongly resembled I_{NaR} previously recorded from calyces in slices (Meredith and Rennie, 2020). **(B)** I_{NaR} was seen in most calyces in crista slices (10 of 15 cells tested at age P13-15), but was rarely observed in isolated calyces (2 of 15 cells tested, age range P15-33). Electrode solution for these recordings contained Cs^+ and the HEPES-based external solution contained 120 mM Na^+.

positive potentials and increase the degree of current available around the resting potential (Yi et al., 2010; Almanza et al., 2012; Meredith et al., 2012; Horwitz et al., 2014; Ventura and Kalluri, 2019). It is unclear if neurotransmitters act to increase I_h via cAMP within afferents *in vivo*, but it is plausible that in addition to modulation of the Na^+ current, dopamine could impact I_h via a cAMP-dependent signaling pathway. Dopamine has been shown to modulate I_h in chemosensory neurons of the carotid body, where it acts to decrease firing through a hyperpolarizing shift in I_h (Zhang et al., 2018). Further examination of the effects of dopamine and associated signaling pathways on other voltage-dependent currents in inner ear afferents could uncover additional modulatory pathways for this candidate efferent transmitter.

Na^+ Current Characteristics in Isolated Calyx Terminals

Voltage-gated Na^+ channels typically produce rapid and transient currents (I_{NaT}) that mediate the upward phase of the action potential. In addition to I_{NaT}, resurgent (I_{NaR}) and persistent Na^+ currents also manifest in certain cell types (Lewis and Raman, 2014). Dopamine has been shown to differentially modulate Na^+ current components in pyramidal neurons isolated from the prefrontal cortex, where it inhibited transient but not persistent Na^+ currents (Maurice et al., 2001). Large and fast activating, rapidly inactivating I_{NaT} are present in all mature vestibular afferent calyx terminals in gerbil crista, whereas much smaller resurgent and persistent Na^+ currents are present in a subset of afferents and all three Na^+ current components are blocked by tetrodotoxin (Meredith and Rennie, 2018, 2020). Nine distinct Na^+ channel α subunits have been identified (Nav1.1-1.9) and several of these are expressed in vestibular ganglion neurons (Liu et al., 2016). Nav1.6 channels are present in both cochlear and vestibular afferents where they contribute to transient and resurgent Na^+ currents (Browne et al., 2017; Meredith and Rennie, 2020). A specific action of dopamine on Nav1.6-mediated currents in inner ear afferents remains to be determined. I_{NaR} and I_{NaT} were detected together in the majority of mature calyx terminals in crista slices (Meredith and Rennie, 2020). In contrast, I_{NaT} was present in all isolated calyces studied here, but I_{NaR} was rarely observed. In both vestibular calyces and spiral ganglion neurons I_{NaR} expression increased with postnatal development suggesting a role for this current in afferent firing in adult inner ear epithelia (Browne et al., 2017; Meredith and Rennie, 2020). Navβ4 subunits, which may be required for I_{NaR} expression (Lewis and Raman, 2014), were detected in vestibular epithelia (Liu et al., 2016) and immunolocalized to the heminode and nodes of Ranvier in cochlear afferent neurons (Browne et al., 2017). Although isolated calyces express several voltage-dependent currents including large I_{NaT}, I_h and a variety of K^+ currents (Hurley et al., 2006; Rennie and Streeter, 2006; Dhawan et al., 2010; Meredith et al., 2011, 2012; Meredith and Rennie, 2015), these solitary calyx terminals for the most part lack axons and could be deficient in endogenous factors needed for I_{NaR} generation. Spike generation likely occurs in afferent terminals at the initial unmyelinated segment close to hair cells (Hossain et al., 2005; Lysakowski et al., 2011), but the precise location of Na^+ channel subtypes remains to be determined.

Efferent Mechanisms in the Inner Ear

Vestibular hair cells and inner hair cells make synapses with afferent terminals to convey sound and balance information to the brain as action potentials, but the auditory and vestibular systems also receive extensive efferent input from the brain. Outer hair cells and type II hair cells are contacted directly

by efferent terminals, but efferent fibers also terminate on unmyelinated vestibular calyx terminals and auditory afferents postsynaptic to inner hair cells. The strategic placement of efferent synapses in the initial segment zone of the axon and calyx outer face could allow modulation of afferent firing close to the site of action potential initiation through receptor-mediated influence on current components mediated through voltage-gated ion Na^+ channels.

Gerbil cristae receive substantial efferent innervation with distinct efferent groups projecting to ipsilateral and contralateral cristae (Purcell and Perachio, 1997). Although acetylcholine is considered a major efferent neurotransmitter, as shown in gerbil not all vestibular efferent neurons are cholinergic (Perachio and Kevetter, 1989). The activation of efferent fibers has been shown to have complex effects (both excitatory and inhibitory) on action potential firing rate in vestibular afferents. Acetylcholine released from efferent terminals can act via both nicotinic and muscarinic receptor signaling pathways (Holt et al., 2015, 2017; Lee et al., 2017; Poppi et al., 2020). Ca^{2+} influx through α9-containing nicotinic receptors activates SK channels producing a hyperpolarization of type II vestibular hair cells and a decrease in membrane resistance and hair cell sensitivity (Poppi et al., 2018, 2020). A similar mechanism exists in the cochlea where the efferent-mediated release of acetylcholine inhibits outer hair cell function through α9 receptors (Fuchs and Lauer, 2019). Conversely, acetylcholine can result in excitation through muscarinic receptor activation which inhibits M-like K^+ currents in calyx afferents of turtle and rat crista (Holt et al., 2017; Ramakrishna et al., 2021). Other transmitters may also contribute to efferent transmission (Lee and Jones, 2017). In rat crista, GABA was recently shown to have an excitatory effect on calyx firing through $GABA_B$ receptor-mediated inhibition of K^+ channels (Ramakrishna and Sadeghi, 2020). Therefore several studies have suggested efferent-mediated modulation of K^+ currents in vestibular hair cells and afferents, but direct effects of potential neuromodulators on Na^+ channels linked to firing have not been reported until now. Our data suggest dopamine release could impact firing in vestibular afferents through activation of D2 receptors and associated intracellular signaling mechanisms resulting in Na^+ channel inhibition within calyx terminals. As described in cochlear afferents, dopamine-mediated reduction of I_{NaT} would result in a decrease in firing in vestibular calyx-bearing neurons.

Dopaminergic efferents are present in the cochlea and may also be present in vestibular epithelia. Tyrosine hydroxylase is required for the synthesis of dopamine and Drescher et al. (2010) identified thin tyrosine hydroxylase-containing nerve fibers in otolith epithelia including the rat saccule and utricle and mouse utricle. These presumed efferent fibers terminated on vestibular hair cells and also on calyces. In addition, D1 (D1A) and D2 (D2L) receptor immunoreactivity was seen within hair cells and neurons supporting a role for dopamine as an efferent neurotransmitter in the vestibular system (Drescher et al., 2010).

CONCLUDING REMARKS

Dopamine may operate as a neuroactive substance at the hair cell/afferent synapse in mammalian auditory and vestibular systems. Through a reduction in sodium channel activity via changes in phosphorylation, dopamine released from efferents may reduce action potential firing in both auditory and vestibular afferents. In the cochlea, dopamine appears to exert its inhibitory effect on afferent firing via two distinct dopaminergic signaling pathways. Our data support a role for D2 receptors in Na^+ current inhibition and the involvement of other dopamine receptor subtypes remains to be elucidated. Disruption to dopaminergic efferent pathways could be associated with auditory and vestibular dysfunction.

DATA AVAILABILITY STATEMENT

The raw data supporting the conclusions of this article will be made available by the authors, without undue reservation.

ETHICS STATEMENT

The animal study was reviewed and approved by University of Colorado Denver Institutional Animal Care and Use Committee.

AUTHOR CONTRIBUTIONS

FM and KR designed the experiments, performed the research experiments, analyzed the data, and prepared the figures. KR wrote the first draft of the manuscript. Both authors contributed to the article and approved the submitted version.

FUNDING

Funding for this work was provided by the National Institute on Deafness and Other Communication Disorders Grants DC016860 and DC018786.

REFERENCES

Almanza, A., Luis, E., Mercado, F., Vega, R., and Soto, E. (2012). Molecular identity, ontogeny, and cAMP modulation of the hyperpolarization-activated current in vestibular ganglion neurons. *J. Neurophysiol.* 108, 2264–2275. doi: 10.1152/jn.00337.2012

Andrianov, G. N., Ryzhova, I. V., and Tobias, T. V. (2009). Dopaminergic modulation of afferent synaptic transmission in the semicircular canals of frogs. *Neurosignals* 17, 222–228. doi: 10.1159/000224632

Browne, L., Smith, K. E., and Jagger, D. J. (2017). Identification of persistent and resurgent sodium currents in spiral ganglion neurons cultured from the mouse Cochlea. *eNeuro* 4:ENEURO.0303-17.2017.

Cantrell, A. R., and Catterall, W. A. (2001). Neuromodulation of Na+ channels: an unexpected form of cellular plasticity. *Nat. Rev. Neurosci.* 2, 397–407. doi: 10.1038/35077553

Dhawan, R., Mann, S. E., Meredith, F. L., and Rennie, K. J. (2010). K+ currents in isolated vestibular afferent calyx terminals. *J. Assoc. Res. Otolaryngol.* 11, 463–476. doi: 10.1007/s10162-010-0213-8

Drescher, M. J., Cho, W. J., Folbe, A. J., Selvakumar, D., Kewson, D. T., Abu-Hamdan, M. D., et al. (2010). An adenylyl cyclase signaling pathway predicts direct dopaminergic input to vestibular hair cells. *Neuroscience* 171, 1054–1074. doi: 10.1016/j.neuroscience.2010.09.051

Eatock, R. A., and Songer, J. E. (2011). Vestibular hair cells and afferents: two channels for head motion signals. *Annu. Rev. Neurosci.* 34, 501–534. doi: 10.1146/annurev-neuro-061010-113710

Fuchs, P. A., and Lauer, A. M. (2019). Efferent Inhibition of the Cochlea. *Cold Spring Harb. Perspect. Med.* 9:a033530. doi: 10.1101/cshperspect.a033530

Goldberg, J. M. (2000). Afferent diversity and the organization of central vestibular pathways. *Exp. Brain Res.* 130, 277–297. doi: 10.1007/s002210050033

Holt, J. C., Jordan, P. M., Lysakowski, A., Shah, A., Barsz, K., and Contini, D. (2017). Muscarinic acetylcholine receptors and M-currents underlie efferent-mediated slow excitation in calyx-bearing vestibular afferents. *J. Neurosci.* 37, 1873–1887. doi: 10.1523/jneurosci.2322-16.2017

Holt, J. C., Kewin, K., Jordan, P. M., Cameron, P., Klapczynski, M., Mcintosh, J. M., et al. (2015). Pharmacologically distinct nicotinic acetylcholine receptors drive efferent-mediated excitation in calyx-bearing vestibular afferents. *J. Neurosci.* 35, 3625–3643. doi: 10.1523/jneurosci.3388-14.2015

Horwitz, G. C., Risner-Janiczek, J. R., and Holt, J. R. (2014). Mechanotransduction and hyperpolarization-activated currents contribute to spontaneous activity in mouse vestibular ganglion neurons. *J. Gen. Physiol.* 143, 481–497. doi: 10.1085/jgp.201311126

Hossain, W. A., Antic, S. D., Yang, Y., Rasband, M. N., and Morest, D. K. (2005). Where is the spike generator of the cochlear nerve? Voltage-gated sodium channels in the mouse cochlea. *J. Neurosci.* 25, 6857–6868. doi: 10.1523/jneurosci.0123-05.2005

Hurley, K. M., Gaboyard, S., Zhong, M., Price, S. D., Wooltorton, J. R., Lysakowski, A., et al. (2006). M-like K+ currents in type I hair cells and calyx afferent endings of the developing rat utricle. *J. Neurosci.* 26, 10253–10269. doi: 10.1523/jneurosci.2596-06.2006

Inoue, T., Matsubara, A., Maruya, S., Yamamoto, Y., Namba, A., Sasaki, A., et al. (2006). Localization of dopamine receptor subtypes in the rat spiral ganglion. *Neurosci. Lett.* 399, 226–229. doi: 10.1016/j.neulet.2006.01.063

Karadaghy, A. A., Lasak, J. M., Chomchai, J. S., Khan, K. M., Drescher, M. J., and Drescher, D. G. (1997). Quantitative analysis of dopamine receptor messages in the mouse cochlea. *Brain Res. Mol. Brain Res.* 44, 151–156. doi: 10.1016/s0169-328x(96)00261-6

Lee, C., Holt, J. C., and Jones, T. A. (2017). Effect of M-current modulation on mammalian vestibular responses to transient head motion. *J. Neurophysiol.* 118, 2991–3006. doi: 10.1152/jn.00384.2017

Lee, C., and Jones, T. A. (2017). Neuropharmacological targets for drug action in vestibular sensory pathways. *J. Audiol. Otol.* 21, 125–132. doi: 10.7874/jao.2017.00171

Lewis, A. H., and Raman, I. M. (2014). Resurgent current of voltage-gated Na(+) channels. *J. Physiol.* 592, 4825–4838. doi: 10.1113/jphysiol.2014.277582

Liu, X. P., Wooltorton, J. R., Gaboyard-Niay, S., Yang, F. C., Lysakowski, A., and Eatock, R. A. (2016). Sodium channel diversity in the vestibular ganglion: NaV1.5, NaV1.8, and tetrodotoxin-sensitive currents. *J. Neurophysiol.* 115, 2536–2555. doi: 10.1152/jn.00902.2015

Lysakowski, A., Gaboyard-Niay, S., Calin-Jageman, I., Chatlani, S., Price, S. D., and Eatock, R. A. (2011). Molecular microdomains in a sensory terminal, the vestibular calyx ending. *J. Neurosci.* 31, 10101–10114. doi: 10.1523/jneurosci.0521-11.2011

Maison, S. F., Liu, X. P., Eatock, R. A., Sibley, D. R., Grandy, D. K., and Liberman, M. C. (2012). Dopaminergic signaling in the cochlea: receptor expression patterns and deletion phenotypes. *J. Neurosci.* 32, 344–355. doi: 10.1523/jneurosci.4720-11.2012

Maurice, N., Tkatch, T., Meisler, M., Sprunger, L. K., and Surmeier, D. J. (2001). D1/D5 dopamine receptor activation differentially modulates rapidly inactivating and persistent sodium currents in prefrontal cortex pyramidal neurons. *J. Neurosci.* 21, 2268–2277. doi: 10.1523/jneurosci.21-07-02268.2001

Meredith, F. L., Benke, T. A., and Rennie, K. J. (2012). Hyperpolarization-activated current (I(h)) in vestibular calyx terminals: characterization and role in shaping postsynaptic events. *J. Assoc. Res. Otolaryngol.* 13, 745–758. doi: 10.1007/s10162-012-0342-3

Meredith, F. L., Li, G. Q., and Rennie, K. J. (2011). Postnatal expression of an apamin-sensitive k(ca) current in vestibular calyx terminals. *J. Membr. Biol.* 244, 81–91. doi: 10.1007/s00232-011-9400-8

Meredith, F. L., and Rennie, K. J. (2015). Zonal variations in K+ currents in vestibular crista calyx terminals. *J. Neurophysiol.* 113, 264–276. doi: 10.1152/jn.00399.2014

Meredith, F. L., and Rennie, K. J. (2016). Channeling your inner ear potassium: K+ channels in vestibular hair cells. *Hear. Res.* 338, 40–51. doi: 10.1016/j.heares.2016.01.015

Meredith, F. L., and Rennie, K. J. (2018). Regional and developmental differences in Na(+) currents in vestibular primary afferent neurons. *Front. Cell. Neurosci.* 12:423. doi: 10.3389/fncel.2018.00423

Meredith, F. L., and Rennie, K. J. (2020). Persistent and resurgent Na(+) currents in vestibular calyx afferents. *J. Neurophysiol.* 124, 510–524. doi: 10.1152/jn.00124.2020

Missale, C., Nash, S. R., Robinson, S. W., Jaber, M., and Caron, M. G. (1998). Dopamine receptors: from structure to function. *Physiol. Rev.* 78, 189–225.

Oestreicher, E., Arnold, W., Ehrenberger, K., and Felix, D. (1997). Dopamine regulates the glutamatergic inner hair cell activity in guinea pigs. *Hear. Res.* 107, 46–52. doi: 10.1016/s0378-5955(97)00023-3

Perachio, A. A., and Kevetter, G. A. (1989). Identification of vestibular efferent neurons in the gerbil: histochemical and retrograde labelling. *Exp. Brain Res.* 78, 315–326.

Perelmuter, J. T., Wilson, A. B., Sisneros, J. A., and Forlano, P. M. (2019). Forebrain dopamine system regulates inner ear auditory sensitivity to socially relevant acoustic signals. *Curr. Biol.* 29:e2193.

Poppi, L. A., Holt, J. C., Lim, R., and Brichta, A. M. (2020). A review of efferent cholinergic synaptic transmission in the vestibular periphery and its functional implications. *J. Neurophysiol.* 123, 608–629. doi: 10.1152/jn.00053.2019

Poppi, L. A., Tabatabaee, H., Drury, H. R., Jobling, P., Callister, R. J., Migliaccio, A. A., et al. (2018). ACh-induced hyperpolarization and decreased resistance in mammalian type II vestibular hair cells. *J. Neurophysiol.* 119, 312–325. doi: 10.1152/jn.00030.2017

Purcell, I. M., and Perachio, A. A. (1997). Three-dimensional analysis of vestibular efferent neurons innervating semicircular canals of the gerbil. *J. Neurophysiol.* 78, 3234–3248. doi: 10.1152/jn.1997.78.6.3234

Ramakrishna, Y., Manca, M., Glowatzki, E., and Sadeghi, S. G. (2021). Cholinergic modulation of membrane properties of calyx terminals in the vestibular periphery. *Neuroscience* 452, 98–110. doi: 10.1016/j.neuroscience.2020.10.035

Ramakrishna, Y., and Sadeghi, S. G. (2020). Activation of GABAB receptors results in excitatory modulation of calyx terminals in rat semicircular canal cristae. *J. Neurophysiol.* 124, 962–972. doi: 10.1152/jn.00243.2020

Rennie, K. J., and Streeter, M. A. (2006). Voltage-dependent currents in isolated vestibular afferent calyx terminals. *J. Neurophysiol.* 95, 26–32. doi: 10.1152/jn.00641.2005

Ruel, J., Wang, J., Dememes, D., Gobaille, S., Puel, J. L., and Rebillard, G. (2006). Dopamine transporter is essential for the maintenance of spontaneous activity of auditory nerve neurones and their responsiveness to sound stimulation. *J. Neurochem.* 97, 190–200. doi: 10.1111/j.1471-4159.2006.03722.x

Sun, W., and Salvi, R. J. (2001). Dopamine modulates sodium currents in cochlear spiral ganglion neurons. *Neuroreport* 12, 803–807. doi: 10.1097/00001756-200103260-00037

Toro, C., Trapani, J. G., Pacentine, I., Maeda, R., Sheets, L., Mo, W., et al. (2015). Dopamine modulates the activity of sensory hair cells. *J. Neurosci.* 35, 16494–16503. doi: 10.1523/jneurosci.1691-15.2015

Valdes-Baizabal, C., Soto, E., and Vega, R. (2015). Dopaminergic modulation of the voltage-gated sodium current in the cochlear afferent neurons of the rat. *PLoS One* 10:e0120808. doi: 10.1371/journal.pone.0120808

Ventura, C. M., and Kalluri, R. (2019). Enhanced activation of HCN channels reduces excitability and spike-timing regularity in maturing vestibular afferent neurons. *J. Neurosci.* 39, 2860–2876. doi: 10.1523/jneurosci.1811-18.2019

Warr, W. B., and Guinan, J. J. Jr. (1979). Efferent innervation of the organ of corti: two separate systems. *Brain Res.* 173, 152–155. doi: 10.1016/0006-8993(79)91104-1

Wersall, J. (1956). Studies on the structure and innervation of the sensory epithelium of the cristae ampulares in the guinea pig; a light and electron microscopic investigation. *Acta Otolaryngol. Suppl.* 126, 1–85.

Wu, J. S., Yi, E., Manca, M., Javaid, H., Lauer, A. M., and Glowatzki, E. (2020). Sound exposure dynamically induces dopamine synthesis in cholinergic LOC efferents for feedback to auditory nerve fibers. *eLife* 9:e52419.

Yi, E., Roux, I., and Glowatzki, E. (2010). Dendritic HCN channels shape excitatory postsynaptic potentials at the inner hair cell afferent synapse in the mammalian cochlea. *J. Neurophysiol.* 103, 2532–2543. doi: 10.1152/jn.00506.2009

Zhang, M., Vollmer, C., and Nurse, C. A. (2018). Adenosine and dopamine oppositely modulate a hyperpolarization-activated current Ih in chemosensory neurons of the rat carotid body in co-culture. *J. Physiol.* 596, 3101–3117. doi: 10.1113/jp274743

Conflict of Interest: The authors declare that the research was conducted in the absence of any commercial or financial relationships that could be construed as a potential conflict of interest.

frontiers in Neuroscience

ERRATUM
published: 15 March 2022
doi: 10.3389/fnins.2022.866989

Erratum: Dopaminergic Inhibition of Na^+ Currents in Vestibular Inner Ear Afferents

*Frontiers Production Office**

Frontiers Media SA, Lausanne, Switzerland

Keywords: calyx, semicircular canal, crista, hair cell, sodium channel

OPEN ACCESS

Approved by:
Frontiers Editorial Office, Frontiers Media SA, Switzerland

***Correspondence:**
Frontiers Production Office
production.office@frontiersin.org

Specialty section:
This article was submitted to Perception Science, a section of the journal Frontiers in Neuroscience

Received: *31 January 2022*
Accepted: *31 January 2022*
Published: *15 March 2022*

Citation:
Frontiers Production Office (2022) Erratum: Dopaminergic Inhibition of Na^+ Currents in Vestibular Inner Ear Afferents. Front. Neurosci. 16:866989. doi: 10.3389/fnins.2022.866989

An Erratum on

Dopaminergic Inhibition of Na^+ Currents in Vestibular Inner Ear Afferents
by Meredith, F. L., and Rennie, K. J. (2021). Front. Neurosci. 15:710321. doi: 10.3389/fnins.2021.710321

Due to an editorial mistake, the acknowledgment for the participation of a third reviewer is missing. The acknowledgment is the following: 'Selina Baeza-Loya, University of Chicago, United States, in collaboration with reviewer RE'. The publisher apologizes for this mistake.

The original article has been updated.

frontiers in Neuroscience

REVIEW
published: 27 September 2021
doi: 10.3389/fnins.2021.695914

A Reversal in Hair Cell Orientation Organizes Both the Auditory and Vestibular Organs

Basile Tarchini[1,2,3]*

[1] The Jackson Laboratory, Bar Harbor, ME, United States, [2] Department of Medicine, Tufts University, Boston, MA, United States, [3] Graduate School of Biomedical Science and Engineering (GSBSE), University of Maine, Orono, ME, United States

Sensory hair cells detect mechanical stimuli with their hair bundle, an asymmetrical brush of actin-based membrane protrusions, or stereocilia. At the single cell level, stereocilia are organized in rows of graded heights that confer the hair bundle with intrinsic directional sensitivity. At the organ level, each hair cell is precisely oriented so that its intrinsic directional sensitivity matches the direction of mechanical stimuli reaching the sensory epithelium. Coordinated orientation among neighboring hair cells usually ensures the delivery of a coherent local group response. Accordingly, hair cell orientation is locally uniform in the auditory and vestibular cristae epithelia in birds and mammals. However, an exception to this rule is found in the vestibular macular organs, and in fish lateral line neuromasts, where two hair cell populations show opposing orientations. This mirror-image hair cell organization confers bidirectional sensitivity at the organ level. Here I review our current understanding of the molecular machinery that produces mirror-image organization through a regional reversal of hair cell orientation. Interestingly, recent evidence suggests that auditory hair cells adopt their normal uniform orientation through a global reversal mechanism similar to the one at work regionally in macular and neuromast organs. Macular and auditory organs thus appear to be patterned more similarly than previously appreciated during inner ear development.

Keywords: cell polarity, hair cell, otolith organ, cochlea, neuromast, stereocilia bundle, hearing, balance

OPEN ACCESS

Edited by:
Gwenaelle S. G. Geleoc, Boston Children's Hospital and Harvard Medical School, United States

Reviewed by:
Paola Perin, University of Pavia, Italy
Hernan Lopez-Schier, Helmholtz Zentrum München, Helmholtz-Gemeinschaft Deutscher Forschungszentren (HZ), Germany

***Correspondence:**
Basile Tarchini
basile.tarchini@jax.org

Specialty section:
This article was submitted to Perception Science, a section of the journal Frontiers in Neuroscience

Received: *15 April 2021*
Accepted: *03 September 2021*
Published: *27 September 2021*

Citation:
Tarchini B (2021) A Reversal in Hair Cell Orientation Organizes Both the Auditory and Vestibular Organs. Front. Neurosci. 15:695914. doi: 10.3389/fnins.2021.695914

INTRODUCTION

The reception and transmission of mechanical stimuli by sensory hair cells (HCs) underlies the ability to hear and to perceive self and environmental motions. Mechanical stimuli range from sound waves in the auditory organ [the cochlea (Schwander et al., 2010)], to head movements and gravity in the balance organs [the vestibular system (Eatock and Songer, 2011)], to water movements in the lateral line system of fish and amphibians (Chitnis et al., 2012). The transduction of physical movements into biological signals occurs in the hair bundle, a critical apical compartment common to all HC types (McGrath et al., 2017; Velez-Ortega and Frolenkov, 2019). Depending on organ type and HC location within the organ, hair bundles differ in the number, dimensions and organization of their individual membrane protrusions, or stereocilia

(Barr-Gillespie, 2015). However, hair bundles conform to some fundamental shared principles. Their stereocilia are supported by an F-actin paracrystal core and are always aligned in multiple rows of graded heights. This slanted, asymmetrical architecture is integral to the directional response of the hair bundle: only deflections of the hair bundle toward the tallest row produce optimal tension on tip links connecting rows of different heights (**Figure 1A**). In turn, this tension favorably influences the opening probability of ion channels located at the lower end of each tip link (Qiu and Muller, 2018; Zheng and Holt, 2021). The influx of ions in stereocilia generates a receptor potential which leads to the depolarization of the HC.

ESTABLISHING AND ORIENTING AN ASYMMETRICAL CYTOSKELETON: TWO DISTINCT POLARITY FEATURES SHARED BY ALL HAIR CELLS

At the single cell level, polarization starts as a break of cytoskeleton symmetry in young post-mitotic HCs. First, the roughly central basal body and the primary cilium it nucleates, termed the kinocilium, shift off-center (**Figure 1B**) (reviewed previously, see for example Deans, 2013; Tarchini and Lu, 2019; Montcouquiol and Kelley, 2020). Of note, the kinocilium is the only true, microtubule-based cilium in HCs. Via still unknown mechanisms, microvilli in the vicinity of the off-center basal body grow in diameter and height to become stable stereocilia. In mouse auditory HCs, stereocilia are corralled by the emergence and expansion of a smooth region of apical membrane between the shifted basal body and the lateral/abneural HC junction, the "bare zone" (**Figure 1B**). The bare zone and molecular links connecting central stereocilia to the kinocilium impart an asymmetrical V-shaped or semicircular edge to the forming hair bundle (**Figure 1B**). Stereocilia become precisely aligned, and the most lateral stereocilia abutting the bare zone grow into the tallest row. Under the apical surface, the hair bundle becomes supported by a pedestal of dense actin meshwork called the cuticular plate (**Figure 1B**). The cuticular plate is itself asymmetrical, as it accommodates the basal body on the bare zone side. Apical microtubules are asymmetrically distributed, because they are excluded and constrained to the basal body side by the cuticular plate. In summary, the hair bundle and external structures like the basal body, cuticular plate and microtubules are intimately interconnected, and become globally planar-polarized. This polarization process occurs at the single cell level, and will confer the hair bundle with an intrinsic directional sensitivity.

The hair bundle can be compared to an antenna. Proper signal detection requires an antenna to be intrinsically sensitive to signal direction, but also to be oriented correctly relative to the source of the signal. A complicated aspect of early HC polarization is that the generation of an asymmetrical cytoskeleton, summarized above, implicitly defines an orientation for each HC at the organ level. Symmetry breaking occurs in a single cell as the kinocilium moves off-center, but the direction of this move at the organ level (i.e., toward the lateral edge of the auditory epithelium in cochlear HCs; **Figure 1C**) also provides the HC with its initial orientation. Establishing cytoskeleton asymmetry in single HCs and orienting the resulting structures at the tissue level may thus appear to be the same polarization process. However, several lines of evidence show that these are, in fact, distinct processes.

The first line of evidence is that HCs can be misoriented from their earliest stage of differentiation and still develop a normal hair bundle and apical cytoskeleton. This was documented in core planar cell polarity (PCP) mutants such as *Vangl2* and double *Fzd3,6* mutants (Montcouquiol et al., 2003; Wang et al., 2006; Song et al., 2010). Core PCP proteins form conserved apical junction complexes that are required for intercellular communication and uniform local cell orientation (Goodrich and Strutt, 2011; Singh and Mlodzik, 2012; Butler and Wallingford, 2017). The VANGL2 and FZD3,6 complexes antagonize and exclude each other inside a single HC or support cell, but they have high affinity for each other in the extracellular space, relaying polarity information across cell neighbors to coordinate their orientation. For example, FZD3,6 located medially in a HC interacts with VANGL2 located laterally in the adjacent support cell (**Figures 1A,B**). Core PCP and its role in patterning the inner ear has been reviewed extensively (see for example Deans, 2013; Tarchini and Lu, 2019; Montcouquiol and Kelley, 2020), and a companion article by Deans and colleagues in this issue provides a useful update. Two results in the core PCP field are particularly worth a mention here. First, core PCP information is already propagated across precursors of HC and support cells (Wang et al., 2005; Montcouquiol et al., 2006), and asymmetrical PCP complexes are observed prior to symmetry breaking in HCs (**Figure 1B**; Deans et al., 2007; Jones et al., 2008). Second, the aberrant position of the basal body following its early off-center shift in the *Vangl2* mutant HCs foretells the pattern of HC misorientation observed at later stages when the hair bundle is differentiated (Montcouquiol et al., 2003). The evidence thus suggests that core PCP proteins provide an early junctional framework throughout the sensory epithelium. This framework instructs the orientation of the early basal body shift in HCs, and by extension, the orientation of the whole HC apical cytoskeleton (**Figure 1B**). Of note, however, core PCP proteins are not required for the shift itself, only for defining its orientation.

A second line of evidence for distinct polarization processes establishing and orienting the asymmetrical cytoskeleton is that HCs with a severely dysmorphic apical cytoskeleton can adopt a largely normal orientation (as judged by the position of the basal body/kinocilium, for example). USHER1 proteins form transient fibrous links interconnecting emerging stereocilia, and the resulting loss of stereocilia cohesion in *Usher1* mutants can give rise to dramatically misshapen hair bundles that lack a distinct V-shape or graded stereocilia heights (Lefevre et al., 2008; Webb et al., 2011). Nevertheless, auditory HCs in *Usher1* mutants are overall oriented laterally based on the position of other apical cytoskeletal elements. It is important to note, however, that misplaced stereocilia will disrupt the precise positioning of physically linked cytoskeletal elements, for example the kinocilium and its associated basal body (Webb et al., 2011).

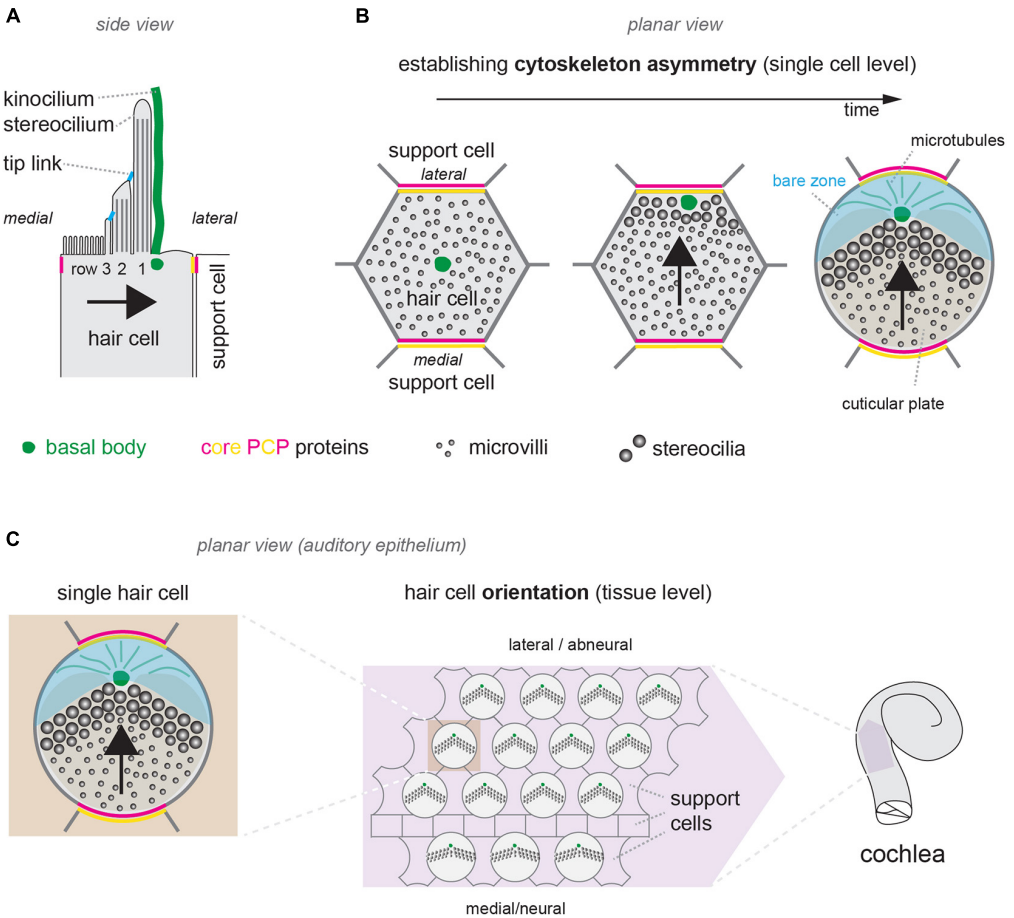

FIGURE 1 | Cytoskeleton asymmetry in single hair cells and hair cell orientation at the tissue level. **(A)** Diagram of the apical surface of a single mouse neonate auditory HC (IHC). Cytoskeleton asymmetry in this side view includes stereocilia with graded heights by row, with the tallest row 1 on the side of the off-center basal body that nucleates the kinocilium (green). **(B)** Planar (en-face) view illustrating symmetry breaking and cytoskeleton asymmetry in a single developing auditory HC during late embryogenesis. The basal body (green) shifts off-center toward the lateral HC junction. Microvilli on the side of the off-center basal body grow in diameter and height to become stereocilia and form the hair bundle. With time, a bare zone deprived of microvilli (blue) emerges between the basal body and the lateral HC junction. In panels **(A,B)** segregation of the two distinct core PCP complexes in single HCs and their juxtaposition at the apical HC-support cell junctions are represented in magenta and yellow (see main text). **(C)** Diagram showing the orientation of auditory HCs in the sensory epithelium around birth. Each HC orients its planar-asymmetric apical cytoskeleton so that the off-center basal body (green) and V-shaped hair bundle point toward the lateral (abneural) side of the auditory epithelium. In all panels, arrows indicate HC orientation based on the position of the basal body/kinocilium, the shape of the hair bundle and other planar-asymmetric cytoskeletal elements.

Although the resulting apical HC defects have frequently been described as HC misorientation (PCP phenotype), the low magnitude of the purported misorientation in comparison to core PCP phenotypes suggests otherwise. In other words, defective morphogenesis in single HCs may be sufficient to account for their mild apparent "misorientation." This conclusion is supported by multiple observations of mildly mispositioned stereocilia or kinocilium when cell adhesion (for example Fukuda et al., 2014) or cell fate determination (for example Kiernan et al., 2005; Zhang et al., 2017) is altered. In these cases, disruptions in the orderly mosaic between HCs and support cells alter junctional tension and might indirectly cause stereocilia and kinocilium mispositioning in HCs.

Another example is provided by a protein complex that forms the bare zone: the inhibitory G proteins (Gαi1-3), the scaffolding protein GPSM2 and the adaptor INSC. Unlike USHER1 proteins, Gαi-GPSM2-INSC is planar-polarized, and occupies the HC apical membrane but not the apical HC junction with neighboring support cells, where core PCP proteins reside (**Figure 1B**). Loss of Gαi3, GPSM2 or INSC variably disrupts stereocilia positioning while also upsetting the position of the basal body/kinocilium, as in *Usher1* mutants. However, auditory HCs also maintain a generally lateral orientation in *Gαi3*, *Gpsm2* or *Insc* mutants (Ezan et al., 2013; Tarchini et al., 2013; Bhonker et al., 2016).

Finally, evidence that distinct polarization processes establish and orient the asymmetrical cytoskeleton was also obtained at later stages of HC differentiation. While the apical cytoskeleton maintains its asymmetry in maturing HCs, HC orientation is not strictly fixed in time. First, following the early off-center

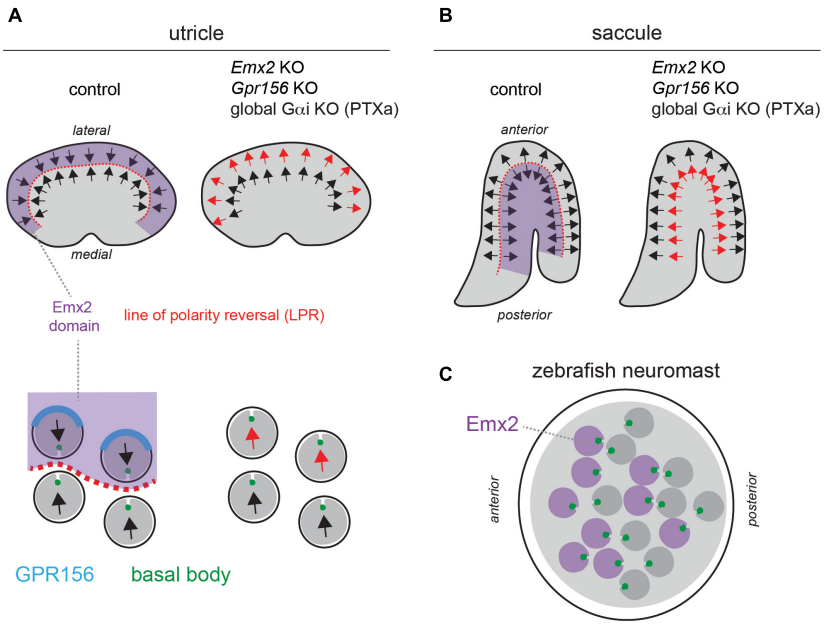

FIGURE 2 | A reversal in hair cell orientation occurs in the macular organs of the vestibular system and in fish neuromasts. **(A,B)** Diagram of HC orientation (arrows) and *Emx2* regional expression (purple) in the mouse utricular **(A)** and saccular **(B)** maculae. A regional reversal in HC orientation in the *Emx2*-positive lateral utricle **(A)** and posterior saccule **(B)** creates a mirror-image organization at the organ level. This organization is lost in *Emx2* and *Gpr156* mutants, as well as upon Pertussis toxin (PTXa) expression. The bottom diagrams in panel **(A)** (utricle) show polarized enrichment of GPR156 (blue) at the lateral HC junction in *Emx2*-positive HCs above the line of polarity reversal (LPR, red), but not in *Emx2*-negative HCs below the LPR. **(C)** Diagram of an anterior-posterior neuromast in the larval zebrafish posterior lateral line. HCs expressing *emx2* are indicated in purple. In all panels, arrows indicate HC orientation based on the position of the basal body/kinocilium (green), the shape of the hair bundle and other planar-asymmetric cytoskeletal elements.

shift of the basal body, HC orientation is refined and becomes more precisely lateral in the cochlea with time (Dabdoub et al., 2003). Second, severe auditory HC misorientation in *Vangl2* and *Fzd3,6* mutants is corrected to a large extent after birth by a still unknown mechanism independent from core PCP (Copley et al., 2013; Nemelka et al., 2020, PS#897). Just as the orientation of an antenna can be adjusted to better capture external signals, the entire HC apical cytoskeleton is rotated during orientation correction, including the hair bundle and external structures. It remains unclear whether the whole HC (including its baso-lateral plasma membrane) is rotated, or only surface structures past the apical junctions.

A REGIONAL REVERSAL IN HAIR CELL ORIENTATION PRODUCES MIRROR-IMAGE ANATOMY IN MACULAR AND NEUROMAST ORGANS

Establishing an asymmetrical cytoskeleton and defining its orientation across neighboring HCs describes the polarization process in avian and mammalian auditory epithelia and in semicircular canal cristae, where HCs detect angular acceleration. However, these mechanisms do not account for an intriguing conserved feature in macular (otolith) organs detecting linear acceleration and gravity, and in fish neuromasts sensing water movements. In maculae and neuromasts, HCs are sorted into two populations with opposing orientations (Flock and Wersall, 1962; Flock, 1964; Lindeman, 1969). HC orientation in the maculae varies across the organ in order to capture head movements in a range of orientations within an approximately horizontal (utricle) or vertical (saccule) plane (**Figures 2A,B**). However, this gradual change is distinct from an abrupt change in HC orientation that is observed across a virtual line of polarity reversal (LPR; **Figures 2A,B**; Li et al., 2008). In fish neuromasts, progenitors undergo a final division and sibling HCs acquire opposing orientations (Lopez-Schier et al., 2004; Chitnis et al., 2012). As a result, neuromasts have two equal populations of HCs with mirror-image orientations, but there is no continuous LPR (**Figure 2C**).

Mirror-image organization implies that opposing HCs in the same organ produce opposite responses to the same stimulus: HC depolarization and increased afferent spike rate on one side, and HC hyperpolarization and decreased spike rate on the other side (Harada et al., 1984; Lu et al., 1998; Lu and Popper, 2001). Mirror-image HC organization endows each neuromast with bidirectional sensitivity to detect predators and prey, for rheotaxis and for schooling behavior (Lopez-Schier et al., 2004; Ghysen and Dambly-Chaudiere, 2007; Chitnis et al., 2012). In contrast, the role of mirror-image HC organization in macular organs remains uncertain. It may complement the incomplete range of HC orientation on either side of the LPR to achieve 360° sensitivity, and/or be a strategy to enhance evoked activity in downstream neurons by combining positive and negative signals.

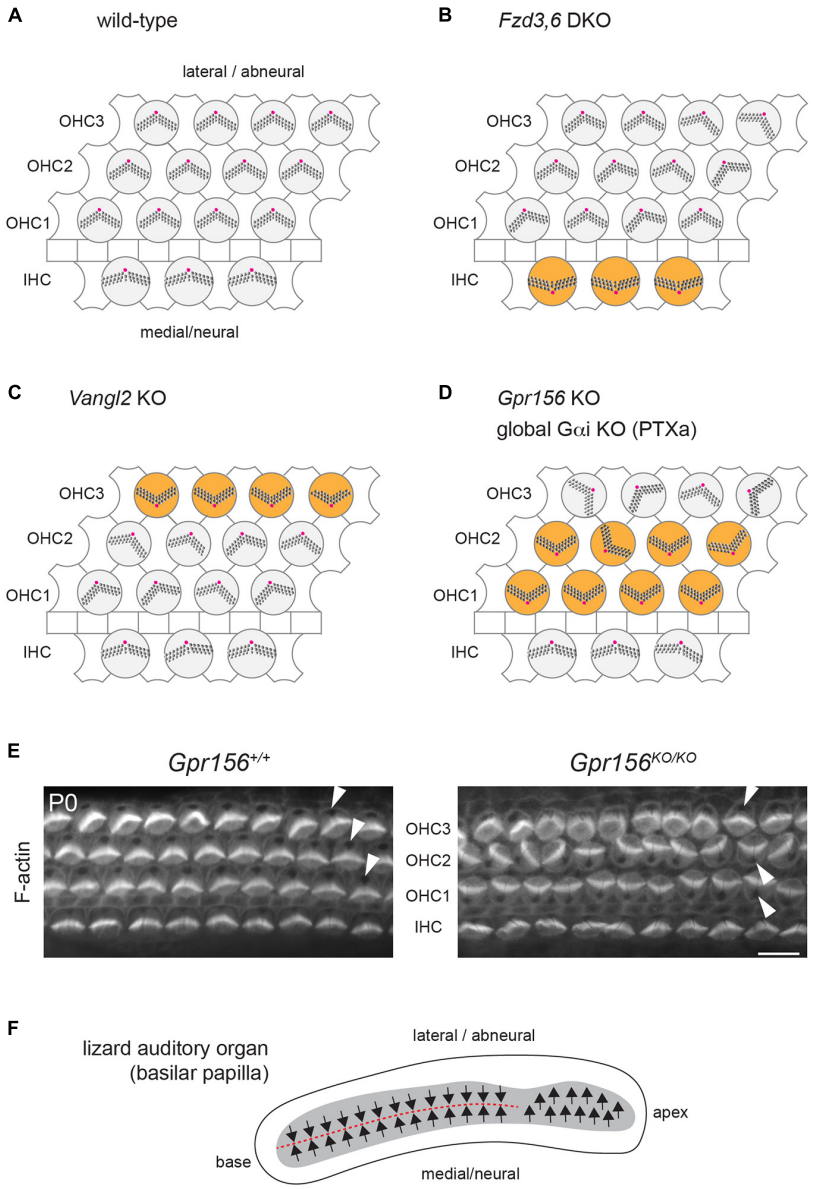

FIGURE 3 | Cellular organization and hair cell orientation in the auditory epithelium of the mouse and oriental garden lizard. **(A–D)** Diagrams of the auditory epithelium in mouse neonates in a wild-type **(A)** or in mutant **(B–D)** cochleae. The off-center basal body located at the vertex of a V-shaped (outer HC, OHC) or semi-circular (inner HC, IHC) hair bundle is indicated in magenta. Note how different HC subtypes are inverted in orientation (orange) in different mutants: IHCs in *Fzd3,6* double mutants (DKO) (Wang et al., 2006), OHC3 in *Vangl2* mutants (KO) (Yin et al., 2012; Copley et al., 2013) and OHC1-2 in *Gpr156* mutants as well as upon Pertussis toxin (PTXa) expression (Kindt et al., 2021). **(E)** Conjugated phalloidin labeling of the mouse auditory epithelium at birth (P0) to reveal F-actin. F-actin is concentrated in the asymmetrical hair bundle, revealing HC orientation along with the absence of signal at the off-center basal body (arrowheads). Note how OHC1-2 are inverted in their orientation in *Gpr156* mutants. Scale bar is 10 μm. **(F)** Diagram of the basilar papilla in the oriental garden lizard after (Bagger-Sjoback and Wersall, 1973). Arrows indicate HC orientation, and the red dashed line indicates the line of polarity reversal. Note how the base of the papilla shows mirror-image HC organization reminiscent of normal macular organs and zebrafish neuromasts (**Figures 2A–C**), and similar to IHC and OHC1-2 orientation in *Gpr156* mouse mutants **(D,E)**.

A critical observation is that the pattern of core PCP protein enrichment is unchanged across the LPR in the macular organs, and thus cannot by itself instruct a reversal in HC orientation in one half of the organ (Deans et al., 2007; Jones et al., 2014). Zebrafish neuromasts similarly show uniform enrichment of core PCP proteins regardless of HC orientation (Mirkovic et al., 2012). This led to the conclusion that asymmetric PCP cues at apical junctions likely act as a framework that can be independently interpreted by other factors in HCs (Deans et al., 2007). Such factors would consequently differ across the LPR, or be limited to one side.

One obvious candidate emerged from studies investigating the gene mutated in the deaf mouse mutant *Pardon*, the homeobox transcription factor *Emx2* (Rhodes et al., 2003). Interestingly,

Emx2 loss-of-function abolishes mirror-image organization and the LPR in macular organs without affecting locally coordinated HC orientation, or the gradual change in HC orientation along the organ (**Figures 2A,B**; Holley et al., 2010). Relatedly, inactivating *emx2* in zebrafish produces neuromasts where a normal number of HCs all adopt the same orientation, leading to unidirectional sensitivity (Jiang et al., 2017).

Regional *Emx2* transcription can fully explain the loss of mirror-image HC organization in the vestibular system and in neuromasts in *Emx2* mutants. In the mouse maculae, *Emx2* transcripts are limited to the lateral utricle and posterior saccule, the specific regions where HCs are flipped by 180° in the mutants (**Figures 2A,B**). Therefore, *Emx2* normally functions to reverse HC orientation there compared to the rest of the macula, creating the LPR (Jiang et al., 2017). *Emx2* regional specificity to one side of the LPR is conserved in the macular organs of the chicken (Jiang et al., 2017). In neuromasts, *emx2* expression is similarly regional and limited to HCs that are flipped in the mutant: HCs that detect anterior (A) > posterior (P) flow in A-P neuromasts, and HCs that detect dorsal (D) > ventral (V) flow in D-V neuromasts (**Figure 2C**; Jiang et al., 2017). Remarkably, forcing *Emx2* expression in all macular or neuromast HCs prompts HCs that normally do not express *Emx2* to reverse their orientation (Jiang et al., 2017). This gain-of-function produces an organ where all HCs adopt a uniform orientation that is opposite from what is observed upon *Emx2* loss-of-function. In summary, *Emx2* is necessary and sufficient to reverse a ground state of HC orientation by 180°.

Logically, *Emx2* expression is absent in the cristae of the semicircular canals that do not harbor mirror-image HC organization (Holley et al., 2010; Jiang et al., 2017). Accordingly, HC orientation is unaltered in *Emx2* mutant cristae (Holley et al., 2010; Jiang et al., 2017).

Together, these regional expression patterns and phenotypes suggest that EMX2 effectors in HCs, perhaps as direct transcriptional target(s), reverse the interpretation of invariant core PCP cues at cell-cell junctions. At early stages, this could reverse the orientation of the basal body shift, which in turn would reverse the orientation of the whole asymmetrical HC cytoskeleton. Support for a reversed shift of the basal body across the LPR was indeed obtained using live-imaging of explanted utricles (Tona and Wu, 2020). Of note, these studies collectively demonstrate that HC orientation is not only regulated by intercellular mechanisms acting at the tissue level (core PCP), but also by a mechanism acting at the single cell level (Emx2-triggered reversal). Distinct HC-instrinsic mechanisms thus influence symmetry breaking (establishing cytoskeleton asymmetry) as well as HC orientation.

In zebrafish neuromasts, uniformly blocking or over-activating Notch signaling also biases HCs toward one orientation (Mirkovic et al., 2012; Dow et al., 2018), in addition to disturbing the production of new HCs from support cells (Haddon et al., 1998; Wibowo et al., 2011). The most recent evidence suggests that Notch-mediated lateral inhibition influences mirror-image HC organization in part by influencing *emx2* expression (Jacobo et al., 2019; Kozak et al., 2020).

Interestingly, *Emx2* is transcribed throughout the auditory epithelium in mouse (Holley et al., 2010; Jiang et al., 2017). A specific role for *Emx2* in auditory HC orientation is difficult to evaluate, however, because constitutive *Emx2* mutants lack outer HCs (OHCs). Inner HC (IHCs) are severely misaligned (Holley et al., 2010), and improper contacts with support cell neighbors may explain their imprecise orientation in *Emx2* mutants (Holley et al., 2010).

A GLOBAL REVERSAL IN HAIR CELL ORIENTATION UNEXPECTEDLY SHAPES THE AUDITORY ORGAN

The auditory epithelium in mammals and birds does not include mirror-image HC organization, and both IHCs and OHCs ("tall" and "short" HCs in the bird basilar papilla) are similarly oriented toward the lateral, or abneural, side of the organ (**Figures 1C**, **3A**). Intriguingly, however, several mouse mutants have presented with a relatively precise inversion of a subset of HCs: IHCs in constitutive *Fzd3,6* double inactivation (Wang et al., 2006) and the third row of OHCs (OHC3) in *Vangl2* inactivation (Yin et al., 2012; Copley et al., 2013; **Figures 3B,C**).

These results are somewhat surprising because FZD3,6 and VANGL2 are transmembrane members of the core PCP family, and core PCP mutants in other systems tend to show randomization, and not inversion, of cell orientation. Randomization is expected, as core PCP proteins are generally dependent on one another for their asymmetric enrichment. A collapse of the communication system at cell-cell junctions is not expected to preserve the axis of polarity and only invert cell orientation along that axis, as reported in *Fzd3,6* and *Vangl2* mutants (the medio-lateral, or radial axis in the cochlea).

An inversion of the complementary HC types, OHC1 and OHC2, was reported in cochlear explants incubated with Pertussis toxin (Ezan et al., 2013) and in mouse models where the Pertussis toxin catalytic subunit (PTXa) is expressed in HCs *in vivo* (Tarchini et al., 2013; Tarchini et al., 2016; **Figure 3D**). Although these results suggest that G protein signaling inhibited by PTXa could be involved in HC orientation, they are equally difficult to interpret in isolation. First, using a bacterial toxin to downregulate functionally redundant Gαi proteins in developing HCs might produce non-physiological outcomes. Second, Gαi has other roles that are well established during HC differentiation. Gαi associates with the scaffolding regulator GPSM2 to form an atypical Gαi(GDP)-GPSM2 polarity complex that notably influences the orientation of the mitotic spindle in dividing progenitors (di Pietro et al., 2016). In post-mitotic HCs, Gαi and GPSM2 regulate cytoskeleton planar asymmetry at the bare zone, as mentioned previously (**Figure 1B**), and later promote stereocilia elongation with the MYO15A complex (Tarchini et al., 2016; Mauriac et al., 2017; Beer-Hammer et al., 2018; Tadenev et al., 2019).

Inactivation of the Gαi-GPSM2 complex at the bare zone is unlikely to explain the inversion of OHC1-2s observed with Pertussis toxin. First, unlike PTXa models, *Gpsm2* mutants do not show inverted OHC1-2s (Ezan et al., 2013; Tarchini et al.,

2013; Bhonker et al., 2016). Second, polarized enrichment of Gαi at the apical membrane is unaffected and remains in register with the apical HC cytoskeleton in *Emx2* mutants both in macular (Jiang et al., 2017) and in zebrafish neuromast HCs (Jacobo et al., 2019). Reasoning that Gαi might play multiple roles in developing HCs, we embarked on a quest to identify alternative Gαi regulators that would strictly influence HC orientation, and not cytoskeleton morphogenesis. As Gαi is a member of the heterotrimeric Gαiβγ complex best characterized to relay GPCR signaling, we focused in particular on GPCRs highly expressed during HC differentiation. The orphan class C (glutamate) GPCR GPR156 proved to be an important missing link for auditory, vestibular and neuromast HC orientation.

In the mouse auditory epithelium, constitutive *Gpr156* mutants fully recapitulate OHC1-2 inversion observed with PTXa (**Figures 3D,E**), validating this defect as physiologically relevant (Kindt et al., 2021). In macular organs, *Gpr156* mutants phenocopy *Emx2* mutants, preventing EMX2-driven HC reversal in the lateral utricle and posterior saccule, and thus abolishing the LPR and mirror-image organization (**Figures 2A,B**). Finally, GPR156 function is highly conserved, as zebrafish *gpr156* mutants have largely unidirectional neuromasts where most HCs adopt the *emx2*-negative orientation (Kindt et al., 2021).

At the mechanistic level, unlike *Emx2*, *Gpr156* transcripts are not limited to the lateral utricle and the posterior saccule, but uniformly detected in all HCs in all inner ear sensory organs. Although *Gpr156* is thus not specifically transcribed by EMX2, EMX2 is necessary and sufficient to enrich and polarize the GPR156 protein at the apical HC junction. GPR156 is consistently detected at the junction opposite from the basal body in HCs from all organs and regions expressing *Emx2*: the auditory epithelium, the lateral utricle and the posterior saccule (**Figure 2A**). Additionally, the GPR156 protein is not enriched apically or polarized in HCs that do not express *Emx2*: HCs in the cristae, the medial utricle and the anterior saccule.

Genetic epistasis experiments also showed that EMX2 and GPR156 act upstream of Gαi. PTXa expression in macular organs leads to a partial or complete loss of regional HC reversal depending on the PTXa mouse strain used (Jiang et al., 2017; Kindt et al., 2021), a phenocopy of *Emx2* and *Gpr156* mutants (**Figures 2A,B**). PTXa can prevent forced HC reversal upon *Emx2* gain-of-function in the medial utricle, showing that Gαi functions downstream of EMX2 (Jiang et al., 2017). Furthermore, PTXa prevents EMX2-driven HC reversal without disturbing the polarized distribution of GPR156 (Kindt et al., 2021). This indicates that properly polarized GPR156 at the HC junction cannot trigger orientation reversal without Gαi function. In summary, an EMX2 > GPR156 > Gαi signaling cascade is required in HCs to trigger their reversal. GPR156 likely signals through heterotrimeric Gαiβγ proteins, as do metabotropic $GABA_B$ receptors that are the closest GPR156 homologs (Kaupmann et al., 1997; Kuner et al., 1999; Robbins et al., 2001).

The distribution of core PCP proteins in the mouse maculae is not affected upon *Emx2* loss- or gain-of-function (Jiang et al., 2017). Similarly, asymmetric Vangl2 enrichment is not affected in neuromast HCs in either *emx2* or *notch* zebrafish mutants (Jacobo et al., 2019). In reciprocal experiments, *emx2* expression remains limited to half the HCs in each neuromast in *vangl2* zebrafish mutants, as in controls (Ji et al., 2018). These results suggest that the EMX2-GPR156-Gαi reversal pathway acts in parallel to core PCP. This conclusion is also supported by normal FZD6 and VANGL2 enrichment in the auditory epithelium of *Gpr156* mutants when the HC-support cell mosaic is intact (Kindt et al., 2021). In a stark departure, however, GPR156 enrichment at the medial HC junction in auditory HCs is missing or altered in *Vangl2 Looptail* mutants (Kindt et al., 2021). This suggests that GPR156 might link the core PCP pathway that regulates cell orientation at cell-cell junctions and the *Emx2* pathway that triggers a reversal of the basal body shift in HCs. In that light, GPR156 might represent one of the inferred effectors that interpret invariant core PCP patterning to make a binary decision on orientation in macular HCs (Wang et al., 2006; Deans et al., 2007). *Emx2* expression polarizes GPR156-Gαi signaling, which in turn seems to prevent the basal body from sitting nearby and prompts it to shift away instead (**Figure 2A**). As GPR156 overlaps in part with FZD6 at the medial HC junction in the auditory epithelium (Kindt et al., 2021), adding GPR156 in the junctional complex may turn FZD3,6 into a repulsive rather than attractive cue for the basal body. Interestingly, FZD6 is proposed to be enriched laterally in utricular HCs (Deans et al., 2007), which means that the basal body shifts toward FZD6 in *Emx2*-negative HCs (medial utricle), but away from FZD6 in *Emx2*-positive HCs that co-enrich GPR156 with FZD6 (lateral utricle, auditory epithelium; **Figure 2A**).

Overall, an evolutionary hypothesis is emerging where *Emx2* expression in select sensory regions of the inner ear and the neuromast triggers a reversal of HC orientation compared to a ground state of orientation defined by the core PCP framework (Jiang et al., 2017). In the vestibular system, EMX2 creates mirror-image HC organization in the maculae, distinguishing these organs from the more ancestral cristae in terms of their polarization patterns. *Emx2* expression in the auditory epithelium may be a carry-over from its local expression in the maculae. Unexpectedly, it appears that the ground state of auditory HC orientation is toward the medial/neural side of the organ, and that different effectors were recruited to globally reverse HC orientation toward the lateral side in mammals and in birds; notably, core PCP proteins for the most peripheral HC types (IHC, OHC3) and GPR156-Gαi for internal HC types (OHC1-2).

Interestingly, the lizard auditory organ (basilar papilla) does not show uniform HC orientation toward the lateral/abneural edge. Instead, the basal region of the papilla has medial HCs with a lateral orientation (like IHCs in mammals and tall HCs in birds), but lateral HCs with a medial orientation (**Figure 3F**; Bagger-Sjoback and Wersall, 1973; Mulroy, 1974). Normal mirror-image auditory HC organization in lizards is reminiscent of opposing IHC and OHC1-2s in *Gpr156* and PTXa mouse mutants (**Figures 3D,E**). The auditory organ from lepidosaurs (including lizards), archosaurs (crocodile, birds) and mammals are believed to have evolved in parallel as a pinch-off from a vestibular organ (Manley, 2000). In contrast to mammals and

birds, it is possible that lizards do not have a basilar papilla fully derived from an *Emx2*-positive vestibular lineage. This may explain opposing HC orientations in lizards: specifically, lateral HCs at the papillar base might lack EMX2-GPR156-Gαi signaling and adopt a medial orientation, as mouse OHC1-2s do in the absence of *Gpr156* (**Figures 3D,E**).

SOME REMAINING QUESTIONS AND FUTURE DIRECTIONS

The link between core PCP and the EMX2-GPR156-Gαi pathway uncovered in *Vangl2 Looptail* mutants needs to be confirmed and explored further using alternative core PCP mutant models. In particular, it will be informative to test *Fzd3,6* mutants and probe for a physical interaction between FZD3,6 and GPR156 as these proteins occupy the same HC junction and are both GPCRs. Like GPR156 and FZD3,6, the adhesion GPCR CELSR1 is also enriched medially in auditory HCs, and is another core PCP candidate to interact with GPR156 (Duncan et al., 2017). Additionally, it remains unclear how, in the auditory epithelium at least, the core PCP proteins VANGL2 and FZD3,6 would both provide an early polarity framework throughout the sensory domain while also acting as effectors for orientation reversal in OHC3 (VANGL2) and IHC (FZD3,6). Perhaps different temporal roles, or different partners (late orientation reversal with GPR156?) can help explain this apparent dual activity.

It will be interesting to determine whether GPR156 activity, and thus HC reversal, depends on an agonist, possibly a secreted ligand or the extracellular domain of an integral protein in the adjacent support cell. In contrast, activation of GPR156 by EMX2 is more likely to result from polarized trafficking or polarized enrichment of the GPR156 receptor, which likely involves factors that remain to be identified. It is interesting to speculate that, unlike *Gpr156*, such factor(s) could be a direct transcriptional target of EMX2 that acts as a chaperone or binding partner to ensure that GPR156 is enriched at the apical junction and is planar polarized there. Alternatively, it is possible that EMX2 might prevent the expression of a factor that degrades GPR156 or somehow prevents GPR156 polarized enrichment. In any case, as originally predicted (Deans et al., 2007), such factor(s) would be regionally limited to one side of the LPR (*Emx2*-positive or *Emx2*-negative regions), providing an effective means to screen future candidates.

AUTHOR CONTRIBUTIONS

The author confirms being the sole contributor of this work and has approved it for publication.

FUNDING

BT was supported by the National Institute on Deafness and Other Communication Disorders (NIDCD) with R01s DC015242 and DC018304.

ACKNOWLEDGMENTS

I am very grateful to Elli Hartig and Dayana Krawchuk for their comments on the manuscript and editing advice.

REFERENCES

Bagger-Sjoback, D., and Wersall, J. (1973). The sensory hairs and tectorial membrane of the basilar papilla in the lizard *Calotes versicolor*. *J. Neurocytol.* 2, 329–350. doi: 10.1007/bf01104034

Barr-Gillespie, P. G. (2015). Assembly of hair bundles, an amazing problem for cell biology. *Mol. Biol. Cell* 26, 2727–2732. doi: 10.1091/mbc.e14-04-0940

Beer-Hammer, S., Lee, S. C., Mauriac, S. A., Leiss, V., Groh, I. A. M., Novakovic, A., et al. (2018). Galphai proteins are indispensable for hearing. *Cell. Physiol. Biochem.* 47, 1509–1532.

Bhonker, Y., Abu-Rayyan, A., Ushakov, K., Amir-Zilberstein, L., Shivatzki, S., Yizhar-Barnea, O., et al. (2016). The GPSM2/LGN GoLoco motifs are essential for hearing. *Mamm. Genome.* 27, 29–46. doi: 10.1007/s00335-015-9614-7

Butler, M. T., and Wallingford, J. B. (2017). Planar cell polarity in development and disease. *Nat. Rev. Mol. Cell Biol.* 18, 375–388.

Chitnis, A. B., Nogare, D. D., and Matsuda, M. (2012). Building the posterior lateral line system in zebrafish. *Dev. Neurobiol.* 72, 234–255. doi: 10.1002/dneu.20962

Copley, C. O., Duncan, J. S., Liu, C., Cheng, H., and Deans, M. R. (2013). Postnatal refinement of auditory hair cell planar polarity deficits occurs in the absence of Vangl2. *J. Neurosci.* 33, 14001–14016. doi: 10.1523/jneurosci.1307-13.2013

Dabdoub, A., Donohue, M. J., Brennan, A., Wolf, V., Montcouquiol, M., Sassoon, D. A., et al. (2003). Wnt signaling mediates reorientation of outer hair cell stereociliary bundles in the mammalian cochlea. *Development* 130, 2375–2384. doi: 10.1242/dev.00448

Deans, M. R. (2013). A balance of form and function: planar polarity and development of the vestibular maculae. *Semin. Cell Dev. Biol.* 24, 490–498. doi: 10.1016/j.semcdb.2013.03.001

Deans, M. R., Antic, D., Suyama, K., Scott, M. P., Axelrod, J. D., and Goodrich, L. V. (2007). Asymmetric distribution of prickle-like 2 reveals an early underlying polarization of vestibular sensory epithelia in the inner ear. *J. Neurosci.* 27, 3139–3147. doi: 10.1523/jneurosci.5151-06.2007

di Pietro, F., Echard, A., and Morin, X. (2016). Regulation of mitotic spindle orientation: an integrated view. *EMBO Rep.* 17, 1106–1130. doi: 10.15252/embr.201642292

Dow, E., Jacobo, A., Hossain, S., Siletti, K., and Hudspeth, A. J. (2018). Connectomics of the zebrafish's lateral-line neuromast reveals wiring and miswiring in a simple microcircuit. *Elife* 7:e33988.

Duncan, J. S., Stoller, M. L., Francl, A. F., Tissir, F., Devenport, D., and Deans, M. R. (2017). Celsr1 coordinates the planar polarity of vestibular hair cells during inner ear development. *Dev. Biol.* 423, 126–137. doi: 10.1016/j.ydbio.2017.01.020

Eatock, R. A., and Songer, J. E. (2011). Vestibular hair cells and afferents: two channels for head motion signals. *Annu. Rev. Neurosci.* 34, 501–534. doi: 10.1146/annurev-neuro-061010-113710

Ezan, J., Lasvaux, L., Gezer, A., Novakovic, A., May-Simera, H., Belotti, E., et al. (2013). Primary cilium migration depends on G-protein signalling control of subapical cytoskeleton. *Nat. Cell Biol.* 15, 1107–1115. doi: 10.1038/ncb2819

Flock, A. (1964). Structure of the macula utriculi with special reference to directional interplay of sensory responses as revealed by morphological polarization. *J. Cell Biol.* 22, 413–431. doi: 10.1083/jcb.22.2.413

Flock, A., and Wersall, J. (1962). A study of the orientation of the sensory hairs of the receptor cells in the lateral line organ of fish, with special reference to the function of the receptors. *J. Cell Biol.* 15, 19–27. doi: 10.1083/jcb.15.1.19

Fukuda, T., Kominami, K., Wang, S., Togashi, H., Hirata, K., Mizoguchi, A., et al. (2014). Aberrant cochlear hair cell attachments caused by Nectin-3 deficiency result in hair bundle abnormalities. *Development* 141, 399–409. doi: 10.1242/dev.094995

Ghysen, A., and Dambly-Chaudiere, C. (2007). The lateral line microcosmos. *Genes Dev.* 21, 2118–2130. doi: 10.1101/gad.1568407

Goodrich, L. V., and Strutt, D. (2011). Principles of planar polarity in animal development. *Development* 138, 1877–1892. doi: 10.1242/dev.054080

Haddon, C., Jiang, Y. J., Smithers, L., and Lewis, J. (1998). Delta-Notch signalling and the patterning of sensory cell differentiation in the zebrafish ear: evidence from the mind bomb mutant. *Development* 125, 4637–4644. doi: 10.1242/dev.125.23.4637

Harada, Y., Shirane, M., Tagashira, N., and Suzuki, M. (1984). Action potential of isolated frog utricle. *Acta Otolaryngol. Suppl.* 406, 143–148. doi: 10.3109/00016488309123023

Holley, M., Rhodes, C., Kneebone, A., Herde, M. K., Fleming, M., and Steel, K. P. (2010). Emx2 and early hair cell development in the mouse inner ear. *Dev. Biol.* 340, 547–556. doi: 10.1016/j.ydbio.2010.02.004

Jacobo, A., Dasgupta, A., Erzberger, A., Siletti, K., and Hudspeth, A. J. (2019). Notch-mediated determination of hair-bundle polarity in mechanosensory hair cells of the zebrafish lateral line. *Curr. Biol.* 29, 3579–3587.e7.

Ji, Y. R., Warrier, S., Jiang, T., Wu, D. K., and Kindt, K. S. (2018). Directional selectivity of afferent neurons in zebrafish neuromasts is regulated by Emx2 in presynaptic hair cells. *Elife* 7:e35796.

Jiang, T., Kindt, K., and Wu, D. K. (2017). Transcription factor Emx2 controls stereociliary bundle orientation of sensory hair cells. *Elife* 6:e23661.

Jones, C., Qian, D., Kim, S. M., Li, S., Ren, D., Knapp, L., et al. (2014). Ankrd6 is a mammalian functional homolog of *Drosophila* planar cell polarity gene diego and regulates coordinated cellular orientation in the mouse inner ear. *Dev. Biol.* 395, 62–72. doi: 10.1016/j.ydbio.2014.08.029

Jones, C., Roper, V. C., Foucher, I., Qian, D., Banizs, B., Petit, C., et al. (2008). Ciliary proteins link basal body polarization to planar cell polarity regulation. *Nat. Genet.* 40, 69–77. doi: 10.1038/ng.2007.54

Kaupmann, K., Huggel, K., Heid, J., Flor, P. J., Bischoff, S., Mickel, S. J., et al. (1997). Expression cloning of GABA(B) receptors uncovers similarity to metabotropic glutamate receptors. *Nature* 386, 239–246. doi: 10.1038/386239a0

Kiernan, A. E., Cordes, R., Kopan, R., Gossler, A., and Gridley, T. (2005). The Notch ligands DLL1 and JAG2 act synergistically to regulate hair cell development in the mammalian inner ear. *Development* 132, 4353–4362.

Kindt, K. S., Akturk, A., Jarysta, A., Day, M., Beirl, A., Flonard, M., et al. (2021). EMX2-GPR156-Galphai reverses hair cell orientation in mechanosensory epithelia. *Nat. Commun.* 12:2861.

Kozak, E. L., Palit, S., Miranda-Rodriguez, J. R., Janjic, A., Bottcher, A., Lickert, H., et al. (2020). Epithelial planar bipolarity emerges from notch-mediated asymmetric inhibition of Emx2. *Curr. Biol.* 30, 1142–1151.e6.

Kuner, R., Kohr, G., Grunewald, S., Eisenhardt, G., Bach, A., and Kornau, H. C. (1999). Role of heteromer formation in GABAB receptor function. *Science* 283, 74–77.

Lefevre, G., Michel, V., Weil, D., Lepelletier, L., Bizard, E., Wolfrum, U., et al. (2008). A core cochlear phenotype in USH1 mouse mutants implicates fibrous links of the hair bundle in its cohesion, orientation and differential growth. *Development* 135, 1427–1437.

Li, A., Xue, J., and Peterson, E. H. (2008). Architecture of the mouse utricle: macular organization and hair bundle heights. *J. Neurophysiol.* 99, 718–733.

Lindeman, H. H. (1969). Regional differences in structure of the vestibular sensory regions. *J. Laryngol. Otol.* 83, 1–17.

Lopez-Schier, H., Starr, C. J., Kappler, J. A., Kollmar, R., and Hudspeth, A. J. (2004). Directional cell migration establishes the axes of planar polarity in the posterior lateral-line organ of the zebrafish. *Dev. Cell* 7, 401–412.

Lu, Z., and Popper, A. N. (2001). Neural response directionality correlates of hair cell orientation in a teleost fish. *J. Comp. Physiol. A* 187, 453–465.

Lu, Z., Song, J., and Popper, A. N. (1998). Encoding of acoustic directional information by saccular afferents of the sleeper goby, *Dormitator latifrons*. *J. Comp. Physiol. A* 182, 805–815.

Manley, G. A. (2000). Cochlear mechanisms from a phylogenetic viewpoint. *Proc. Natl. Acad. Sci. U.S.A.* 97, 11736–11743. doi: 10.1073/pnas.97.22.11736

Mauriac, S. A., Hien, Y. E., Bird, J. E., Carvalho, S. D., Peyroutou, R., Lee, S. C., et al. (2017). Defective Gpsm2/Galphai3 signalling disrupts stereocilia development and growth cone actin dynamics in Chudley-McCullough syndrome. *Nat. Commun.* 8:14907. doi: 10.1038/ncomms14907

McGrath, J., Roy, P., and Perrin, B. J. (2017). Stereocilia morphogenesis and maintenance through regulation of actin stability. *Semin. Cell Dev. Biol.* 65, 88–95. doi: 10.1016/j.semcdb.2016.08.017

Mirkovic, I., Pylawka, S., and Hudspeth, A. J. (2012). Rearrangements between differentiating hair cells coordinate planar polarity and the establishment of mirror symmetry in lateral-line neuromasts. *Biol. Open* 1, 498–505. doi: 10.1242/bio.2012570

Montcouquiol, M., and Kelley, M. W. (2020). Development and patterning of the cochlea: from convergent extension to planar polarity. *Cold Spring. Harb. Perspect. Med.* 10:a033266. doi: 10.1101/cshperspect.a033266

Montcouquiol, M., Rachel, R. A., Lanford, P. J., Copeland, N. G., Jenkins, N. A., and Kelley, M. W. (2003). Identification of Vangl2 and Scrb1 as planar polarity genes in mammals. *Nature* 423, 173–177. doi: 10.1038/nature01618

Montcouquiol, M., Sans, N., Huss, D., Kach, J., Dickman, J. D., Forge, A., et al. (2006). Asymmetric localization of Vangl2 and Fz3 indicate novel mechanisms for planar cell polarity in mammals. *J. Neurosci.* 26, 5265–5275. doi: 10.1523/JNEUROSCI.4680-05.2006

Mulroy, M. J. (1974). Cochlear anatomy of the alligator lizard. *Brain Behav. Evol.* 10, 69–87. doi: 10.1159/000124303

Nemelka, J., Park, S., and Deans, M. (2020). "Stereociliary Bundle Reorientation in the Absence of PCP Signaling and Proper Tectorial Membrane Development" in *Poster at the Mid-winter meeting of the Association for Research in Otolaryngology (ARO)*, New Jersey.

Qiu, X., and Muller, U. (2018). Mechanically gated ion channels in mammalian hair cells. *Front. Cell. Neurosci.* 12:100. doi: 10.3389/fncel.2018.00100

Rhodes, C. R., Parkinson, N., Tsai, H., Brooker, D., Mansell, S., Spurr, N., et al. (2003). The homeobox gene Emx2 underlies middle ear and inner ear defects in the deaf mouse mutant pardon. *J. Neurocytol.* 32, 1143–1154. doi: 10.1023/B:NEUR.0000021908.98337.91

Robbins, M. J., Calver, A. R., Filippov, A. K., Hirst, W. D., Russell, R. B., Wood, M. D., et al. (2001). GABA(B2) is essential for g-protein coupling of the GABA(B) receptor heterodimer. *J. Neurosci.* 21, 8043–8052. doi: 10.1523/JNEUROSCI.21-20-08043.2001

Schwander, M., Kachar, B., and Muller, U. (2010). Review series: the cell biology of hearing. *J. Cell Biol.* 190, 9–20. doi: 10.1083/jcb.201001138

Singh, J., and Mlodzik, M. (2012). Planar cell polarity signaling: coordination of cellular orientation across tissues. *Wiley Interdiscip. Rev. Dev. Biol.* 1, 479–499. doi: 10.1002/wdev.32

Song, H., Hu, J., Chen, W., Elliott, G., Andre, P., Gao, B., et al. (2010). Planar cell polarity breaks bilateral symmetry by controlling ciliary positioning. *Nature* 466, 378–382. doi: 10.1038/nature09129

Tadenev, A. L. D., Akturk, A., Devanney, N., Mathur, P. D., Clark, A. M., Yang, J., et al. (2019). GPSM2-GNAI specifies the tallest stereocilia and defines hair bundle row identity. *Curr. Biol.* 29, 921–934.e4. doi: 10.1016/j.cub.2019.01.051

Tarchini, B., and Lu, X. (2019). New insights into regulation and function of planar polarity in the inner ear. *Neurosci. Lett.* 709:134373. doi: 10.1016/j.neulet.2019.134373

Tarchini, B., Jolicoeur, C., and Cayouette, M. (2013). A molecular blueprint at the apical surface establishes planar asymmetry in cochlear hair cells. *Dev. Cell* 27, 88–102. doi: 10.1016/j.devcel.2013.09.011

Tarchini, B., Tadenev, A. L., Devanney, N., and Cayouette, M. (2016). A link between planar polarity and staircase-like bundle architecture in hair cells. *Development* 143, 3926–3932. doi: 10.1242/dev.139089

Tona, Y., and Wu, D. K. (2020). Live imaging of hair bundle polarity acquisition demonstrates a critical timeline for transcription factor Emx2. *Elife* 9:e59282. doi: 10.7554/eLife.59282.sa2

Velez-Ortega, A. C., and Frolenkov, G. I. (2019). Building and repairing the stereocilia cytoskeleton in mammalian auditory hair cells. *Hear. Res.* 376, 47–57. doi: 10.1016/j.heares.2018.12.012

Wang, J., Mark, S., Zhang, X., Qian, D., Yoo, S. J., Radde-Gallwitz, K., et al. (2005). Regulation of polarized extension and planar cell polarity in the cochlea by the vertebrate PCP pathway. *Nat. Genet.* 37, 980–985. doi: 10.1038/ng1622

Wang, Y., Guo, N., and Nathans, J. (2006). The role of Frizzled3 and Frizzled6 in neural tube closure and in the planar polarity of inner-ear sensory hair cells. *J. Neurosci.* 26, 2147–2156. doi: 10.1523/JNEUROSCI.4698-05.2005

Webb, S. W., Grillet, N., Andrade, L. R., Xiong, W., Swarthout, L., Della Santina, C. C., et al. (2011). Regulation of PCDH15 function in mechanosensory hair cells by alternative splicing of the cytoplasmic domain. *Development* 138, 1607–1617. doi: 10.1242/dev.060061

Wibowo, I., Pinto-Teixeira, F., Satou, C., Higashijima, S., and Lopez-Schier, H. (2011). Compartmentalized Notch signaling sustains epithelial mirror symmetry. *Development* 138, 1143–1152. doi: 10.1242/dev.060566

Yin, H., Copley, C. O., Goodrich, L. V., and Deans, M. R. (2012). Comparison of phenotypes between different vangl2 mutants demonstrates dominant effects of the Looptail mutation during hair cell development. *PLoS One* 7:e31988. doi: 10.1371/journal.pone.0031988

Zhang, T., Xu, J., Maire, P., and Xu, P. X. (2017). Six1 is essential for differentiation and patterning of the mammalian auditory sensory epithelium. *PLoS Genet.* 13:e1006967. doi: 10.1371/journal.pgen.1006967

Zheng, W., and Holt, J. R. (2021). The mechanosensory transduction machinery in inner ear hair cells. *Annu. Rev. Biophys.* 50, 31–51. doi: doi: 10.1146/annurev-biophys-062420-081842

Conflict of Interest: The author declares that the research was conducted in the absence of any commercial or financial relationships that could be construed as a potential conflict of interest.

frontiers in Neuroscience

ORIGINAL RESEARCH
published: 12 October 2021
doi: 10.3389/fnins.2021.710275

Similarities in the Biophysical Properties of Spiral-Ganglion and Vestibular-Ganglion Neurons in Neonatal Rats

*Radha Kalluri**

Caruso Department of Otolaryngology-Head and Neck Surgery, Zilkha Neurogenetics Institute, Keck School of Medicine of University of Southern California, Los Angeles, CA, United States

The membranes of auditory and vestibular afferent neurons each contain diverse groups of ion channels that lead to heterogeneity in their intrinsic biophysical properties. Pioneering work in both auditory- and vestibular-ganglion physiology have individually examined this remarkable diversity, but there are few direct comparisons between the two ganglia. Here the firing patterns recorded by whole-cell patch-clamping in neonatal vestibular- and spiral ganglion neurons are compared. Indicative of an overall heterogeneity in ion channel composition, both ganglia exhibit qualitatively similar firing patterns ranging from sustained-spiking to transient-spiking in response to current injection. The range of resting potentials, voltage thresholds, current thresholds, input-resistances, and first-spike latencies are similarly broad in both ganglion groups. The covariance between several biophysical properties (e.g., resting potential to voltage threshold and their dependence on postnatal age) was similar between the two ganglia. Cell sizes were on average larger and more variable in VGN than in SGN. One sub-group of VGN stood out as having extra-large somata with transient-firing patterns, very low-input resistance, fast first-spike latencies, and required large current amplitudes to induce spiking. Despite these differences, the input resistance per unit area of the large-bodied transient neurons was like that of smaller-bodied transient-firing neurons in both VGN and SGN, thus appearing to be size-scaled versions of other transient-firing neurons. Our analysis reveals that although auditory and vestibular afferents serve very different functions in distinct sensory modalities, their biophysical properties are more closely related by firing pattern and cell size than by sensory modality.

Keywords: ion channels, voltage threshold, vestibular ganglion neurons, spiral ganglion neurons, firing patterns, current threshold, neuronal excitability, biophysical properties

OPEN ACCESS

Edited by:
Soroush G. Sadeghi,
University at Buffalo, United States

Reviewed by:
Sonja Pyott,
University Medical Center Groningen, Netherlands
Ruth Anne Eatock,
University of Chicago, United States
Selina Baeza-Loya,
University of Chicago, United States,
in collaboration with reviewer RE

***Correspondence:**
Radha Kalluri
radha@usc.edu

Specialty section:
This article was submitted to Perception Science, a section of the journal Frontiers in Neuroscience

Received: *15 May 2021*
Accepted: *07 September 2021*
Published: *12 October 2021*

Citation:
Kalluri R (2021) Similarities in the Biophysical Properties of Spiral-Ganglion and Vestibular-Ganglion Neurons in Neonatal Rats. Front. Neurosci. 15:710275. doi: 10.3389/fnins.2021.710275

INTRODUCTION

Auditory and vestibular afferents are bipolar neurons that receive, filter, and transmit information from the sensory epithelium to the brainstem. In both systems, the afferents are each comprised of functionally distinct neuronal sub-groups that convey different qualities of sensory information to the brainstem (e.g., rapid and slow head movements in the vestibular system; or sound intensity in

the auditory system). Previous work in auditory and vestibular physiology classified neuronal sub-groups by their dendritic morphology, synaptic specializations, and patterns of connectivity with hair cells to account for these parallel information pathways.

When considered across the two systems, inner-ear afferents are remarkably diverse in dendritic and terminal morphologies (**Figure 1**). Some vestibular afferents make spatially compact connections by forming giant cup-like (calyx) terminals around the entire basal pole of one or more hair cells, while others form large spatially extended dendritic arbors that contact hundreds of hair cells with varying combinations of calyces and tiny bouton-like terminals (e.g., Goldberg et al., 1990). In contrast to the varied combination of inputs driving vestibular afferents, the Type I auditory neurons (the primary cell type in the auditory nerve) make a single bouton-like connection opposing a single synaptic ribbon (Liberman, 1982).

Despite the many morphological and functional differences between auditory and vestibular afferents, many of the individual components of their synapses are similar. For example, in both systems, sensory hair cells bearing synaptic ribbons (Merchan-Perez and Liberman, 1996; Lysakowski and Goldberg, 2008) release glutamate to drive post-synaptic glutamate receptors (Glowatzki and Fuchs, 2002; Songer and Eatock, 2013; Sadeghi et al., 2014). Spiking is likely triggered at ion channel dense hemi-nodes located on peripheral dendrites close to the sensory epithelium (see red shading in **Figure 1** schematizing the putative spike initiation zone) (Hossain, 2005; Lysakowski et al., 2012). Most relevant to this paper is that *in vitro* studies have shown that the neurons are biophysically diverse in both systems. Some neurons respond only to the onset of current injections (temporal differentiation), while others also respond to the continuous portion of the stimulus (temporal integration) (described further in **Figure 2**). Such diversity allows the neuronal subgroups to encode specific features of the incoming sensory information.

Biophysical diversity arises from differences in ion channel composition. Across many studies in both systems, gradients in the same two classes of ionic currents – low-voltage gated potassium currents driven by Kv1 and KCNQ channels (I_{KL}) and hyperpolarization-activated cationic currents conducted through HCN channels (I_h) – are proposed as being crucial for driving biophysical diversity (Mo and Davis, 1997a,b; Mo et al., 2002; Iwasaki et al., 2008; Kalluri et al., 2010; Yi et al., 2010; Almanza et al., 2012; Yoshimoto et al., 2015). Despite the many qualitative similarities between the intrinsic properties of vestibular- and spiral ganglion neurons, there are no direct comparisons between the two groups. Here i take the first steps by comparing firing patterns and neuronal excitability from patch-clamp recordings made in our laboratory from spiral- and vestibular-ganglion neurons.

MATERIALS AND METHODS

Preparation

Patch-clamp recordings were made from spiral-ganglion somata in semi-intact cochlear whole-mount preparations and vestibular-ganglion somata from disassociated neurons. Neuron preparations were from Long-Evans rats from either sex ranging in age from postnatal day (P)1 through P18.

Animals were handled according to the National Institutes of Health Guide for the Care and Use of Laboratory Animals. All procedures were approved by the animal care committee of the Massachusetts Eye and Ear Infirmary, The House Research Institute, or the University of Southern California.

The data presented have appeared in previous publications. Readers interested in detailed descriptions of the methods can refer to the original manuscripts (Kalluri et al., 2010; Ventura and Kalluri, 2019; Markowitz and Kalluri, 2020). The following is a summary.

Cochlear and vestibular ganglion were bathed in and perfused throughout the dissection and recording session with Liebovitz medium supplemented with 10 mM HEPES and titrated with NaOH to 7.35 pH (L-15).

Spiral Ganglion: Cochlear middle turns were dissected from the middle turn and mounted as whole-mount epithelia under nylon threads on a glass coverslip as previously described in Markowitz and Kalluri (2020). The preparations were treated with an enzymatic cocktail containing L-15, 0.05% collagenase, and 0.25% trypsin for 15–20 min at 37 degrees C and subsequently perfused with fresh oxygenated L-15 during the entire recording. Recordings were made from the cell bodies (somata) of the bipolar spiral ganglion neurons. The semi-intact preparation contained the peripheral dendrites of the bipolar neurons and their hair cell connections. Recordings began and ended between 1 and 5 h after dissection.

Vestibular Ganglion: The superior vestibular ganglion was dissected, dissociated, and cultured as previously described (Kalluri et al., 2010; Ventura and Kalluri, 2019). Briefly, vestibular ganglia were treated with the same trypsin/collagenase cocktail described above for spiral ganglion. Enzymatic incubation lasted between 20 and 40 min, depending on age. Ganglia were passed through a series of fire-polished Pasteur pipettes to dissociate cells mechanically. Disassociated cells were plated onto coated coverslips (poly-d-lysine coated glass-bottomed culture dishes or polyethlylamine coated coverslips) and cultured overnight in DMEM with 10 mM HEPES, penicillin-streptomycin, 5% FBS, as previously described.

Enzymatic digestion helps to remove the myelin layers that wrap around the somata of spiral and vestibular ganglion neurons. Demyelination allows electrodes to access the neuronal membrane for patch-clamp recording. Some enzymes are known to impact the function of ion channels (Quandt, 1987; Armstrong and Roberts, 1998). For example, papain distorts the inactivation properties of BK channels by cleaving their extracellular domains (Armstrong and Roberts, 1998). Here we treat both the VGN and SGN with the same enzymatic cocktail containing trypsin and collagenase, thus providing consistency across the two systems. In both systems, the incubation time in enzyme was empirically titrated at each age range to maximize cell yield.

Electrophysiology

Cochlear preparations were viewed at X630 using a Zeiss Axio-Examiner D1 microscope fitted with Zeiss W Plan-Aprochromat

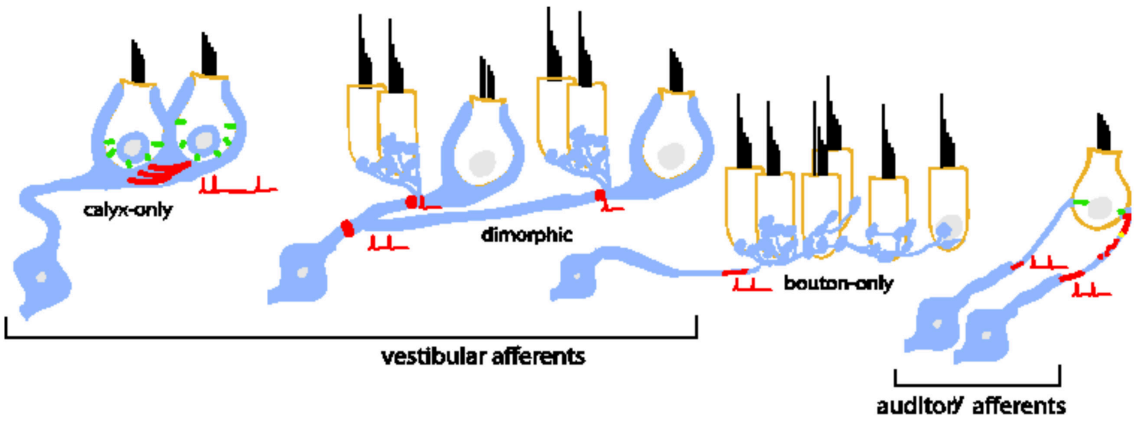

FIGURE 1 | Bipolar neurons of the inner ear are diverse in their morphology, dendritic arborization, and patterns of connectivity with inner hair cells. Type I spiral ganglion afferents in the auditory nerve have a single dendritic terminal that receives input from a single ribbon synapse at an inner hair cell. An individual inner hair cell has many synaptic ribbons that provide input to many Type I spiral ganglion neurons with a wide range of sound intensity thresholds. Vestibular afferents have diverse dendritic morphologies. Some neurons form post-synaptic calyx terminals that envelop the entire basal pole of Type I vestibular hair cells. Other neurons branch extensively to make many bouton terminals on Type II hair cells. A large group of neurons is dimorphic because the neurons form both calyceal and bouton terminals on Type I and Type II hair cells. The prevalence of dendritic morphology changes based on epithelial zone. Pure calyx afferents tend to be found in the central zones of vestibular epithelia where irregular-timing spiking is prevalent *in vivo*. Bouton afferents are found in the peripheral zones where regular-timing spiking is prevalent. Dimorphic afferents are found throughout. In both bipolar neuron groups, spike initiation occurs on the dendrite near the terminals.

optics. Vestibular ganglion preparations were viewed at X430 on an inverted microscope fitted with DIC optics (e.g., Zeiss Axiovert 135). Signals were driven, recorded, and amplified by either an Axoclamp 200B or Multiclamp 700B amplifier, Digidata 1440 board, and pClamp software.

Recording pipettes were fabricated using filamented borosilicate glass. Pipettes were fired polished to yield an access resistance between 5 and 7 MΩ. The tip of each recording pipette was covered in a layer of parafilm or sylgard to reduce pipette capacitance. Cochlear recordings were made in ruptured patch mode with recording pipettes filled with the following standard internal solution (in mM): 135 KCl, 3.5 $MgCl_2$, 3 Na_2ATP, 5 HEPES, 5 EGTA, 0.1 $CaCl_2$, 0.1 Li-GTP, 100 cAMP, and titrated with KOH to a pH of 7.35. This yielded a total potassium concentration of 165 mM with a total osmolality of 300 mmol/kg.

Vestibular ganglion recordings were made in either ruptured-patch mode with a similar standard internal solution (see above) or in perforated-patch mode. The perforated-patch internal solution contained (in mM): 75 K_2SO_4, 25 KCl, 5 $MgCl_2$, 5 HEPES, 5 EGTA, 0.1 $CaCl_2$, and titrated with 1M KOH to a pH of 7.4. Amphotericin B (240/ml, 158 Sigma-Aldrich) was dissolved in DMSO and added to the perforated patch solution on the day of recording. I pooled the data from perforated and ruptured-patch recordings as the gross electrophysiological features were not dependent on the recording mode. Voltages are reported without correcting a junction potential of approximately 3.8 mV in ruptured-patch or 5.5 mV in perforated-patch (calculated by JPCalc as implemented in pClamp 10.7, Barry 1994).

Analysis

Spike features were analyzed from current-clamp recordings in response to families of depolarizing current steps. Current steps were either 200 or 400 ms in duration and incremented from −120 to 200 pA in 10 pA increments. In some cells, current injection levels were increased to 400 pA. Cells were first qualitatively classified based on the pattern of spike accommodation in response to injected currents. I characterized resting potential, cell size as inferred from capacitance, input resistance near resting potential, current threshold, voltage threshold, and first spike latency.

Resting potential (V_{rest}, mV) was estimated as the cell membrane potential averaged before step current injection.

Input resistance (R_{in}, GOhm) was calculated as the slope of the voltage-current relationship produced 100 ms after a ± 10-pA step current injection.

Membrane capacitance (C_m, pF) was estimated in voltage clamp from the built-in membrane test protocol in pClamp and capacitance estimation circuitry of the amplifier. Note that this is different from our previous papers where we estimated C_m from current-clamp recordings by fitting an exponent to the voltage response for a small hyperpolarizing current step. However, measuring capacitance in current clamp can lead to errors in capacitance estimation for spatially extended neurons and if the activation of voltage-gated channels distorts the time course of membrane charging. Because of this potential for error, we only report cell capacitance when it was measured in voltage clamp. Note also that this resulted in fewer cells in which we have C_m estimates than cells in which we recorded firing patterns.

Voltage Threshold (V_{thresh}, mV). Voltage threshold was the membrane voltage V_m at which dV_m/dt changes rapidly. A 5 mV/ms threshold criterion was suitable for detecting action potentials in both vestibular and auditory ganglion neurons. The criterion value was defined to reliably detect spikes while avoiding graded depolarizations and spurious depolarizations due to capacitance artifacts and noise. Some cells, like the

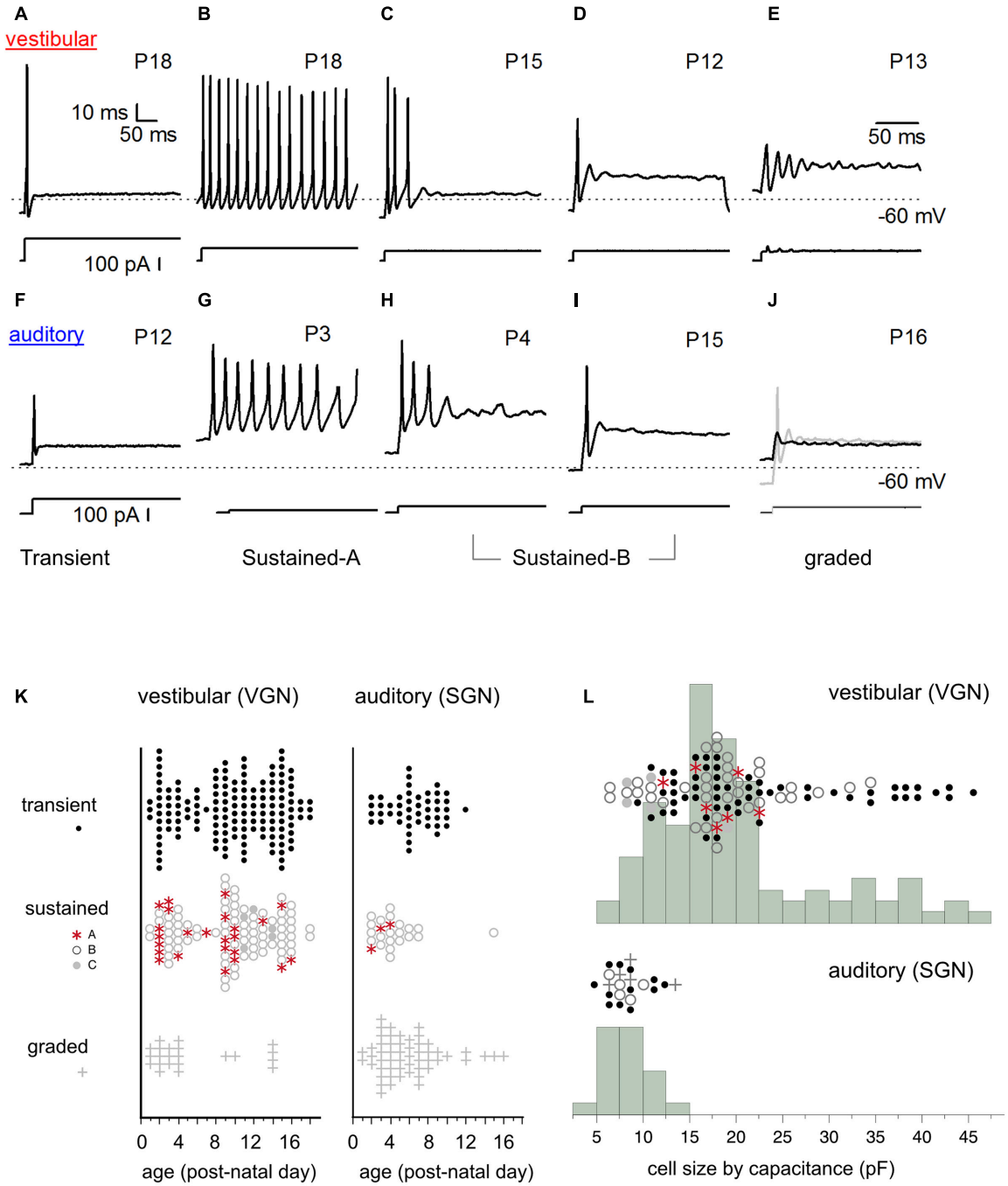

FIGURE 2 | Diversity of *in vitro* firing patterns in response to step current injection. **(A–E)** Firing patterns in five example vestibular ganglion neurons. Transient-spiking **(A)**, sustained-A spiking **(B)**, sustained-B spiking **(C,D)**. Non-spiking/graded responses **(E)**. Dashed line indicates –60 mV. Traces below the firing patterns indicate stimulus. **(F–J)** Similar range of firing patterns in five example spiral ganglion neurons (auditory). Transient-spiking **(F)**, sustained-A spiking **(G)**, sustained-B spiking **(H,I)**. Non-spiking/graded response (black trace). **(J)** Spiking is induced by injecting a –10 pA hyperpolarizing current before applying the current step (gray trace) **(J)**. **(K)** Prevalence of firing patterns as a function of postnatal age in VGN (left) and SGN (right). **(L)** Distribution of somatic cell size in vestibular and spiral ganglion. Cell capacitance values were available in fewer cells than shown in **(K)**. In **(K,L)**, symbols indicate firing patterns as follows: Transient (black dots), sustained-A (red asterisks), sustained-B (open gray circles), non-spiking plus graded (plus sign).

graded-firing group in SGN and sustained-C group in VGN, were excluded from subsequent analysis because their stimulus-induced depolarizations did not meet the criterion value.

Relative Voltage Threshold (δV_{th}, *mV*) is the depolarization needed relative to resting potential to initiate an action potential. $\delta V_{th} = V_{thresh} - V_{rest}$.

Current Threshold (I_{thresh}, pA) was defined as the minimum current required (in 10 pA increments) to produce an action potential.

Response Latency (L, ms) was defined as the delay between the onset of stimulus current and the peak of the first action potential induced by the stimulus at current threshold.

Net Excitability (mV/pA or GOhms): The ratio of relative voltage threshold to current threshold $(V_{thresh}\text{-}V_{rest})/I_{thresh}$

Charge Threshold (Q, femto Coulombs): The charge threshold was defined as the product between the current threshold and first spike latency. For a step current injection, this approximates the charge delivered to evoke the first action potential.

Statistical Analysis

pClamp software was used to gather raw data from electrophysiological recordings. MATLAB was used to batch process and uniformly quantify the firing pattern features from all recordings. Statistical analysis was performed in JMP software package. Student's *t*-test was used to compare the means of two distributions with equal variance (as determined by Levine's test). Regression slope analyses are reported in the figure captions. One-way analysis of covariance was used to compare groups when one covariate was a continuous variable (e.g., when comparing resting potential vs. age in firing-pattern groups). *Post-hoc* Tukey HSD tests compared the least squared adjusted means. The results of the ANCOVA analyses are shown in **Table 1**. All the individual data points with regressions and 95% confidence intervals are shown in figures. An alpha level of 0.05 was used for all statistical tests.

RESULTS

Heterogeneity of Firing Patterns

The somata of spiral and vestibular ganglia respond with a wide range of firing patterns to injected currents (**Figures 2A–E** spiral ganglion, **Figures 2F–J** vestibular ganglion). We broadly grouped cells based on these firing patterns (readers can find more details about this classification scheme in Kalluri et al., 2010; Markowitz and Kalluri, 2020). Here the same naming convention previously applied to the vestibular ganglion (blue text under the firing patterns) is applied to the spiral ganglion.

I classified neurons into two broad firing pattern groups, transient-firing and sustained-firing. Transient-firing neurons produce a single action potential (spike) at the onset of the current step (**Figures 2A,F**; VGN and SGN, respectively). For current injections greater than threshold, the firing pattern of most transient-spiking neurons is invariant to intensity. In contrast, sustained-firing neurons vary in the degree of accommodation. Some neurons have slowly accommodating firing patterns with long trains of spikes throughout the depolarizing step (sustained-A firing patterns, **Figures 2B,G**). Other neurons have intermediate degrees of accommodation (sustained-B; **Figures 2C,D,H,I**, respectively). The degree of accommodation observed in sustained-firing patterns varies from cell to cell and depends on current amplitude.

In both vestibular and spiral ganglion, some cells do not fire robust action potentials. We classified these non-spiking responses as graded (**Figures 2E,J**). The presence of an action potential was defined as reaching a criterion depolarization rate of 5 mV/ms. We previously classified non-spiking cells with prominent voltage oscillations follow a short first spike or voltage depolarization as sustained-C/resonant (**Figure 2E**). Here, non-spiking cells with and without voltage oscillations were classified as graded. Notably, non-spiking cells in both the vestibular and spiral ganglion could produce an action potential if they were first hyperpolarized to below their natural resting potential before applying current steps (gray curve in **Figure 2J** shows an example in spiral ganglion).

Spike patterns were analyzed in 131 spiral ganglion neurons and 294 vestibular ganglion neurons. In both spiral and vestibular ganglion, the different spike patterns were not uniformly prevalent. Most cells producing action potentials had transient-firing patterns (151/294 VGN; **Figure 2K**, left; 47/131 SGN; **Figure 2K**, black dots). Within the sustained group (106/294 VGN, 24/131 SGN), we encountered sustained-B firing patterns (76/106 VGN; 21/24 SGN, **Figure 2K**) more often than sustained-A firing patterns (25/106 VGN, 3/24 SGN). Graded or non-spiking cells formed a significant proportion of the data set in the spiral ganglion (54/131) but were less frequently encountered in vestibular ganglion (22/294 VGN). This could be due to methodological differences because SGN recordings were from semi-intact acute preparations. In contrast, the VGN recordings were from dissociated cultured preparations (see section "Discussion" on this point).

The prevalence of different firing-pattern groups changes with development, with the number of sustained-A firing neurons decreasing with postnatal age in both VGN and SGN. To illustrate the age-dependent change in firing pattern prevalence, we grouped the data as $<$ P10 and $\geq$ P10. Below P10, 16 out of 48 sustained-spiking responses in VGN (∼33%) were sustained-A patterns. After P10, 8 out of 54 sustained-spiking responses (∼15%) were sustained-A firing patterns. In spiral ganglion, the dataset is much more limited in terms of postnatal age, so we did not quantify prevalence in a similar way. However, only 3 out of 23 sustained-spiking responses were classified as sustained-A; all three observations were recorded before P4.

Cell Size

One of the most striking differences between vestibular and spiral ganglion neurons is somatic size (as inferred from the membrane capacitance estimates from voltage-clamp measurements). Vestibular neurons have a wide range of membrane capacitance, ranging from 5 to 45 pF (**Figure 2L**). Note that the number of cells in which capacitance measurements were available for comparison is fewer than we measured firing patterns (104/294 in VGN and 23/131 in SGN). This is because the present analysis was limited to those cells in which capacitance measurements were made in voltage-clamp. This constraint was applied because voltage-clamp based capacitance estimates are less likely to be distorted voltage gated currents like I_{KL} or by the extended neuronal morphology in the semi-intact spiral ganglion preparation (Golowasch et al., 2009).

The distribution of cell size is bimodal in VGN (**Figure 2L**, top). Most VGN (∼80%) are small to intermediate-sized cells with capacitance values ranging between 5 and 25 pF. Both transient-firing and sustained-firing cells are found in the first mode (**Figure 2L**; firing type is indicated by the same symbols as defined in **Figure 2K**). The remaining ∼20% of VGN are large cells with capacitance values between 30 and 45 pF. In this size range, transient-firing patterns are the dominant group (16/21 cells, **Figure 2L**).

In contrast to the wide range of cells sizes seen in vestibular ganglion, spiral ganglion somata are smaller and more homogeneous in cell size (with capacitance values ranging between 6 and 10 pF; **Figure 2L**, bottom). Based on confocal scans in the neonatal rat spiral ganglion, Markowitz and Kalluri (2020) estimated that the SGN reported in this study had average diameters around 12.7 ± 0.3 μm, n = 28. These values are consistent with measurements made in other mammalian species where the mature somatic diameters of SGN range between 10 and 15 μm (Romand and Romand, 1990; Berglund and Ryugo, 1991; Tsuji and Liberman, 1997; Nayagam et al., 2011). Assuming an unmyelinated spherical soma (with a specific capacitance around ∼1 μF/cm^2), the somatic capacitance would be around 5.1 ± 0.2 pF. Based on the similarities in values between the capacitance as estimated from voltage clamp and estimated cell diameters, we conclude that small capacitance (in comparison to vestibular ganglion) is representative of spiral ganglion neurons.

TABLE 1 | Analysis of covariance.

	Source	Nparm	DF	Sum of squares	F ratio	Prob > F
Figure 3	Ganglion	1	1	732.2971	12.1165	0.0006
V_{rest} (mV)	Age (post-natal days)	1	1	3463.6387	57.3088	<0.0001
	Ganglion*age (post-natal days)	1	1	10.2708	0.1699	0.6806
Figure 3A V_{rest}	Age (post-natal days)	1	1	1981.3045	35.2857	<0.0001
Transient	Ganglion (VGN/SGN)	1	1	545.8877	9.7219	0.0023
	Age*ganglion	1	1	13.395	0.2386	0.6261
Figure 3B V_{rest}	Age (post-natal days)	1	1	1459.5773	22.6073	<0.0001
Sustained (a+b)	Ganglion	1	1	3.3321	0.0516	0.8209
	Ganglion*age (post-natal days)	1	1	7.7828	0.1205	0.7293
Figure 3C V_{rest}	Age of animal (post-natal days)	1	1	1603.5887	48.311	< 0.0001
Graded	Ganglion	1	1	536.4468	16.1614	0.0001
	Ganglion*age (post-natal days)	1	1	1.0542	0.0318	0.8591
Figure 4A	Ganglion	1	1	299.4174	6.03	0.0151
V_{thresh} (mV); n = 164	V_{rest}, (mV)	1	1	2965.569	59.7241	<0.0001
	GanglionV_{rest}, (mV)	1	1	0.0209	0.0004	0.9837
Figure 4D	V_{rest}, (mV)	1	1	52.32906	0.7889	0.3768
ΔV_{thresh} (mV)	Ganglion	1	1	315.8627	4.7619	0.0317
Transient; n = 93	Ganglion* V_{rest}, (mV)	1	1	0.06481	0.001	0.9751
Figure 4E	V_{rest}, (mV)	1	1	335.095	19.8699	<0.0001
ΔV_{thresh} (mV)	Ganglion	1	1	29.41228	1.744	0.1911
Sustained (a+b); n = 71	Ganglion* V_{rest}, (mV)	1	1	0.004	0.0002	0.9878
Figure 5A	V_{rest}, (mV)	1	1	67150.39	14.0502	0.0003
I_{thresh} (pA)	Firing Pattern	1	1	233488.9	48.854	<0.0001
VGN	V_{rest}, (mV) * Firing pattern	1	1	25456.27	5.3263	0.0225
Figure 5B	V_{rest}, (mV)	1	1	2750.983	4.7693	0.0325
I_{thresh} (pA)	Firing pattern	1	1	9951.6	17.2527	<0.0001
SGN	V_{rest}, (mV) * Firing pattern	1	1	494.1974	0.8568	0.358
Figure 5D	V_{rest}, (mV)	1	1	8.577368	47.4505	<0.0001
Net excitability (gOhm)	Firing Pattern	1	1	1.05186	5.8189	0.0174
VGN	V_{rest}, (mV) * Firing Pattern	1	1	0.211134	1.168	0.282
Figure 5E	V_{rest}, (mV)	1	1	0.081531	1.7086	0.1988
Net excitability (gOhm)	Firing pattern	1	1	0.001529	0.032	0.8589
SGN	V_{rest}, (mV) * Firing pattern	1	1	0.027033	0.5665	0.4562
Figure 6A	R_{in} *(gOhm)*	1	1	5.439455	42.2084	<0.0001
Net excitability (*gOhm*)	Firing pattern	1	1	5.426628	42.1089	<0.0001
	R_{in} * Firing pattern	1	1	0.071217	0.5526	0.4583
Figure 6B	C_m (pF)	1	1	231.62668	6.6882	0.0110
Response latency	Firing type	1	1	296.73012	8.5681	0.0041
	C_m (pF)*Firing type	1	1	0.26040	0.0075	0.9311

** indicates the interaction between two source variables.*

The differences in cell-capacitance between spiral and vestibular ganglion is unlikely to be driven by the difference in the average age of the present comparison.

Overall, somatic size is more variable in vestibular ganglion neurons than it is in spiral ganglion neurons. However, cell size was not a robust predictor of firing pattern in either VGN or SGN, excepting the largest VGN, which are predictably transient-firing.

Comparing the Excitability of Vestibular and Spiral Ganglion Neurons

I measured resting potential, voltage threshold relative to resting potential, current threshold, and first-spike latency to quantify cell excitability. I examined the covariances between these features, which then compared across vestibular and spiral ganglion to identify similar and different features between the systems.

Resting potential hyperpolarizes with postnatal age (**Figure 3**) in both spiral and vestibular ganglion ($p < 0.0001$). As illustrated in **Figure 3**, the age-dependent hyperpolarization in resting potential is evident in all three firing pattern groups (transient-firing **Figure 3A**, sustained-A + sustained-B pooled **Figure 3B**, and graded/non-spiking **Figure 3C**). This hyperpolarization of resting potential is consistent with previous findings in both VGN and SGN showing that maturing ganglion neurons acquire larger potassium currents (Mo et al., 2002; Kalluri et al., 2010; Iwasaki et al., 2012; Markowitz and Kalluri, 2020). The spiral and vestibular ganglion neurons data are plotted together but indicated by color for easy identification (red for VGN and blue for SGN).

The dependence of resting potential on age is similar for both spiral ganglion and vestibular ganglion neurons [ANCOVA, Age*Ganglion, $F(1, 1) = 0.17$, $p = 0.68$; see **Table 1**]. The mean resting potential of SGN neurons (least-squares adjusted mean) is on average more depolarized than that of VGN neurons (-58.3 ± 0.90 vs. -61.6 ± 0.65 mV). The SGN data skew toward a younger range with more graded-responding cells than VGN. These two features may partly account for the more depolarized resting potentials of the SGN population.

Excitability by Voltage Threshold

Voltage threshold is the minimum voltage needed to produce an action potential. It is mainly dependent on the availability of sodium and calcium channels to open in a positive feedback loop to generate the upstroke of an action potential (Bean, 2007; Platkiewicz and Brette, 2010, 2011). Voltage threshold is not a fixed quantity but can vary from cell to cell and in an individual cell depending on its recent history. In the present data set, the voltage threshold varies anywhere from -65 to -10 mV. This wide range can be partly attributed to the wide range of resting potentials found in the two ganglion groups. The relationship between voltage threshold and resting potential is illustrated in **Figure 4**. Voltage threshold hyperpolarizes with resting potential (**Figure 4**, regression for pooled VGN (red symbols) and SGN (blue symbols), $p < 0.001$). Since resting potential depends on age (**Figure 3**), hyperpolarization of voltage threshold with resting potential is equivalent to hyperpolarization of voltage threshold with postnatal age ($p < 0.001$, regression not shown).

The hyperpolarization of voltage threshold with resting potential is consistent with the idea that the inactivation properties of sodium channels shape voltage threshold. As the resting potential of cells hyperpolarizes, a smaller proportion of the available sodium channels is likely to be inactivated. The greater availability of sodium channels would lower voltage threshold. As described in the modeling of Platkiewicz and Brette (2010), the rate at which voltage threshold changes over a range of membrane potentials depends on the voltage-inactivation range of sodium channels. Voltage threshold becomes most sensitive to membrane potential near the half-inactivation voltage. Conversely, it becomes insensitive to membrane potential at voltages where the sodium channels are wholly relieved from inactivation. In the VGN, the trend for voltage threshold to hyperpolarize persists even at the most negative resting potentials (between -80 and -90 mV). This suggests that the sodium channels in VGN are likely to be partly inactivated even at these more negative resting potentials. Whether this is also true in SGN is not clear since the resting potentials of the SGN did not extend as far negative as in the VGN, presumably due to skew in SGN data toward younger ages when neurons are more depolarized.

An analysis of covariance revealed that the dependence of voltage threshold on resting potential is similar between the two ganglion groups [ANCOVA: Vrest*Ganglion, $F(1, 1) = 1.85$, $p = 0.175$]. This suggests that over a similar range of resting potentials, the average half-inactivation voltage and slope factor for sodium currents is similar between the two ganglion groups.

Although voltage threshold hyperpolarizes with resting potential, this does not mean that the cells are more excitable. This is because the voltage threshold does not change at the same rate as the resting potential (compare the slope of the voltage threshold regression to the dashed line marking the resting potential). Indicating a decrease in excitability, the relative voltage threshold ($\triangle V_{th} = V_{thresh} - V_{rest}$) increases as resting potential hyperpolarizes [$F(1, 171)$, $p < 0.001$].

$\triangle V_{th}$ was notably more variable in transient-firing neurons than in sustained-firing neurons (compare the spread in the dots vs. circles in **Figure 4B**). **Figure 4C** shows example action potential traces from three transient-spiking neurons (numbers in the figure indicate the cell ID) that were similar in resting potential but had very different voltage thresholds. The difference in the range of $\triangle V_{th}$ between transient and sustained-firing groups is illustrated by the regressions plotted for each firing type in **Figures 4D,E**, respectively. When broken down by firing pattern, the least square adjusted mean of $\triangle V_{th}$ was smaller for SGN than in VGN for transient-spiking neurons ($22\pm$ 3.5 mV vs. 30 ± 1.0 mV, SGN, and VGN, respectively) but was not different for sustained-spiking neurons (22 ± 1.5 mV vs. $24\pm$ 0.6 mV, SGN and VGN, respectively). More data in SGN at older ages is needed to understand if the younger age of SGN accounts for the difference between sustained groups in SGNN and VGN. Another possibility is that the transient-spiking neurons with high thresholds in VGN belong to a distinct subgroup of cells that are considerably larger than any of the other cells in VGN and SGN.

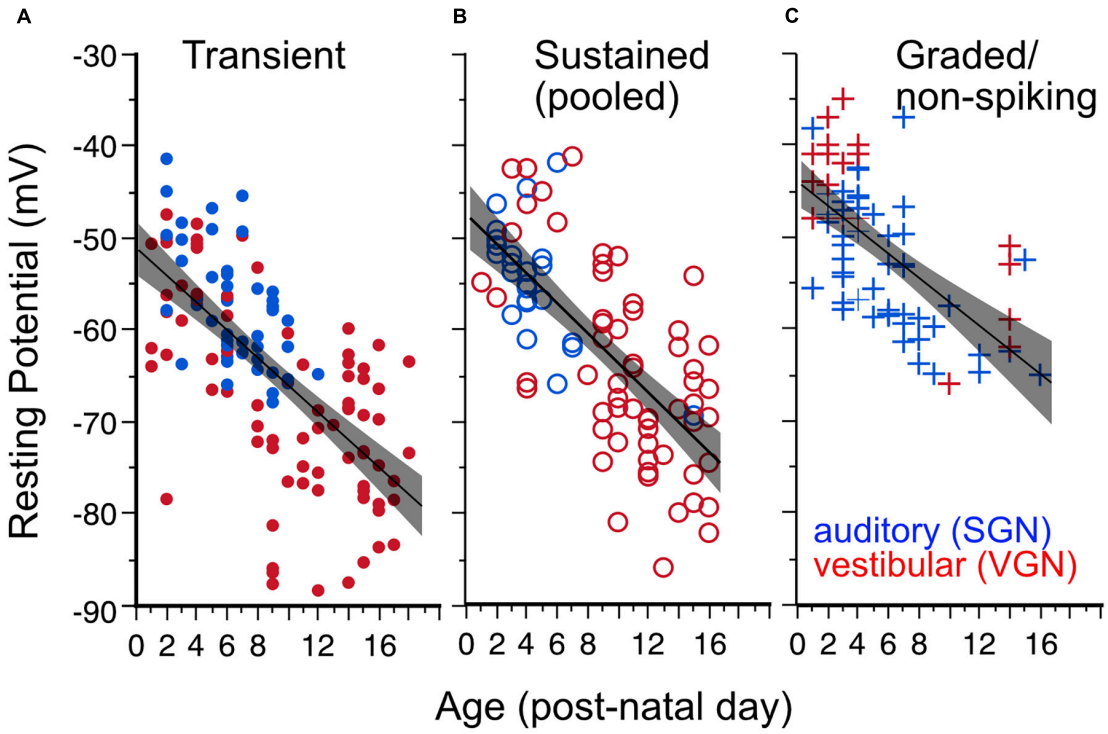

FIGURE 3 | Resting potential hyperpolarizes with age for all firing pattern groups. Lines plus shaded areas show linear regressions plus 95% confidence intervals. Blue symbols indicate spiral ganglion neurons, whereas red symbols indicate vestibular ganglion neurons. Each data point represents the resting potential of individual ganglion neurons. **(A)** Resting potential vs. postnatal age in transient-spiking somata. Y (Resting Potential) = –1 – 1.49*X (post-natal age). $F(1, 129) = 100.92$, $p = 0.0001$. **(B)** Resting potential vs. postnatal age in sustained-spiking neurons. Here sustained-A and sustained-B groups are pooled together and represented by open circles. Y = –47.56 – 1.615*X. $F(1, 82) = 80.10$, $p \leq 0.0001$. **(C)** Resting potential vs. postnatal age in non-spiking/graded neurons. Y = –44–1.306*X, $F(1,69) = 45$, $p < = 0.0001$.

Excitability by Current Threshold

Figures 5A,B plot the minimum current intensity required to induce spiking from VGN and SGN neurons, respectively. As in **Figure 4**, the current threshold is plotted against resting potential to evaluate if the variance in this biophysical measure is also related to the maturational change in resting potential. In both VGN and SGN, there is a significant correlation between resting potential and current threshold ($p = 0.0003$ in VGN, $p = 0.0325$ in SGN). Overall, larger stimulus currents are needed to induce spiking in transient-spiking neurons than in sustained-spiking neurons (compare the offset between the magenta and green regression lines in **Figures 5A,B**). This is consistent with transient-spiking neurons in VGN and SGN having larger low-voltage gated potassium currents., which oppose membrane depolarization (Mo et al., 2002; Kalluri et al., 2010).

One distinct difference between the VGN and SGN is the range of current thresholds observed. Some VGN neurons required as much as 350 pA current injection to generate an action potential. Part of the differences could be due to the SGN dataset being limited to a younger age range where resting potentials are more depolarized and current thresholds are generally smaller in both VGN and SGN. Another more significant factor is that transient firing neurons have a much wider range of cell sizes (refer back to **Figure 2L**). **Figure 5C** (inset into **Figure 5B**) shows that the current thresholds of SGN neurons is similar to that of the small-intermediate sized (< 25 pF) transient neurons from the VGN. The largest current thresholds are from the large VGN neurons (> 25 pF).

The combination of voltage threshold and current threshold determine the net excitability of a neuron. Indicative of their greater net excitability, the ratio between the relative voltage threshold and current threshold was larger in sustained-spiking neurons than in transient-spiking neurons in VGN (**Figure 5D** in VGN). Although the trend was similar in SGN, it did not reach statistical significance (**Figure 5E**, effect tests based on ANCOVA summarized in **Table 1**).

The Mutual Dependence of Current Threshold and First-Spike Latency on Input Resistance and Cell Size

Not surprisingly, net excitability (which has units of resistance) is positively correlated with input resistance (**Figure 6A**). However, when cells with the same input impedance are compared, sustained-spiking cells are more excitable than are transient-spiking cells (larger ratio of voltage threshold/current threshold). This means that the difference in excitability between sustained-firing and transient-firing neurons is not just a reflection of differences in resting membrane properties but also dependent

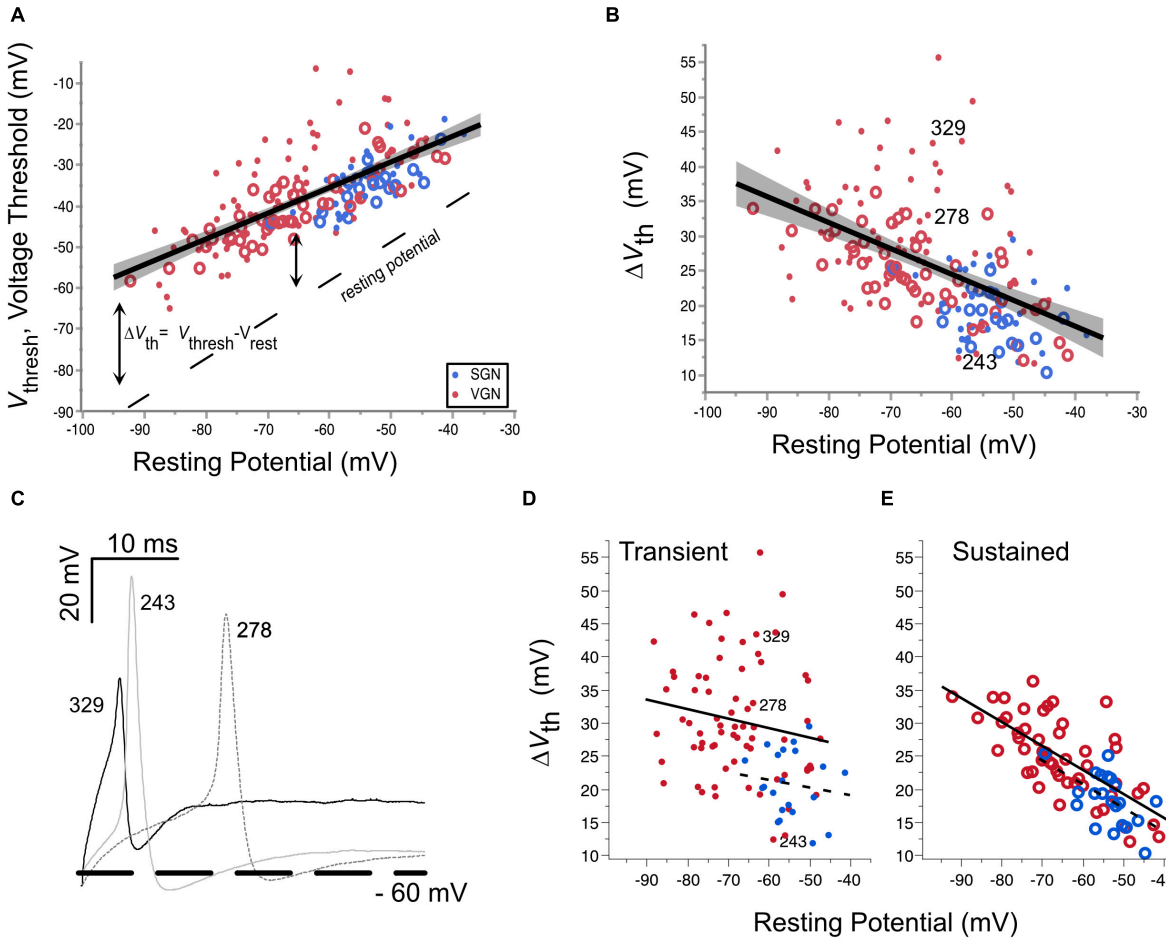

FIGURE 4 | Voltage threshold hyperpolarizes with resting potential in both spiral ganglion and vestibular ganglion. **(A)** Voltage threshold as a function of resting potential in spiral (blue) and vestibular ganglion neurons (red). Sustained-spiking neurons are drawn with open circles, transient-spiking neurons are drawn with small solid circles. Linear regression through all the SGN and VGN data pooled with 95% confidence intervals drawn as a solid line with gray shading. $F(1, 171) = 171.8$, $p < 0.0001$. The dashed line indicates the resting potential. **(B)** Relative voltage threshold (voltage threshold minus the resting potential) plotted as a function of resting potential. $F(1, 171) = 61.6$, $p < 0.0001$. **(C)** Example spike waveforms illustrating the range of voltage thresholds possible for three transient-spiking neurons from VGN. The cells were chosen to have similar resting potentials near –60 mV. The number next to each trace indicates the cell ID. A thick dashed line is drawn at –60 mV. **(D)** Voltage thresholds compared between SGN (dashed regression line) and VGN (solid regression line) for cells with transient-firing patterns (dots). **(E)** Voltage thresholds compared between SGN and VGN for sustained-firing patterns (open circles). Note that sustained-**(A,B)** firing patterns are pooled together. The cell ID indicates the three cells from **(C)**.

on the voltage-gated currents that shape membrane potential between rest and threshold (e.g., I_{KL}).

First-spike latency reflects the temporal integration properties of ganglion neurons. The time to generate a spike is expected to be determined by both the membrane capacitance and input resistance of the cell; membrane time constant ($\tau = R_{in}C_m$). When input-impedance is considered on its own (e.g., for cells of uniform size), cells with larger input impedance would take longer to reach voltage threshold, albeit with smaller amplitude current injections. In SGN where cell size is relatively uniform, first-spike latency varies with terminal contact position in inner hair cells; modiolar-contacting SGN have shorter first-spike latencies than pillar-contacting SGN (Markowitz and Kalluri, 2020). Based, in part, on this variation in first spike-latency and uniformity in cell size, Markowitz and Kalluri (2020) concluded that modiolar-contacting SGN have larger net conductance when compared to pillar-contacting SGN.

Suppose cell capacitance was considered on its own. In that case, one might expect first-spike latency to be the longest in the largest cells, but this is not the case (**Figure 6B**). Some of the fastest first-spike latencies are from the largest cells in the VGN and the longest latencies are small cells from SGN. ANCOVA effect test showing a significant effect of capacitance and firing pattern on latency is reported in **Table 1**.

The large capacitance of the large somata in VGN is balanced by these cells also having the smallest input resistance. Indeed, cell size and input resistance are covarying. The systematic covariance between input-resistance (R_{in}) and membrane capacitance (C_m) is illustrated in **Figure 6C**. The relationship is fit by a function with the form $R_{in} = A/C_m$. A straightforward interpretation of

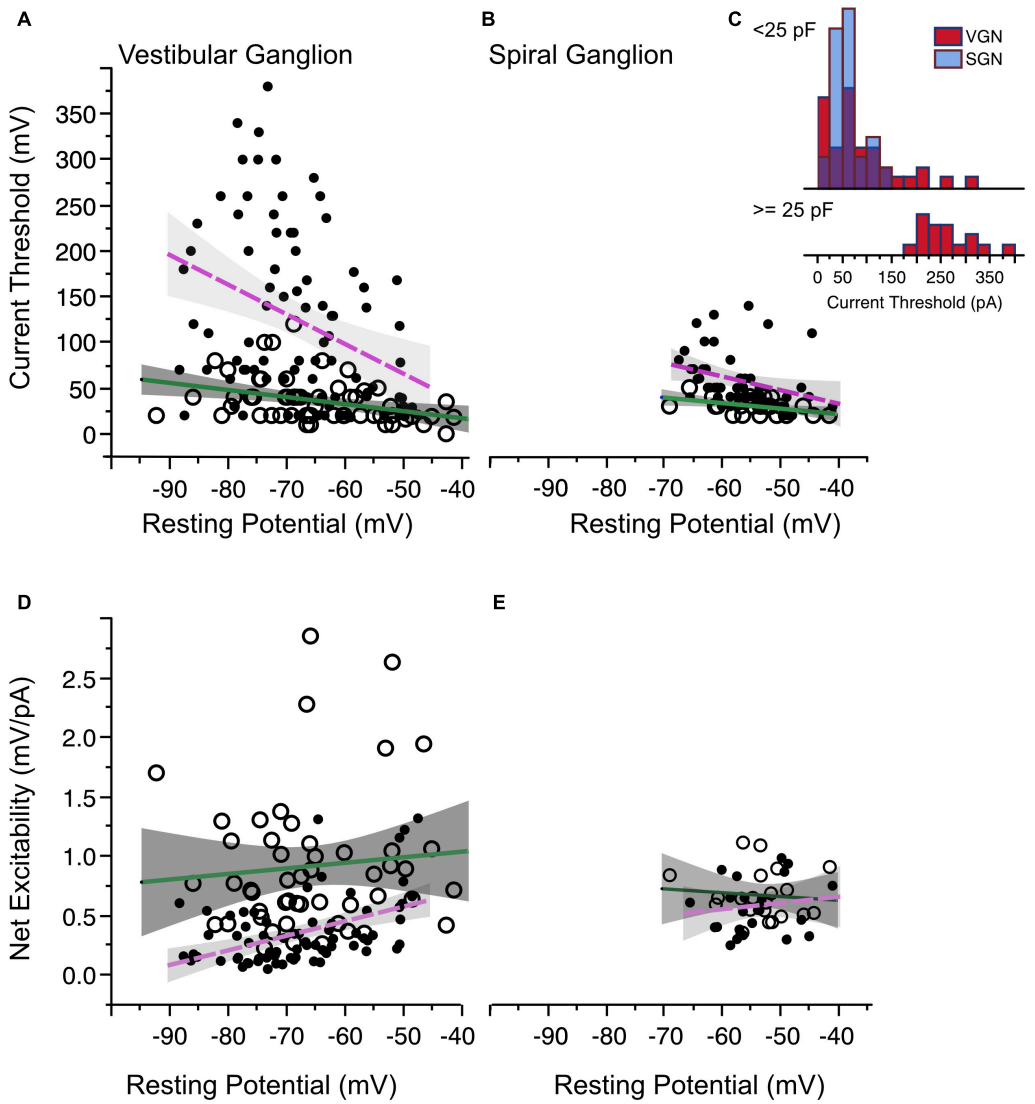

FIGURE 5 | Current threshold and net excitability. **(A)** Current threshold as a function of resting potential in vestibular ganglion neurons. Sustained-spiking neurons are drawn with open circles, transient-spiking neurons are drawn with small solid circles. Lines with gray shading show linear regressions with 95% confidence intervals (dashed magenta line for transient-firing and solid green line for sustained-firing). **(B)** Current threshold vs. resting potential for spiral ganglion neurons. Symbols and regression lines as in **(A)**. **(C)** Histogram of current thresholds in transient spiking neurons. The top histogram is for small to medium-sized cells with capacitance values less than 25 pF. All SGN are assumed to belong to this group. The bottom histogram is for large-sized cells with capacitance values greater than 25 pF. Current thresholds are larger for these cells than for the rest of the SGN and VGN combined. Blue bars indicate SGN and red bars indicate VGN. **(D,E)** The ratio between voltage and current threshold (net excitability) is plotted against resting potential for VGN and SGN.

this relationship is that small and large cells are approximately scaled versions of each other with similar ion channel density per unit area of the membrane (i.e., the specific membrane resistance, *A*, is constant as cell diameter increases). Since input resistance and capacitance scale together, this accounts for why first-spike latency does not increase with cell size. If one views the value of *A* as the specific-membrane resistance, then the lower value of *A* for transient-firing neurons compared to sustained-firing neurons remains consistent with this group of neurons expressing large low-voltage gated potassium conductances (Mo et al., 2002; Iwasaki et al., 2008; Kalluri et al., 2010).

By Ohm's Law, the amount of current needed to effect a fixed change in voltage is expected to increase with input resistance (**Figure 7A.1** for SGN and **Figure 7B.1** for VGN). Related by their mutual dependence on input resistance, current threshold is covariant with first-spike latency (*L*) in both SGN and VGN (**Figure 7A.2** for SGN and **Figure 7B.2** for VGN). Another way to express the excitability of these ganglion neurons is to look at the minimum charge delivered to excite an action potential (*Q*). Multiplying the current threshold by the first spike latency ($Q = I_{threshold}{}^{*}L$) roughly estimates the charge. Since the stimulus is a current step, this value is equivalent to the area under the

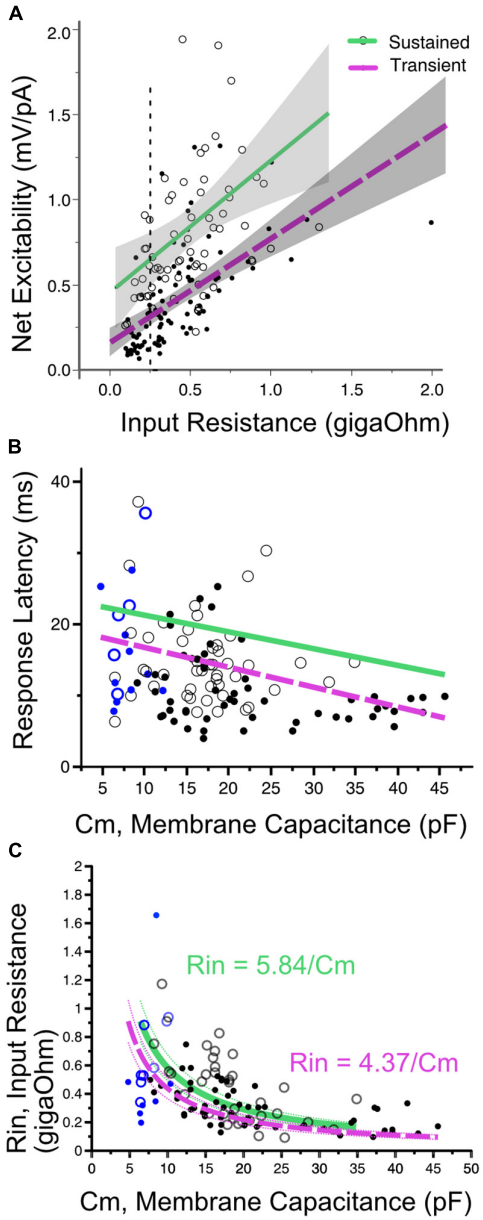

FIGURE 6 | (A) Net excitability vs. input resistance for transient- (solid dots) and sustained-spiking neurons (open circles) in VGN and SGN pooled. Regression lines plus 95% confidence intervals are drawn through each firing pattern group. Sustained and transient-spiking neurons with magenta and green lines, respectively. Cells with similar input resistance (e.g., 0.25 gOhms, dotted verticle line) differ in net-excitability, with sustained-spiking neurons being more excitable than transient-spiking neurons. **(B)** Indicative of covariance between input resistance and cell size, first-spike latency decreases with increasing membrane capacitance. Solid magenta and dashed green lines show linear regressions through sustained- and transient-spiking cells. VGN and SGN data are distinguished by black and blue symbols, respectively. Symbols defined as in A. ANCOVA effect tests comparing regressions are shown in **Table 1**. **(C)** Input resistance decreases with membrane capacitance (C_m). The data are fit with two functions in the form $R_{in} = A/C_m$. A is equivalent to the specific membrane resistance and is larger for sustained-spiking neurons than for transient spiking neurons. The relationship between R_{in} and C_m is consistent with the idea that the number of *(Continued)*

FIGURE 6 | (Continued)
ion channels grows with cell size, but channel density remains approximately constant. The fits are drawn through the sustained and transient-spiking neurons with magenta and green lines, respectively. Dotted lines are 95% confidence intervals. Blue symbols indicate spiral ganglion neurons and black symbols indicate vestibular ganglion neurons.

stimulus from onset of the current step to the first-spike. Q depends on both cell size and firing pattern (**Figure 7C**). For any fixed cell size, the sustained-A group requires the smallest charge transfer to trigger spiking. This was followed by sustained-B and then transient-spiking neurons. If we consider all SGN as small cells (including cells without capacitance measurements), transient-firing SGN require significantly more charge to trigger spiking than do sustained-B firing SGN (758 ± 3, n = 46 vs. 546 = /−44 n = 24; t-test, df = 66, $p < 0.001$).

The systematic dependence of Q on cell size and firing pattern group reveals an inherent structure to the biophysical heterogeneity seen across the two ganglia. As the regression lines in **Figure 7C** show, Q is sensitive to cell size, but this sensitivity differs between firing pattern groups; note that the slopes of the regression lines are steeper for the transient and sustained-B cells than for the sustained-A cells. Indeed, Q is relatively invariant to cell size in the sustained-A firing group. The relative insensitivity to cell size is consistent with the idea that sustained-A neurons have the largest specific membrane resistance and thus have the slowest rate of change in input resistance with cell size. In contrast, Q is sensitive to cell size in sustained-B neurons and most sensitive to cell size in transient-spiking neurons. The dependence of Q on cell size reflects the neurons' inherent sensitivity to depolarization rate. The steady-state activation of low-voltage gated channels means that transient-firing neurons have low input impedance, which requires larger currents to depolarize the neuron to voltage threshold. The activation kinetics of the potassium currents sets a time limit within which the membrane potential must reach spike threshold.

DISCUSSION

Spiral Ganglion Neurons and Vestibular Ganglion Are Part of the Same Biophysical Continuum

Heterogeneity in the ion channel properties of spiral and vestibular ganglion has long been evident in the diversity of firing patterns observed in response to current injections. Many *in vitro* studies in both sensory systems have described this diversity independently; revealing qualitative similarities in firing patterns and in the types of ion channels responsible for shaping the firing patterns (Mo and Davis, 1997a; Mo et al., 2002; Risner and Holt, 2006; Iwasaki et al., 2008; Hight and Kalluri, 2016). Indicative of the overall heterogeneity in their ion channel composition, our combined analysis of vestibular and spiral ganglion neurons revealed a wide range of firing patterns, resting potentials, voltage thresholds, current thresholds, and first-spike latencies.

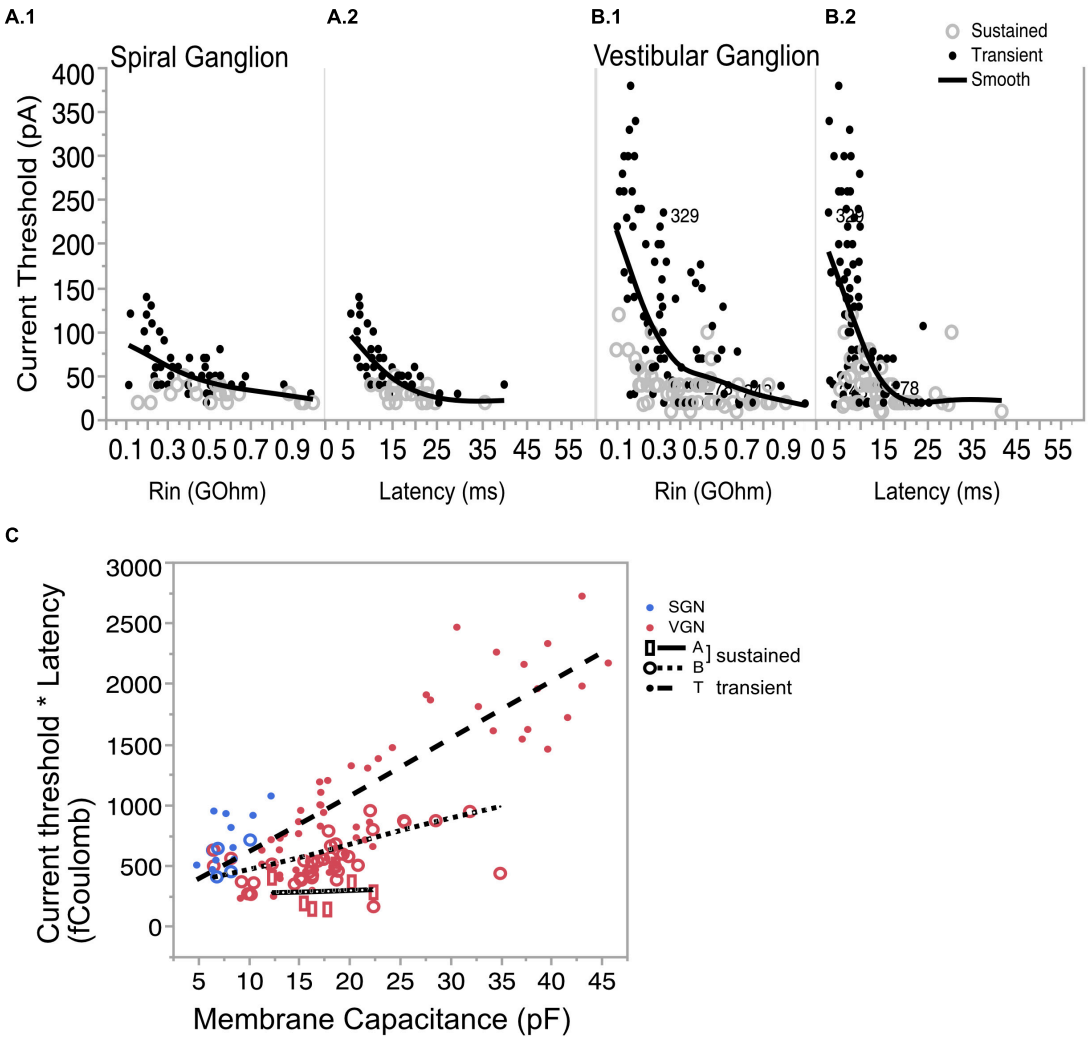

FIGURE 7 | Covariation of current threshold and first-spike latency. **(A.1)** Current threshold decreases with input resistance for sustained- and transient-spiking neurons in SGN. **(A.2)** Current threshold as a function of response latency showing that cells with large thresholds are also the cells with short latencies. **(B.1,B.2)** Same as **(A.1,A.2)** but for VGN. Solid lines in **(A.1,A.2,B1,B.2)** are smoothed spline curves drawn through the pooled transient- and sustained-spiking groups. **(C)** Charge (*Q*) that is required to reach action-potential peak plotted as a function of membrane capacitance. *Q* is estimated by multiplying (*) the current threshold by the first-spike latency. Symbols with regression lines indicate transient-spiking (dots/dash line), sustained-B spiking (open circles/dotted line) and sustained-A spiking (open rectangles/solid line). Spiral ganglion neurons are indicated in blue symbols and vestibular ganglion neurons are indicated by red symbols. * indicated multiplication of the two quantities.

Transient-spiking and sustained-spiking patterns were found in both ganglion groups. The biophysical distinctions between these two firing pattern groups neurons are qualitatively similar across the two ganglia. For example, transient-firing neurons were less excitable than sustained-spiking neurons in both SGN and VGN. These differences are consistent with previous patch-clamping studies in each system, showing that the presence of low-voltage gated potassium currents (e.g., conducted through Kv1 and KCNQ channels) is responsible for spike-train accommodation (Mo et al., 2002; Iwasaki et al., 2008; Kalluri et al., 2010). The role of low-voltage gated potassium currents in shaping firing patterns and excitability is not unique to the inner ear ganglion neurons. Similar firing pattern groups have also been described in auditory brainstem neurons (Oertel, 1983; Rothman and Manis, 2003). Bushy and Octopus cells are both known to have low impedance and produce transient-firing patterns because they contain large low-voltage gated potassium currents. In contrast, stellate cells either lack or have smaller potassium currents to produce more sustained responses.

In both SGN and VGN, the prevalence of ganglion neurons with sustained-A firing patterns decreased with postnatal age. Developmental changes in firing patterns were accompanied by an overall hyperpolarization in resting potential, a decrease in input resistance, and an increase in current threshold. The covariances between biophysical properties such as resting potential and voltage threshold and their dependence on postnatal age were similar between the two ganglia. For example, resting potential changed with postnatal age and

voltage threshold changed with resting potential. Notably, the rate of hyperpolarization in resting potential and voltage threshold was statistically similar for spiral and vestibular ganglion neurons. These developmental trends are consistent with previous electrophysiological studies showing that the density of low-voltage gated potassium currents (which regulate spike patterns and resting potentials) increase during maturation (reviewed in Davis and Crozier, 2015 for SGN; Ventura and Kalluri, 2019 for VGN). Consistent with electrophysiology, recent RNA sequencing results in SGN show enrichment of potassium channels during postnatal maturation (Shrestha et al., 2018; Sun et al., 2018; Petitpré et al., 2018). Similarly, immunohistochemistry and pharmacology in VGN provide evidence for a developmental upregulation in low-voltage gated potassium currents and their underlying channels (Rennie and Streeter, 2006; Pérez et al., 2009; Kalluri et al., 2010; Meredith and Rennie, 2015). For example, KCNQ channels (which carry part of low-voltage gated potassium currents) are initially confined to a subset of neurons innervating the central/striolar zones of the vestibular sensory epithelia. The expression pattern spreads to include peripheral/extrastiolar zones during postnatal development (Hurley et al., 2006). By P21, nearly all VGNs in mice immunolabel for KCNQ channels (Rocha-Sanchez et al., 2007). Developmental upregulation of these channels can account for the hyperpolarization of resting potentials and the tendency for firing patterns to become more phasic transient- and sustained-B firing patterns.

Although there are significant qualitative similarities in the biophysical properties of VGN and SGN, there are quantitative differences. In most of the biophysical measures, VGN have a broader range of values than in the SGN. This included more hyperpolarized resting potentials, a wider range of voltage thresholds, a larger range of current thresholds, and more diversity in cell size as probed by membrane capacitance in VGN than in SGN. This may partly be because the VGN data extend to older ages than the SGN. Since there are biophysical changes due to developmental in both neuronal groups, this likely contributes to some of the absolute differences in biophysical properties. Differences in cell size likely contribute to biophysical differences between SGN and VGN. Based on the membrane capacitance, spiral ganglion neurons are small and relatively homogenous in cell size, whereas vestibular ganglion neurons are more heterogenous with a bi-modally distribution in cell sizes. The electrophysiological estimates of cell sizer are consistent with previous morphological analyses; SGN somata have relatively homogenous cross-sectional areas (e.g., Nayagam et al., 2011) when compared to VGN, which are more variable in somatic size (Kevetter and Leonard, 2002).

The electrophysiological properties of large-bodied VGN stood out as being distinct from the rest of the VGN and SGN. These cells had the largest current thresholds, low input impedance, very fast first spike latencies, and fired predominantly with transient-spiking. Even though the biophysical features of these large VGN stand out as being distinct from SGN, the analysis presented here suggests that the large VGN are size-scaled versions of smaller transient-firing neurons in SGN and VGN. For example, the larger current thresholds and faster first spike latencies in the large VGN neurons make sense if the input resistance changes as expected when cell diameter increases while holding channel densities constant. Related by cell size, the biophysical properties of SGN and VGN can be thought of as belonging to the same size-scaled biophysical continuum.

Limitations

One advantage of the present comparison between SGN and VGN is that the recordings were made under similar conditions (internal solution composition, recording protocols, and enzymatic treatment), and uniform criteria were applied to quantify the biophysical properties of each neuron. However, there are methodological differences that are important to consider. First, SGN recordings are skewed to a younger age range because the dissection for the semi-intact preparation becomes more difficult as the otic capsule ossifies with maturation. In contrast, because the VGN were disassociated and cultured, the dataset extends to older ages. Second, the difference between acute and cultured preparations means that the somatic membranes may be in different states. Previous work has shown that time in culture and culture conditions have can impact firing patterns (Adamson et al., 2002; Zhou et al., 2005; Sun and Salvi, 2009). This may be why there is a greater prevalence of graded-firing neurons in the acute SGN than in cultured VGN. Indeed, graded responses are reported in other studies where SGN were prepared without a significant period in culture (Santos-sacchi, 1993; Jagger and Housley, 2003). This may be because ion channels redistribute to portions of the membrane otherwise covered by myelin in the endogenous condition (as described in CNS by Shrager, 1993).

Which Ion Channel Combinations Are Driving Biophysical Diversity?

In both the spiral and vestibular ganglion, similar groups of ion channels are thought to be important for shaping firing patterns (Mo et al., 2002; Liu and Davis, 2007; Iwasaki et al., 2008; Kalluri et al., 2010; Yoshimoto et al., 2015). Our previous work and that of many others have focused on currents conducted by low-voltage gated potassium channels (I_{KL}), like Kv1 and KCNQ, and currents conducted by hyperpolarization-activated cyclic-nucleotide gated channels, HCN (I_H). These currents are powerful modulators of neuronal activity because they have voltage-gated properties that make the currents available between rest and threshold. They can influence cell excitability by regulating resting potential, input resistance, membrane integration times, and firing patterns.

Based on pharmacology and modeling, spike-train accommodation is regulated by the density of I_{KL} (e.g., Mo et al., 2002; Iwasaki et al., 2008; Kalluri et al., 2010; Hight and Kalluri, 2016). I_{KL} prevents repetitive spiking because activation between rest and threshold prevents the cell from recovering to threshold after the first spike. Because I_{KL} is typically active at resting potential, cells having these currents tend to have hyperpolarized resting potential and lower input resistance. Ultimately, in neurons that express large I_{KL}, the race between reaching threshold and the activation of I_{KL} makes these neurons

sensitive to the rate of voltage depolarizations. As a result, cells with large I_{KL} respond to the sharp onsets of step stimuli in response to current steps but not to the sustained portion of the stimulus.

Voltage threshold can be regulated by the type, density, and inactivation properties of sodium channels and by the presence of potassium/leak channels that counter the depolarization force of sodium channels (Platkiewicz and Brette, 2010, 2011). As a result, voltage threshold can vary from cell to cell and depend on a cell's history. Here the more negative the resting potential of a cell, the more hyperpolarized the voltage threshold. This can broadly be understood as resulting from fewer sodium channels being inactivated at rest for cells with more hyperpolarized resting potentials. According to the modeling by Platkiewicz and Brette (2011), voltage threshold is likely to be most sensitive to membrane voltage near the half-inactivation voltage for sodium currents. The finding voltage threshold is similarly dependent on resting potential in VGN and SGN is consistent with the idea that the sodium currents are primarily carried by TTX sensitive transient Nav1.6 channels (Hossain, 2005; Lysakowski et al., 2011).

Despite the broad similarity in the threshold's dependence on resting potential, there is also significant cell to cell variability in threshold, suggesting that variations in sodium channel density and sub-unit composition could further regulate threshold. For example, VGN neurons express various sodium channels, including Nav 1.5 and Nav 1.8 (Liu et al., 2016) and sodium-dependent potassium channels (e.g., Reijntjes et al. (2019) in SGN) which can impact voltage threshold. The variable expression for Nav1.8 in calretinin positive vs. calretinin negative vestibular ganglion neurons provides evidence for differences in sodium channels composition across different cell groups (Liu et al., 2016). Recent analysis in vestibular calyx recordings also suggests that there are zonal and maturational differences in sodium current properties, with peripheral zone neurons having larger resurgent sodium currents which may make those neurons more excitable (Meredith and Rennie, 2020).

Voltage thresholds are more variable in transient-spiking vestibular neurons than in sustained-spiking neurons. A similar difference between firing pattern groups was previously noted in spiral ganglion, where neurons that fired only a single action potential had the most varied and depolarized voltage thresholds (Crozier and Davis, 2014). In addition to sodium channels, Kv1 and HCN channels, which are known to be important for transient firing, are known to regulate voltage threshold in SGN (Liu et al., 2014). Given the similar roles played by Kv1 and HCN channels in transient-firing neurons, it seems highly likely that they are similarly impacting voltage threshold in VGN, but this remains to be directly tested.

Relating Biophysical Diversity to Functional Diversity

On the surface, it seems peculiar that auditory and vestibular neurons, each with such diverse morphologies and functions, share so many common traits. Many of the individual components of the afferent synapses are similar in the two systems. For example, the synapses between hair cells and afferent neurons are composed of electron-dense ribbon-bearing pre-synaptic active zones that drive post-synaptic glutamate receptors. Across many studies, gradients in the same two classes of ionic currents (low-voltage gated potassium currents, I_{KL} and hyperpolarization-activated cationic currents, I_h) of the post-synaptic neurons are proposed as being crucial to diverse neuronal functions (Mo and Davis, 1997a,b; Mo et al., 2002; Risner and Holt, 2006; Kalluri et al., 2010; Yi et al., 2010; Horwitz et al., 2011; Almanza et al., 2012). The analysis here shows that the biophysical properties of the post-synaptic neurons are not just qualitatively similar but can be quantitatively related.

Neurons with large I_{KL} having low-input resistance, large current thresholds, fast membrane time constants, and sensitivity to rate of depolarization have also been described in the timing pathways of the auditory brainstem (Bal and Oertel, 2001; Ferragamo and Oertel, 2002; Rothman and Manis, 2003). There the presence of I_{KL} is critical for coincidence detection (reviewed in Golding and Oertel, 2012). Similarly, in vestibular afferents, the short temporal integration time in the presence of I_{KL} drives *in vitro* neurons to produce irregular spiking by allowing them to respond preferentially to rapid and randomly timed changes in simulated synaptic current (Kalluri et al., 2010). In contrast, *in vitro* ganglion neurons lacking I_{KL} (possibly combined with HCN mediated currents) have long integration times to smooth the rapid fluctuations in the incoming stimulus to generate highly regular spiking. These ideas about the possible impact of biophysical diversity on afferent responses are based on *in vitro* experiments where the somata lack normal synaptic input, dendritic filtering and efferent modulation. To make definitive associations between *in vitro* and *in vivo* patterns will require future work to test if somata with distinct firing patterns belong to afferent neurons with distinct morphology or patterns of spatial connectivity within the epithelium.

Consistent with the idea that *in vitro* neuronal classes can be related to *in vivo* classes, the large, transient-firing somata in the vestibular ganglion likely belong to the irregular-firing afferents innervating the central zones of vestibular epithelia. This is based on the observation (based on molecular expression patterns) that the somata of irregularly firing afferents from central epithelial zones tend to be larger than that of regular-firing vestibular afferents (Leonard and Kevetter, 2002). Like the large-bodied somatata, calyx terminals in striolar zone mouse vestibular epithelia produce transient-spiking and express large Kv1 and KCNQ channels when compared to extrastriolar calyces (Songer and Eatock, 2013). The morphology of pure-calyx bearing neurons suggests that these neurons are designed to respond to large, temporally compact inputs; this is the type of synaptic input one might expect from the synchronous release of neurotransmitters from many synaptic ribbons driven by small groups (1–3) of closely spaced hair cells. The arrangement of the hair cells and their ribbon synapses suggests that they might produce highly synchronized fast onset synaptic events such as those predicted by Holmes et al. (2017) to drive irregular spiking.

In contrast to the diverse range of dendritic morphologies found in vestibular afferents, the morphology of auditory afferents is homogenous. Liu and Davis (2007) proposed the idea

intrinsic diversity in voltage thresholds contributes to functional diversity I the auditory nerve (i.e., diversity in sound-intensity threshold and spontaneous rates across auditory neurons). Recent work in spiral ganglion shows that the biophysical diversity and transcriptomic diversity of ganglion neurons aligns (Petitpré et al., 2018; Shrestha et al., 2018; Sun et al., 2018; Markowitz and Kalluri, 2020) with a previously described spatial map for spontaneous rates and sound- intensity thresholds (Liberman, 1982). The somata of auditory nerve fibers contacting the pillar face of inner hair cells (putative high-spontaneous rate fibers) have lower current thresholds, higher-input impedance, and longer first-spike latencies compared to the somata of fibers contacting the modiolar face of the inner hair cell (putative low-spontaneous rate fibers) (Markowitz and Kalluri, 2020). Differences in temporal integration could contribute to the response of SR-groups by making neurons selective to the different kinetics of synaptic current. For example, synaptic events at inner hair cells are characterized by a combination of multi-phasic slow-onset events and monophasic fast-onset events (Grant et al., 2010). With shorter synaptic integration windows (reflected in first-spike latency) and lower input impedance, low-SR fibers would need large, fast onset currents to reach threshold. In contrast, the longer integration windows and lower current thresholds of pillar-contacting fibers could support faster spike rates by allowing the neuron to respond to a greater variety of synaptic inputs; e.g., both mono-phasic and multi-phasic events.

Diversity in intrinsic biophysics is only one of several factors that combine to produce an afferent neuron's response. This means that neuronal membranes with similar intrinsic biophysical properties could produce very different responses depending on the input. As schematized in **Figure 1**, the bipolar neurons of auditory and vestibular nerves are diverse in many ways. They vary in the type and number of hair cells providing input to the neurons. The temporal features of synaptic input are likely to be complex, depending on the makeup of the hair cells providing input to hair cells. For example, vestibular hair cells transmit information through both chemical and non-chemical mechanisms (Songer and Eatock, 2013; Sadeghi et al., 2014; Contini et al., 2019). Moreover, the complex dendritic arbors of vestibular neurons are likely to filter synaptic input differently than the unitary short dendrite of auditory afferents. Models of vestibular neuron activity predict that regular- and irregular-timed spiking is determined both by the intrinsic biophysical properties of the neuron and by the nature of the synaptic input (Smith and Goldberg, 1986; Hight and Kalluri, 2016). For example, modeled sustained-A neurons are equally capable of producing regular and irregular firing depending on how much of the temporal fluctuations in the synaptic signals are allowed through to the spike initiation zone (Hight and Kalluri, 2016). Future work will need to consider how dendritic morphology, synaptic specializations, and ion channel properties combine to produce functionally distinct neuronal subgroups in the auditory and vestibular nerve.

DATA AVAILABILITY STATEMENT

The original contributions presented in the study are included in the article/supplementary material, further inquiries can be directed to the corresponding author/s.

ETHICS STATEMENT

The animal study was reviewed and approved by the Institutional Animal Care and Use Committee at the University of Southern California.

AUTHOR CONTRIBUTIONS

RK: conceptualization, resources, data curation, software, formal analysis, supervision, funding acquisition, validation, investigation, visualization, methodology, project administration, writing—original draft, and editing.

FUNDING

Funding for this work was provided by the NIH-NIDCD sponsored grant R01DC015512 to RK and a Dean's Pilot grant from the Keck School of Medicine.

ACKNOWLEDGMENTS

I acknowledge the following for their contributions to the original data collection included in the current analysis: Alexander Markowitz (SGN), Christopher Ventura (VGN), and Daniel Bronson (VGN). Some of the data from early postnatal vestibular ganglion were collected by the author in partnership with Jing Bing Xue and Ruth Anne Eatock when at the Massachusetts Eye and Ear Infirmary (previously published).

REFERENCES

Adamson, C. L., Reid, M. A., and Davis, R. L. (2002). Opposite actions of brain-derived neurotrophic factor and neurotrophin-3 on firing features and ion channel composition of murine spiral ganglion neurons. *J. Neurosci.* 22, 1385–1396.

Almanza, A., Luis, E., Mercado, F., Vega, R., and Soto, E. (2012). Molecular identity, ontogeny, and cAMP modulation of the hyperpolarization-activated current in vestibular ganglion neurons. *J. Neurophysiol.* 108, 2264–2275. doi: 10.1152/jn.00337.2012

Armstrong, C. E., and Roberts, W. M. (1998). Electrical properties of frog saccular hair cells: distortion by enzymatic dissociation. *J. Neurosci.* 18, 2962–2973. doi: 10.1523/jneurosci.18-08-02962.1998

Bal, R., and Oertel, D. (2001). Potassium currents in octopus cells of the mammalian cochlear nucleus. *J. Neurophysiol.* 86, 2299–2311. doi: 10.1152/jn.2001.86.5.2299

Bean, B. P. (2007). The action potential in mammalian central neurons. *Nat. Rev. Neurosci.* 8, 451–465. doi: 10.1038/nrn2148

Berglund, A. M., and Ryugo, D. K. (1991). Neurofilament antibodies and spiral ganglion neurons of the mammalian cochlea. *J. Comp. Neurol.* 306, 393–408.

Contini, D., Holstein, G. R., and Art, J. J. (2019). Synaptic cleft microenvironment influences potassium permeation and synaptic transmission in hair cells surrounded by calyx afferents in the turtle. *J. Physiol.* 4, 853–889. doi: 10.1113/jp278680

Crozier, R. A., and Davis, R. L. (2014). Unmasking of spiral ganglion neuron firing dynamics by membrane potential and neurotrophin-3. *J. Neurosci.* 34, 9688–9702. doi: 10.1523/jneurosci.4552-13.2014

Davis, R. L., and Crozier, R. A. (2015). Dynamic firing properties of type I spiral ganglion neurons. *Cell Tissue Res.* 361, 115–127. doi: 10.1007/s00441-014-2071-x

Ferragamo, M. J., and Oertel, D. (2002). Octopus cells of the mammalian ventral cochlear nucleus sense the rate of depolarization. *J. Neurophysiol.* 87, 2262–2270.

Glowatzki, E., and Fuchs, P. (2002). Transmitter release at the hair cell ribbon synapse. *Nat. Neurosci.* 5, 147–154. doi: 10.1038/nn796

Goldberg, J. M., Lysakowski, A., and Fernández, C. (1990). Morphophysiological and ultrastructural studies in the mammalian cristae ampullares. *Hear Res.* 49, 89–102. doi: 10.1016/0378-5955(90)90097-9

Golding, N. L., and Oertel, D. (2012). Synaptic integration in dendrites: exceptional need for speed. *J. Physiol.* 590, 5563–5569. doi: 10.1113/jphysiol.2012.229328

Golowasch, J., Thomas, G., Taylor, A. L., Patel, A., Pineda, A., Khalil, C., et al. (2009). Membrane capacitance measurements revisited: dependence of capacitance value on measurement method in nonisopotential neurons. *J. Neurophysiol.* 102, 2161–2175. doi: 10.1152/jn.00160.2009

Grant, L., Yi, E., and Glowatzki, E. (2010). Two modes of release shape the postsynaptic response at the inner hair cell ribbon synapse. *J. Neurosci.* 30, 4210–4220. doi: 10.1523/jneurosci.4439-09.2010

Hight, A. E., and Kalluri, R. (2016). A biophysical model examining the role of low-voltage-activated potassium currents in shaping the responses of vestibular ganglion neurons. *J. Neurophysiol.* 116, 503–521. doi: 10.1152/jn.00107.2016

Horwitz, G. C., Risner-Janiczek, J. R., Jones, S. M., and Holt, J. R. (2011). HCN channels expressed in the inner ear are necessary for normal balance function. *J. Neurosci.* 31, 16814–16825. doi: 10.1523/jneurosci.3064-11.2011

Hossain, W. A. (2005). Where is the spike generator of the cochlear nerve? Voltage Gated Sodium Channels in the Mouse Cochlea. *J. Neurosci.* 25, 6857–6868. doi: 10.1523/jneurosci.0123-05.2005

Hurley, K. M., Gaboyard, S., Zhong, M., Price, S. D., Wooltorton, J. R. A., Lysakowski, A., et al. (2006). M-like K+ currents in type I hair cells and calyx afferent endings of the developing rat utricle. *J. Neurosci.* 26, 10253–10269.

Iwasaki, S., Chihara, Y., Komuta, Y., Ito, K., and Sahara, Y. (2008). Low-voltage-activated potassium channels underlie the regulation of intrinsic firing properties of rat vestibular ganglion cells. *J. Neurophysiol.* 100, 2192–2204. doi: 10.1152/jn.01240.2007

Iwasaki, S., Nakajima, T., Chihara, Y., Inoue, A., Fujimoto, C., and Yamasoba, T. (2012). Developmental changes in the expression of Kv1 potassium channels in rat vestibular ganglion cells. *Brain Res.* 2:1429.

Jagger, D. J., and Housley, G. D. (2003). Membrane properties of type II spiral ganglion neurones identified in a neonatal rat cochlear slice. *J. Physiol.* 552, 525–533.

Kalluri, R., Xue, J., and Eatock, R. A. (2010). Ion channels set spike timing regularity of mammalian vestibular afferent neurons. *J. Neurophysiol.* 104, 2034–2051. doi: 10.1152/jn.00396.2010

Kevetter, G. A., and Leonard, R. B. (2002). Molecular probes of the vestibular nerve II. characterization of neurons in Scarpa's ganglion to determine separate populations within the nerve. *Brain Res.* 928, 18–29.

Leonard, R. B., and Kevetter, G. A. (2002). Molecular probes of the vestibular nerve. I. peripheral termination patterns of calretinin, calbindin and peripherin containing fibers. *Brain Res.* 928, 8–17. doi: 10.1016/s0006-8993(01)03268-1

Liberman, M. C. (1982). Single-neuron labeling in the cat auditory nerve. *Science* 216, 1239–1241.

Liu, Q., and Davis, R. L. (2007). Regional specification of threshold sensitivity and response time in CBA/CaJ mouse spiral ganglion neurons. *J. Neurophysiol.* 98, 2215–2222. doi: 10.1152/jn.00284.2007

Liu, Q., Lee, E., and Davis, R. L. (2014). Heterogeneous intrinsic excitability of murine spiral ganglion neurons is determined by Kv1 and HCN channels. *Neuroscience* 257, 96–110.

Liu, X.-P., Wooltorton, J., Gaboyard-Niay, S., Yang, F.-C., Lysakowski, A., and Eatock, R. A. (2016). Sodium channel diversity in the vestibular ganglion: Tetrodotoxin-sensitive, Nav1.5 and Nav1.8 currents. *J. Neurophysiol.* 115, 2536–2555. doi: 10.1152/jn.00902.2015

Lysakowski, A., and Goldberg, J. M. (2008). Ultrastructural analysis of the cristae ampullares in the squirrel monkey (*Saimiri sciureus*). *J. Comput. Neurol.* 511, 47–64. doi: 10.1002/cne.21827

Lysakowski, A., Gaboyard-Niay, S., Calin-Jageman, I., and Chatlani, S. (2012). Molecular microdomains in a sensory terminal, the vestibular calyx ending. *J. Neurosci.* 31, 10101–10114.

Lysakowski, A., Gaboyard-Niay, S., Calin-Jageman, I., Chatlani, S., Price, S. D., and Eatock, R. A. (2011). Molecular microdomains in a sensory terminal, the vestibular calyx ending. *J. Neurosci.* 31, 10101–10114.

Markowitz, A. L., and Kalluri, R. (2020). Gradients in the biophysical properties of neonatal auditory neurons align with synaptic contact position and the intensity coding map of inner hair cells. *Elife* 9, 1–33.

Merchan-Perez, A., and Liberman, M. C. (1996). Ultrastructural differences among afferent synapses on cochlear hair cells: correlations with spontaneous discharge rate. *J. Comput. Neurol.* 371, 208–221. doi: 10.1002/(sici)1096-9861(19960722)371:2<208::aid-cne2>3.0.co;2-6

Meredith, F. L., and Rennie, K. J. (2015). Zonal variations in k+currents in vestibular crista calyx terminals. *J. Neurophysiol.* 113, 264–276.

Meredith, F. L., and Rennie, K. J. (2020). Persistent and resurgent na currents in vestibular calyx afferents. *J. Neurophysiol.* 124, 510–524.

Mo, Z. L., and Davis, R. L. (1997a). Endogenous firing patterns of murine spiral ganglion neurons. *J. Neurophysiol.* 77, 1294–1305. doi: 10.1152/jn.1997.77.3.1294

Mo, Z. L., and Davis, R. L. (1997b). Heterogeneous voltage dependence of inward rectifier currents in spiral ganglion neurons. *J Neurophysiol* 78, 3019–3027. doi: 10.1152/jn.1997.78.6.3019

Mo, Z.-L., Adamson, C. L., and Davis, R. L. (2002). Dendrotoxin-sensitive K+ currents contribute to accommodation in murine spiral ganglion neurons. *J. Physiol.* 542, 763–778. doi: 10.1113/jphysiol.2002.017202

Nayagam, B. A., Muniak, M. A., and Ryugo, D. K. (2011). The spiral ganglion: connecting the peripheral and central auditory systems. *Hear Res.* 278, 2–20. doi: 10.1016/j.heares.2011.04.003

Oertel, D. (1983). Synaptic responses and electrical properties of cells in brain slices of the mouse anteroventral cochlear nucleus. *J. Neurosci.* 3, 2043–2053.

Petitpré, C., Wu, H., Sharma, A., Tokarska, A., Fontanet, P., Wang, Y., et al. (2018). Neuronal heterogeneity and stereotyped connectivity in the auditory afferent system. *Nat. Commun.* 9:3691.

Pérez, C., Limón, A., Vega, R., and Soto, E. (2009). The muscarinic inhibition of the potassium M-current modulates the action-potential discharge in the vestibular primary-afferent neurons of the rat. *Neuroscience* 158, 1662–1674.

Platkiewicz, J., and Brette, R. (2010). A threshold equation for action potential initiation. *PLoS Comput. Biol.* 6:25.

Platkiewicz, J., and Brette, R. (2011). Impact of fast sodium channel inactivation on spike threshold dynamics and synaptic integration. *PLoS Comput. Biol.* 7:e1001129.

Quandt, F. N. (1987). Burst kinetics of sodium channels which lack fast inactivation in mouse neuroblastoma cells. *J. Physiol.* 392, 563–585.

Reijntjes, D. O. J., Lee, J. H., Park, S., Schubert, N. M. A., van Tuinen, M., Vijayakumar, S., et al. (2019). Sodium-activated potassium channels shape peripheral auditory function and activity of the primary auditory neurons in mice. *Sci. Rep.* 9:2573.

Rennie, K. J., and Streeter, M. A. (2006). Voltage-dependent currents in isolated vestibular afferent calyx terminals. *J. Neurophysiol.* 95, 26–32.

Risner, J. R., and Holt, J. R. (2006). Heterogeneous potassium conductances contribute to the diverse firing properties of postnatal mouse vestibular ganglion neurons. *J. Neurophysiol.* 96, 2364–2376.

Rocha-Sanchez, S. M. S., Morris, K. A., Kachar, B., Nichols, D., Fritzsch, B., and Beisel, K. W. (2007). Developmental expression of Kcnq4 in vestibular neurons and neurosensory epithelia. *Brain Res.* 1139, 117–125.

Romand, M.-R., and Romand, R. (1990). Development of spiral ganglion cells in mammalian cochlea. *J. Electron. Microsc.* Tech. 15, 144–154.

Rothman, J. S., and Manis, P. B. (2003). The roles potassium currents play in regulating the electrical activity of ventral cochlear nucleus neurons. *J. Neurophysiol.* 89, 3097–3113. doi: 10.1152/jn.00127.2002

Sadeghi, S. G., Pyott, S. J., Yu, Z., and Glowatzki, E. (2014). Glutamatergic signaling at the vestibular hair cell calyx synapse. *J. Neurosci.* 34, 14536–14550. doi: 10.1523/jneurosci.0369-13.2014

Santos-sacchi, J. (1993). Voltage-dependent ionic conductances cells from the guinea pig inner ear. *J. Neurosci.* 13, 3599–3611.

Shrager, P. (1993). Axonal coding of action potentials in demyelinated nerve fibers. *Brain Res.* 619, 278–290. doi: 10.1016/0006-8993(93)91622-y

Shrestha, B. R., Chia, C., Wu, L., Kujawa, S. G., Liberman, M. C., and Goodrich, L. V. (2018). Sensory neuron diversity in the inner ear is shaped by activity. *Cell* 174, 1229–1246.e17.

Smith, C. E., and Goldberg, J. M. (1986). A stochastic afterhyperpolarizaton model of repetitive activity in vestibular afferents. *Biol. Cybern.* 54, 41–51. doi: 10.1007/bf00337114

Songer, J. E., and Eatock, R. A. (2013). Tuning and timing in mammalian type i hair cells and calyceal synapses. *J. Neurosci.* 33, 3706–3724. doi: 10.1523/jneurosci.4067-12.2013

Sun, W., and Salvi, R. J. (2009). BDNF and NT-3 modulate neurotransmitter receptor expressions on developing spiral ganglion neurons. *Neuroscience* 164, 1854–1866. doi: 10.1016/j.neuroscience.2009.09.037

Sun, S., Babola, T., Pregernig, G., So, K. S., Nguyen, M., Su, S. S. M., et al. (2018). Hair Cell mechanotransduction regulates spontaneous activity and spiral ganglion subtype specification in the auditory system. *Cell* 174, 1247–1263.e15.

Tsuji, J., and Liberman, M. C. (1997). Intracellular labeling of auditory nerve fibers in guinea pig: central and peripheral projections. *J. Comp. Neurol.* 202, 188–202.

Ventura, C. M., and Kalluri, R. (2019). Enhanced activation of HCN channels reduces excitability and spike-timing regularity in maturing vestibular afferent neurons. *J. Neurosci.* 39, 2860–2876. doi: 10.1523/jneurosci.1811-18.2019

Yi, E., Roux, I., and Glowatzki, E. (2010). Dendritic HCN channels shape excitatory postsynaptic potentials at the inner hair cell afferent synapse in the mammalian cochlea. *J. Neurophysiol.* 103, 2532–2543.

Yoshimoto, R., Iwasaki, S., Takago, H., Nakajima, T., Sahara, Y., and Kitamura, K. (2015). Developmental increase in hyperpolarization-activated current regulates intrinsic firing properties in rat vestibular ganglion cells. *Neuroscience* 284, 632–642. doi: 10.1016/j.neuroscience.2014.10.034

Zhou, Z., Liu, Q., and Davis, R. L. (2005). Complex regulation of spiral ganglion neuron firing patterns by neurotrophin-3. *J. Neurosci.* 25, 7558–7566. doi: 10.1523/jneurosci.1735-05.2005

Conflict of Interest: The author declares that the research was conducted in the absence of any commercial or financial relationships that could be construed as a potential conflict of interest.

Publisher's Note: All claims expressed in this article are solely those of the authors and do not necessarily represent those of their affiliated organizations, or those of the publisher, the editors and the reviewers. Any product that may be evaluated in this article, or claim that may be made by its manufacturer, is not guaranteed or endorsed by the publisher.

frontiers in Neuroscience

ORIGINAL RESEARCH
published: 14 October 2021
doi: 10.3389/fnins.2021.741571

Sound-Evoked Responses in the Vestibulo-Ocular Reflex Pathways of Rats

Tianwen Chen[1†], Jun Huang[1†], Yue Yu[1†], Xuehui Tang[1], Chunming Zhang[2], Youguo Xu[1], Alberto Arteaga[1], Jerome Allison[1,3], William Mustain[1], Matthew C. Donald[4], Tracy Rappai[4], Michael Zhang[5], Wu Zhou[1,3,6] and Hong Zhu[1,3]**

[1] Department of Otolaryngology-Head and Neck Surgery, University of Mississippi Medical Center, Jackson, MS, United States, [2] Department of Otolaryngology, First Affiliated Hospital, Shanxi Medical University, Taiyuan, China, [3] Department of Neurobiology and Anatomical Sciences, University of Mississippi Medical Center, Jackson, MS, United States, [4] School of Medicine, University of Mississippi Medical Center, Jackson, MS, United States, [5] Summer Undergraduate Research Program, University of Mississippi Medical Center, Jackson, MS, United States, [6] Department of Neurology, University of Mississippi Medical Center, Jackson, MS, United States

OPEN ACCESS

Edited by:
Soroush G. Sadeghi,
University at Buffalo, United States

Reviewed by:
Natela Shanidze,
Smith-Kettlewell Eye Research Institute, United States
Martha Bagnall,
Washington University in St. Louis, United States

***Correspondence:**
Wu Zhou
wzhou@umc.edu
Hong Zhu
hozhu@umc.edu

[†] These authors have contributed equally to this work

Specialty section:
This article was submitted to Perception Science, a section of the journal Frontiers in Neuroscience

Received: 14 July 2021
Accepted: 22 September 2021
Published: 14 October 2021

Citation:
Chen T, Huang J, Yu Y, Tang X, Zhang C, Xu Y, Arteaga A, Allison J, Mustain W, Donald MC, Rappai T, Zhang M, Zhou W and Zhu H (2021) Sound-Evoked Responses in the Vestibulo-Ocular Reflex Pathways of Rats. Front. Neurosci. 15:741571. doi: 10.3389/fnins.2021.741571

Vestibular evoked myogenic potentials (VEMP) have been used to assess otolith function in clinics worldwide. However, there are accumulating evidence suggesting that the clinically used sound stimuli activate not only the otolith afferents, but also the canal afferents, indicating canal contributions to the VEMPs. To better understand the neural mechanisms underlying the VEMPs and develop discriminative VEMP protocols, we further examined sound-evoked responses of the vestibular nucleus neurons and the abducens neurons, which have the interneurons and motoneurons of the vestibulo-ocular reflex (VOR) pathways. Air-conducted clicks (50–80 dB SL re ABR threshold, 0.1 ms duration) or tone bursts (60–80 dB SL, 125–4,000 Hz, 8 ms plateau, 1 ms rise/fall) were delivered to the ears of Sprague-Dawley or Long-Evans rats. Among 425 vestibular nucleus neurons recorded in anesthetized rats and 18 abducens neurons recorded in awake rats, sound activated 35.9% of the vestibular neurons that increased discharge rates for ipsilateral head rotation (Type I neuron), 15.7% of the vestibular neurons that increased discharge rates for contralateral head rotation (Type II neuron), 57.2% of the vestibular neurons that did not change discharge rates during head rotation (non-canal neuron), and 38.9% of the abducens neurons. Sound sensitive vestibular nucleus neurons and abducens neurons exhibited characteristic tuning curves that reflected convergence of canal and otolith inputs in the VOR pathways. Tone bursts also evoked well-defined eye movements that increased with tone intensity and duration and exhibited peak frequency of ∼1,500 Hz. For the left eye, tone bursts evoked upward/rightward eye movements for ipsilateral stimulation, and downward/leftward eye movements for contralateral stimulation. These results demonstrate that sound stimulation results in activation of the canal and otolith VOR pathways that can be measured by eye tracking devices to develop discriminative tests of vestibular function in animal models and in humans.

Keywords: vestibular-evoked myogenic potential (VEMP), single unit recording, vestibulo ocular reflex, otolith, canal, eye movement, abducens nucleus

INTRODUCTION

Since the discovery of the vestibular-evoked myogenic potentials (VEMPs) (Colebatch and Halmagyi, 1992), there has been a rapid growth of VEMP research and investigators worldwide have used the VEMPs to characterize a variety of vestibulopathies, including Tullio/superior canal dehiscence syndrome, vestibular neuritis, Ménière's disease, and vestibular schwannoma (Minor et al., 1998; Rauch, 2006; Rosengren et al., 2010). Although the VEMPs have been widely used, important issues on the neural basis remain to be elucidated in order to develop more discriminative VEMP protocols and interpretative guidelines. Because early animal studies showed that loud sound primarily activates the otolith afferents (Murofushi et al., 1995; Murofushi and Curthoys, 1997), the VEMPs are presently used to test otolith function. However, there are studies suggesting that loud sound also activates other vestibular end organs. For example, Young et al. (1977) and Carey et al. (2004) reported that long duration tones activated both the canals and the otoliths in monkeys and chinchillas, respectively. We further found that the clinical VEMP stimuli activated both the canal and otolith afferents in rats (Zhu et al., 2011b, 2014). Consistent with these single unit recording results, our intra-axonal labeling studies provided anatomical evidence that sound sensitive afferents innervate horizontal and anterior cristae as well as saccular and utricular macule (Zhu et al., 2014).

The goal of the present study was to extend the studies of sound activation of the vestibular afferents to examine sound activation of the vestibular nucleus neurons and the abducens neurons, which mediate the ocular VEMP (oVEMP) recorded over the extraocular muscles (Wilson and Schor, 1999; Uchino et al., 2005; Uchino and Kushiro, 2011). Furthermore, we employed a video-based eye tracker to examine tone burst-evoked eye movements in awake rats. These results show that sound activation of the vestibular afferents are processed by the vestibular nucleus neurons, which then activate the VOR motoneurons to generate sound-evoked eye movements. This knowledge not only provides insight into neural mechanisms underlying the VEMPs, but also provides evidence showing the potentials of sound-evoked eye movement as a test of vestibular function in animal models and in humans.

MATERIALS AND METHODS

Adult male Sprague-Dawley (SD) rats weighing 250–350 g (Harlan, Indianapolis, IN, United States) were used in the experiments of recording vestibular nucleus neurons in anesthetized condition. Adult female Long-Evens (LE) rats weighing 175–225 g (Harlan, Indianapolis, IN, United States) were used in the experiments of single unit recording of the abducens neurons and recording of eye movements in awake condition. The abducens recording and sound-evoked eye movement experiments were initiated after completion of the vestibular nucleus recording experiments. These experiments need to be performed in a different strain of rats (i.e., Long-Evans rats) because we found out that SD rats were albino and their pupils could not be tracked by the ISCAN eye tracker. All procedures were approved by the Institutional Animal Care and Use Committee at University of Mississippi Medical Center.

Single Unit Recording of the Vestibular Nucleus Neurons

Surgeries

Sound-evoked responses in vestibular nuclei were first studied in anesthetized animals by Murofushi et al. (1996). To be comparable to the literature, we performed vestibular nucleus neuron recordings in anesthesia rats (sodium pentobarbital, 50 mg/kg, i.p.). The animals' core body temperature was monitored and maintained at 36–37°C with a heating pad (Frederick Haer & Company, Bowdoinham, ME, United States). A midline dorsal cranial skin incision was made and soft tissues were cleared to expose skull suture landmarks bregma and lambda. A small stainless steel cylinder was cemented on the skull by dental acrylic for stabilization of the rat's head during recording experiments. The head was stabilized on a stereotaxic frame with the head holder by a Kopf stereotaxic carriage (David Kopf Instruments, Tujunga, CA, United States). A burr-hole was made in the skull over the coordinates corresponding to the vestibular nuclei (From Lamda, L 1.5–2.0 mm, AP 3.6–4.6 mm, D 7–8 mm, Paxinos and Watson, 1998). A microelectrode (Sutter Instruments, Novato, CA, United States) filled with 3M sodium chloride (5 MΩ) that was mounted on a microdrive was then advanced into the vestibular nuclei. Signals were amplified and filtered by a MNAP system (Plexon Inc., Dallas, TX, United States). Once a unit was isolated, at least 30 s background discharge activity was recorded. Then the unit's responses to head rotation and sound stimulation were recorded.

Vestibular Stimulation

The animal's body was restrained in a nylon jacket and stabilized in the stereotaxic instrument. The stereotaxic instrument was mounted on a custom-made rotation device that allowed us to deliver head rotations. In order to stimulate horizontal and vertical canals, the head was tilted 30° nose down and 15° left ear down (Estes et al., 1975; Daunicht and Pellionisz, 1987; Blanks and Torigoe, 1989) and subjected to sinusoidal earth-horizontal rotations (1 Hz, 10°, peak velocity of 62.8 deg/s). Single unit data along with horizontal and vertical head position signals were recorded for at least 10 cycles.

Sound Stimulation

Sound was generated by a MA3 stereo microphone amplifier (DT system, Tucker-Davis Technologies, Alachua, FL, United States) and delivered via an insert ear phone (ER-3A). A hard plastic infant tip adapter was placed at the end of a sound conducting tubing and placed into a speculum which was sealed in the ear canal. Before and after the speculum was inserted, the ear canal was checked with an otoscope to ensure that it was patent. To ensure comparability of results between animals, sound intensity was referred to the threshold of the auditory brainstem response (ABR) of individual animals. ABR threshold was determined for each rat using stainless steel subdermal needle electrodes placed at the vertex (active), behind the stimulated ear (reference) and in the hind leg (ground) (Simpson et al., 1985). Differentially

recorded signals were amplified (100,000×), filtered (100 Hz–3 kHz) and digitized at 20 kHz over a 15 ms epoch (ICS Chartr EP 200 evoked potential assessment device, GN Otometrics, Taastrup, Denmark). Stimulus was a 0.1 ms click of alternating polarity, delivered through the earphone at a rate of 25.1/s. ABR threshold was determined by averaging 2,000 responses. Animals with elevated thresholds were excluded to eliminate the effects of a possible conductive hearing loss.

Air-conducted clicks (50–80 dB re ABR threshold, 0.1 ms duration, rarefaction or condensation) or tone bursts with various frequencies and intensities (125–4,000 Hz; 8 ms plateau, 1 ms rise/fall; 60–80 dB SL re ABR threshold) were delivered randomly at a rate of 5 Hz to the ear ipsilateral to the recording site. Typically, 150 trials were obtained for each condition (100 ms pre-stimulus to 100 ms post-stimulus).

Single Unit Recording of the Abducens Neurons

Under general anesthesia, a burr hole (∼3 mm) was made in the skull over the coordinates corresponding to the abducens nucleus (From Lamda, L 0–0.5 mm, AP 3.6–4.0 mm, D 8–8.5 mm, Paxinos and Watson, 1998) and the dura was removed. The craniotomy was closed by bone wax and protected by a recording chamber secured to the skull by dental acrylic. The chamber was covered by a cap. Rats were given at least 7 days to allow a full recovery. Because a pilot study showed that few abducens neurons were activated by sound stimulation in anesthetized rats, in this study, we performed single unit recordings of the abducens neurons in awake LE rats. Each rat was briefly anesthetized with isoflurane and the head was stabilized on a stereotaxic frame via the head holder. To avoid bleeding due to hitting the sinus, the head was positioned 18° downward with respect to the horizontal arm of the stereotaxic instrument. A microelectrode was advanced downward by a microdrive to search for abducens neurons. Once a neuron was isolated, its responses to spontaneous eye movements and eye movements evoked by passive head rotations were recorded. Then its responses to air-conduced clicks or tone bursts delivered to the ipsilateral and contralateral ears were recorded. While the atlas coordinates were used as the guide to search for abducens neurons, the final identification of abducens neurons was based on their eye movement sensitivity and histological reconstruction.

Eye Movement Recording

Female LE rats were used to study sound-evoked eye movements since their pupils are better tracked for eye movement recording and they have been shown to tolerate the restraint method well (Quinn et al., 1998). The rat eye movement was recorded using a video-based eye tracker (ISCAN ETS-200, ISCAN, Burlington, MA, United States) as described in our previous study (Stewart et al., 2016). Briefly, a rat's head and body was secured on a stereotaxic instrument that was mounted on a servo-controlled rotator. An infrared camera equipped with a zoom lens (Computar TV Zoom Lens, Computar Optics Group, Japan) was attached to the platform of the rotator and was focused on the eye. The rat's left eye was illuminated by a standard ISCAN multiple infrared LED illuminator attached to the camera mount on a flexible arm to produce a reference corneal reflection (CR). The ISCAN system tracks the centers of the pupil and CR and provides real-time signals related to pupil position and CR position, which were digitized and sampled at 1 kHz with head position signals by a CED Power 1401 system (Cambridge Electronics Devices, Cambridge, United Kingdom). Calibration was achieved by rotating the camera by ±10° around the vertical axis of the turntable.

Histology

After completion of the single unit recording experiments, a dye deposit was made in the recording site by injecting of 7% fast green with a current of 7 μA for 10 min. Brain sections (45 μm) were cut and stained with cresyl violet to recover the recording sites.

Data Acquisition and Data Analysis

Extracellular voltage signals were filtered and sampled by a CED Power 1401 system (Cambridge Electronics Devices, Cambridge, United Kingdom) at 20 kHz with 16-bit resolution and a temporal resolution of 0.01 ms. Signals of horizontal and vertical head positions and sound stimulation were sampled at 1 kHz. These signals were stored on a hard disk for offline analyses. Data analysis was performed on PC workstations using Spike 2 (Cambridge Electronics Devices, Cambridge, United Kingdom), MatLab (The MathWorks, Inc. Natick, MA, United States) and SigmaPlot (Systat Software, Inc., San Jose, CA, United States). Coefficient of variation (CV) of interspike intervals was used to assess regularity of spontaneous discharge of vestibular nucleus neurons. For vestibular afferents in rodents, CV has been shown to be dependent on firing rate and CV* has been used to normalize CV (Lasker et al., 2008). For vestibular nucleus neurons, however, the relationship between CV and firing rate has not been established. Thus, we did not attempt to adopt the CV* approach to normalize CV in vestibular nucleus neurons. Head motion signals and neuronal firing rate data were averaged over multiple sinusoidal cycles. A fast Fourier transform (FFT) analysis was performed to compute the gain and phase of the unit with respect to the fundamental frequency. Gain and phase relative to head velocity were calculated at the fundamental stimulus frequency (∼0.5 Hz). Neurons that were excited by ipsilateral head rotation were classified as Type I neurons. Vestibular nucleus neurons that were excited by contralateral head rotation were classified as Type II neurons. This classification was adopted from Scudder and Fuchs (1992). Because we were unable to test type-II neurons for pitch rotations, type-II neurons likely include both true-Type II neurons and vertical canal neurons. Neurons that were not modulated during head rotation likely received inputs from otolith afferents and were classified as non-canal neurons.

Sound sensitivity of the vestibular nucleus neurons and abducens neurons was quantified by computing the cumulative probability of evoking a spike (CPE) (Broussard and Lisberger, 1992; Broussard et al., 1995; Zhu et al., 2011b, 2014) which was able to accurately compute the latency and amplitude of

the sound-evoked responses and to quantitatively assess relative sound sensitivity among different neurons. To compute the CPE, first, the latency between the click or tone burst and the foot of the first action potential after sound onset was measured for 150 sound stimuli. Then the latencies were arranged in ascending order and were paired with an ascending series of probabilities ranging in equal increments from 1/150 to 1.0. To estimate the time course of the probability of firing after sound onset, probability of firing was plotted as a function of the time after sound onset ("click," **Figure 1C**, left panel). To take into account the probability that the neuron would have fired in the absence of sound, the same analysis was performed beginning 30 ms before sound onset ("no-click," **Figure 1C**, left panel). Linear regression was used to fit a line to the "no-click" data and the Y-value of the line was subtracted from each "click" value to yield the probability of evoking a spike as a function of time (**Figure 1C**, right panel). The latency of the sound-evoked response was defined as the onset of the abrupt increase in firing probability (**Figure 1C**, right panel, the point of divergence between the line and the data points in the Click condition). The amplitude of the neuron response was measured by the height of the rapid change in firing probability. A neuron was classified as sound sensitive if its CPE was larger than 0.1, i.e., clicks or tones increased firing probability by 0.1.

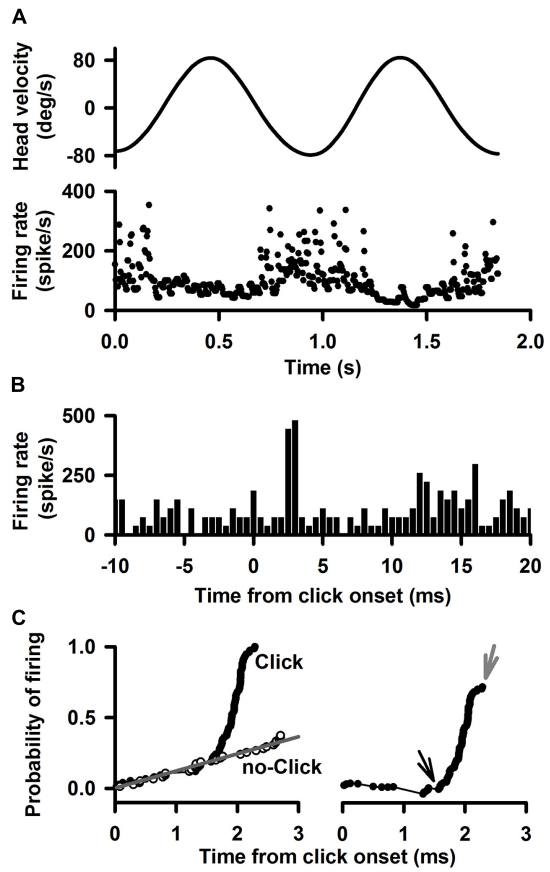

FIGURE 1 | A representative Type I neuron's responses to clicks (0.1 ms, rarefaction, 50–80 dB SL, 0 dB is referred to the threshold of the ABR) delivered to the ipsilateral ear. **(A)** Upper trace: head velocity. Lower trace: firing rate of the neuron in response to 1 Hz horizontal rotation. **(B)** Peristimulus histograms of click-evoked responses at 80 dB SL. Bin size is 0.5 ms. **(C)** Quantitative measurement of the time course of the click-evoked excitatory response. *Left panel* probability of evoking a spike. The black curve labeled "click" plots the probability that the neuron fired as a function of time after click onset. The gray curve labeled "no click" plots the probability that the neuron fired as a function of time during spontaneous discharging. *Right panel* Probability of evoking a spike as a function of time, obtained by subtracting the regression line (no-click, gray) in the upper panel from the data for "click" case. Amplitude of evoked-response is defined by cumulative probability of evoking a spike (CPE), which is estimated as peak probability (gray arrow) minus the baseline probability (black arrow). Latency of click-evoked response is defined as the onset of the sharp increase in firing probability (black arrow).

Statistical Analysis

Statistical analyses were performed using SigmaPlot. Differences among experimental groups were analyzed by one-way or two-way ANOVAs. Differences between two experimental groups were analyzed by *t*-tests or paired *t* tests. *P* values of less than 0.05 were considered statistically significant. Mean values $\pm$ SE are presented.

RESULTS

Sound-Evoked Responses of the Vestibular Nucleus Neurons

A total of 425 vestibular nucleus neurons were recorded from 62 rats (**Table 1**). **Figure 1** shows typical responses to click of a Type I vestibular nucleus neuron, which increased its firing rate to ipsilateral head rotation (1 Hz) with a gain of 0.45 (spike/s)/(deg/s) and a phase lag of 3.5° with respect to the ipsilateral head velocity (**Figure 1A**). The peristimulus histograms exhibit short-latency excitatory responses to clicks of 80 dB SL (**Figure 1B**). The cumulative probability of evoking a spike, i.e., CPE, as a function of time was computed to measure latency and amplitude of the sound-evoked responses (**Figure 1C**). Latency of the sound-evoked response was defined as the onset of the sharp increase in firing probability (**Figure 1C**, right panel, black arrow). Amplitude of the sound-evoked

TABLE 1 | Summary of the responses of vestibular nucleus neurons to clicks or tone bursts.

	Clicks			Tones		
	Type I	Type II	Non-canal	Type I	Type II	Non-canal
SS	42	7	37	24	7	50
NSS	64	54	13	54	21	52
Total	106	61	50	78	28	102
% of SS	39.6%	11.5%	74%	30.8%	25%	49%

Data are presented as number of neurons or and percentage of sound sensitive neuron. Neurons that were excited by ipsilateral earth-horizontal rotations were classified as Type I neurons. Neurons that were excited by contralateral earth-horizontal rotations were classified as Type II neurons. Neurons that were not modulated during earth-horizontal rotation were classified as non-canal neurons. SS, sound sensitive neuron; NSS, non-sound sensitive neurons. A SS neuron is defined as CPE values are above 0.1. See text for statistical analysis.

response was estimated as the difference between the peak probability (gray arrow) and the baseline probability (black arrow). This Type I vestibular neuron has a latency of 1.36 ms and an amplitude of 0.81 for clicks at 80 dB SL.

Click-Evoked Responses of Vestibular Nucleus Neurons

Click-evoked responses were studied in 217 of the 425 vestibular nucleus neurons. There were more sound sensitive Type I neurons than Type II neurons (39.6 vs. 11.5%, Chi-square test, $P < 0.001$) and more sound sensitive non-canal neurons (74%) than the Type I or Type II neurons (Chi-square test, $P < 0.032$ and $P < 0.001$, respectively) (**Table 1**). A two-way ANOVA of 35 vestibular nucleus neurons (17 Type I, 3 Type II, and 15 non-canal) that were tested with four intensity levels (50–80 dB SL) revealed significant effects of click intensity ($P < 0.001$, $F_{3,139} = 40.3$) and neuron type ($P < 0.001$, $F_{2,139} = 8.6$) on CPE but no significant interaction between the two factors ($F_{6,139} = 1.8$, $P = 0.097$). *Post hoc* analysis (Holm-Sidak) revealed that all types of neurons showed increased responses with higher sound intensities ($P < 0.05$), but there was no significant difference between 50 and 60 dB conditions ($P = 0.846$; **Figure 2**). The threshold to activate the non-canal neurons was 70 dB SL while the threshold to activate the canal sensitive neurons was 80 dB SL. The non-canal neurons had larger CPEs than the Type I ($T = 3.77$, $P < 0.001$) and Type II neurons ($T = 2.80$, $P = 0.012$). There was no significant difference in CPE amplitudes between Type I and Type II neurons ($T = 0.69$, $P = 0.49$).

The vestibular nucleus neurons responded to both rarefaction and condensation clicks. Click polarity exhibited no significant effects on the CPE amplitudes of the Type I, Type II, and non-canal neurons. **Figures 3A,B** show the latency distributions for sound sensitive vestibular nucleus neurons. Averaged response latencies to rarefaction clicks and condensation clicks were

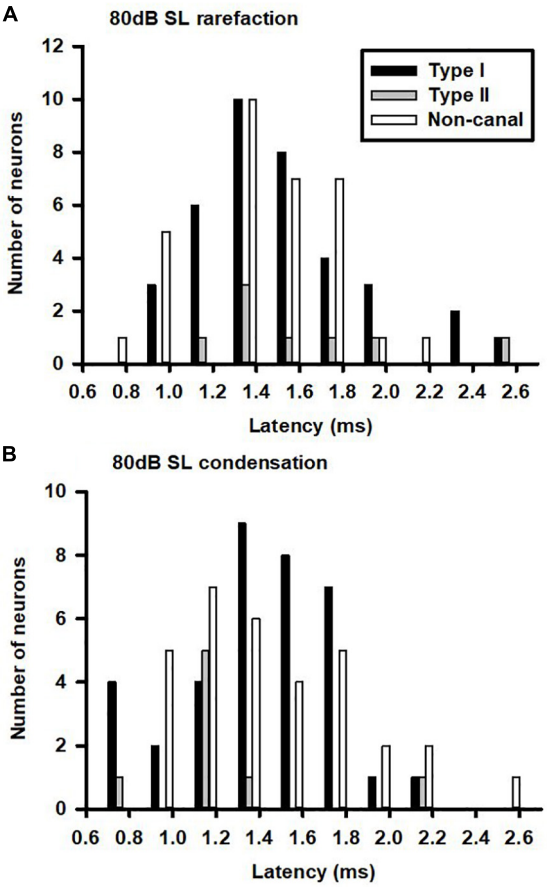

FIGURE 3 | Latency distributions of click-evoked responses in vestibular nucleus neurons. **(A)** Rarefaction and **(B)** condensation.

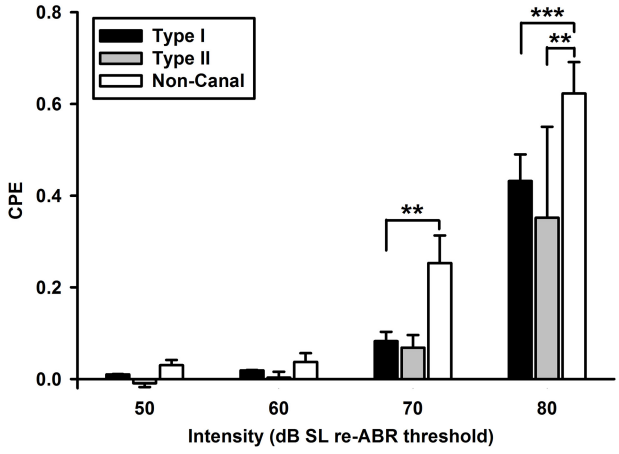

FIGURE 2 | Click-evoked responses of vestibular nucleus neurons (Type I, Type II, and non-canal neurons) as a function of click intensity. All types of neurons showed increased responses with higher sound intensities. The non-canal neurons had larger click-evoked responses than Type I and Type II neurons. ***$P < 0.001$, **$P < 0.01$.

1.43 ± 0.04 and 1.37 ± 0.04 ms, respectively. Overall, there was no significant difference in the response latencies between the two conditions (Paired-*t* test, $t = 1.44$, $P > 0.05$). One way ANOVA analysis showed no significant difference in response latency among different types of neurons for rarefaction and condensation clicks.

The sound sensitive neurons (SS) and the non-sound sensitive neurons (NSS) exhibited significant differences in spontaneous firing rates and regularity (**Figure 4**). For Type II neurons (*t*-test, $P < 0.05$, $T = 1.703$) and non-canal neurons (*t*-test, $P < 0.05$, $T = 1.72$), CV of the SS neurons were significantly larger than CV of the NSS neurons (**Figure 4A**). While the SS Type I neurons exhibited larger CV than the NSS type I neurons, the difference did not reach significance (*t*-test, $P = 0.09$, $T = 1.359$). It is important to note that in this analysis, CV of the vestibular nucleus neurons is not normalized with respect to firing rate. When future studies establish the relationship between CV and firing rate for vestibular nucleus neurons, this issue needs to be revisited. The spontaneous firing rates for sound sensitive Type II (*t*-test, $P < 0.05$, $T = 2.02$) and non-canal neurons (*t*-test, $P < 0.0005$, $T = 3.95$) were significantly higher than that of the non-sound sensitive neurons (**Figure 4B**). A correlation analysis

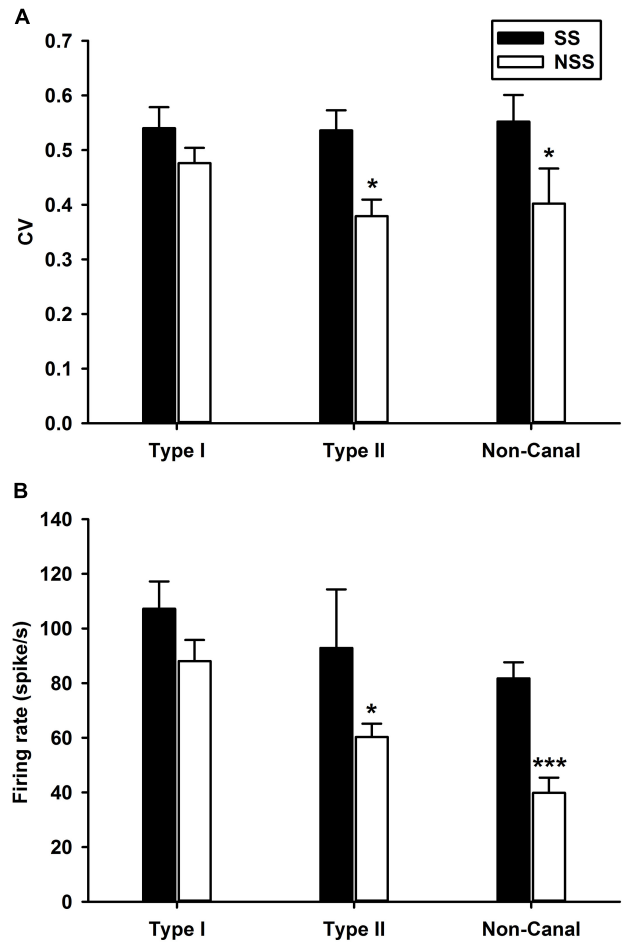

FIGURE 4 | Comparisons of spontaneous firing rates and regularity (CV) between sound sensitive (SS) and non-sound sensitive (NSS) vestibular nucleus neurons. **(A)** CV. The SS Type II and non-canal neurons were more irregular than NSS neurons. **(B)** Spontaneous firing rates. The SS Type II and non-canal neurons had higher spontaneous firing rates than NSS neurons. ***$P < 0.001$, *$P < 0.05$.

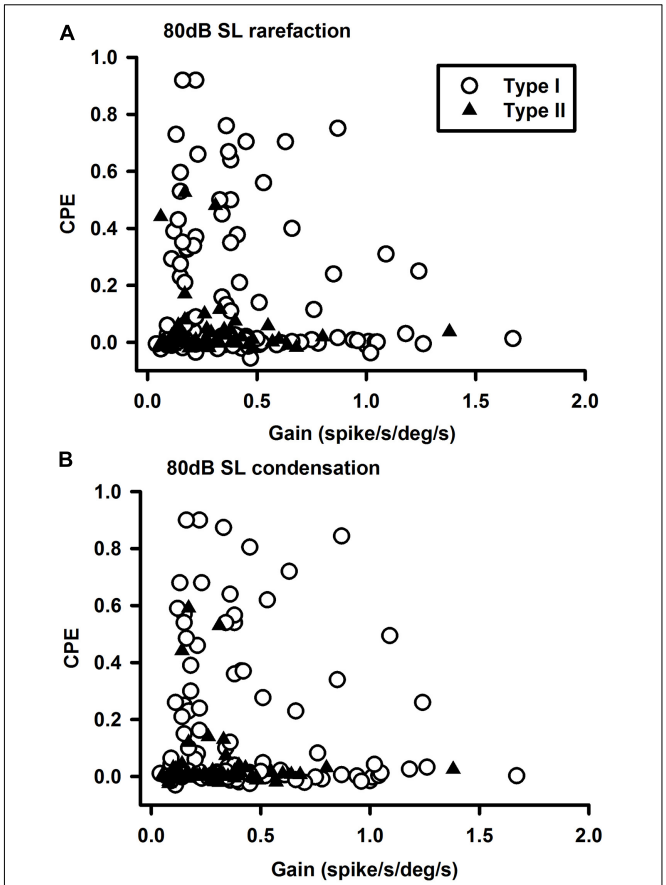

FIGURE 5 | Relationships between vestibular nucleus neuron's sensitivities to clicks and head rotation at 80 dB SL. **(A)** Rarefaction and **(B)** condensation. The sound sensitivities (CPEs) of the Type I neurons were inversely correlated with their sensitivities to head rotations (gains).

was performed to examine the relationship between sensitivity to head rotation and sound sensitivity for Type I and Type II sound sensitive neurons (**Figure 5**). The Type I neurons' CPEs were weakly inversely correlated with their gains ($R = 0.35$, $P = 0.022$, open symbols). There was no significant correlation for the Type II neurons. Histology showed that sound sensitive neurons were distributed through the vestibular nuclei. There were no clusters of sound sensitive neurons or non-sound sensitive neurons.

Tone Burst-Evoked Responses of Vestibular Nucleus Neurons

Tone-evoked responses were examined in 208 neurons. Similar to the click-evoked responses, tone evoked more responses in the non-canal neurons (49%) than in the Type I neurons (31%, Chi-square test, $P < 0.05$) and the Type II units (25%, Chi-square test, $P < 0.001$; **Table 1**). The vestibular nucleus neurons exhibited well-defined tuning curves, which exhibited peak responses at around 1,500 Hz at 70 and 80 dB (**Figure 6**). An earlier study of vestibular afferent tuning curves revealed that an important difference between the otolith afferents and the canal afferents is that low frequency tones of 350 Hz can activate the otolith afferents, but not the canal afferents (Zhu et al., 2011a). Thus, if a vestibular nucleus neuron only receives inputs from canal afferents, it would not be activated by low frequency tones. However, if it receives inputs from the otolith afferents, it would be activated by low frequency tones. In this study, we classified the neurons that exhibited significant responses to tones of 350 Hz (CPEs > 0.1) as low frequency threshold neuron (LFT, red) and the neurons that did not exhibit responses to tones of 350 Hz as high frequency threshold neurons (HFT, black). The Type I and Type II neurons, which included the canal-only and the otolith-canal convergent neurons, had both HFT and LFT responses. However, the non-canal neurons, which were the otolith-only neurons, had only LFT responses. Consistent with the assumption of their inputs from both the otolith afferents and canal afferents, the Type I and Type II LFT neurons exhibited larger tone-evoked responses than those of the non-canal neurons. One way ANOVA analysis revealed that the peak

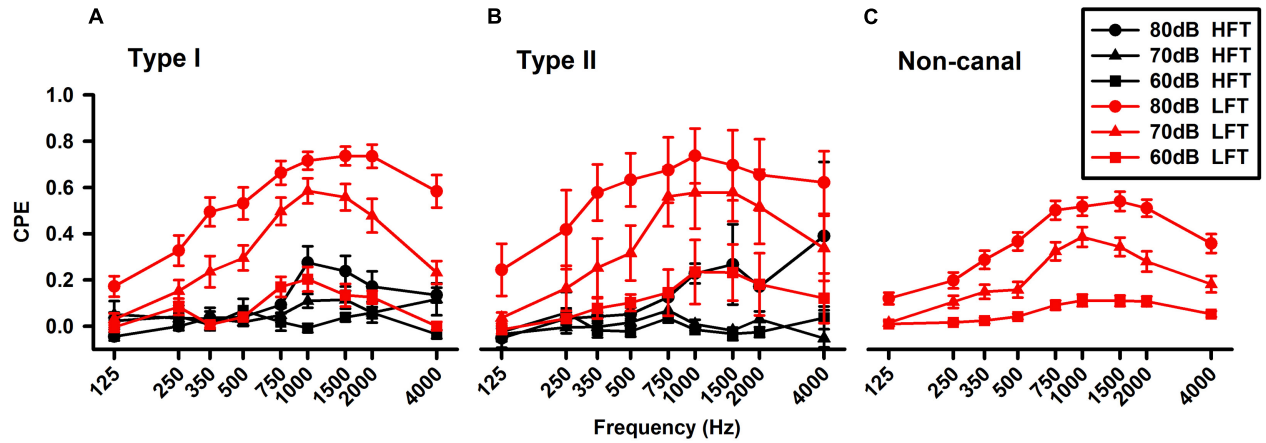

FIGURE 6 | Averaged frequency tuning of the vestibular nucleus neurons. **(A)** Type I vestibular neurons. **(B)** Type II vestibular neurons. **(C)** Non-canal vestibular neurons. The sound sensitive neurons were further classified as LFT (low frequency threshold, red lines) and HFT (high frequency threshold, black lines) neurons. The Type I and II neurons, which included canal-only and canal-otolith convergent neurons, exhibited both HFT and LFT responses, while the non-canal neurons (otolith only) exhibited only LFT responses.

responses of non-canal neurons were significant lower than those of the Type I neurons ($P < 0.05$, 1,500 Hz, 80 dB SL). It is important to note that the HFT/LFT classification is solely based on tone-evoked responses and their anatomical connections to the vestibular afferents need to be confirmed by future studies.

Sound Sensitivity of the Abducens Neurons

In a pilot study, we examined the responses of abducens neurons to sound stimulation in 19 rats under isoflurane anesthesia. Among 90 abducens neurons tested with clicks, only two neurons were activated by the ipsilateral ear stimulation. Among 50 neurons tested with tone bursts, only one neuron was activated by sound stimulation to either the ipsilateral or contralateral ear. Thus, different from the vestibular afferents and the vestibular nuclei, sound activation of abducens neurons could be suppressed by anesthesia. In the current study, abducens neuron responses to tone bursts or clicks were studied in awake rats. **Figure 7** shows typical responses of an abducens neuron during fixations and horizontal eye movements evoked by head rotation. The neuron exhibited a burst during a saccade in its on-direction and a pause during a saccade in its off-direction (**Figure 7A**, top and middle panels). The abducens neuron firing rate was linearly related to horizontal eye position with a sensitivity of 8.9 spike/s/deg (**Figure 7A**, lower panel). **Figures 7B,C** show rasters and spike densities of the neuron in response to tone bursts (1,000 Hz, 8 ms plateau, 1 ms rise/fall, 80 dB SL) delivered to the ipsilateral or contralateral ear, respectively. CPEs were computed to quantify the neuron's sound sensitivity (**Figure 7D**). **Figure 7E** shows the tuning curves of the abducens neuron to tones delivered into the ipsilateral and contralateral ears. While this neuron exhibited responses to tone bursts in both ears, its responses to the contralateral stimulation, which was mediated by the horizontal canal inputs, were much larger than that to the ipsilateral stimulation, which was mediated by the utricule inputs (Uchino et al., 1996). Among 18 abducens neurons studied, seven of them exhibited well-defined responses to tone bursts or clicks. Four neurons exhibited excitatory response to both ipsilateral and contralateral sound, indicating convergence of inputs from both the canal and the utricular afferents. Two neurons only responded to contralateral tones, but not to the ipsilateral tones, indicating inputs only from the canal afferents. One neuron exhibited responses only to the ipsilateral sound, indicating inputs from the otolith afferents. Similar to the vestibular nucleus neurons, the abducens neurons exhibited both LFT and HFT responses to tone stimulation (**Figure 8**).

On average, the click-evoked responses of the abducens neurons had a latency of 2.95 ± 0.45 ms and CPE of 0.162 ± 0.05 to ipsilateral stimulation, and a latency of 3.09 ± 0.68 ms and CPE of 0.157 ± 0.05 to contralateral stimulation. Similar to the latencies of click-evoked responses in the vestibular nucleus neurons (2nd order VOR neurons), which were longer than that in the vestibular afferents (1st order VOR neurons) (∼0.7 ms) (Zhu et al., 2011b), the latencies of click-evoked responses in the abducens neurons (3rd order VOR neurons) were longer than that in the vestibular nucleus neurons (∼1.5 ms).

Tone Burst-Evoked Eye Movements

Tone-evoked eye movements were studied in the left eye of five female LE rats. **Figure 9** shows typical changes in horizontal and vertical eye position and velocity to tone bursts of 1,000 Hz at 80 dB SL delivered to the ipsilateral (black lines) or contralateral ear (gray lines). In the horizontal direction, tone bursts evoked small eye movements at a latency of ∼4.4 ms, which moved toward the nose for the ipsilateral stimulation, and toward the ear for the contralateral stimulation (**Figure 9A**). In the vertical direction, tone bursts evoked upward eye movements for the ipsilateral stimulation and downward eye movements for the contralateral stimulation (**Figure 9B**). The tone-evoked eye movements exhibited a bell shape response in position with a

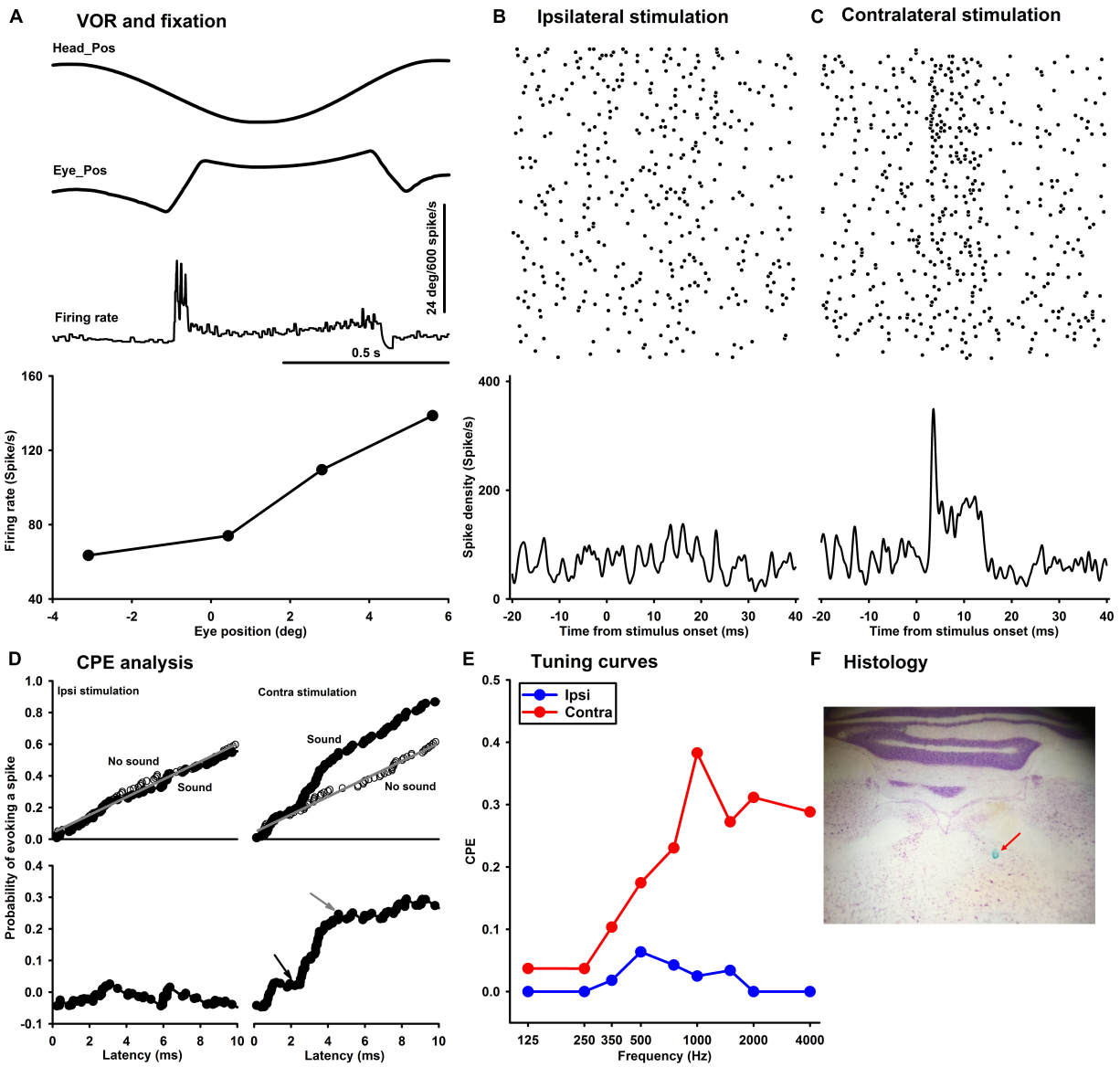

FIGURE 7 | Sound-evoked responses in a representative abducens neuron in an awake rat. **(A)** Discharge activities during eye movements in response to head rotation (**A**, top and middle panels) and fixations (**A**, lower panel). Raster of the abducens neuron in response to 1,000 Hz tone bursts delivered into the ipsilateral ear **(B)** or the contralateral ear **(C)**. **(D)** CPE analysis of tone-evoked responses in the abducens neuron. **(E)** Tuning curves of the abducens neurons for ipsilateral (blue) and contralateral (red) ear stimulation. **(F)** Histological verification of a recording site in the abducens nucleus.

peak latency of ∼20.7 ms and a biphasic response in velocity with a first peak latency of ∼15.9 ms. To quantitatively examine how tone-evoked eye movements are dependent on tone frequency, tuning curves were compiled using the first peak of eye velocity response. **Figure 10** shows tuning curves in the horizontal and vertical directions for the ipsilateral (black lines) and contralateral (gray lines) stimulation in the group of rats. Each rat was tested for three consecutive days to examine repeatability of the tone-evoked eye movements (**Figure 10**, three black lines and three gray lines in each panel). While there were individual variability and day-to-day variability, tone bursts consistently evoked well-defined tuning curves for the vertical eye movements with peak frequencies at ∼1,500 Hz. The tone-evoked horizontal eye movements, however, not only were smaller than tone-evoked vertical eye movements (horizontal peak velocity: 13.7 deg/s, vertical peak velocity: 36.8 deg/s), but also increased with tone frequencies up to 4,000 Hz. An important feature of the tone-evoked eye movements is that tone bursts with 350 Hz or lower evoked well-defined eye movements, consistent with convergence of canal and otolith contributions on the abducens neurons.

To examine effects of intensity on tone-evoked eye movements, we compiled the tuning curves for tone bursts at three intensities (60, 70, 80 dB SL) (**Figure 11**). To quantitatively assess effects of intensity on horizontal and

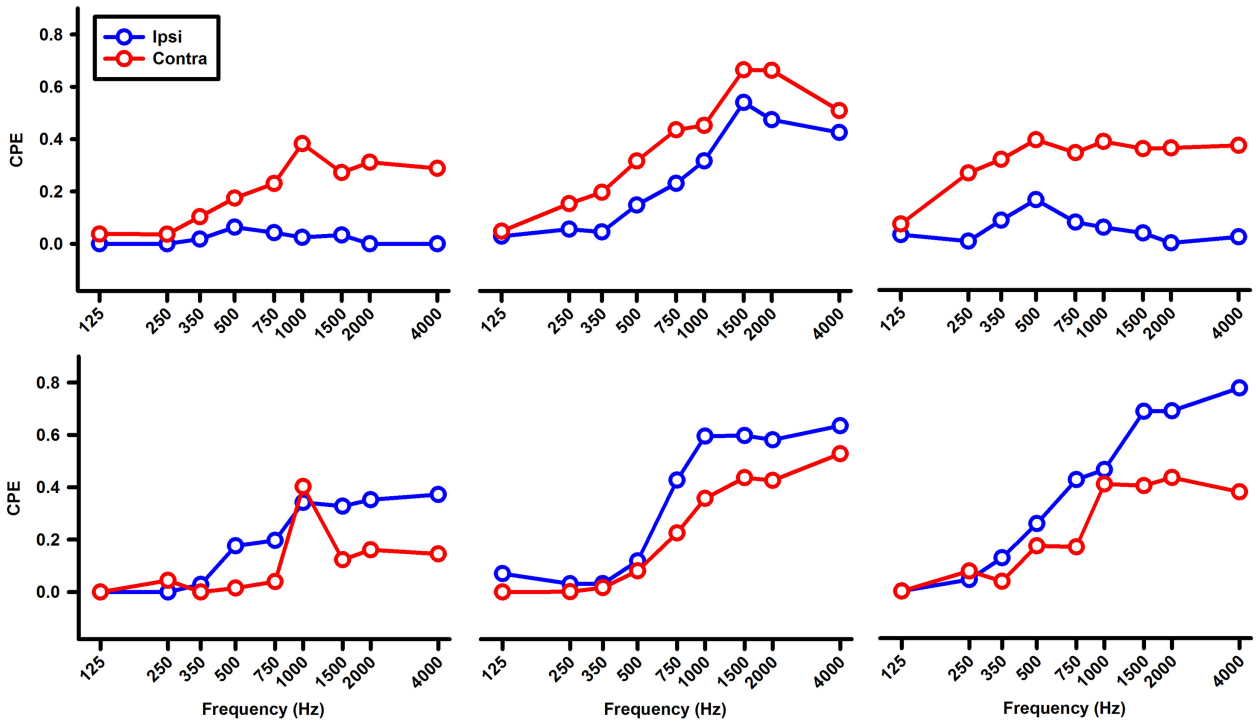

FIGURE 8 | Tuning curves of six abducens neurons for ipsilateral (blue) and contralateral (red) ear tone stimulation.

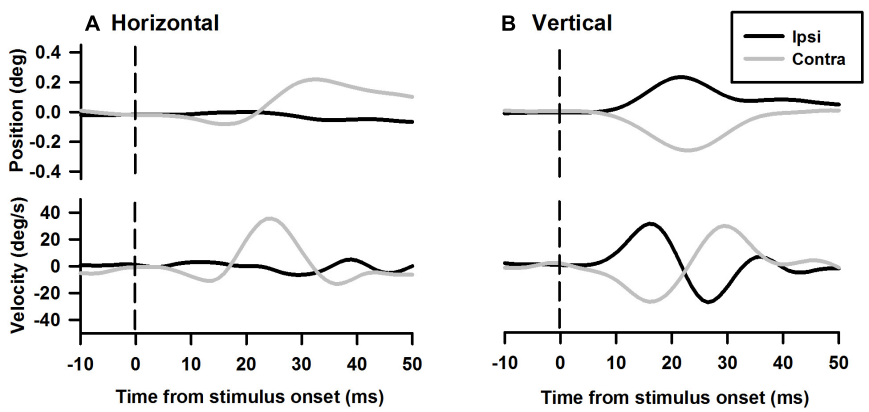

FIGURE 9 | Representative eye movement responses to tone bursts of 1,000 Hz. **(A)** Tone-evoked horizontal eye movement responses in position (*upper panel*) and velocity (*lower panel*). **(B)** Tone-evoked vertical eye movement responses in position and velocity (*lower panel*).

vertical eye movements, peak velocities of 1,500 Hz tone-evoked eye movements were plotted as a function of intensity for ipsilateral (black lines) and contralateral (gray lines) stimulation (**Figure 12**). While sound-evoked vertical eye movements increased with tone intensity for either ipsilateral (slope: 1.47 deg/s/dB, R^2 = 0.99) or contralateral (slope: -1.38 deg/s/dB, R^2 = 0.93) stimulation, sound-evoked horizontal eye movements increased with tone intensity only for contralateral (slope: -0.5 deg/s/dB, R^2 = 0.93) stimulation, but not for ipsilateral (slope: 0.07 deg/s/dB, R^2 = 0.15) stimulation. **Figure 13** further showed how tone-evoked eye movements were dependent on tone duration. When tone duration was increased, tone-evoked changes in eye position were increased only in the vertical direction. The peak velocities in the horizontal and vertical directions, however, were not changed.

DISCUSSION

In the present study, we extended the early studies of sound-activation of the vestibular afferents and further examined how sound activates the other components of the VOR pathways,

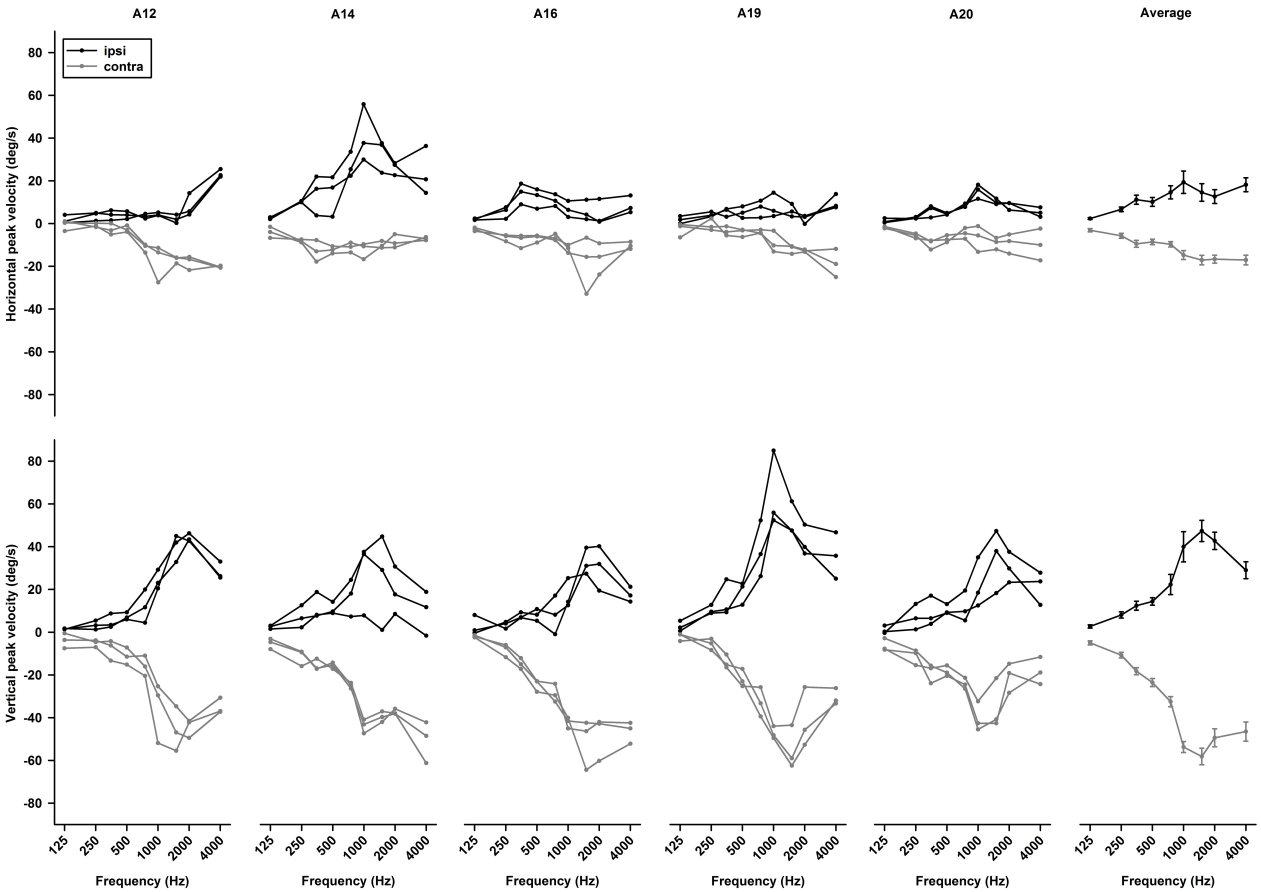

FIGURE 10 | Repeatability of tone bursts-evoked eye movements. *Upper panels* are horizontal eye movement tuning curves of five rats obtained in three consecutive days. *Lower panels* are vertical eye movement tuning curves of rats obtained in three consecutive days. The last *right panels* are averaged tuning curves from the five rats.

i.e., the vestibular nucleus neurons, the abducens neurons and finally the eye movements. The main finding is that sound-activation of the vestibular nucleus neurons, abducens neurons, and eye movements reflects summation of sound activation of the canal and otolith afferents. These results provide insight into understanding the neural mechanisms underlying the VEMPs and developing discriminative VEMP protocols utilizing tone bursts-evoked eye movements in animal models and in humans. Since eye movements are controlled by interactions of agonist-antagonist pairs of extraocular muscles, sound-evoked eye movements need to be interpreted as interactions of sound activation of multiple VOR pathways.

Sound-Activation of the Vestibular Nucleus Neurons

Click-evoked responses in the vestibular nuclei were reported in anesthetized guinea pigs (Murofushi et al., 1996). In the study, some of the sound sensitive vestibular nucleus neurons were found to respond to head tilt, indicating their inputs from the otolith afferents. The present study extended the previous study by quantitatively examining tone burst-evoked responses in the rat vestibular nucleus neurons, which were further classified into three categories based on their responses to head rotation, i.e., the Type I, Type II, and non-canal neurons (Scudder and Fuchs, 1992). The Type I and Type II neurons exhibited increased and decreased firing rates to ipsilateral head rotation, respectively. The non-canal neurons exhibited no modulation to head rotation. While the non-canal neurons likely only receive otolith inputs, the Type I and Type II neurons may consist of neurons that only receive canal inputs and neurons that also receive otolith inputs (Uchino et al., 2005). As shown in our earlier studies of tone-evoked activation of the vestibular afferents, the canal and otolith afferents exhibit distinct characteristics to tone frequency (Zhu et al., 2011a). First, the canal afferents exhibited no responses to tones with frequencies at 350 Hz or lower, even at the highest intensity tested (80 dB SL). However, the otolith afferents exhibited well-defined responses to tones of 350 Hz, even at the moderate intensity (70 dB SL). Second, tones of 1,500 Hz activate both canal and otolith afferents at intensities of 70 dB or higher, but only the otolith afferents at the intensity of 60 dB SL. For the Type I/II neurons that only receive the canal inputs, they would be expected to exhibit responses to tones with frequencies higher than 350 Hz, i.e.,

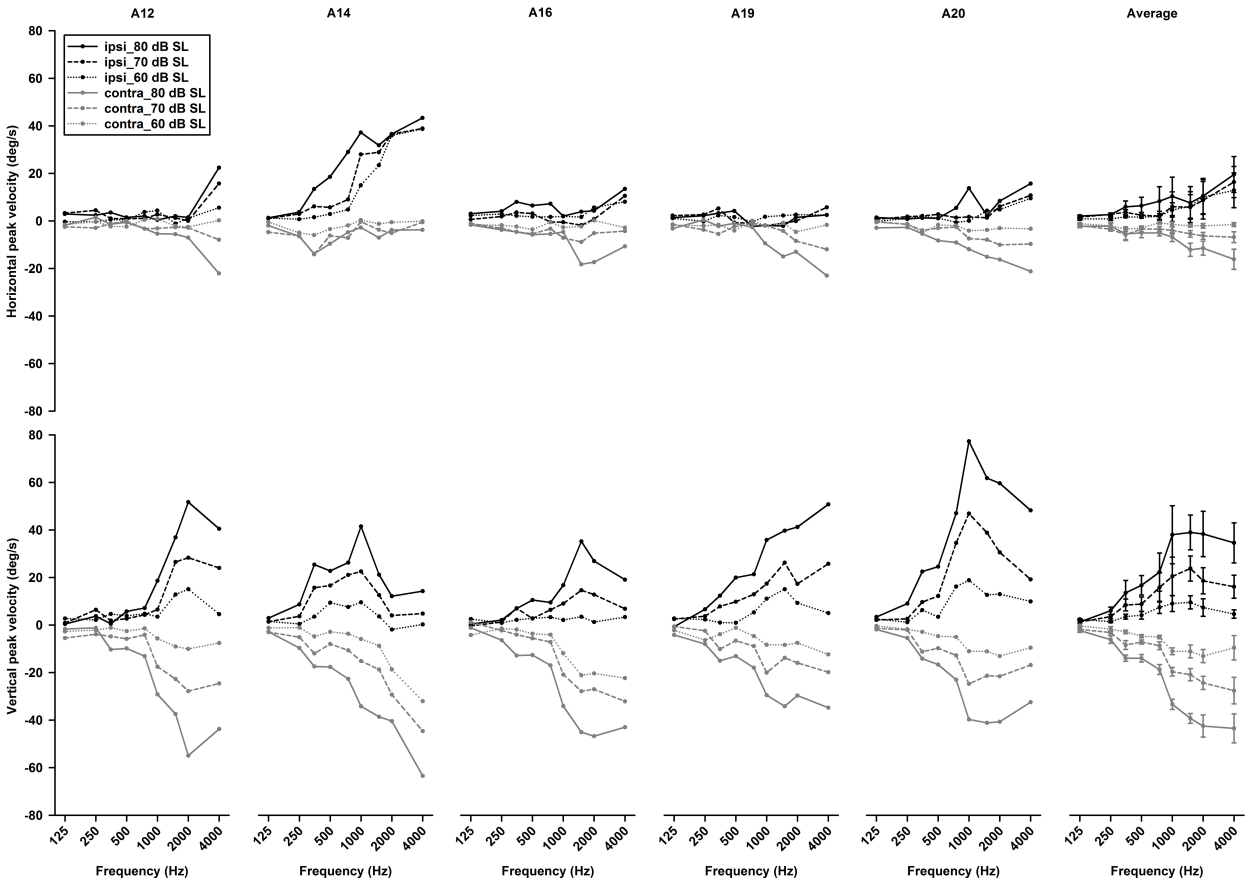

FIGURE 11 | Effects of intensity on tone bursts-evoked horizontal (*upper panels*) and vertical (*lower panels*) eye movements in five rats (the left five panels). The last right panels are the averaged tuning curves of the five rats.

high frequency threshold (HFT). For the Type I/Type II neurons that receive both the canal and otolith inputs, they would be expected to exhibit responses to tones with frequencies at 350 Hz or lower, i.e., low frequency threshold (LFT). Indeed, the non-canal neurons were all responsive to low frequency tones (i.e., HFT neurons), indicating their inputs from the otolith afferents. Similarly, the Type I/II neurons have both LFT neurons and HFT neurons, indicating some of them receiving inputs from both the canal afferents and the otolith afferents. Furthermore, the LFT Type I/II neurons exhibited larger tone-evoked responses than the LFT non-canal neurons, consistent with the assumption of their converged inputs from the canal and otolith afferents. These results suggest that in the vestibular nuclei, the sound-evoked afferent responses are primarily carried by the otolith only neurons and the canal/otolith convergence neurons.

Sound Activation of the Abducens Neurons

The abducens nucleus has the final neurons of the VOR pathways. On one hand, they receive canal inputs from the VOR interneurons in the contralateral vestibular nuclei and otolith inputs from the ipsilateral utricular afferents. On the other hand, abducens neurons innervate the lateral rectus of the ipsilateral eye via its motoneurons and the medial rectus of the contralateral eye via its internuclear neurons (Highstein and Baker, 1978). Thus, for the eye ipsilateral to the stimulated ear, its abducens neurons receive utricular inputs either directly from the ipsilateral utricular afferents or indirectly from the secondary vestibular nucleus neurons that receive utricular afferent inputs (Uchino et al., 1996). For the eye contralateral to the stimulated ear, its abducens neurons receive inputs from the canal afferents from the stimulated side. It is important to note that some vestibular nucleus neurons receive inputs from both the canal afferents and the otolith afferents, such as those Type I and Type II vestibular nucleus neurons that exhibit low frequency threshold responses. As a result of the convergence, the abducens neurons in the contralateral VOR pathways are activated by sound activation of the otolith afferents, such as the neurons in **Figures 7**, **8**. While click-evoked responses have been studied in monkey abducens neurons (Zhou et al., 2007; Xu et al., 2009), to the best of our knowledge, this was the first study that examined tone burst-evoked responses in the abducens neurons in awake rats. The results show that sound activation of the vestibular afferents results in activations of abducens neurons in the

ipsilateral and contralateral sides, which contribute to the sound-evoked eye movements measured by a video-based eye tracker (**Figures 9–13**).

Tone Bursts-Evoked Eye Movements

The sound-evoked responses in the vestibular nucleus neurons and abducens neurons suggest that sound activation of the vestibular afferents, the first neuron in the three-neuron arc of the VOR pathways, results in a robust activation of the second and third order neurons of the circuits, which is expected to generate measurable tone-evoked eye movements. Indeed, using a video-based eye tracker, we observed well-defined tone-evoked eye movements, which were dependent on frequency, duration, and intensity. To interpret the sound-evoked horizontal and vertical eye movements, it is important to note that eye movements are generated not by actions of a single extraocular muscle, but by actions of agonist-antagonist pairs of the extraocular muscles. For example, the horizontal eye movements of the left eye are determined by the actions of the medial rectus and the lateral rectus, which are innervated by motoneurons in the oculomotor nuclei and abducens nuclei, respectively. As shown in **Figures 11**, **12**, the effects of intensity on the horizontal eye movements evoked by the ipsilateral stimulation were quite different from that evoked by the contralateral stimulation. Whereas the contralateral stimulation-evoked eye movements were increased with tone intensity, the ipsilateral stimulation-evoked eye movements exhibited little changes as intensity were increased (**Figure 12**). The results suggest that the ipsilateral stimulation evoked two types of eye movements that were in opposite directions. One type of eye movement was generated by activation of the utricular-abducens pathways that moved the left eye to the left, and the other type of eye movement was generated by the canal-oculomotor pathways (via the abducens internuclear neurons) that moved the left eye to the right. The observed eye movements was the summation of the two types of eye movements that were in opposite directions. Since the canal pathways generated larger activation of the medial rectus, the eye moved to the right with reduced amplitudes. Thus, although the amplitudes of both types of eye movements increased with tone intensity, the summed results exhibited little changes with different intensities.

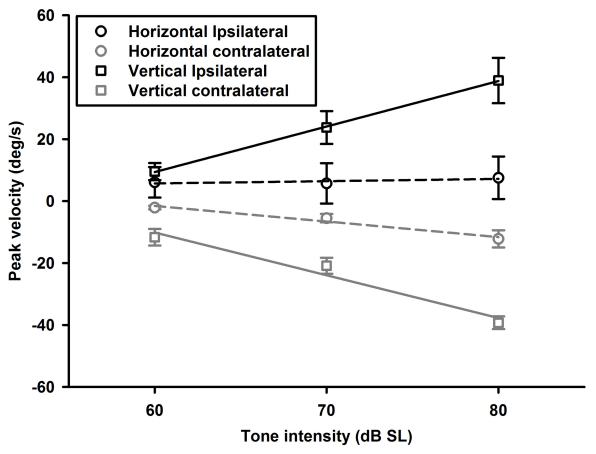

FIGURE 12 | Averaged peak velocities of 1,500 Hz tone burst-evoked horizontal (circles) and vertical (squares) eye movements as a function of tone intensity. Black lines and symbols are for contralateral ear stimulation, and gray lines and symbols are for ipsilateral ear stimulation.

Sound evoked different eye movements in the horizontal and vertical directions. First, sound- evoked horizontal movements in the two eyes were in the same direction, i.e., away from the stimulated ear, and sound evoked vertical eye movements in the two eyes were in opposite directions, i.e., upward in the ipsilateral eye and downward in the contralateral eye. Second, the sound-evoked vertical eye movements were much larger than the horizontal eye movements. In fact, the vertical eye movement were about three times larger than the horizontal eye movements. Third, low frequency tone bursts (350 Hz) evoked minimal eye movement in the horizontal direction, but evoked robust responses in the vertical direction in both eyes. As shown in **Table 2**, the vertical eye movements evoked by ipsilateral stimulation are the summed results of four VOR pathways, i.e., the anterior canal-superior rectus and the utricule-superior rectus pathways that move the eye upward, and the posterior canal-superior oblique muscle and the utricle-superior oblique muscle pathways that move the eye downward (McCrea et al., 1987a,b; Uchino et al., 1996). In contrast to the superior rectus that is the main extraocular muscle that rotates the eye upward, the superior oblique muscle rotates the eye partially downward and partially clockwise. If there is a similar sound activation in the two extraocular muscles, the superior rectus action is the dominant force and the eye rotates upward. Similar interpretation applies to the tone-evoked downward eye movement in the eye contralateral to the stimulated ear, which are the summed results of four VOR pathways (**Table 2**), i.e., the posterior canal-inferior rectus and the utricule-inferior rectus pathways that move the eye downward, and the anterior canal-inferior oblique muscle and the utricle-inferior oblique muscle pathways that move the eye upward. In this case, the inferior rectus action is the dominant force that rotates the contralateral eye downward. The vertical eye movement responses to low frequency tones are consistent with the contributions from sound activation of the utricular pathways.

Our earlier studies showed that clicks and tone bursts evoked well-defined eye movements in monkeys (Zhou et al., 2004, 2007; Xu et al., 2009). It is worth comparing sound-evoked eye movements in rats and monkeys. On one hand, sound evokes conjugate horizontal eye movements in both rats and monkeys. On the other hand, there are notable differences in sound-evoked responses in the two animal models. First, sound evoked disjunctive vertical eye movements in all five rats tested, but it evoked conjugate vertical eye movements in one monkey and disjunctive vertical eye movements in another monkey. Second, the amplitudes of tone-evoked vertical eye movements in rats are about 20 times larger than that in monkeys. Third, the tone bursts-evoked horizontal eye movements in the eye ipsilateral to the stimulated ear were increased with sound intensity in monkeys, but not in rats. In humans, the click-evoked VOR responses have been studied in normal subjects and in patients

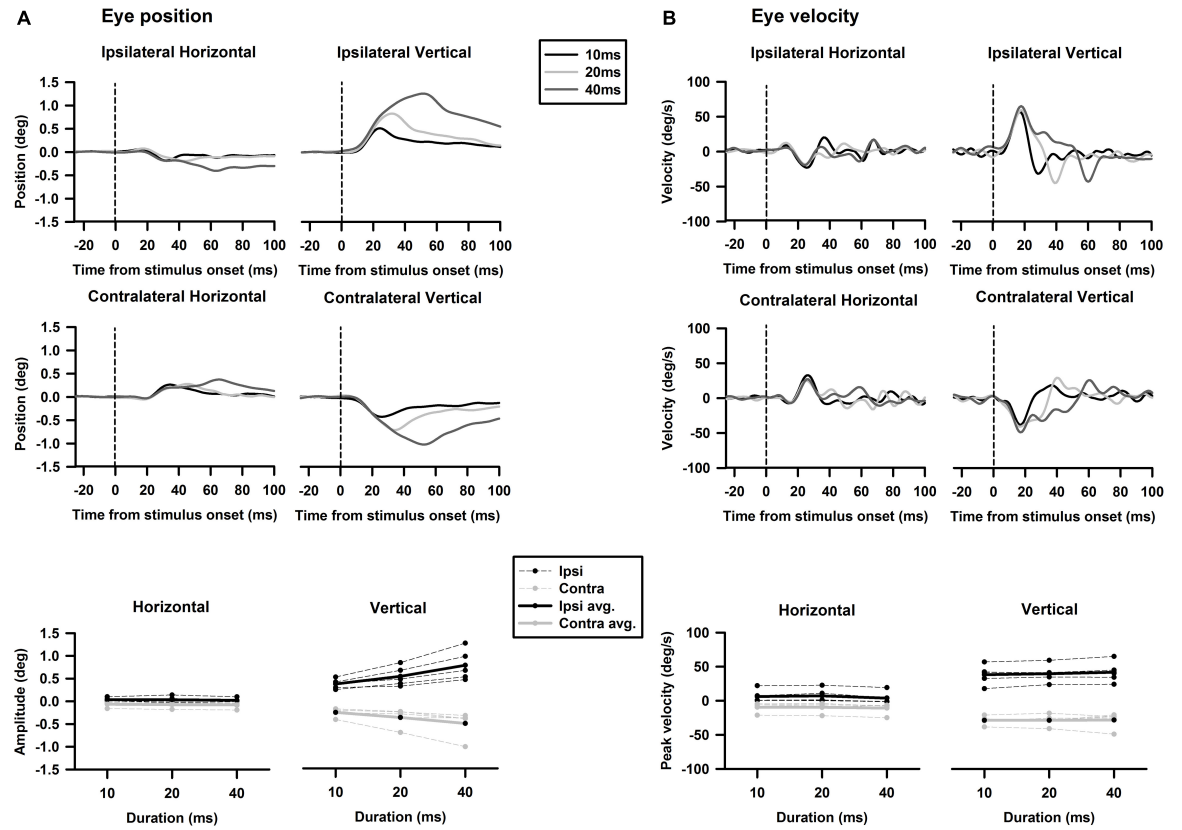

FIGURE 13 | Effects of duration on tone-bursts-evoked horizontal and vertical eye movements. **(A)** Tone-evoked changes in eye position. **(B)** Tone-evoked changes in eye velocity.

with superior canal dehiscence (SCD). Although clicks evoked well-defined eye movements in SCD patients, the studies detected minimal eye movements in normal humans (Aw et al., 2006).

Summary and Future Studies

In this study, we provided evidence that sound activation of the vestibular afferents further leads to activation of the VOR interneurons and motoneurons, which produces sound-evoked eye movements that can be measured by a video-based eye tracker. Consistent with convergence of canal and otolith inputs on the vestibular nucleus neurons, we showed that the vestibular nucleus neurons exhibited well-defined tone bursts-evoked activation that reflected activation of both the canal and otolith afferents. This convergence of sound activation of the canal and otolith afferents were further observed in the abducens neurons and the tone burst-evoked eye movements. An interesting finding of the study is that tone bursts-evoked robust eye movements in rats were much larger than that reported in monkeys and humans, which can be measured by a video-based eye tracker. Since the tone bursts-evoked eye movements reflect sound-activation of both the canals and the otoliths, it can be developed into an important biomarker for assessing unilateral vestibular functions in diseased conditions in animal models. Furthermore, it calls for reexamination of the protocols used in studies of sound-evoked eye movements in humans. For example, instead of using clicks that primarily contains high frequency components, our results suggest that tone bursts of various frequencies should be employed and binocular eye movements should be measured. Sound activation of both the canals and otoliths needs to be taken into consideration when interpreting sound-evoked eye movements in humans.

TABLE 2 | Vestibulo-ocular reflex (VOR) pathways that connect vestibular end organs to extraocular muscles of the left eye.

	Horizontal EM		Vertical EM	
Ipsilateral ear stimulation	HC-I-MR → U-I-MR → U-I-LR ←	→	AC-I-SR ↑ U-I-SR ↑ U-I-SO ↓ PC-I-SO ↓	↑
Contralateral ear stimulation	HC-C-LR ← U-C-LR ← U-C-MR →	←	AC-C-IO ↑ U-C-IO ↑ U-C-IR ↓ PC-C-IR ↓	↓

HC, horizontal canal; AC, anterior canal; PC, posterior canal; U, utricule; LR, lateral rectus; MR, medial rectus; SR, superior rectus; SO, superior oblique; IR, inferior rectus; IO, inferior oblique; I, ipsilateral; C, contralateral; →, rightward eye movement; ←, leftward eye movement; ↑, upward eye movement; ↓, downward eye movement.

DATA AVAILABILITY STATEMENT

The original contributions presented in the study are included in the article/supplementary material, further inquiries can be directed to the corresponding authors.

ETHICS STATEMENT

The animal study was reviewed and approved by IACUC of University of Mississippi Medical Center.

AUTHOR CONTRIBUTIONS

HZ and WZ designed the research. TC, JH, YY, XT, CZ, YX, AA, JA, WM, MD, TR, MZ, HZ, and WZ performed data acquisition and data analysis. HZ and WZ wrote the manuscript. All authors contributed to the article and approved the submitted version.

FUNDING

This research was supported by grants NIHR01DC012060, NIH R21 DC017293, and NIH R01 DC018919.

REFERENCES

Aw, S. T., Todd, M. J., Aw, G. E., Magnussen, J. S., Curthoys, I. S., and Halmagyi, G. M. (2006). Click-evoked vestibulo-ocular reflex: stimulus-response properties in superior canal dehiscence. *Neurology* 66, 1079–1087. doi: 10.1212/01.wnl.0000204445.81884.c7

Blanks, R. H., and Torigoe, Y. (1989). Orientation of the semicircular canals in rat. *Brain Res.* 487, 278–287. doi: 10.1016/0006-8993(89)90832-9

Broussard, D. M., DeCharms, R. C., and Lisberger, S. G. (1995). Inputs from the ipsilateral and contralateral vestibular apparatus to behaviorally characterized abducens neurons in rhesus monkeys. *J. Neurophysiol.* 74, 2445–2459. doi: 10.1152/jn.1995.74.6.2445

Broussard, D. M., and Lisberger, S. G. (1992). Vestibular input to brain stem neurons that participate in motor learning in the primate vestibuloocular reflex. *J. Neurophysiol.* 68, 1906–1909. doi: 10.1152/jn.1992.68.5.1906

Carey, J. P., Hirvonen, T. P., Hullar, T. E., and Minor, L. B. (2004). Acoustic responses of vestibular afferents in a model of superior canal dehiscence. *Otol. Neurotol.* 25, 345–352. doi: 10.1097/00129492-200405000-00024

Colebatch, J. G., and Halmagyi, G. M. (1992). Vestibular evoked potentials in human neck muscles before and after unilateral vestibular deafferentation. *Neurology* 42, 1635–1636. doi: 10.1212/wnl.42.8.1635

Daunicht, W. J., and Pellionisz, A. J. (1987). Spatial arrangement of the vestibular and the oculomotor system in the rat. *Brain Res.* 435, 48–56. doi: 10.1016/0006-8993(87)91585-x

Estes, M. S., Blanks, R. H. I., and Markham, C. H. (1975). Physiological characteristics of vestibular first-order canal neurons in the cat. I. response plane determination and resting discharge characteristics. *J. Neurophysiol.* 38, 1232–1249. doi: 10.1152/jn.1975.38.5.1232

Highstein, S. M., and Baker, R. (1978). Excitatory termination of abducens internuclear neurons on medial rectus motoneurons: relationship to syndrome of internuclear ophthalmoplegia. *J. Neurophysiol.* 41, 1647–1661. doi: 10.1152/jn.1978.41.6.1647

Lasker, D. M., Han, G. C., Park, H. J., and Minor, L. B. (2008). Rotational responses of vestibular–nerve afferents innervating the semicircular canals in the C57BL/6 mouse. *J. Assoc. Res. Otolaryngol.* 9, 334–348. doi: 10.1007/s10162-008-0120-124

McCrea, R., Strassman, A., and Highstein, S. (1987a). Anatomical and physiological characteristics of vestibular neurons mediating the vertical vestibulo-ocular reflexes of the squirrel monkey. *J. Comp. Neurol.* 264, 571–597. doi: 10.1002/cne.902640409

McCrea, R., Strassman, A., May, E., and Highstein, S. (1987b). Anatomical and physiological characteristics of vestibular neurons mediating the horizontal vestibulo-ocular reflexes of the squirrel monkey. *J. Comp. Neurol.* 264, 547–570. doi: 10.1002/cne.902640408

Minor, L. B., Solomon, D., Zinreich, J. S., and Zee, D. S. (1998). Sound- and/or pressure-induced vertigo due to bone dehiscence of the superior semicircular canal. *Arch. Otolaryngol. Head Neck Surg.* 124, 249–258. doi: 10.1001/archotol.124.3.249

Murofushi, T., and Curthoys, I. S. (1997). Physiological and anatomical study of click-sensitive primary vestibular afferents in the guinea pig. *Acta Otolaryngol.* 117, 66–72. doi: 10.3109/00016489709117994

Murofushi, T., Curthoys, I. S., and Gilchrist, D. P. (1996). Response of guinea pig vestibular nucleus neurons to clicks. *Exp. Brain Res.* 111, 149–152. doi: 10.1007/BF00229565

Murofushi, T., Curthoys, I. S., Topple, A. N., Colebatch, J. G., and Halmagyi, G. M. (1995). Responses of guinea pig primary vestibular neurons to clicks. *Exp. Brain Res.* 103, 174–178. doi: 10.1007/BF00241975

Paxinos, G., and Watson, C. (1998). *The Rat Brain in Stereotaxic Coordinates*. San Diego, CA: Academic Press.

Quinn, K. J., Rude, S. A., Brettler, S. C., and Baker, J. F. (1998). Chronic recording of the vestibulo-ocular reflex in the restrained rat using a permanently implanted scleral search coil. *J. Neurosci. Methods* 80, 201–208. doi: 10.1016/s0165-0270(98)00005-3

Rauch, S. D. (2006). Vestibular evoked myogenic potentials. *Curr. Opin. Otolaryngol. Head. Neck. Surg.* 14, 299–304. doi: 10.1097/01.moo.0000244185.65022.01

Rosengren, S. M., Welgampola, M. S., and Colebatch, J. G. (2010). Vestibular evoked myogenic potentials: past, present and future. *Clin. Neurophysiol.* 121, 636–651. doi: 10.1016/j.clinph.2009.10.016

Scudder, C. A., and Fuchs, A. F. (1992). Physiological and behavioral identification of vestibular nucleus neurons mediating the horizontal vestibuloocular reflex in trained rhesus monkeys. *J. Neurophysiol.* 68, 244–264. doi: 10.1152/jn.1992.68.1.244

Simpson, G. V., Knight, R. T., Brailowsky, S., Prospero-Garcia, O., and Scabini, D. (1985). Altered peripheral and brainstem auditory function in aged rats. *Brain Res.* 348, 28–35. doi: 10.1016/0006-8993(85)90355-5

Stewart, C., Yu, Y., Huang, J., Maklad, A., Tang, X., Allison, J., et al. (2016). Effects of high intensity noise on the vestibular system in rats. *Hear. Res.* 335, 118–127. doi: 10.1016/j.heares.2016.03.002

Uchino, Y., and Kushiro, K. (2011). Differences between otolith- and semicircular canal-activated neural circuitry in the vestibular system. *Neurosci. Res.* 71, 315–327. doi: 10.1016/j.neures.2011.09.001

Uchino, Y., Sasaki, M., Sato, H., Bai, R., and Kawamoto, E. (2005). Otolith and canal integration on single vestibular neurons in cats. *Exp. Brain Res.* 164, 271–285. doi: 10.1007/s00221-005-2341-7

Uchino, Y., Sasaki, M., Sato, H., Imagawa, M., Suwa, H., and Isu, N. (1996). Utriculoocular reflex arc of the cat. *J. Neurophysiol.* 76, 1896–1903. doi: 10.1152/jn.1996.76.3.1896

Wilson, V. J., and Schor, R. H. (1999). The neural substrate of the vestibulocollic reflex: what needs to be learned. *Exp. Brain Res.* 129, 483–493. doi: 10.1007/s002210050918

Xu, Y., Simpson, I., Tang, X., and Zhou, W. (2009). Acoustic clicks activate both the canal and otolith vestibulo-ocular reflex pathways in behaving monkeys. *JARO* 10, 569–577. doi: 10.1007/s10162-009-0178-7

Young, E. D., Fernandez, C., and Goldberg, J. M. (1977). Responses of squirrel monkey vestibular neurons to audio-frequency sound and head vibration. *Acta Otolaryngol.* 84, 352–360. doi: 10.3109/00016487709123977

Zhou, W., Mustain, W., and Simpson, I. (2004). Sound-evoked vestibulo-ocular reflexes (VOR) in trained monkeys. *Exp. Brain Res.* 156, 129–134. doi: 10.1007/s00221-003-1778-9

Zhou, W., Xu, Y., Simpson, I., and Cai, Y. D. (2007). Multiplicative computation in the vestibulo-ocular reflex (VOR). *J. Neurophysiol.* 97, 2780–2789. doi: 10.1152/jn.00812.2006

Zhu, H., Tang, X., Wei, W., Maklad, A., Mustain, W., Rabbitt, R., et al. (2014). Input-output functions of vestibular afferent responses to air-conducted clicks in rats. *JARO* 15, 73–86. doi: 10.1007/s10162-013-0428-6

Zhu, H., Tang, X., Wei, W., Xu, Y., Mustain, W., and Zhou, W. (2011b). Click-evoked responses in vestibular afferents in rats. *J. Neurophysiol.* 106, 754–763. doi: 10.1152/jn.00003.2011

Zhu, H., Tang, X., Wei, W., Mustain, W., Wood, P., Xu, X., et al. (2011a). "Air-conducted short tone bursts-evoked vestibular responses in rats," in *Proceedings of the Annual Meeting of Society for Neuroscience. Control/Tracking Number:* 2011-S-2626-SfN (Washington, DC).

Conflict of Interest: The authors declare that the research was conducted in the absence of any commercial or financial relationships that could be construed as a potential conflict of interest.

frontiers in Neuroscience

REVIEW
published: 18 October 2021
doi: 10.3389/fnins.2021.742391

Conserved and Divergent Principles of Planar Polarity Revealed by Hair Cell Development and Function

Michael R. Deans[1,2]*

[1] Department of Surgery, Division of Otolaryngology, University of Utah School of Medicine, Salt Lake City, UT, United States,
[2] Department of Neurobiology, University of Utah School of Medicine, Salt Lake City, UT, United States

Planar polarity describes the organization and orientation of polarized cells or cellular structures within the plane of an epithelium. The sensory receptor hair cells of the vertebrate inner ear have been recognized as a preeminent vertebrate model system for studying planar polarity and its development. This is principally because planar polarity in the inner ear is structurally and molecularly apparent and therefore easy to visualize. Inner ear planar polarity is also functionally significant because hair cells are mechanosensors stimulated by sound or motion and planar polarity underlies the mechanosensory mechanism, thereby facilitating the auditory and vestibular functions of the ear. Structurally, hair cell planar polarity is evident in the organization of a polarized bundle of actin-based protrusions from the apical surface called stereocilia that is necessary for mechanosensation and when stereociliary bundle is disrupted auditory and vestibular behavioral deficits emerge. Hair cells are distributed between six sensory epithelia within the inner ear that have evolved unique patterns of planar polarity that facilitate auditory or vestibular function. Thus, specialized adaptations of planar polarity have occurred that distinguish auditory and vestibular hair cells and will be described throughout this review. There are also three levels of planar polarity organization that can be visualized within the vertebrate inner ear. These are the intrinsic polarity of individual hair cells, the planar cell polarity or coordinated orientation of cells within the epithelia, and planar bipolarity; an organization unique to a subset of vestibular hair cells in which the stereociliary bundles are oriented in opposite directions but remain aligned along a common polarity axis. The inner ear with its complement of auditory and vestibular sensory epithelia allows these levels, and the inter-relationships between them, to be studied using a single model organism. The purpose of this review is to introduce the functional significance of planar polarity in the auditory and vestibular systems and our contemporary understanding of the developmental mechanisms associated with organizing planar polarity at these three cellular levels.

Keywords: hair cell, vestibular, auditory, planar cell polarity (PCP), planar polarity

OPEN ACCESS

Edited by:
Gwenaelle S. G. Geleoc, Boston Children's Hospital and Harvard Medical School, United States

Reviewed by:
Xiaowei Lu, University of Virginia, United States
Matthew William Kelley, National Institutes of Health (NIH), United States

***Correspondence:**
Michael R. Deans
michael.deans@utah.edu

Specialty section:
This article was submitted to Perception Science, a section of the journal Frontiers in Neuroscience

Received: *16 July 2021*
Accepted: *28 September 2021*
Published: *18 October 2021*

Citation:
Deans MR (2021) Conserved and Divergent Principles of Planar Polarity Revealed by Hair Cell Development and Function. Front. Neurosci. 15:742391. doi: 10.3389/fnins.2021.742391

INTRODUCTION

Planar polarity is the coordinated organization of cellular polarities within the plane of an epithelial layer. It is frequently manifest in the organization of apical structures such as the stereociliary bundles of vertebrate mechanosensory hair cells that are the focus of this review, or the trichome hairs projecting from *Drosophila* wing cells that have been a longstanding model for planar polarity

research (Goodrich and Strutt, 2011). Small cohorts of cells or functional cell clusters are also often organized as planar polarized groups. For example, the hair follicles distributed throughout mammalian skin consist of cell clusters coordinately oriented to project a single hair in a uniform direction (Devenport and Fuchs, 2008), and the chiral organization of photoreceptors in the ommatidia of the insect's compound eye has a stereotyped planar polarity reflecting ommatidia position (Jenny, 2010). These examples share a common two-fold organization in which cells or cellular clusters are intrinsically polarized and that polarity is coordinated with neighboring cells or clusters throughout the epithelium. The mechanisms coordinating neighboring cells are largely conserved between tissues and across species, and are encoded by the Planar Cell Polarity (PCP) genes (Goodrich and Strutt, 2011). These genes function upstream of the cell and tissue-specific effectors that mediate cell-intrinsic polarity. In vertebrates, PCP gene function has also been linked to other developmental processes such as synapse formation and axon guidance (Nagaoka et al., 2014; Thakar et al., 2017), but it is unclear how much this reflects a conserved planar polarity activity or the repurposing of signaling molecules whose primary function in *Drosophila* is restricted to planar polarity. Conversely, vertebrate genes not commonly associated with planar polarity in *Drosophila* have clear roles in planar polarization during vertebrate development (Montcouquiol et al., 2003; Lu et al., 2004). For the purposes of this review, any cellular process or structure that is organized parallel to the plane of an epithelium will be considered planar polarized, and any proteins contributing to their maintenance or development have planar polarity functions.

Planar polarization is essential for the auditory and vestibular functions of the vertebrate inner ear because it underlies the mechanism by which mechanosensory hair cells detect sound or motion. Projecting from the apical surface of hair cells is a bundle of stereocilia arranged in rows of increasing height with the tallest positioned next to a single, laterally displaced kinocilium. Stereocilia are specialized microvilli composed of filamentous actin, whereas the kinocilium is a true tubulin-based cilium anchored at a basal body located beneath the apical cell surface (Schwander et al., 2010). The planar polarity of individual hair cells is manifest in two ways, the orientation of the staircase of stereocilia progressing from rows of shorter to longer length, and the lateral position of the kinocilium. This organization underlies hair cell function because stereocilia in adjacent rows are interconnected by protein crosslinks called tip-links that couple mechanically gated ion channels on the tips of shorter stereocilia with the shafts of their taller neighbors. As a result, mechanical stimuli deflecting the bundle toward the kinocilium generates tension that opens these channels and depolarizes the cell. Deflections in the opposite direction reduces tension, closing channels and moving the hair cell to a more hyperpolarized state. This mechanism underlies mechanotransduction in both auditory and vestibular hair cells, and in each the stereocilia are deflected by overlying extracellular matrices that move in response to sound or motion (Hudspeth, 1989; Gillespie and Muller, 2009). As a result, there is a direct link between the planar polarization of the stereociliary bundle and mechanotransduction, and building a polarized bundle that is properly oriented relative to these extracellular matrices is essential for hearing and balance function.

The planar polarized organization of hair cell stereociliary bundles can be visualized at three levels. At a cellular level, intrinsic planar polarity is readily evident in the organization of stereocilia and kinocilium within the bundle. At a tissue level, planar polarity is evident in the organization of hair cells within the auditory and vestibular sensory epithelia where it is commonly called Planar Cell Polarity (PCP) (Tarchini and Lu, 2019). For each, the orientation of stereociliary bundles is coordinated between neighboring hair cells, and the population of cells are aligned relative to the functional anatomy of the sensory epithelium within which they reside. This two-fold organization of planar polarity occurs across diverse tissues and species. The third level of planar polarity is only found in the otolithic organs (utricle and saccule) of the vestibule (Deans, 2013) and the lateral line neuromasts of fish, where it was recently described as planar bipolarity (Kozak et al., 2020). In these systems, the hair cells are distributed between two groups that are aligned along a common polarity axis but differ in that their stereociliary bundles are oriented in opposite directions. For the utricle these groups are easily distinguished and meet at an intercellular boundary called the Line of Polarity Reversal (LPR). In the saccule and mature lateral line neuromasts the boundary constituting the LPR is less defined, and cells of opposite stereociliary bundle orientation may be intermixed. Previously planar bipolarity was proposed to be a manifestation of a broader tissue level or global organization (Deans, 2013). However, as mechanisms that establish planar bipolarity are tightly linked to intrinsic planar polarity, and do not appear to impact tissue-level PCP, this hierarchical organization seems less likely (Kindt et al., 2021). As I will describe, the mechanisms generating planar bipolarity would be better viewed as tissue-specific modulators of intrinsic cell polarity. These three aspects of inner ear planar polarity are mediated by separate signaling pathways encoded by different groups of polarity genes, but their coordinated activities are necessary for building functional auditory and vestibular sensory organs.

The goal of this review is to describe the commonalities and differences in hair cell planar polarity that occur in the auditory and vestibular structures of the vertebrate inner ear. In general, aspects of intrinsic planar polarity essential for mechanotransduction and planar cell polarity are shared between these modalities, while planar bipolarity has evolved to facilitate the specific functions of the otolithic organs. These areas of divergence make the inner ear a powerful system to study developmental mechanisms guiding planar polarity that can be applied to other systems. For example, the precise organization of stereociliary bundles in the organ of Corti allows for subtle mutant phenotypes to be rapidly identified, while planar bipolarity makes the otolithic organs an ideal system to study how overlapping signaling pathways modulate the output of planar polarization. This review will contain a combination of anatomical and physiological observations relating to the functional significance of planar polarity as well as molecular mechanisms that have been identified that build these systems,

with differences and similarities between auditory and vestibular highlighted throughout.

FUNCTIONAL SIGNIFICANCE

Auditory Hair Cells of the Mammalian Cochlea

The proper orientation of hair cell stereociliary bundles relative to the anatomy of the cochlear duct is essential for their function as mechanosensory receptors (**Figure 1**). Auditory hair cells are located within the organ of Corti that spirals along the length of the mammalian cochlea. They are precisely patterned within four rows and surrounded by supporting cells that provide structural support. The most medial row contains Inner Hair Cells (IHC) that detect the sound contributing to auditory perception while the remaining three rows contain Outer Hair Cells (OHC) that facilitate frequency tuning and amplification mechanisms. The stereociliary bundles of both IHCs and OHCs are oriented with the excitatory axis of their bundles oriented parallel to the short axis of the cochlea and as a result, bundle deflections toward the lateral edge of the cochlear spiral are excitatory (**Figure 1C**). On IHCs the rows of stereocilia are flat with the kinocilium centrally positioned adjacent to the tallest row and laterally displaced on the cell surface. On OHCs the rows of stereocilia rows arranged in a V-shape with the kinocilium located at the vertex where it is also laterally displaced and adjacent to the tallest stereocilia. The kinocilium is a transient component of auditory bundles that is lost near the onset of hearing, likely to facilitate high frequency hearing (Elliott et al., 2018). However, the basal body that anchored the kinocilium is maintained in this lateral position for the life of the cell. OHC stereocilia contact the overlying tectorial membrane and are deflected when the overlying tectorial and underlying basilar membranes vibrate in response to sound. IHC stereocilia are similarly deflected by fluid flow beneath the tectorial membrane as the result of these motions (Schwander et al., 2010). Since the tectorial membrane is attached on its medial side to the spiral limbus and therefore fixed in position it is critical that the hair cell planar polarity axis is oriented parallel to the short axis of the cochlear spiral so that hair cells are properly stimulated by sound.

The relationship between the direction of bundle deflection and the physiological response of individual hair cells has been directly measured following mechanical stimulation *in vitro* (Hudspeth and Corey, 1977; Shotwell et al., 1981) and using calcium imaging in zebrafish (Kindt et al., 2021). In these studies, maximal responses were only found when the bundle was deflected toward taller stereocilia while deflections in the opposite direction were inhibitory due to the closure of channels that had remained open at rest. In general, hair cells do not depolarize when bundles are deflected orthogonal to the axis of the staircase because this motion fails to place adequate tension on the tip links. When modeled, the relationship between the vector of the mechanical stimulus and the hair cell response *in vitro* is best fit by a cosine relationship (Shotwell et al., 1981). As a result, auditory function is likely quite tolerant to minor changes in bundle orientation since deviations of 20 degrees in either direction are only predicted to produce a 6% reduction in hair cell activation (100%-Cos20). Unfortunately, it is not straightforward to test the impact of stereociliary bundle misorientation on auditory function in the hearing mouse because mutations producing these phenotypes are pleiotropic with phenotypes impacting supporting cell morphology (Copley et al., 2013) and hair cell innervation (Ghimire et al., 2018; Ghimire and Deans, 2019; Jean et al., 2019), in addition to neural tube closure (Curtin et al., 2003; Montcouquiol et al., 2003; Lu et al., 2004; Wang J. et al., 2006; Wang Y. et al., 2006) and kidney development (Derish et al., 2020; Torban and Sokol, 2021). Until the significance of bundle orientation can be tested in isolation, we are left with the scientific irony that the precise organization of auditory hair cell leaves the smallest of changes readily visible to the experimentalist, yet may only have minor impacts on auditory function.

Vestibular Hair Cells of the Semi-Circular Canal Cristae

Similar to auditory hair cells, the vestibular hair cells in the semi-circular canal cristae must be coordinately oriented with the anatomy of their associated non-sensory structure, the semi-circular canal, for proper function. Cristae hair cells detect rotational accelerations of the head and mediate the vestibular ocular reflexes (VOR) essential for maintaining visual gaze (Fetter, 2007). These hair cells are distributed between the three cristae of the anterior, posterior and lateral semi-circular canals (**Figures 1B,D,F**). Cristae hair cells are stimulated by inertial fluid movements within the canals that occur in response to rotational head movements. These fluid movements impinge on an extracellular matrix called the cupula that surrounds and deflects the hair cell stereociliary bundles. As a result of this anatomical organization, the stereociliary bundles must be oriented with the excitation axis of their stereociliary bundles aligned parallel to the semi-circular canal in order for the hair cell to be stimulated by cupula movements. Therefore, the direction of motion that may be detected by cristae hair cells is determined solely by the orientation of the lateral, anterior or posterior canal. In addition, the hair cells are oriented in a single direction within the cristae so rotations in one direction are excitatory while rotations in the opposite are inhibitory. Since the two ears are mirror images of one another, rotational movements excite hair cells in the cristae of one ear while simultaneously inhibiting hair cells in the complementary cristae of the opposite ear. The full range of head rotations are perceived through the integration of cristae output from the left and right ears by the vestibular nucleus of the hindbrain. As a result, coordinating the planar cell polarity of hair cells within cristae and relative to the associated semi-circular canals is critical for vestibular function.

Vestibular Hair Cells of the Utricle and Saccule

The sensory epithelia of the utricle and saccule contain hair cells that detect gravity and linear acceleration. Their stereociliary bundles contact an overlying extracellular matrix that is embedded with calcium carbonate crystals, called the

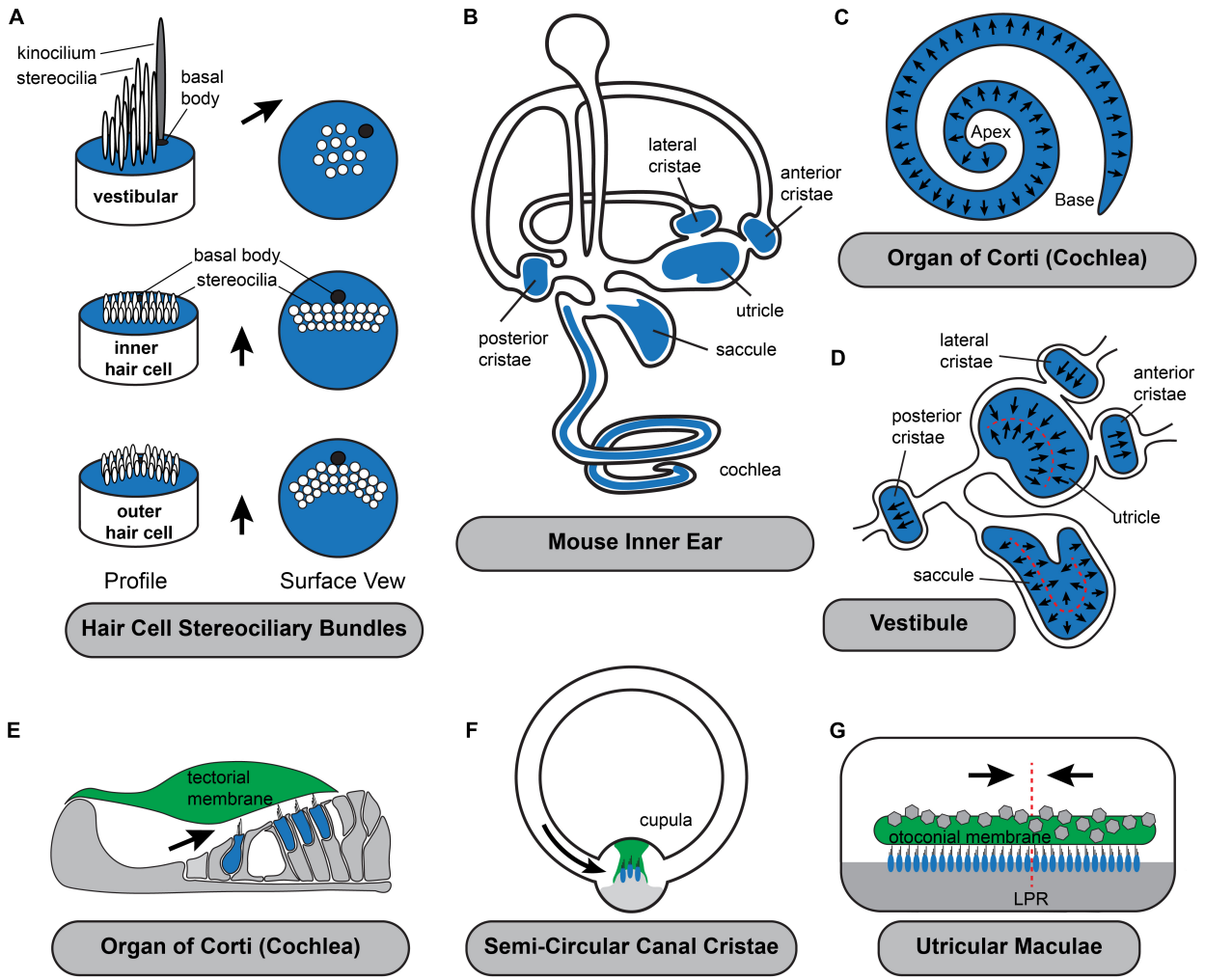

FIGURE 1 | Planar polarization of the stereociliary bundle is coordinated with the anatomy of the inner ear. **(A)** The intrinsic polarization of auditory and vestibular hair cells is evident in the organization of stereocilia into rows of increasing height with the longest adjacent to the laterally displaced kinocilium and its associated basal body. While stereocilia length and organization varies the polarized organization is shared by all hair cell types. **(B)** Hair cells are located in the sensory epithelia (blue shading) with auditory hair cells located in the organ of Corti in the cochlea and vestibular hair cells distributed between the three semi-circular canal cristae and two otolithic organs, the utricle and saccule. **(C)** Throughout the organ of Corti, hair cells are oriented with their stereociliary bundles pointed toward the lateral edge of the cochlear spiral. **(D)** In the vestibule, the orientation of cristae hair cells is aligned with the associated semi-circular canal. In the utricle and saccule there is an array of stereociliary bundle orientations and the hair cells are divided between two groups patterned about the Line of Polarity Reversal (LPR, red dashed line). **(E–G)** Schematic cross-sections of the three types of sensory epithelia illustrating the direction of excitatory hair cell deflections. Stereociliary bundles are deflected by overlying extracellular matrices which are either fixed in place such as the tectorial membrane **(E)**, aligned with the associated semi-circular canals like the cupula of the cristae **(F)**, or in the **(G)** utricle and saccule are capable of moving in response to acceleration or tilt across 360 degrees of space. Black arrows in all panels illustrate the excitatory axis of stereociliary bundle deflection.

otoconial membrane that moves in response to acceleration and has sufficient mass to detect gravity. Unlike the tectorial membrane of the cochlea or the cupula in the cristae, the otoconial membrane is not physically tethered to non-sensory structures and therefore is capable of deflecting vestibular hair cell in response to movements across a 360 degree range. The planar polarized organization of utricular and saccular hair cells reflects this because their stereociliary bundles are similarly distributed across a range of orientations (**Figure 1D**) while remaining tightly aligned with their nearest neighbors.

The most salient aspect of planar polarity in the otolithic organs is the division of hair cells between two groups aligned along a common PCP axis, but with oppositely oriented stereociliary bundles (Deans, 2013). In the utricle the bundles of the two groups are oriented with their kinocilia on the side of the cell pointed toward each other while in the saccule the bundles are oriented with their kinocilia pointed away. A similar planar bipolarity organization is seen in the lateral line of fish and has been studied extensive using the zebrafish model (Lopez-Schier and Hudspeth, 2006; Ji et al., 2018; Jacobo et al., 2019; Navajas Acedo et al., 2019;

Kozak et al., 2020). As a result of this organization, stimuli will produce parallel streams of excitation and inhibition since movements of the tectorial membrane will deflect the bundles in opposite directions. These two groups are innervated by distinct populations of afferent neurons that transmit parallel streams of information through the VIIIth cranial nerve. In the mouse it has been further demonstrated that these streams have distinct central projections with neurons innervating the medial regions of the utricle projecting to the vestibular nuclei and neurons innervating the lateral region projecting to the cerebellum (Maklad et al., 2010). Afferent innervation in the zebrafish is also coordinated with bundle orientation because peripheral axons only contact hair cells of one type and maintain this preference even after the axon is severed and allowed to re-innervate the neuromast (Lozano-Ortega et al., 2018).

In the mouse utricle and saccule, the boundary between hair cells with oppositely oriented stereociliary bundles is described as the line of polarity reversal (LPR). There is not a distinct landmark or structure that constitutes the LPR, and often two hair cells with opposing bundle orientations are separated by just a single intervening supporting cell. The LPR is closely associated with the striola, a physiologically specialized area in the medial region of the maculae enriched with hair cells contacted by afferent neurons that form complex calyceal endings surrounding multiple hair cells. The striolar region can be molecularly distinguished because striolar hair cells express the calcium binding protein oncomodulin while the afferent neurons innervating them express calretinin. In the mouse utricle the LPR runs along the lateral edge of the striolar region and occasionally these features are described synonymously despite being anatomically and developmentally distinct. For example, the LPR actually passes through the striolar region of the mouse saccule and during development the striolar region is positioned by a gradient of retinoic acid signaling that is independent of the LPR which persists when this gradient is disrupted (Desai et al., 2005; Ono et al., 2020). The LPR is also variable in its organization and can appear as a smooth boundary when mapped in the mouse utricle and a jagged boundary in the mouse saccule where hair cells with oppositely oriented bundles are more often interspersed at this border (Stoller et al., 2018).

In addition to planar bipolarity, the organization of stereociliary bundles in the maculae differs from the cochlea and the cristae because bundle orientation gradually radiates across the width of the sensory epithelia. As a result, even for hair cells restricted to one side of the LPR, the orientation of individual bundles located on opposite sides of the sensory epithelia may differ by more than 100 degrees (**Figure 1D**). Since the range of motion that can be detected by an individual hair cell is determined by the orientation of its stereociliary bundle, the planar polarity organization of the vestibular maculae results in individual cells that are orientated to be optimally stimulated by motions spanning a 360 degree range. Furthermore, the overlying otoconial membrane is not anchored within the vestibule, therefore linear accelerations and tilt can provide stimuli throughout this function range. Thus, unlike the cristae where the direction of rotational acceleration that can be detected is determined by the position of the semi-circular canals, in the vestibular maculae the range of linear acceleration that can be detected is determined by the organization of the mechanosensory hair cells themselves. Theoretically this organization could constitute a sensory representation of motion across 360 degrees of space, although the level of resolution maintained by the utricle or saccule have not been established, and likely differs between species with different locomotive behaviors. Foremost, the resolution imparted by an individual hair cell is diminished by the cosine rule and mechanical characteristics of bundle deflection (Shotwell et al., 1981). It is also impacted by the morphology of afferent neurons which branch and contact multiple neighboring hair cells which may have a modest range of bundle orientations depending on their distribution (Eatock and Songer, 2011). Despite these anatomical considerations, it remains clear that the organization of bundle orientations allow the vestibular maculae to resolve motions in opposite directions and that this resolution is maintained in their central projections to either the vestibular nuclei or the cerebellum. Regardless of the level of resolution, the planar polarized organization of hair cell stereociliary bundles in the maculae establishes a sensory representation of linear acceleration and gravitational tilt within the peripheral end organ and this representation is dependent upon planar polarity.

DEVELOPMENTAL MECHANISMS

The developmental mechanisms that guide hair cell planar polarity are generally shared between auditory and vestibular hair cells. The differences that do occur underlie specialized evolutions unique to the structure and function of the sensory epithelia in which the hair cells reside rather than functional differences between the hair cells themselves. As a result, greater differences in planar polarity occur between vestibular hair cells of the maculae and the semi-circular canal cristae than between the hair cells of the cristae and cochlea. Mechanisms guiding hair cell planar polarity development can be broadly divided between three signaling pathways acting at distinct anatomical scales (Deans, 2013). Common to all hair cells is the cell intrinsic polarization that directly regulates morphogenesis of the stereociliary bundle. The second is planar cell polarity, a tissue level organization that aligns cell intrinsic polarities along a common polarity axis. The third level of organization is unique to the otolithic organs and distinguishes hair cells in the utricle and saccule from the other sensory organs of the inner ear. This organization is epithelial planar bipolarity, and describes the division of hair cells between two groups patterned about the LPR. Planar bipolarity is also seen in the organization of neuromast hair cells of the zebrafish lateral line and developmental events guiding this process are conserved between systems (Jiang et al., 2017; Kozak et al., 2020; Kindt et al., 2021). Additional features distinguishing auditory and vestibular hair

cells that are not directly related to bundle polarity, including stereociliary length and retention of the kinocilium will not be discussed in detail.

Cell Intrinsic Signaling Pathways Polarize the Stereociliary Bundle

Within an individual hair cell, planar polarity is evident in the organization of the stereociliary bundle, and the position of the kinocilium with its associated basal body on the apical cell surface (**Figure 1A**). Consistent with this, the signaling mechanisms guiding intrinsic planar polarity are closely linked to actin-based mechanisms regulating stereocilia length and staircase formation, and the cytoskeletal regulators that position the basal body at the lateral edge of the apical cell surface (Grimsley-Myers et al., 2009; Sipe and Lu, 2011; Tarchini et al., 2016; Tadenev et al., 2019). Thus, mechanisms guiding cell intrinsic polarity regulate both the actin and tubulin cytoskeletal networks. Morphological observations made during hair cell development and differentiation suggest a sequential model in which cell intrinsic polarization is guided by the kinocilium with crosslinks between the kinocilium and the adjacent stereocilia regulating the actin-based processes determining stereocilia length (Tilney et al., 1992; Lefevre et al., 2008; Richardson and Petit, 2019). Consistent with this idea, the basal body appears in a lateral position before stereocilia elongation and staircase formation (Denman-Johnson and Forge, 1999). Experimentally it is also common to rely exclusively on the position of the basal body for defining hair cell polarity because it occurs early and is not impacted by disruptions of bundle morphology. This application has only reinforced acceptance of the sequential model of bundle orientation. However, more recent genetic studies (discussed below) suggest that basal body positioning and asymmetric actin dynamics are established independently and that subsequent interactions between the kinocilium and stereocilia actually reinforce and maintain the polarized structure of the bundle. Consistent with these observations, when intrinsic polarity is disrupted the kinocilium is often dissociated from the stereocilia which themselves may assemble in malformed or disorganized rows (Tarchini and Lu, 2019).

One distinctly polarized signaling pathway is the Par3-Rac1-PAK cascade which was one of the first associated with the development of intrinsic polarity (Grimsley-Myers et al., 2009). Intrinsic polarity is significantly disrupted following mutations in the small GTPase Rac1, with kinocilia that are dissociated from the stereocilia and malformed bundles that are frequently fragmented. Although Rac1 is present throughout auditory hair cells, its downstream effector PAK (P21 activated kinase) is only detected in its phosphorylated active state along the lateral cell boundary. PAK is a known regulator of cytoskeletal dynamics (Bokoch, 2003) and in this lateral location activated PAK is in the vicinity of the sub-apical microtubule network and kinocilium, supporting a model in which interactions between the basal body and hair cell junction are stabilized by cortical Rac-PAK signaling (Grimsley-Myers et al., 2009). Interestingly, the lateral activation of PAK by Rac1 is dependent upon Par3, a polarity molecule better known for its function opposite of the Par6/aPKC complex during apical-basolateral polarization of epithelial cells. This pathway is also active in hair cells where it patterns the apical cell surface, and Par3 is required for Rac1 activation of PAK. Conversely, expression of an activated Rac1 rescues the *Par3* mutant phenotype demonstrating that these molecules act in a linear path to regulate intrinsic polarity (Landin Malt et al., 2019).

The most distinctive feature of intrinsic polarity is the staircase array of stereocilia suggesting that factors regulating filamentous actin assembly should have an important role in regulating intrinsic hair cell polarity. Therefore, it is surprising that a set of molecules typically associated with mitotic spindles and the regulation of cortical force during cell division contributes to this aspect of intrinsic planar polarity in hair cells (Morin and Bellaiche, 2011). This includes the G-protein inhibitory subunit GNAI (Tarchini et al., 2013) and its associated regulatory protein GPSM2 (also known as LGN) (Ezan et al., 2013). GPSM2 maintains GNAI in a GDP-bound state and this complex is enriched near the lateral hair cell boundary early in development (**Figure 2A**). Although this localization coincides with the lateral movement of the basal body these processes are not spatially coordinated making it unlikely that either one guides the other. GNAI/GPSM2 sculpts formation of the stereociliary bundle by establishing a microvilli free zone on the apical cell surface between the lateral cell boundary and the kinocilium, promoting extension of the longest row of stereocilia, and redistributing Par3 and aPKC to lateral and medial positions, respectively (Tarchini et al., 2013; Tadenev et al., 2019). Patterning of the apical cell surface by Par3 and aPKC promotes formation of a compact stereociliary bundle at the region between. This apical blueprint is maintained through neonatal development in the mouse by the multiple PDZ domain (MPDZ) protein which is required to maintain segregation of GNAI/GPSM2 and aPKC (Jarysta and Tarchini, 2021). Despite these advances it remains unclear what initiates the polarized distribution of GNAI-GPSM2 within hair cells nor whether GNAI-GPSM2 regulates Par3 upstream of the Par3-Rac1-PAK cascade.

Subsequent to polarization, maintenance of the kinocilium at the lateral edge of the apical cell surface is dependent upon a microtubule array assembled beneath the cell surface. The distribution of the microtubule binding protein EB1 in auditory hair cells indicates that the microtubule plus-ends are enriched at the lateral edge of auditory hair cells where the basal body is located (Ezan et al., 2013). Moreover, disruptions of the microtubule network following mutation of the cytosolic dynein regulatory gene *Lis1* results in displaced basal bodies and associated stereociliary bundle defects (Sipe et al., 2013). The kinesin motor component Kif3a, better known for its role in intraflagellar transport, also contributes to protein trafficking along microtubule networks in hair cells and contributes to the lateral Rac1-PAK signaling pathway (Sipe and Lu, 2011). In its absence auditory hair cells also have displaced basal bodies and stereociliary bundle defects. However, neither Lis1 or Kif3a mutations impact the initial movement of the basal body to the lateral edge suggesting instead that the microtubule network is necessary for maintaining rather than initiating intrinsic polarity. As the basal body is a well known microtubule organizing center

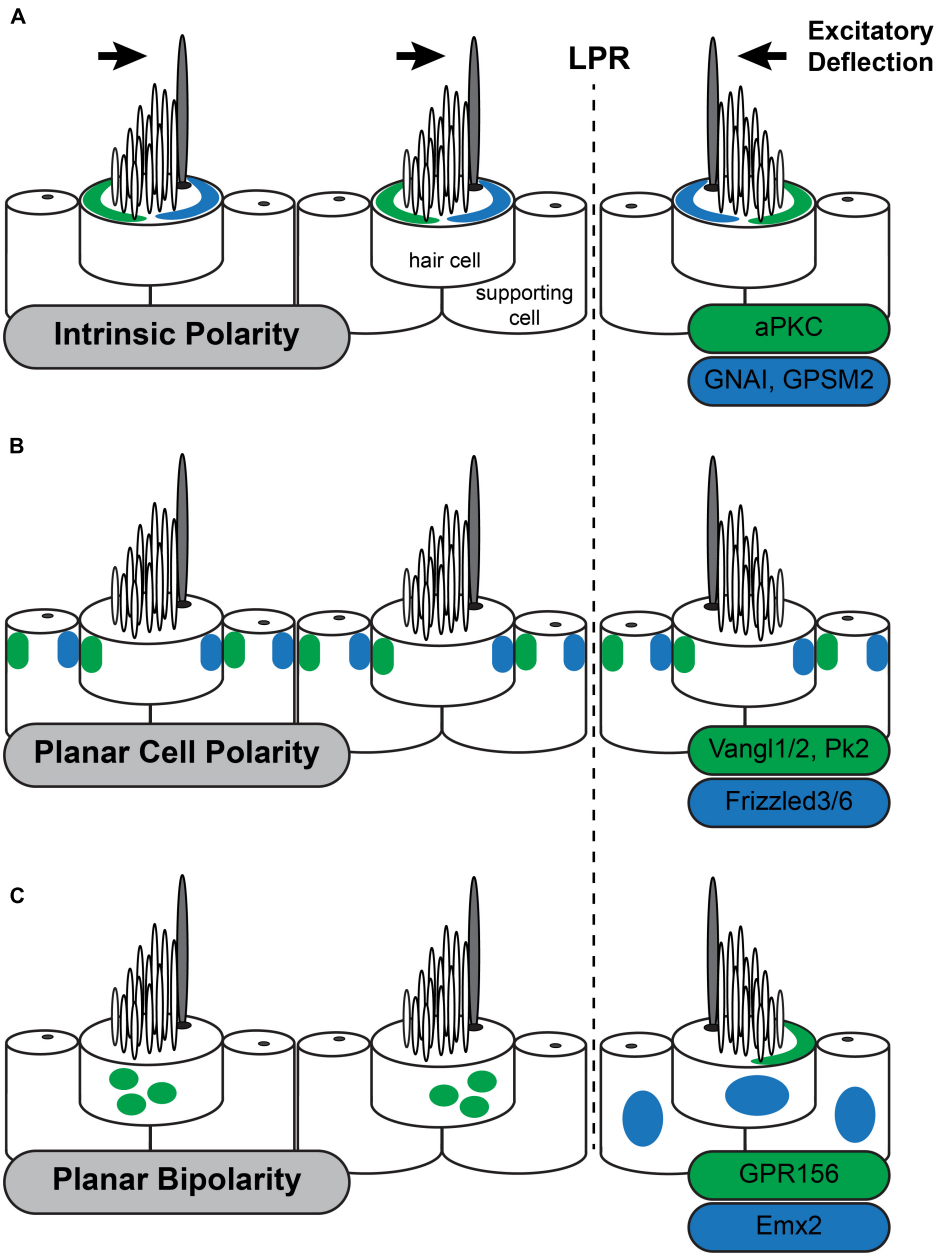

FIGURE 2 | Three planar polarity signaling pathways organize stereociliary bundles in the utricle. The three levels of planar polarity organization in the sensory epithelia of the mouse inner ear utilize distinct sets of signaling proteins during their development. Each set of proteins is uniquely distributed throughout the sensory epithelia or within hair cells. **(A)** The Intrinsic polarity factors GNAI/GPSM2 are enriched at the apical cell surface in the stereocilia bare zone adjacent to the kinocilium while aPKC is enriched on the opposite side of the cell surface. The relative position of GNAI/GPSM2 and the kinocilium is constant and as a result the position of GNAI/GPMS2 is reversed in hair cells on opposite sides of the Line of Polarity Reversal (LPR) similar to stereociliary bundle orientation. **(B)** The Planar Cell Polarity proteins Vangl1/2 and Pk2 are asymmetrically distributed opposite of Fzd3/6 within hair cells and supporting cells throughout the sensory epithelia of the utricle and saccule. This distribution is unchanged at the LPR, and as a result the kinocilium is adjacent to Fzd3/6 in the medial utricle and opposite of Fzd3/6 in the lateral utricle. **(C)** Planar Bipolarity and the position of the LPR are established by the transcription factor Emx2 which is expressed in hair cells and supporting cells throughout the lateral utricle. GPR156 is expressed in all hair cells but is only present delivered to the apical cells surface in hair cells that also express Emx2. In these cells GRP156 is always enriched at the cell boundary opposite of the kinocilium.

(MTOC) it would be logical that once asymmetrically positioned it would maintain this localization through the microtubule cytoskeleton. Lastly, while the kinocilium and stereocilia appear to be positioned independently, subsequent interactions between these structures likely reinforce their polarization and maintain cohesion of the bundle (Lefevre et al., 2008).

Planar Cell Polarity Signaling Establishes and Maintains Tissue Polarity

Hair cell planar cell polarity is established by intercellular signals that coordinate the orientation of neighboring cells and a global organizer that orients the population within the sensory epithelia. The most salient example of inner ear planar polarity is the coordinated orientation of stereociliary bundles between neighboring hair cells in the organ of Corti. The genes regulating this coordination were first identified in *Drosophila* and described the organization of epidermal cells on the wing and body that project trichomes or hairs toward the wing tip and tail (Vladar et al., 2009; Goodrich and Strutt, 2011). *Drosophila* PCP genes encode the Wnt receptor Frizzled, the transmembrane protein Van Gogh and the seven-pass transmembrane cadherin Flamingo/Starry Night which are asymmetricaly distributed at apical cell boundaries with Frizzled and Flamingo or Van Gogh and Flamingo enriched at opposite poles. The cytoplasmic proteins Disheveled and Diego colocalize with Frizzled, while Prickle colocalizes with Van Gogh. In general, it is thought that transmembrane proteins form an intercellular signaling complex that coordinates polarity between neighboring cells while cytoplasmic factors contribute to intracellular feedback that reinforces the molecular polarization of individual cells.

The initial suggestion that PCP genes could function in the inner ear was presented in an essay by Julian Lewis and Alex Davies (Lewis and Davies, 2002). They predicted that, based on their anatomical organization, hair cell polarization would require multiple levels of organization and that PCP signaling was appropriate for coordinating the orientation of intrinsic polarities between neighboring hair cells. The conservation of PCP gene function between *Drosophila* wing hairs and inner ear hair cells was subsequently demonstrated by Curtin et al. (2003) and Montcouquiol et al. (2003) who observed that *Vangl2*, the vertebrate ortholog of the *Drosophila* gene *vang gogh*, and *CELSR1*, the vertebrate ortholog of *flamingo/starry night* were required for the coordinated alignment of auditory hair cell stereocilia. Although they impacted different populations of hair cells, a common attribute of these phenotypes was that the intrinsic polarization of the stereociliary bundle was maintained while stereociliary bundles were misoriented between neighboring cells and the tissue axis. This is in contrast with *Drosophila* phenotypes where both intrinsic and tissue polarity are disrupted, with the cell's hair or basal body appearing in a central location on the apical cell surface (Carvajal-Gonzalez et al., 2016; Garrido-Jimenez et al., 2018). This difference is likely due to the intrinsic polarity pathways that are unique to hair cells (Tarchini and Lu, 2019). PCP signaling in the vertebrate ear coordinates intrinsic polarity between neighboring cells and this signal is relayed by an intercellular signaling complex comprised of Vangl1 and Vangl2 (Vangl1/2) (Montcouquiol et al., 2003; Yin et al., 2012; Stoller et al., 2018), Frizzled3 and Frizzled6 (Fzd3/6) (Wang Y. et al., 2006) receptors with their associated transduction partner Disheveled1/2/3 (Wang J. et al., 2006), and the atypical cadherin CELSR1/2/3 (Flamingo in *Drosophila*) (Curtin et al., 2003; Duncan et al., 2017; **Figure 2B**). These factors are conserved between vertebrates and invertebrates and have been described as the Core PCP proteins. Common phenotypes to core PCP mutants are hair cell polarity defects and profound neural tube defects called craniorachischisis in which the neural tube fails to close along the entire length of the body. Craniorachischisis is also seen in *Scribble* (Scrb) (Murdoch et al., 2001) and *Ptk7* mutants (Lu et al., 2004) which indicates a role in PCP signaling though these functions appear to be vertebrate specific. In contrast the vertebrate ortholog of Drosophila Prickle (Prickle-like2, PK2) is asymmetrically localized in hair cells and supporting cells of the inner ear like other PCP proteins (Deans et al., 2007) but bundle orientation phenotypes have not been reported for *Pk2* mutants nor identified in *Pk1* mutant mice (Yang et al., 2017). One explanation may be that Prickle functions in *Drosophila* to reinforce intracellular polarization but that is redundant with the intrinsic polarization mechanisms functioning in hair cells.

Several lines of evidence argue that that PCP signaling functions in parallel to the intrinsic planar polarity and planar bipolarity signaling pathways in hair cells. Foremost, the asymmetric distribution of PCP proteins is not changed when intrinsic signaling through the GNAI pathways is disrupted (Tarchini et al., 2013). Similarly, in *Rac1* conditional knockouts Fzd3 is asymmetrically distributed at cellular junctions during early development (prior to E17.5) though it is lost during subsequent hair cell maturation (Grimsley-Myers et al., 2009). The changes in Frizzled localization in *Rac1* cKOs are not sufficient to produce phenotypes resembling *Fzd3/6* mutants (Wang Y. et al., 2006). However, these changes do suggest there may be some cross talk between the pathways. Conversely, in PCP mutants hair cells are misoriented relative to each other yet continue to form polarized stereociliary bundles, and the intrinsic factors remain polarized and are properly distributed relative to those bundles (Grimsley-Myers et al., 2009; Tarchini et al., 2013). PCP signaling also appears independent of planar bipolarity because the asymmetric distributions of PCP proteins do not change at the LPR or in mutants with disrupted planar bipolarity (Deans et al., 2007; Jiang et al., 2017). This has led to the general view that PCP signaling functions as a compass that coordinates the orientation of individual cells relative to the tissue axes rather than an effector directing polarization of the stereociliary bundle.

The evidence that core PCP proteins mediate intercellular signaling is based on the domineering non-autonomy phenotypes seen in *Drosophila* where the orientation of wild type cells is disrupted if they are adjacent to PCP mutant clones. When similar mutant boundaries are generated in the vestibular maculae using restricted expression of Cre recombinase, the adjacent wild type cells are also misoriented and turn away from the boundary (Stoller et al., 2018). Similar domineering non-autonomy phenotypes have been seen after Vangl2 overexpression in the chick basilar papillae (Sienknecht et al., 2011) and transplant experiments in the frog epidermis that evaluated the planar polarity of multiciliated cells (Mitchell et al., 2009). In each of these systems wild type cells became

misoriented when neighboring experimental cells in which PCP signaling is manipulated, demonstrating the conservation of intercellular signal between vertebrates and *Drosophila*. Signaling is dependent upon the asymmetric distribution of Frizzled and Vangl2 to opposite sides of cells and polarity signals are relayed across intercellular space by Frizzled and Vangl2 acting as a receptor ligand pair (Wu and Mlodzik, 2008) or *via* Flamingo/CELSR bridges (Struhl et al., 2012). Surprisingly, this complex appears to be restricted to just one side of cochlear hair cells with Frizzled3 on the medial side of the hair cell and Vangl2 on the lateral side of the adjacent supporting cell (Wang Y. et al., 2006; Giese et al., 2012). In contrast, immunofluorescent labeling suggests that PCP proteins are on both sides of supporting cell junctions (Duncan et al., 2017). One interpretation of these distributions is that PCP is communicated across inner ear sensory epithelia by supporting cells, and that hair cells receive polarization cues without contributing to their propagation. In the vestibular system it is unclear whether PCP guides supporting cell development because they lack distinct structural features whereas in the organ of Corti where supporting cells have more structural complexity it is clear that Vangl2 is required for their polarized development (Copley et al., 2013).

The outstanding unanswered question for both the auditory and vestibular sensory epithelia is what determines the tissue-wide organization and acts as the global organizer of PCP. For example, in the cristae what aligns the PCP axis with the semi-circular canal, and how does this signaling mechanism establish the opposite orientation of hair cells in the lateral and anterior cristae (**Figure 1D**). Intercellular signaling suggests that once initiated, PCP could be relayed to new cells or maintained during cellular movements and that an organizer could be transient. It had been anticipated that an extracellular morphogen would be this cue, with Wnts proposed as a ligand since the Wnt receptor Frizzled is also a core PCP protein (Yang and Mlodzik, 2015). However, when Wnt is removed from the inner ear, planar polarity is only mildly impacted (Ghimire and Deans, 2019; Najarro et al., 2020). Similarly, in *Drosophila* when all *Wnt* genes are deleted there is no impact on epithelial wing cell PCP (Ewen-Campen et al., 2020; Yu et al., 2020). While Wnts may not define the tissue PCP vector for the inner ear, recently findings suggest that non-canonical Wnt/G-protein signaling may instead act to coordinate cell-intrinsic and tissue-level PCP (Landin Malt et al., 2020, 2021). Thus, instead of establishing bundle orientation, Wnts may function to refine bundle orientation, particularly for the last row of OHCs (Dabdoub, 2003). Because PCP is reinforced and propagated by intercellular signaling an exciting hypothesis is that signals polarizing the early otocyst establish a PCP axis in the poresensory domain that is maintained throughout morphogenesis (Deans, 2013).

Planar Bipolarity Distinguishes the Vestibular Maculae and Lateral Line

Vestibular hair cells in the utricle and saccule are distributed between two groups with oppositely oriented stereociliary bundles that meet at the LPR. In the utricle, hair cells are organized so that their stereociliary bundles are pointed toward each other while in the saccule the bundles point away, but in either case, the hair cells are oriented along the same PCP axis. Similar organization is seen in the lateral line neuromast of zebrafish where hair cells are oriented along a common axis yet are divided into two groups with stereociliary bundles oriented in opposite directions. While previously described as a readout of global planar polarity (Deans, 2013), planar bipolarity is more likely a specialized from of intrinsic polarity that is dependent upon the PCP axis that underlies tissue polarity. Moreover, as described in greater detail below, the LPR is now known to be established through the regulation of cell intrinsic events rather than global patterning mechanisms.

The LPR is not organized by PCP signaling because the subcellular distribution of these factors is not altered at the LPR (Deans et al., 2007). Instead, the LPR is formed by transcriptional activity of Emx2 which is expressed by hair cells and supporting cells in the lateral region of the utricle (**Figure 2C**) and medial region of the saccule in a pattern matching the LPR. In the absence of Emx2 hair cells point in a single direction while overexpression using viral vectors or genetic tools in mouse gives the opposite result (Jiang et al., 2017). Since the distribution of PCP proteins are not altered in *Emx2* mutants, this transcription factor is likely to act as a molecular switch regulating intrinsic polarity. However, Emx2 is also expressed in the cochlea and mutant phenotyping reveals developmental roles extending beyond planar polarity because the absence of Emx2 OHCs fail to differentiate (Holley et al., 2010). The basis of this phenotype has not been determined though one possibility is that Emx2 influences regional patterning and that auditory and vestibular hair cell phenotypes emerge because cells in these regions are not properly differentiated. Consistent with this possibility, the vestibular macuale are smaller in one Emx2 mutant line (Holley et al., 2010), though this has not been apparent in others where macular area was measured (Jiang et al., 2017). Thus, it remains unclear whether Emx2 acts atop a gene regulatory network that establishes regional identity with bundle polarity being one downstream feature, or if Emx2 directly regulates the expression of effectors that determine stereociliary bundle orientation.

An important downstream effector of Emx2 function is the orphan G-protein coupled receptor GPR156 which gives similar phenotypes to Emx2 when mutated (Kindt et al., 2021). Interestingly GPR156 cannot be a direct Emx2 target because GPR156 is expressed in all hair cells. Instead it is only functional in cells expressing Emx2 where it is delivered to the apical surface suggesting that GPR156 trafficking pathways are regulated by Emx2. In cells on the opposite side of the LPR, GPR156 is not apical and appears to be retained in intracellular organelles (**Figure 2C**). Remarkably pertussis toxin-mediated inhibition of GNAI suggest that these G-proteins act downstream of GPR156 because blocking GNAI function in this way gives phenotypes resembling both *Emx2* and *GPR156* mutants. Further genetic interaction studies confirm a functional hierarchy of Emx2, GPR156 and GNAI. This study further suggests that GNAI has parallel functions in regulating intrinsic polarity and planar bipolarity because the regulatory protein GPSM2 is not required

for planar bipolarity. An exciting possibility is that GNAI could function in an activated GTP-bound state downstream of GRP156 though this has not been demonstrated. Regardless, the function of this Emx2-GPR156-GNAI signaling cascade is to determine the position of the kinocilium relative to the PCP axis. In cells expressing Emx2 the kinocilium is always opposite of Fzd3/6 as seen in the organ of Corti (Wang Y. et al., 2006) and inferred from the distribution of PCP proteins in supporting cells of the utricle (Deans et al., 2007). Thus, Emx2-dependent planar bipolarity regulates how intrinsic planar polarity is organized relative to the planar cell polarity axis.

CELLULAR MOVEMENTS

One aspect of inner ear development that distinguishes auditory from vestibular hair cells are the dynamic cellular movements that pattern the precisely aligned rows of hair cells within the organ of Corti. Evidence from live imaging suggests that cochlear extension occurs through radial intercalation, directional migration of supporting cells and tissue growth (Driver et al., 2017). The precisely aligned rows of hair cells are generated through convergent extension movements in which newly specified hair cells converge along the radial axis and extend along the long axis of the cochlear spiral. Convergent extension is the result of collective cell migrations and are seen in multiple morphogenic events during embryonic development that include gastrulation and lengthening of the body axis prior to neuralation. During neural tube closure, cellular convergence at the midline lengthens the anterior:posterior body axis and brings the neural folds into closer proximity so that they may fuse to form the dorsal most neural tube. The directed cell migration underlying convergent extension movements requires PCP signaling, and when that is disrupted polarized cellular movements are randomized. As a result, a common phenotype associated with vertebrate PCP gene mutations including *Vangl2*, *Dsh,* and *Fzd3/6* is an open neural tube defect extending from the midbrain-hindbrain boundary to the tail called craniorachischisis (Copp et al., 2003; Greene et al., 2009).

Similar disruptions in the convergent extension movements of hair cells in *vangl2*, *Dsh* and *Fzd3/6* double mutants have been attributed to the formation of supernumerary rows of OHCs in the cochlear apex, and cochlea that are significantly reduced in length (Montcouquiol et al., 2003; Wang J. et al., 2005; Wang Y. et al., 2006). One interpretation of these phenotypes is that PCP dependent convergent extension of hair cells drives cochlear duct extension. Indeed, organ of Corti cells appear to migrate away from the apical end of cochlear ducts when grown *in vitro* (Wang J. et al., 2005). However, these mutant phenotypes are pleiotropic and it is also possible that cochlear phenotypes are secondary to craniorachischisis which disrupts morphogenesis of the inner ear because they are displaced in a medial-lateral orientation within the embryo, and because they are exposed to embryonic fluids of the yolk sac. Indeed, for *vangl2* CKOs in which craniorachischisis does not occur, the length of the cochlear duct is not altered and supernumerary OHC rows cannot be detected despite comparable changes to stereociliary bundle orientation to *Looptail* mutants (Copley et al., 2013). This *vangl2* CKO phenotype is not consistent with hair cell convergence producing a driving force that extends the cochlear duct, and a simpler explanation is that PCP signaling keeps cells properly oriented relative to each other as they undergo large collective movements. A definitive experiment to distinguish these alternatives would be to analyze hair cell patterning in a CKO in which gene deletion is restricted to the dorsal neural tube thereby producing craniorachischisis without impacting PCP gene expression in the ear itself.

The relative orientation of the stereociliary bundle is also dynamic and auditory stereociliary bundle orientation can change over time. While it is not clear whether this involves rotation of apical cell components or rotational movements of the entire hair cell, rotational movements have been inferred in both wild type and mutant states. This is most obvious for *vangl2* CKO where misoriented bundles are largely corrected during early postnatal development (Copley et al., 2013). However, in wild type mice the bundles atop third row OHCs also reorient over this time through a refinement process that involves Wnt (Dabdoub, 2003). The vertebrate PCP factor PTK7 may also play an important role in reorienting cells so that they are aligned along a common planar polarity axis by regulating actomyosin contractility at hair cell and supporting cell junctions (Lee et al., 2012; Andreeva et al., 2014). Despite these mechanisms, not all hair cells are capable of rotation. For example hair cells in the cochlear apex are never corrected in *vangl2* CKOs (Copley et al., 2013) and first row OHCs never reorient in *GPR156* mutants (Kindt et al., 2021). An interesting explanation is that shear forces that organize and pattern supporting cells in the abneural organ of Corti also drive hair cell rotation which is why it is a phenomenon primarily seen for the third row of OHCs (Cohen et al., 2020).

Hair cells develop in a gradient from base to apex with progressive maturation of bundle characteristics, gene expression and innervation. Similarly, the final orientation of hair cells is progressive, particularly for OHCs with bundles rotating from an initial tilt toward the cochlear apex toward the abneural boundary. This has significant experimental consequences if not properly controlled. For example, since bundles tilt toward cochlear apex, and cochlea chirality differs between left and right ear, samples from opposite ears cannot be pooled for quantification unless images from one ear are "mirrored" prior to analysis. Furthermore, because the cochlea develops as a gradient from base to apex, bundle orientation can differ significantly between OHCs located in the base versus the apex, and between cochlea harvested at different developmental stages. As a result, mutant models where overall embryo development is delayed often show OHC bundle orientations that accurately reflect their developmental stage but may be mistaken for a planar polarity phenotype when compared to fully developed littermate controls.

OUTSTANDING QUESTIONS

Comparing planar polarity development and function between the auditory and vestibular systems has led to significant advances

in our understanding of the molecular mechanisms guiding cellular polarization at the intrinsic and tissue levels. Despite this progress there remain several outstanding questions. Foremost, is there a global organizer that establishes the initial PCP axis, and does this organizer have a conserved role across different species and planar polarity model systems? Current work from *Drosophila* indicates that Wnt is not likely to have a role in that process and an exciting possibility is that alternatives could be identified by research in the inner ear. For example, morphogens that contribute to patterning the major axes of the developing otocyst that include BMP, Sonic Hedgehog and Retinoic Acid. One possibility is that a polarity axis is established by one of these morphogens in the early prosensory domain that is maintained throughout morphogenesis by interecellular PCP signaling.

It will also be important to establish whether or not regenerated hair cells, whether they are stem cell derived or endogenous, are capable of establishing these three levels of planar polarity. Will hair cells re-introduced into damaged tissue be able to adopt a proper orientation for their organ and location? And will this support auditory and vestibular function? A compelling set of regeneration experiments in the chick suggest this may the case and that PCP proteins in supporting cells are available to guide the planar polarization of new hair cells (Warchol and Montcouquiol, 2010). For the vestibular system, how is bundle orientation correlated with innervation and will reinnervation respect LPR? Studies in zebrafish suggest that bundle orientation and hair cell identity are linked to innervation patterns and that reinnervation mechanisms will be resilient and accurate (Pujol-Marti et al., 2014) though whether this is maintained in mammals is yet to be determined. While it is clear there remains significant work to be done to answer these questions, the breadth of studies completed to date demonstrate that we remain pointed in the right direction.

AUTHOR CONTRIBUTIONS

MRD wrote, revised, and reviewed the manuscript.

FUNDING

This work was supported by the National Institute on Deafness and Other Communication Disorders of the NIH (R01DC013066 and R01DC018040) and the University of Utah Department of Surgery, Division of Otolaryngology Professional Development Fund.

REFERENCES

Andreeva, A., Lee, J., Lohia, M., Wu, X., Macara, I. G., and Lu, X. (2014). PTK7-Src signaling at epithelial cell contacts mediates spatial organization of actomyosin and planar cell polarity. *Dev. Cell* 29, 20–33. doi: 10.1016/j.devcel.2014.02.008

Bokoch, G. M. (2003). Biology of the p21-activated kinases. *Annu Rev. Biochem.* 72, 743–781. doi: 10.1146/annurev.biochem.72.121801.161742

Carvajal-Gonzalez, J. M., Roman, A. C., and Mlodzik, M. (2016). Positioning of centrioles is a conserved readout of Frizzled planar cell polarity signalling. *Nat. Comm.* 7:11135. doi: 10.1038/ncomms11135

Cohen, R., Amir-Zilberstein, L., Hersch, M., Woland, S., Loza, O., Taiber, S., et al. (2020). Mechanical forces drive ordered patterning of hair cells in the mammalian inner ear. *Nat. Comm.* 11:5137. doi: 10.1038/s41467-020-18894-8

Copley, C. O., Duncan, J. S., Liu, C., Cheng, H., and Deans, M. R. (2013). Postnatal refinement of auditory hair cell planar polarity deficits occurs in the absence of Vangl2. *J. Neurosci.* 33, 14001–14016. doi: 10.1523/JNEUROSCI.1307-13.2013

Copp, A. J., Greene, N. D., and Murdoch, J. N. (2003). The genetic basis of mammalian neurulation. *Nat. Rev. Genet.* 4, 784–793. doi: 10.1038/nrg1181

Curtin, J. A., Quint, E., Tsipouri, V., Arkell, R. M., Cattanach, B., Copp, A. J., et al. (2003). Mutation of Celsr1 Disrupts Planar Polarity of Inner Ear Hair Cells and Causes Severe Neural Tube Defects in the Mouse. *Curr. Biol.* 13, 1129–1133. doi: 10.1016/S0960-9822(03)00374-9

Dabdoub, A. (2003). Wnt signaling mediates reorientation of outer hair cell stereociliary bundles in the mammalian cochlea. *Development* 130, 2375–2384. doi: 10.1242/dev.00448

Deans, M. R. (2013). A balance of form and function: planar polarity and development of the vestibular maculae. *Sem. Cell Dev. Biol.* 24, 490–498. doi: 10.1016/j.semcdb.2013.03.001

Deans, M. R., Antic, D., Suyama, K., Scott, M. P., Axelrod, J. D., and Goodrich, L. V. (2007). Asymmetric distribution of prickle-like 2 reveals an early underlying polarization of vestibular sensory epithelia in the inner ear. *J. Neurosci.* 27, 3139–3147. doi: 10.1523/JNEUROSCI.5151-06.2007

Denman-Johnson, K., and Forge, A. (1999). Establishment of hair bundle polarity and orientation in the developing vestibular system of the mouse. *J. Neurocytol.* 28, 821–835. doi: 10.1023/A:1007061819934

Derish, I., Lee, J. K. H., Wong-King-Cheong, M., Babayeva, S., Caplan, J., Leung, V., et al. (2020). Differential role of planar cell polarity gene Vangl2 in embryonic and adult mammalian kidneys. *PLoS One* 15:e0230586. doi: 10.1371/journal.pone.0230586

Desai, S. S., Zeh, C., and Lysakowski, A. (2005). Comparative morphology of rodent vestibular periphery. I. Saccular and utricular maculae. *J. Neurophys.* 93, 251–266. doi: 10.1152/jn.00746.2003

Devenport, D., and Fuchs, E. (2008). Planar polarization in embryonic epidermis orchestrates global asymmetric morphogenesis of hair follicles. *Nat. Cell Biol.* 10, 1257–1268. doi: 10.1038/ncb1784

Driver, E. C., Northrop, A., and Kelley, M. W. (2017). Cell migration, intercalation and growth regulate mammalian cochlear extension. *Development* 144, 3766–3776. doi: 10.1242/dev.151761

Duncan, J. S., Stoller, M. L., Francl, A. F., Tissir, F., Devenport, D., and Deans, M. R. (2017). Celsr1 coordinates the planar polarity of vestibular hair cells during inner ear development. *Dev. Biol.* 423, 126–137. doi: 10.1016/j.ydbio.2017.01.020

Eatock, R. A., and Songer, J. E. (2011). Vestibular hair cells and afferents: two channels for head motion signals. *Ann. Rev. Neurosci.* 34, 501–534. doi: 10.1146/annurev-neuro-061010-113710

Elliott, K. L., Fritzsch, B., and Duncan, J. S. (2018). Evolutionary and Developmental Biology Provide Insights Into the Regeneration of Organ of Corti Hair Cells. *Front. Cell Neurosci.* 12:252. doi: 10.3389/fncel.2018.00252

Ewen-Campen, B., Comyn, T., Vogt, E., and Perrimon, N. (2020). No Evidence that Wnt Ligands Are Required for Planar Cell Polarity in Drosophila. *Cell Rep.* 32:108121. doi: 10.1016/j.celrep.2020.108121

Ezan, J., Lasvaux, L., Gezer, A., Novakovic, A., May-Simera, H., Belotti, E., et al. (2013). Primary cilium migration depends on G-protein signalling control of subapical cytoskeleton. *Nat. Cell Biol.* 15, 1107–1115. doi: 10.1038/ncb2819

Fetter, M. (2007). Vestibulo-ocular reflex. *Dev. Ophthalmol.* 40, 35–51. doi: 10.1159/000100348

Garrido-Jimenez, S., Roman, A. C., Alvarez-Barrientos, A., and Carvajal-Gonzalez, J. M. (2018). Centriole planar polarity assessment in Drosophila wings. *Development* 2018:145. doi: 10.1242/dev.169326

Ghimire, S. R., and Deans, M. R. (2019). Frizzled3 and Frizzled6 Cooperate with Vangl2 to Direct Cochlear Innervation by Type II Spiral Ganglion Neurons. *J. Neurosci.* 39, 8013–8023. doi: 10.1523/JNEUROSCI.1740-19.2019

Ghimire, S. R., Ratzan, E. M., and Deans, M. R. (2018). A non-autonomous function of the core PCP protein VANGL2 directs peripheral axon turning in the developing cochlea. *Development* 2018:145. doi: 10.1242/dev.159012

Giese, A. P., Ezan, J., Wang, L., Lasvaux, L., Lembo, F., Mazzocco, C., et al. (2012). Gipc1 has a dual role in Vangl2 trafficking and hair bundle integrity in the inner ear. *Development* 139, 3775–3785. doi: 10.1242/dev.074229

Gillespie, P. G., and Muller, U. (2009). Mechanotransduction by hair cells: models, molecules, and mechanisms. *Cell* 139, 33–44. doi: 10.1016/j.cell.2009.09.010

Goodrich, L. V., and Strutt, D. (2011). Principles of planar polarity in animal development. *Development* 138, 1877–1892. doi: 10.1242/dev.054080

Greene, N. D., Stanier, P., and Copp, A. J. (2009). Genetics of human neural tube defects. *Hum. Mol. Genet.* 18, R113–R129. doi: 10.1093/hmg/ddp347

Grimsley-Myers, C. M., Sipe, C. W., Geleoc, G. S., and Lu, X. (2009). The small GTPase Rac1 regulates auditory hair cell morphogenesis. *J. Neurosci.* 29, 15859–15869. doi: 10.1523/JNEUROSCI.3998-09.2009

Holley, M., Rhodes, C., Kneebone, A., Herde, M. K., Fleming, M., and Steel, K. P. (2010). Emx2 and early hair cell development in the mouse inner ear. *Dev. Biol.* 340, 547–556. doi: 10.1016/j.ydbio.2010.02.004

Hudspeth, A. J. (1989). How the ear's works work. *Nature* 341, 397–404. doi: 10.1038/341397a0

Hudspeth, A. J., and Corey, D. P. (1977). Sensitivity, polarity, and conductance change in the response of vertebrate hair cells to controlled mechanical stimuli. *Proc. Natl. Acad. Sci. U S A* 74, 2407–2411. doi: 10.1073/pnas.74.6.2407

Jacobo, A., Dasgupta, A., Erzberger, A., Siletti, K., and Hudspeth, A. J. (2019). Notch-Mediated Determination of Hair-Bundle Polarity in Mechanosensory Hair Cells of the Zebrafish Lateral Line. *Curr. Biol.* 357:e7. doi: 10.1016/j.cub.2019.08.060

Jarysta, A., and Tarchini, B. (2021). Multiple PDZ domain protein maintains patterning of the apical cytoskeleton in sensory hair cells. *Development* 2021:148. doi: 10.1242/dev.199549

Jean, P., Ozcete, O. D., Tarchini, B., and Moser, T. (2019). Intrinsic planar polarity mechanisms influence the position-dependent regulation of synapse properties in inner hair cells. *Proc. Natl. Acad. Sci. U S A* 116, 9084–9093. doi: 10.1073/pnas.1818358116

Jenny, A. (2010). Planar cell polarity signaling in the Drosophila eye. *Curr. Topics Dev. Biol.* 93, 189–227. doi: 10.1016/B978-0-12-385044-7.00007-2

Ji, Y. R., Warrier, S., Jiang, T., Wu, D. K., and Kindt, K. S. (2018). Directional selectivity of afferent neurons in zebrafish neuromasts is regulated by Emx2 in presynaptic hair cells. *Elife* 2018:7. doi: 10.7554/eLife.35796

Jiang, T., Kindt, K., and Wu, D. K. (2017). Transcription factor Emx2 controls stereociliary bundle orientation of sensory hair cells. *Elife* 2017:6. doi: 10.7554/eLife.23661

Kindt, K. S., Akturk, A., Jarysta, A., Day, M., Beirl, A., Flonard, M., et al. (2021). EMX2-GPR156-Galphai reverses hair cell orientation in mechanosensory epithelia. *Nat. Comm.* 12:2861. doi: 10.1038/s41467-021-22997-1

Kozak, E. L., Palit, S., Miranda-Rodriguez, J. R., Janjic, A., Bottcher, A., Lickert, H., et al. (2020). Epithelial Planar Bipolarity Emerges from Notch-Mediated Asymmetric Inhibition of Emx2. *Curr. Biol.* 114:e6. doi: 10.1016/j.cub.2020.01.027

Landin Malt, A., Clancy, S., Hwang, D., Liu, A., Smith, C., Smith, M., et al. (2021). Non-Canonical Wnt Signaling Regulates Cochlear Outgrowth and Planar Cell Polarity via Gsk3beta Inhibition. *Front. Cell Dev. Biol.* 9:649830. doi: 10.3389/fcell.2021.649830

Landin Malt, A., Dailey, Z., Holbrook-Rasmussen, J., Zheng, Y., Hogan, A., Du, Q., et al. (2019). Par3 is essential for the establishment of planar cell polarity of inner ear hair cells. *Proc. Natl. Acad. Sci. U S A* 116, 4999–5008. doi: 10.1073/pnas.1816333116

Landin Malt, A., Hogan, A. K., Smith, C. D., Madani, M. S., and Lu, X. (2020). Wnts regulate planar cell polarity via heterotrimeric G protein and PI3K signaling. *J. Cell Biol.* 2020:219. doi: 10.1083/jcb.201912071

Lee, J., Andreeva, A., Sipe, C. W., Liu, L., Cheng, A., and Lu, X. (2012). PTK7 regulates myosin II activity to orient planar polarity in the mammalian auditory epithelium. *Curr. Biol.* 22, 956–966. doi: 10.1016/j.cub.2012.03.068

Lefevre, G., Michel, V., Weil, D., Lepelletier, L., Bizard, E., Wolfrum, U., et al. (2008). A core cochlear phenotype in USH1 mouse mutants implicates fibrous links of the hair bundle in its cohesion, orientation and differential growth. *Development* 135, 1427–1437. doi: 10.1242/dev.012922

Lewis, J., and Davies, A. (2002). Planar cell polarity in the inner ear: how do hair cells acquire their oriented structure? *J. Neurobiol.* 53, 190–201. doi: 10.1002/neu.10124

Lopez-Schier, H., and Hudspeth, A. J. (2006). A two-step mechanism underlies the planar polarization of regenerating sensory hair cells. *Proc. Natl. Acad. Sci. U S A* 103, 18615–18620. doi: 10.1073/pnas.0608536103

Lozano-Ortega, M., Valera, G., Xiao, Y., Faucherre, A., and Lopez-Schier, H. (2018). Hair cell identity establishes labeled lines of directional mechanosensation. *PLoS Biol.* 16:e2004404. doi: 10.1371/journal.pbio.2004404

Lu, X., Borchers, A. G., Jolicoeur, C., Rayburn, H., Baker, J. C., and Tessier-Lavigne, M. (2004). PTK7/CCK-4 is a novel regulator of planar cell polarity in vertebrates. *Nature* 430, 93–98. doi: 10.1038/nature02677

Maklad, A., Kamel, S., Wong, E., and Fritzsch, B. (2010). Development and organization of polarity-specific segregation of primary vestibular afferent fibers in mice. *Cell Tissue Res.* 340, 303–321. doi: 10.1007/s00441-010-0944-1

Mitchell, B., Stubbs, J. L., Huisman, F., Taborek, P., Yu, C., and Kintner, C. (2009). The PCP pathway instructs the planar orientation of ciliated cells in the Xenopus larval skin. *Curr. Biol.* 19, 924–929. doi: 10.1016/j.cub.2009.04.018

Montcouquiol, M., Rachel, R. A., Lanford, P. J., Copeland, N. G., Jenkins, N. A., and Kelley, M. W. (2003). Identification of Vangl2 and Scrb1 as planar polarity genes in mammals. *Nature* 423, 173–177. doi: 10.1038/nature01618

Morin, X., and Bellaiche, Y. (2011). Mitotic spindle orientation in asymmetric and symmetric cell divisions during animal development. *Dev. Cell* 21, 102–119. doi: 10.1016/j.devcel.2011.06.012

Murdoch, J. N., Rachel, R. A., Shah, S., Beermann, F., Stanier, P., Mason, C. A., et al. (2001). Circletail, a new mouse mutant with severe neural tube defects: chromosomal localization and interaction with the loop-tail mutation. *Genomics* 78, 55–63. doi: 10.1006/geno.2001.6638

Nagaoka, T., Ohashi, R., Inutsuka, A., Sakai, S., Fujisawa, N., Yokoyama, M., et al. (2014). The Wnt/planar cell polarity pathway component Vangl2 induces synapse formation through direct control of N-cadherin. *Cell Rep.* 6, 916–927. doi: 10.1016/j.celrep.2014.01.044

Najarro, E. H., Huang, J., Jacobo, A., Quiruz, L. A., Grillet, N., and Cheng, A. G. (2020). Dual regulation of planar polarization by secreted Wnts and Vangl2 in the developing mouse cochlea. *Development* 2020:147.

Navajas Acedo, J., Voas, M. G., Alexander, R., Woolley, T., Unruh, J. R., Li, H., et al. (2019). PCP and Wnt pathway components act in parallel during zebrafish mechanosensory hair cell orientation. *Nat. Comm.* 10:3993. doi: 10.1038/s41467-019-12005-y

Ono, K., Sandell, L. L., Trainor, P. A., and Wu, D. K. (2020). Retinoic acid synthesis and autoregulation mediate zonal patterning of vestibular organs and inner ear morphogenesis. *Development* 2020:147. doi: 10.1242/dev.192070

Pujol-Marti, J., Faucherre, A., Aziz-Bose, R., Asgharsharghi, A., Colombelli, J., Trapani, J. G., et al. (2014). Converging axons collectively initiate and maintain synaptic selectivity in a constantly remodeling sensory organ. *Curr. Biol.* 24, 2968–2974. doi: 10.1016/j.cub.2014.11.012

Richardson, G. P., and Petit, C. (2019). Hair-Bundle Links: Genetics as the Gateway to Function. *Cold Spr. Harb Perspect Med.* 2019:9. doi: 10.1101/cshperspect.a033142

Schwander, M., Kachar, B., and Muller, U. (2010). Review series: The cell biology of hearing. *J. Cell Biol.* 190, 9–20. doi: 10.1083/jcb.201001138

Shotwell, S. L., Jacobs, R., and Hudspeth, A. J. (1981). Directional sensitivity of individual vertebrate hair cells to controlled deflection of their hair bundles. *Ann. N. Y. Acad. Sci.* 374, 1–10. doi: 10.1111/j.1749-6632.1981.tb30854.x

Sienknecht, U. J., Anderson, B. K., Parodi, R. M., Fantetti, K. N., and Fekete, D. M. (2011). Non-cell-autonomous planar cell polarity propagation in the auditory sensory epithelium of vertebrates. *Dev. Biol.* 352, 27–39. doi: 10.1016/j.ydbio.2011.01.009

Sipe, C. W., and Lu, X. (2011). Kif3a regulates planar polarization of auditory hair cells through both ciliary and non-ciliary mechanisms. *Development* 138, 3441–3449. doi: 10.1242/dev.065961

Sipe, C. W., Liu, L., Lee, J., Grimsley-Myers, C., and Lu, X. (2013). Lis1 mediates planar polarity of auditory hair cells through regulation of microtubule organization. *Development* 140, 1785–1795. doi: 10.1242/dev.089763

Stoller, M. L., Roman, O. Jr., and Deans, M. R. (2018). Domineering non-autonomy in Vangl1;Vangl2 double mutants demonstrates intercellular PCP signaling in the vertebrate inner ear. *Dev. Biol.* 437, 17–26. doi: 10.1016/j.ydbio.2018.02.021

Struhl, G., Casal, J., and Lawrence, P. A. (2012). Dissecting the molecular bridges that mediate the function of Frizzled in planar cell polarity. *Development* 139, 3665–3674. doi: 10.1242/dev.083550

Tadenev, A. L. D., Akturk, A., Devanney, N., Mathur, P. D., Clark, A. M., Yang, J., et al. (2019). GPSM2-GNAI Specifies the Tallest Stereocilia and Defines Hair Bundle Row Identity. *Curr. Biol.* 29, 921–934e4. doi: 10.1016/j.cub.2019.01.051

Tarchini, B., and Lu, X. (2019). New insights into regulation and function of planar polarity in the inner ear. *Neurosci. Lett.* 709:134373. doi: 10.1016/j.neulet.2019.134373

Tarchini, B., Jolicoeur, C., and Cayouette, M. (2013). A molecular blueprint at the apical surface establishes planar asymmetry in cochlear hair cells. *Dev. Cell* 27, 88–102. doi: 10.1016/j.devcel.2013.09.011

Tarchini, B., Tadenev, A. L., Devanney, N., and Cayouette, M. (2016). A link between planar polarity and staircase-like bundle architecture in hair cells. *Development* 143, 3926–3932. doi: 10.1242/dev.139089

Thakar, S., Wang, L., Yu, T., Ye, M., Onishi, K., Scott, J., et al. (2017). Evidence for opposing roles of Celsr3 and Vangl2 in glutamatergic synapse formation. *Proc. Natl. Acad. Sci. U S A* 114, E610–E618. doi: 10.1073/pnas.1612062114

Tilney, L. G., Tilney, M. S., and DeRosier, D. J. (1992). Actin filaments, stereocilia, and hair cells: how cells count and measure. *Annu. Rev. Cell Biol.* 8, 257–274. doi: 10.1146/annurev.cb.08.110192.001353

Torban, E., and Sokol, S. Y. (2021). Planar cell polarity pathway in kidney development, function and disease. *Nat. Rev. Nephrol.* 17, 369–385. doi: 10.1038/s41581-021-00395-6

Vladar, E. K., Antic, D., and Axelrod, J. D. (2009). Planar cell polarity signaling: the developing cell's compass. *Cold Spr. Harbor Perspect. Biol.* 1:a002964. doi: 10.1101/cshperspect.a002964

Wang, J., Hamblet, N. S., Mark, S., Dickinson, M. E., Brinkman, B. C., Segil, N., et al. (2006). Dishevelled genes mediate a conserved mammalian PCP pathway to regulate convergent extension during neurulation. *Development* 133, 1767–1778. doi: 10.1242/dev.02347

Wang, J., Mark, S., Zhang, X., Qian, D., Yoo, S. J., Radde-Gallwitz, K., et al. (2005). Regulation of polarized extension and planar cell polarity in the cochlea by the vertebrate PCP pathway. *Nat. Genet.* 37, 980–985. doi: 10.1038/ng1622

Wang, Y., Guo, N., and Nathans, J. (2006). The role of Frizzled3 and Frizzled6 in neural tube closure and in the planar polarity of inner-ear sensory hair cells. *J. Neurosci.* 26, 2147–2156. doi: 10.1523/JNEUROSCI.4698-05.2005

Warchol, M. E., and Montcouquiol, M. (2010). Maintained expression of the planar cell polarity molecule Vangl2 and reformation of hair cell orientation in the regenerating inner ear. *J. Assoc. Res. Otolaryngol.* 11, 395–406. doi: 10.1007/s10162-010-0209-4

Wu, J., and Mlodzik, M. (2008). The frizzled extracellular domain is a ligand for Van Gogh/Stbm during nonautonomous planar cell polarity signaling. *Dev. Cell* 15, 462–469. doi: 10.1016/j.devcel.2008.08.004

Yang, T., Kersigo, J., Wu, S., Fritzsch, B., and Bassuk, A. G. (2017). Prickle1 regulates neurite outgrowth of apical spiral ganglion neurons but not hair cell polarity in the murine cochlea. *PLoS One* 12:e0183773. doi: 10.1371/journal.pone.0183773

Yang, Y., and Mlodzik, M. (2015). Wnt-Frizzled/planar cell polarity signaling: cellular orientation by facing the wind (Wnt). *Annu. Rev. Cell Dev. Biol.* 31, 623–646. doi: 10.1146/annurev-cellbio-100814-125315

Yin, H., Copley, C. O., Goodrich, L. V., and Deans, M. R. (2012). Comparison of phenotypes between different vangl2 mutants demonstrates dominant effects of the Looptail mutation during hair cell development. *PLoS One* 7:e31988. doi: 10.1371/journal.pone.0031988

Yu, J. J. S., Maugarny-Cales, A., Pelletier, S., Alexandre, C., Bellaiche, Y., Vincent, J. P., et al. (2020). Frizzled-Dependent Planar Cell Polarity without Secreted Wnt Ligands. *Dev. Cell* 54, 583–592e5. doi: 10.1016/j.devcel.2020.08.004

Conflict of Interest: The author declares that the research was conducted in the absence of any commercial or financial relationships that could be construed as a potential conflict of interest.

Publisher's Note: All claims expressed in this article are solely those of the authors and do not necessarily represent those of their affiliated organizations, or those of the publisher, the editors and the reviewers. Any product that may be evaluated in this article, or claim that may be made by its manufacturer, is not guaranteed or endorsed by the publisher.

frontiers in Neuroscience

ORIGINAL RESEARCH
published: 25 October 2021
doi: 10.3389/fnins.2021.733291

Expression and Physiology of Voltage-Gated Sodium Channels in Developing Human Inner Ear

*Rikki K. Quinn[1,2], Hannah R. Drury[1,2], Ethan T. Cresswell[1,2], Melissa A. Tadros[1,2], Bryony A. Nayagam[3], Robert J. Callister[1,2], Alan M. Brichta[1,2] and Rebecca Lim[1,2]**

[1] School of Biomedical Sciences and Pharmacy, The University of Newcastle, Callaghan, NSW, Australia, [2] Hunter Medical Research Institute, The University of Newcastle, New Lambton Heights, NSW, Australia, [3] Department of Audiology and Speech Pathology, The University of Melbourne, Parkville, VIC, Australia

OPEN ACCESS

Edited by:
Soroush G. Sadeghi,
University at Buffalo, United States

Reviewed by:
Katie Rennie,
University of Colorado, Denver, United States
Radha Kalluri,
University of Southern California, United States

***Correspondence:**
Rebecca Lim
Rebecca.Lim@newcastle.edu.au

Specialty section:
This article was submitted to Perception Science, a section of the journal Frontiers in Neuroscience

Received: 30 June 2021
Accepted: 29 September 2021
Published: 25 October 2021

Citation:
Quinn RK, Drury HR, Cresswell ET, Tadros MA, Nayagam BA, Callister RJ, Brichta AM and Lim R (2021) Expression and Physiology of Voltage-Gated Sodium Channels in Developing Human Inner Ear. Front. Neurosci. 15:733291. doi: 10.3389/fnins.2021.733291

Sodium channel expression in inner ear afferents is essential for the transmission of vestibular and auditory information to the central nervous system. During development, however, there is also a transient expression of Na^+ channels in vestibular and auditory hair cells. Using qPCR analysis, we describe the expression of four Na^+ channel genes, SCN5A (Nav1.5), SCN8A (Nav1.6), SCN9A (Nav1.7), and SCN10A (Nav1.8) in the human fetal cristae ampullares, utricle, and base, middle, and apex of the cochlea. Our data show distinct patterns of Na^+ channel gene expression with age and between these inner ear organs. In the utricle, there was a general trend toward fold-change increases in expression of SCN8A, SCN9A, and SCN10A with age, while the crista exhibited fold-change increases in SCN5A and SCN8A and fold-change decreases in SCN9A and SCN10A. Fold-change differences of each gene in the cochlea were more complex and likely related to distinct patterns of expression based on tonotopy. Generally, the relative expression of SCN genes in the cochlea was greater than that in utricle and cristae ampullares. We also recorded Na^+ currents from developing human vestibular hair cells aged 10–11 weeks gestation (WG), 12–13 WG, and 14+ WG and found there is a decrease in the number of vestibular hair cells that exhibit Na^+ currents with increasing gestational age. Na^+ current properties and responses to the application of tetrodotoxin (TTX; 1 μM) in human fetal vestibular hair cells are consistent with those recorded in other species during embryonic and postnatal development. Both TTX-sensitive and TTX-resistant currents are present in human fetal vestibular hair cells. These results provide a timeline of sodium channel gene expression in inner ear neuroepithelium and the physiological characterization of Na^+ currents in human fetal vestibular neuroepithelium. Understanding the normal developmental timeline of ion channel gene expression and when cells express functional ion channels is essential information for regenerative technologies.

Keywords: vestibular, cochlea, human, development, PCR, sodium channel, electrophysiology, inner ear

INTRODUCTION

Voltage-gated sodium channels are essential for the propagation of action potentials in neurons. There are nine different α-subunits in Na^+ voltage-gated ion channels that are expressed in the central and peripheral nervous systems that are critical for neuronal excitability and function (Wang et al., 2017). In sensory afferent fibers there are different patterns of Na^+ channel subunit expression during development, that likely influences the sensitivity and firing patterns of these neurons (Thun et al., 2009; Tadros et al., 2015; Kim and Rutherford et al., 2016; Meredith and Rennie, 2020). In the central nervous system, there is a developmentally regulated expression of sodium channel genes specifically targeting excitatory or inhibitory neurons which is likely to establish distinct firing rates (Du et al., 2020). In addition to the essential role in action potential discharge, Na^+ channel expression during development has a role in synaptogenesis (Chabbert et al., 2003; Brugeaud et al., 2007; Zu et al., 2021) and may be important for cell differentiation and afferentation (Oliver et al., 1997; Wooltorton et al., 2007).

There is a diversity in the expression of Na^+ channel genes including Nav 1.1–Nav 1.9 in the inner ear at different stages of development (Mechaly et al., 2005; Wooltorton et al., 2007; Fryatt et al., 2009; Frucht et al., 2011; Yoshimura et al., 2014; Liu et al., 2016), that is thought to be important for establishing appropriate neural connections. The β-subunits of voltage-gated Na^+ channels, encoded by SCNB genes have also been tracked in the developing the inner ear (Wooltorton et al., 2007; Liu et al., 2016). Complementing these molecular results are anatomical investigations that have documented the expression and location of various Na^+ channel α-subunits within hair cells, afferent terminals, and ganglia of the auditory and vestibular systems (Wooltorton et al., 2007; Lysakowski et al., 2011; Eckrich et al., 2012; Kim and Rutherford et al., 2016; Liu et al., 2016; Zhou et al., 2020). Functional studies have characterized the presence of different types of Na^+ currents (attributable to α- and β-subunits) in both developing and mature vestibular and auditory hair cells and ganglion neurons of rat, mouse, and gerbil (Santos-Sacchi, 1993; Rüsch and Eatock, 1996; Chabbert et al., 1997; Marcotti et al., 2003; Geleoc et al., 2004; Wooltorton et al., 2007; Li et al., 2010; Liu et al., 2016; Browne et al., 2017). In vestibular type I and type II hair cells, there is evidence for the presence of both tetrodotoxin (TTX)-insensitive and TTX-sensitive Na^+ channels, respectively, and that Na^+ channel expression in utricle is developmentally regulated (Wooltorton et al., 2007). By postnatal day (PND) 21, there is a loss of TTX-sensitive Na^+ channels in type II hair cells and a significant down-regulation of TTX-insensitive Na^+ channels in type I hair cells (Wooltorton et al., 2007). This transient Na^+ channel expression is reduced after synaptogenesis and the establishment of afferent contacts (Wooltorton et al., 2007). In the cochlea, the expression of Na^+ channels during development in outer hair cells (OHCs) may be linked to establishing and refining afferent and efferent connections (Oliver et al., 1997). In inner hair cells (IHCs), during embryonic and early postnatal development (embryonic E16.5 – PND 12), there is a transient expression of Na^+ channels that are responsible for modulating spike frequency of Ca^{2+}-evoked action potentials (Marcotti et al., 2003; Eckrich et al., 2012). With the onset of hearing (after PND 12 in mice), there is a down-regulation of these Na^+ channels in IHCs.

The expression of voltage-gated Na^+ channels in auditory and vestibular ganglion neurons is essential for action potential generation and propagation of auditory and vestibular information from the periphery to the central nervous system. Vestibular ganglion neurons, like afferent fibers have a diversity of spike frequencies and timing, i.e., regular versus irregular discharge, which is likely due to the expression of different Na^+ channels including persistent and resurgent Na^+ channels (Liu et al., 2016; Meredith and Rennie, 2018, 2020). Similarly, the high frequency of auditory afferent discharge and requirement for precise timing and localization of auditory inputs is dependent on the expression of a combination of TTX-sensitive, TTX-insensitive, persistent, and resurgent Na^+ channels in spiral ganglion neurons (Santos-Sacchi, 1993; Browne et al., 2017).

In summary, our current understanding of Na^+ channel expression in the auditory and vestibular systems has arisen almost exclusively from developing and mature animal models. Some work on human tissue has described ion channel expression, however, this has been restricted to immunolabelling in diseased adult tissue (Hotchkiss et al., 2005). No studies have characterized the expression and few have described the function of Na^+ channel physiology in developing human hair cells (Lim et al., 2014). To address this deficit, we examined mRNA expression of four Na^+ channel types that are known to be functionally important in cochlea and vestibular end organs during embryonic and postnatal development in other species. We also characterize Na^+ channel physiology in developing vestibular hair cells using patch clamp electrophysiology. Our experimental approach uses human fetal inner ear neuroepithelia aged between 10 and 17 WG, a period of human inner ear development when rapid changes are occurring (see review Lim and Brichta, 2016).

MATERIALS AND METHODS

Tissue Collection

Tissue samples were obtained from elective terminations (10–17 WG). All procedures were approved by The University of Newcastle Human Ethics Committee and complied with Australia's National Health and Medical Research Council, National Statement on Ethical Conduct in Human Research regulations. Written consent was obtained from all donors and no identifying information was supplied to researchers. No samples were collected with known medical or genetic anomalies. Gestational age was determined by three criteria: (1) date of last menstrual period, (2) ultrasound measurement of crown – rump length, and (3) foot length (Hern, 1984). Products of conception (POC) were collected in a cold glycerol-based artificial cerebrospinal fluid (ACSF) containing (in mM); 250 glycerol, 26 $NaHCO_3$, 11 glucose, 2.5 KCl, 1.2 NaH_2PO_4, 1.2 $MgCl_2$, and 2.5 $CaCl_2$ and then transported to a PC2 laboratory at The University of Newcastle. All samples arrived at our laboratory within 60 min of the termination procedure. All

experiments were also approved by the University of Newcastle Institutional Biosafety Committee.

Tissue Preparation

Inner ears were obtained from POC and transferred to a dissecting well filled with fresh glycerol-based ACSF that was bubbled with 5% CO_2/95% O_2 as previously described (Lim et al., 2014). At the developmental stages we examined (10–17 WG), the precursor of the bony labyrinth is cartilaginous and not calcified. Consequently, it was peeled away to expose the underlying membranous labyrinth. The neuroepithelium of the vestibular organs (cristae ampullares and utricle) and cochlea were micro dissected and the membranes overlying the neuroepithelium were removed. The vestibular organs were used for either molecular biology analysis or electrophysiological experiments. For molecular biology experiments, the vestibular organs (cristae ampullares, utricle) and the cochlea were transferred to a vial of RNAlater (Merck, Australia), stored at 4°C overnight and then at −20°C for processing at a later date. Hair cell layers were not further dissected in either cochlea or vestibular organs. Thus, our qPCR results measure gene expression from epithelium containing hair cells, afferent and efferent terminals, and stromal cells. For electrophysiology experiments, whole vestibular organs were transferred to a recording chamber (Lim et al., 2014) containing oxygenated Liebovitz's L15 cell culture medium containing (in mM); 1.26 $CaCl_2$, 0.98 $MgCl_2$, 0.81 $MgSO_4$, 5.33 KCl, 44 KH_2PO_4, 137.93 NaCl, 1.34 NaH_2PO_4 (Life Technologies, Australia; pH 7.45, 305 mOsM), and perfused at an exchange rate of 3 ml/min.

RNA Extraction

For each sensory region (cristae ampullares, utricle, and cochlea) from an individual POC sample aged 10–17 WG, RNA was extracted using QIAGEN miRNeasy Kit (QIAGEN, Australia) according to manufacturer's instructions. Briefly, sensory regions were homogenized in 700 μl QIAzol lysis reagent and incubated at room temperature for 5 min. Samples were loaded into QIAGEN miRNeasy spin columns and total and small RNA were isolated. RNA quality and quantity were determined using Nanospectrophotometry.

DNase I Treatment

Total RNA (60–200 ng) was treated with 1 μl DNase I (ThermoFisher Scientific, Australia), 1 μl DNase I buffer, and molecular biology grade water to total volume = 10 μl and incubated at room temperature for 15 min. Next, 1 μl of 25 mM EDTA was added and samples incubated for 10 min at 65°C.

Reverse Transcription

Reverse transcription was performed using SuperScript III (ThermoFisher Scientific, Australia), according to the manufacturer's instructions. Briefly, 30–100 ng of total RNA, 1 μl oligo(dT)18 primers, 1 μl of random hexamer, 1 μl of 10 mM dNTP, and molecular biology grade water to total volume = 13 μl, were mixed and heated for 5 min at 65°C. After incubation, 4 μl 5× first-strand buffer, 1 μl of 0.1 M DTT, 1 μl RiboSafe RNase Inhibitor (40 U/μl) and 1 μl SuperScript III RT (200 U/μl) were added and samples incubated for 60 min at 50°C, followed by 15 min at 70°C.

qPCR

All qPCR primers were designed using NCBI Primer-BLAST (see **Table 1**). Primer efficiencies, specificity, and optimal cDNA quantities were determined using serial dilutions of neuronal cDNA from human POCs. Reactions contained 6.25 μl 2× SensiFAST SYBR® Lo-ROX (Bioline, Australia), 1–4 ng cDNA, 200 nm each of forward and reverse primers and molecular biology grade water to total volume = 12.5 μl. Reactions were performed in triplicate on an ABI 7500 Real-Time PCR System (Applied Biosystems, United States) and analyzed using the Applied Biosystems 7500 Sequence Detection software (version 1.4). Delta Ct (ΔCt, threshold cycle) was determined for each gene relative to the housekeeping gene β-Actin (ACTB). Expression of a second housekeeping gene (GAPDH) was also done. Our analysis found there was a potential age-related change in GAPDH in inner ear samples. Consequently, GAPDH was not used as a reference gene, rather, β-actin was used for sample normalization. To confirm the use of β-actin as a reliable and valid housekeeping gene with stable expression, the entire data set was screened using RefFinder (Xie et al., 2012). The ΔΔCt method was employed to compare gene expression across the three different age groups (10–11 WG, 12–13 WG, and 14+ WG).

Data Presentation and Statistical Analysis

Plots of ΔΔCt for each gene were generated by normalizing data in each tissue sample to 10–11 WG values and represented as ***fold change*** to compare developmental changes. Comparisons of gene expression between tissue samples (i.e., utricle versus base of cochlea) for a single age group are described as ***relative expression*** to the housekeeping gene, β-actin.

In figures that show fold change, each data point represents the mean fold change ± SEM (fold change ratio) for the gestational ages shown.

As our data were not normally distributed, differences were described by relative expression of the median and were

TABLE 1 | Primer sequences for SCN5A, SCN8A, SCN9A, and SCN10A.

Gene	Forward sequence	Reverse Sequence	Primer efficiency
SCN5A	GAGTACACCTTCAC CGCCAT	TCACACTAAAGTCCA GCCAGTT	93.7%
SCN8A	ATTTGAAGGGATGAG GGTGGTG	AAGCAGTAGTGGTA CTTTCCC	105.8%
SCN9A	ACCCCCAATCAGTC ACCACT	GACTTGTTCTGCTG CTTCGC	83.0%
SCN10A	TCGCTAATCCGACT GTGTGG	TCCTGCTGTCCTTTG GGGAT	106.1%

analyzed by the Mann–Whitney *U* test. Effect size following Mann–Whitney *U* test was calculated by the following formula:

$$\eta^2 = Z^2/N$$

Effect size was calculated to compare relative gene expression across ages and tissue regions. An advantage of calculating effect size is the independence from sample size (Schafer and Schwarz, 2019). This increases the likelihood of detecting biologically relevant results within a small sample set. Effect sizes for η^2 are $\eta^2 > 0.01$ = small effect size, $\eta^2 > 0.06$ = medium effect size, and $\eta^2 > 0.14$ = large effect size (Cohen, 1988). Effect sizes of median gene expression were calculated between the three age groups for each tissue and between tissues at each age group.

Electrophysiological Recordings

Whole cell patch clamp recordings of voltage-gated Na^+ channel activity were made from tissue samples aged between 10 and 16 WG. Hair cell recordings began within 90–120 min from the time of the termination procedure and tissue was viable for up to 5 h post-procedure. Whole vestibular organs (individual crista, utricle, or vestibular triad) were transferred to the recording chamber. Borosilicate glass pipettes (3–5 MΩ) were used and filled with KCl/gluconate based internal solution. The KCl/gluconate based internal solution contained (in mM); 42 KCl, 98 K-gluconate, 4 HEPES, 0.5 EGTA, 1 $MgCl_2$, 5 Na-ATP, and pH 7.3 (Poppi et al., 2018). All recordings were made at room temperature (22–25°C). Hair cells were recorded from the explant and identified using either a Zeiss Axioscope 2 FS or Olympus BX51WI microscope with infra-red differential interference contrast optics. In some experiments TTX (Alomone, Israel; 1 μM) and cadmium (Sigma Aldrich, Australia; 300 μM) were added to the perfusate. Recordings were collected using either an Axopatch 1D or MultiClamp 200B amplifier, both using Axograph X software. Data were sampled at 20 kHz and filtered at 2–10 kHz. Series resistance (R_s) was monitored throughout the recording sessions and data were rejected if R_s changed by more than 20%. The mean R_s was 14.3 ± 1.4 MΩ. Data were recorded from hair cells of both the cristae and utricle. Data are presented as mean ± SEM. Data were analyzed by Mann–Whitney *U* statistical test since data were not normally distributed.

RESULTS

Gene expression data were collected from inner ear samples aged 10–17 WG from a total of 47 donations. Data were grouped into the following age categories; 10–11, 12–13, and 14+ WG. Changes in mRNA expression of four different Na^+ channel genes, SCN5A, SCN8A, SCN9A, and SCN10A were tracked during fetal development. These genes were chosen as changes in their expression has been reported in other species during development (Wooltorton et al., 2007; Fryatt et al., 2009; Liu et al., 2016; Zhou et al., 2020). For each gene we first describe ***fold changes*** in gene expression over time for each inner ear region (i.e., crista, utricle, base, middle, and apex of the cochlea, respectively). These fold changes are shown in **Figures 1–4** where data points represent the mean fold change ± SEM (i.e., fold change ratio) for the gestational ages shown. We then compare ***relative gene expression*** between vestibular and auditory regions. These data are presented in **Tables 2–4**.

SCN5A (Nav1.5) mRNA Expression

SCN5A gene expression between 10–11 WG and 14+ WG in cristae and utricle were not statistically significantly different (crista; 10–11 WG median = 5.2×10^{-3}, $n = 12$, 14+ WG median = 1.8×10^{-2}, $n = 9$, $U = 31$, $p = 0.102$, utricle; 10–11 WG median = 0.02, $n = 8$, 14+ WG median = 0.015, $n = 12$, $U = 47$, $p = 0.97$). There was, however, a threefold change in SCN5A expression between 10–11 WG and 14 WG in crista (**Figure 1A**). In the base of the cochlea, there was a threefold increase in SCN5A gene expression between 12–13 WG and 14+ WG, and was statistically significantly different. SCN5A expression in the 14+ WG age group (median = 15.8×10^{-2}, $n = 8$) was significantly greater than the 12–13 WG age group (median = 1.8×10^{-2}, $n = 8$; $U = 13$, $p = 0.046$) with a large

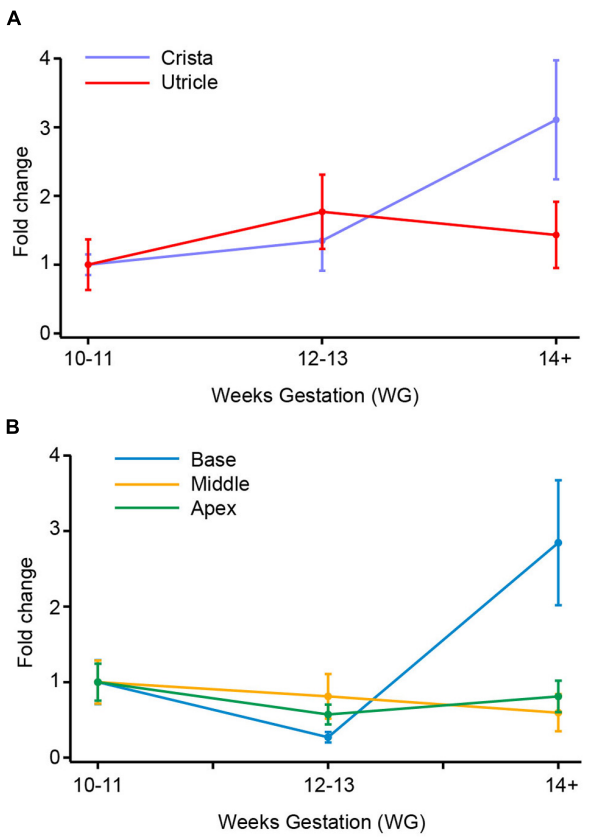

FIGURE 1 | SCN5A (Nav1.5) mRNA in vestibular organs and cochlea. **(A)** In utricle there is no difference in the expression of SCN5A across the three age groups. In crista, there is a threefold increase in SCN5A from 10–11 WG to 14+ WG. **(B)** In cochlea there is a 2.8-fold increase in expression of SCN5A mRNA between 10–11 WG and 14+ WG. There were no changes in expression of SCN5A in middle or apex of cochlea.

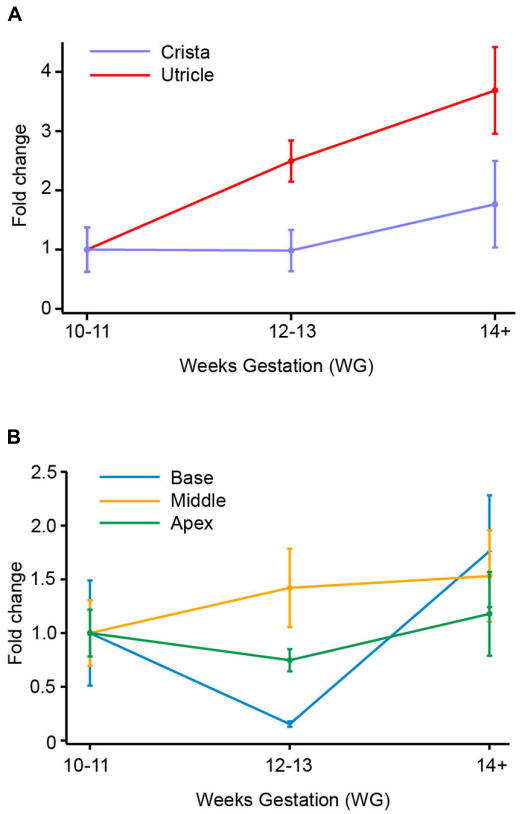

FIGURE 2 | SCN8A (Nav1.6) mRNA in vestibular organs and cochlea. **(A)** Both crista and utricle exhibit an increase in SCN8A mRNA expression with age. At the ages examined there was a peak in fold change at 14+ WG in both crista (1.8-fold) and utricle (3.7-fold). **(B)** There were smaller fold changes in the cochlea compared to vestibular organs. The base and apex of the cochlea show decreases in SCN8A expression at 12–13 WG compared to 10–11 WG. At 14+ WG both base and apex then have increases in mRNA expression, greater than that at 10–11 WG and 12–13 WG. The increase in SCN8A mRNA expression in the base of the cochlea was significantly greater at 14+ WG than at 12–13 WG. In contrast to the base and apex, the middle turn of the cochlea had a slight increase in mRNA expression at 12–13 WG compared to 10–11 WG, which plateaued at 14+ WG.

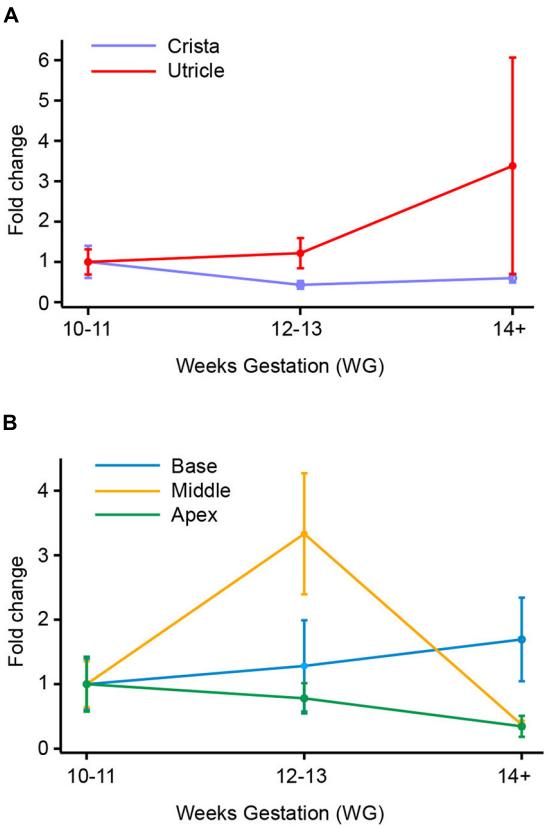

FIGURE 3 | SCN9A (Nav1.7) mRNA in vestibular organs and cochlea. **(A)** There was a slight decrease in SCN9A expression with age in the crista, with the lowest expression level at 12–13 WG (0.4-fold change). In utricle, there was a slight increase in SCN9A expression at 12–13 WG, to peak at 14+ WG with a 3.4-fold change in SCN9A expression relative to the 10–11 WG age group. **(B)** SCN9A expression in the base of the cochlea increased with age to peak at 14+ WG with a 1.7-fold increase compared to 10–11 WG. There was a 3.3-fold increase in SCN9A expression in the middle region of the cochlea at 12–13 WG, which then dramatically decreased at 14+ WG resulting in a 0.4-fold decrease compared to 10–11 WG. There was a decrease in SCN9A expression with age in the apex of the cochlea with lowest expression at 14+ WG (0.006-fold compared to 10–11 WG).

effect size ($\eta^2 = 0.25$). There were no other significant changes in expression of SCN5A with age in the other regions (middle and apex) of the cochlea.

There were several age-dependent differences in the relative expression of SCN5A between inner ear regions. For the vestibular system, the relative expression of SCN5A was significantly higher in the utricle at 10–11 WG (median = 20.7×10^{-3}, $n = 8$) compared to the cristae (median = 5.2×10^{-3}, $n = 12$, $U = 15$, $p = 0.011$), but not at other ages. For the cochlea, the relative expression of SCN5A at 14+ WG was significantly greater in the base compared to all other inner ear regions (see **Table 2**).

SCN8A (Nav1.6) mRNA Expression

There is a general trend toward an increase in SCN8A gene expression in vestibular organs with age (**Figure 2A**). This increase in SCN8A expression is significant between 10–11 WG (median = 2.4×10^{-2}, $n = 8$) and 14+ WG (median = 8.9×10^{-2}, $n = 11$) in the utricle ($U = 17$, $p = 0.026$) reflecting a large effect size ($\eta^2 = 0.26$). However, there were no differences in the expression of SCN8A in the cristae ampullares with age. But there is a significantly greater relative expression of SCN8A in the utricle compared to the cristae at each age group (see **Table 3**).

Fold changes in the relative expression of SCN8A in regions of the cochlea are shown in **Figure 2B**. In the base of the cochlea, there is a decrease in SCN8A expression between 10–11 WG and 12–13 WG, followed by a marked increase in SCN8A expression between 12–13 WG and 14+ WG. This increased SCN8A mRNA expression between 12–13 WG (median = 9.6×10^{-3}, $n = 8$) and 14+ WG (median 78.7×10^{-3}, $n = 8$) was statistically significant ($U = 12$, $p = 0.036$), with a large effect size ($\eta^2 = 0.27$). It should be noted that at 14+ WG the increase in SCN8A expression is

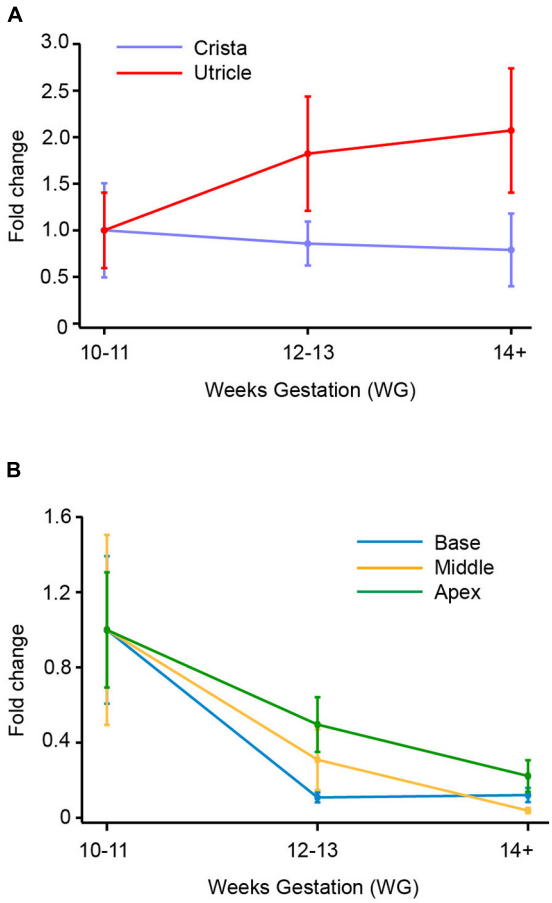

FIGURE 4 | SCN10A (Nav1.8) mRNA in vestibular organs and cochlea. **(A)** In crista there was a decrease in expression of SCN10A between 10–11 WG and 14+ WG. At 14 WG, SCN10A expression was 0.8-fold less than that observed at 10–11 WG. In contrast, in the utricle, SCN10A expression steadily increased to peak at 14+ WG where expression was twofold greater than the youngest age. **(B)** In the base, middle, and apex of the cochlea there was a consistent decrease in expression of SCN10A between 10–11 WG and 14+ WG. SCN10A expression was lowest at 14+ WG within the cochlea, decreasing to 0.003-fold in the middle region of the cochlea.

1.8-fold greater than that at 10–11 WG, but relative expression between these two ages was not statistically significantly different. There were no changes in SCN8A expression in the middle turn or apex of the cochlea with age. The apex showed a similar aged-related pattern of expression as observed in the base, but the magnitude of the fold changes was not as great and not significant.

At 12–13 WG, the relative expression of SCN8A in the apex was significantly greater than relative expression in both the base and middle regions of the cochlea, in both instances this represents a large effect size (see **Table 4**). Relative expression of SCN8A was greater in the base, middle, and apex of the cochlea compared to the cristae ampullares at the ages investigated (see **Supplementary Tables 1–3**). In contrast to the crista, the relative expression of SCN8A was greater in the utricle compared to the middle of the cochlea at 10–11 WG and 14+ WG (see **Supplementary Table 4**) and the apex of the cochlea at 12–13 WG and 14+ WG (see **Supplementary Table 5**).

TABLE 2 | Relative expression of SCN5A in base of cochlea compared to other inner ear regions at 14+ WG.

Region	*N*	Median	*U*	Significance
Base	8	15.8×10^{-2}		
Utricle	12	1.5×10^{-2}	21	0.037*
Crista	9	1.8×10^{-2}	15	0.043*
Middle	9	0.85×10^{-2}	14	0.034*
Apex	8	0.45×10^{-2}	11	0.028*

*$p < 0.05$.

SCN9A (Nav1.7) mRNA Expression

In the utricle and crista, there are no significant differences in expression of SCN9A expression with gestational age (**Figure 3A**). There was in the utricle, however, a strong trend toward increased expression of SCN9A between 10–11 WG and 14+ WG (i.e., 3.4-fold increase), but this was not significant. There are significant differences in the relative expression of SCN9A between the two vestibular regions (see **Table 3**). There were greater levels of expression in the utricle compared to the crista at all three age groups as evidenced by large effect sizes.

SCN9A fold changes in the cochlea are shown in **Figure 3B**. There were no significant differences in SCN9A expression in the base with age. In the middle region of the cochlea, there is a 3.5-fold increase in SCN9A expression between 10–11 WG and 12–13 WG, but this was not statistically significant. Between 12–13 WG (median = 5.8×10^{-2}, $n = 9$) and 14+ WG (median = 0.4×10^{-2}, $n = 9$) there is a significant decrease in SCN9A expression ($U = 11$, $p = 0.009$) with a large effect size ($\eta^2 = 0.38$). In the apex there was a consistent decrease in the expression of SCN9A with age. SCN9A expression at 10–11 WG (median = 17.3×10^{-3}, $n = 9$) is significantly higher than at 14+ WG (median = 5.0×10^{-3}, $n = 8$; $U = 14$, $p = 0.034$).

At the two younger age groups, 10–11 WG and 12–13 WG, the cristae ampullares and base of the cochlea had significantly lower relative expression of SCN9A compared to the utricle, middle, and apex of the cochlea.

SCN10A (Nav1.8) mRNA Expression

There were no significant differences in SCN10A expression with age in either the crista or utricle. The utricle did show a twofold increase in the expression of SCN10A between 10–11 WG and 14+ WG (**Figure 4A**), but this was not statistically significant. In contrast, the crista showed a 0.8-fold decrease in the expression of SCN10A by 14+ WG (**Figure 4A**). SCN10A expression was significantly higher in the utricle compared to the crista at each age group (see **Table 3**).

In the cochlea, SCN10A expression declined between 10–11 WG and 14+ WG in base, middle, and apex (**Figure 4B**). However, these decreases in SCN10A expression with age in each region of the cochlea were not statistically significant.

The relative expression of SCN10A was significantly greater in the base, middle, and apex of the cochlea compared to the

TABLE 3 | Relative expression of SCN8A, SCN9A, and SCN10A in utricle compared to cristae ampullares during fetal development.

	Age	Utricle		Crista		*U*	Significance	η^2
		Median	*N*	Median	*N*			
SCN8A	10–11 WG	2.4×10^{-2}	8	4.0×10^{-4}	11	0	$p < 0.001$**	0.69
	12–13 WG	3.8×10^{-2}	11	6.3×10^{-4}	8	7	$p = 0.002$**	0.49
	14+ WG	8.9×10^{-2}	11	1.4×10^{-3}	9	0	$p < 0.001$**	0.70
SCN9A	10–11 WG	10.2×10^{-3}	7	1.2×10^{-3}	9	6	$p = 0.007$**	0.45
	12–13 WG	21.0×10^{-3}	9	1.4×10^{-3}	8	2	$p = 0.001$**	0.63
	14+ WG	13.3×10^{-3}	9	1.8×10^{-3}	8	0	$p = 0.001$*	0.71
SCN10A	10–11 WG	17.4×10^{-4}	6	1.7×10^{-4}	4	2	$p = 0.03$*	0.45
	12–13 WG	24.5×10^{-4}	8	1.3×10^{-4}	6	4	$p = 0.01$**	0.48
	14+ WG	38.4×10^{-4}	8	0.4×10^{-4}	7	0	$p = 0.001$**	0.70

*$p < 0.05$.
**$p < 0.01$.

crista during development (see **Supplementary Tables 6–8**). There were no significant differences in the relative expression of SCN10A between the utricle and regions of the cochlea. Similarly, there were no differences in relative expression of SCN10A between cochlea regions at any age.

Electrophysiological Recordings

Electrophysiological data were collected from a total of 73 donor samples ranging in age from 10 WG to 16 WG.

Na^+ Currents

All recordings were made using a KCl/gluconate based internal solution. From a total of 181 hair cell recordings, ∼30% ($n = 57$) exhibited presumptive Na^+ currents. Close inspection showed 40 cells were suitable for detailed analysis (17 were removed because of series resistance changes). All cells selected for analysis exhibited whole-cell currents that were consistent with type II vestibular hair cells. The characteristic whole-cell current associated with type I vestibular hair cells, $I_{k,l}$, was not present in any recorded cells at any age. Sodium current peak amplitude varied markedly (−42.5 to −747.6 pA) across the three age groups. **Figure 5A** compares mean Na^+ current amplitude for the three age groups. Mean peak current was similar in the three age groups (10–11 WG = 310.6 ± 69.2 pA, 12–13 WG = 266.8 ± 42.4 pA, and 14+ WG = 326.0 ± 122.7 pA).

TABLE 4 | Relative expression of SCN8A in apex compared to base and middle of cochlea at 12–13 WG.

Apex		Middle		*U*	Significance	η^2
Median	*N*	Median	*N*			
19.3×10^{-3}	10	6.7×10^{-3}	8	13	$p = 0.016$*	0.32
		Base				
		Median	*N*	*U*	Significance	η^2
		9.6×10^{-3}	8	10	$p = 0.008$**	0.39

*$p < 0.05$.
**$p < 0.01$.

Na^+ currents were present in 38% of all hair cells recorded at 10–11 WG and 37% of hair cells aged 12–13 WG. However, in the 14+ WG age group, only three hair cells possessed Na^+ currents, constituting 11% of all total cells recorded at this age group. Activation and inactivation curves for the three age groups is shown in **Figure 5B**.

Previous studies have shown two types of Na^+ current in developing vestibular hair cells, with different inactivation kinetics ($V_{1/2}$) (Wooltorton et al., 2007). For inactivation, cells were held at various potentials then stepped to −30 mV (**Figure 5C** inset **). Na^+ currents are classified as Na_1 or Na_2 when their $V_{1/2}$ inactivation, is more negative than −81 mV or more positive than −81 mV, respectively. Based on this classification, the $V_{1/2}$ inactivation, G_{max}, and current slope of Na^+ currents were obtained during inactivation (**Figure 5C** inset **). Values for the three age groups are shown in **Table 5**. We only provide statistics for the 12–13 WG age group as the number of hair cells in other age groups exhibiting Na^+ currents were too small. For this age group, $V_{1/2}$ inactivation for cells classified as Na_1 (median = 89.7 mV, $n = 9$) was significantly more negative than those classified as Na_2 (median = 74.5, $n = 19$, $U = 0$, $p < 0.001$). The G_{max} and slope values for inactivation were not different. Given the difficulty of obtaining a sufficient number of human fetal hair cells at each age group that possessed Na^+ currents, we could not further analyze data according to $V_{1/2}$ inactivation.

The sensitivity to TTX varies depending on Na^+ channel type/expression in different tissues (Zimmer, 2010; Marler et al., 2018; de Oliveira et al., 2019) and this variability in TTX sensitivity is also evident in vestibular hair cells (Wooltorton et al., 2007). Accordingly, in a subset of recordings ($n = 17$), we assessed the sensitivity of Na^+ currents to TTX (1 μM). Our data shows that TTX blocked Na^+ currents in each age group. Peak Na^+ current amplitude, half maximal activation ($V_{1/2}$), and slope for Na^+ channel activation, at each age group before and after the application of TTX is shown in **Table 6**. TTX (1 μM) blocked 60% and 56% of the Na^+ current, at 10–11 WG ($n = 6$) and 12–13 WG ($n = 10$), respectively. Only one cell was tested in the older group. **Figure 5C** shows an inward current with a peak current of ∼ −700 pA in control solution. This inward current was partially

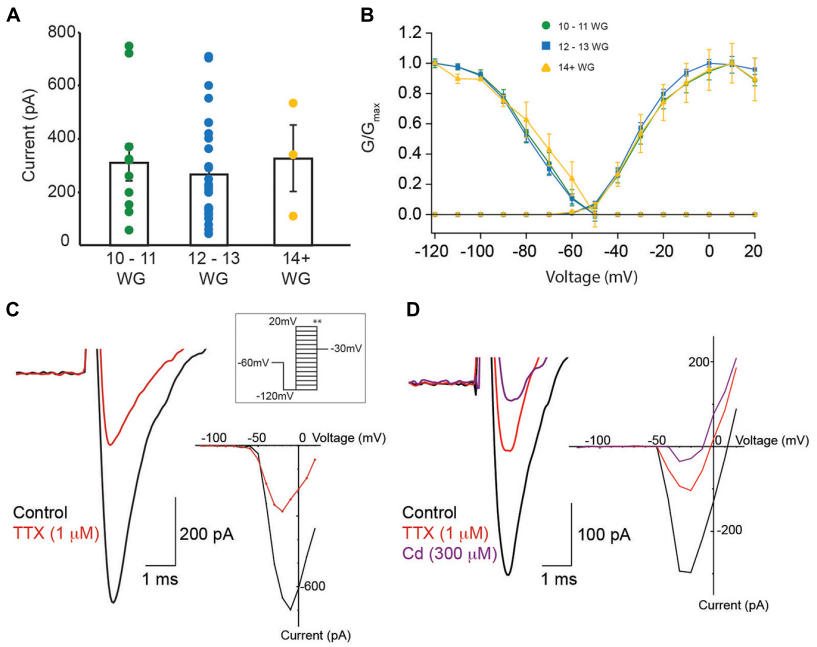

FIGURE 5 | Na^+ currents in fetal vestibular hair cells. **(A)** The mean Na^+ current amplitude recorded from vestibular hair cells in three age groups, 10–11 WG, 12–13 WG, and 14+ WG. Scatter of individual Na^+ current amplitudes for each cell in each age group is shown. **(B)** Activation and inactivation plots for Na^+ currents for three age groups. **(C)** Left panel: a representative example of a Na^+ current from hair cell aged 12 WG in control L15 media (black trace) and in the presence of TTX (1 μM; red trace). **(C)** Right panel: the I–V plot for the cell shown in **(C)** *left panel* in control solution (black trace) and in 1 μM TTX (red trace). **(D)** Left panel: a representative example of a Na^+ current from cristae hair cell aged 11 WG in control L15 media (black trace), in the presence of TTX (1 μM; red trace), and in the presence of both TTX and cadmium (300 μM; purple trace). The Na^+ current was evoked by stepping from −120 to −20 mV. **(D)** Right panel: the I–V plot for the cell shown in **(D)** *left panel* in control solution (black trace), 1 μM TTX (red trace), and 300 μM cadmium (purple trace). **(A,B)** Mean and SEM are shown.

TABLE 5 | $V_{1/2}$ inactivation, G_{max}, and slope values for Na^+ currents in response to inactivation protocol.

	$V_{1/2inact}$ (mV)		G_{max}		Slope	
	Na_1	Na_2	Na_1	Na_2	Na_1	Na_2
10–11 WG	−86.4 ± 4.0 (2)	−73.3 ± 1.7 (9)	4.9 ± 2.0 (2)	4.4 ± 0.8 (9)	6.0 ± 0.5 (2)	7.7 ± 0.4 (9)
12–13 WG	−89.7 ± 2.5 (9)	−74.5 ± 1.0 (19)	4.9 ± 0.8 (9)	3.5 ± 0.6 (19)	6.9 ± 0.7 (9)	7.8 ± 0.4 (19)
14+ WG	−85.0 ± 0 (1)	−72.4 ± 2.1 (2)	1.8 (1)	6.9 ± 2.1 (2)	7.6 (1)	9.5 ± 0.5 (2)

Number of cells in each age group is shown in brackets ().

TABLE 6 | Peak Na^+ current amplitude, $V_{1/2}$, and slope for each age group, before and after, the addition of TTX (1 μM).

Age	*n*	Peak amplitude (pA)		$V_{1/2}$ (mV)		Slope	
		Control	TTX	Control	TTX	Control	TTX
10–11 WG	6	−336.3 ± 85.6	−133.2 ± 37.3	−40.5 ± 2.1	−48.1 ± 3.3	4.8 ± 0.4	4.4 ± 0.8
12–13 WG	10	−341.5 ± 7.3	−191.3 ± 51.7	−38.7 ± 0.8	−50.5 ± 2.8	5.0 ± 0.5	5.0 ± 0.7
14+ WG	1	−531.6	−128.1	−42.9	−75.5	4.3	14.5

blocked by the Na^+ channel antagonist TTX (1 μM) in a hair cell aged 12–13 WG (red trace, **Figure 5C**).

Interestingly, in the two younger age groups, 1 μM TTX did not completely block Na^+ currents, suggesting a component of the inward current in human fetal hair cells is TTX resistant. This somewhat matches a previous report describing TTX resistant Na^+ currents in vestibular hair cells, albeit using a lower TTX concentration (500 nM versus 1 μM) (Wooltorton et al., 2007). In our study, while 1 μM TTX was found to block a significant proportion of the inward Na^+ current, there remains a considerable component of the inward current in human fetal hair cells that is TTX resistant. It is possible that in response to depolarization, the residual inward current that remains after TTX exposure is due to Ca^{2+} influx. To test this, we applied the Ca^{2+} channel blocker cadmium (**Figure 5D**). Cadmium (300 μM) partly blocked the inward current, suggesting some

fraction of the inward current in human fetal hair cells may be due to Ca^{2+} influx. However, in some instances, cadmium has also been shown to block a component of Na^+ currents (Wooltorton et al., 2007). The cadmium-sensitive component accounts for approximately 31% of the total inward current ($n = 4$ cells). Consequently, our results suggest the inward current has three components: TTX-sensitive, TTX-insensitive, and a Ca^{2+} channel component.

DISCUSSION

Here we targeted four different Na^+ channel genes, SCN5A, SCN8A, SCN9A, and SCN10A corresponding to Nav1.5, Nav1.6, Nav1.7, and Nav1.8 channels, respectively, which are either TTX sensitive (Nav1.6 and Nav1.7) or TTX insensitive and TTX resistant (Nav1.5 and Nav 1.8, respectively). This is the first time that each of the four genes investigated have been shown to be expressed in human fetal auditory and vestibular neuroepithelium. Due to the difficulty of isolating sufficient tissue for qPCR analysis, across all age fetal groups, Na^+ channel gene expression was measured from cochlea and vestibular neuroepithelium, that contained a combination of hair cells, afferent, and efferent terminals, and stromal cells. There is a diversity of Na^+ channel gene expression throughout the body, Nav 1.5 is mainly expressed in cardiac myocytes, while Nav 1.6 expression is primarily in the central nervous system. Nav1.7 and Nav1.8 expression is found in the peripheral nervous system, specifically in dorsal root ganglion neurons and are thought to have a role in nocioception (Tan et al., 2014; Hameed, 2019). The genes investigated in this study were selected based on previous studies which showed expression in both auditory and vestibular systems in other species (Chabbert et al., 1997; Wooltorton et al., 2007; Liu et al., 2016; Zhou et al., 2020).

In all rodents studied to date, there is an initial embryonic and early postnatal developmental expression of Na^+ channels in hair cells of the vestibular and cochlea neuroepithelium, which declines postnatally (Marcotti et al., 2003; Geleoc et al., 2004; Wooltorton et al., 2007; Meredith and Rennie, 2020). The initial developmental expression was thought to be important for recruiting appropriate afferent connections during development. In the cochlea, IHCs express Na^+ channels and also spontaneously discharge action potentials, where Na^+ channel activation is believed to play a role in modulating action potential frequency (Marcotti et al., 2003). In contrast, mouse and rat vestibular hair cells do not spontaneously discharge (Geleoc et al., 2004), and rat utricular hair cells often required a brief hyperpolarization followed by a depolarizing pulse before they fire a single action potential (Wooltorton et al., 2007).

Tetrodotoxin-Sensitive Na^+ Channel Expression in Vestibular Neuroepithelium

In rats, genes for six TTX-sensitive Na^+ channels (Nav1.1, Nav1.2, Nav1.3, Nav 1.4, Nav1.6, and Nav1.7) were reported in utricular epithelium at PND 1 (Mechaly et al., 2005; Wooltorton et al., 2007; Liu et al., 2016). Indeed, there is considerable cell-to-cell variability in the expression of Na^+ channel subtypes in rat utricular hair cells aged postnatal days 1–2 (Chabbert et al., 2003). However, by PND 21 expression of Nav1.3 and Nav1.4 was absent in rat utricle (Wooltorton et al., 2007). Electrophysiological and anatomical data suggest that Na^+ channel activity in rat utricular hair cells is confined to the first postnatal week of development (Chabbert et al., 2003), but there is evidence for Na^+ currents in hair cells of the rat crista until 3 weeks and 35 days in gerbil (Li et al., 2010). Within the first week, single cell RT-PCR from rat utricular hair cells report the expression of Nav1.2, Nav1.3, with Nav1.6 having the most prominent Na^+ channel expression (Chabbert et al., 2003). Immunolabelling studies show Nav1.6 localized to afferent fibers (Lysakowski et al., 2011) and physiological studies show Nav1.6 is present in mature calyx afferent terminals rather than immature terminals (Meredith and Rennie, 2018). In particular, Nav1.6 is more highly expressed in peripheral zone calyces that are responsible for high firing rates and regular discharge (Meredith and Rennie, 2020). In human fetal epithelium, our qPCR data shows a 3.7 and 1.7-fold-increase in SCN8A (Nav1.6) expression in utricle and crista, respectively, between 10–11 WG and 14+ WG (see **Figure 2**). Expression of another TTX-sensitive subunit gene, SCN9A (Nav1.7) also showed a threefold increase in expression between 10–11 WG and 14+ WG, but only in the utricle (**Figure 3**). Functionally, at both the younger ages of development investigated (10–11 WG and 12–13 WG), hair cells with Na^+ currents have a significant proportion that is blocked by the application of TTX (1 μM). This supports the notion that the TTX sensitive component is due to either Nav1.6 or Nav1.7 channels expressed in human fetal vestibular hair cells.

Tetrodotoxin-Insensitive/Resistant Na^+ Channel Expression in Vestibular Neuroepithelium

Embryonic mouse utricular hair cells possess TTX-resistant Na^+ currents, that peak at embryonic day 16 and are absent at birth (Geleoc et al., 2004). Likewise in rat, TTX-resistant Nav1.8/Nav1.9 channels are absent from utricle at PND 1 (Mechaly et al., 2005; Wooltorton et al., 2007). The gene for the TTX-insensitive channel, Nav1.5 is expressed at PND 1 and PND 21 in utricle (Wooltorton et al., 2007). Nav1.5 has been shown to be localized to the inner face of calyceal terminals, particularly in the striola and may have a role establishing zonal differences in discharge regularity (Lysakowski et al., 2011). Our qPCR data suggest the presence of both TTX-insensitive, Nav1.5 and TTX-resistant, Nav1.8, Na^+ channel subtypes within the vestibular neuroepithelium during human fetal development. Electrophysiological recordings show the persistence of Na^+ channel activation in hair cells in the presence of TTX. At 10–11 WG and 12–13 WG, approximately 40% of the inward current remained in the presence of 1 μM TTX, a concentration that blocks TTX-sensitive Na^+ subunits (typically blocked by 50 nM TTX) and the TTX-insensitive subunit, Nav1.5 (typically blocked by 500 nM TTX). Although we did not attempt to further pharmacologically dissect the contribution of Nav1.5 subunits to the Na^+ current, our qPCR data suggests an increased contribution of Nav1.5 to the TTX-insensitive component of the Na^+ current. We showed a 3.1-fold-change increase in expression of SCN5A in crista between 10–11 WG and 14+ WG (see

Figure 1). TTX-resistant Na^+ currents have also been recorded in mammalian vestibular hair cells (Rüsch and Eatock, 1997; Geleoc et al., 2004). In immature gerbil calyceal afferent terminals and vestibular hair cells, the application of 1 μM TTX reveals both TTX-sensitive and TTX-resistant Na^+ currents, with the TTX-resistant component likely due to expression of Nav 1.8 channels (Meredith and Rennie, 2018). Similarly, in human fetal vestibular hair cells the remaining TTX-resistant component is likely due to expression of Nav1.8. However, our qPCR data shows an increase in SCN10A (Nav1.8) expression in the utricle during fetal development but a concomitant decrease in SCN10A expression in the crista during the same period. One reason for the discrepancy in SCN10A expression with age, between utricle and crista may be that our utricular dissections inadvertently included nearby vestibular ganglion neurons, which have been shown to express Nav1.8 subunits (Liu et al., 2016).

Na^+ Channel Characteristics in Vestibular Epithelium

Na^+ channel activation and inactivation parameters have been measured in rat, mouse, and gerbil vestibular periphery (Geleoc et al., 2004; Wooltorton et al., 2007; Liu et al., 2016; Meredith and Rennie, 2018). To compare G_{max}, $V_{1/2}$ and slope for the Na^+ current inactivation to previous studies, we classified cells according to $V_{1/2}$ inactivation; $Na_1 < 81$ mV and $Na_2 \geq 81$ mV (Wooltorton et al., 2007). The $V_{1/2}$ inactivation of human fetal hair cells at 12–13 WG classified as Na_2 (~ -73 mV) was similar to that obtained in immature rat hair cells (~ -74 mV), while human fetal hair cells classified as Na_1 (~ -86 mV) had slightly more positive $V_{1/2}$ inactivation than previously reported in mouse (−88 mV; Geleoc et al., 2004), rat (−92 mV; Wooltorton et al., 2007), and gerbil hair cells (−90 mV; Li et al., 2010), but more negative than another study in rat (−80 mV; Chabbert et al., 2003). In rat, Na_1 was TTX-insensitive and expressed by all type I hair cells (Wooltorton et al., 2007). Our data suggest that Na^+ currents in developing human vestibular hair cells are comparable to those in immature rat at early stages of development and hair cells with Na_1 may even be an early indicator of a type I hair cell. The presence of Na^+ currents in hair cells, at least from 10 WG, also indicates that these currents have a significant role during development. Na^+ channel associated action potentials are thought to be responsible for release of brain derived neurotrophic factor (BDNF) in rat utricle at P0 (Chabbert et al., 2003). BDNF is proposed to have a role in establishing appropriate afferent neural connections and synaptogenesis.

Previous studies have shown a down regulation of Na^+ currents with postnatal age (Chabbert et al., 2003; Geleoc et al., 2004; Wooltorton et al., 2007; Li et al., 2010). In human fetal neuroepithelium, the incidence of hair cells with Na^+ currents decrease with age: from 38% of all recorded cells at 10 −11 WG to 11% of all recorded hair cells at 14+ WG. This suggests there is a similar decline in Na^+ channel expression in human hair cells, *in utero*. It has been suggested that cell specific Na^+ currents may have a function in establishing appropriate afferent connections for either bouton terminal or simple or complex calyces (Wooltorton et al., 2007). This would mean, by 14+ WG, the role of Na^+ currents in vestibular hair cell development is nearing an end. This notion is supported by our recordings of the first indisputable electrophysiological activity from human calyceal terminals at 14 WG (Lim et al., 2014). By this time in development, calyces had formed and presumably made appropriate connections. For technical reasons, we were unable to record from developing human calyceal terminals prior to 14 WG and therefore could not confirm the presence of Na^+ channel expression as they developed their connections. Our molecular data, however, suggest there are increases in several Na^+ channel genes throughout the time period examined, which is consistent with a continuing role in Na^+ channel expression in afferent terminals and fibers.

Na^+ Channel Expression in Cochlea Neuroepithelium

In immature mice (P3–P7) genes for six TTX-sensitive Na^+ channels were detected with different abundance in inner and OHCs, Nav1.1, Nav1.2, Nav1.3, Nav1.4, Nav1.6, and Nav1.7, while genes for TTX-insensitive Na^+ channels, Nav1.5, Nav1.8, and Nav1.9 were also detected but with much lower relative expression (Zhou et al., 2020). In human fetal cochlea neuroepithelium, we detected expression of genes for Nav1.5, Nav1.6, Nav1.7, and Nav1.8 from 10 WG through to 14+ WG. Additional experiments are required to determine of other subunits are also conserved in human cochlea and to establish the cell expression of these genes.

Tetrodotoxin-Sensitive Na^+ Channel Genes SCN8A and SCN9A in the Cochlea

For the TTX-sensitive channel Na^+ gene SCN8A (Nav1.6), there is a general trend toward fold-change increases in each region of the cochlea between 10–11 WG and 14+ WG, but particularly between 12–13 WG and 14+ WG at the base of the cochlea. In addition to these fold-change increases relative to the 10–11 WG age group, our data also shows a greater relative expression of SCN8A in the apex of the cochlea compared to the base and middle regions at 12–13 WG. Similarly, microarray analysis of various ion channel genes in mice describes greater expression of SCN8A in the apex of the cochlea than the middle and base regions (Yoshimura et al., 2014). It should be noted that there is greater relative expression of SCN8A in base, middle, and apex of the cochlea compared to the crista, but there is similar relative expression to the utricle.

Expression of the other TTX-sensitive gene, SCN9A (Nav1.7) in human fetal cochlea shows a downward trend between 10–11 WG and 14+ WG in the apex of the cochlea, while at the base of the cochlea, the trend is reversed and there is an increased expression with age. At the two younger age groups, SCN9A relative expression in the base is significantly less than the middle and apex of the cochlea. In the middle region of the cochlea there is a peak in SCN9A expression at 12–13 WG, followed by a decline in relative expression. Taken together, this expression pattern suggests an apex-to-base tonotopic gradient of expression. Relative expression of SCN9A may have already peaked in the apex resulting in a consistent decrease with age,

while the middle region peaks at 12–13 WG, followed by a decrease in relative expression. During the same time period, SCN9A relative expression in the base increases with age. This would contrast with the base-to-apex tonotopic differentiation that occurs in human cochlea hair cells (Pujol and Lavigne-Rebillard, 1985; Locher et al., 2013). IHCs at the base of the cochlea first differentiate from 12 WG and differentiation continues along the tonotopic access toward the middle and apex by 14 WG, while three rows of OHCs have differentiated at the base at 14 WG (Locher et al., 2013).

However, a tonotopic gradient of expression for at least one other ion channel (Cav1.3) and calcium binding proteins show a similar apex-to-base expression (reviewed in Mann and Kelley, 2011). To our knowledge there are no studies describing the tonotopic gradient for Na^+ channel genes in any mammal.

Our data in human fetal cochlea are similar to results in developing mouse cochlea, which found SCN9A to have the highest expression of all Na^+ channels genes (Zhou et al., 2020). Tonotopy of SCN9A expression was evident between mouse IHCs and OHCs, with greater SCN9A relative expression in IHCs in the apex of the cochlea compared to the base, while in OHCs, the reverse was true, with greater SCN9A relative expression in the base (Zhou et al., 2020). In this study we were not able to make comparisons between the two cochlear hair cell types.

Electrophysiological studies in the cochlea suggest the vast majority of Na^+ currents in IHCs and OHCs are TTX-sensitive (Marcotti et al., 2003; Zhou et al., 2020). In mice, the most predominant Na^+ channel gene encoded is Nav1.7, a TTX-sensitive channel (Zhou et al., 2020). Interestingly, the sensitivity to TTX differed significantly between the two hair cell types. Na^+ currents in IHCs were blocked by 1 μM TTX, while OHCs required 10 μM TTX (Zhou et al., 2020). Another study, also in mice reports the K_d for TTX in IHC Na^+ currents was 4.8 nM, suggesting Nav1.7 as the predominant Na^+ channel in IHCs (Marcotti et al., 2003). Our data support the presence of both SCN8A and SCN9A Na^+ channel genes (Nav1.6 and Nav1.7 channels, respectively) in developing human cochlea neuroepithelium. Future electrophysiological studies will be needed to: determine whether human fetal IHCs and OHCs also have differing TTX sensitivity and to establish which Na^+ channel gene predominates in each hair cell type.

Tetrodotoxin-Insensitive Na^+ Channel Genes SCN5A and SCN10A in the Cochlea

Compared to TTX-sensitive SCN genes, there is a consistent decline in the TTX-insensitive/resistant Na^+ channel genes SCN5A (Nav1.5) and SCN10A (Nav1.8) in cochlea neuroepithelium during human fetal development, with the exception of a peak 2.8-fold-change increase in relative expression of Nav1.5 in the base of the cochlea at 14+ WG compared to 10–11 WG.

In mouse cochlea epithelia, the expression of SCN5A was greater in the apex compared to the base during early postnatal development (Zhou et al., 2020). In contrast to these mouse data, in fetal cochlea neuroepithelium, there were no differences in SCN5A expression levels between cochlea regions, until 14+ WG. At this stage, relative expression in the base was significantly greater than that recorded in middle or apex of the cochlea. It is possible that these are species differences or alternatively, it could be due to the different developmental plan and timeline. With the exception of Zhou et al. (2020), these TTX-insensitive/resistant Na^+ channel genes have not been investigated in the cochlea – due in part to their low expression levels (Fryatt et al., 2009). Our results, however, show that these two Na^+ channel genes are expressed in the cochlea epithelium during human fetal development, albeit briefly. The relative expression of SCN5A at 14+ WG is significantly higher in the cochlea base, than all other inner ear regions including the utricle and crista. Similarly, the relative expression of SCN10A is greater in all cochlea regions compared to the crista at 12–13 WG and 14+ WG. It is possible that the transient expression of SCN5A and SCN10A is necessary for establishing appropriate neural connections in specific cell types or may have a tonotopic gradient profile that was not evident during the timeframe investigated. Alternately, these genes may have a more important role during human development than in other species.

CONCLUSION

The expression of Na^+ channels in hair cells of the developing human inner ear is transient, but coincides with a critical period when afferent connections and synapses are being formed. This study has identified different patterns of expression of four Na^+ channel genes in vestibular and cochlear neuroepithelium during human fetal development and has characterized Na^+ currents in human vestibular hair cells. We show significant differences in gene expression with age and between different inner ear regions. In particular, our data in human fetal inner ear shows there is likely a greater role for TTX-sensitive Nav1.6 (SCN8A) Na^+ channels in vestibular neuroepithelium, while Nav1.7 (SCN9A) has a greater contribution in cochlea neuroepithelium. Our data also suggest there are tonotopy-related differences in the expression of Nav1.7 in the cochlea. In contrast, regional differences in gene expression in vestibular organs such as, *central* versus *peripheral* in the crista and *striola* versus *extrastriola* in the utricle were not investigated due to technical limitations of differentiating between these regions in developing neuroepithelium. This was made more difficult because patterns of "mature" markers of these regions (e.g., calbindin and calretinin) are not yet established.

Another noted difference in Na^+ channel gene expression between vestibular and cochlear neuroepithelium was the presence of TTX-insensitive Na^+ channel genes, SCN5A and SCN10A. Results suggest SCN5A and SCN10 contribute to a proportion of the Na^+ current in developing vestibular hair cells. In contrast, in developing human cochlea there is predominately a down-regulation of SCN5A and SCN10A with age. In other species, there is little evidence for either of these two genes in cochlea development.

There is a transient expression of Na^+ channels in hair cells of the inner ear of several mammalian species (Chabbert et al., 2003;

Marcotti et al., 2003; Geleoc et al., 2004; Wooltorton et al., 2007). Our results suggest Na^+ channel expression in human fetal vestibular and cochlea neuroepithelia are consistent with those from other species. The brief expression of Na^+ channels in hair cells may have a similar purported role in establishing appropriate afferent contacts and synapse formation. Therefore, these two processes are critical during development to establish normal function. The onset and continued expression of Na^+ channels in afferent terminals and fibers are essential for the transmission of auditory and vestibular information. During human fetal development, vestibular and auditory reflexes which are indicative of functional afferent activity have been recorded at 19 WG and 24 WG, respectively (Humphrey, 1964; Lecanuet and Schaal, 1996).

Understanding the significant differences and commonalities in expression and timing between the vestibular and auditory systems in human tissue is essential if we are to incorporate appropriate and representative hair cells in human stem-cell derived inner ear organoids (Koehler et al., 2017; Jeong et al., 2018; Lahlou et al., 2018; Mattei et al., 2019). Our current understanding of the chronology of hair cell development and maturation arises primarily from studies in animals. Animal models, such as mice, have helped us understand basic principles, however, their compressed developmental timeline means the often, brief expression of some transcription factors means their functional significance is not always clear. Using human fetal vestibular and cochlear tissue to determine which genes are expressed, and when, and for how long, in each inner ear organ is needed to establish the precise timeline of gene expression and fundamental information for driving potential regenerative technologies that are optimized specifically for humans.

DATA AVAILABILITY STATEMENT

The raw data supporting the conclusions of this article will be made available by the authors, without undue reservation.

ETHICS STATEMENT

The studies involving tissue donation made by human participants were reviewed and approved by the University of Newcastle Human Research Ethics Committee. The patients/participants provided their written informed consent to participate in this study.

AUTHOR CONTRIBUTIONS

RQ, HD, EC, and RL completed the data collection and analysis. MT and BN provided manuscript feedback. RC, AB, and RL conceptualized the project and wrote the manuscript. All authors contributed to the article and approved the submitted version.

FUNDING

Funding for this research was provided by the Garnett Passe and Rodney Williams Memorial Foundation and National Health and Medical Research Council of Australia APP1048232.

ACKNOWLEDGMENTS

The authors would like to acknowledge clinic staff and donors for making this research possible. Thank you to D. W. Smith for discussions regarding analysis of gene expression data.

SUPPLEMENTARY MATERIAL

The Supplementary Material for this article can be found online at: https://www.frontiersin.org/articles/10.3389/fnins.2021.733291/full#supplementary-material

REFERENCES

Browne, L., Smith, K. E., and Jagger, D. J. (2017). Identification of Persistent and Resurgent Sodium Currents in Spiral Ganglion Neurons Cultured from the Mouse Cochlea. *eNeuro* 2017:4.

Brugeaud, A., Travo, C., Dememes, D., Lenoir, M., Llorens, J., Puel, J. L., et al. (2007). Control of hair cell excitability by vestibular primary sensory neurons. *J. Neurosci.* 27, 3503–3511. doi: 10.1523/jneurosci.5185-06.2007

Chabbert, C., Chambard, J. M., Valmier, J., Sans, A., and Desmadryl, G. (1997). Voltage-activated sodium currents in acutely isolated mouse vestibular ganglion neurones. *Neuroreport* 8, 1253–1256. doi: 10.1097/00001756-199703240-00039

Chabbert, C., Mechaly, I., Sieso, V., Giraud, P., Brugeaud, A., Lehouelleur, J., et al. (2003). Voltage-gated Na+ channel activation induces both action potentials in utricular hair cells and brain-derived neurotrophic factor release in the rat utricle during a restricted period of development. *J. Physiol.* 553, 113–123. doi: 10.1113/jphysiol.2003.043034

Cohen, J. (1988). *Statistical power analysis for the behavioral sciences*. Hillsdale, N.J.: Erlbaum Associates.

de Oliveira, R. B., Petiz, L. L., Lim, R., Lipski, J., Gravina, F. S., Brichta, A. M., et al. (2019). Crosstalk between mitochondria, calcium channels and actin cytoskeleton modulates noradrenergic activity of locus coeruleus neurons. *J. Neurochem.* 149, 471–487. doi: 10.1111/jnc.14692

Du, J., Simmons, S., Brunklaus, A., Adiconis, X., Hession, C. C., Fu, Z., et al. (2020). Differential excitatory vs inhibitory SCN expression at single cell level regulates brain sodium channel function in neurodevelopmental disorders. *Eur. J. Paediatr. Neurol.* 24, 129–133. doi: 10.1016/j.ejpn.2019.12.019

Eckrich, T., Varakina, K., Johnson, S. L., Franz, C., Singer, W., Kuhn, S., et al. (2012). Development and function of the voltage-gated sodium current in immature mammalian cochlear inner hair cells. *PLoS One* 7:e45732. doi: 10.1371/journal.pone.0045732

Frucht, C. S., Uduman, M., Kleinstein, S. H., Santos-Sacchi, J., and Navaratnam, D. S. (2011). Gene expression gradients along the tonotopic axis of the chicken auditory epithelium. *J. Assoc. Res. Otolaryngol.* 12, 423–435. doi: 10.1007/s10162-011-0259-2

Fryatt, A. G., Vial, C., Mulheran, M., Gunthorpe, M. J., and Grubb, B. D. (2009). Voltage-gated sodium channel expression in rat spiral ganglion neurons. *Mol. Cell Neurosci.* 42, 399–407. doi: 10.1016/j.mcn.2009.09.001

Geleoc, G. S., Risner, J. R., and Holt, J. R. (2004). Developmental acquisition of voltage-dependent conductances and sensory signaling in hair cells of the embryonic mouse inner ear. *J. Neurosci.* 24, 11148–11159. doi: 10.1523/jneurosci.2662-04.2004

Hameed, S. (2019). Nav1.7 and Nav1.8: Role in the pathophysiology of pain. *Mol. Pain* 15:1744806919858801.

Hern, W. M. (1984). Correlation of fetal age and measurements between 10 and 26 weeks of gestation. *Obstet. Gynecol.* 63, 26–32.

Hotchkiss, K., Harvey, M., Pacheco, M., and Sokolowski, B. (2005). Ion channel proteins in mouse and human vestibular tissue. *Otolaryngol. Head Neck Surg.* 132, 916–923. doi: 10.1016/j.otohns.2005.01.022

Humphrey, T. (1964). "Some correlations between the appearance of human fetal reflexes and the development of the nervous system," in *Growth and Maturation of the Brain*, ed. D. P. S. Schade (Amsterdam: Elsevier), 93–135. doi: 10.1016/s0079-6123(08)61273-x

Jeong, M., O'Reilly, M., Kirkwood, N. K., Al-Aama, J., Lako, M., Kros, C. J., et al. (2018). Generating inner ear organoids containing putative cochlear hair cells from human pluripotent stem cells. *Cell Death Dis.* 9, 922.

Kim, K. X., and Rutherford, M. A. (2016). Maturation of NaV and KV Channel Topographies in the Auditory Nerve Spike Initiator before and after Developmental Onset of Hearing Function. *J. Neurosci.* 36, 2111–2118. doi: 10.1523/jneurosci.3437-15.2016

Koehler, K. R., Nie, J., Longworth-Mills, E., Liu, X. P., Lee, J., Holt, J. R., et al. (2017). Generation of inner ear organoids containing functional hair cells from human pluripotent stem cells. *Nat. Biotechnol.* 35, 583–589. doi: 10.1038/nbt.3840

Lahlou, H., Nivet, E., Lopez-Juarez, A., Fontbonne, A., Assou, S., and Zine, A. (2018). Enriched Differentiation of Human Otic Sensory Progenitor Cells Derived From Induced Pluripotent Stem Cells. *Front. Mol. Neurosci.* 11:452.

Lecanuet, J. P., and Schaal, B. (1996). Fetal sensory competencies. *Eur. J. Obstet. Gynecol. Reprod. Biol.* 68, 1–23. doi: 10.1016/0301-2115(96)02509-2

Li, G. Q., Meredith, F. L., and Rennie, K. J. (2010). Development of K(+) and Na(+) conductances in rodent postnatal semicircular canal type I hair cells. *Am. J. Physiol. Regul. Integr. Comp. Physiol.* 298, R351–R358. doi: 10.1007/bf00197284

Lim, R., and Brichta, A. M. (2016). Anatomical and physiological development of the human inner ear. *Hear Res.* 338, 9–21. doi: 10.1016/j.heares.2016.02.004

Lim, R., Drury, H. R., Camp, A. J., Tadros, M. A., Callister, R. J., and Brichta, A. M. (2014). Preliminary characterization of voltage-activated whole-cell currents in developing human vestibular hair cells and calyx afferent terminals. *J. Assoc. Res. Otolaryngol.* 15, 755–766. doi: 10.1007/s10162-014-0471-y

Liu, X. P., Wooltorton, J. R., Gaboyard-Niay, S., Yang, F. C., Lysakowski, A., and Eatock, R. A. (2016). Sodium channel diversity in the vestibular ganglion: NaV1.5, NaV1.8, and tetrodotoxin-sensitive currents. *J. Neurophysiol.* 115, 2536–2555. doi: 10.1152/jn.00902.2015

Locher, H., Frijns, J. H., van Iperen, L., de Groot, J. C., Huisman, M. A., and Chuva de Sousa Lopes, S. M. (2013). Neurosensory development and cell fate determination in the human cochlea. *Neural. Dev.* 8:20.

Lysakowski, A., Gaboyard-Niay, S., Calin-Jageman, I., Chatlani, S., Price, S. D., and Eatock, R. A. (2011). Molecular microdomains in a sensory terminal, the vestibular calyx ending. *J. Neurosci.* 31, 10101–10114. doi: 10.1523/jneurosci.0521-11.2011

Mann, Z. F., and Kelley, M. W. (2011). Development of tonotopy in the auditory periphery. *Hear Res.* 276, 2–15. doi: 10.1016/j.heares.2011.01.011

Marcotti, W., Johnson, S. L., Rusch, A., and Kros, C. J. (2003). Sodium and calcium currents shape action potentials in immature mouse inner hair cells. *J. Physiol.* 552, 743–761. doi: 10.1113/jphysiol.2003.043612

Marler, T. L., Wright, A. B., Elmslie, K. L., Heier, A. K., Remily, E., Kim-Han, J. S., et al. (2018). NaV1.9 channels in muscle afferent neurons and axons. *J. Neurophysiol.* 120, 1032–1044. doi: 10.1152/jn.00573.2017

Mattei, C., Lim, R., Drury, H., Nasr, B., Li, Z., Tadros, M. A., et al. (2019). Generation of Vestibular Tissue-Like Organoids From Human Pluripotent Stem Cells Using the Rotary Cell Culture System. *Front. Cell Dev. Biol.* 7:25.

Mechaly, I., Scamps, F., Chabbert, C., Sans, A., and Valmier, J. (2005). Molecular diversity of voltage-gated sodium channel alpha subunits expressed in neuronal and non-neuronal excitable cells. *Neuroscience* 130, 389–396.

Meredith, F. L., and Rennie, K. J. (2018). Regional and Developmental Differences in Na(+) Currents in Vestibular Primary Afferent Neurons. *Front. Cell Neurosci.* 12:423.

Meredith, F. L., and Rennie, K. J. (2020). Persistent and resurgent Na(+) currents in vestibular calyx afferents. *J. Neurophysiol.* 124, 510–524. doi: 10.1152/jn.00124.2020

Oliver, D., Plinkert, P., Zenner, H. P., and Ruppersberg, J. P. (1997). Sodium current expression during postnatal development of rat outer hair cells. *Pflugers Arch.* 434, 772–778. doi: 10.1007/s004240050464

Poppi, L. A., Tabatabaee, H., Drury, H. R., Jobling, P., Callister, R. J., Migliaccio, A. A., et al. (2018). ACh-induced hyperpolarization and decreased resistance in mammalian type II vestibular hair cells. *J. Neurophysiol.* 119, 312–325. doi: 10.1152/jn.00030.2017

Pujol, R., and Lavigne-Rebillard, M. (1985). Early stages of innervation and sensory cell differentiation in the human fetal organ of Corti. *Acta Otolaryngol. Suppl.* 423, 43–50. doi: 10.3109/00016488509122911

Rüsch, A., and Eatock, R. A. A. (1996). delayed rectifier conductance in type I hair cells of the mouse utricle. *J. Neurophysiol.* 76, 995–1004. doi: 10.1152/jn.1996.76.2.995

Rüsch, A., and Eatock, R. A. (1997). "Sodium currents in hair cells of the mouse utricle," in *Diversity in Auditory Mechanics*, eds E. R. Lewis, G. R. Long, R. F. Lyon, C. R. Steele, P. M. Narins, and E. Hecht-Poinar (Singapore: World Scientific), 549–555.

Santos-Sacchi, J. (1993). Voltage-dependent ionic conductances of type I spiral ganglion cells from the guinea pig inner ear. *J. Neurosci.* 13, 3599–3611. doi: 10.1523/jneurosci.13-08-03599.1993

Schafer, T., and Schwarz, M. A. (2019). The Meaningfulness of Effect Sizes in Psychological Research: Differences Between Sub-Disciplines and the Impact of Potential Biases. *Front. Psychol.* 10:813.

Tadros, M. A., Farrell, K. E., Graham, B. A., Brichta, A. M., and Callister, R. J. (2015). Properties of sodium currents in neonatal and young adult mouse superficial dorsal horn neurons. *Mol. Pain* 11:17.

Tan, Z. Y., Piekarz, A. D., Priest, B. T., Knopp, K. L., Krajewski, J. L., McDermott, J. S., et al. (2014). Tetrodotoxin-resistant sodium channels in sensory neurons generate slow resurgent currents that are enhanced by inflammatory mediators. *J. Neurosci.* 34, 7190–7197. doi: 10.1523/jneurosci.5011-13.2014

Thun, J., Persson, A. K., and Fried, K. (2009). Differential expression of neuronal voltage-gated sodium channel mRNAs during the development of the rat trigeminal ganglion. *Brain Res.* 11-22:2009.

Wang, J., Ou, S. W., and Wang, Y. J. (2017). Distribution and function of voltage-gated sodium channels in the nervous system. *Channels* 11, 534–554. doi: 10.1080/19336950.2017.1380758

Wooltorton, J. R., Gaboyard, S., Hurley, K. M., Price, S. D., Garcia, J. L., Zhong, M., et al. (2007). Developmental changes in two voltage-dependent sodium currents in utricular hair cells. *J. Neurophysiol.* 97, 1684–1704. doi: 10.1152/jn.00649.2006

Xie, F., Xiao, P., Chen, D., Xu, L., and Zhang, B. (2012). miRDeepFinder: a miRNA analysis tool for deep sequencing of plant small RNAs. *Plant Mol. Biol.* 2012:3.

Yoshimura, H., Takumi, Y., Nishio, S. Y., Suzuki, N., Iwasa, Y., and Usami, S. (2014). Deafness gene expression patterns in the mouse cochlea found by microarray analysis. *PLoS One* 9:e92547. doi: 10.1371/journal.pone.0092547

Zhou, Y., Xia, C., Yin, M., Wang, X., Wu, H., and Ji, Y. (2020). Distribution and Functional Characteristics of Voltage-Gated Sodium Channels in Immature Cochlear Hair Cells. *Neurosci. Bull.* 36, 49–65. doi: 10.1007/s12264-019-00415-3

Zimmer, T. (2010). Effects of tetrodotoxin on the mammalian cardiovascular system. *Mar. Drugs* 8, 741–762. doi: 10.3390/md8030741

Zu, M., Guo, W. W., Cong, T., Ji, F., Zhang, S. L., Zhang, Y., et al. (2021). SCN11A gene deletion causes sensorineural hearing loss by impairing the ribbon synapses and auditory nerves. *BMC Neurosci.* 22:18.

Conflict of Interest: The authors declare that the research was conducted in the absence of any commercial or financial relationships that could be construed as a potential conflict of interest.

Publisher's Note: All claims expressed in this article are solely those of the authors and do not necessarily represent those of their affiliated organizations, or those of the publisher, the editors and the reviewers. Any product that may be evaluated in this article, or claim that may be made by its manufacturer, is not guaranteed or endorsed by the publisher.

frontiers in Neuroscience

ORIGINAL RESEARCH
published: 01 November 2021
doi: 10.3389/fnins.2021.750596

Implication of Vestibular Hair Cell Loss of Planar Polarity for the Canal and Otolith-Dependent Vestibulo-Ocular Reflexes in *Celsr1*$^{-/-}$ Mice

François Simon[1,2]*, *Fadel Tissir*[3,4], *Vincent Michel*[5], *Ghizlene Lahlou*[6,7], *Michael Deans*[8,9] *and Mathieu Beraneck*[1]*

[1] Université de Paris, INCC UMR 8002, CNRS, Paris, France, [2] Service d'ORL et de Chirurgie Cervico-Faciale Pédiatrique, AP-HP, Hôpital Necker-Enfants Malades, Paris, France, [3] Institut de Neuroscience, Université Catholique de Louvain, Brussels, Belgium, [4] College of Health and Life Sciences, Hamad Bin Khalifa University, Doha, Qatar, [5] Institut de l'Audition, Institut Pasteur, INSERM, Paris, France, [6] Institut de l'Audition/Institut Pasteur, Technologies et thérapie génique pour la surdité, Paris, France, [7] Service d'ORL et de Chirurgie Cervico-Faciale Pédiatrique, APHP, Sorbonne Université, Hôpital Pitié-Salpétrière, Paris, France, [8] Department of Neurobiology and Anatomy, University of Utah School of Medicine, Salt Lake City, UT, United States, [9] Division of Otolaryngology, Department of Surgery, University of Utah School of Medicine, Salt Lake City, UT, United States

OPEN ACCESS

Edited by:
Soroush G. Sadeghi, University at Buffalo, United States

Reviewed by:
Michael C. Schubert, Johns Hopkins University, United States
Kathleen Cullen, McGill University, Canada

***Correspondence:**
François Simon
f.simon@aphp.fr
Mathieu Beraneck
mathieu.beraneck@u-paris.fr

Specialty section:
This article was submitted to Perception Science, a section of the journal Frontiers in Neuroscience

Received: *30 July 2021*
Accepted: *04 October 2021*
Published: *01 November 2021*

Citation:
Simon F, Tissir F, Michel V, Lahlou G, Deans M and Beraneck M (2021) Implication of Vestibular Hair Cell Loss of Planar Polarity for the Canal and Otolith-Dependent Vestibulo-Ocular Reflexes in Celsr1$^{-/-}$ Mice. Front. Neurosci. 15:750596. doi: 10.3389/fnins.2021.750596

Introduction: Vestibular sensory hair cells are precisely orientated according to planar cell polarity (PCP) and are key to enable mechanic-electrical transduction and normal vestibular function. PCP is found on different scales in the vestibular organs, ranging from correct hair bundle orientation, coordination of hair cell orientation with neighboring hair cells, and orientation around the striola in otolithic organs. Celsr1 is a PCP protein and a Celsr1 KO mouse model showed hair cell disorganization in all vestibular organs, especially in the canalar ampullae. The objective of this work was to assess to what extent the different vestibulo-ocular reflexes were impaired in Celsr1 KO mice.

Methods: Vestibular function was analyzed using non-invasive video-oculography. Semicircular canal function was assessed during sinusoidal rotation and during angular velocity steps. Otolithic function (mainly utricular) was assessed during off-vertical axis rotation (OVAR) and during static and dynamic head tilts.

Results: The vestibulo-ocular reflex of 10 Celsr1 KO and 10 control littermates was analyzed. All KO mice presented with spontaneous nystagmus or gaze instability in dark. Canalar function was reduced almost by half in KO mice. Compared to control mice, KO mice had reduced angular VOR gain in all tested frequencies (0.2–1.5 Hz), and abnormal phase at 0.2 and 0.5 Hz. Concerning horizontal steps, KO mice had reduced responses. Otolithic function was reduced by about a third in KO mice. Static ocular-counter roll gain and OVAR bias were both significantly reduced. These results demonstrate that canal- and otolith-dependent vestibulo-ocular reflexes are impaired in KO mice.

Conclusion: The major ampullar disorganization led to an important reduction but not to a complete loss of angular coding capacities. Mildly disorganized otolithic hair cells were associated with a significant loss of otolith-dependent function. These results suggest that the highly organized polarization of otolithic hair cells is a critical factor for the accurate encoding of the head movement and that the loss of a small fraction of the otolithic hair cells in pathological conditions is likely to have major functional consequences. Altogether, these results shed light on how partial loss of vestibular information encoding, as often encountered in pathological situations, translates into functional deficits.

Keywords: vestibulo ocular reflex, planar cell polarity (PCP), vestibular system, CELSR1, mouse model, hair cell

INTRODUCTION

Sensory hair cells play a key role in the vestibular system as they enable the transduction of mechanical head movements into the electrical signals that will inform the brain about the head movements and position in 3D space. This is made possible by the organization and polarization of the stereociliary bundle, a group of actin-made stereocilia on the apical hair cell surface that are arranged in rows of increasing height leading up to a microtubule-based kinocilium (Barr-Gillespie, 2015). Mechanical movement may deflect the bundle toward the kinocilium, placing tension on the tip-links, a think link connecting the tip of each stereocilium to the side of its taller neighbor and opening mechanoelectrical transducers (MET) channels, thus depolarizing the hair cell and sending an excitatory signal to the vestibular neurons (Nam et al., 2019). Movement away from the kinocilium conversely closes MET and results in an inhibitory stimulus. Each hair cell therefore has a specific directional sensitivity that corresponds to its polarity axis (Shotwell et al., 1981). In both the semicircular canals (SCC) and otolithic organs, hair cells are arranged and coordinated according to their neighboring cells during vestibular morphogenesis (Yang et al., 2017). In the SCC, the stereociliary bundles are all orientated in the same direction parallel to the SCC axis and are thus all stimulated at the same time. In the utricular and saccular maculae, orientation of the hair cells cover 360° and are all organized in a mirror-like fashion around a cell boundary called Line of Polarity Reversal (LPR), which runs along the center of the macula in close proximity to the striolar region (Deans, 2013; Yang et al., 2017).

This complex organization, termed planar cell polarity (PCP), may be found on different scales: intra-cellular scale within the stereociliary bundle, inter-cellular scale where hair cell orientation depends on the orientation of neighboring hair cells, and in the otolithic organs on a macular scale, as each head movement combines an excitatory and inhibitory stimulus on either side of the LPR (Deans, 2013). PCP proteins are key in all vertebrate systems to enable cell communication and coordination between hair cells and supporting cells, as well as between supporting cells (Deans, 2013; Tissir and Goffinet, 2013; Hakanen et al., 2019), notably in the inner ear (Tarchini and Lu, 2019). In humans, the CELSR1 molecule (Cadherin EGF LAG Seven-pass G-type Receptor 1), a PCP protein, has been linked to neural tube defects and caudal agenesis (Allache et al., 2012; Robinson et al., 2012), although no specific vestibular function anomaly has been reported.

To better study the effect of the Ceslr1 molecule, *Celsr1*$^{-/-}$ mice have been developed introducing a frameshift that leads to a premature stop preventing translation of the cytoplasmic domain. Most *Celsr1* knocked-out (KO) mice are not viable due to neural tube defects: 20% die *in utero* and more than half of the remaining die before weaning (Ravni et al., 2009). Indeed, Celsr1 is a protein involved in PCP formation but is also linked to several severe defects in neurological development. Various *Celsr1* mouse mutants also present with severe neural tube defects ranging from craniorachischisis to loop-tails (Greene et al., 2009), behavioral impairment (Boucherie et al., 2018), alterations of skin hair pattern (Ravni et al., 2009), endothelial valve formation (Tatin et al., 2013), and oviduct development (Shi et al., 2014).

Concerning the labyrinth, auditory hair cell misorientation has been reported (Curtin et al., 2003). Those *Celsr1* KO mice that survive were not found to have any auditory impairment, which may be due to compensation by other *Celsr* genes in the KO that does not occur in other *Celsr1* mutant lines (Tissir and Goffinet, 2013; Duncan et al., 2017). The mice, however, presented with typical vestibular postural and locomotor disorders such as head bobbing, circling, and spinning when suspended by the tail (Curtin et al., 2003; Duncan et al., 2017). Although associated with vestibular malfunction, these postural impairments are largely non-specific and do not allow us to distinguish SCC- from otolith-based deficits (Beraneck et al., 2014). Hence, immunofluorescent imaging of the vestibular organs showed that in the absence of Celsr1, stereociliary bundles were misoriented relative to their neighbors, especially in the SCC (**Figure 1A**). On the other hand, the orientation at the level of the maculae was found to be only mildly affected (Duncan et al., 2017; **Figure 1B**). To which extent the functionality of vestibular-dependent reflexes relies on the precise orientation of the population of hair cells in the ampullae and maculae remains to our knowledge completely unexplored.

The objective of this study was therefore to precisely quantify in the *Celsr1* KO adult mice how the differential disorganization of the vestibular hair cells polarity affects the canalar- and otolithic-dependent vestibulo-ocular reflexes.

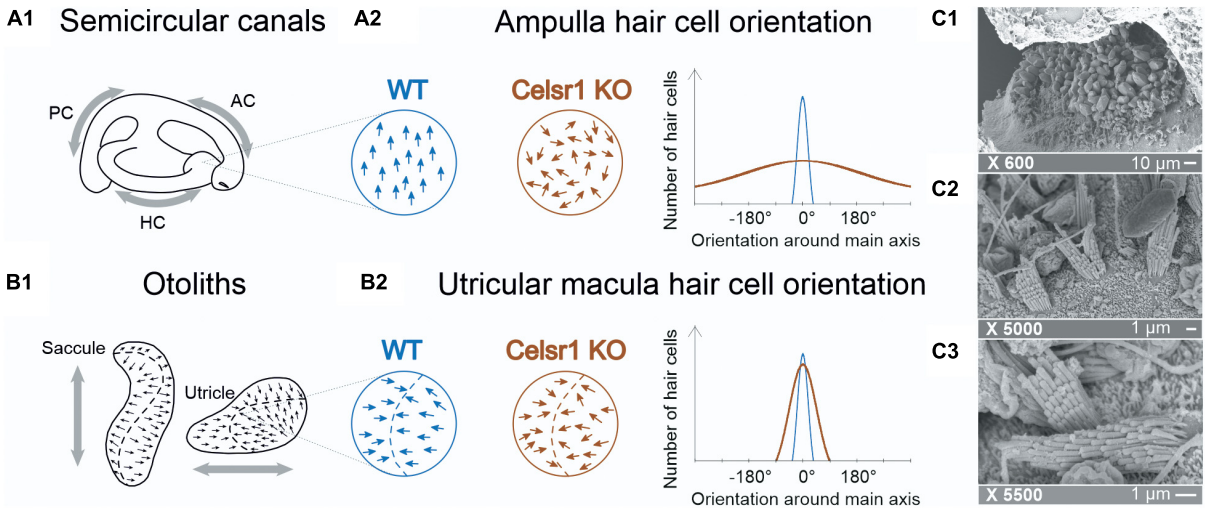

FIGURE 1 | Hair cell orientation of semicircular canal ampullae and otolithic maculas in wild-type and *celsr1*$^{-/-}$ mice. In semicircular canals, the ampullae **(A1)** are stimulated following a rotation, whereas **(B1)** the utricule and saccule are stimulated following translational movements. The organization of hair cells in the ampulla **(A2)** are normally all orientated in the same direction, whereas in *celsr1*$^{-/-}$ mice, 80% of hair cells are misorientated. The organization in the macula **(B2)** is more complex with hair cells orientated toward the striola (in the utricule shown here), and moderate misorientation in *celsr1*$^{-/-}$ mice. Hair cell orientation of wild type (WT) and *celsr1*$^{-/-}$ are schematically represented based on results from Duncan et al. (2017). Transmission electronic microscope of the saccular macula of a KO mouse. The × 600 **(C1)** image shows an overall maintained saccular structure with otoconia and sensory hair cells beneath; **(C2)** × 5,000 shows mostly stereociliary bundles and **(C3)** × 5,500 shows a clear misalignment of two neighboring hair cells, confirming the previous study (Duncan et al., 2017).

MATERIALS AND METHODS

Animals were used in accordance with the European Communities Council Directive 2010/63/EU. All efforts were made to minimize suffering and reduce the number of animals included in the study. All procedures were approved by the ethical committee for animal research of the University of Paris. Animals from the *Celsr1* KO line (Ravni et al., 2009) were provided by the Université Catholique de Louvain. 10 *Celsr1*$^{-/-}$ and 10 littermate control mice were analyzed.

To perform pupil position recording with a fixed head, a head post was implanted at least 48 h before vestibular exploration to the skull (Beraneck and Cullen, 2007; Beraneck et al., 2012; França de Barros et al., 2019). All eye movement recordings were made in the dark using an infrared video system (ETL-200, ISCAN, Burlington MA), recording pupil, and corneal reflection (CR) position (Beraneck and Cullen, 2007; Beraneck and Lambert, 2009; Beraneck et al., 2012; Beraneck and Idoux, 2012). Eye movements were recorded using non-invasive video-oculography (Stahl et al., 2000). The experimental setup, apparatus, and methods of data acquisition were similar to those described previously (Beraneck et al., 2012; Carcaud et al., 2017; Idoux et al., 2018). Briefly, mice were head-fixed at a ∼30° nose-down position to align the horizontal canals with the yaw plane (Calabrese and Hullar, 2006). Myosis was induced with topical 2% pilocarpine applied 10 min before experimentation. Recorded eye and head position signals were sampled at 1 kHz, digitally recorded (CED power1401 MkII) using Spike 2 software and later exported into the Matlab programming environment for off-line analysis (Matlab, The MathWorks). Videonystagmography recorded spontaneous eye movement without vestibular stimulation and eye movement with the three sequential following stimulations: sinusoidal rotation for horizontal angular vestibulo-ocular reflex (aVOR), off-vertical axis rotation (OVAR) for maculo-ocular reflex (MOR), bias and modulation and static and dynamic head tilt roll for the ocular counterroll (OCR) (Beraneck et al., 2012; Romand et al., 2013; Simon et al., 2020).

First, aVOR was tested during horizontal sinusoidal rotation of the turntable (at 0.2, 0.5, 0.8, 1, and 1.5 Hz; peak velocity 30°/s), analyzing gain and phase. The gain was the ratio between the velocity of the eye (response) and head (stimulus) rotations. Since the animal was head-fixed to the rotating table, head movements and table movements were identical. The phase was the temporal shift between the eye and table rotations, expressed in degrees as ratio of the sinusoidal cycle (2 pi). Details for gain and phase calculation were reported in Carcaud et al. (2017). Values with VAF (Variance-accounted-for) under 0.5 were discarded (Beraneck and Cullen, 2007). During OVAR test (Hess and Dieringer, 1990), axis of rotation was tilted from the vertical by 17°. Rotations were performed at constant speed (50°/s) for at least 10 rotations both in clockwise (CW) and counterclockwise (CCW) directions. During rotations, the velocity of horizontal slow phases is modulated around a constant bias. All methods and analysis during OVAR are similar to those in Beraneck et al., 2012. The MOR corresponds to an otolithic response, but also critically depends on an efficient central vestibular system (Hess and Dieringer, 1990; Beraneck et al., 2012). The static OCR tests more specifically the static utricular function. Vertical pupil position according to the head tilt angle was measured first with the mouse maintained at a 0° horizontal position. The platform was then tilted into different roll positions, at 10°, 20°, 30°, and

40° alternatively to the right and to the left. Measurements were made in a static position during at least 15 s to identify the stable pupil position. The vertical eye angle was then calculated from the raw vertical CR and pupil position (Oommen and Stahl, 2008). The OCR gain was calculated corresponding to the slope of a linear regression of both variables (vertical eye angle and head tilt degree). Dynamic roll head tilt was also tested during sinusoidal roll motion at 0.5 Hz from left to right at three different roll angles: −10° to 10°, −20° to 20°, and −30° to 30° corresponding to three different roll amplitudes: 20°, 40°, and 60°. Maximal amplitude of the sinusoidal vertical pupil position was calculated for each condition and dynamic $_{tilt}$VOR gain was calculated corresponding to the amplitude of the vertical eye position on amplitude of the roll rotation. Finally, angular velocity steps in the horizontal plane (hsteps) were performed at a speed of 50°/s. The horizontal slow phase velocity decay was fitted to an exponential curve [$f(x) = a^*\exp(b^*x)$] and the time constant τ was then calculated as $\tau = -1/b$. Gain was calculated from the peak slow phase velocity on table velocity. The time constant of the slow phase exponential velocity decay and gain was calculated for per-rotatory and post-rotatory nystagmus for CW and CCW rotations. CCW per-rotatory and CW post-rotatory values, and CCW post-rotatory and CW per-rotatory values, were combined to assess left and right vestibular functions, respectively. Directional preponderance was calculated using the Jongkees formula and gain value: $DP = Left\ gain - Right\ gain Left\ gain + Right\ gain$ The "saccade main sequence" (Bahill et al., 1975) was analyzed by comparing the relationship between fast phases' peak velocity, duration, and amplitude (Stahl, 2008) to assess the ability of the ocular motor system to generate force (Leigh and Zee, 2015) and integrity of premotor oculomotor pathway (Gibaldi and Sabatini, 2021). For each individual, at least 15 fast phases with peak velocity above 80°/s produced during the OVAR test were analyzed. Onsets and offsets were defined using a ± 20°/s gaze velocity criterion (Beraneck and Cullen, 2007).

Once vestibular exploration was complete, mice were euthanized. In three mice (two Celsr1 KO and one WT), temporal bones were dissected and an opening was made in the apex of the cochlea before fixation in 2.5% glutaraldehyde in cacodylate buffer pH 7.4 at 4°C for 2 h. Vestibular organs were later microdissected and processed for scanning electronic microscopy by alternating incubations in 1% osmium tetroxide and 0.1 M thiocarbohydrazide (OTOTO), as previously described (Furness et al., 2008), to check the disorganization of the morphology of hair bundles in the sensory cells (**Figure 1C**).

Statistical analysis was made using XLstats (Addinsoft, New York, NY). All data are reported as mean and standard deviation. Normal distribution of values was verified using the Kolmogorov–Smirnov test. Two-way ANOVA was used to compare aVOR gain and phase (mouse type and frequency) and the parameters of the Saccade Main Sequence (mouse type and parameters). One-way ANOVA was used to compare static and dynamic roll head tilt amplitudes. *Post-hoc* comparisons were performed where appropriate using the Tukey HSD test. Student's *t*-test (or Wilcoxon if appropriate) was used for MOR bias and modulation static OCR and dynamic $_{tilt}$VOR. For fast phase analysis, a detection of outliers was performed using Routs method and all statistics on regression lines were performed using GraphPad Prism software. Values of $p < 0.05$ were considered significant.

RESULTS

Behavioral and Spontaneous Observations

A total of 10 *Celsr1*$^{-/-}$ (KO mice) and 10 control littermates/wild type (WT) were tested at adult age, and the characteristics of both groups are reported in **Table 1**. All KO mice had abnormal swimming behavior, circling, and head tilt, but none of them drowned.

Videonystagmography recording eye stability in the dark without any vestibular stimulation showed abnormal eye movements in the KO group only. Five mice had spontaneous horizontal nystagmus with the rapid eye movement always beating in the same direction. The five other mice had spontaneous horizontal nystagmus, which could beat in either direction. The KO mice had 10.8 ± 7 spontaneous nystagmus beating per minute (regardless of direction). The presence of spontaneous horizontal nystagmus in all KO mice shows that the disorganization of the vestibular hair cells planar polarity probably affects the balance between the mass discharge within bilateral vestibular complex, which is a major determinant of the stability of gaze in the horizontal plane.

Canal-Dependent Vestibulo-Ocular Reflex Assessment

The amplitude of the eye movements evoked by sinusoidal horizontal rotations was reduced in KO compared to controls (**Figure 2A1**). The gain and phase of the angular horizontal vestibulo-ocular reflex are illustrated in **Figures 2A2,A3** and values are reported in **Table 2**. KO mice had significantly lower gain over all frequencies [two-way ANOVA model, $F(9, 100) = 17.1$, $p < 0.001$], with a reduction of about 50% of the amplitude of eye movements in all tested conditions. This deficit was accompanied with a significant phase lead observed in the lower frequencies only [two-way ANOVA model, $F(9, 100) = 37.9$, $p < 0.001$].

Function of the horizontal aVOR was further tested during velocity steps at 50°/s. At the onset of the movement, horizontal eye movements were typically observed as a succession of compensatory slow phases interrupted by fast phases that recentered the eye. In WT mice, the responses

TABLE 1 | Characteristics of mice tested.

Type of mice	Number of mice	Number of males	Age (weeks) when tested	Number of loop-tails
Celsr1$^{-/-}$	10	2	13 ± 9	6
WT	10	6	15 ± 9	0

Age reported as mean ± standard deviation.

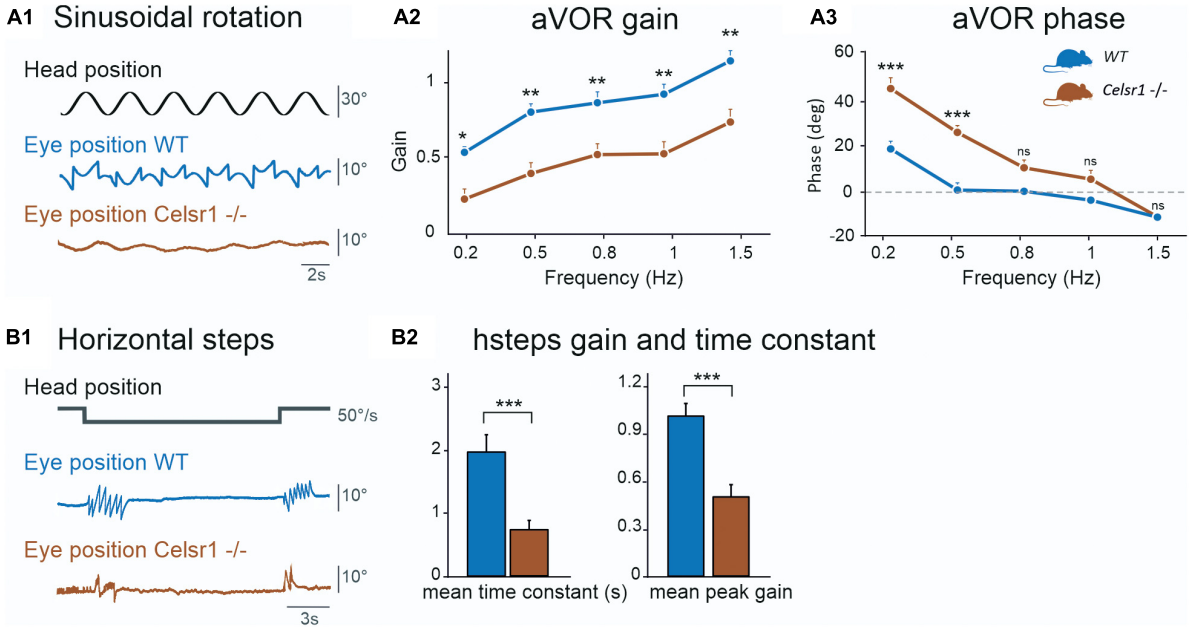

FIGURE 2 | Semicircular canal function. The horizontal semicircular canal (SCC) was tested. Horizontal sinusoidal rotation **(A)** tested for horizontal aVOR. Traces in **(A1)** show head position (corresponding to table position) and horizontal eye movement. KO mice show clear reduction in the amplitude of the eye movement. aVOR gain **(A2)** for maximum 30°/s velocity showed reduced gain for all frequencies of stimulation. aVOR phase **(A3)** for maximum 30°/s velocity showed increased phase for all frequencies of stimulation except 1.5 Hz. Horizontal steps **(B1)** at 50°/s were performed. Traces show head position and horizontal eye position, during per-rotatory nystagmus at the start of a CCW stimulation. In this example trace, only two fast phases can be identified at velocity changes for the KO mouse compared to seven for the WT. Time constant (**B2**, left) and peak gain (**B2**, right) are both decreased for Celsr1 KO mice, for hsteps at 50°/s, for per- and post-rotatory nystagmus during CW and CCW steps. *aVOR* angular vestibulo-ocular reflex, *CW* Clockwise, *CCW* Counterclockwise, *hsteps* horizontal steps, *WT* wild type. *$p < 0.05$; **$p < 0.01$; ***$p < 0.001$.

lasted several seconds while it only lasted 1–2 s in KO (**Figure 2B1**). Hsteps results are reported in **Table 3**. Overall, peak-velocity gain and time constant were both significantly reduced in KO mice (**Figure 2B2**). This confirms the general hypofunction of the canal-dependent aVOR. To further quantify asymmetry of the responses, results are reported according to side of stimulation (**Table 3**). Gains and time constants were reduced in *Celsr1* KO mice in both ears. Directional preponderance (**Table 3**, see section "Materials and Methods") was significantly increased in KO mice compared to WT, regardless of the direction. Thus, although no side stood out, there was an overall increased instability and variability in the preponderance of the deficit in the KO mice, compatible with the gaze instability observed at rest, which was not always in the same direction. No statistical correlation was found between the directional preponderance and nystagmus direction. During both sinusoidal angular rotation or horizontal steps, compensatory eye movements were restricted to the horizontal plane, with minimal vertical component, as observed in WT mice, suggesting that the spatial tuning of the canal-dependent VOR was unaffected by the disorganization of hair cell polarity.

TABLE 2 | Horizontal angular vestibulo-ocular reflex.

Frequency	0.2 Hz	0.5 Hz	0.8 Hz	1 Hz	1.5 Hz
aVOR gain					
Celsr1$^{-/-}$	0.24 ± 0.22	0.42 ± 0.24	0.55 ± 0.21	0.55 ± 0.27	0.77 ± 0.27
WT	0.56 ± 0.13	0.84 ± 0.19	0.91 ± 0.24	0.97 ± 0.22	1.20 ± 0.22
p	***0.044***	***0.002***	***0.015***	***0.002***	***0.002***
aVOR phase					
Celsr1$^{-/-}$	48.7 ± 16.2	28.0 ± 10.4	11.4 ± 10.4	6.1 ± 11.7	−11.6 ± 3.8
WT	20.3 ± 11.5	1.0 ± 10.7	0.4 ± 5.7	−3.8 ± 4.7	−11.8 ± 6.6
p	***<0.001***	***<0.001***	*0.266*	*0.423*	*1*

All values are represented as mean ± SD (standard deviation). Statistical significance of the difference between wild type (WT) and Celsr1 KO mice is shown, significant values are in bold (normal distribution). aVOR angular Vestibular-ocular reflex; p values shown in italic.

Otolith-Dependent Vestibulo-Ocular Reflex Assessment

To specifically test the otolith-dependent vestibulo-ocular reflexes, WT and KO mice were tested using roll head tilt (Simon et al., 2020), which activates the ocular counter rotation reflex (OCR), and during OVAR, which activates the MOR (Beraneck et al., 2012). Results of both tests are illustrated in **Figures 3A,B**, respectively. Static OCR gain and MOR bias and modulation values are reported in **Table 4**.

Figure 3A1 illustrates the vertical eye movements observed during the static roll head tilt. The amplitude of the OCR responses was clearly reduced in KO mice compared to controls.

TABLE 3 | Horizontal steps.

	Left gain	Right gain	Left τ	Right τ	Overall gain	Overall τ	Directional preponderance
Celsr1$^{-/-}$	0.48 ± 0.22	0.53 ± 0.31	0.70 ± 0.50	0.81 ± 0.50	0.51 ± 0.25	0.76 ± 0.48	0.18 ± 0.11
WT	0.97 ± 0.22	1.08 ± 0.31	2.18 ± 0.82	1.88 ± 1.05	1.03 ± 0.26	2.03 ± 0.90	0.06 ± 0.06
p	–	–	–	–	***<0.001***	***0.001***	***0.009***

All values are represented as mean ± SD (standard deviation). Overall gain and τ values correspond to the mean value of CCW and CW per- and post-rotatory values. τ is in seconds. Absolute values were used to calculate directional preponderance mean. Statistical comparison was made using Student's t-test (normal distribution). τ time constant. Significant values are shown in bold.

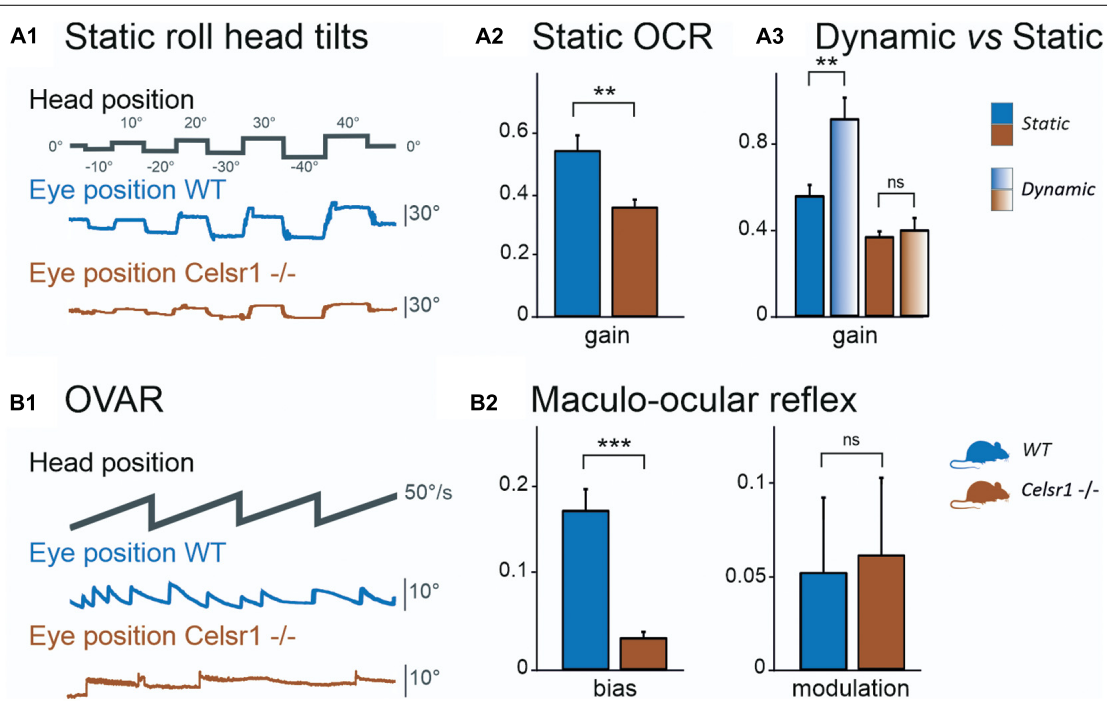

FIGURE 3 | Otolithic system function. Static roll head tilts **(A1)** were performed to determine OCR testing utricular function. Traces show head position (corresponding to table position) and vertical eye movement. KO mouse had preserved function with about 1/3 poorer gain. Vertical eye position in degrees was calculated for OCR according to roll head tilt degree. The static left eye pupil position was measured; tilts with positive degrees were toward the left side and those with negative degrees were toward the right side. OCR gain **(A2)** was significantly reduced in KO mice. The dynamic (gradient fill) head tilt gain was compared to the static (solid fill) OCR gain **(A3)**. In KO mice, the amplitude was not significantly changed between static and dynamic stimulations, whereas it was in WT mice. The Maculo-ocular reflex was studied with the off-vertical axis rotations **(B1)** at 50°/s. Traces show head position and horizontal eye position, during CW stimulation. KO mouse in this example has poor response, seen as the absence of the MOR nystagmus. We report MOR bias (**B2**, left), which is significantly reduced in KO mice, and modulation (**B2**, right), which is similar in both groups. *CW* Clockwise, *CCW* Counterclockwise, *MOR* Maculo-ocular reflex, *OCR* Ocular counterroll, *OVAR* Off-vertical axis rotation, *WT* wild type. *$p < 0.05$; **$p < 0.01$; ***$p < 0.001$.

TABLE 4 | Static OCR and OVAR–maculo-ocular vestibular reflexes.

MOR	Static ocular counterroll			Off-vertical axis rotation			
	40° left	40° right	Gain	CCW bias	CW bias	Overall bias	Overall gain mod.
Celsr1$^{-/-}$	14.7 ± 8.2	−16.9 ± 8.1	0.37 ± 0.09	−0.02 ± 0.03	0.04 ± 0.04	0.03 ± 0.03	0.06 ± 0.04
WT	17.7 ± 7.4	−29.0 ± 13.0	0.56 ± 0.17	−0.17 ± 0.10	0.17 ± 0.11	0.17 ± 0.10	0.05 ± 0.04
p	–	–	***0.008***	–	–	< ***0.001***	*0.38*

All values are represented as mean ± SD (standard deviation). OCR is reported as the left eye vertical angle at 40° static head tilt to the left and to the right and gain (slope value of vertical eye angle and head tilt degree). Maculo-ocular reflex during OVAR is reported with the bias value, during CCW and CW stimulations, and overall bias mean. MOR modulation is also reported (overall CW and CCW values). Statistical comparison was made using Student's t-test (normal distribution).
CCW counterclockwise, CW clockwise, MOR maculo-ocular reflex.
Significant values are shown in bold.

The static OCR gain in KO mice was reduced by about 1/3 compared to WT mice, with mean amplitude gain (vertical eye amplitude/tilt amplitude) of 0.34 ± 0.07 vs. 0.57 ± 0.20, $p = 0.062$, for KO and WT mice, respectively (**Figure 3A2**). The responses of dynamic OCR were then tested in response to dynamic head roll tilts performed as 0.5-Hz sinusoidal rotations in the roll axis. The gain of dynamic OCR was of 0.40 ± 0.19 vs. 0.93 ± 0.31, $p < 0.001$, for KO and WT mice, respectively [ANOVA model $F(3, 40) = 17.5$, $p < 0.001$]. No significant difference was found in the responses between static and dynamic OCR in the KO mice, whereas the responses were significantly better during dynamic OCR than static OCR in the WT mice (**Figure 3A3**).

The responses of WT and KO mice to OVAR stimulation are presented in **Figure 3B1** and **Table 4**. Again, a clear hypofunction was found in KO mice, as an absence of the OVAR-evoked nystagmus (**Figure 3B2**). Quantification revealed an absence of MOR in KO mice during both clockwise and counterclockwise rotations. Overall, the results of the head roll and OVAR tests reveal major deficits in the otolith-dependent reflexes. Both OCR and MOR appeared significantly impaired in KO compared to WT. Altogether, these results show that a mild impairment in the orientation of the hair cells on the maculae leads to severe dysfunction affecting the otolith-dependent vestibulo-ocular reflexes.

Assessment of the Ocular Motor Pathway

The Celsr1 KO mouse is a model of planar cell polarization loss in the vestibular organs. However, several other abnormalities have been reported in this strain (Curtin et al., 2003; Tatin et al., 2013; Shi et al., 2014; Boucherie et al., 2018), which clearly demonstrates deficits in the central nervous system. To determine whether the reduced responses recorded during VOR tests could relate to a deficit in the ability of the ocular motor system to generate force (Leigh and Zee, 2015), we quantified the so-called "saccade main sequence" (Bahill et al., 1975; Gibaldi and Sabatini, 2021). The quantification of the peak velocity, amplitude, and duration of fast phases produced during vestibular stimulation (OVAR test) demonstrated no statistically significant difference between WT and KO (**Table 5**). There was no significant difference in the relationship between amplitude and duration either ($p = 0.11$, **Figure 4A**). As previously reported in several species (Stahl, 2008), horizontal fast phases exhibited a rather linear relationship between velocity and amplitude for WT mice ($R^2 = 0.61$, $p < 0.001$, **Figure 4B**); KO mice demonstrated a less robust relationship ($R^2 = 0.24$, $p < 0.001$), with a reduced slope compared to WT ($p < 0.001$). While informative, this analysis is based on oculomotor responses generated by vestibular stimulation. Specific oculomotor tests are needed to confirm whether KO mouse show normal or altered ocular motor function for eye movements evoked via other means (optokinetic nystagmus for example).

TABLE 5 | Saccade main sequence.

	Peak velocity (°/s)	Amplitude (°)	Duration (s)
Celsr1$^{-/-}$	353.3 ± 124.4	13.2 ± 3.8	0.041 ± 0.013
WT	370.0 ± 166.6	12.7 ± 4.8	0.036 ± 0.010
p	*0.44*	*1*	*1*

All values are represented as mean ± SD (standard deviation). For each group, a minimum of 15 fast phases were analyzed per mice; n = 186 and n = 159 for Celsr1$^{-/-}$ *and WT, respectively. Statistical comparison was made using a two-way ANOVA model [two-way ANOVA model, F(5, 1035) = 821.3, p < 0.001] with Tukey post-hoc tests (normal distribution).*

DISCUSSION

It has previously been shown that in *Celsr1* KO mice, SCC ampullar hair cells were particularly disorganized, with approximately less than 20% of hair cells correctly oriented, whereas the loss of polarity was milder in the otolithic organs with approximately more than 80% of hair bundles in the appropriate direction (**Figure 1**; Duncan et al., 2017). This disorganization was confirmed in our KO mouse population. Although morphological, locomotor, and postural behavioral studies had already been undertaken, the effect of stereociliary bundle polarity loss on the capacity of the vestibular system to encode precise directional signals during head movements had not yet been studied.

It must be noted that the mutated *celsr1* not only affects the peripheral vestibular system but also has multiple other consequences including severe neurological defects such as neural tube defects and caudal agenesis (Curtin et al., 2003; Boucherie et al., 2018). Thus, it seems likely that *Celsr1* KO mice have altered central processing due to major developmental perturbation in addition to altered PCP formation in the vestibular periphery. This should be kept in mind when analyzing the results, as all differences between KO and WT mice may not simply be due to peripheral organ disorganization but may be partly linked to central pathway and/or premotor ocular anomalies.

In our study, we found that the canalar function was severely altered, with aVOR gain in KO approximately half of that of WT mice on all frequencies. A statistically significant phase lead was, however, only found in the lower frequencies at 0.2 and 0.5 Hz, and became progressively identical to WT phases at high frequencies (>1.5 Hz). This suggests that loss of cell polarity impairs the amplitude of compensatory eye movement at all frequencies, and the timing of the aVOR more specifically at lower frequencies. A hypothesis to explain this result would be that, angular accelerations being lower at those frequencies, the misoriented hair cells are likely not stimulated or weakly stimulated, leading to an abnormally decreased population encoding of the movement. This probably impairs the capacity of central vestibular neurons to appropriately encode the amplitude and timing of the head movement. In higher frequencies, a larger proportion of hair cells would be stimulated at the onset of movement, facilitating the event detection of movement and enabling a VOR response with a normal phase. Whichever the frequency, the reduced number of correctly aligned stereocilia bundles depolarized during canalar stimulation could explain the reduced gain over the entire frequency range tested. This

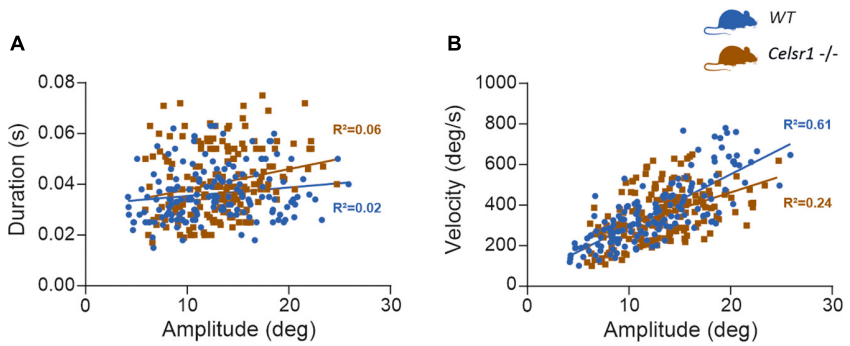

FIGURE 4 | Saccade main sequence. At least 15 fast phases generated by WT (n = 10) and KO mouse (n = 10) during OVAR stimulation were analyzed, for a total 159 and 186 fast phases, respectively. The amplitude, duration, and peak velocity were quantified using a 20°/s threshold for saccade onset and offset (Beraneck and Cullen, 2007). **(A)** Shows the relation between amplitude and duration. For WT, linear regression parameters were: $Y = 0.0003x + 0.032$; $R^2 = 0.024$; $F(1, 157) = 3.93$, $p = 0.049$. For KO, linear regression parameters were: $Y = 0.0008x + 0.030$; $R^2 = 0.055$; $F(1, 184) = 10.64$, $p = 0.001$. Regression were not significantly different [$F(1, 341) = 2.53$, $p = 0.113$]. **(B)** Shows the relation between amplitude and velocity. For WT, linear regression parameters were: $Y = 25.38x + 44.02$; $R^2 = 0.607$; $F(1, 155) = 239.3$, $p < 0.0001$. For KO, linear regression parameters were: $Y = 16.08x + 140.7$; $R^2 = 0.242$; $F(1, 184) = 58.59$, $p < 0.0001$. Regression were significantly different [$F(1, 339) = 12.24$, $p < 0.001$].

was confirmed by analyzing the mean peak gain during the hsteps stimulation, in response to a transient angular stimulation. Indeed, a 0.51 vs. 1.03 gain was measured, showing the loss of approximately half of the canalar gain, yet unexpectedly high considering that more than 80% of ampulla hair cells were disorganized. Overall, it should be noted that despite an extensive disorganization of the hair cell orientation in the ampullae, the signals originating from one SCC could be centrally interpreted as a directional activation in the plane of the canal, thus preserving the directionality of the generated eye movement. Overall, these results suggest that a major loss of information encoding at the level of the semicircular canal, as probably occurs in many inner ear pathologies such labyrinthitis or ototoxicity (Cassel et al., 2019), can partly be compensated by the central vestibular complex. It further suggests that the decoding of directionality of the movement is mostly accounted for by the orientation of the semicircular canals and not by hair cell orientation *per se*.

Otolithic-dependent VOR were significantly decreased in the *Celsr1* KO mice; however, the residual function was sufficient to maintain a static OCR gain at approximately two-thirds of WT mice gain, which could explain why none of the *Celsr1* KO mice drowned in our study. Considering the minor loss of hair cell polarization in the utricle previously reported morphologically (Duncan et al., 2017), functional loss may be considered excessive compared to the ampulla. This may be due to the fact that the otolithic system contains less redundancy in hair cell direction (as hair cells tend to follow the axis of the striola perpendicularly), compared to the ampulla where all hair cells are normally orientated in the same direction (Deans, 2013). This result demonstrates that the spatial organization of the hair cells in the maculae is a critical factor allowing the precise decoding of the spatial directionality of the head movements by central vestibular structures. Thus, in the otolithic system, a small proportion of hair cells misoriented may incur major functional impairment.

A number of other tests assessed more integrated and complex vestibular functions, such as the velocity storage (which requires SCC function and the integrity of a central vestibular and cerebellar neural circuit), MOR (the bias corresponding to a complex otolithic response, but which also requires the integrity of canalar and velocity storage system), and the dynamic roll head tilt (which recruits both utricular and vertical canal function, with an increase in gain compared to the static tilt OCR (Maruta et al., 2001)). No test was able to specifically assess vertical SCC function, although we may expect from this last test that the reduction in vertical SCC function might be comparable to that of horizontal SCC function, as a comparable hair cell disruption has been found in both (Duncan et al., 2017). Differences between KO and WT mice were strongly significant concerning hsteps time constant and peak gain, as well as MOR bias and dynamic roll head tilt. This suggests that the central vestibular complex is not able to compensate for the accumulated peripheral deficits by integrating information originating from different vestibular organs.

CONCLUSION

Previous studies demonstrated that during development, the acquisition of optimal canal and otolith-based responses are mutually dependent, that is, a deficit in one set of organs might affect the maturation of the other. In otolith-deficient mice that lack otolith-based reflexes, the spatial tuning of the aVOR was thus found to be impaired (Beraneck et al., 2012). Similarly, early alteration of semicircular canals was demonstrated to affect the translational, otolithic-dependent, VOR in *Xenopus laevis* (Branoner and Straka, 2015, 2018). One objective of our study was thus to confirm which characteristics (amplitude of response, timing of the response, and directional tuning) of the canal and otolith-dependent VOR were affected by the peripheral vestibular hair cell loss of planar polarity.

This study first confirms the previous morphological results (Duncan et al., 2017), showing that in *Celsr1* KO mice, vestibulo-ocular functional reflexes depending on canal or otolith organs are both impaired. Overall, the major ampullar disorganization led to a reduction, but not to a complete loss of angular coding capacities, and no abnormal spatial tuning. On the other hand, mildly disorganized otolithic hair cells were associated with a marked hypofunction. These results therefore suggest that the highly organized polarization of otolithic hair cells is a critical factor for the accurate encoding of the head movement and that the loss of a small fraction of the otolithic hair cells is likely to have major functional consequences. These results shed light on how partial loss of vestibular information encoding, as often encountered in pathological situations, translates into functional deficits.

Although *CELSR1* missense or dinucleotide repeat mutations have been associated with neural tube defect studies (Allache et al., 2012; Robinson et al., 2012; Lei et al., 2014; Zhan et al., 2016), vestibular function in these patients has never been reported. Considering their neurological background, exploration of vestibular function may not be sufficiently considered in patients with neural tube defects who present with posture, reaching, or orientation issues. Bearing in mind our results, we believe that clinical research studies should assess vestibular function in patients with neural tube defects and especially with *CELSR1* mutations, as vestibular disorders may be diagnosed and appropriate rehabilitation may be prescribed.

DATA AVAILABILITY STATEMENT

The raw data supporting the conclusions of this article will be made available by the authors, without undue reservation.

ETHICS STATEMENT

The animal study was reviewed and approved by Ethical Committee for Animal Research of the University of Paris.

AUTHOR CONTRIBUTIONS

FS and MB carried out the experiment. FS wrote the manuscript with support from FT, VM, GL, MD, and MB. FT produced the *Celsr1* knockout mice. MD and FT helped supervise the project. MB and MD conceived the original idea. MB supervised the project. All authors edited the manuscript and approved its content.

FUNDING

This work was supported by the *Centre National d'Etudes Spatiales*, the *Centre National de la Recherche Scientifique*, and the *Université de Paris*. This study contributes to the IdEx Université de Paris ANR-18-IDEX-0001. This work has benefited from the support and expertise of the animal facility of BioMedTech Facilities at Université de Paris (Institut National de la Santé et de la Recherche Médicale Unité S36/Unité Mixte de Service 2009). MB and FS received support from Marc Boulet Audition.

ACKNOWLEDGMENTS

We are grateful to Michele Tagliabue and Louise Schenberg for their help in the analysis of the data.

REFERENCES

Allache, R., De Marco, P., Merello, E., Capra, V., and Kibar, Z. (2012). Role of the planar cell polarity gene CELSR1 in neural tube defects and caudal agenesis. *Birt. Defects Res. A Clin. Mol. Teratol.* 94, 176–181. doi: 10.1002/bdra.23002

Bahill, A. T., Clark, M. R., and Stark, L. (1975). The main sequence, a tool for studying human eye movements. *Math Biosci.* 24, 191–204. doi: 10.1016/0025-5564(75)90075-9

Barr-Gillespie, P.-G. (2015). Assembly of hair bundles, an amazing problem for cell biology. *Mol. Biol. Cell.* 26, 2727–2732. doi: 10.1091/mbc.E14-04-0940

Beraneck, M., and Cullen, K. E. (2007). Activity of vestibular nuclei neurons during vestibular and optokinetic stimulation in the alert mouse. *J. Neurophysiol.* 98, 1549–1565. doi: 10.1152/jn.00590.2007

Beraneck, M., and Idoux, E. (2012). Reconsidering the role of neuronal intrinsic properties and neuromodulation in vestibular homeostasis. *Front. Neurol.* 3:25. doi: 10.3389/fneur.2012.00025

Beraneck, M., and Lambert, F. M. (2009). Impaired perception of gravity leads to altered head direction signals: what can we learn from vestibular-deficient mice? *J. Neurophysiol.* 102, 12–14. doi: 10.1152/jn.00351.2009

Beraneck, M., Bojados, M., Le Seac'h, A., Jamon, M., and Vidal, P. P. (2012). Ontogeny of mouse vestibulo-ocular reflex following genetic or environmental alteration of gravity sensing. *PLoS One* 7:e40414. doi: 10.1371/journal.pone.0040414

Beraneck, M., Lambert, F. M., and Sadeghi, S. G. (2014). "Functional development of the vestibular system: sensorimotor pathways for stabilization of gaze and posture," in *Development of Auditory and Vestibular Systems*, eds R. Romand and I. Varela-Nieto (Elsevier), 449–487.

Boucherie, C., Boutin, C., Jossin, Y., Schakman, O., Goffinet, A. M., Ris, L., et al. (2018). Neural progenitor fate decision defects, cortical hypoplasia and behavioral impairment in celsr1-deficient mice. *Mol. Psychiatry* 23, 723–734. doi: 10.1038/mp.2017.236

Branoner, F., and Straka, H. (2015). Semicircular canal-dependent developmental tuning of translational vestibulo-ocular reflexes in *Xenopus laevis*. *Dev. Neurobiol.* 75, 1051–1067. doi: 10.1002/dneu.22234

Branoner, F., and Straka, H. (2018). Semicircular canal influences on the developmental tuning of the translational vestibulo-ocular reflex. *Front. Neurol.* 9:404. doi: 10.3389/fneur.2018.00404

Calabrese, D. R., and Hullar, T. E. (2006). Planar relationships of the semicircular canals in two strains of mice. *J. Assoc. Res. Otolaryngol. JARO* 7, 151–159. doi: 10.1007/s10162-006-0031-1

Carcaud, J., França de Barros, F., Idoux, E., Eugène, D., Reveret, L., Moore, L. E., et al. (2017). Long-lasting visuo-vestibular mismatch in freely-behaving mice reduces the vestibulo-ocular reflex and leads to neural changes in the direct vestibular pathway. *eNeuro* 4:ENEURO.0290-16.2017. doi: 10.1523/ENEURO.0290-16.2017

Cassel, R., Bordiga, P., Carcaud, J., Simon, F., Beraneck, M., Le Gall, A., et al. (2019). Morphological and functional correlates of vestibular synaptic deafferentation and repair in a mouse model of acute onset vertigo. *Dis. Model Mech.* 12:dmm.039115. doi: 10.1242/dmm.039115

Curtin, J. A., Quint, E., Tsipouri, V., Arkell, R. M., Cattanach, B., Copp, A. J., et al. (2003). Mutation of celsr1 disrupts planar polarity of inner ear hair

cells and causes severe neural tube defects in the mouse. *Curr. Biol. CB* 13, 1129–1133.

Deans, M. R. (2013). A balance of form and function: planar polarity and development of the vestibular maculae. *Semin. Cell. Dev. Biol.* 24, 490–498. doi: 10.1016/j.semcdb.2013.03.001

Duncan, J. S., Stoller, M. L., Francl, A. F., Tissir, F., Devenport, D., and Deans, M. R. (2017). Celsr1 coordinates the planar polarity of vestibular hair cells during inner ear development. *Dev. Biol.* 423, 126–137. doi: 10.1016/j.ydbio.2017.01.020

França de Barros, F., Carcaud, J., and Beraneck, M. (2019). Long-term sensory conflict in freely behaving mice. *J. Vis. Exp.* doi: 10.3791/59135

Furness, D. N., Katori, Y., Nirmal Kumar, B., and Hackney, C. M. (2008). The dimensions and structural attachments of tip links in mammalian cochlear hair cells and the effects of exposure to different levels of extracellular calcium. *Neuroscience* 154, 10–21. doi: 10.1016/j.neuroscience.2008.02.010

Gibaldi, A., and Sabatini, S. P. (2021). The saccade main sequence revised: a fast and repeatable tool for oculomotor analysis. *Behav. Res. Methods* 53, 167–187. doi: 10.3758/s13428-020-01388-2

Greene, N. D. E., Stanier, P., and Copp, A. J. (2009). Genetics of human neural tube defects. *Hum. Mol. Genet.* 18, R113–R129. doi: 10.1093/hmg/ddp347

Hakanen, J., Ruiz-Reig, N., and Tissir, F. (2019). Linking cell polarity to cortical development and malformations. *Front. Cell Neurosci.* 13:244. doi: 10.3389/fncel.2019.00244

Hess, B. J. M., and Dieringer, N. (1990). Spatial organization of the maculo-ocular reflex of the rat: responses during off-vertical axis rotation. *Eur. J. Neurosci.* 2, 909–919.

Idoux, E., Tagliabue, M., and Beraneck, M. (2018). No gain no pain: relations between vestibulo-ocular reflexes and motion sickness in mice. *Front. Neurol.* 9:918. doi: 10.3389/fneur.2018.00918

Lei, Y., Zhu, H., Yang, W., Ross, M. E., Shaw, G. M., and Finnell, R. H. (2014). Identification of novel CELSR1 mutations in spina bifida. *PLoS One* 9:e92207. doi: 10.1371/journal.pone.0092207

Leigh, R. J., and Zee, D. S. (2015). *The Neurology of Eye Movements*. (Contemporary Neurology Series, Oxford University Press).

Maruta, J., Simpson, J. I., Raphan, T., and Cohen, B. (2001). Orienting otolith-ocular reflexes in the rabbit during static and dynamic tilts and off-vertical axis rotation. *Vision Res.* 41, 3255–3270. doi: 10.1016/s0042-6989(01)00091-8

Nam, J.-H., Grant, J. W., Rowe, M. H., and Peterson, E. H. (2019). Multiscale modeling of mechanotransduction in the utricle. *J. Neurophysiol.* 122, 132–150. doi: 10.1152/jn.00068.2019

Oommen, B. S., and Stahl, J. S. (2008). Eye orientation during static tilts and its relationship to spontaneous head pitch in the laboratory mouse. *Brain Res.* 1193, 57–66. doi: 10.1016/j.brainres.2007.11.053

Ravni, A., Qu, Y., Goffinet, A. M., and Tissir, F. (2009). Planar cell polarity cadherin celsr1 regulates skin hair patterning in the mouse. *J. Invest. Dermatol.* 129, 2507–2509. doi: 10.1038/jid.2009.84

Robinson, A., Escuin, S., Doudney, K., Vekemans, M., Stevenson, R. E., Greene, N. D., et al. (2012). Mutations in the planar cell polarity genes CELSR1 and SCRIB are associated with the severe neural tube defect craniorachischisis. *Hum. Mutat.* 33, 440–447. doi: 10.1002/humu.21662

Romand, R., Krezel, W., Beraneck, M., Cammas, L., Fraulob, V., Messaddeq, N., et al. (2013). Retinoic acid deficiency impairs the vestibular function. *J. Neurosci.* 33, 5856–5866. doi: 10.1523/jneurosci.4618-12.2013

Shi, D., Komatsu, K., Hirao, M., Toyooka, Y., Koyama, H., Tissir, F., et al. (2014). Celsr1 is required for the generation of polarity at multiple levels of the mouse oviduct. *Dev. Camb. Engl.* 141, 4558–4568. doi: 10.1242/dev.115659

Shotwell, S. L., Jacobs, R., and Hudspeth, A. J. (1981). Directional sensitivity of individual vertebrate hair cells to controlled deflection of their hair bundles. *Ann. N.Y. Acad. Sci.* 374, 1–10. doi: 10.1111/j.1749-6632.1981.tb30854.x

Simon, F., Pericat, D., Djian, C., Fricker, D., Denoyelle, F., and Beraneck, M. (2020). Surgical techniques and functional evaluation for vestibular lesions in the mouse: unilateral labyrinthectomy (UL) and unilateral vestibular neurectomy (UVN). *J. Neurol.* 267, 51–61. doi: 10.1007/s00415-020-09960-8

Stahl, J. S. (2008). *Characteristics and Applications of Mouse Eye Movements*, Eds. L. M. Chalupa, R. W. Williams (The MIT Press). 87–105.

Stahl, J. S., Averbuch-Heller, L., and Leigh, R. J. (2000). Acquired nystagmus. *Arch. Ophthalmol. Chic. Ill* 1960, 544–549. doi: 10.1001/archopht.118.4.544

Tarchini, B., and Lu, X. (2019). New insights into regulation and function of planar polarity in the inner ear. *Neurosci. Lett.* 709:134373. doi: 10.1016/j.neulet.2019.134373

Tatin, F., Taddei, A., Weston, A., Fuchs, E., Devenport, D., Tissir, F., et al. (2013). Planar cell polarity protein celsr1 regulates endothelial adherens junctions and directed cell rearrangements during valve morphogenesis. *Dev. Cell.* 26, 31–44. doi: 10.1016/j.devcel.2013.05.015

Tissir, F., and Goffinet, A. M. (2013). Shaping the nervous system: role of the core planar cell polarity genes. *Nat. Rev. Neurosci.* 14, 525–535. doi: 10.1038/nrn3525

Yang, X., Qian, X., Ma, R., Wang, X., Yang, J., Luo, W., et al. (2017). Establishment of planar cell polarity is coupled to regional cell cycle exit and cell differentiation in the mouse utricle. *Sci. Rep.* 7:43021. doi: 10.1038/srep43021

Zhan, Y.-H., Luo, Q.-C., Zhang, X.-R., Xiao, N. A., Lu, C. X., Yue, C., et al. (2016). CELSR1 is a positive regulator of endothelial cell migration and angiogenesis. *Biochem. Biokhimiia* 81, 591–599. doi: 10.1134/S0006297916060055

Conflict of Interest: The authors declare that the research was conducted in the absence of any commercial or financial relationships that could be construed as a potential conflict of interest.

Publisher's Note: All claims expressed in this article are solely those of the authors and do not necessarily represent those of their affiliated organizations, or those of the publisher, the editors and the reviewers. Any product that may be evaluated in this article, or claim that may be made by its manufacturer, is not guaranteed or endorsed by the publisher.

frontiers in Neuroscience

ORIGINAL RESEARCH
published: 08 December 2021
doi: 10.3389/fnins.2021.749483

Current Response in $Ca_V1.3^{-/-}$ Mouse Vestibular and Cochlear Hair Cells

Marco Manca[1,2†], Piece Yen[2†], Paolo Spaiardi[1], Giancarlo Russo[1], Roberta Giunta[1], Stuart L. Johnson[2,3], Walter Marcotti[2,3] and Sergio Masetto[1]*

[1] Department of Brain and Behavioral Sciences, University of Pavia, Pavia, Italy, [2] School of Biosciences, University of Sheffield, Sheffield, United Kingdom, [3] Sheffield Neuroscience Institute, University of Sheffield, Sheffield, United Kingdom

Signal transmission by sensory auditory and vestibular hair cells relies upon Ca^{2+}-dependent exocytosis of glutamate. The Ca^{2+} current in mammalian inner ear hair cells is predominantly carried through $Ca_V1.3$ voltage-gated Ca^{2+} channels. Despite this, $Ca_V1.3$ deficient mice ($Ca_V1.3^{-/-}$) are deaf but do not show any obvious vestibular phenotype. Here, we compared the Ca^{2+} current (I_{Ca}) in auditory and vestibular hair cells from wild-type and $Ca_V1.3^{-/-}$ mice, to assess whether differences in the size of the residual I_{Ca} could explain, at least in part, the two phenotypes. Using 5 mM extracellular Ca^{2+} and near-body temperature conditions, we investigated the cochlear primary sensory receptors inner hair cells (IHCs) and both type I and type II hair cells of the semicircular canals. We found that the residual I_{Ca} in both auditory and vestibular hair cells from $Ca_V1.3^{-/-}$ mice was less than 20% (12–19%, depending on the hair cell type and age investigated) compared to controls, indicating a comparable expression of $Ca_V1.3$ Ca^{2+} channels in both sensory organs. We also showed that, different from IHCs, type I and type II hair cells from $Ca_V1.3^{-/-}$ mice were able to acquire the adult-like K^+ current profile in their basolateral membrane. Intercellular K^+ accumulation was still present in $Ca_V1.3^{-/-}$ mice during $I_{K,L}$ activation, suggesting that the K^+-based, non-exocytotic, afferent transmission is still functional in these mice. This non-vesicular mechanism might contribute to the apparent normal vestibular functions in $Ca_V1.3^{-/-}$ mice.

Keywords: auditory, vestibular, development, calcium current, potassium current, hair cells

OPEN ACCESS

Edited by:
Gwenaelle S. G. Geleoc, Boston Children's Hospital and Harvard Medical School, United States

Reviewed by:
Sungchil Yang, City University of Hong Kong, Hong Kong SAR, China
Ivan Milenkovic, University of Oldenburg, Germany

****Correspondence:***
Sergio Masetto
smasetto@unipv.it;
sergio.masetto@unipv.it

† These authors have contributed equally to this work

Specialty section:
This article was submitted to Perception Science, a section of the journal Frontiers in Neuroscience

Received: *29 July 2021*
Accepted: *01 November 2021*
Published: *08 December 2021*

Citation:
Manca M, Yen P, Spaiardi P, Russo G, Giunta R, Johnson SL, Marcotti W and Masetto S (2021) Current Response in $Ca_V1.3^{-/-}$ Mouse Vestibular and Cochlear Hair Cells. Front. Neurosci. 15:749483. doi: 10.3389/fnins.2021.749483

INTRODUCTION

The inner ear houses the auditory and the balance organs. In mammals, the primary sensory cells are the inner hair cells (IHCs) of the cochlea, and the type I and type II hair cells of the vestibular system. Acoustic stimuli or head movements cause change in the hair cell membrane potential, which modulates Ca^{2+} inflow and related neurotransmitter (glutamate) exocytosis (Bonsacquet et al., 2006; Dulon et al., 2009; Songer and Eatock, 2013; Sadeghi et al., 2014; Vincent et al., 2014; Kirk et al., 2017). Both auditory and vestibular hair cells express voltage-gated L-type Ca^{2+} channels containing the pore-forming $Ca_V1.3$ subunit (previously known as α1D), which are characterized by a negative voltage of activation (about −60 mV) and negligible voltage-dependent

inactivation (Platzer et al., 2000; Bao et al., 2003; Johnson and Marcotti, 2008; Zampini et al., 2013). Pharmacologically, L-type ($Ca_V1.1$ to $Ca_V1.4$) Ca^{2+} channels are identified by their sensitivity to dihydropyridines (DHPs) such as nimodipine and nifedipine (antagonists) or BayK 8644 (agonist), which do not affect the other voltage-gated Ca^{2+} channels (Ca_V2 and Ca_V3). However, the $Ca_V1.3$ subunit is relatively insensitive to DHP antagonists compared to $Ca_V1.1$, 1.2, and 1.4 subunits (Koschak et al., 2001; Xu and Lipscombe, 2001).

The majority (∼90%) of the Ca^{2+} current in IHCs is carried by the $Ca_V1.3$ subunit (Platzer et al., 2000; Jeng et al., 2020a). The nature of the remaining ∼10% of the Ca^{2+} current is still unknown (see Pangrsic et al., 2018), although previous work has indicated that it could be carried by the $Ca_V1.4$ subunit (Brandt et al., 2003). Consistent with the critical role of $Ca_V1.3$ channels in hair cell Ca^{2+} dependent exocytosis, $Ca_V1.3^{-/-}$ mice are deaf (Platzer et al., 2000; Brandt et al., 2003), but do not show vestibular deficits (Platzer et al., 2000; Dou et al., 2004). A pharmacological study from rat semicircular canal crista hair cells has indicated that the level of expression of $Ca_V1.3$ Ca^{2+} channels is comparable to that of the cochlear IHCs (Bao et al., 2003). However, vestibular utricle hair cells from $Ca_V1.3^{-/-}$ mice appear to express a large residual Ca^{2+} current (∼50%, Dou et al., 2004), which could potentially drive some signal transmission to the afferent fibers, at least during linear horizontal head accelerations. Currently, it is unknown whether a substantial residual Ca^{2+} current is also expressed in $Ca_V1.3^{-/-}$ semicircular canal hair cells, which could compensate for rotation-related reflexes (e.g., vestibulo-ocular reflexes), and whether its size is similar between type I and type II hair cells. The possible presence of large residual Ca^{2+} currents in vestibular hair cells from $Ca_V1.3^{-/-}$ mice, together with the recently identified non-quantal, Ca^{2+}-independent, signal transmission at type I hair cell synapses (Eatock, 2018) could contribute, at least in part, to the milder vestibular phenotype present in $Ca_V1.3^{-/-}$ mice. Non-quantal transmission, which has not been reported in auditory hair cells, involves intercellular K^+ accumulation in the synaptic cleft occurring during the activation of a hyperpolarizing-activated outward rectifying K^+ current $I_{K,L}$ (Lim et al., 2011; Contini et al., 2012, 2017, 2020; Spaiardi et al., 2017, 2020a).

Here, we have performed whole-cell patch clamp recordings from IHCs and both type I and type II hair cells from the mammalian crista of $Ca_V1.3^{-/-}$ mice using the same experimental conditions in terms of extracellular Ca^{2+} and temperature. We have found that both IHCs and vestibular hair cells from $Ca_V1.3^{-/-}$ mice have < 20% of residual Ca^{2+} current compared to control mice. Thus, differences in $Ca_V1.3$ Ca^{2+} channel expression among vestibular organs (saccule vs. semicircular canals) may exist, possibly allowing hair cells from some vestibular organs to retain some Ca^{2+}-dependent neurotransmitter exocytosis. We have also found that, different from cochlear IHCs, $Ca_V1.3$ Ca^{2+} channels are not required for the normal maturation of the biophysical properties (K^+ channel expression) of both type I and type II hair cells. Since $I_{K,L}$ and intercellular K^+ accumulation in the synaptic cleft of type I hair cells were normal in $Ca_V1.3^{-/-}$ mice, non-quantal signal transmission might also contribute to the vestibular functioning of $Ca_V1.3^{-/-}$ mice.

MATERIALS AND METHODS

Ethics Statement

All animal work was performed at the University of Sheffield (United Kingdom), licensed by the Home Office under the Animals (Scientific Procedures) Act 1986 (PPL_PCC8E5E93) and approved by the University of Sheffield Ethical Review Committee (180626_Mar). For all *in vitro* work, mice were culled by cervical dislocation, which is a schedule 1 method.

Tissue Preparation

Experiments were performed using $Ca_V1.3$ knockout mice ($Ca_V1.3^{-/-}$) on a C57BL/6N background and control mice (littermate heterozygous or C57BL/6N). Mice from both sexes were used and ranging from postnatal day 4 (P4) to P35. The semicircular canals with their *ampullae* and cochleae (apical turn) were dissected out from the inner ear as reported previously (Jeng et al., 2020a, 2021; Spaiardi et al., 2020a; Carlton et al., 2021), using an extracellular solution composed of (in mM) 135 NaCl, 5.8 KCl, 1.3 $CaCl_2$, 0.9 $MgCl_2$, 0.7 NaH_2PO_4, 5.6 D-glucose, and 10 HEPES-NaOH. Sodium pyruvate (2 mM), amino acids, and vitamins were added from concentrates (Thermo Fisher Scientific, United Kingdom). The pH was adjusted to 7.5 (osmolality ∼308 mmol kg^{-1}). The dissected organs were fixed at the bottom of the recording chamber by a nylon-meshed silver ring and were continuously perfused with the above extracellular solution (0.5 ml/min) using a peristaltic pump (Masterflex L/S, Cole Palmer, United States). Hair cells were viewed using a upright microscopes (Olympus BX51; Leica DM-LFS) equipped with Nomarski Differential Interface Contrast (DIC) optics with a 60X or 64X water immersion objective and x15 eyepieces.

Whole-Cell Electrophysiology

Voltage-clamp whole-cell experiments were performed at room temperature (18–22°C) for K^+ current recordings, and near-body temperature (32–36°C) for Ca^{2+} currents recordings using an Optopatch amplifier (Cairn Research Ltd., United Kingdom) as previously described (Johnson and Marcotti, 2008; Jeng et al., 2020b; Spaiardi et al., 2020b). The patch pipettes were pulled to 2–3 MΩ tip resistance from soda glass capillaries (Hilgenberg, Germany) and coated with surf-wax (Mr. Zoggs SexWax, United States) to minimize the fast capacitance transient across the wall of the patch pipette. For K^+ current recordings, the patch pipette filling solution contained (in mM): KCl 131, Na_2-Phosphocreatine 10, $MgCl_2$ 3, EGTA-KOH 1, Na_2ATP 5, and HEPES 5; pH adjusted to 7.28 with KOH (osmolality was 294 mmol kg^{-1}). For Ca^{2+} current recordings, the pipette intracellular solution contained (in mM): 106 Cs-glutamate, 20 CsCl, 3 $MgCl_2$, 1 EGTA-CsOH, 5 Na_2ATP, 0.3 Na_2GTP, 5 HEPES-CsOH, 10 Na_2-phosphocreatine, pH 7.3 with CsOH (294 mmol kg^{-1}). Data acquisition was controlled by pClamp software using a Digidata board (Molecular Devices, United States). Recordings were low-pass filtered at either 2.5 or 5 kHz (8-pole Bessel),

sampled at 5, 10, or 100 kHz and stored on computer for off-line analysis using Clampfit (Molecular Devices, United States) and Origin (OriginLab, United States) software. Membrane potentials reported in the text and figures were corrected for the uncompensated residual series resistance (R_s) and the liquid junction potential (LJP), which was either −4 mV for the K^+-based and −11 mV for the Cs^+-glutamate-based intracellular solution, measured between electrode and bath solutions. For K^+ current recordings from vestibular hair cells, R_s was calculated off-line from the capacitive artifact elicited by applying a voltage step from either −74 to −64 mV in type II and −124 to −44 mV in type I hair cells. The different voltage step was used in order to minimize artifact contamination by inward and outward rectifier voltage-gated channels in the two hair cell types (Spaiardi et al., 2017). Voltage clamp protocols are referred to a holding potential of −64 mV for the K^+-based intracellular solution or −91 mV for the Cs^+-based intracellular solution.

For Ca^{2+} current recordings, the composition of the extracellular solution contained (in mM): NaCl 101, $CaCl_2$ 5, CsCl 5.8, $MgCl_2$ 0.9, HEPES 10, glucose 5.6, tetraethylammonium (TEA) 30, 4-aminopyridine (4AP) 15 (pH adjusted with HCl was 7.5; osmolality: 312 mOsm/kg). The higher Ca^{2+} concentration (5 mM) was used to better visualize the Ca^{2+} current in $Ca_V1.3^{-/-}$ mice. Extracellular TEA, 4AP, and intracellular Cs^+ (see above) were used to block the K^+ channels (cochlear IHCs: Marcotti et al., 2003; Jeng et al., 2020b, 2021; vestibular hair cells: Rennie and Correia, 1994; Biel et al., 2009). Moreover, the K^+ channel blockers linopirdine (80 μM; Tocris, United Kingdom) was also used to block $I_{K,n}$ in adult IHCs (Marcotti et al., 2003). In some experiments, $CdCl_2$ 0.1 mM was also added to the above extracellular solution to block the Ca^{2+} current (Hille, 2001) in vestibular hair cells. The amplitude of the Ca^{2+} current was measured by either subtracting the linear leakage current component, measured between −81 and −91 mV, or the current blocked by Cd^{2+} from the current recorded in the presence of TEA and 4AP (see above).

Statistics Analysis

Statistical comparisons of means were made by Student's two-tailed *t*-test or, for multiple comparisons, analysis of variance (one-way or two-way ANOVA) was applied. $P < 0.05$ was selected as the criterion for statistical significance. Mean values are quoted as means ± SD.

RESULTS

Potassium Currents Recorded From Type I and Type II Crista Hair Cells From Control and $Ca_V1.3^{-/-}$ Mice

Type I hair cells of the *ampullae* sensory epithelium (the *crista*) exhibit a large low-voltage activated outward rectifying K^+ currents, named $I_{K,L}$ (Rennie and Correia, 1994; Rüsch and Eatock, 1996), which was recorded in both adult wild-type (**Figure 1A**) and $Ca_V1.3^{-/-}$ mice (**Figure 1B**). Since $I_{K,L}$ is almost completely activated at −60 mV, hyperpolarizing voltages from the holding potential of −64 mV produced deactivating tail currents (e.g., −104 and −124 mV: **Figures 1A,B**), while depolarizations elicit an instantaneous increase of the outward currents. The mean steady-state current-voltage (*I-V*) relationship for the total current recorded in type I hair cells was not significantly different between wild-type (P17-P22; $n = 12$) and $Ca_V1.3^{-/-}$ mice (P19-P20; $n = 6$) ($P = 0.9742$, $F = 0.4149$, DFn = 15, two-way ANOVA, **Figure 1C**). The negligible steady-state current at −124 mV is consistent with $I_{K,L}$ being fully deactivated at this potential, and with the absence of inward rectifier currents in mouse *crista* type I hair cells (Spaiardi et al., 2020a). Note that the outward tail currents in type I hair cells, which were recorded at −44 mV, were smaller following the voltage step to −24 mV than those at −44 mV in both wild-type (**Figures 1A,D**) and $Ca_V1.3^{-/-}$ mice (**Figures 1B,E,F**). The presence of progressively smaller outward tail current following larger outward K^+ currents (**Figures 1D,E**), which in some cases includes tail current reversal (**Figure 1F**), is consistent with intercellular (e.g., in the calyceal synaptic cleft) K^+ accumulation inducing a shift in the K^+ equilibrium potential (Lim et al., 2011; Contini et al., 2012, 2017, 2020; Spaiardi et al., 2020a). Progressive intercellular K^+ accumulation during depolarization is also responsible for the "apparent" inactivation of the outward current, which is due to the progressive decrease of the driving force for K^+ to exit the hair cells (e.g., Spaiardi et al., 2017).

Different from the type I hair cells, the macroscopic current recorded from adult type II hair cells is not dominated by $I_{K,L}$ (**Figures 1G,H**), but instead express several other currents that have been previously described in great details (Meredith and Rennie, 2016). This include a transient ($I_{K,A}$) and a delayed rectifying ($I_{K,v}$) outward K^+ current, an inward rectifying K^+ current ($I_{K,1}$), and the mixed inward rectifying Na^+/K^+ current (I_h). All these currents were evident from the inward and outward current profile recorded from type II hair cells of $Ca_V1.3^{-/-}$ mice (**Figure 1H**). The mean steady-state *I-V* for the total current recorded in type II hair cells was also not significantly different between wild-type (P17-P22; $n = 4$) and $Ca_V1.3^{-/-}$ mice (P18-P19; $n = 4$) ($P = 0.7010$, $F = 0.7756$, DFn = 15, two-way ANOVA, **Figure 1I**).

The above results demonstrate that the absence of the $Ca_V1.3$ Ca^{2+} channel subunit does not impair the normal developmental acquisition of voltage-dependent K^+ currents in vestibular type I and II hair cells in the *crista*. This is different from the cochlea, where the normal expression of the K^+ currents characteristic of adult inner hair cells (IHCs), which are the fast activating BK current $I_{K,f}$ and negatively activating delayed rectifier $I_{K,n}$ (Kros et al., 1998; Marcotti et al., 2003; Oliver et al., 2003), was either prevented (apical-coil) or reduced (basal-coil) in $Ca_V1.3^{-/-}$ mice (Brandt et al., 2003; Jeng et al., 2020a).

Calcium Currents in Type I and Type II Hair Cells in Control and $Ca_V1.3^{-/-}$ Mice

Although type I and type II hair cells are morphologically distinct, this is not always visible when working with the intact organ. Therefore, the correct identification of type I hair cells relies on the presence of $I_{K,L}$ (**Figure 1**). Recordings were

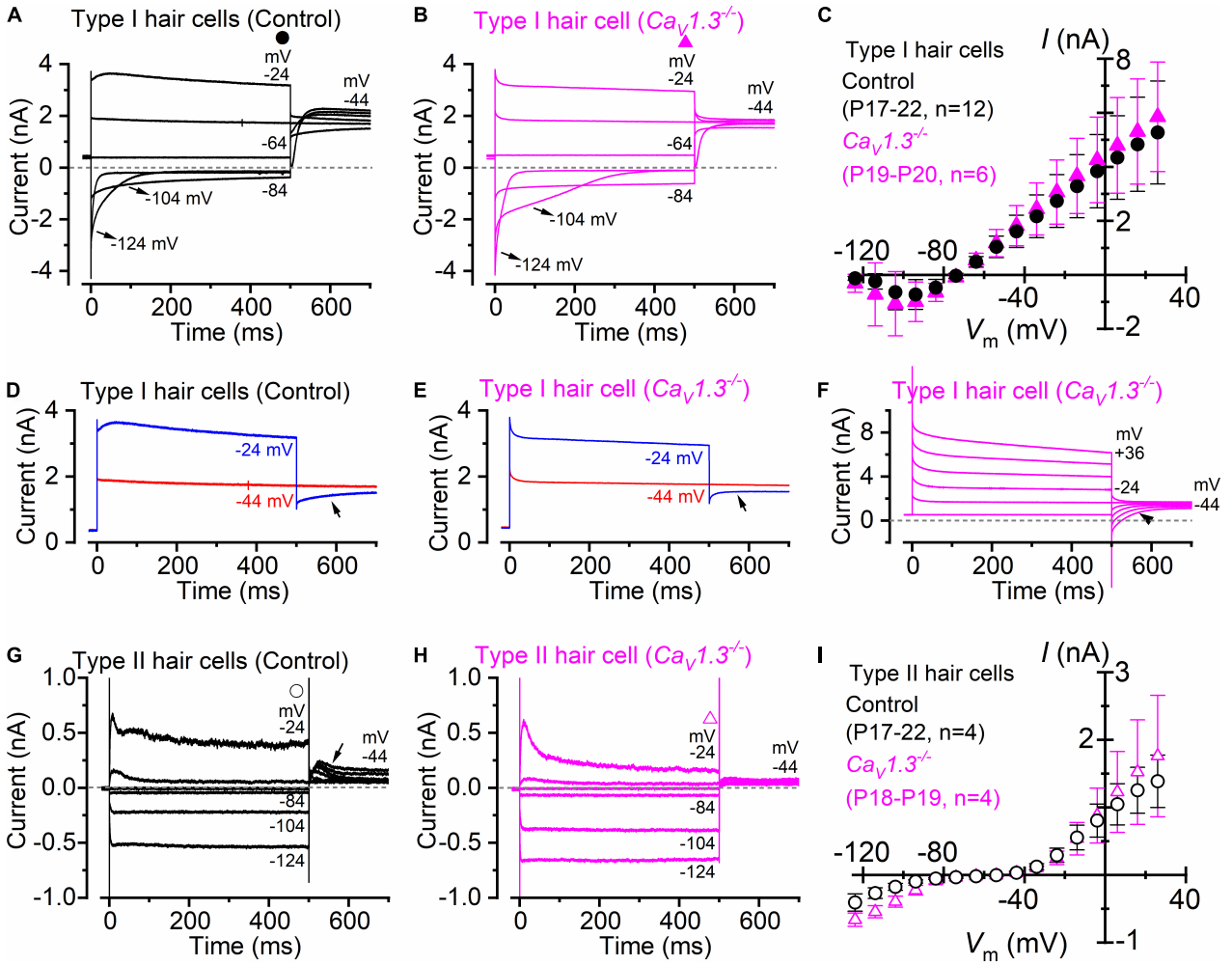

FIGURE 1 | Type I and type II crista hair cells express normal K^+ currents in control and $Ca_V1.3^{-/-}$ adult mice. **(A,B)** Membrane current responses from type I hair cells of control [**(A)**, P18] or $Ca_V1.3^{-/-}$ [**(B)** P20] adult mice were performed by applying 500 ms depolarizing voltage steps of 10 mV nominal increment from −124 mV, starting from a holding potential of −64 mV. For clarity, only a few test potentials are shown. **(C)**, Steady-state current-voltage (*I-V*) curves obtained from type I hair cells of control (P17–22) and $Ca_V1.3^{-/-}$ (P19–20) mice. **(D,E)** Current responses from panels **(A,B)** but at only two membrane potentials that better emphasize the tail currents. **(F)** Potassium current recorded from a type I hair cell of a $Ca_V1.3^{-/-}$ mouse (P19). The tail currents at −44 mV were elicited following 500 ms voltage steps between −64 to 40 mV in 20 mV nominal increments (actual membrane potential is shown near some of the traces). The instantaneous tail current reverse (arrow) following the two most depolarized voltage steps. The horizontal dashed line represents the zero-current level. For a detailed explanation of the above phenomenon, see Spaiardi et al. (2017). **(G,H)** Membrane current responses from type II hair cells of control [**(G)**, P17] or $Ca_V1.3^{-/-}$ [**(H),** P19] adult mice obtained using the voltage protocol described above. Note that the larger tail outward currents at −44 mV [arrow in panel **(G)**], elicited following the 500 ms hyperpolarizing voltage steps, were due to progressive removal of $I_{K,A}$ inactivation. **(I)** Steady-state *I-V* curves obtained from type I hair cells of control (P17–22) and $Ca_V1.3^{-/-}$ (P18–19) mice. In panels **(C,I)** values are shown as mean ± S.D.

performed using intracellular Cs^+, which is known to block I_h (Biel et al., 2009) and the outward rectifying K^+ currents (Bao et al., 2003) in type II hair cells while having little effect on $I_{K,L}$ (Griguer et al., 1993; Rüsch and Eatock, 1996; Chen and Eatock, 2000; Rennie and Correia, 2000). An additional consideration affecting the correct identification of $I_{K,L}$ is its state of deactivation at the holding potential used for the recordings, which is generally set at −90 mV. **Figures 2A,C** shows representative current responses recorded from a type I hair cell with a largely deactivated $I_{K,L}$, as indicated by the small inward current at −91 mV, and the small instantaneous current upon depolarizing and hyperpolarizing voltage steps. In the example shown in **Figures 2B,C**, however, $I_{K,L}$ is largely activated at −91 mV and exhibits large instantaneous currents. Although this variability has previously been reported (Hurley et al., 2006; Spaiardi et al., 2017), we found that the reversal potential for the macroscopic current was significantly more hyperpolarised in type I hair cells showing a largely activated $I_{K,L}$ at −91 mV (**Figure 2C**). While a deactivated $I_{K,L}$ at the holding potential was primarily recorded in early postnatal hair cells (n = 15), more mature cells tend to exhibit a largely activated current (n = 8) (**Figure 2D**). Since the reversal potential of the macroscopic K^+

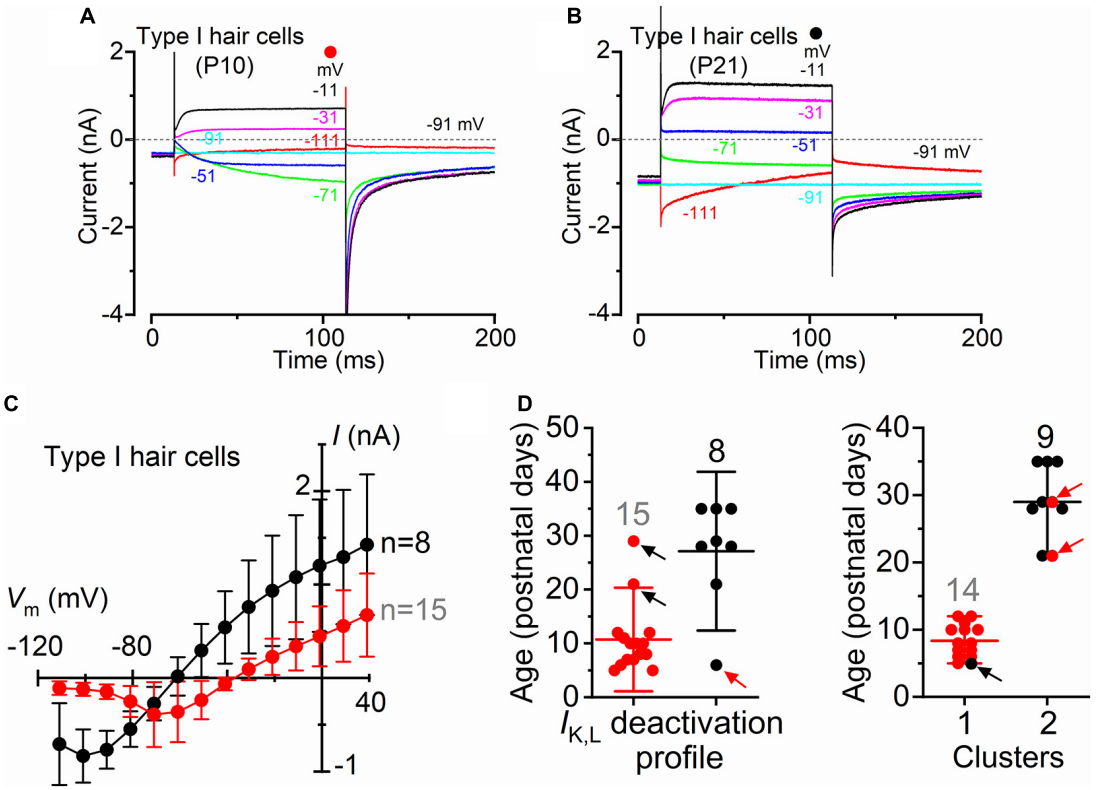

FIGURE 2 | Type I crista hair cells can be identified by their large permeability to Cs^+ in wild-type neonatal and adult mice. **(A,B)** Representative membrane current responses recorded from type I hair cells of control mice of different age with Cs^+ as main ion carrier in the intracellular solution [**(A),** P10; **(B),** P21]. Currents were elicited by 500 ms depolarizing voltage steps of 10 mV nominal increment from −111 mV starting from a holding potential of −91 mV. For clarity, only a few test potentials are shown. **(C)** Steady-state *I-V* curves obtained from type I hair cells arbitrarily subdivided into two groups depending if the inward current through the K,L channels was (red), or was not (black), completely deactivated at −111 mV. Values are shown as mean ± SD. **(D)** Left: Age distribution of type I hair cells expressing $I_{K,L}$ that was (red), or was not (black), completely deactivated at −111 mV. Each symbol refers to the steady-state value of $I_{K,L}$ measured in each cell at −111 mV. Right: same data as in the left panel but subdivided into type I hair cells that are completely deactivated (red) and not deactivated (black) at −111 mV clusters using k-means clustering. Arrows indicate the hair cells that are located in one cluster but have $I_{K,L}$ properties that fit best the other cluster.

current in type I hair cells is primarily determined by the ions flowing through the K,L channels, it should reach values near the reversal potential of the mixed Cs^+/K^+ current (called a "biionic potential"; see Hille, 2001) through K,L channels in the presence of a large $I_{K,L}$ and intracellular Cs^+ (Spaiardi et al., 2020a). Given the reported permeability ratio of Cs^+ to K^+ of about 0.31 (Rüsch and Eatock, 1996; Spaiardi et al., 2020a), the reversal potential should be close to −40 mV. The finding that the reversal potential in older hair cells (**Figure 2C**) is close to −60 mV could indicate that the relative permeability of K,L channels to Cs^+ is likely to be larger than that previously estimated, at least in more mature type I hair cells. However, the presence of a residual calyx might also produce a shift of the mixed Cs^+/K^+ equilibrium potential toward more negative voltages during inward currents (Spaiardi et al., 2017, 2020a). This would imply a tighter attachment of the calyx to more mature type I hair cells.

The above results are consistent with $I_{K,L}$ increasing in amplitude and activating at more hyperpolarized potentials during post-natal development, as also previously shown in rat type I hair cells (Hurley et al., 2006). Different K^+ channels subunits have also been found to be expressed by rodent type I hair cells during postnatal development which may account for the above changes (Hurley et al., 2006; Spitzmaul et al., 2013).

Following the positive identification of the patched hair cell as type I, a small inward current (**Figure 3A**, upper panel) became visible when superfusing the cells with an extracellular solution containing the K^+ channel blockers TEA and 4AP, in the presence of 5 mM Ca^{2+} (see section "Materials and Methods"). In a subset of type I hair cells (n = 8), we found that the addition of 0.1 mM Cd^{2+} to the extracellular solution fully blocked the inward current, confirming its identity as I_{Ca} (**Figure 3A**, lower panel). The isolated I_{Ca} was obtained by subtracting the current recorded in the presence of TEA, 4AP, and Cd^{2+} to that obtained in the absence of Cd^{2+} (**Figure 3B**). Under this experimental condition, the inward current activated at about −61 mV and peaked near −21 mV (**Figures 3B,D**). Comparable results were obtained when I_{Ca} was isolated by performing the leakage-subtraction procedure (see section "Materials and Methods") to the currents recorded in TEA and 4AP (**Figures 3C,D**).

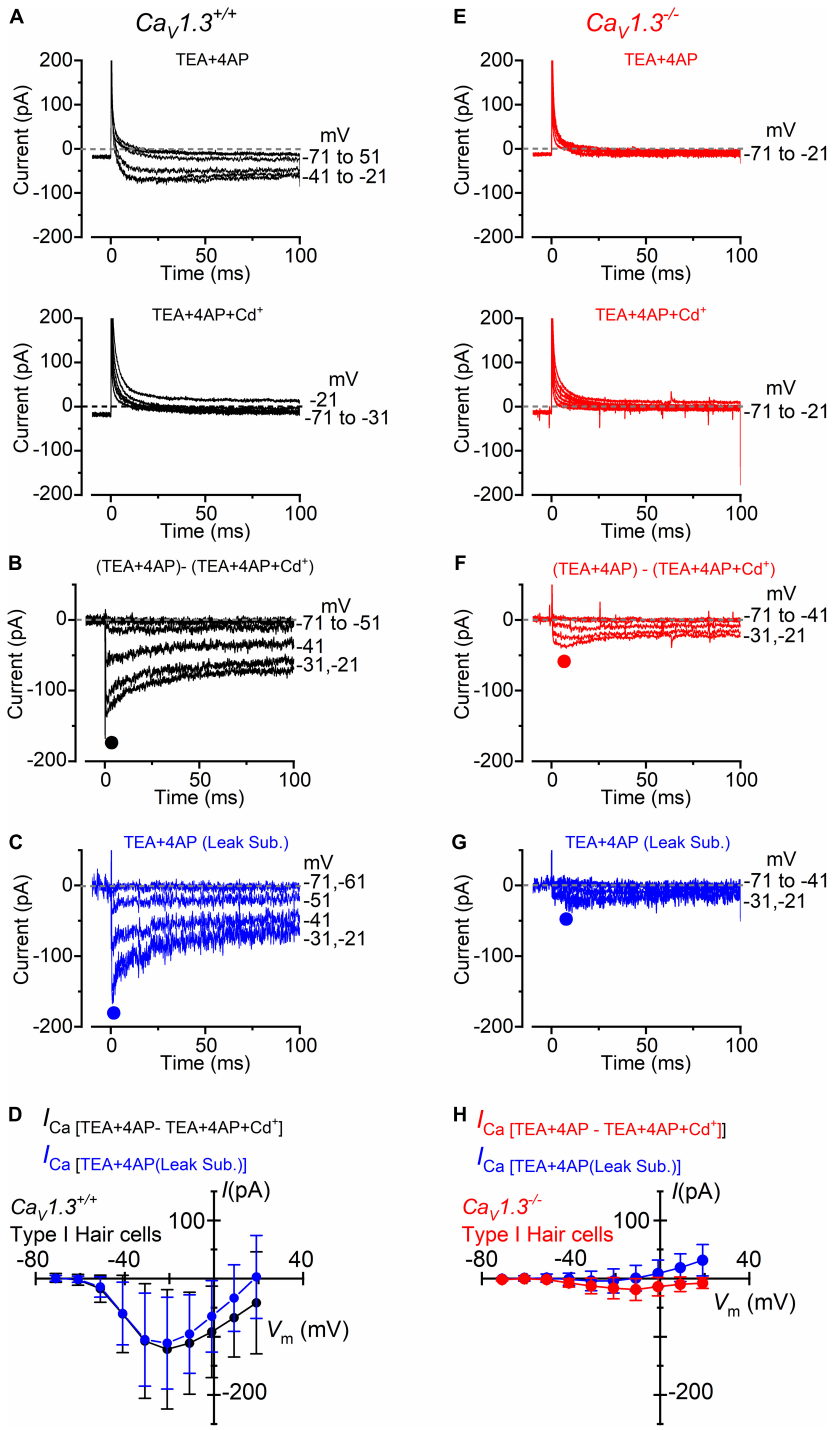

FIGURE 3 | Calcium currents in type I crista hair cells from wild-type and $Ca_V1.3^{-/-}$ mice. **(A)** Upper panel: current recorded from a type I hair cell of a wild-type mouse (P5) in the presence of 30 mM TEA and 15 mM 4AP in the extracellular solution and Cs^+ as the main ion carrier in the intracellular solution. Currents were elicited by 100 ms depolarizing voltage steps of 10 mV nominal increment (holding potential of −91 mV). For clarity, only a few test potentials are shown. Lower panel: current recorded from the same cell and solution shown in the top panel but with the additional 0.1 mM Cd^{2+} (Ca^{2+} channel blocker). **(B)** Inward Ca^{2+} current from the same wild-type hair cell shown in panel **(A)** obtained by subtracting the current recorded in extracellular TEA, 4AP, and 0.1 mM Cd^{2+} to that recorded in TEA and 4AP. **(C)** Inward current obtained by leakage subtraction of the current recorded from the cell in panel **(A)**, upper panel. **(D)** Peak inward *I-V* curves for the current obtained as the Cd^{2+}-sensitive current (black symbols, n = 8) or after leakage subtraction (blue symbols; n = 17). **(E–G)** Currents recorded from a type I hair cell from a $Ca_V1.3^{-/-}$ (P5) mouse obtained as described in panels **(A–C)**. **(H)** Peak inward *I-V* curves for the current obtained as the Cd^{2+}-sensitive current (red symbols, n = 10) or after leakage subtraction (blue symbols; n = 36). Values in panels **(D,H)** are shown as mean ± SD.

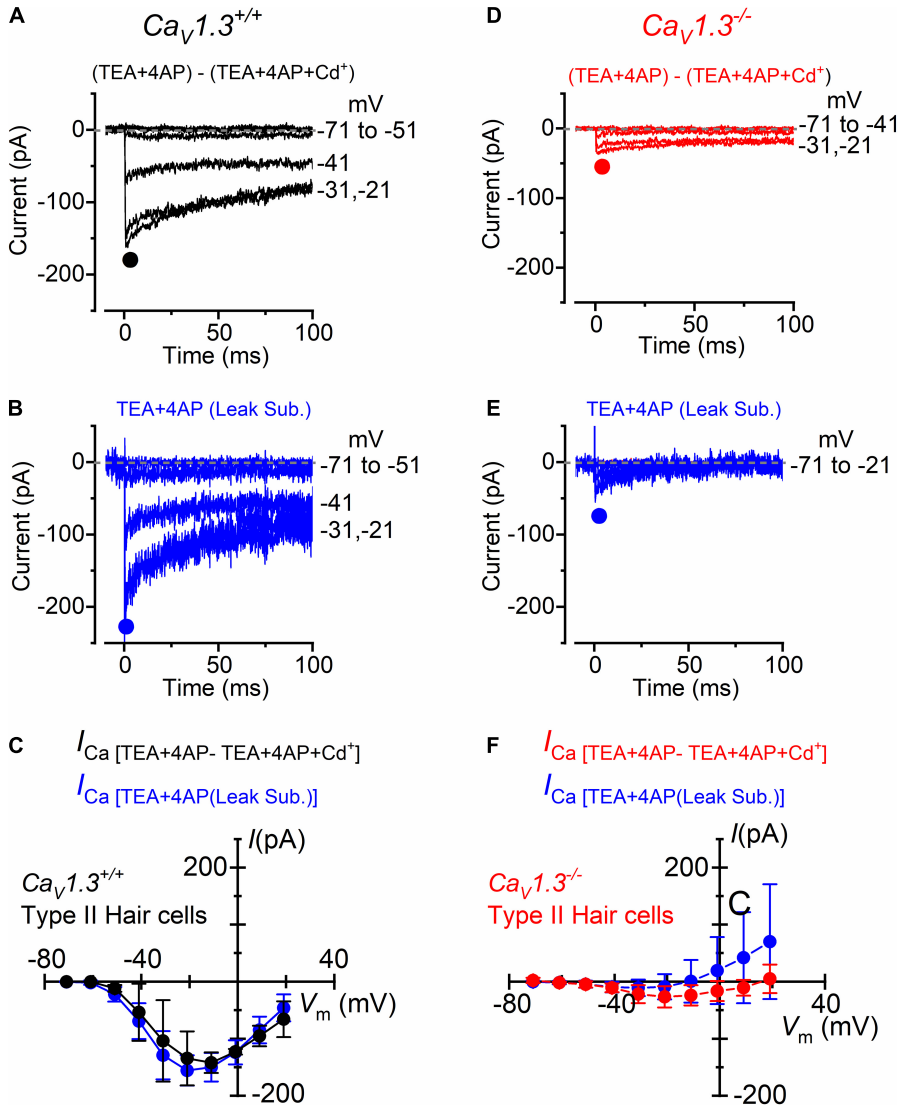

FIGURE 4 | Calcium currents in type II crista hair cells from wild-type and $Ca_V1.3^{-/-}$ mice. **(A,B)** Inward current recorded from a type II hair cell of a wild-type mouse (P5) using the same experimental conditions described in **Figures 3B,C**. For clarity, only a few test potentials are shown. **(C)** Peak inward *I-V* curves for the Cd^{2+}-sensitive current (black symbols, $n = 2$) or for the current after leakage subtraction (blue symbols; $n = 5$). **(D,E)** Inward currents recorded from a type II hair cell from a $Ca_V1.3^{-/-}$ (P5) mouse obtained as described in panels **(A,B)**. **(F)** Peak inward *I-V* curves for the current obtained as the Cd^{2+}-sensitive current (red symbols, $n = 3$) or after leakage subtraction (blue symbols; $n = 12$). Values in panels **(C,F)** are shown as mean ± SD.

In $Ca_V1.3^{-/-}$ mice, the inward current was barely visible in type I hair cells when the extracellular solution contained TEA, 4AP, and 5 mM Ca^{2+} (**Figure 3E**). Following the isolation of I_{Ca} with Cd^{2+} (**Figure 3F**), or after leakage subtraction (**Figure 3G**), it became more easily detectable. The inward current peaked near −11 mV (**Figure 3H**). In type I hair cells, the mean peak I_{Ca} after Cd^{2+}-subtraction was 121 pA in wild-type and 19 pA in $Ca_V1.3^{-/-}$ mice (15.7% of the wilt-type value).

For type II hair cells, the isolation of the Ca^{2+} current was performed as shown in **Figure 3**, using either the isolated Cd^{2+}-procedure (**Figures 4A,D**) or after leakage subtraction (**Figures 4B,E**) in both wild-type and $Ca_V1.3^{-/-}$ mice, respectively. In WT type II hair cells the amplitude of the Cd^{2+}-sensitive current (I_{Ca}: **Figures 4A,C**) was not significantly different to that obtained by leakage-subtraction (**Figures 4B,C**: $P < 0.9336$, $F = 0.3916$, DFn = 9, two-way ANOVA), or to the Cd^{2+}-sensitive current measured in wild-type type I hair cells (**Figures 3B,D**: $P < 0.8457$, two-way ANOVA). The size of the Cd^{2+}-sensitive I_{Ca} recorded in type II hair cells of $Ca_V1.3^{-/-}$ mice (**Figures 4D,F**) was very similar to that measured in type I hair cells (**Figures 3F,H**, $P < 0.7677$, $F = 0.6319$, DFn = 9, two-way ANOVA). In type II hair cells, the mean peak I_{Ca} after Cd^{2+}-subtraction was 142 pA in wild-type and 27 pA in $Ca_V1.3^{-/-}$ mice (19.0% of the wild-type value).

We tested whether the size of I_{Ca} changed with age in hair cells from wild-type and $Ca_V1.3^{-/-}$ mice. The peak I_{Ca} amplitude,

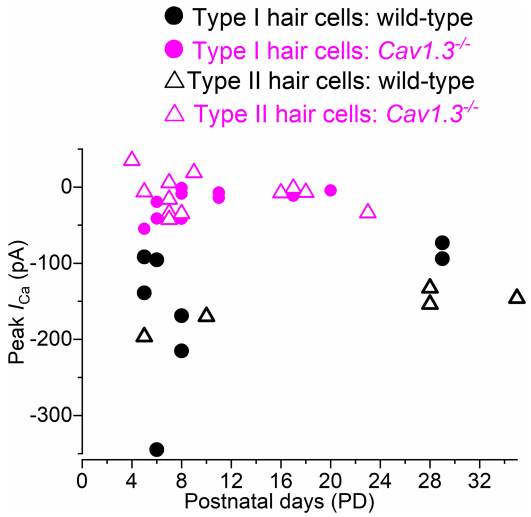

FIGURE 5 | Calcium current in type I and type II hair cells as a function of postnatal age in mice. Peak of the Ca^{2+} current measured as a function of postnatal age in type I and type II hair cells from both wild-type and $Ca_V1.3^{-/-}$ mice. Single data points are shown.

which was detected between −21 and −10 mV, was plotted as a function of postnatal day (**Figure 5**). The size of I_{Ca} in both type I and type II hair cells appears to be comparable between early and late postnatal ages in both wild-type and $Ca_V1.3^{-/-}$ mice.

Calcium Currents in the Inner Hair Cells of the Mouse Cochlea From $Ca_V1.3^{-/-}$ Mice

We investigated I_{Ca} in cochlear IHCs by performing whole-cells recordings at 32–36 °C and with the same solutions used for the above vestibular hair cell recordings (intracellular Cs^+, extracellular TEA and 4AP, and 5 mM Ca^{2+} (**Figure 6**). About 10% of the total I_{Ca} in apical IHCs has been shown to be carried by Ca^{2+} channels other than $Ca_V1.3$ (Platzer et al., 2000; Michna et al., 2003). Indeed, we found that the size of I_{Ca}, measured after leakage-subtraction, was largely reduced in IHCs from $Ca_V1.3^{-/-}$ mice compared to littermate controls at both immature ($P < 0.0001$, $F = 63.70$, DFn = 9) and adult ages (**Figure 6G**, $P < 0.0001$, $F = 20.33$, DFn = 9, between the same voltage range used for the vestibular hair cells: −61 to +29 mV, two-way ANOVA). The nature of the residual Ca^2 channels in immature (∼16% of the wild-type value) and adult (∼12%) IHCs is unknown, but previous suggestions included $Ca_V1.4$ (Brandt et al., 2003) or, in immature avian auditory hair cells, $Ca_V3.1$ T-type subunits (Levic and Dulon, 2012).

DISCUSSION

In the present study, we compared the level of expression of the Ca^{2+} current in hair cells of the crista and cochlear IHCs from wild-type and $Ca_V1.3^{-/-}$ mice. We also investigated whether the normal developmental acquisition of the mature-like K^+ current in the crista hair cells was dependent on the presence of $Ca_V1.3$ Ca^{2+} channels, as previous demonstrated for the IHCs (Brandt et al., 2003; Jeng et al., 2020a). We found that the adult-like K^+ currents in type I and type II hair cells were similarly present in both wild-type and $Ca_V1.3^{-/-}$ mice. We also showed that the IHCs and crista hair cells from $Ca_V1.3^{-/-}$ mice exhibit a residual Ca^{2+} current that was only < 20% to that of control cells (ranging between 12 and 19% depending on hair-cell type and age investigated). The data provided have highlighted some differences in the way inner ear organs regulate the development of hair cells.

It is well established that the development of IHCs and outer hair cells (OHCs) in the cochlea is tightly linked to their ability to elicit Ca^{2+} dependent action potentials during pre-hearing stages (Corns et al., 2014; Ceriani et al., 2019), where hearing onset occurs at P12 in most altricial rodents. One of the basolateral biophysical characteristics of cochlear hair cells, which is controlled by this spiking activity, is the expression of adult-like K^+ channels. Cochlear hair cells from pre-hearing $Ca_V1.3^{-/-}$ mice, which are unable to elicit Ca^{2+} action potentials retain an immature K^+ current profile even at adult stages (Brandt et al., 2003; Ceriani et al., 2019; Jeng et al., 2020a). We found that the absence of the $Ca_V1.3$ Ca^{2+} current does not, however, influence the maturation of vestibular hair cells, most likely because these cells seem not to elicit action potentials during early postnatal developmental stages.

The absence of $Ca_V1.3$ Ca^{2+} channels in both mice (Platzer et al., 2000; Dou et al., 2004) and humans (Baig et al., 2011) is associated with deafness but not visible vestibular dysfunctions. Thus, it is not clear why vestibular function is not suppressed or largely reduced by the absence of Ca^{2+}-dependent exocytosis in hair cells. Different from hearing, partial vestibular compensation may occur by other sensory systems (e.g., proprioception and vision), so that specific vestibular tests such as vestibular evoked potentials (VsEPs) are likely to be required to unveil subtle vestibular impairments (Jones and Jones, 2014). This has been previously demonstrated for another synaptic protein, otoferlin, which is expressed in both cochlear and vestibular hair cells. Otoferlin knockout mice are deaf but do not show gross vestibular dysfunction (abnormal posturing, imbalance or nystagmus; Roux et al., 2006), although subtle vestibular deficits can be unveiled by VsEPs (Dulon et al., 2009).

Similar to cochlear IHCs, type I and type II hair cells from the crista of $Ca_V1.3^{-/-}$ mice exhibit a small (<20%) residual Ca^{2+} current, indicating that the $Ca_V1.3$ subunit carries the large majority of the current. This result differs from a previous study performed on early postnatal hair cells from the utricle of $Ca_V1.3^{-/-}$ mice (P1–P10: Dou et al., 2004), which exhibit a much larger (about 50%) residual inward Ba^{2+} current through voltage-gated Ca^{2+} channels. It is unlikely that age difference among studies is the reason for this discrepancy because we observed a similar residual Ca^{2+} current in both neonatal and adult vestibular hair cells from $Ca_V1.3^{-/-}$ mice.

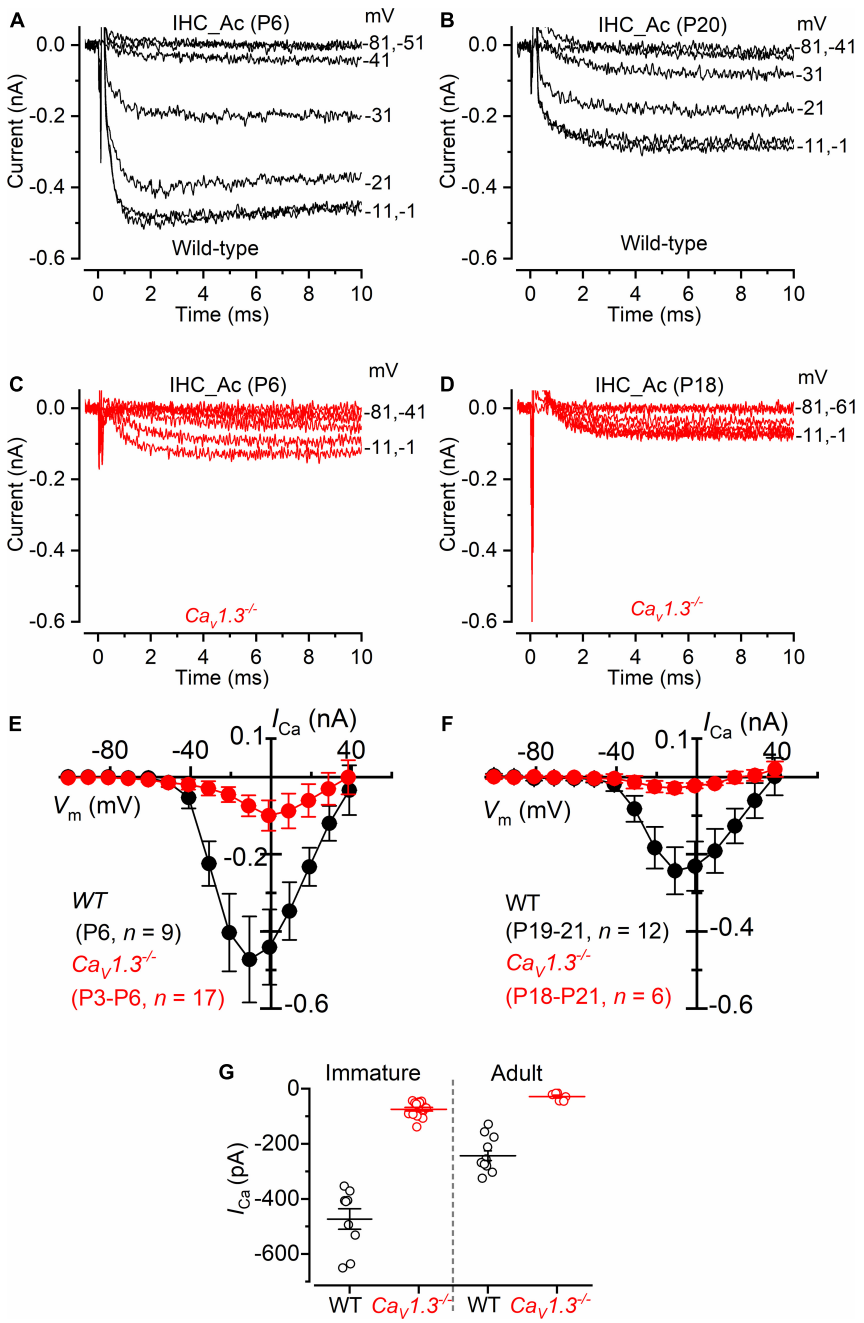

FIGURE 6 | Calcium currents in IHCs from $Ca_V1.3^{-/-}$ mice. **(A,B)** Calcium currents recorded from immature [**(A)**, P6] and adult [**(B)**, P20] IHCs of wild-type mice. Currents were elicited by depolarizing voltage steps of 10 mV increments (10 ms in duration) starting from the holding potential of −81 mV. **(C,D)** Calcium currents from immature [**(C),** P6] and adult [**(D)**, P18] IHCs of $Ca_V1.3^{-/-}$ mice. For clarity, in panels **(A–D)** only some of the traces are shown. Actual test potentials, corrected for voltage drop across uncompensated R_s, are shown next to the traces. **(E,F),** *I-V* curves for the inward Ca^{2+} current in immature **(E)** and adult **(F)** IHCs from both wild-type and $Ca_V1.3^{-/-}$ mice. **(G)** Peak Ca^{2+} current in both genotypes at immature and adult IHCs. One-way ANOVA (overall: $P < 0.0001$, $F = 98.98$, DFn = 43) Tukey's post-test analysis: wild-type immature (−473 ± 112 pA, $n = 9$) vs. $Ca_V1.3^{-/-}$ immature (−74 ± 27 pA, $n = 17$), $P < 0.0001$; wild-type adult (−243 ± 61 pA, $n = 12$) vs. $Ca_V1.3^{-/-}$ adult (−28 ± 14 pA, $n = 6$), $P < 0.001$; wild-type immature vs. wild-type adult, $P < 0.001$; wild-type immature vs. $Ca_V1.3^{-/-}$ adult, $P < 0.001$; $Ca_V1.3^{-/-}$ immature vs. wild-type adult, $P < 0.001$; $Ca_V1.3^{-/-}$ immature vs. $Ca_V1.3^{-/-}$ adult, $P > 0.05$. Data are reported as mean ± SD.

An alternative explanation is that the expression level of the $Ca_V1.3$ subunit is different between utricle and crista hair cells. In principle, the residual Ca^{2+} current in some type I and type II vestibular hair cells could at least in part reduce the vestibular phenotype in $Ca_V1.3^{-/-}$ mice, provided that the remaining Ca^{2+} channels are capable of driving

some exocytosis. An attractive possibility for the absence of vestibular phenotypes in $Ca_V1.3^{-/-}$ mice, however, is likely to be associated with the presence of non-quantal synaptic transmission in vestibular type I hair cells, but not cochlear IHCs (Yamashita and Ohmori, 1990; Holt et al., 2007; Songer and Eatock, 2013). This non-conventional, K^+-based synaptic transmission relays on intercellular K^+ increase in the extended narrow synaptic cleft between the basolateral membrane of type I hair cells and the inner face of the afferent calyx terminal (Lim et al., 2011; Contini et al., 2012, 2017; Spaiardi et al., 2020a) and fast, direct resistive coupling between pre- and postsynaptic K^+ channels facing the synaptic cleft (Contini et al., 2020). $I_{K,L}$, which is normally present in $Ca_V1.3^{-/-}$ mice, plays a major role in this K^+-based signal transmission at the calyx synapse (Eatock, 2018). Indeed, we found that intercellular K^+ increase still occurs in $Ca_V1.3^{-/-}$ mice (**Figure 1**), suggesting that calyces develop normally around the type I hair cell basolateral membrane. Non-synaptic activation of the calyx has also been described during the mechanical deflection of the hair bundle of the type I hair cells (Songer and Eatock, 2013). The presence of this K^+-based afferent transmission, which is unlikely to be affected in $Ca_V1.3^{-/-}$ mice, might contribute to the absence of obvious vestibular dysfunction in these mice.

DATA AVAILABILITY STATEMENT

The original contributions presented in the study are included in the article/supplementary material, further inquiries can be directed to the corresponding author/s.

ETHICS STATEMENT

The animal study was reviewed and approved by University of Sheffield Ethical Review Committee.

AUTHOR CONTRIBUTIONS

WM and SM conceived and coordinated the study. All authors helped with the collection and analysis of the data.

FUNDING

This work was supported by the BBSRC (BB/T004991/1) to WM and University of Pavia to SM.

REFERENCES

Baig, S. M., Koschak, A., Lieb, A., Gebhart, M., Dafinger, C., Nürnberg, G., et al. (2011). Loss of Ca(v)1.3 (CACNA1D) function in a human channelopathy with bradycardia and congenital deafness. *Nat. Neurosci.* 14, 77–84. doi: 10.1038/nn.2694

Bao, H., Wong, W. H., Goldberg, J. M., and Eatock, R. A. (2003). Voltage-gated calcium channel currents in type I and type II hair cells isolated from the rat crista. *J. Neurophysiol.* 90, 155–164. doi: 10.1152/jn.00244.2003

Biel, M., Wahl-Schott, C., Michalakis, S., and Zong, X. (2009). Hyperpolarization-activated cation channels: from genes to function. *Physiol. Rev.* 89, 847–885. doi: 10.1152/physrev.00029.2008

Bonsacquet, J., Brugeaud, A., Compan, V., Desmadryl, G., and Chabbert, C. (2006). AMPA type glutamate receptor mediates neurotransmission at turtle vestibular calyx synapse. *J. Physiol.* 576, 63–71. doi: 10.1113/jphysiol.2006.116467

Brandt, A., Striessnig, J., and Moser, T. (2003). CaV1.3 channels are essential for development and presynaptic activity of cochlear inner hair cells. *J. Neurosci.* 23, 10832–10840. doi: 10.1523/JNEUROSCI.23-34-10832.2003

Carlton, A. J., Halford, J., Underhill, A., Jeng, J. Y., Avenarius, M. R., Gilbert, M. L, et al. (2021). Loss of Baiap2l2 destabilizes the transducing stereocilia of cochlear hair cells and leads to deafness. *J. Physiol* 599, 1173–1198. doi: 10.1113/JP280670

Ceriani, F., Hendry, A., Jeng, J. Y., Johnson, S. L., Stephani, F., Olt, J., et al. (2019). Coordinated calcium signalling in cochlear sensory and non-sensory cells refines afferent innervation of outer hair cells. *EMBO J.* 38:e99839. doi: 10.15252/embj.201899839

Chen, J. W., and Eatock, R. A. (2000). Major potassium conductance in type I hair cells from rat semicircular canals: characterization and modulation by nitric oxide. *J. Neurophysiol.* 84, 139–151. doi: 10.1152/jn.2000.84.1.139

Contini, D., Holstein, G. R., and Art, J. J. (2020). Synaptic cleft microenvironment influences potassium permeation and synaptic transmission in hair cells surrounded by calyx afferents in the turtle. *J. Physiol.* 598, 853–889. doi: 10.1113/JP278680

Contini, D., Price, S. D., and Art, J. J. (2017). Accumulation of K+ in the synaptic cleft modulates activity by influencing both vestibular hair cell and calyx afferent in the turtle. *J. Physiol.* 595, 777–803. doi: 10.1113/JP273060

Contini, D., Zampini, V., Tavazzani, E., Magistretti, J., Russo, G., Prigioni, I., et al. (2012). Intercellular K+ accumulation depolarizes Type I vestibular hair cells and their associated afferent nerve calyx. *Neuroscience* 227, 232–246. doi: 10.1016/j.neuroscience.2012.09.051

Corns, L. F., Bardhan, T., Houston, O., Olt, J., Holley, M. C., Masetto, S., et al. (2014). "Functional development of hair cells in the mammalian inner ear," in *Development of Auditory and Vestibular Systems*, eds R. Romand and I. Varela-Nieto (, NY: Academic Press), 155–188.

Dou, H., Vazquez, A. E., Namkung, Y., Chu, H., Cardell, E. L., Nie, L., et al. (2004). Null Mutation of α1D Ca2+ channel gene results in deafness but no vestibular defect in Mice. *J. Assoc. Res. Otolaryngol.* 5, 215–226. doi: 10.1007/s10162-003-4020-3

Dulon, D., Safieddine, S., Jones, S. M., and Petit, C. (2009). Otoferlin is critical for a highly sensitive and linear calcium-dependent exocytosis at vestibular hair cell ribbon synapses. *J. Neurosci.* 29, 10474–10487. doi: 10.1523/JNEUROSCI.1009-09.2009

Eatock, R. A. (2018). Specializations for fast signaling in the amniote vestibular inner ear. *Integr. Comp. Biol.* 58, 341–350. doi: 10.1093/icb/icy069

Griguer, C., Sans, A., and Lehouelleur, J. (1993). Non-typical K(+)-current in cesium-loaded guinea pig type I vestibular hair cell. *Pfluegers Arch.* 422, 407–409. doi: 10.1007/BF00374300

Hille, B. (2001). *Ion Channels of Excitable Membranes*, 3rd Edn. Sunderland, MA: Sinauer Associates, Inc.

Holt, J. C., Chatlani, S., Lysakowski, A., and Goldberg, J. M. (2007). Quantal and nonquantal transmission in calyx-bearing fibers of the turtle posterior crista. *J. Neurophysiol.* 98, 1083–1101. doi: 10.1152/jn.00332.2007

Hurley, K. M., Gaboyard, S., Zhong, M., Price, S. D., Wooltorton, J. R., Lysakowski, A., et al. (2006). M-like K+ currents in type I hair cells and calyx afferent endings of the developing rat utricle. *J. Neurosci.* 26, 10253–10269. doi: 10.1523/JNEUROSCI.2596-06.2006

Jeng, J. Y., Carlton, A. J., Johnson, S. L., Brown, S. D. M., Holley, M. C., Bowl, M. R., et al. (2021). Biophysical and morphological changes in inner hair cells and their efferent innervation in the ageing mouse cochlea. *J. Physiol.* 599, 269–287. doi: 10.1113/JP280256

Jeng, J. Y., Ceriani, F., Hendry, A., Johnson, S. L., Yen, P., Simmons, D. D., et al. (2020a). Hair cell maturation is differentially regulated along the tonotopic axis of the mammalian cochlea. *J. Physiol.* 598, 151–170. doi: 10.1113/JP279012

Jeng, J. Y., Ceriani, F., Olt, J., Brown, S. D. M., Holley, M. C., Bowl, M. R., et al. (2020b). Pathophysiological changes in inner hair cell ribbon synapses in the ageing mammalian cochlea. *J. Physiol.* 598, 4339–4355. doi: 10.1113/JP280018

Johnson, S. L., and Marcotti, W. (2008). Biophysical properties of CaV1.3 calcium channels in gerbil inner hair cells. *J. Physiol.* 586, 1029–1042. doi: 10.1113/jphysiol.2007.145219

Jones, S. M., and Jones, T. A. (2014). Genetics of peripheral vestibular dysfunction: lessons from mutant mouse strains. *J. Am. Acad. Audiol.* 25, 289–301. doi: 10.3766/jaaa.25.3.8

Kirk, M. E., Meredith, F. L., Benke, T. A., and Rennie, K. J. (2017). AMPA receptor- mediated rapid EPSCs in vestibular calyx afferents. *J. Neurophysiol.* 17, 2312–2323. doi: 10.1152/jn.00394.2016

Koschak, A., Reimer, D., Huber, I., Grabner, M., Glossmann, H., Engel, J., et al. (2001). α1D (Cav1.3) Subunits Can Form L-type Ca2+ Channels Activating at Negative Voltages. *J. Biol. Chem.* 276, 22100–22106. doi: 10.1074/jbc.M101469200

Kros, C. J., Ruppersberg, J. P., and Rüsch, A. (1998). Expression of a potassium current in inner hair cells during development of hearing in mice. *Nature* 394, 281–284. doi: 10.1038/28401

Levic, S., and Dulon, D. (2012). The temporal characteristics of Ca2+ entry through L-type and T-type Ca2+ channels shape exocytosis efficiency in chick auditory hair cells during development. *J. Neurophysiol.* 108, 3116–3123. doi: 10.1152/jn.00555.2012

Lim, R., Kindig, A. E., Donne, S. W., Callister, R. J., and Brichta, A. M. (2011). Potassium accumulation between type I hair cells and calyx terminals in mouse crista. *Exp. Brain. Res.* 210, 607–621. doi: 10.1007/s00221-011-2592-4

Marcotti, W., Johnson, S. L., Holley, M. C., and Kros, C. J. (2003). Developmental changes in the expression of potassium currents of embryonic, neonatal and mature mouse inner hair cells. *J. Physiol.* 548, 383–400. doi: 10.1113/jphysiol.2002.034801

Meredith, F. L., and Rennie, K. J. (2016). Channeling your inner ear potassium: K(+) channels in vestibular hair cells. *Hear. Res.* 338, 40–51. doi: 10.1016/j.heares.2016.01.015

Michna, M., Knirsch, M., Hoda, J., Muenkner, S., Langer, P., Platzer, J., et al. (2003). Cav 1.3 (α1D) Ca2+ currents in neonatal outer hair cells of mice. *J. Physiol.* 553, 747–758. doi: 10.1113/jphysiol.2003.053256

Oliver, D., Knipper, M., Derst, C., and Fakler, B. (2003). Resting potential and submembrane calcium concentration of inner hair cells in the isolated mouse cochlea are set by KCNQ-type potassium channels. *J. Neurosci.* 23, 2141–2149. doi: 10.1523/JNEUROSCI.23-06-02141.2003

Pangrsic, T., Singer, J. H., and Koschak, A. (2018). Voltage-gated calcium channels: key players in sensory coding in the retina and the inner ear. *Physiol. Rev.* 98, 2063–2096. doi: 10.1152/physrev.00030.2017

Platzer, J., Engel, J., Schrott-Fischer, A., Stephan, K., Bova, S., Chen, H., et al. (2000). Congenital deafness and sinoatrial node dysfunction in mice lacking class D L-type Ca2+ channels. *Cell* 102, 89–97. doi: 10.1016/s0092-8674(00)00013-1

Rennie, K. J., and Correia, M. J. (1994). Potassium currents in mammalian and avian isolated Type I semicircular canal hair cells. *J. Neurophysiol.* 71, 317–329. doi: 10.1152/jn.1994.71.1.317

Rennie, K. J., and Correia, M. J. (2000). Effects of cationic substitutions on delayed rectifier current in type I vestibular hair cells. *J. Membr. Biol.* 173, 139–148. doi: 10.1007/s002320001015

Roux, I., Safieddine, S., Nouvian, R., Grati, M., Simmler, M. C., Bahloul, A., et al. (2006). Otoferlin, defective in a human deafness form, is essential for exocytosis at the auditory ribbon synapse. *Cell* 127, 277–289. doi: 10.1016/j.cell.2006.08.040

Rüsch, A., and Eatock, R. A. (1996). A delayed rectifier conductance in Type I hair cells of the mouse utricle. *J. Neurophysiol.* 76, 995–1004. doi: 10.1152/jn.1996.76.2.995

Sadeghi, S. G., Pyott, S. J., Yu, Z., and Glowatzki, E. (2014). Glutamatergic signaling at the vestibular hair cell calyx synapse. *J. Neurosci.* 34, 14536–14550. doi: 10.1523/JNEUROSCI.0369-13.2014

Songer, J. E., and Eatock, R. A. (2013). Tuning and timing in mammalian type I hair cells and calyceal synapses. *J. Neurosci.* 33, 3706–3724. doi: 10.1523/JNEUROSCI.4067-12.2013

Spaiardi, P., Tavazzani, E., Manca, M., Milesi, V., Russo, G., Prigioni, I., et al. (2017). An allosteric gating model recapitulates the biophysical properties of IK,L expressed in mouse vestibular type I hair cells. *J. Physiol.* 595, 6735–6750. doi: 10.1113/JP274202

Spaiardi, P., Tavazzani, E., Manca, M., Russo, G., Prigioni, I., Biella, G., et al. (2020a). K+ accumulation and clearance in the calyx synaptic cleft of type i mouse vestibular hair cells. *Neuroscience* 426, 69–86. doi: 10.1016/j.neuroscience.2019.11.028

Spaiardi, P., Marcotti, W., Masetto, S., and Johnson, S. L. (2020b). Exocytosis in mouse vestibular Type II hair cells shows a high-order Ca2+ dependence that is independent of synaptotagmin-4. *Physiol. Rep.* 8:e14509. doi: 10.14814/phy2.14509

Spitzmaul, G., Tolosa, L., Winkelman, B. H. J., Heidenreich, M., Frens, M. A., Chabbert, C., et al. (2013). Vestibular role of KCNQ4 and KCNQ5 K+ channels revealed by mouse models. *J. Biol. Chem.* 288, 9334–9344. doi: 10.1074/jbc.M112.433383

Vincent, P. F. Y., Bouleau, Y., Safieddine, S., Petit, C., and Dulon, D. (2014). Exocytotic machineries of vestibular type I and cochlear ribbon synapses display similar intrinsic otoferlin-dependent Ca2+ sensitivity but a different coupling to Ca2+ channels. *J. Neurosci.* 34, 10853–10869. doi: 10.1523/JNEUROSCI.0947-14.2014

Xu, W., and Lipscombe, D. (2001). Neuronal Ca(V)1.3 alpha (1) L-type channels activate at relatively hyperpolarized membrane potentials and are incompletely inhibited by dihydropyridines. *J. Neurosci.* 21, 5944–5951. doi: 10.1523/JNEUROSCI.21-16-05944.2001

Yamashita, M., and Ohmori, H. (1990). Synaptic responses to mechanical stimulation in calyceal and bouton type vestibular afferents studied in an isolated preparation of semicircular canal ampullae of chicken. *Exp. Brain Res.* 80, 475–488. doi: 10.1007/BF00227989

Zampini, V., Johnson, S. L., Franz, C., Knipper, M., Holley, M. C., Magistretti, J., et al. (2013). Burst activity and ultrafast activation kinetics of CaV1.3 Ca^{2+} channels support presynaptic activity in adult gerbil hair cell ribbon synapses. *J. Physiol.* 591, 3811–3820. doi: 10.1113/jphysiol.2013.251272

Conflict of Interest: The authors declare that the research was conducted in the absence of any commercial or financial relationships that could be construed as a potential conflict of interest.

Publisher's Note: All claims expressed in this article are solely those of the authors and do not necessarily represent those of their affiliated organizations, or those of the publisher, the editors and the reviewers. Any product that may be evaluated in this article, or claim that may be made by its manufacturer, is not guaranteed or endorsed by the publisher.

frontiers in Neuroscience

ORIGINAL RESEARCH
published: 14 December 2021
doi: 10.3389/fnins.2021.754585

Characterizing the Access of Cholinergic Antagonists to Efferent Synapses in the Inner Ear

*Choongheon Lee[1], Anjali K. Sinha[2], Kenneth Henry[1,2], Anqi W. Walbaum[3], Peter A. Crooks[3] and Joseph C. Holt[1,2,4]**

[1] Department of Otolaryngology, University of Rochester, Rochester, NY, United States, [2] Department of Neuroscience, University of Rochester, Rochester, NY, United States, [3] Department of Pharmaceutical Sciences, College of Pharmacy, University of Arkansas for Medical Sciences, Little Rock, AR, United States, [4] Department of Pharmacology & Physiology, University of Rochester, Rochester, NY, United States

OPEN ACCESS

Edited by:
Soroush G. Sadeghi, University at Buffalo, United States

Reviewed by:
Amanda Lauer, Johns Hopkins University, United States
Juan D. Goutman, CONICET Instituto de Investigaciones en Ingeniería Genética y Biología Molecular "Dr. Héctor N. Torres" (INGEBI), Argentina

***Correspondence:**
Joseph C. Holt
joseph_holt@urmc.rochester.edu

Specialty section:
This article was submitted to Perception Science, a section of the journal Frontiers in Neuroscience

Received: *06 August 2021*
Accepted: *15 November 2021*
Published: *14 December 2021*

Citation:
Lee C, Sinha AK, Henry K, Walbaum AW, Crooks PA and Holt JC (2021) Characterizing the Access of Cholinergic Antagonists to Efferent Synapses in the Inner Ear. Front. Neurosci. 15:754585. doi: 10.3389/fnins.2021.754585

Stimulation of cholinergic efferent neurons innervating the inner ear has profound, well-characterized effects on vestibular and auditory physiology, after activating distinct ACh receptors (AChRs) on afferents and hair cells in peripheral endorgans. Efferent-mediated fast and slow excitation of vestibular afferents are mediated by α4β2*-containing nicotinic AChRs (nAChRs) and muscarinic AChRs (mAChRs), respectively. On the auditory side, efferent-mediated suppression of distortion product otoacoustic emissions (DPOAEs) is mediated by α9α10nAChRs. Previous characterization of these synaptic mechanisms utilized cholinergic drugs, that when systemically administered, also reach the CNS, which may limit their utility in probing efferent function without also considering central effects. Use of peripherally-acting cholinergic drugs with local application strategies may be useful, but this approach has remained relatively unexplored. Using multiple administration routes, we performed a combination of vestibular afferent and DPOAE recordings during efferent stimulation in mouse and turtle to determine whether charged mAChR or α9α10nAChR antagonists, with little CNS entry, can still engage efferent synaptic targets in the inner ear. The charged mAChR antagonists glycopyrrolate and methscopolamine blocked efferent-mediated slow excitation of mouse vestibular afferents following intraperitoneal, middle ear, or direct perilymphatic administration. Both mAChR antagonists were effective when delivered to the middle ear, contralateral to the side of afferent recordings, suggesting they gain vascular access after first entering the perilymphatic compartment. In contrast, charged α9α10nAChR antagonists blocked efferent-mediated suppression of DPOAEs only upon direct perilymphatic application, but failed to reach efferent synapses when systemically administered. These data show that efferent mechanisms are viable targets for further characterizing drug access in the inner ear.

Keywords: vestibular efferents, auditory efferents, nicotinic, muscarinic, mouse, DPOAE

INTRODUCTION

Efferent innervation of the mammalian inner ear begins as bilateral clusters of predominantly cholinergic neurons in several distinct nuclei within the pontomedullary regions of the brainstem. The cell bodies of vestibular and auditory efferent neurons are found in group e and the superior olivary complex, respectively (Warr, 1975; Goldberg and Fernández, 1980; Leijon and Magnusson, 2014). They give rise to axons that collect in the eighth cranial nerve on both sides and travel to the inner ear to innervate hair cells and/or primary afferents in the vestibular endorgans and cochlea (Guinan, 2006; Maison et al., 2013; Holt, 2020; Poppi et al., 2020). In both efferent systems, contralateral efferent neurons, destined to innervate the ipsilateral ear, cross the midline just below the floor of the fourth ventricle. This anatomical confluence has provided a convenient place to electrically stimulate both vestibular and auditory efferent neurons in studies that seek to characterize peripheral efferent synaptic mechanisms and how they impact inner ear function (Goldberg and Fernández, 1980; Sridhar et al., 1995; Maison et al., 2007; Schneider et al., 2021). Many inner ear efferent neurotransmitters have been identified (Guth et al., 1998; Holt et al., 2011; Sewell, 2011; Kitcher et al., 2021), but much of the pharmacology regarding electrical stimulation of inner ear efferents has demonstrated a major role for acetylcholine (ACh). Targeting these cholinergic efferent mechanisms in the inner ear are not only critical to understanding their roles in vestibular and auditory behaviors, but also offer an opportunity to characterize how different cholinergic agents access the intact inner ear.

Electrical stimulation of vestibular efferent neurons in mammals alters the excitability of primary vestibular afferents along several time scales indicating roles for multiple postsynaptic mechanisms (Goldberg and Fernández, 1980; McCue and Guinan, 1994; Marlinski et al., 2004; Schneider et al., 2021). Recent pharmacological evidence in mice has identified at least three distinct cholinergic mechanisms. Efferent-mediated slow excitation requires activation of afferent muscarinic ACh receptors (mAChRs) while efferent-mediated fast excitation depends on activation of afferent α4β2*-containing nicotinic AChRs (nAChRs) (Ramakrishna et al., 2020; Schneider et al., 2021). Efferent-mediated inhibition of vestibular afferents is thought to proceed through the sequential activation of α9α10nAChRs and SK2 potassium channels in type II vestibular hair cells (Poppi et al., 2018, 2020; Yu et al., 2020). While patch clamp recordings demonstrate that α9α10nAChRs and SK2 are widely expressed in type II hair cells, direct observations of efferent-mediated inhibition of mammalian vestibular afferents are infrequent (Goldberg and Fernández, 1980; Marlinski et al., 2004; Schneider et al., 2021). Efferent-mediated inhibition is likely obscured by contemporaneous efferent-mediated afferent excitation (Holt et al., 2015). As such, selective pharmacological blockade of the excitatory components, particularly fast excitation, is needed to unmask the underlying efferent-mediated inhibition, before confirming that α9α10nAChRs and SK2 are involved. Fortunately, an alternative and reliable source of efferent-mediated activation of the same inhibitory mechanism in the inner ear can be found on the auditory side. Electrical stimulation of medial olivocochlear efferent neurons also activates α9α10nAChRs and SK2 to hyperpolarize outer hair cells (OHCs). This hyperpolarization results in a robust suppression of distortion product otoacoustic emissions (DPOAEs) and compound action potentials (CAPs) (Sridhar et al., 1995; Maison et al., 2007), which could be reliably monitored to determine whether selective α9α10nAChR antagonists access the inner ear.

Many pharmacological studies characterizing the underlying cholinergic efferent receptor mechanisms in the mammalian inner ear have been carried out in anesthetized or reduced preparations (Sridhar et al., 1995; Maison et al., 2007; Poppi et al., 2018; Ramakrishna et al., 2020; Schneider et al., 2021), while insights into vestibular and auditory efferent function in behaving animals have been primarily performed in transgenic animals missing key efferent synaptic mechanisms (Lauer and May, 2011; May et al., 2011; Luebke et al., 2014; Hübner et al., 2015, 2017; Terreros et al., 2016; Clause et al., 2017; Morley et al., 2017; Tu et al., 2017; Jones et al., 2018; Wang et al., 2021). The further incorporation of pharmacological tools in probing efferent function in behaving animal models could be used to corroborate those observations in transgenic animals, provided that the drugs used are selective and their application can be restricted to the inner ear while limiting CNS entry. Drug entry into the inner ear has been modeled in part on entry of the same drugs into the CNS given some similarities between the blood–brain barrier (BBB) and the blood-labyrinth barrier (BLB) (Salt and Hirose, 2018; Salt and Plontke, 2018; Nyberg et al., 2019; Walia et al., 2021), although the BLB is thought to be more permeable than the BBB. To date, systemically-administered drugs used to block inner ear efferent mechanisms in mammals, including atropine, scopolamine, dihydro-β-erythroidine, and strychnine (Maison et al., 2007; Schneider et al., 2021), are all small-molecular weight tertiary amines that also cross the BBB. Alternatively, some selective cholinergic antagonists have charged quaternary ammonium heads which can significantly limit their access into the CNS, but details about whether they can access the inner ear are unknown. Previous experiments using the ionic tracer trimethylphenylammonium (TMPA) or the biscationic AMPA receptor blockers IEM1460 and IEM1925 reveal that some positively-charged substances can enter the ear upon systemic administration (Mikulec et al., 2009; Walia et al., 2021). While the IEM compounds retain key physiochemical properties that favor CNS entry, TMPA does not (Daina et al., 2017). This begs the question as to whether charged cholinergic drugs, particularly those that exhibit little to no BBB permeability, can also travel to the inner ear.

In this study, using different drug administration routes, we utilized a combination of vestibular afferent and DPOAE recordings during electrical stimulation of vestibular and auditory efferent neurons, before and after the administration of charged mAChR and α9α10nAChR antagonists with limited BBB permeability. Our pharmacological data reveal that charged mAChR antagonists access the inner ear independent of the administration route and can move from one ear to the other, while the charged α9α10nAChR antagonists appear effective only when injected directly into the perilymphatic compartment.

Charge, structure, and size of the drug molecules likely contribute to their relative access among the various compartments.

MATERIALS AND METHODS

Animals

All animal procedures were performed in accordance with NIH's Guide for the Care and Use of Laboratory Animals, and approved by the University Committee for Animal Resources (UCAR) at the University of Rochester Medical Center (URMC). Mice: Both sexes of C57BL/6 mice (Jackson Laboratory), weighing 20–30 g, and aged 49–180 days were housed in a one-way room with a standard 12-h light:dark cycle and free access to food and water. Turtle: Both sexes of Red-eared slider turtles (*Trachemys scripta elegans,* 100–500 g, ∼7–18 cm carapace length) were obtained from Cyr Biology Company (Ponchatoula, LA, United States). They were group-housed in large polycarbonate tanks with running water, basking structures, heat lamps, and 12-h light:dark cycle.

Mouse Preparation

Details of our mouse preparation were previously published (Schneider et al., 2021). Briefly, mice were deeply anesthetized with (IP) urethane (1.6 g/kg) and xylazine (20 mg/kg). Heart rate was continuously monitored using a 3-lead EKG and body temperature (∼36.5-37.5°C) was maintained using a homeothermic monitoring system (Harvard Apparatus). A tracheostomy was performed for intubation and mechanical ventilation at a rate of 100 bpm (model 683, Harvard Apparatus). After the head was secured in a stereotaxic frame (Stoelting), a posterior craniotomy and cerebellar aspiration were performed to expose cranial nerve VIII on the right side just before it enters the otic capsule and/or the floor of the 4th ventricle.

Turtle Preparation

Details of the turtle preparation were published previously (Holt et al., 2006, 2015, 2017). Briefly, turtles were deeply anesthetized with Euthasol (40–100 mg/kg). Once areflexic, they were decapitated and the head was split along the sagittal axis. The left half was immersed in an oxygenated artificial perilymph (AP) solution (in mM): 105 NaCl, 4 KCl, 0.8 $MgCl_2$, 2 $CaCl_2$, 25 $NaHCO_3$, 2 Na-pyruvate, 0.5 glutamine, 10 glucose, pH 7.2–7.3 during continuous bubbling with 95% O_2/5% CO_2. Much of the remaining brain in the left half-head was removed and a small opening made in the temporal bone exposed the posterior ampullary nerve with its two branches to the crista epithelium, whereby connective tissues on the nerve's surface were carefully peeled back with a fine tungsten hook. The half-head preparation, anchored into a plastic recording chamber using cyanoacrylate, was moved to the recording rig whereby the exposed posterior ampullary nerve was continuously supplied with oxygenated AP.

Afferent Recordings

Sharp microelectrodes, with impedances of 40–120 MΩ, were pulled from borosilicate glass tubing (BF150-86-10, Sutter Instrument), filled with 3 M KCl, and inserted into an electrode sleeve connected to a single axis motorized micromanipulator (IVM, Scientifica). After connecting to a preamplifier headstage (Biomedical Engineering, Thornwood, NY, United States), microelectrodes were lowered into the superior division of nerve VIII in mouse or the posterior crista nerve of turtle to record extracellular spike activity from spontaneously-discharging vestibular afferents. Afferent signals were low-pass filtered (1 kHz, four-pole Bessel; Wavetek), sampled at 10 kHz, and recorded using in-house acquisition scripts in Spike2 (Cambridge Electronic Design) on a PC with a micro1401 interface. Spike2 data files, exported as general text files, were processed with custom macros in IgorPro 8.02 (WaveMetrics). Afferent discharge in mice and turtle was classified according to CV*, a normalized measurement of discharge regularity (Brichta and Goldberg, 2000a; Schneider et al., 2021). Mouse afferents were classified as regularly-discharging when CV* < 0.1, while afferents with CV* > 0.1 were classified as irregularly-discharging. A total of 58 mice and 16 turtles were used for afferent recordings in this study.

Distortion Product Otoacoustic Emissions

Stimulus components F1 (10 KHz) and F2 (12 KHz) were presented independently using separate Etymotic ER2 earphones coupled to the ear canal through a 3-mm tip and an ER10-B+ low-noise microphone system. F1 and F2 were generated with 16-bit resolution on two analog output channels of a data acquisition card (PCIe-6251; National Instruments) and scaled to the desired level with two programmable attenuators (PA5; Tucker Davis Technologies). F1 level ranged 40–70 dB SPL with F2 always 10 dB $<$ F1. Two headphone drivers (−27 dB gain; HB7; Tucker Davis Technologies) powered the earphones. Microphone output was amplified (40 dB gain; ER10-B+) and sampled using the same data acquisition card. Sampling frequencies of analog I/O were 50 kHz. DPOAE recordings were controlled with custom programs written in MATLAB (The MathWorks). F1/F2 stimuli were presented every 2.3 s (2.05 s w/0.025-s cosine-squared onset/offset ramps and 0.25 s of silence). DPOAE amplitudes were measured during the unramped period by first dividing the sampled microphone input into four 0.5 s segments and then averaged to reduce noise levels. DPOAE amplitude (dB SPL) and noise level were calculated from the Fourier transform of the average response at 2*F1 – F2. Noise level was estimated from subtracting the average responses of segments 1 and 3 from segments two and four. The stimulus frequencies and levels used in this study are typically associated with a 5–15 dB suppression of DPOAEs during efferent stimulation and thought to target some of the peak efferent innervation densities along the outer hair cell region (Maison et al., 2003, 2007). A total of 44 mice were used for DPOAE recordings in this study.

Efferent Stimulation

In mice, a platinum-iridium rake of four separate electrodes was lowered into the floor of the 4th ventricle along the midline and just caudal to the facial colliculi (Schneider et al., 2021). At this location, the same electrode configuration can stimulate both medial olivocochlear efferents and contralateral vestibular efferents crossing over to innervate the contralateral ear. To

stimulate efferent neurons in turtle, the tip of one Teflon-coated silver/silver chloride wire (AG10T; Medwire, Mt. Vernon, NY, United States) was placed on the cross-bridge, a small nerve bundle of predominantly efferent fibers connecting the anterior and posterior divisions of the VIIIth nerve (Fayyazuddin et al., 1991), while a second electrode was placed on nearby bone. For both preparations, efferent stimuli were produced using laboratory-designed Spike2 scripts on a PC where TTL pulses from a digital-output port of a micro1401 interface (Cambridge Electronic Design) triggered a stimulus isolator (model A360; World Precision Instruments, Sarasota, FL, United States) to deliver current pulses to efferent electrodes. In all preparations, electrical stimuli consisted of trains of 100–150 μs constant-current shock pulses delivered from the stimulus isolator to any single electrode pairs. We varied the amplitude of shock pulses to determine the threshold (T, 20–50 μA) and maxima (75–800 μA) that elicited robust suppression of DPOAEs or afferent responses without antidromic activation. Shock trains consisted of 20 shocks at 200/s in turtle, 333 shocks/s for 5 s for mouse vestibular afferent recordings, and 200 shocks/s for 70 s for mouse DPOAE recordings. Inter-trial intervals between successive shock trains were 3–5, 60–75, and 250–350 s for the three preparations, respectively. These intervals were needed for efferent-mediated responses to return to baseline values before the arrival of the next shock train.

Efferent shock artifacts were canceled off-line after computing an average artifact and subtracting it from corresponding records. Mean afferent or DPOAE responses to efferent stimulation were calculated by averaging 3–25 trials during each experimental condition. Shock train start was always set to $t = 0$ and spike times or DPOAE amplitude measurements were specified for each trial starting at 0.5–40 seconds before the efferent shock train and ending at 0.5–40 seconds before the next efferent shock train. Responses to successive efferent shock trains were also displayed as continuous response graphs to capture the succession of sequential shock trains and reveal the serial effects of a particular treatment. As a function of efferent stimulation paradigms and the resulting kinetics of different efferent-mediated responses, response amplitudes were measured from different time segments in each species in accordance with previously published work (Brichta and Goldberg, 2000b; Maison et al., 2007; Holt et al., 2015; Schneider et al., 2021). For turtle vestibular afferent recordings, the mean amplitude of efferent-mediated inhibition or excitation was calculated from the first 100-ms segment of the average response histogram immediately following the efferent shock train. In mice, mean peak amplitude of efferent-mediated fast excitation was tabulated from the first 500-ms segment of the average response histogram starting at $t = 0$ s. The mean peak amplitude of efferent-mediated slow excitation was computed from a 1-s segment at $t = 6$–7 s, a region typically including the maximum efferent-mediated slow excitation but excluding any efferent-mediated fast excitation. Finally, in the mice DPOAE recordings, measurements of peak efferent-mediated DPOAE suppression were taken from the minimal DPOAE amplitude observed during the first 10 s of the efferent stimulus for each average response under control conditions. Subsequent measures of efferent-mediated suppression of DPOAE amplitude during drug administration were measured using the same time point as the respective control records. To avoid contamination by efferent-mediated suppression, the mean amplitude of the efferent-mediated slow enhancement was calculated from the range of DPOAE values taken at 140–155 s after shock-train onset. All reported mean response amplitudes include a subtraction of mean prestimulus background discharge rates or DPOAE amplitudes taken from the 0.5–10 s of the prestimulus period ($t = -40$ to 0).

Drug Administration

Afferent or DPOAE responses to efferent stimulation were acquired before, during, and after the administration of pharmacological agents. In turtle, drugs were prepared in turtle Ringers and administered directly to the neuroepithelium using a gravity-fed, multibarrel pipette. In mice, administration routes included intraperitoneal (IP) injection, delivery into the middle ear space using an intrabulla (IB) approach, or direct perilymphatic delivery via an intracanal (IC) approach through the posterior canal. For the IB approach, we first made a small incision behind the right pinna and then retracted the underlying muscles to identify the posterior bulla. We made a small opening in the otic bulla using a 30-G needle where we inserted the pulled 50–200 μm tip of a plastic 1-ml syringe and then sealed with cyanoacrylate glue. We elected to use an IB route over an intratympanic route as it permitted a bottom-up approach to completely fill the middle ear and submerge the round/oval window without having to contend with residual air pockets that could alter drug movement into the inner ear. The IB route also avoided damage to the tympanic membrane, associated middle ear ossicles, and linkage to the oval window.

The IC approach to access the mouse inner ear has been described (Suzuki et al., 2017; Isgrig and Chien, 2018; Talaei et al., 2019). In short, a postauricular incision behind the ear was made with a micro-scissors and the muscles underlying the temporal bone were separated and retracted, exposing the bony wall of the posterior semicircular canal. In preparation for fenestration of the bony surface, the mucosa was removed and the area was dried with a soft cotton tip. A small area on the posterior semicircular canal was fenestrated (∼150 to 200 μm diameter) with a myringotomy blade (Beaver-Visitec). The perfused solutions for IC administration were prepared in mouse artificial perilymph (in mM: 150 NaCl, 4 KCl, 8 Na2HPO4, 2 NaH2PO4, 1.5 CaCl2, 1 MgCl2, and 10 glucose; pH 7.4). The selected solution was loaded into a 10-μl gastight Hamilton syringe that was connected to a customized polypropylene tube (OD ∼100–120 μm). The distal end of the polypropylene tube was inserted and sealed into the posterior canal with a thin layer of cyanoacrylate glue (Permabond) to prevent leakage of perilymph. The sealed surface was monitored for more than 15 min to confirm that there was no obvious fluid leakage. Typically, a total volume of 1–2 μL was manually delivered into the perilymph over ∼30–60 s at an approximate perfusion rate of ∼33 nL/s. In some cases, multiple IC injections were given in the same animal.

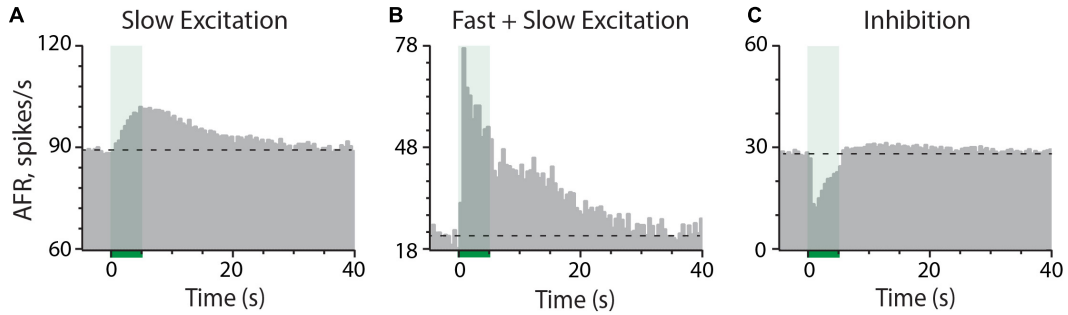

FIGURE 1 | Electrical stimulation of vestibular efferent neurons can elicit three distinct effects on afferent discharge including **(A)** slow excitation, **(B)** combined fast and slow excitation, and **(C)** inhibition. In **(A–C)**, an average response histogram to 7, 6, and 8 efferent shock trains (each 333 shocks/s for 5 s, green column at t = 0–5 s) were constructed for the three different afferents, respectively, from three different animals. Dashed horizontal lines represent the prestimulus baseline afferent firing rate. Binning in all panels is 500 ms.

Drugs Used

The neuromuscular blocker *d*-tubocurarine (dTC, 0.625 mg/kg, IP) was used to suppress muscle contractions occasionally seen with brainstem stimulation. Experimental drugs used in this study included the mAChR antagonists glycopyrrolate (GLY) and methscopolamine (MSC) as well as the α9α10nAChR antagonists strychnine (STR), Cmpd7a (aka ZZ1-61c), Cmpd10c (aka GZ556A), and Cmpd11e (aka ZZ204G). IP doses were as follows: (1) A dose of 2 mg/kg for GLY and MSC was selected in order to compare their effectiveness in this preparation to previously characterized mAChR antagonists (i.e., atropine and scopolamine) (Schneider et al., 2021); (2) The dose for STR (6 mg/kg) was based on previous cochlear efferent studies (Maison et al., 2007); (3) Initial doses for Cmpd7a (1–38 mg/kg), Cmpd10c (2.5–49 mg/kg), and Cmpd11e (2.5–5 mg/kg) in mice were chosen based on previous pharmacological characterization in rodents (Holtman et al., 2011; Wala et al., 2012), while higher doses were sought when lower doses failed to produce an effect; and (4) The concentration range for Cmpds 7a, 10c, and 11e (0.01–2 μM) used in turtle afferent recordings were determined from previous pharmacological characterization in *Xenopus* oocytes (Zheng et al., 2011). IB delivery of glycopyrrolate and methscopolamine typically used ∼30 μL of a 0.2 mg/ml stock for a final concentration of ∼0.5 mM for either drug. IC delivery of glycopyrrolate, Cmpd7a, Cmpd10c, Cmpd11e typically used a 1–2 μL injection volume with drug concentrations ranging from 0.3 to 5 mM. Source of drugs used in this study: Glycopyrrolate, methscopolamine (URMC pharmacy or Sigma); strychnine, dTC (Sigma); Cmpds7a (ZZ1-61c), 10c (GZ556A), and 11e (ZZ204G) were synthesized by the Crooks Lab according to Zhang et al. (2008).

Statistical Procedures

The effects of different pharmacological treatments on efferent-mediated changes in afferent discharge rate or DPOAE response amplitudes were assessed using a paired *t*-test. A one-way ANOVA was used to compare block times among different drug administration routes. One-sample *t*-test was used to evaluate if means differed from zero. All statistical analyses were done in Graph Pad-Prism (GraphPad). Values, expressed as means ± SEM, and outcome parameters including *p*-values, *F*-statistics, *t*-statistics, and effect sizes (Cohen's *d*) are reported in the text and/or figures. For paired *t*-tests, Cohen's *d* (*d*) was tabulated using the equation $d = t \div \sqrt{N}$ where *t* is the *t*-statistic and *N* is the sample size.

RESULTS

Mouse vestibular afferents exhibit multiple response components to electrical stimulation of the efferent vestibular system (EVS). The most common response, observed in nearly all afferent recordings, is an efferent-mediated slow excitation (**Figure 1A**) that takes seconds to develop and persists for tens of seconds after termination of the stimulus. The kinetics and pharmacology of this response are consistent with an efferent-mediated activation of mAChRs (Holt et al., 2017; Ramakrishna et al., 2020; Schneider et al., 2021). The second most common response, seen in approximately one-third of our afferent recordings, is an efferent-mediated fast excitation with peak amplitudes ranging from 5 to 75 spikes/s. Efferent-mediated fast excitation peaks within the first 500-ms of the stimulus and quickly returns to baseline upon stimulus termination (**Figure 1B**). While it can occur in isolation, efferent-mediated fast excitation, as the example shows, typically develops in tandem with efferent-mediated slow excitation. The kinetics and pharmacology of efferent-mediated fast excitation are in line with the activation of α4β2*nAChR (Holt et al., 2015; Schneider et al., 2021). Lastly, in less than 1% of our afferent recordings, an efferent-mediated fast inhibition is observed (**Figure 1C**). Similar to efferent-mediated fast excitation, the kinetics of efferent-mediated inhibition closely follow the onset and termination of the efferent stimulus. Given its infrequent observations in mouse, the pharmacology of efferent-mediated inhibition of vestibular afferents has not been well characterized. However, its similarity with efferent-mediated afferent inhibition in other vestibular preparations suggests it is mediated by the activation of α9α10nAChRs and SK potassium channels in type II hair cells (Sugai et al., 1992; Holt et al., 2001, 2015; Parks et al., 2017). Patch clamp recordings confirm that both

components are present in mouse type II vestibular hair cells (Poppi et al., 2018, 2020; Yu et al., 2020), but it has not been pharmacologically confirmed in afferent recordings during efferent stimulation. The prevalence of α9α10nAChRs in mouse type II hair cells suggests that efferent-mediated inhibition should be more common, but it may be obscured in many of our afferent recordings after summating with the ongoing efferent-mediated fast and slow excitation. During the prestimulus time domain where the three efferent-mediated responses can overlap, selective cholinergic blockers would be helpful in isolating each EVS-activated mechanism.

Drug Access and Charged mAChR Antagonists

Understanding what cholinergic drugs can actually reach the intact inner ear and their resulting dose-response relationships will be key in isolating specific efferent synaptic mechanisms as well as probing the potential functional roles that each of these mechanisms play in vestibular-related behaviors. Previously-characterized cholinergic drugs, when administered systemically (IP), are known to enter the CNS and also block EVS-mediated responses in the ear (Schneider et al., 2021). In the current study, in what was intended to be a negative control, we sought to determine whether the inverse would be true. Would cholinergic drugs, having little to no CNS entry, fail to enter the inner ear to block EVS-mediated afferent responses?

Intraperitoneal Administration of Charged mAChR Antagonists

To test this idea, we first characterized extracellular spike responses of mouse vestibular afferents during EVS stimulation before and after the systemic administration of the peripherally-acting mAChR antagonist glycopyrrolate (**Figures 2A–D**). Glycopyrrolate has a singly-charged, quaternary ammonium head (**Figure 2B**), which significantly limits its ability to cross the BBB (Proakis and Harris, 1978; Kaila et al., 1990; Chabicovsky et al., 2019). A continuous rate histogram from a regularly-discharging vestibular afferent is shown in **Figure 2A**. Repeated electrical stimulation of vestibular efferents in the brainstem (333 shocks/s for 5 s, multiple green bars) routinely elicited an excitation characterized as slow given its time to peak and return to baseline (**Figures 2A,B**). Note the shortening of interspike intervals in raw spike traces. At the 350-s mark, glycopyrrolate (2 mg/kg) was administered via an intraperitoneal (IP) injection. Following IP glycopyrrolate (green-shaded region), the amplitude of efferent-mediated slow excitation remained relatively unchanged for another 6–7 min, but then began to exhibit some variability in subsequent trials that fell short of matching control responses. After just over 12 min post IP glycopyrrolate, efferent stimuli elicited little to no slow excitation suggesting that glycopyrrolate does in fact reach mAChRs in the inner ear. This is nearly double the 6–8 min previously observed for blockade of efferent-mediated responses by atropine, scopolamine, and DHβE (Schneider et al., 2021). Baseline discharge rates also began to fall about the same time. The average response histograms for this unit show the differences in discharge rates during baseline and peak slow excitation (**Figure 2B**), where a mean slow excitation of ∼10 spikes/s was almost completely blocked and the baseline fell by about 10 spikes/s. In ten animals, IP glycopyrrolate was tested in 10 afferents (3 regular, 7 irregular) where it significantly blocked 93% of the mean efferent-mediated slow excitation [12.1 ± 2.1 vs. 0.9 ± 0.3 spikes/s, $t(9) = 5.138$, $d = 1.625$; **Figure 2C**] and significantly reduced baseline discharge rates [47.0 ± 7.3 vs. 38.8 ± 7.7 spikes/s, $t(9) = 2.780$, $d = 0.8791$; **Figure 2D**]. Blockade of slow excitation and baseline reduction with glycopyrrolate are similar to previous observations with IP administration of the mAChR antagonists atropine and scopolamine (Schneider et al., 2021).

We were surprised that glycopyrrolate was able to make its way into the inner ear given its reported restricted access to the CNS. These observations suggested the rules governing the entry of some drugs to the ear vary from the brain, presumably-based on relative differences in blood–brain barrier (BBB) and blood-labyrinth barrier (BLB) permeability. We wondered whether such entry was applicable to other charged mAChR antagonists. To test further, we employed the use of methscopolamine, which like glycopyrrolate also has a single, positively-charged, quaternary ammonium group (**Figure 2E**), and does not readily cross the BBB (Domino and Corssen, 1967; Freedman et al., 1989; Callegari et al., 2011). Systemically-administered methscopolamine, at doses of 2–10 mg/kg, fails to block central mAChRs in a number of experimental preparations including rats (Westerberg and Corcoran, 1987; Roth et al., 1989; Dringenberg and Vanderwolf, 1996) and mice (Lamberty and Gower, 1991; Bymaster et al., 1998; Singer and Yee, 2012; Brulet et al., 2017). Like IP glycopyrrolate, similar effects on efferent-mediated slow excitation were also seen with IP methscopolamine (**Figure 2E**). In seven afferents from seven animals (2 regular, 5 irregular; **Figure 2F**), IP methscopolamine significantly blocked nearly 92% of the mean efferent-mediated slow excitation [12.3 ± 2.0 vs. 0.9 ± 0.4 spikes/s, $t(6) = 6.194$, $d = 2.529$], but unlike glycopyrrolate, there was no significant difference between mean afferent background discharge rates before and after methscopolamine [36.9 ± 9.9 vs. 33.8 ± 9.2 spikes/s, $t(6) = 1.012$; **Figure 2G**]. Blockade of efferent-mediated slow excitation by glycopyrrolate and methscopolamine indicated that some cholinergic antagonists with poor CNS penetration can enter the ear. That methscopolamine does not consistently decrease baseline activity suggests that blockade of mAChRs underlying efferent-mediated slow excitation are not always tied to decreases in baseline activity. These observations also suggest that methscopolamine may have limited access to or interactions with the mechanism(s) underlying changes in baseline discharge seen with IP glycopyrrolate. This, in turn could be related to differences in the chemical structures of these two mAChR antagonists.

Intrabullar Administration of Charged mAChR Antagonists

We next asked whether glycopyrrolate and methscopolamine might also block efferent-mediated slow excitation if they were instead delivered to the middle ear using an intrabullar (IB) route. Many drugs, when placed in the middle ear,

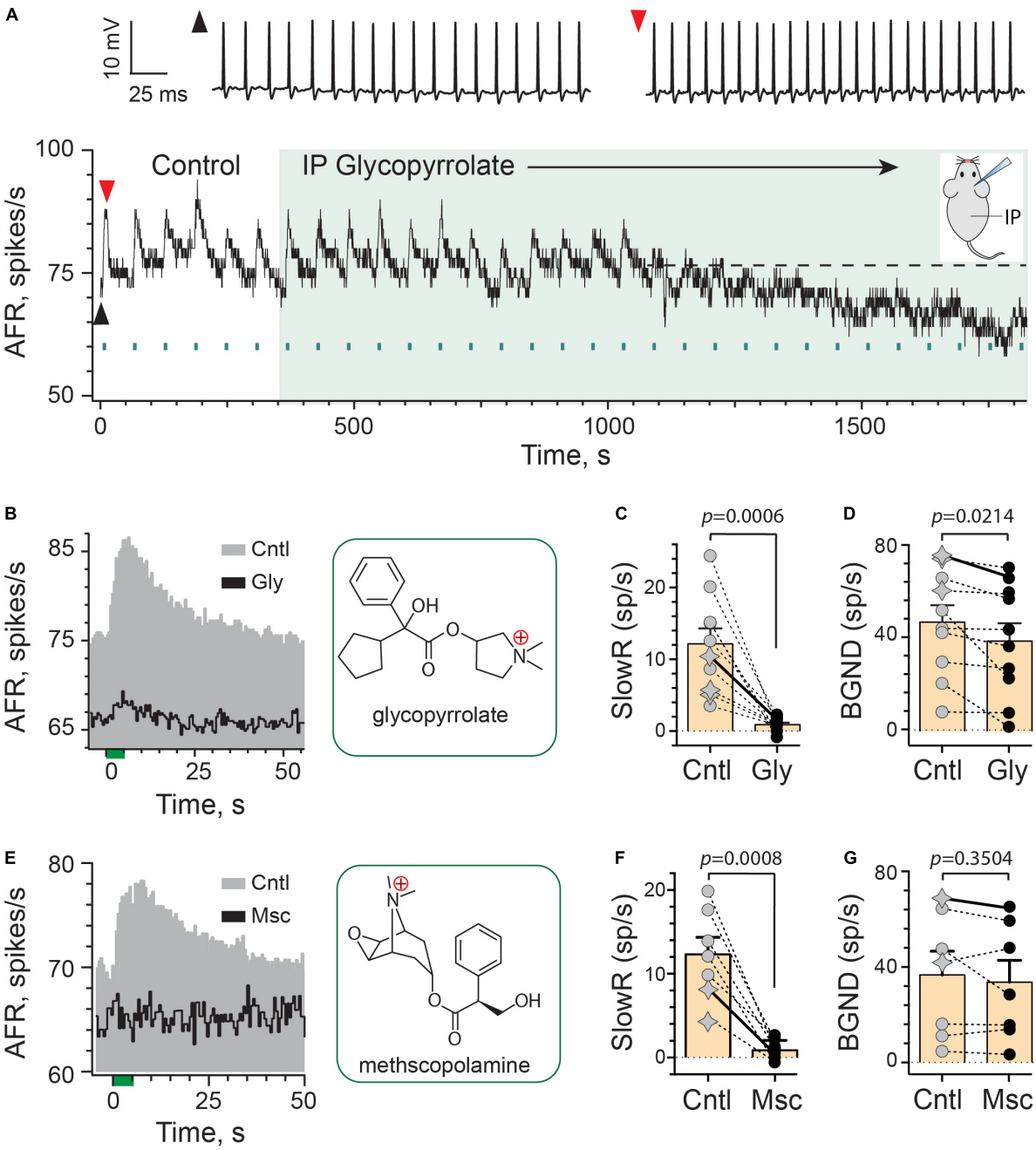

FIGURE 2 | Efferent-mediated slow excitation of vestibular afferents is antagonized by peripheral mAChR antagonists. **(A)** Continuous response histogram from a regular afferent shows changes in afferent firing rate (AFR) during midline efferent stimulation (green bars, 333/s for 5 s every 60 s) before and after administering glycopyrrolate (IP, 2 mg/kg) at t = 360 s (green box). Raw spike data from baseline (black arrowhead) and peak efferent-mediated slow excitation (red arrowhead) are shown above the histogram. Inset: mouse diagram – afferent recording from right ear during IP drug delivery. **(B)** Corresponding average response histograms from the same afferent in **(A)** were generated separately for 6 efferent shock trains during control conditions (Cntl) and 10 trials starting at t = 1,150 s during IP glycopyrrolate (Gly). Chemical structure for glycopyrrolate is shown in green box. **(C,D)** Mean peak slow excitation (SlowR) and background discharge rates (BGND) are plotted for 10 afferents from 10 animals before (Cntl, gray) and after IP glycopyrrolate (Gly, black). Star symbols and filled circles in control column indicate regular and irregular afferents, respectively. Orange bars with error bars reflect the population mean and SEM. Solid line shows values from histograms in **(B)**. Indicated p-values from paired t-test. **(E)** Average response histograms showing the effects of midline efferent stimulation in an irregular afferent before (Cntl, gray) and after IP administration of 2 mg/kg methscopolamine (Msc, black). Chemical structure for methscopolamine is shown in green box. **(F,G)** Mean peak slow excitation (SlowR) and background discharge rates (BGND) are plotted for seven afferents from seven animals before (Cntl, gray) and after IP methscopolamine (Msc, black). Orange bars with error bars reflect the population mean and SEM. Solid line shows values from histograms in **(E)**. Indicated p-values from paired t-test. Binning in **(A,B,E)** is 500 ms.

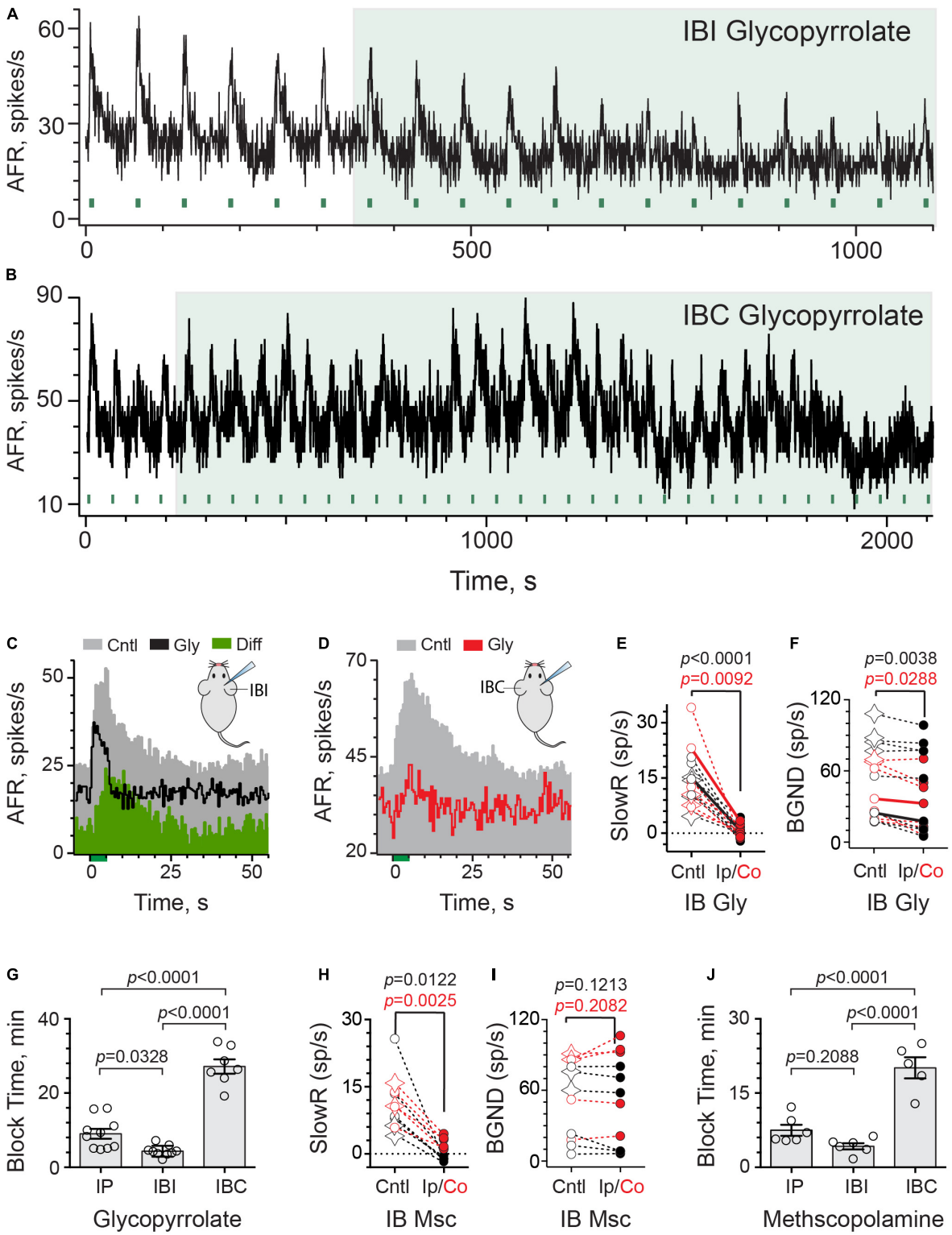

FIGURE 3 | Intrabulla application of glycopyrrolate and methscopolamine also blocks efferent-mediated slow excitation in mouse vestibular afferents. **(A)** Continuous response histogram from an irregular afferent shows changes in afferent firing rate (AFR) during midline efferent stimulation (green bars, 333/s for 5 s every 60 s) before and after the ipsilateral intrabulla delivery of glycopyrrolate (30 μl at 0.5 mM), starting at t = 360 s (green box). **(B)** Continuous response histogram from an irregular afferent shows changes in afferent firing rate (AFR) during midline efferent stimulation (green bars, 333/s for 5 s every 60 s) before and after the contralateral

(Continued)

FIGURE 3 | intrabulla delivery of glycopyrrolate (30 μl at 0.5 mM), starting at t = 220 s (green box). **(C)** Corresponding average response histograms from the same afferent in **(A)** were generated separately for 6 efferent shock trains delivered before and after block by ipsilateral IB glycopyrrolate (Gly). The afferent unit displayed both fast and slow excitation and IP glycopyrrolate blocked the slow with no change on the fast. The green difference histogram, had by subtracting the Gly trace from the Cntl trace, reveals the glycopyrrolate-sensitive slow excitation. **(D)** Corresponding average response histograms from the same afferent in **(B)** were generated separately for 23 and 5 efferent shock trains, delivered before and after block by contralateral IB glycopyrrolate (Gly), respectively. **(E,F)** Values of mean peak slow excitation and background rates, respectively, during control (Cntl) and ipsilateral IB (black, Ip) or contralateral IB glycopyrrolate (red, Co). Star symbols and filled circles in control column indicate regular and irregular afferents, respectively. Solid black and red line show values from histograms in **(C,D)**, respectively. Indicated p-values from paired t-test. **(G)** Times to maximum block for IP, IBI, and IBC glycopyrrolate are compared. Indicated p-values from one-way ANOVA. **(H,I)** Values of mean peak slow excitation and background rates, respectively, during control (cntl) and ipsilateral IB (black, Ip) or contralateral IB methscopolamine (red, Co). Star symbols and filled circles in control column indicate regular and irregular afferents, respectively. Indicated p-values from paired t-test. **(J)** Times to maximum block for IP, IBI, and IBC methscopolamine are compared. Indicated p-values from one-way ANOVA. Binning in **(A–D)** is 500 ms.

move across the round window membrane (RWM) into the perilymphatic compartment where they can directly interact with inner ear tissues (McCall et al., 2010; Salt and Hirose, 2018; Salt and Plontke, 2018; Patel et al., 2019). This approach, previously characterized for atropine and scopolamine (Schneider et al., 2021), delivers drugs to the inner ear faster than IP administration and may offer an opportunity to avoid/delay systemic off-target effects potentially including drug-mediated decreases in baseline discharge. Secondly, the IB route bypasses the BLB and previous evidence has revealed that the round window behaves as a semipermeable membrane where positively-charged molecules can cross quite easily (Goycoolea and Lundman, 1997; Goycoolea, 2001; Liu et al., 2013). To better understand how IB glycopyrrolate may enter the mouse ear and delineate local versus systemic access, we characterized both the effects of ipsilateral (IBI) and contralateral (IBC) delivery of glycopyrrolate, relative to the right side from which afferent recordings were made (**Figures 3A,B**). The continuous rate histogram in **Figure 3A** demonstrates the effects of IBI glycopyrrolate (30 μl @ 0.5 mM, large green box) on an irregularly-discharging afferent's response to repeated efferent shock trains (333 shocks/s for 5 s, green bars). In this particular example, efferent stimulation elicited both a fast and slow excitation. The efferent-mediated fast excitation can be identified as the immediate jump in firing rate at the beginning of the stimulus (**Figure 3C**, green bar at t = 0). We specifically chose this record to demonstrate that glycopyrrolate, while it completely antagonized efferent-mediated slow excitation, had little effect on efferent-mediated fast excitation. Similar pharmacological observations were made with glycopyrrolate in two other units showing both efferent-mediated fast and slow excitation. In the unit shown, the first observation that glycopyrrolate is affecting the size and shape of the efferent-mediated slow excitation is 4–5 min after drug delivery. That IBI glycopyrrolate was blocking efferent-mediated slow excitation in this example is revealed in the difference histogram (Diff), generated by subtracting the Gly histogram from the Cntl histogram. As was the case with IP glycopyrrolate, IBI glycopyrrolate also reduced background discharge.

Surprisingly, contralateral IB glycopyrrolate (IBC) also produced similar blockade of efferent-mediated slow excitation and reduction of background discharge rates (**Figures 3B,D**), but the time to these effects was much more protracted than with either IBI or IP administration. Note, in this unit, that it takes nearly 20 min before IBC glycopyrrolate begins to impact the amplitude of efferent-mediated slow excitation and reduce background discharge. This presumably reflects the time it takes for glycopyrrolate to move from the contralateral to the ipsilateral ear. These observations also indicate that the changes in response amplitude and baseline firing are related to the arrival of glycopyrrolate and not some time-dependent decline in afferent viability. In 16 animals, the effects of IB glycopyrrolate were characterized in 16 afferents (6 regular, 10 irregular; **Figure 3E**), where it significantly blocked almost 98% of efferent-slow excitation using either the IBI [13.9 ± 1.6 vs. 0.3 ± 0.6 spikes/s, $t(8) = 8.081$, $d = 2.694$] or IBC route [15.2 ± 3.8 vs. 0.4 ± 0.7 spikes/s, $t(6) = 3.782$, $d = 1.429$]. Background discharge rates (**Figure 3F**) were also significantly reduced in both IBI [55.1 ± 11.6 vs. 48.2 ± 12.4 spikes/s, $t(8) = 4.031$, $d = 1.344$] and IBC animals [43.2 ± 8.7 vs. 33.9 ± 8.9 spikes/s, $t(6) = 2.861$, $d = 1.081$].

Comparison of Block Times for Intraperitoneal and Intrabullar Routes

Our motivation to use IBC glycopyrrolate was sparked by questions about how IBI glycopyrrolate arrives in the ipsilateral perilymphatic space. Conventional thinking would suggest that, upon delivery, it moves across the round and/or oval windows into the perilymphatic fluid and then diffuses to block mAChRs in the vestibular neuroepithelium (Salt and Hirose, 2018; Salt et al., 2018b; Patel et al., 2019). Alternatively, its entry into local vascular components might also rapidly deliver it to the ear in a manner similar to IP administration, but presumably faster given its proximity. Comparable entry into the local vasculature of the contralateral ear might be expected to arrive at the ipsilateral ear after some short delay needed for delivering the drug via the bloodstream. That delay might be longer if the drug must first enter the contralateral perilymph before re-entering the systemic circulation. We reasoned that these two access scenarios (i.e., round window versus local vasculature entry) could be distinguished by determining if differences existed in arrival times to the ipsilateral ear between IBI and IBC administration. Block times for IP, IBI, and IBC glycopyrrolate were revealing in this regard (**Figure 3G**). First, consistent with previous observations with atropine and scopolamine (Schneider et al., 2021), glycopyrrolate is significantly faster when given IBI than when given via the IP route (4.3 ± 0.5 vs. 9.0 ± 1.3 min) and both IP and IBI were significantly faster than IBC (27.2 ± 1.9 min) as determined by one-way ANOVA [$F(2,23) = 77.29$, $p < 0.0001$]. The threefold difference

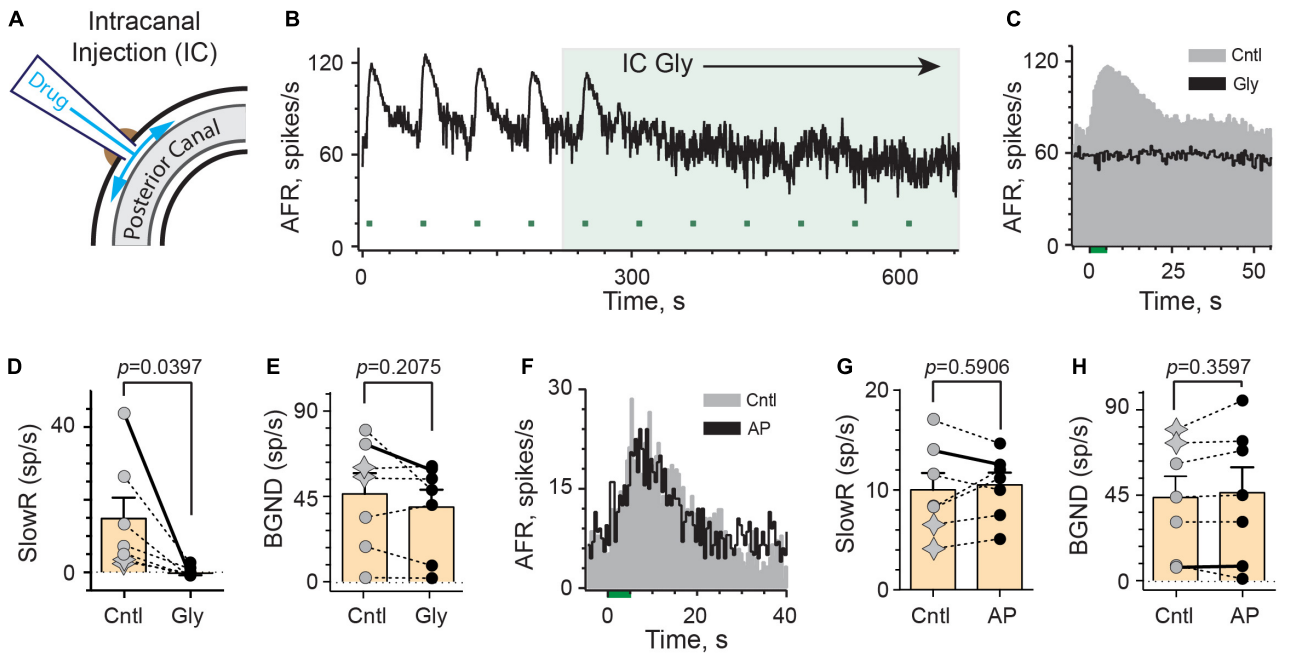

FIGURE 4 | Intracanal application of glycopyrrolate rapidly blocks efferent-mediated slow excitation in mouse vestibular afferents. **(A)** Our intracanal perilymphatic injection (IC) is made possible by inserting and sealing a small plastic tube within the bony wall of the posterior canal. When connected to a Hamilton syringe, 1–2 μl volumes can be slowly delivered to the perilymph within the posterior canal to then diffuse to the vestibule and cochlea. **(B)** Continuous response histogram from an irregular afferent shows changes in afferent firing rate (AFR) during midline efferent stimulation (green bars, 333/s for 5 s every 60 s) before and after perilymphatic injection of glycopyrrolate (1 μl at 0.5 mM) through the bony posterior canal wall. Glycopyrrolate was slow injected over 30 s starting at t = 220 s (green box). **(C)** Corresponding average response histograms from the same afferent in **(B)** were generated separately for the first four and last five efferent shock trains, delivered before (Cntl) and after IC glycopyrrolate (Gly), respectively. **(D,E)** Values of mean peak slow excitation (SlowR) and background discharge rates (BGND), respectively, during control (Cntl) and IC glycopyrrolate (Gly). Star symbols and filled circles in control column indicate regular and irregular afferents, respectively. Orange bars with error bars reflect the population mean and SEM. Solid line shows values from histograms in **(C)**. Indicated p-value from paired t-test. **(F)** Average response histograms for another afferent were generated for efferent shock trains, delivered before (Cntl) and after the IC injection of artificial perilymph (AP). Star symbols and filled circles in control column indicate regular and irregular afferents, respectively. **(G,H)** Values of mean peak slow excitation (SlowR) and background discharge rates (BGND), respectively, during control (Cntl) and IC artificial perilymph (AP). Orange bars with error bars reflect the population mean and SEM. Solid line shows values from histograms in **(F)**. Indicated p-value from paired t-test. Binning in **(B,C,F)** is 500 ms.

in block times between IBI and IBC administration is consistent with glycopyrrolate gaining direct access to the perilymphatic compartment through the round/oval windows, but the fact that IBC glycopyrrolate also reached the ipsilateral ear suggests it does eventually gain vascular access. The difference in timing may also be dependent on glycopyrrolate's effective concentration in the ipsilateral ear as a function of where it was administered. Systemic redistribution following IBC administration should result in lower glycopyrrolate concentrations reaching the ipsilateral side, which has been seen with fluorescein (Salt et al., 2018a).

Similar experiments for IB methscopolamine were performed and characterized in 11 afferents (4 regular and 7 irregular) from 11 animals (**Figures 3H,I**). IB methscopolamine significantly blocked 99% of efferent-mediated slow excitation using the IBI route [11.1 ± 3.2 vs. −0.9 ± 0.4 spikes/s, $t(5) = 3.831$, $d = 1.564$] and 77% using the IBC route [11.4 ± 1.7 vs. 2.6 ± 0.6 spikes/s, $t(4) = 6.729$, $d = 3.009$]. The effects of methscopolamine on background discharge rates, however, were neither as pronounced nor consistent as glycopyrrolate. Background rates were not significantly different before and after IBI [43.0 ± 13.4 vs. 38.8 ± 14.2 spikes/s, $t(5) = 1.864$] or IBC methscopolamine (68.6 ± 13.3 vs. 74.6 ± 15.5 spikes/s, $t(4) = 1.499$) (**Figure 3I**). Block times for IP, IBI, and IBC methscopolamine are also presented (**Figure 3J**). While block times for IP (7.5 ± 1.1 min) and IBI methscopolamine (4.2 ± 0.6 min) were not significantly different, both IP and IBI routes were shorter than IBC (19.6 ± 1.8 min) as determined using a one-way ANOVA [$F(2,15) = 39.44$, $P < 0.0001$]. Again, consistent with a direct entry into the inner ear, ipsilateral IB methscopolamine was faster than contralateral IB administration.

Despite their presumed limited access to the CNS, it is clear from the data above that methscopolamine, regardless of the route of administration or time to blockade, does not significantly impact background discharge in the same way that glycopyrrolate does. With all three administration routes (i.e., IP vs. IBI vs. IBC), glycopyrrolate significantly decreased background discharge while methscopolamine did not. With methscopolamine, the effects on background discharge were quite variable. Since mammalian efferent-mediated afferent responses are typically larger in irregularly-discharging afferents than in regularly-discharging afferents (Goldberg and Fernández, 1980; Marlinski et al., 2004; Schneider et al., 2021), it might be

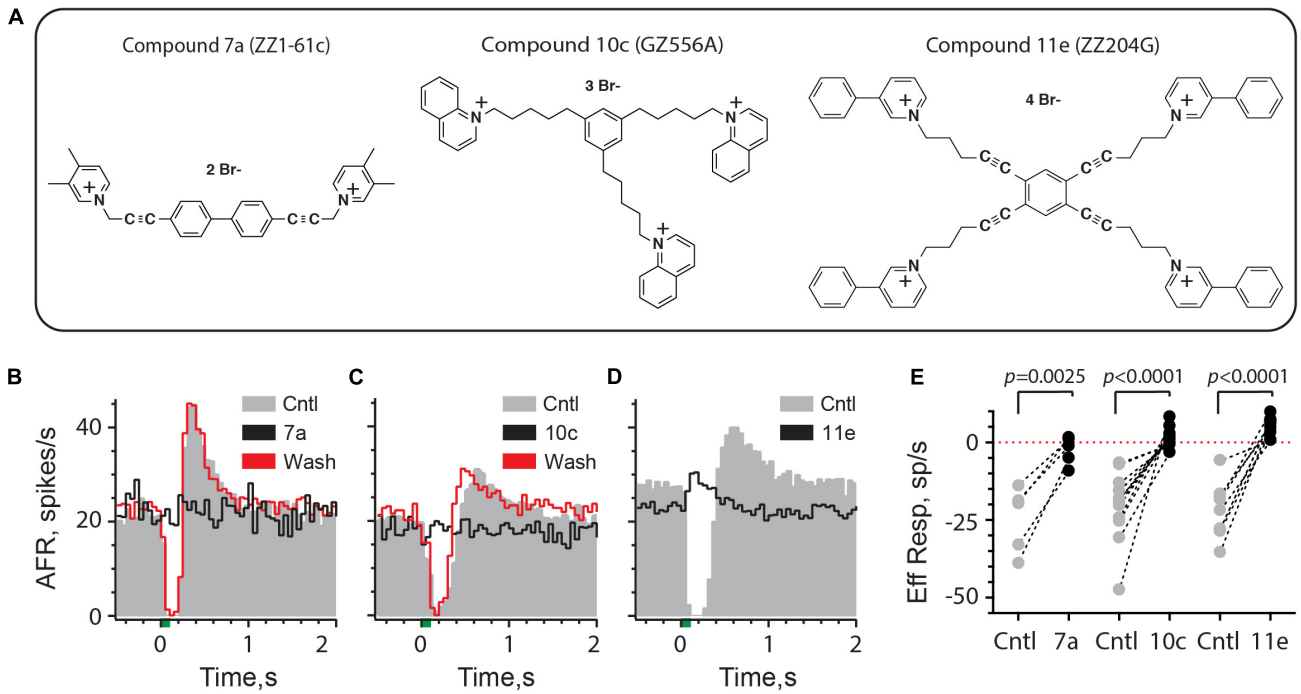

FIGURE 5 | Efferent-mediated inhibition of turtle vestibular afferents is antagonized by charged α9α10nAChR blockers. **(A)** Chemical structures of bis, tris, and tetrakis quaternary ammonium compounds 7a, 10c, and 11e are shown (see also Zheng et al., 2011). **(B–D)** Average response histograms showing the effects of efferent stimulation in turtle bouton afferents before (Cntl, gray) and during the application of Compound 7a, 10c, or 11e (Black trace), respectively. Efferent-mediated inhibition was recovered after washout (Wash, red trace) with Compounds 7a and 10c. Efferent shock trains (20 shocks at 200/s, green bar at $t = 0$) were repeated every 3 s and all histograms were based on at least 20 shock train presentations. **(E)** Mean afferent responses to efferent stimulation (Eff Resp) are plotted for multiple afferents before (Cntl, gray-filled circles) and after the application of Compound 7a, 10c, or 11e (black-filled circles). Negative values indicate inhibition while positive values reveal efferent-mediated excitatory effects. Indicated p-values from comparisons made using a paired t-test. Binning in **(B–D)** is 50 ms.

argued that the effects of mAChR antagonists on background discharge, if related to activation of the same mAChRs, might also be larger in irregular afferents and that an overrepresentation of regularly-discharging afferents in a sampling population might mask detection of significant mean differences between control and post-drug background discharge rates. As seen in **Figures 2D,G, 3F,I**, about one-third of units (15 of 44) are regularly-discharging suggesting that they are not particularly overrepresented. However, to identify if significant differences in background discharge rates exist between regular and irregular afferents following glycopyrrolate or methscopolamine, we pooled the data from all three administration routes for each drug and then separated them into regular ($CV^* < 0.1$) and irregular ($CV^* > 0.1$) groups. Pooling was justified given their significant effect (i.e., glycopyrrolate) or lack thereof (i.e., methscopolamine) on mean background discharge rates among all three administration routes. Background rates before and after glycopyrrolate were significantly different in both regular [78.0 ± 4.6 vs. 72.5 ± 4.6 spikes/s, paired t-test, $p = 0.0290$, $t(8) = 2.655$, $d = 0.9386$] and irregular afferents [33.3 ± 4.2 vs. 23.9 ± 4.3 spikes/s, paired t-test, $p = 0.0002$, $t(17) = 4.731$, $d = 1.183$], while background rates before and after methscopolamine were not significantly different in either regular [71.1 ± 7.4 vs. 73.8 ± 9.1 spikes/s, paired t-test, $p = 0.5115$, $t(7) = 0.7063$] or irregular afferents [39.2 ± 8.2 vs. 37.0 ± 8.7 spikes/s, paired t-test, $p = 0.3619$, $t(11) = 0.9349$]. These observations suggest that the different effects of glycopyrrolate and methscopolamine on an afferent's background discharge does not seem to be related to differences in discharge regularity.

Intracanal Administration of Charged mAChR Antagonists

As governed by its ability to block efferent-mediated slow excitation of vestibular afferents, glycopyrrolate and methscopolamine eventually reach the perilymphatic compartment following intraperitoneal injection or delivery into either middle ear. Glycopyrrolate also significantly reduces background discharge via IP or IB routes suggesting that it might alter afferent excitability through some peripheral mechanism. In order to confirm that these effects are specifically related to the delivery of glycopyrrolate to the inner ear, we administered the drug directly into the perilymph using an intracanal (IC) injection. After making a small hole in the wall of the bony posterior canal, the tip of a polypropylene microcannula, connected to a Hamilton syringe filled with glycopyrrolate in artificial perilymph (AP), was inserted and sealed in place using cyanoacrylate glue (**Figure 4A**). In the continuous rate histogram shown (**Figure 4B**), efferent shock trains (333 shocks/s for 5 s, multiple green bars) repeatedly elicited a large slow excitation in an irregularly-discharging

vestibular afferent. After the fourth efferent stimulus, 1 μl of glycopyrrolate (0.2 mg/ml in AP; 0.5 mM) was injected over 30 s near the 220-s mark (green-shaded box). The afferent response to the first efferent stimulus following IC glycopyrrolate was unremarkable and appears comparable to those observed during control conditions. However, by the second post-drug efferent shock train, the afferent failed to respond to efferent stimulation and efferent-mediated slow excitation remains blocked for subsequent efferent stimuli. The average response histograms demonstrate that a peak slow excitation of more than 40 spikes/s is completely blocked following the IC injection (**Figure 4C**). In seven animals, the effects of IC glycopyrrolate were characterized in seven afferents (2 regular and 5 irregular) where it significantly blocked 98% of efferent-mediated slow excitation [14.7 ± 5.7 vs. −0.3 ± 0.5 spikes/s, $t(6) = 2.617$, $d = 0.9891$] (**Figure 4D**). The mean time to block for the IC route was 2.4 ± 0.6 min which was significantly shorter than the IBI route ($p = 0.0240$, Unpaired t-test). While a baseline reduction was associated with IC glycopyrrolate in the example shown in **Figure 4B**, this effect was not consistent and there was not a significant reduction in background activity before and after glycopyrrolate across the seven units [46.0 ± 10.8 vs. 39.1 ± 9.1 spikes/s; $t(6) = 1.413$; **Figure 4E**]. Importantly, as a control measure, IC injection of artificial perilymph (AP) had little effect on efferent-mediated slow excitation (**Figure 4F**). In seven units (2 regular and 5 irregular) from four animals, IC AP had no significant effect on efferent-mediated slow excitation [9.9 ± 1.7 vs. 10.5 ± 1.2 spikes/s, $t(6) = 0.5681$; **Figure 4G**] or background discharge [43.4 ± 11.2 vs. 46.0 ± 13.3 spikes/s, $t(6) = 0.9916$; **Figure 4H**]. Collectively, these data indicate that blockade of efferent-mediated slow excitation by glycopyrrolate, regardless of administration route, is attributed to blockade of mAChRs in the inner ear.

Assessing the Entry of Quaternary Alpha9-nAChR Antagonists Into the Inner Ear

These observations suggest we may be able to identify a number of additional charged drugs with the ability to block a host of synaptic mechanisms in the inner ear without targeting similar components in the brain. We also wanted to explore if charged nAChR antagonists could be used to investigate efferent-mediated inhibition or efferent-mediated fast excitation of vestibular afferents. To this end, Zheng et al. (2007, 2011) and López-Hernández et al. (2009) have developed a series of novel *bis*-, *tris*-, and *tetrakis*-azaaromatic quaternary ammonium analogs that function as potent nAChR antagonists. On basis of potency and selectivity, three compounds, referred to as Cmpd7a, 10c, and 11e (**Figure 5A**), were shown to block α9α10nAChR-mediated responses in *Xenopus* oocytes (Zheng et al., 2011). However, their effectiveness at blocking α9α10nAChRs in the inner ear has not been characterized. In order to better understand how these analogs could be used in this regard, we asked several broad questions: (1) Are these compounds, in fact, potent inhibitors of efferent-mediated processes in the inner ear attributed to activation of α9α10nAChRs?; (2) How quickly do they block? and (3) Because Cmpd7a, 10c, and 11e possess two, three, or four quaternary ammonium heads, respectively, could they block α9α10nAChR-mediated responses in the mammalian inner ear if administered systemically, in a manner similar to blockade of mAChRs with glycopyrrolate and methscopolamine?

Charged α9α10nAChR Antagonists Block Efferent-Mediated Inhibition of Turtle Vestibular Afferents

To answer the first two questions, we first characterized the effects of Cmpd7a, 10c and 11e on efferent-mediated inhibition of vestibular afferents innervating the turtle posterior crista. This preparation is advantageous in that it allows direct drug application to the crista neuroepithelium while electrically stimulating vestibular efferent neurons, and that the pharmacology of the underlying efferent mechanisms are well understood (Holt et al., 2006, 2015, 2017; Parks et al., 2017). With direct drug access, we can also approximate minimal blocking concentrations and the length of time needed to achieve complete blockade, which are useful benchmarks for probing similar mechanisms in mice.

Efferent-mediated inhibition in turtle may be purely inhibitory or followed by a post-inhibitory excitation (PIE), but both responses are blocked by α9α10nAChR antagonists including strychnine, tropisetron, α-bungarotoxin, and α-conotoxin RgIa (Holt et al., 2006, 2015). Furthermore, PIE is mostly dependent on the preceding inhibition and will also be blocked by α9α10nAChR antagonists. Consistent with its effect on α9α10nAChRs in Xenopus oocytes (Zheng et al., 2011), superfusion of Cmpd7a, at a concentration of 100 nM, completely blocked both efferent-mediated inhibition and the subsequent PIE in a turtle afferent (**Figure 5B**). The blockade was reversible as evidenced by return of the efferent-mediated inhibition and PIE during the washout period. The effect of Cmpd7a (0.1–1 μM) was evaluated in five afferents from four animals (**Figure 5E**), where it significantly blocked 89% of efferent-mediated inhibition [−24.7 ± 4.7 vs. −2.8 ± 2.0 spikes/s, $t(4) = 6.737$, $d = 3.013$]. Similar observations in 12 afferents from 7 animals were made for Cmpd10c (**Figures 5C,E**) whose superfusion at concentrations of 0.1–1 μM significantly blocked 108% of efferent-mediated inhibition [−20.8 ± 3.2 vs. 1.6 ± 0.9 spikes/s, $t(11) = 5.922$, $d = 1.710$]. The greater than 100% blockade is a reflection of efferent-mediated fast excitation which is often unmasked after applying α9α10nAChR antagonists (Holt et al., 2015). This excitation can be identified in several units where the post-blockade values in Cmpd10c are above the zero-line indicating that the direction of the response has reversed (**Figure 5E**). Finally, consistent with previous characterization in Xenopus oocytes (Zheng et al., 2011), the most potent of the three analogs was Cmpd11e which completely blocked efferent-mediated inhibition in our preparation down to concentrations as low as 10 nM. In the example shown in **Figure 5D**, 100 nM Cmpd11e completely antagonized the inhibitory response and unmasked an efferent-mediated excitatory response. The effects of Cmpd11e (0.01–2 μM) were tested in nine afferents from 5 animals (**Figure 5E**), where it significantly blocked 122% of the efferent-mediated inhibition

[−22.5 ± 2.9 vs. 5.0 ± 1.0 spikes/s, $t(8) = 7.97$, $d = 2.657$]. Again, the unmasking of efferent-mediated excitation is reflected in the positive post-blockade values for Cmpd11e. Mean block times for 7a (11.4 ± 2.7 min), 10c (11.2 ± 1.9 min), and 11e (12.2 ± 3.1 min) were not significantly different [Kruskal–Wallis: $H(2) = 0.1054$, $P = 0.9487$). Collectively, these data demonstrate that these charged compounds are potent inhibitors of α9α10nAChRs present on vestibular type II hair cells in the turtle inner ear.

Quaternary α9α10nAChR Antagonists in the Mouse Inner Ear

We next sought to determine if Cmpd7a, 10c, and 11e could block α9α10nAChR-mediated responses in the mammalian inner ear if administered systemically. Our data with glycopyrrolate and methscopolamine indicated that the systemic administration of some charged compounds can make it to the inner ear. Although α9α10nAChRs are expressed in mammalian vestibular endorgans and their activation gives rise to hyperpolarization of type II hair cells (Poppi et al., 2018, 2020; Yu et al., 2020), direct observations of efferent-mediated inhibition of mouse vestibular afferents are infrequent (Goldberg and Fernández, 1980; Schneider et al., 2021; also see **Figure 1A**). One likely explanation is that the inhibitory component of efferent-mediated afferent responses is obscured by efferent-mediated fast excitation (Holt et al., 2015). As such, it would be experimentally challenging to identify if these quaternary α9α10nAChR antagonists, when given systemically, were in fact directly blocking α9α10nAChRs in the peripheral vestibular system.

However, a much more reliable and robust source of α9α10nAChR activation in the inner ear can be found on the auditory side. By recording distortion product otoacoustic emissions (DPOAEs) during electrical stimulation of medial olivocochlear (MOC) efferent neurons, we can probe the activation of α9α10nAChRs on outer hair cells (OHCs). Activation of MOC neurons in mice, on average, can produce a 5–15 dB peak suppression of DPOAE levels (Maison et al., 2007; Vetter et al., 2007). That this suppression is mediated by α9α10nAChRs is supported by selective pharmacological blockade, its notable absence in α9 and α10 nAChR subunit knockout mice, and enhancement in α9 gain-of-function mutants (Vetter et al., 1999, 2007; Maison et al., 2007; Taranda et al., 2009). Using a similar approach, we wanted to characterize the effects of MOC stimulation on DPOAE levels before and after the IP administration of Cmpd7a, 10c, and 11e. Under control conditions (**Figure 6A**), repeated delivery of the MOC efferent shock train (200 shock/s for 70 s, green bars) resulted in a ∼8 dB peak suppression of DPOAE levels near the onset of the efferent stimulus. Over the length of the stimulus, efferent suppression of DPOAEs exhibited variable levels of decay toward baseline and the post-stimulus period was often marked by a slow enhancement in DPOAEs levels that could persist for hundreds of seconds (**Figure 6B**). For the 44 animals used in this study, the mean efferent-mediated suppression and enhancement of DPOAEs was −11.5 ± 0.6 dB and 1.1 ± 0.2 dB, respectively.

We wanted to confirm that the observed suppression was in fact mediated by α9α10nAChRs. At the end of the third efferent shock train, a single dose of the α9α10nAChR antagonist strychnine (6 mg/kg) was delivered by IP injection where it completely blocked the efferent-mediated suppression in just under 10 min while leaving efferent-mediated slow enhancement intact (**Figures 6A,B**). IP strychnine (6 mg/kg) significantly blocked 92% of the efferent suppression [−10.8 ± 0.9 vs. −0.9 ± 0.2 dB, $t(18) = 11.57$, $d = 2.654$; **Figure 6C**] in 19 animals without significant effects on efferent-mediated slow enhancement [0.8 ± 0.2 vs. 1.3 ± 0.4 dB, paired t-test, $t(18) = 0.9489$, $p = 0.3552$; data not shown]. The waveforms associated with efferent-mediated suppression and slow enhancement of DPOAEs as well as their differential sensitivity to strychnine are consistent with previous data (Maison et al., 2007).

Using the same preparation, we then asked whether the IP administration of any of the charged α9α10nAChR antagonists would also affect efferent-mediated suppression of DPOAEs. We started with Cmpd7a which exhibits a similar blocking potency as strychnine (i.e., IC50: 16 nM vs. 20 nM, respectively) in blocking α9α10nAChRs in Xenopus oocytes (Elgoyhen et al., 2001; Zheng et al., 2011). Given equipotency, we reasoned that similar IP doses of Cmpd7a should block the efferent-mediated suppression provided that the drug can actually access the inner ear in sufficient concentrations. **Figure 6D** shows another continuous recording of DPOAEs during efferent stimulation. Efferent shock trains (200 shocks/s for 70 s, green bars) produced a ∼10 dB peak suppression. At the 10-min mark, a single IP injection of Cmpd7a (2.5 mg/kg, blue arrowhead) failed to block the suppression to the next two efferent shock trains. At that time, a second IP injection of Cmpd7a at the same dose (2nd blue arrowhead) was administered which again failed to block the efferent-mediated suppression. Ironically, the amplitude of the efferent-mediated suppression was larger, in this example, after the second dose of Cmpd7a. As a positive control, IP strychnine (6 mg/kg, red arrowhead) was administered and blocked over half the suppression by the next shock train. Mean responses are shown in **Figure 6E**. Blockade by strychnine was complete in just over 10 min post-injection, consistent with the time course in **Figure 6A**. This suggests that the effects of strychnine blockade were not accelerated by the pretreatment with Cmpd7a, which would likely be observed if Cmpd7a had any inner ear access. Given the differences in charge, molecular weight, and structure, one might posit that the fraction of Cmpd7a that enters the inner ear after IP administration is lower than that seen with strychnine. However, doses as large as 38 mg/kg with an average exposure time near 30 min failed to block the efferent-mediated suppression. In four animals, a total of six IP injections of Cmpd7a (1–38 mg/kg) had no significant effect on efferent-mediated suppression [−9.3 ± 0.9 vs. −9.8 ± 1.2 dB, $t(5) = 0.7221$; **Figure 6F**] or slow enhancement [0.8 ± 0.2 vs. 0.4 ± 0.1 dB, paired t-test, $t(5) = 1.888$, $p = 0.1177$; data not shown]. Unlike glycopyrrolate and methscopolamine, these data suggest that Cmpd7a fails to access the inner ear when administered systemically.

If the inability of Cmpd7a to find its way into the perilymphatic compartment is attributed to its two quaternary ammonium heads, then the other charged analogs will likely be

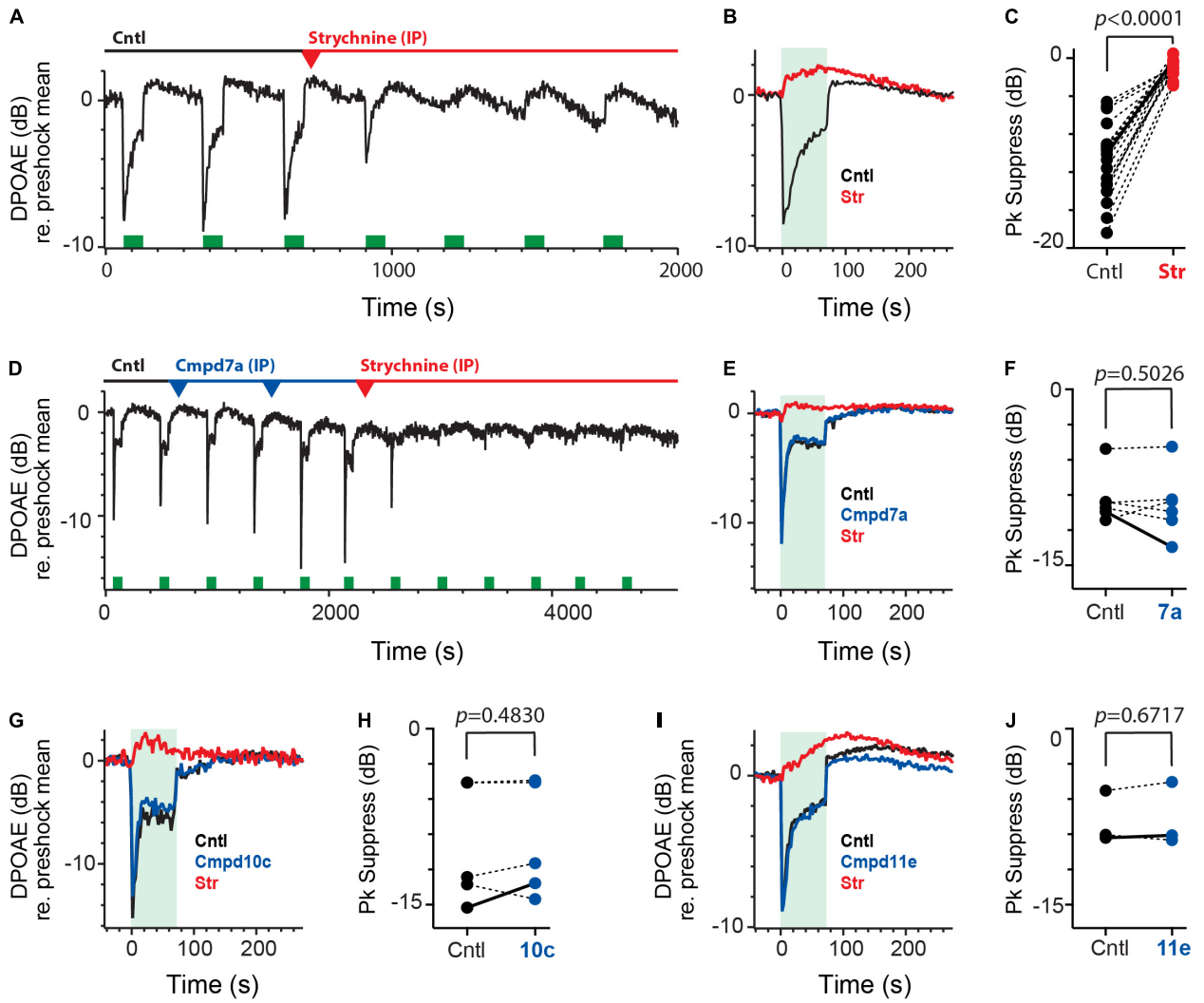

FIGURE 6 | Intraperitoneal administration of charged α9α10nAChR blockers fail to block efferent-mediated suppression of mice DPOAEs. **(A)** Continuous recording of mouse DPOAEs during midline stimulation of MOC efferent neurons (green bars, 200 shock/s for 70 s), before (Cntl) and after IP administration of strychnine at t = 700 s. (red arrowhead, 6 mg/kg). **(B)** Mean responses, from **(A)**, showing the effect of midline efferent stimulation (70-s duration @ 200 shocks/s, green box) on DPOAE amplitude before (Cntl, black trace) and after IP administration of strychnine (Str, red). **(C)** Peak values of efferent-mediated DPOAE suppression (Pk Suppress) are plotted for multiple animals before (Cntl, black) and after the application of strychnine (Str, red). Solid line shows values from mean traces in **(B)**. **(D)** Continuous recording of mouse DPOAEs during midline stimulation of MOC efferent neurons (green bars, 200 shock/s for 70 s), before (Cntl) and after two IP doses of Cmpd7a (2.5 mg/kg each, blue arrowheads) and subsequent IP strychnine (6 mg/kg, red arrowhead). **(E)** Mean responses, from **(D)**, showing the effect of midline efferent stimulation (70-s duration @ 200 shocks/s, green box) on DPOAE amplitude before (Cntl, black trace) and after IP delivery of Cmpd7a (blue trace) and then strychnine (red trace). **(F,H,J)** Peak values of efferent-mediated DPOAE suppression (Pk Suppress) are plotted for multiple animals before (Cntl, black) and after the application of Cmpd7a, 10c, or 11e (blue). Solid line shows values from corresponding traces in **(E,G,I)**. **(G,I)** Mean responses showing the effect of midline efferent stimulation (70-s duration @ 200 shocks/s, green box) on DPOAE amplitude before (Cntl, black trace) and after IP delivery of Cmpd10c (2.5 mg/Kg, blue trace) or Cmpd11e (2.5 mg/kg, blue trace), respectively. Both are then followed by IP strychnine (6 mg/Kg, red trace). Indicated p-values in **(C,F,H,J)** were computed using a paired t-test. Binning in **(A,B,D,E,G,I)** is 2.3 s.

excluded as well. DPOAE suppression assays were repeated for Cmpd10c (**Figures 6G,H**) and Cmpd11e (**Figures 6I,J**), whose reported IC50 values of blocking α9α10nAChRs in Xenopus oocytes (i.e., 4.2 and 0.56 nM, respectively) are nearly 5- and 40-fold more potent than strychnine or Cmpd7a (Elgoyhen et al., 2001; Zheng et al., 2011). However, IP Cmpd10c and Cmpd11e at a range of doses were without effects on efferent-mediated suppression (**Figures 6G,I**). The effects of five IP injections of Cmpd10c (2.5–49 mg/kg) at exposure times ranging from 13 to 40 min were evaluated in four animals where it had no significant effect on efferent-mediated suppression [−10.1 ± 2.3 vs. −9.6 ± 2.2 dB, $t(4)$ = 0.7723; **Figure 6H**] or changes in measurements of the slow enhancement [−0.3 ± 0.2 vs. −0.4 ± 0.2 dB, paired t-test, $t(4)$ = 0.3582, p = 0.7383; data not shown]. Similarly, in three animals, IP Cmpd11e (2.5–5 mg/kg) at a mean exposure time near 40 min had no significant effect on

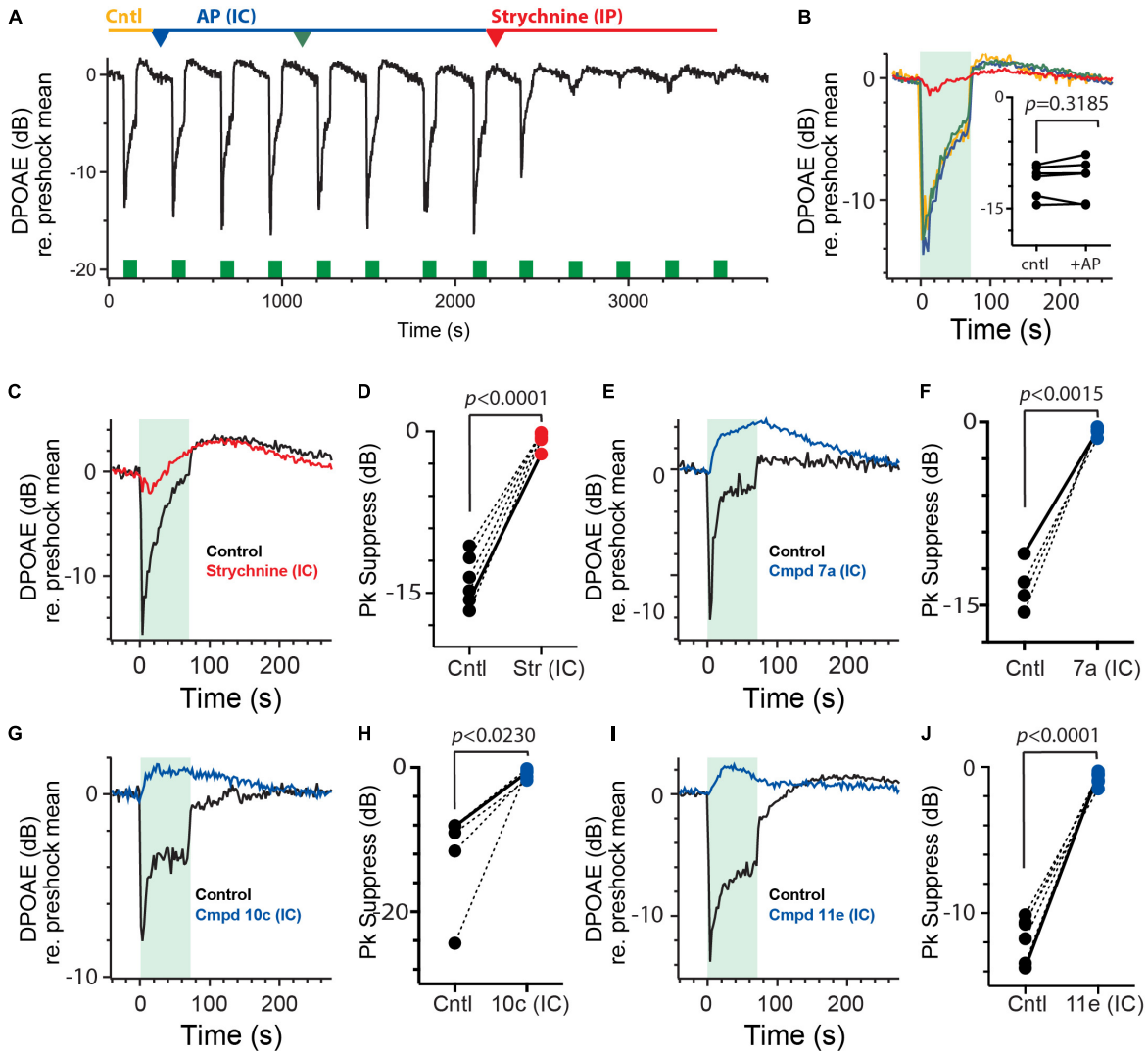

FIGURE 7 | Intracanal administration of charged α9α10nAChR antagonists blocks efferent-mediated suppression of mice DPOAEs. **(A)** Continuous recording of mouse DPOAEs during midline stimulation of MOC efferent neurons (green bars, 200 shock/s for 70 s), before (Cntl) and after two IC injections of artificial perilymph (AP, 1–1.5 μl each, blue and green arrowheads) and subsequent IP strychnine (6 mg/Kg, red arrowhead). **(B)** Mean responses, from **(A)**, showing the effect of midline efferent stimulation (70-s duration @ 200 shocks/s, green box) on DPOAE amplitude before (Cntl, yellow trace) and after two IC injections of artificial perilymph (AP, blue and green traces) and subsequent strychnine (red trace). Inset: peak values of efferent-mediated DPOAE suppression are plotted for multiple animals before (Cntl) and after the IC injection of AP (+AP). Indicated *p*-values were computed using a paired *t*-test. **(C,E,G,I)** Mean responses showing the effect of midline efferent stimulation (70-s duration @ 200 shocks/s, green box) on DPOAE amplitude before (Cntl, black trace) and after IC injection of strychnine (1.5 μl @1.6 mM, red trace), Cmpd7a (1 μl @ 5 mM, blue trace), Cmpd10c (3 μl @ 2.5 mM, blue trace), or Cmpd11e (1.5 μl @ 3 mM, blue trace), respectively. **(D,F,H,J)** Peak values of efferent-mediated DPOAE suppression (Pk Suppress) are plotted for multiple animals before (Cntl, black) and after IC injection of strychnine, Cmpd7a, Cmpd10c, or Cmpd11e (red or blue trace), respectively. Solid line shows values from corresponding traces in **(C,E,G,I)**. Indicated *p*-values were computed using a paired *t*-test. Binning in **(A–C,E,G,I)** is 2.3 s.

efferent suppression [-7.9 ± 1.3 vs. -7.7 ± 1.6 dB, $t(2) = 0.4915$; **Figure 6J**] or slow enhancement [1.9 ± 0.6 vs. 1.3 ± 0.6 dB, paired *t*-test, $t(2) = 1.065$, $p = 0.3984$; data not shown]. In both cases, complete blockade by subsequent IP strychnine (**Figures 6G,I**) suggest that, like Cmpd7a, Cmpd10c, and Cmpd11e fail to reach the inner ear in sufficient concentrations to block α9α10nAChRs. Post-drug block times for strychnine in all cases were similar [11.5 ± 1.2 (Cntl) vs. 11.5 ± 2.4 (7a) vs. 9.0 ± 1.1 (10c) vs. 12.3 ± 3.9 (11e)].

In order to demonstrate that the failure of these compounds to block α9α10nAChR-mediated efferent suppression of DPOAEs was attributed to their inability to gain access to the inner ear, we asked if direct injection into the perilymphatic compartment would result in successful blockade. Here, we revisited the IC approach by which we can introduce small volumes of drugs into the perilymph via a small fenestra made in the bony wall of the posterior canal. While we demonstrated earlier that IC administration of artificial perilymph (AP) had no significant

effect on efferent-mediated slow response of vestibular afferents (**Figure 4F**), we wanted to be sure that similar AP injections were without effect on efferent-mediated changes in DPOAEs. In the continuous DPOAE recording shown in **Figure 7A**, efferent shock trains (200 shocks/s for 70 s, green boxes) gave rise to a characteristic suppression followed by a slow enhancement. As anticipated, repeated AP injections into the posterior canal (1.5 μl each, blue/green arrowheads) failed to modify the response waveform in any consistent way, while a single IP dose of strychnine (6 mg/kg, red arrowhead) blocked the suppression. Mean responses under each condition are shown in **Figure 7B**. In three animals, 6 separate IC injections of AP had no significant effect on efferent-mediated DPOAE suppression [−11.2 ± 0.9 vs. 11.0 ± 1.1, $t(5) = 0.5468$; **Figure 7B** inset] or slow enhancement [0.6 ± 0.1 vs. 0.7 ± 0.1 dB, paired *t*-test, $t(5) = 1.513$, $p = 0.1908$; data not shown]. As a positive control that our IC drug injections do in fact reach cochlear OHCs, we also evaluated the effects of IC strychnine on efferent-mediated suppression (**Figure 7C**). Similar to IP administration, IC strychnine also blocks efferent-mediated suppression without effects on the slow enhancement. In six animals, IC strychnine (0.5–2.5 μl @ 1.6–3.2 mM) significantly blocked 95% of the efferent suppression [−13.8 ± 0.9 vs. −0.6 ± 0.3 dB; $t(5) = 16.69$; $d = 6.814$; **Figure 7D**] without any significant effects on the slow enhancement [2.7 ± 0.5 vs. 2.1 ± 0.4, paired *t*-test; $t(5) = 1.081$; $p = 0.3290$; data not shown].

The next obvious step was to administer the charged α9α10nAChR antagonists via the IC route to determine if having direct access to the perilymph results in blockade of the efferent-mediated DPOAE suppression. In contrast to IP administration, IC delivery of Cmpd7a, Cmpd 10c, and Cmpd11e blocked most of the efferent suppression of DPOAEs without any consistent effect on the slow enhancement (**Figures 7E,G,I**). In 4, 5, and 6 animals, Cmpd7a (1–4 μl @ 1–5 mM), Cmpd10c (0.5–3 μl @ 2.5 mM), and Cmpd11e (1–3.5 μl @ 0.3–3 mM) significantly blocked 94% [−13.4 ± 1.0 vs. −0.8 ± 0.2 dB, $t(3) = 11.32$, $d = 6.53$; **Figure 7F**], 93% [−12.2 ± 3.1 vs. −0.9 ± 0.3 dB, $t(4) = 3.587$, $d = 1.604$; **Figure 7H**], and 93% [−11.7 ± −0.6 vs. −0.8 ± 0.2 dB, $t(5) = 14.45$, $d = 5.90$; **Figure 7J**] of the efferent-mediated suppression, respectively. However, as with strychnine application, efferent-mediated slow enhancement was not significantly affected with either Cmpd7a [1.2 ± 0.2 vs. 1.9 ± 0.6 dB, paired *t*-test, $p = 0.4758$, $t(3) = 0.8129$], Cmpd10c [1.5 ± 0.6 vs. 0.6 ± 0.2 dB, paired *t*-test, $p = 0.1817$, $t(4) = 1.615$], or Cmpd11e [1.2 ± 0.7 vs. 1.5 ± 0.9 dB, paired *t*-test, $p = 0.5562$, $t(5) = 0.6302$] (data not shown). These data demonstrate that in order for these charged α9α10nAChR antagonists to block α9α10nAChRs in the inner ear, they must be applied directly into the perilymph, as systemic administration fails to reach the inner ear, at least with the doses and exposure times studied here.

DISCUSSION

We have had a long-standing interest in identifying pharmacological agents with high selectivity toward the various cholinergic receptors utilized by the peripheral EVS. Ideally, each selective drug would block the receptor in question while, depending on the dose, would have little to no effect on the others. To this end, we have previously demonstrated in the turtle posterior crista that α-bungarotoxin (αBTX), strychnine, and α-conotoxin RgIA (αCtxRgIA) potently antagonize α9α10nAChRs underlying efferent-mediated afferent inhibition, while DHβE, αCtxMII and bPiDDb potently block α4α6β2nAChRs underlying efferent-mediated fast excitation, and mAChR agents selectively targeted efferent-mediated slow excitation (Holt et al., 2006, 2015, 2017).

The turtle crista preparation is well-suited for pharmacological characterization of vestibular efferent synaptic mechanisms as these cholinergic drugs could be directly applied to the neuroepithelium without access issues. Ease of drug access has also been advantageous in characterizing efferent cholinergic mechanisms in vestibular endorgan preparations from mice (Poppi et al., 2018, 2020; Ramakrishna et al., 2020; Yu et al., 2020). However, in characterizing efferent-mediated afferent responses in the intact ear of anesthetized mice, there had to be considerations about whether some of the aforementioned drugs would make it to the perilymphatic space during systemic or middle ear administration. Our recent vestibular work as well as previous studies investigating cochlear efferents have demonstrated that many of these drugs including DHβE, atropine, scopolamine, and strychnine do, in fact, reliably access the mouse inner ear on a reasonably quick time scale (Maison et al., 2007; Schneider et al., 2021). While these drugs are tertiary amine compounds with small molecular weights (MW < 500 Da) that favor movement into the CNS as well as the ear, we questioned whether larger MW compounds like αBTX, αCtxRgIA, αCtxMII or charged drugs like bPiDDb would have similar access? We also wanted to identify if BBB permeability was a prerequisite for getting these cholinergic drugs into the ear. Selectively targeting the inner ear while avoiding confounding CNS effects would be instrumental in probing efferent synaptic mechanisms in behaving animal models, particularly for vestibular efferents where there is still debate as to what their physiological role is (Raghu et al., 2019; Cullen and Wei, 2021; Schneider et al., 2021). Identification of ear-specific drugs combined with local administration strategies could be helpful in this regard.

Predicting Inner Ear Drug Access

A comprehensive, computational model was recently made available at the SwissADME website[1] that consider a drug's physiochemical properties (e.g., lipid solubility, size, polar surface, etc.) and pharmacokinetic profile to predict how readily that drug may pass through biological membranes, with a focus on the BBB and absorption in the gut (Daina and Zoete, 2016; Daina et al., 2017). Recent studies characterizing drug entry into the cochlea have made good use of this model (Salt et al., 2019; Walia et al., 2021), with the reasonable assumption that drugs demonstrating BBB permeability might be expected to also penetrate the BLB during systemic administration or the round window during middle ear application. Based on

[1] http://www.swissadme.ch

their chemical structures, the online portal predicts that DHβE, atropine, scopolamine, and strychnine will have access to the CNS and presumably the inner ear, a prediction certainly confirmed in this and previous physiological studies (Maison et al., 2007; Schneider et al., 2021).

However, the SwissADME model indicates that the singly-charged mAChR antagonists glycopyrrolate and methscopolamine should not cross the BBB, and yet in this study we demonstrated they both can enter the perilymph to block efferent-mediated slow excitation after both IP and IB administration. Similar observations apply to the ionic tracer TMPA (Inamura and Salt, 1992; Mikulec et al., 2009). Collectively, these results demonstrate that BBB permeability is not necessarily the only predictor for entry into the ear. In contrast, the charged AMPA receptor antagonist IEM1460 was found in both CSF and perilymph following IP administration, in agreement with SwissADME predictions (Walia et al., 2021). These observations suggest that additional properties simply beyond MW and polarity influence what drugs enter the CNS, ear, or both. Last but not least, we also explored whether the bis, tris, and tetrakis quaternary ammonium α9α10nAChR antagonists Cmpd7a, 10c, and 11e could be used to block efferent-mediated suppression of DPOAEs. The multiple quaternary ammonium heads suggest that they will exhibit low to no BBB permeability (Wala et al., 2012; Walbaum, 2017). The SwissADME may be less useful here in that the molecular weights and structures of Cmpd7a, 10c, and 11e exceed some of the defined parametric ranges thus rendering subsequent predictions suboptimal. That being said, these drugs were only effective in blocking α9α10nAChR-mediated cochlear responses when directly injected into the perilymphatic compartment, but not when given systemically. These observations are consistent with an inability of these drugs to cross the BBB and BLB, at least within the time frame studied here.

In a limited survey of charged compounds that access the inner ear, those that gain access (i.e., glycopyrrolate, methscopolamine, and IEM1460) are aliphatic quaternary ammonium analogs while the α9α10nAChR antagonists Cmpd7a, 10c, and 11e are aromatic quaternary ammonium analogs. There are key differences in how aliphatic and aromatic compounds interact with lipid membranes as well as a variety of transporter and efflux mechanisms that might facilitate drug permeability (Metzner et al., 2006; Geldenhuys et al., 2010; Lind et al., 2021). Whether some of these differences contribute to the entry or efflux of these cholinergic drugs in or out of the inner ear and brain remains to be determined, but some cholinergic drugs are substrates for choline transporter uptake and *P*-glycoprotein-mediated efflux which may heavily influence drug accumulation in a particular compartment (Daneman et al., 2010; Geldenhuys et al., 2010; Wakuda et al., 2019).

It will be important to quantify the concentrations of cholinergic drugs reaching the inner ear and CNS as a function of the starting dose and administration site (i.e., IP vs. IB). Direct measurements of drug levels in these compartments, however, will require perilymphatic and CSF sampling which are beyond the scope of the current study. However, we do have some insight into this relationship for a number of other substances which generally reach higher levels with middle ear applications than with systemic administration. With the IV/IP routes, perilymphatic levels of fluorescein, TMPA, salicylate, and IEM-1460 were 0.05–1.4% of the administered dose (Boettcher et al., 1990; Inamura and Salt, 1992; Hirose et al., 2014; Salt et al., 2018a; Walia et al., 2021). With round window application, the percentage of gentamicin, Dex-P, TMPA, and fluorescein found in the perilymph are typically higher ranging from 1 to 6% (Plontke et al., 2008; Mikulec et al., 2009; Salt et al., 2018a). Since blocking times are a function of drug levels reaching efferent synapses, it is important to compare similar final perilymphatic concentrations with different administration routes. For a 20 g mouse in our Gly and Msc experiments, we used the same stock solution (0.2 mg/ml), but different delivery volumes for IP (0.2 ml for 2 mg/kg) and IB (0.03 ml) to arrive at starting drug amounts of 40 and 6 μg, respectively. Assuming a ∼1 and 5% differential perilymphatic access among the IP and IB routes, estimates of final drug amounts reaching efferent synapses would be similar (i.e., 0.4 μg for IP and 0.3 μg for IB). For IC glycopyrrolate, assuming all of the drug administered (1 μl of 0.2 mg/ml stock solution) makes it into the perilymph, a final drug amount of 0.2 μg is within the same range. Future direct measurements of drug levels in the perilymph are needed to confirm if this relationship holds for glycopyrrolate and methylscopolamine as well as the other cholinergic efferent drugs. In accordance with existing literature (Domino and Corssen, 1967; Proakis and Harris, 1978; Freedman et al., 1989; Callegari et al., 2011; Wala et al., 2012; Walbaum, 2017; Chabicovsky et al., 2019), we postulate that these cholinergic drugs exhibit poor BBB penetration, but measurements of CSF drug levels in mice will also be important in determining to what extent, if any, these drugs have access to the CNS in our preparation.

Delineating Peripheral Versus Central Actions of mAChR Antagonist

For glycopyrrolate and methscopolamine, we are relying on literature in multiple species and preparations using a variety of biochemical, electrophysiological, and behavioral assays to document that these drugs have little access across the BBB. But, direct measurements of drug levels in blood, perilymph, and CSF in our mouse preparation would be more reassuring. We know that the effectiveness of mAChR and nAChR antagonists to block efferent-mediated slow and fast excitation, respectively, occurs in the vestibular periphery and not as a function of changing the sensitivity of central efferent neurons to efferent stimulation. We know this because efferent-mediated fast excitation remains unchanged during mAChR blockade and efferent-mediated slow excitation remains unchanged during nAChR blockade. However, some mAChR blockers systematically affect background discharge and we have routinely, as a matter of transparency, described this phenomenon in our mouse efferent work.

While the effects on baseline discharge could be attributed to central effects with certain mAChR antagonists, we have not identified the specific target for these effects nor determined that similar mechanisms are involved with each mAChR

antagonist. Schneider et al. (2021) demonstrated that the mAChR antagonists atropine and scopolamine, which do enter the CNS, affected background discharge when administered through the IP route but not the IB route suggesting that other central and/or peripheral mAChR targets may underlie this effect. However, in the current study, both IP and IB glycopyrrolate significantly decreased background discharge suggesting that the effects are peripheral. This can be contrasted with IP and IB methscopolamine where the effects on afferent background rates are neither consistent nor as pronounced, suggesting that perhaps differences in chemical structures between these two charged mAChR antagonists may permit glycopyrrolate, but not methscopolamine, to modify afferent discharge. Further exploration of the dose response relationship for these different mAChR antagonists may find doses where the effect on efferent-mediated slow excitation and background discharge can be easily separated.

The effect of mAChR antagonists on baseline discharge might be interpreted as a role for efferent tone, which would be consistent with recent data indicating that optothermal inhibition of vestibular efferent neurons in mice gives rise to decreased spontaneous activity in vestibular afferents (Raghu et al., 2019). Such efferent tone, if present in our anesthetized preparation, might result in the release of efferent neurotransmitters (e.g., ACh) that activate mAChRs and/or other peripheral vestibular efferent mechanisms to augment afferent discharge under control conditions. Subsequent blockade of central mAChRs could inhibit neurons in the vestibular nuclei, reticular formation, and/or *e* group to give rise to a decrease in efferent input at the end organ level that ultimately reduces afferent firing (Metts et al., 2006; Soto and Vega, 2010; Idoux et al., 2018). This scenario is consistent with our observations with IP atropine and IP scopolamine, and could be extended to IP and IB glycopyrrolate provided that appreciable amounts of drug, in both cases, reached the brainstem. In turn, IC glycopyrrolate, IP methscopolamine, and IB methscopolamine fail to breach the CNS and therefore do not impact the supposed efferent tone. The challenge with this interpretation is the difficulties in reconciling how IB administration of scopolamine and atropine do not target those same central mechanisms. Along the same lines, activation of the mAChRs that give rise to efferent-mediated slow excitation of vestibular afferents likely does not underlie the decreases in afferent firing seen with mAChR antagonists given the lack of correspondence between these two effects with different drugs and different routes. While previous sectioning experiments suggest that there is little efferent tone or basal activity in our preparation (Schneider et al., 2021), the effects of different anesthetic regimens (i.e., ketamine/xylazine vs. urethane/xylazine) on efferent tone cannot be ruled out as well as any interactions that may exist between each anesthetic cocktail and the different mAChR antagonists.

Alternatively, it is entirely conceivable that electrical stimulation of efferent neurons in our preparation could produce other long-term changes (over 10 s of minutes) in afferent firing, in addition to efferent-mediated slow excitation, that are both sensitive to mAChR blockade. This could all happen in the periphery without involving central efferent circuitry. We know from the literature, that there is also evidence for mAChRs on type II hair cells and vestibular supporting cells (Liu and Wangemann, 1998; Derbenev et al., 2005; Li et al., 2007; Li and Correia, 2011), whose activation could give rise to slower changes in afferent discharge rates. Access time to these receptors may lag behind those needed to block mAChRs on the afferent and thus may contribute to the failure to see background changes when the drugs are delivered quickly to the inner ear like IB scopolamine, IB atropine, and IC glycopyrrolate. When access times are longer, however, blockade of both groups of mAChRs will overlap as is the case with IP scopolamine and IP atropine (Schneider et al., 2021) as well as both IP and IB glycopyrrolate (this study). Longer incubation times with different routes might be helpful here. However, the lack of a consistent effect of methscopolamine on baseline, with either route, is hard to reconcile with such timing differences. The observations that IP and IB methscopolamine do not have significant effects on baseline firing could suggest that specific properties of methscopolamine (e.g., chemical structure, specificity, potency, etc.) may account for the differences. Binding kinetic parameters do vary among the different mAChR antagonists (Riddy et al., 2015). Currently, there is no single or unifying conclusion that satisfactorily explains our data collectively, suggesting that multiple mechanisms are likely involved.

Drug Movement Between Ears

Another interesting outcome of this study was the observation that the contralateral middle ear application of glycopyrrolate and methscopolamine eventually reached the ipsilateral ear. A number of inner ear studies have reported similar observations with a number of different substances (Bath et al., 1999; Stöver et al., 2000; Landegger et al., 2017; Salt et al., 2018a; Lee et al., 2020; Lentz et al., 2020), but the current study, for the first time, tried to monitor the time course of drug communication between ears in mice. While the mechanism by which mAChR antagonists gain access to the ipsilateral ear in our preparation is unknown, possible routes from the contralateral to the ipsilateral ear include a perilymph to vascular route, perilymph to CSF route via the cochlear aqueduct, lymphatic pathways, and/or the eustachian tube (Salt and Hirose, 2018; Talaei et al., 2019; Lee et al., 2020). Fluorescent gentamicin, after injection into the perilymph of the posterior semicircular canal in mice, makes its way out into the systemic circulation in short as 1 h or less (Talaei et al., 2019). The time course for movement of contralateral glycopyrrolate and methscopolamine to the ipsilateral ear overlaps that of the fluorescent gentamicin suggesting similar mechanisms for both. Drug movement between ears may complicate the characterization of drug effects following local application to the ear, particularly with those drugs that can enter the CNS upon systemic redistribution. Further insight into these processes might be had after determining whether contralateral IC injection of glycopyrrolate also blocks efferent-mediated slow excitation in the ipsilateral ear. This approach could be used to exclude the eustachian tube route. Contralateral IC injection of the charged α9α10nAChR antagonists might also

differentiate between a perilymph to systemic circulation route from a perilymph to CSF route.

Significance of Glycopyrrolate and Methscopolamine in Understanding Efferent Vestibular System Function

It has been long recognized that mAChR antagonists like scopolamine are effective in alleviating motion sickness (Yates et al., 1998; Renner et al., 2005; Golding, 2016). The general consensus has been that scopolamine's effectiveness is attributed to mAChR blockade in central vestibular circuitry (Soto and Vega, 2010; Idoux et al., 2018). But evidence regarding efferent activation of mAChRs on vestibular afferents and its sensitivity to mAChR antagonists, now including glycopyrrolate and methscopolamine, suggest we include mAChRs in the vestibular periphery as potential contributors (Weerts et al., 2015; Holt et al., 2017; Ramakrishna et al., 2020; Schneider et al., 2021). While differences in the effectiveness of peripherally and centrally-active mAChR antagonists in alleviating motion sickness are mixed (Kirsten and Schoener, 1975; Uijdehaage et al., 1993; Hasler et al., 1995; Lang et al., 1999; Spinks and Wasiak, 2011; Qi et al., 2019), glycopyrrolate has been utilized as a vestibular suppressant in Meniere's patients and for treating vertigo after cochleostomy during cochlear implants (Storper et al., 1998; Chakrabarty et al., 2011). Collectively, these data suggest that pharmacological targeting of mAChRs in the vestibular periphery may be of some utility in treating motion sickness, and that glycopyrrolate and methscopolamine could be used to distinguish the role of mAChRs in peripheral and central vestibular circuitry. Revisiting the effect of motion sickness on VOR efficacy (Idoux et al., 2018), and assessing susceptibility to charged mAChR antagonists could be instructive in this regard.

DATA AVAILABILITY STATEMENT

The raw data supporting the conclusions of this article will be made available by the authors, without undue reservation.

ETHICS STATEMENT

The animal study was reviewed and approved by University Committee for Animal Resources (UCAR) at the University of Rochester Medical Center (URMC).

AUTHOR CONTRIBUTIONS

CL, PC, and JH contributed to study concept and design. CL, AS, AW, KH, and JH were instrumental in the acquisition of electrophysiological and pharmacological data. CL, JH, and KH were involved in the analysis and interpretation of the data. The manuscript was written and revised by all authors.

FUNDING

This research was supported by NIH/NIDCD Grants R01DC0016974 (JH) and R01DC008891 (JH).

REFERENCES

Bath, A. P., Walsh, R. M., Bance, M. L., and Rutka, J. A. (1999). Ototoxicity of topical gentamicin preparations. *Laryngoscope* 109, 1088–1093.

Boettcher, F. A., Bancroft, B. R., and Salvi, R. J. (1990). Concentration of salicylate in serum and perilymph of the chinchilla. *Arch. Otolaryngol. Head Neck Surg.* 116, 681–684. doi: 10.1001/archotol.1990.01870060039005

Brichta, A. M., and Goldberg, J. M. (2000a). Morphological identification of physiologically characterized afferents innervating the turtle posterior crista. *J. Neurophysiol.* 83, 1202–1223. doi: 10.1152/jn.2000.83.3.1202

Brichta, A. M., and Goldberg, J. M. (2000b). Responses to efferent activation and excitatory response-intensity relations of turtle posterior-crista afferents. *J. Neurophysiol.* 83, 1224–1242. doi: 10.1152/jn.2000.83.3.1224

Brulet, R., Zhu, J., Aktar, M., Hsieh, J., and Cho, K. O. (2017). Mice with conditional NeuroD1 knockout display reduced aberrant hippocampal neurogenesis but no change in epileptic seizures. *Exp. Neurol.* 293, 190–198. doi: 10.1016/j.expneurol.2017.04.005

Bymaster, F. P., Carter, P. A., Peters, S. C., Zhang, W., Ward, J. S., Mitch, C. H., et al. (1998). Xanomeline compared to other muscarinic agents on stimulation of phosphoinositide hydrolysis in vivo and other cholinomimetic effects. *Brain Res.* 795, 179–190. doi: 10.1016/s0006-8993(98)00267-4

Callegari, E., Malhotra, B., Bungay, P. J., Webster, R., Fenner, K. S., Kempshall, S., et al. (2011). A comprehensive non-clinical evaluation of the CNS penetration potential of antimuscarinic agents for the treatment of overactive bladder. *Br. J. Clin. Pharmacol.* 72, 235–246. doi: 10.1111/j.1365-2125.2011.03961.x

Chabicovsky, M., Winkler, S., Soeberdt, M., Kilic, A., Masur, C., and Abels, C. (2019). Pharmacology, toxicology and clinical safety of glycopyrrolate. *Toxicol. Appl. Pharmacol.* 370, 154–169.

Chakrabarty, A., Tarneja, V. K., Singh, V. K., Roy, P. K., Bhargava, A. K., and Sreevastava, D. K. (2011). Cochlear implant: anaesthesia challenges, armed force. *Med. J. Armed Forces India* 60, 351–356. doi: 10.1016/S0377-1237(04)80009-1

Clause, A., Lauer, A. M., and Kandler, K. (2017). Mice lacking the alpha9 subunit of the nicotinic acetylcholine receptor exhibit deficits in frequency difference limens and sound localization. *Front. Cell Neurosci.* 11:167. doi: 10.3389/fncel.2017.00167

Cullen, K. E., and Wei, R. H. (2021). Differences in the Structure and function of the vestibular efferent system among vertebrates. *Front. Neurosci.* 15:684800.

Daina, A., Michielin, O., and Zoete, V. (2017). SwissADME: a free web tool to evaluate pharmacokinetics, drug-likeness and medicinal chemistry friendliness of small molecules. *Sci. Rep.* 7:42717. doi: 10.1038/srep42717

Daina, A., and Zoete, V. (2016). A BOILED-egg to predict gastrointestinal absorption and brain penetration of small molecules. *ChemMedChem* 11, 1117–1121. doi: 10.1002/cmdc.201600182

Daneman, R., Zhou, L., Agalliu, D., Cahoy, J. D., Kaushal, A., and Barres, B. A. (2010). The mouse blood-brain barrier transcriptome: a new resource for understanding the development and function of brain endothelial cells. *PLoS One* 5:e13741.

Derbenev, A. V., Linn, C. L., and Guth, P. S. (2005). Muscarinic ACh receptor activation causes transmitter release from isolated frog vestibular hair cells. *J. Neurophysiol.* 94, 3134–3142. doi: 10.1152/jn.00131.2005

Domino, E. F., and Corssen, G. (1967). Central and peripheral effects of muscarinic cholinergic blocking agents in man. *Anesthesiology* 28, 568–574.

Dringenberg, H. C., and Vanderwolf, C. H. (1996). Cholinergic activation of the electrocorticogram: an amygdaloid activating system. *Exp. Brain Res.* 108, 285–296. doi: 10.1007/BF00228101

Elgoyhen, A. B., Vetter, D. E., Katz, E., Rothlin, C. V., Heinemann, S. F., and Boulter, J. (2001). Alpha10, a determinant of nicotinic cholinergic receptor function in mammalian vestibular and cochlear mechanosensory hair cells. *Proc. Natl. Acad. Sci.U.S.A.* 98, 3501–3506. doi: 10.1073/pnas.051622798

Fayyazuddin, A., Brichta, A. M., and Art, J. J. (1991). Organization of eighth nerve efferents in the turtle, *Pseudemys scripta*. *Soc. Neurosci. Abstr.* 17:312.

Freedman, S. B., Harley, E. A., and Patel, S. (1989). Direct measurement of muscarinic agents in the central nervous system of mice using ex vivo binding. *Eur. J. Pharmacol.* 174, 253–260. doi: 10.1016/0014-2999(89)90317-8

Geldenhuys, W. J., Manda, V. K., Mittapalli, R. K., Van der Schyf, C. J., Crooks, P. A., Dwoskin, L. P., et al. (2010). Predictive screening model for potential vector-mediated transport of cationic substrates at the blood-brain barrier choline transporter. *Bioorg. Med. Chem. Lett.* 20, 870–877. doi: 10.1016/j.bmcl.2009.12.079

Goldberg, J. M., and Fernández, C. (1980). Efferent vestibular system in the squirrel monkey: anatomical location and influence on afferent activity. *J. Neurophysiol.* 43, 986–1025. doi: 10.1152/jn.1980.43.4.986

Golding, J. F. (2016). Motion sickness. *Handb. Clin. Neurol.* 137, 371–390.

Goycoolea, M. V. (2001). Clinical aspects of round window membrane permeability under normal and pathological conditions. *Acta Otolaryngol.* 121, 437–447. doi: 10.1080/000164801300366552

Goycoolea, M. V., and Lundman, L. (1997). Round window membrane. Structure function and permeability: a review. *Microsc. Res. Tech.* 36, 201–211. doi: 10.1002/(sici)1097-0029(19970201)36:3<201::aid-jemt8>3.0.co;2-r

Guinan, J. J. Jr. (2006). Olivocochlear efferents: anatomy, physiology, function, and the measurement of efferent effects in humans. *Ear. Hear.* 27, 589–607. doi: 10.1097/01.aud.0000240507.83072.e7

Guth, P. S., Perin, P., Norris, C. H., and Valli, P. (1998). The vestibular hair cells: post-transductional signal processing. *Prog. Neurobiol.* 5, 193–247. doi: 10.1016/s0301-0082(97)00068-3

Hasler, W. L., Kim, M. S., Chey, W. D., Stevenson, V., Stein, B., and Owyang, C. (1995). Central cholinergic and alpha-adrenergic mediation of gastric slow wave dysrhythmias evoked during motion sickness. *Am. J. Physiol.* 268, G539–G547. doi: 10.1152/ajpgi.1995.268.4.G539

Hirose, K., Hartsock, J. J., Johnson, S., Santi, P., and Salt, A. N. (2014). Systemic lipopolysaccharide compromises the blood-labyrinth barrier and increases entry of serum fluorescein into the perilymph. *J. Assoc. Res. Otolaryngol.* 15, 707–719. doi: 10.1007/s10162-014-0476-6

Holt, J. C. (2020). "Synaptic and pharmacological organization of efferent In?uences on hair cells and vestibular afferent fibers," in *The Senses: A Comprehensive Reference*, Vol. 6, eds B. Fritzsch and H. Straka (Amsterdam: Elsevier), 526–554.

Holt, J. C., Lysakowski, A., and Goldberg, J. M. (2006). Mechanisms of efferent-mediated responses in the turtle posterior crista. *J. Neurosci.* 26, 13180–13193.

Holt, J. C., Lioudyno, M., Athas, G., Garcia, M. M., Perin, P., and Guth, P. S. (2001). The effect of proteolytic enzymes on the alpha9-nicotinic receptor-mediated response in isolated frog vestibular hair cells. *Hear. Res.* 152, 25–42. doi: 10.1016/s0378-5955(00)00225-2

Holt, J. C., Kewin, K., Jordan, P. M., Cameron, P., Klapczynski, M., McIntosh, J. M., et al. (2015). A Pharmacologically distinct nicotinic acetylcholine receptors drive efferent-mediated excitation in calyx-bearing vestibular afferents. *J. Neurosci.* 35, 3625–3643. doi: 10.1523/JNEUROSCI.3388-14.2015

Holt, J. C., Jordan, P. M., Lysakowski, A., Shah, A., Barsz, K., and Contini, D. (2017). Muscarinic acetylcholine receptors and m-currents underlie efferent-mediated slow excitation in calyx-bearing vestibular afferents. *J. Neurosci.* 37, 1873–1887. doi: 10.1523/JNEUROSCI.2322-16.2017

Holt, J. C., Lysakowski, A., and Goldberg, J. M. (2011). "Chapter 6: efferent vestibular system," in *Springer Handbook of Auditory Research: Auditory and Vestibular Efferents*, eds D. K. Ryugo, R. R. Fay, and A. N. Popper (New York, NY: Springer), 135–186.

Holtman, J. R., Dwoskin, L. P., Dowell, C., Wala, E. P., Zhang, Z., Crooks, P. A., et al. (2011). The novel small molecule α9α10 nicotinic acetylcholine receptor antagonist ZZ-204G is analgesic. *Eur. J. Pharmacol.* 670, 500–508. doi: 10.1016/j.ejphar.2011.08.053

Hübner, P. P., Khan, S. I, and Migliaccio, A. A. (2015). The mammalian efferent vestibular system plays a crucial role in the high-frequency response and short-term adaptation of the vestibuloocular reflex. *J. Neurophysiol.* 114, 3154–3165. doi: 10.1152/jn.00307.2015

Hübner, P. P., Khan, S. I, and Migliaccio, A. A. (2017). The mammalian efferent vestibular system plays a crucial role in vestibulo-ocular reflex compensation after unilateral labyrinthectomy. *J. Neurophysiol.* 117, 1553–1568. doi: 10.1152/jn.01049.2015

Idoux, E., Tagliabue, M., and Beraneck, M. (2018). No gain no pain: relations between vestibulo-ocular reflexes and motion sickness in mice. *Front. Neurol.* 9:918. doi: 10.3389/fneur.2018.00918

Inamura, N., and Salt, A. N. (1992). Permeability changes of the blood-labyrinth barrier measured in vivo during experimental treatments. *Hear. Res.* 61, 12–18. doi: 10.1016/0378-5955(92)90030-q

Isgrig, K., and Chien, W. W. (2018). Posterior semicircular canal approach for inner ear gene delivery in neonatal mouse. *J. Vis. Exp.* 133:56648.

Jones, S. M., Vijayakumar, S., Dow, S. A., Holt, J. C., Jordan, P. M., and Luebke, A. E. (2018). Loss of α-calcitonin gene-related peptide (αCGRP) reduces otolith activation timing dynamics and impairs balance. *Front. Mol. Neurosci.* 11:289. doi: 10.3389/fnmol.2018.00289

Kaila, T., Ali-Melkkilä, T., Iisalo, E., and Kanto, J. (1990). Radioreceptor assay for pharmacokinetic studies of glycopyrrolate. *Pharmacol. Toxicol.* 67, 313–316. doi: 10.1111/j.1600-0773.1990.tb00836.x

Kirsten, E. B., and Schoener, E. P. (1975). Motion-modulated vestibular neurons: central versus peripheral effects of cholinergic blocking agents. *Experientia* 31, 575–576. doi: 10.1007/BF01932466

Kitcher, S. R., Pederson, A. M., and Weisz, C. J. C. (2021). Diverse identities and sites of action of cochlear neurotransmitters. *Hear. Res. May* 24:108278. doi: 10.1016/j.heares.2021.108278

Lamberty, Y., and Gower, A. J. (1991). Cholinergic modulation of spatial learning in mice in a Morris-type water maze. *Arch. Int. Pharmacodyn. Ther.* 309, 5–19.

Landegger, L. D., Pan, B., Askew, C., Wassmer, S. J., Gluck, S. D., Galvin, A., et al. (2017). A synthetic AAV vector enables safe and efficient gene transfer to the mammalian inner ear. *Nat. Biotechnol.* 35, 280–284. doi: 10.1038/nbt.3781

Lang, I. M., Sarna, S. K., and Shaker, R. (1999). Gastrointestinal motor and myoelectric correlates of motion sickness. *Am. J. Physiol.* 277, G642–G652. doi: 10.1152/ajpgi.1999.277.3.G642

Lauer, A. M., and May, B. J. (2011). The medial olivocochlear system attenuates the developmental impact of early noise exposure. *J. Assoc. Res. Otolaryngol.* 12, 329–343. doi: 10.1007/s10162-011-0262-7

Lee, S. Y., Kim, J., Oh, S., Jung, G., Jeong, K. J., Tan Tran, V., et al. (2020). Contralateral spreading of substances following intratympanic nanoparticle-conjugated gentamicin injection in a rat model. *Sci. Rep.* 10:18636. doi: 10.1038/s41598-020-75725-y

Leijon, S., and Magnusson, A. K. (2014). Physiological characterization of vestibular efferent brainstem neurons using a transgenic mouse model. *PLoS One* 9:e98277. doi: 10.1371/journal.pone.0098277

Lentz, J. J., Pan, B., Ponnath, A., Tran, C. M., Nist-Lund, C., Galvin, A., et al. (2020). Direct delivery of antisense oligonucleotides to the middle and inner ear improves hearing and balance in usher mice. *Mol. Ther.* 28, 2662–2676. doi: 10.1016/j.ymthe.2020.08.002

Li, G. Q., and Correia, M. J. (2011). Responses of pigeon vestibular hair cells to cholinergic agonists and antagonists. *Brain Res.* 1373, 25–38. doi: 10.1016/j.brainres.2010.12.016

Li, G. Q., Kevetter, G. A., Leonard, R. B., Prusak, D. J., Wood, T.G., and Correia, M. J. (2007). Muscarinic acetylcholine receptor subtype expression in avian vestibular hair cells, nerve terminals and ganglion cells. *Neuroscience* 146, 384–402. doi: 10.1016/j.neuroscience.2007.02.019

Lind, C., Pandey, P., Pastor, R. W., and MacKerell, A. D. Jr. (2021). Functional group distributions, partition coefficients, and resistance factors in lipid bilayers using site identification by ligand competitive saturation. *J. Chem. Theory Comput.* 17, 3188–3202. doi: 10.1021/acs.jctc.1c00089

Liu, J., and Wangemann, P. (1998). Pharmacological evidence for the M3 muscarinic receptor mediating inhibition of K^+ secretion in vestibular dark cells and strial marginal cells. *Assoc. Res. Otolaryngol.* 21:113.

Liu, H., Chen, S., Zhou, Y., Che, X., Bao, Z., Li, S., et al. (2013). The effect of surface charge of glycerol monooleate-based nanoparticles on the round window membrane permeability and cochlear distribution. *J. Drug Target* 21, 846–854. doi: 10.3109/1061186X.2013.829075

López-Hernández, G. Y., Thinschmidt, J. S., Zheng, G., Zhang, Z., Crooks, P. A., Dwoskin, L. P., et al. (2009). Selective inhibition of acetylcholine-evoked responses of alpha7 neuronal nicotinic acetylcholine receptors by novel tris-

and tetrakis-azaaromatic quaternary ammonium antagonists. *Mol. Pharmacol.* 76, 652–666. doi: 10.1124/mol.109.056176

Luebke, A. E., Holt, J. C., Jordan, P. M., Wong, Y. S., Caldwell, J. S., and Cullen, K. E. (2014). Loss of α-calcitonin gene-related peptide (αCGRP) reduces the efficacy of the Vestibulo-ocular Reflex (VOR). *J. Neurosci.* 34, 10453–10458. doi: 10.1523/jneurosci.3336-13.2014

Maison, S. F., Adams, J. C., and Liberman, M. C. (2003). Olivocochlear innervation in the mouse: immunocytochemical maps, crossed versus uncrossed contributions, and transmitter colocalization. *J. Comp. Neurol.* 455, 406–416. doi: 10.1002/cne.10490

Maison, S. F., Vetter, D. E., and Liberman, M. C. (2007). A novel effect of cochlear efferents: in vivo response enhancement does not require alpha9 cholinergic receptors. *J. Neurophysiol.* 97, 3269–3278. doi: 10.1152/jn.00067.2007

Maison, S. F., Usubuchi, H., and Liberman, M. C. (2013). Efferent Feedback minimizes cochlear neuropathy from moderate noise exposure. *J. Neurosci.* 33, 5542–5552. doi: 10.1523/jneurosci.5027-12.2013

Marlinski, V., Plotnik, M., and Goldberg, J. M. (2004). Efferent actions in the chinchilla vestibular labyrinth. *J. Assoc. Res. Otolaryngol.* 5, 126–143.

May, B. J., Lauer, A. M., and Roos, M. J. (2011). Impairments of the medial olivocochlear system increase the risk of noise-induced auditory neuropathy in laboratory mice. *Otol. Neurotol.* 32, 1568–1578. doi: 10.1097/MAO.0b013e31823389a1

McCall, A. A., Swan, E. E., Borenstein, J. T., Sewell, W. F., Kujawa, S. G., and McKenna, M. J. (2010). Drug delivery for treatment of inner ear disease: current state of knowledge. *Ear. Hear.* 31, 156–165. doi: 10.1097/aud.0b013e3181c351f2

McCue, M. P., and Guinan, J. J. (1994). Influence of efferent stimulation on acoustically responsive vestibular afferents in the cat. *J. Neurosci.* 14, 6071–6083. doi: 10.1523/JNEUROSCI.14-10-06071.1994

Metts, B. A., Kaufman, G. D., and Perachio, A. A. (2006). Polysynaptic inputs to vestibular efferent neurons as revealed by viral transneuronal tracing. *Exp. Brain Res.* 172, 261–274. doi: 10.1007/s00221-005-0328-z

Metzner, L., Neubert, K., and Brandsch, M. (2006). Substrate specificity of the amino acid transporter PAT1. *Amino Acids* 31, 111–117. doi: 10.1007/s00726-005-0314-6

Mikulec, A. A., Plontke, S. K., Hartsock, J. J., and Salt, A. N. (2009). Entry of substances into perilymph through the bone of the otic capsule after intratympanic applications in guinea pigs: implications for local drug delivery in humans. *Otol. Neurotol.* 30, 131–138. doi: 10.1097/mao.0b013e318191bff8

Morley, B. J., Lysakowski, A., Vijayakumar, S., Menapace, D., and Jones, T. A. (2017). Nicotinic acetylcholine receptors regulate vestibular afferent gain and activation timing. *J. Comp. Neurol.* 525, 1216–1233. doi: 10.1002/cne.24131

Nyberg, S., Abbott, N. J., Shi, X., Steyger, P. S., and Dabdoub, A. (2019). Delivery of therapeutics to the inner ear: the challenge of the blood-labyrinth barrier. *Sci. Transl. Med.* 11:eaao0935. doi: 10.1126/scitranslmed.aao0935

Parks, X. X., Contini, D., Jordan, P. M., and Holt, J. C. (2017). Confirming a role for α9nAChRs and SK Potassium channels in type II hair cells of the turtle posterior crista. *Front. Cell Neurosci.* 11:356. doi: 10.3389/fncel.2017.00356

Patel, J., Szczupak, M., Rajguru, S., Balaban, C., and Hoffer, M. E. (2019). Inner ear therapeutics: an overview of middle ear delivery. *Front Cell Neurosci* 13:261.

Plontke, S. K., Biegner, T., Kammerer, B., Delabar, U., and Salt, A. N. (2008). Dexamethasone concentration gradients along scala tympani after application to the round window membrane. *Otol. Neurotol.* 29, 401–406. doi: 10.1097/mao.0b013e318161aaae

Poppi, L. A., Holt, J. C., Lim, R., and Brichta, A. M. (2020). A review of efferent cholinergic synaptic transmission in the vestibular periphery and its functional implications. *J. Neurophysiol.* 123, 608–629. doi: 10.1152/jn.00053.2019

Poppi, L. A., Tabatabaee, H., Drury, H. R., Jobling, P., Callister, R. J., Migliaccio, A. A., et al. (2018). ACh-induced hyperpolarization and decreased resistance in mammalian type II vestibular hair cells. *J. Neurophysiol.* 119, 312–325. doi: 10.1152/jn.00030.2017

Proakis, A. G., and Harris, G. B. (1978). Comparative penetration of glycopyrrolate and atropine across the blood–brain and placental barriers in anesthetized dogs. *Anesthesiology* 48, 339–344. doi: 10.1097/00000542-197805000-00007

Qi, R., Su, Y., Pan, L., Mao, Y., Liang, L., Dai, Z., et al. (2019). Anticholinergics mecamylamine and scopolamine alleviate motion sickness-induced gastrointestinal symptoms through both peripheral and central actions. *Neuropharmacology* 146, 252–263. doi: 10.1016/j.neuropharm.2018.12.006

Raghu, V., Salvi, R., and Sadeghi, S. G. (2019). Efferent inputs are required for normal function of vestibular nerve afferents. *J. Neurosci.* 39, 6922–6935. doi: 10.1523/JNEUROSCI.0237-19.2019

Ramakrishna, Y., Manca, M., Glowatzki, E., and Sadeghi, S. G. (2020). Cholinergic modulation of membrane properties of calyx terminals in the vestibular periphery. *Neuroscience* 452, 98–110. doi: 10.1016/j.neuroscience.2020.10.035

Renner, U. D., Oertel, R., and Kirch, W. (2005). Pharmacokinetics and pharmacodynamics in clinical use of scopolamine. *Ther. Drug. Monit.* 27, 655–665. doi: 10.1097/01.ftd.0000168293.48226.57

Riddy, D. M., Valant, C., Rueda, P., Charman, W. N., Sexton, P. M., Summers, R. J., et al. (2015). Label-free kinetics: exploiting functional hemi-equilibrium to derive rate constants for muscarinic receptor antagonists. *Mol. Pharmacol.* 88, 779–790. doi: 10.1124/mol.115.100545

Roth, D., Hamburger-Bar, R., and Lerer, B. (1989). Peripheral versus central manifestations in the toxic interaction of lithium and pilocarpine. *Biol. Psychiatry.* 25, 153–158. doi: 10.1016/0006-3223(89)90159-5

Salt, A., Hartsock, J., Gill, R., and Plontke, S. (2018a). Pathways for Drug Transfer Between the Two Ears. *Assoc. Res. Otolaryngol. Midwinter Meet. Abstr.* 41:430.

Salt, A. N., Hartsock, J. J., Piu, F., and Hou, J. (2018b). Dexamethasone and dexamethasone phosphate entry into perilymph compared for middle ear applications in guinea pigs. *Audiol. Neurootol.* 23, 245–257. doi: 10.1159/000493846

Salt, A. N., and Hirose, K. (2018). Communication pathways to and from the inner ear and their contributions to drug delivery. *Hear. Res.* 362, 25–37. doi: 10.1016/j.heares.2017.12.010

Salt, A. N., and Plontke, S. K. (2018). Pharmacokinetic principles in the inner ear: influence of drug properties on intratympanic applications. *Hear. Res.* 368, 28–40. doi: 10.1016/j.heares.2018.03.002

Salt, A. N., Hartsock, J. J., Hou, J., and Piu, F. (2019). Comparison of the pharmacokinetic properties of triamcinolone and dexamethasone for local therapy of the inner ear. *Front. Cell Neurosci.* 13:347. doi: 10.3389/fncel.2019.00347

Schneider, G. T., Lee, C., Sinha, A. K., Jordan, P. M., and Holt, J. C. (2021). The mammalian efferent vestibular system utilizes cholinergic mechanisms to excite primary vestibular afferents. *Sci. Rep.* 11:1231. doi: 10.1038/s41598-020-80367-1

Sewell, W. F. (2011). "Pharmacology and neurochemistry of olivocochlear efferents," in *Springer Handbook of Auditory Research - Auditory and Vestibular Efferents*, eds D. Ryugo and R. Fay (Cham: Springer), 83–103. doi: 10.1007/978-1-4419-7070-1_4

Singer, P., and Yee, B. K. (2012). Reversal of scopolamine-induced disruption of prepulse inhibition by clozapine in mice. *Pharmacol. Biochem. Behav.* 101, 107–114. doi: 10.1016/j.pbb.2011.12.010

Soto, E., and Vega, R. (2010). Neuropharmacology of vestibular system disorders. *Curr. Neuropharmacol.* 8, 26–40. doi: 10.2174/157015910790909511

Spinks, A., and Wasiak, J. (2011). Scopolamine (hyoscine) for preventing and treating motion sickness. *Cochrane Database Syst. Rev.* 2011:CD002851.

Sridhar, T. S., Liberman, M. C., Brown, M. C., and Sewell, W. F. (1995). A novel cholinergic "slow effect" of efferent stimulation on cochlear potentials in the guinea pig. *J. Neurosci.* 15, 3667–3678. doi: 10.1523/jneurosci.15-05-03667.1995

Storper, I. S., Spitzer, J. B., and Scanlan, M. (1998). Use of glycopyrrolate in the treatment of Meniere's disease. *Laryngoscope* 108, 1442–1445. doi: 10.1097/00005537-199810000-00004

Stöver, T., Yagi, M., and Raphael, Y. (2000). Transduction of the contralateral ear after adenovirus-mediated cochlear gene transfer. *Gene Ther.* 7, 377–383. doi: 10.1038/sj.gt.3301108

Sugai, T., Yano, J., Sugitani, M., and Ooyama, H. (1992). Actions of cholinergic agonists and antagonists on the efferent synapse in the frog sacculus. *Hear. Res.* 61, 56–64. doi: 10.1016/0378-5955(92)90036-m

Suzuki, J., Hashimoto, K., Xiao, R., Vandenberghe, L. H., and Liberman, M. C. (2017). Cochlear gene therapy with ancestral AAV in adult mice: complete transduction of inner hair cells without cochlear dysfunction. *Sci. Rep.* 7:45524.

Talaei, S., Schnee, M. E., Aaron, K. A., and Ricci, A. J. (2019). Dye tracking following posterior semicircular canal or round window membrane injections suggests a role for the cochlea aqueduct in modulating distribution. *Front. Cell Neurosci.* 13:471. doi: 10.3389/fncel.2019.00471

Taranda, J., Maison, S. F., Ballestero, J. A., Katz, E., Savino, J., Vetter, D. E., et al. (2009). A point mutation in the hair cell nicotinic cholinergic receptor prolongs cochlear inhibition and enhances noise protection. *PLoS Biol.* 7:e18. doi: 10.1371/journal.pbio.1000018

Terreros, G., Jorratt, P., Aedo, C., Elgoyhen, A. B., and Delano, P. H. (2016). Selective attention to visual stimuli using auditory distractors is altered in alpha-9 nicotinic receptor subunit knock-out mice. *J. Neurosci.* 36, 7198–7209. doi: 10.1523/jneurosci.4031-15.2016

Tu, L., Poppi, L., Rudd, J., Cresswell, E. T., Smith, D. W., Brichta, A., et al. (2017). Alpha-9 nicotinic acetylcholine receptors mediate hypothermic responses elicited by provocative motion in mice. *Physiol. Behav.* 174, 114–119. doi: 10.1016/j.physbeh.2017.03.012

Uijdehaage, S. H. J., Stern, R. M., and Koch, K. L. (1993). Effects of scopolamine on autonomic profiles underlying motion sickness susceptibility. *Aviat. Space Environ. Med.* 64, 1-8.

Vetter, D. E., Katz, E., Maison, S. F., Taranda, J., Turcan, S., Ballestero, J., et al. (2007). The alpha10 nicotinic acetylcholine receptor subunit is required for normal synaptic function and integrity of the olivocochlear system. *Proc. Natl. Acad. Sci.U.S.A.* 104, 20594–20599. doi: 10.1073/pnas.0708545105

Vetter, D. E., Liberman, M. C., Mann, J., Barhanin, J., Boulter, J., Brown, M. C., et al. (1999). Role of alpha9 nicotinic ACh receptor subunits in the development and function of cochlear efferent innervation. *Neuron* 23, 93–103. doi: 10.1016/s0896-6273(00)80756-4

Wakuda, H., Okura, T., Maruyama-Fumoto, K., Kagota, S., Ito, Y., Miyauchi-Wakuda, S., et al. (2019). Effects of anticholinergic drugs used for the therapy of overactive bladder on p-glycoprotein activity. *Biol. Pharm. Bull.* 42, 1996–2001. doi: 10.1248/bpb.b19-00407

Wala, E. P., Crooks, P. A., McIntosh, J. M., and Holtman, J. R. Jr. (2012). Novel small molecule α9α10 nicotinic receptor antagonist prevents and reverses chemotherapy-evoked neuropathic pain in rats. *Anesth Analg.* 115, 713–720. doi: 10.1213/ANE.0b013e31825a3c72

Walbaum, A. B. (2017). *α9α10 Nicotinic Acetylcholine Receptor Antagonists as Pain Modulators,* Ph. D thesis*, 2017*. Little Rock, AR: University of Arkansas for Medical Sciences.

Walia, A., Lee, C., Hartsock, J., Goodman, S. S., Dolle, R., Salt, A. N., et al. (2021). reducing auditory nerve excitability by acute antagonism of Ca2+-permeable AMPA receptors. *Front. Synaptic Neurosci.* 13:680621. doi: 10.3389/fnsyn.2021.680621

Wang, Y., Sanghvi, M., Gribizis, A., Zhang, Y., Song, L., Morley, B., et al. (2021). Efferent feedback controls bilateral auditory spontaneous activity. *Nat. Commun.* 12:2449.

Warr, W. B. (1975). Olivocochlear and vestibular efferent neurons of the feline brain stem: their location, morphology and number determined by retrograde axonal transport and acetylcholinesterase histochemistry. *J. Comp. Neurol.* 161, 159–181. doi: 10.1002/cne.901610203

Weerts, A. P., Putcha, L., Hoag, S. W., Hallgren, E., Van Ombergen, A., Van de Heyning, P. H., et al. (2015). Intranasal scopolamine affects the semicircular canals centrally and peripherally. *J. Appl. Physiol.* 119, 213–218. doi: 10.1152/japplphysiol.00149.2015

Westerberg, V., and Corcoran, M. E. (1987). Antagonism of central but not peripheral cholinergic receptors retards amygdala kindling in rats. *Exp. Neurol.* 95, 194–206. doi: 10.1016/0014-4886(87)90017-3

Yates, B. J., Miller, A. D., and Lucot, J. B. (1998). Physiological basis and pharmacology of motion sickness: an update. *Brain Res. Bull.* 47, 395–406. doi: 10.1016/s0361-9230(98)00092-6

Yu, Z., McIntosh, J. M., Sadeghi, S. G., and Glowatzki, E. (2020). Efferent synaptic transmission at the vestibular type II hair cell synapse. *J. Neurophysiol.* 12, 360–374.

Zhang, Z., Zheng, G., Pivavarchyk, M., Deaciuc, A. G., Dwoskin, L. P., and Crooks, P. A. (2008). Tetrakis-azaaromatic quaternary ammonium salts: novel subtype-selective antagonists at neuronal nicotinic receptors that mediate nicotine-evoked dopamine release. *Bioorg. Med. Chem. Lett.* 18, 5753–5757. doi: 10.1016/j.bmcl.2008.09.084

Zheng, G., Zhang, Z., Dowell, C., Wala, E., Dwoskin, L. P., Holtman, J. R., et al. (2011). Discovery of non-peptide, small molecule antagonists of alpha9alpha10 nicotinic acetylcholine receptors as novel analgesics for the treatment of neuropathic and tonic inflammatory pain. *Bioorg. Med. Chem. Lett.* 21, 2476–2479. doi: 10.1016/j.bmcl.2011.02.043

Zheng, G., Zhang, Z., Pivavarchyk, M., Deaciuc, A. G., Dwoskin, L. P., and Crooks, P. A. (2007). Bis-azaaromatic quaternary ammonium salts as antagonists at nicotinic receptors mediating nicotine-evoked dopamine release: an investigation of binding conformation. *Bioorg. Med. Chem. Lett.* 17, 6734–6738. doi: 10.1016/j.bmcl.2007.10.052

Conflict of Interest: The authors declare that the research was conducted in the absence of any commercial or financial relationships that could be construed as a potential conflict of interest.

Publisher's Note: All claims expressed in this article are solely those of the authors and do not necessarily represent those of their affiliated organizations, or those of the publisher, the editors and the reviewers. Any product that may be evaluated in this article, or claim that may be made by its manufacturer, is not guaranteed or endorsed by the publisher.

frontiers in Neural Circuits

ORIGINAL RESEARCH
published: 28 January 2022
doi: 10.3389/fncir.2021.751850

The Long and Winding Road—Vestibular Efferent Anatomy in Mice

David Lorincz[1], Lauren A. Poppi[1], Joseph C. Holt[2], Hannah R. Drury[1], Rebecca Lim[1] and Alan M. Brichta[1]*

[1]School of Biomedical Sciences and Pharmacy, The University of Newcastle, Callaghan, NSW, Australia, [2]Department of Otolaryngology, University of Rochester, Rochester, NY, United States

The precise functional role of the Efferent Vestibular System (EVS) is still unclear, but the auditory olivocochlear efferent system has served as a reasonable model on the effects of a cholinergic and peptidergic input on inner ear organs. However, it is important to appreciate the similarities and differences in the structure of the two efferent systems, especially within the same animal model. Here, we examine the anatomy of the mouse EVS, from its central origin in the Efferent Vestibular Nucleus (EVN) of the brainstem, to its peripheral terminations in the vestibular organs, and we compare these findings to known mouse olivocochlear anatomy. Using transgenic mouse lines and two different tracing strategies, we examine *central* and *peripheral* anatomical patterning, as well as the anatomical pathway of EVS axons as they leave the mouse brainstem. We separately tag the left and right efferent vestibular nuclei (EVN) using Cre-dependent, adeno-associated virus (AAV)-mediated expression of fluorescent reporters to map their central trajectory and their peripheral terminal fields. We couple this with Fluro-Gold retrograde labeling to quantify the proportion of ipsi- and contralaterally projecting cholinergic efferent neurons. As in some other mammals, the mouse EVN comprises one group of neurons located dorsal to the facial genu, close to the vestibular nuclei complex (VNC). There is an average of just 53 EVN neurons with rich dendritic arborizations towards the VNC. The majority of EVN neurons, 55%, project to the contralateral eighth nerve, crossing the midline rostral to the EVN, and 32% project to the ipsilateral eighth nerve. The vestibular organs, therefore, receive bilateral EVN innervation, but without the distinctive zonal innervation patterns suggested in gerbil. Similar to gerbil, however, our data also suggest that individual EVN neurons do not project bilaterally in mice. Taken together, these data provide a detailed map of EVN neurons from the brainstem to the periphery and strong anatomical support for a dominant contralateral efferent innervation in mammals.

Keywords: vestibular, efferents, anterograde, retrograde, mouse, cre-dependent

OPEN ACCESS

Edited by:
Soroush G. Sadeghi, University at Buffalo, United States

Reviewed by:
Amanda Lauer, Johns Hopkins University, United States
Anna Lysakowski, University of Illinois at Chicago, United States

****Correspondence:***
David Lorincz
David.Lorincz@uon.edu.au

Received: *24 August 2021*
Accepted: *23 December 2021*
Published: *28 January 2022*

Citation:
Lorincz D, Poppi LA, Holt JC, Drury HR, Lim R and Brichta AM (2022) The Long and Winding Road—Vestibular Efferent Anatomy in Mice. Front. Neural Circuits 15:751850. doi: 10.3389/fncir.2021.751850

INTRODUCTION

Two separate and distinct efferent systems transmit information from the central nervous system to peripheral inner ear organs (**Figure 1**). (1) The olivocochlear (OC) system comprises medial and lateral olivocochlear neurons that innervate the cochlea; and (2) efferent vestibular system (EVS) consisting of efferent vestibular nucleus (EVN) neurons that innervate the vestibular organs

(Ryugo et al., 2011; Cullen and Wei, 2021). Superficially, the two systems share similarities in form and function, and therefore it has been tempting to consider them as operationally equivalent. Indeed, both auditory and vestibular efferent neurons are localized to the brainstem and they both have a similar mechanism of action, using cholinergic and peptidergic neurotransmitters to modify peripheral hair cell and primary afferent activity (Ryugo et al., 2011; Cullen and Wei, 2021). Both groups of efferent neurons are also proportionately fewer in number when compared to their afferent counterparts, and both efferent systems branch extensively to provide a significant peripheral terminal distribution within their respective inner ear organs (Brown, 2011; Holt et al., 2011). However, closer inspection reveals there are key differences that are likely to influence their function. For example, despite being in the brainstem, the location of the auditory and vestibular efferent neurons are different and therefore descending influences are likely dissimilar. OC neurons are found ventrally in the trapezoid body and the lateral superior olive (Brown, 2011), while EVN neurons are typically more dorsal, lying above the facial genu and below the vestibular nucleus complex (Holt et al., 2011). Both efferent systems receive innervation from targets of their afferent counterparts. Thus, OC neurons receive innervation from the cochlear nucleus, while EVN neurons receive innervation from the vestibular nucleus complex. To examine these differences further, however, requires a detailed anatomical understanding of both efferent systems in the same animal model. While auditory efferents have been studied broadly across many species, vestibular efferents have received much less attention. To date, the gerbil is the only rodent model for which there is detailed information on both central and peripheral vestibular efferent anatomy (Perachio and Kevetter, 1989; Purcell and Perachio, 1997). In mouse, a more common laboratory animal and for which there is the requisite detail on auditory efferent anatomy, there are only isolated studies of EVN neurons (Leijon and Magnusson, 2014; Mathews et al., 2015) and even less anatomical data on vestibular efferent central pathways or peripheral innervation patterns (Jordan et al., 2015). Therefore, our study has attempted to fill in the anatomical gaps of the mouse EVS so that it would be possible to examine both the auditory and vestibular efferent systems in the same species.

We used three transgenic mouse lines and two different tracing strategies to examine *central* and *peripheral* vestibular efferent anatomy. By using Cre-dependent, AAV-mediated expression of fluorescent reporters we were able to label the left and right EVN neurons, separately, with different colored fluorophores. The labeling included cell bodies, dendritic architecture, axonal projections, and efferent terminals in vestibular neuroepithelia. EVN dendritic arborization extended well into adjacent dorsal and medial regions including the vestibular nucleus complex. We traced their respective axonal trajectories as they exited the mouse brainstem with the vestibulocochlear nerve. In addition, we were able to follow these color-coded axons to their peripheral terminal fields in the same vestibular organs. We coupled these anterograde results with Fluro-Gold retrograde labeling to quantify the proportion of ipsi- and contralaterally projecting cholinergic efferent neurons. Our results support the absence of individual EVN neurons projecting bilaterally and confirm previous studies that identified the location of mouse EVN neurons (Leijon and Magnusson, 2014; Mathews et al., 2015). However, our results are in contrast with the peripheral innervation patterns described in the gerbil (Purcell and Perachio, 1997). This suggests there may be significant interspecies differences in the organization, and perhaps the function, of the EVS. Therefore, as suggested previously, caution should not only be exercised when extrapolating EVS results from other vertebrate classes to mammals (Holt et al., 2011), but even among members of the same order, such as rodents.

MATERIALS AND METHODS

Bioethics Statement

All experimental procedures were approved by The University of Newcastle Animal Care and Ethics Committee prior to experiments. Adult mice (4–8 months and both sexes) from three transgenic mouse strains were used in this study. **Strain 1**, "*Chat-Cre*" (B6;129S6-*Chat*$^{tm2(cre)Lowl}$/MwarJ; JAX #028861), is a homozygous driver mouse line expressing Cre recombinase in cholinergic neurons. **Strain 2**, "*Chat-ChR2*", is the heterozygous line resulting from the crossing of homozygous *Chat-Cre* mice with homozygous Ai32 mice (B6.Cg-*Gt(ROSA)26Sor*$^{tm32(CAG-COP4*H134R/EYFP)Hze}$/J; JAX #024109). *Chat-ChR2* mice co-express the light-sensitive channel, channelrhodopin-2, and enhanced yellow fluorescent protein (ChR2-eYFP) in cholinergic neurons. **Strain 3**, "*Chat-gCaMP6$_f$*", is the heterozygous line resulting from the crossing of homozygous Chat-Cre mice with homozygous Ai95D mice (B6J.Cg-*Gt(ROSA)26Sor*$^{tm95.1(CAG-GCaMP6f)Hze}$/MwarJ; JAX #028865). *Chat-gCaMP6$_f$* mice express the calcium indicator protein GCaMP6$_f$ in cholinergic neurons. Strain 1, *Chat-Cre* mice, were used for Cre-dependent anterograde viral tracing studies and as a foundation line for *Chat-ChR2* and *Chat-GCaMP6$_f$* strains. *Chat-ChR2* mice were used for general anatomical mapping of cholinergic neurons, and *Chat-GCaMP6$_f$* mice were used for retrograde labeling studies. Genotyping was done in conjunction with Australian BioResources and the Garvan Institute, using the standard forward and reverse primer sequences recommended by the Jackson Laboratory for these commercially available live strains.

Anterograde Tracing With Adeno-Associated Viruses (AAVs)

Chat-Cre mice were anesthetized using isoflurane (5% induction, 1.5–2% maintenance) and placed in a standard head-fixed mouse stereotaxic frame (David Kopf Instruments, USA). Two different adeno-associated viruses (AAVs) were injected unilaterally into the brainstem, to produce either *Cre*-dependent ChR2-mCherry (AAV5/Efla-DIO-hChR2-(H134R)-mCherry, Addgene, #20297) or *Cre*-dependant ChR2-eYFP (AAV5/Efla-DIO-hChR2-(H134R)-eYFP, Addgene, #20298) expression on opposite sides of the brainstem. In wild type mice (C57BL6) antibody labeling against ChAT protein allows for the location of cholinergic cell bodies but does not provide clear labeling

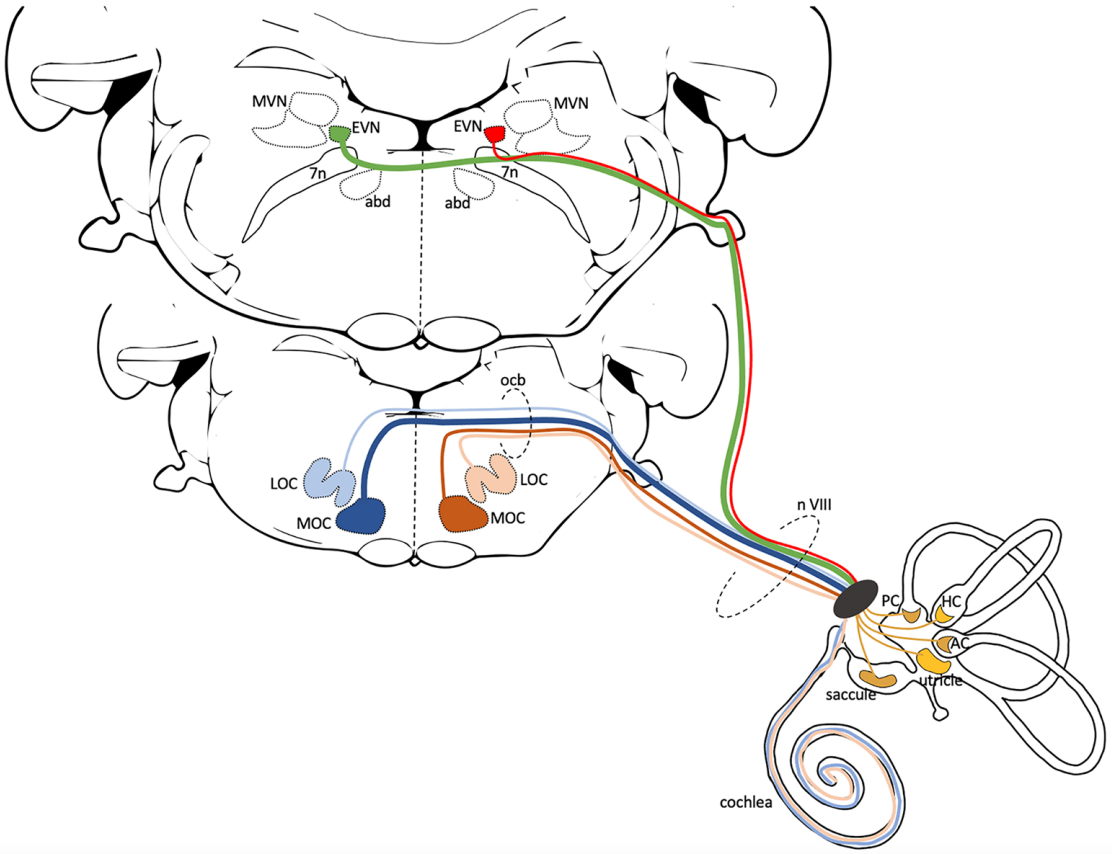

FIGURE 1 | Central anatomy of the Cochlear and Vestibular Efferent System. This schematic illustrates the generic central pathways of the cochlear and vestibular efferent systems in mammals. Both efferent systems have ipsi- and contralateral projections, but here only the left side projections are illustrated. The lower brainstem slice (more rostral) shows the position of lateral and medial olivocochlear neurons (LOC, MOC). Blue lines represent contralateral, beige and brown lines represent ipsilateral efferent cochlear projections. In mice, the majority of the 475 cochlear efferent axons that innervate a cochlea are LOC neurons (~65%). Most of these LOC axons originate from the ipsilateral side (beige—99%) with only a few from the contralateral side (light blue—1%). MOC axons contribute ~35% to cochlea efferent input. Most of the MOC axons originate from the contralateral side (dark blue—75%) and the remaining from the ipsilateral side (brown—25%) (Campbell and Henson, 1988). The upper brainstem slice (more caudal) shows the position of EVN, dorsolateral to the facial nerve and genu (7n) and neighboring regions, the Medial Vestibular Nucleus (MVN), and the abducens nucleus (abd). To date, in mice, it is unclear the number or percentage of EVN cells that send ipsilateral (red line), contralateral (green line), or perhaps bilateral projections. The cochlear and vestibular efferents join the vestibulocochlear nerve (n VIII) as it exits the brainstem and travel together to the inner ear. The cochlear projections innervate the inner hair cells (LOC efferents) and outer hair cells (MOC efferents) in the organ of Corti. The efferent vestibular projections innervate Type II hair cells, afferent nerve fibers, and afferent calyx terminals in the five vestibular organs: saccule, utricle, anterior crista (AC), horizontal crista (HC), posterior crista (PC).

that spans the dendritic and axonal fields of Efferent Vestibular Nucleus (EVN) neurons. Therefore, using ChR2, which is commonly used as a light-sensitive circuit mapping tool, here we exploit its membrane-bound properties for anatomical purposes. The dense and uniform distribution of ChR2, together with co-expressed eYFP, within the membranes of cell bodies, dendrites, and axons allowed for enhanced cytoarchitectural labeling of EVN neurons, both centrally and peripherally. AAVs generating ChR2-mCherry and ChR2-eYFP were injected into the left and right EVN, respectively. For comparison, in two cases we reversed the injection sites, mCherry virus into the right side, and eYFP into the left. No difference in label or distribution was observed. Using pulled glass micropipettes (Drummond glass, 3.5", 3000203G/X), the virus was injected intracranially (200–400 nl) using a microinjection system (Nanoinject II, Drummond SCI, USA) at a rate of 1nl/s. The coordinates of the EVN were initially determined using Mouse Brain Atlas (Paxinos and Franklin, 2001) but were later modified in response to more detailed targeting studies (**Figure 2**). In a typical 26 g adult mouse, AAV injections used the following co-ordinates: $X = \pm 0.7$, $Y = 5.8$, $Z = 4.5$ mm from bregma, where X represents the interaural axis (or distance from the mid-line), Y the anteroposterior line (rostrocaudal) axis, and Z is the dorsoventral distance (or depth) from the bony surface of the skull at bregma. Using these co-ordinates, we specifically labeled the EVN, without interfering or labeling the large cholinergic abducens nucleus located more ventrally (**Figures 3A,B**). Mice were closely monitored during and after the surgeries in accordance with an institutionally approved animal ethics protocol and for

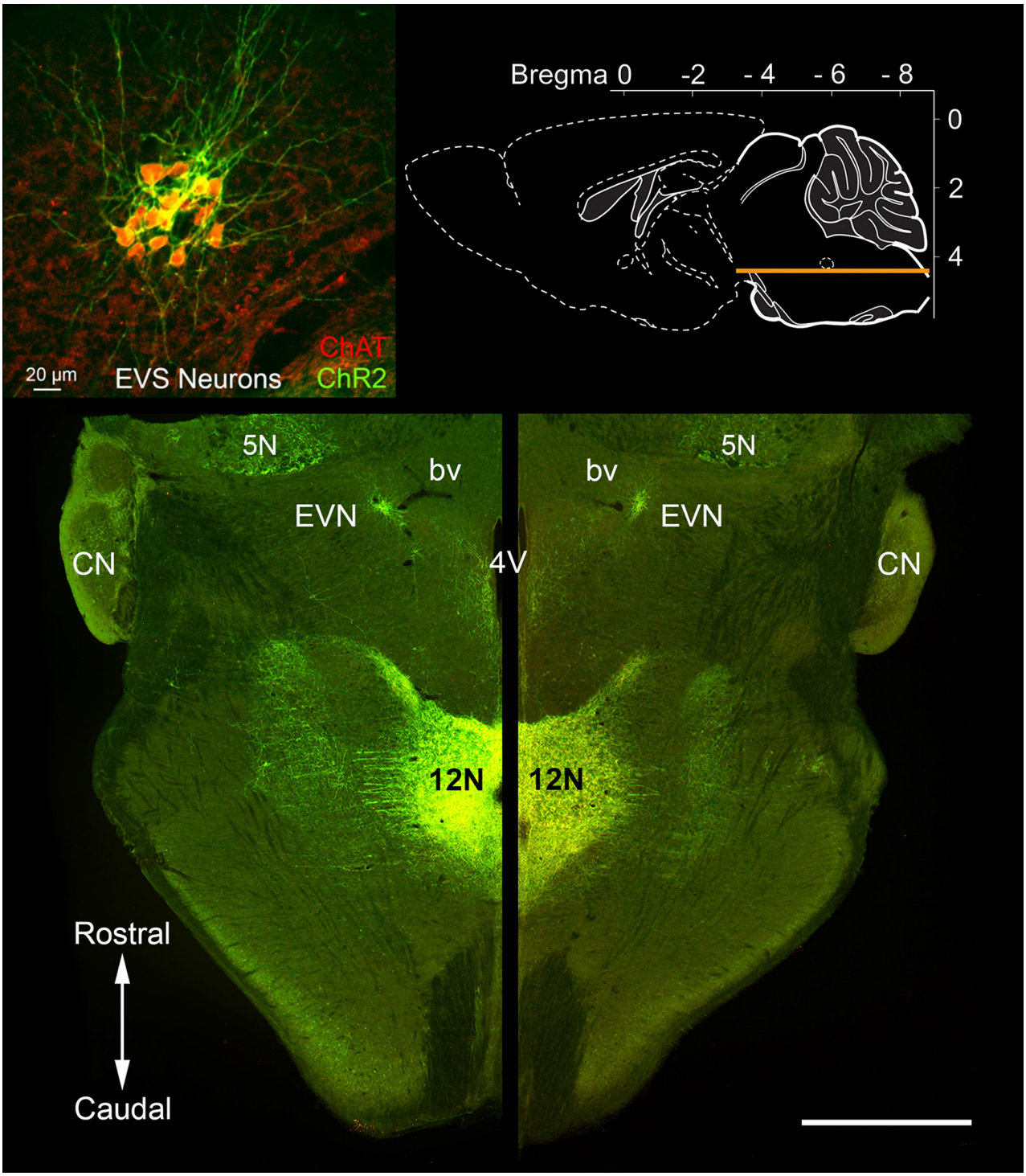

FIGURE 2 | Rostrocaudal location of the Efferent Vestibular Nucleus (EVN). A horizontal section through the brainstem (see top right inset) of a *Chat-ChR2* mouse, where enhanced yellow fluorescent protein (EYFP) and the light-sensitive channels, Channelrhodopsin-2 (ChR2), are co-expressed in cholinergic neurons. The tightly packed Efferent Vestibular Nucleus (EVN) neurons, which are the source of efferent input to the vestibular periphery, are fluorescently labeled and localized at the same level as the floor of the fourth ventricle (4V). EVN neurons were confirmed as cholinergic by double-labeling with antibodies against EYFP (ChR2) and choline acetyltransferase (ChAT), the enzyme responsible for the synthesis of acetylcholine. There was a complete overlap of the two labels as shown in the top-left inset. Similar one-to-one overlap was also observed with our *Chat-gCaMP6f* mouse strain. A characteristic feature seen in both horizontal and transverse slices is the close association between the EVN and nearby blood vessels (bv) as can be seen on both left and right sides. CN = Cochlea Nucleus; 5N = Trigeminal nucleus; 12N Hypoglossal nucleus. Scale bar: 1 mm.

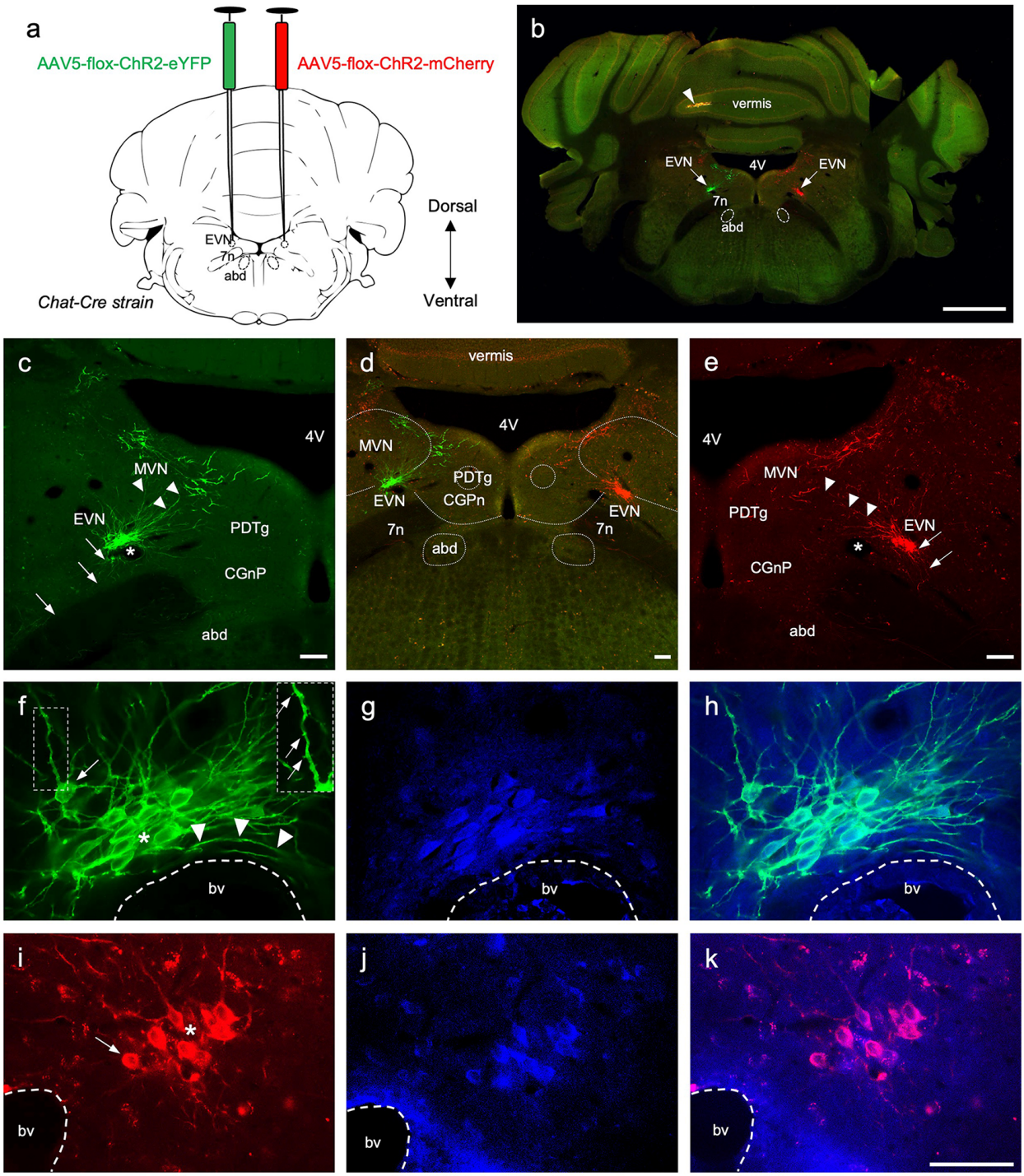

FIGURE 3 | The central components of the Efferent Vestibular System. **(A)** A schematic of a transverse section showing the double intracranial virus injection experiments in *Chat-Cre* strain. AAV5-flox-ChR2-eYFP virus was injected in the left Efferent Vestibular Nucleus, EVN (green), and AAV5-flox-ChR2-mCherry virus were injected in the right EVN (red). 7n—genu of the facial nerve, abd—abducens nucleus. **(B)** Photo-merged image of brainstem transverse section at the level of the EVN following adenovirus injection. The right side of the cerebellum was purposely nicked, prior to sectioning, to help orient sections when mounting. Arrows point at the viral-induced expression of EYFP (green) on the left, and mCherry (red) on the right. 4V—4th ventricle, arrowhead—yellow fluorescent signal in the cerebellar vermis. Scale bar: 1 mm. **(C–E)** Left panel, EVN (green channel), middle panel composite image (red and green channels), and right panel EVN (red channel). Both EVNs show extensive dorsomedial branching towards neighboring brain regions, which include MVN—Medial Vestibular Nucleus, PDTg—posterodorsal tegmental nucleus, CGPn—central gray of the pons. Arrows indicate descending axonal projections; arrowheads indicate dendritic branches; (*Continued*)

FIGURE 3 | Continued
asterisks show lumen of blood vessels. Fluorescent dendritic fibers were observed beyond the arrowheads (on both sides) and a subgroup of cholinergic MVN neurons which had more robust dendritic architecture and could be easily distinguished from EVN dendrites. Scale bar: 100 μm. **(F–H)** Left and middle panels, higher magnification of EVN following GFP (green) and ChAT (blue) immunohistochemistry. Right panel, a composite. Right Inset panel **(F)**: dendrite, arrows pointing to dendritic spines. Arrowheads in **(F)**—fibers curved around the blood vessel. bv—blood vessel; asterisk—tightly packed EVN cells; arrow in **(F)**—cell at the periphery of the tightly packed EVN group. **(I–K)** Right and middle panel, EVN following RFP (red) and ChAT (blue) immunohistochemistry. The right panel is the composite image. bv—blood vessel, asterisk—tightly packed EVN cells, arrow—EVN cell at the periphery of the nucleus. Scale bar **(F–K)**: 50 μm.

optimal viral transduction were allowed to recover for up to 3 weeks.

Fifteen (nine males, six females) animals were used for intracranial bilateral virus injection. The brain and vestibular tissue were processed for anatomical studies from all animals. The virus injection surgeries were successful in eight animals (six males, two females), and these were used for final anatomical validation, where the processed tissue was of good quality and fluorescent protein was strongly expressed in the brain and inner ear tissue for confocal imaging. **Figures 3–5** are from three of these mice.

Retrograde Tracing With Fluoro-Gold

Chat-GCaMP6$_f$ mice were anesthetized and placed in a stereotaxic frame, as described above for anterograde labeling experiments. For retrograde injections, we used a trans-canicular approach based on a procedure described by Guo et al. (2018). The head was rolled 45 degrees to one side allowing easier access for a post-auricular incision. The skin was reflected and the translucent temporal bone, overlying the posterior canal, was exposed, and pierced using a fine 30G needle allowing direct access to the underlying membranous posterior semicircular canal. Fluoro-Gold (FG; 4 μl; Fluorochrome, LLC; Denver, CO) was slowly injected by hand over a 5-min period using a pulled glass electrode (Drummond, 3.5", 3000203G/X) attached and sealed with dental wax to a Hamilton syringe. After injection, the hole in the bony semicircular canal was plugged with dried muscle tissue, held in place with adhesive (Vetbond, 3M, No.14690), and the skin incision closed with sutures. The mice were regularly monitored during the recovery and post-operative period that ranged from 3 to 7 days.

From the *Chat-GCaMP6$_f$* strain four animals (all males) were used for the quantification of retrograde tracing. Two females were also injected in the inner ear, however, labeling was unsuccessful in their case. Images from two mice are shown on **Figure 6** as representative images for retrograde Fluoro Gold labeling.

Tissue Preparation and Immunofluorescent Labeling

After the respective post-surgical recovery times, mice were deeply anesthetized with an intraperitoneal cocktail of ketamine (100 mg.kg^{-1}) and xylazine (0.01 ml/g). Once deeply anesthetized, mice were transcardially perfused with heparinized saline, followed by 4% paraformaldehyde in 0.1 M phosphate-buffered saline (PFA). The brainstem and inner ears were isolated and post-fixed for 3 h in fresh PFA. After rinsing in phosphate-buffered saline (PBS), the inner ears were isolated under a dissecting stereo microscope (Leica, M165 FC), the triad of the anterior and horizontal ampullae, and the utricle were gently freed from the surrounding bone and the overlying ampullary and utricular membrane was detached using a fine scissor to expose the vestibular neuroepithelia and to remove otolith crystals from the utricles. Isolated individual posterior cristae were processed similarly. Following the inner ear dissections, the vestibular organs were mounted on a concave microscope slide, cover-slipped using 50% glycerol/PBS solution, and were imaged as wholemounts. After imaging, triads were cryoprotected in 30% sucrose/PBS solution overnight, prior to sectioning at 30–50 μm using a Leica CM1950 cryostat. For anterograde labeling of fine processes in brainstem slices (dendrites, axons) and peripheral vestibular organ slices (axon terminal fields), we used immunofluorescent labeling to enhance red fluorescent protein (mCherry) and eYFP signal. Triads were embedded in OTC mounting media and were sectioned (30 μm) in a cryostat.

For retrograde FG labeling experiments, EVN cells were visualized in the *Chat-gCaMP6$_f$* mice, through immunolabeling amplification of GFP signal. In a subset of virally transfected EVN neurons we also immunolabeled ChAT-positive cell bodies in brainstem slices and efferent terminals in the peripheral vestibular organs.

Brainstem and vestibular organ sections were incubated in primary antibodies (anti-RFP, 1:200, Chromotek; anti-GFP, 1:200, Abcam; and anti-ChAT, 1:150, Merck) for 2 days. After primary antibody incubation, the tissue was washed three times in 0.1 M PBS for 10 min and then incubated in secondary antibodies (Alexa 405, 1:50; Alexa 488, 1:200; and Alexa 594, 1:200, Abcam) for 2 h then washed in 0.1 M PBS, mounted and cover-slipped in 50% glycerol PBS mounting solution.

Microscopy and Image Processing

EVN neurons in brainstem sections and their efferent terminals in vestibular organs were imaged using a Nikon C1 confocal microscope with 20×, 40×, and 60× objectives. To count the number of GFP- and FG-labeled EVN neurons, the brainstem slices were imaged with a z-stack step size of 0.7 μm. To visualize the efferent terminal fields z-stack images were collected at step size 0.65 μm. Images were processed and reconstructed as maximum intensity projections or 3D reconstructions using ImageJ (NIH Image) and FluoRender (Scientific Computing and Imaging Institute, University of Utah) software.

Statistics

GraphPad Prism software (version 9.2.0, GraphPad Software, Inc, CA, USA) was used for statistical analysis. When analyzing the frequency of GFP-positive ipsilateral and contralateral EVN neurons, with and without Fluorogold (FG) labeling, we used 2 × 2 contingency tables in which the G-Statistic test of independence was computed with a Williams' correction for type

I errors (Sokal and Rohlf, 1981). Statistical significance was set at $p < 0.05$. A significant result indicated that the distribution of FG-positive cells constituted a separate population from those that were FG-negative.

RESULTS

The Central Efferent Vestibular System (EVS)

We used a *Chat-ChR2* mouse line ($n = 5$; two males and three females) to explore the precise location and co-ordinates of the EVN nucleus. Horizontal brainstem sections like that shown in **Figure 2**, provided the rostrocaudal location, and coronal sections provided the dorsoventral location of the EVN (**Figure 3**). Expression of eYFP in *Chat-ChR2* animals showed a one-to-one colocalization with ChAT labeling (inset, **Figure 2**).

To target the EVN specifically, we intracranially injected Cre-dependant AAVs into Chat-*Cre* mice. This resulted in strong endogenous expression of eYFP and mCherry in the left and the right EVN, respectively (**Figures 3A,B** arrows), and could be clearly visualized using confocal microscopy without amplification with antibodies (**Figure 3B**). Using this approach, we were able to avoid off-target labeling of nearby cholinergic populations such as the abducens nucleus (abd) and the olivocochlear system. In two cases, we reversed the injection sites, such that the left EVN was injected with the ChR2-mCherry virus and the right EVN was injected with the ChR2-eYFP virus (**Figure 5a1**). Both viruses strongly expressed the fluorescent marker proteins in the brain and vestibular tissue, although in most cases the eYFP signal was more intense than that of mCherry under our confocal microscopy conditions. Both viruses effectively labeled EVN cell bodies, their primary and distal dendrites, their axon fibers, and peripheral terminals (**Figures 3–5**).

Nearly all eYFP- and mCherry-labeled cell bodies were contained tightly within a single EVN. Sporadically, some labeled cell bodies were found above the injection site in the Medial Vestibular Nucleus (MVN) close to the ventricular border (**Figures 3C–E**). The dendrites of these MVN labeled neurons could be easily distinguished from those of the EVN neurons as they were thicker and located well above (dorsal to) the EVN. Our results suggested only one EVN population or cluster on each side of the brainstem in mice and this was confirmed by our retrograde labeling results (see below). The EVN nucleus was located dorsolateral to the genu of the facial nerve bundle (g7n), approximately 0.7 mm from the midline, and −5.8 mm caudal from Bregma (Paxinos and Franklin, 2001). Distinctive features of the EVN are its relatively small size compared to the abducens nucleus, dense neuronal packing, and rich dendritic projections. The majority of EVN cell bodies formed the "core" of the EVN nucleus and overlapped with one another (**Figures 3F,I**, asterisk). However, some labeled EVN neurons were found further away from the dense core (**Figures 3F,I**, arrow), although still within 50 μm of the core cluster.

EVN neurons exhibit extensive dendritic branching, mainly dorsal and dorsomedial, infiltrating the ventral parts of the neighboring MVN (**Figures 3C,E**; arrowheads). In addition, dendritic fibers were also found reaching towards the *posterodorsal tegmental nucleus* (*PDTg*) and the *central gray of the pons* (*CGnP*; **Figure 3D**).

EVN axon fibers, thinner than primary dendrites, were also visualized. Originating from the ventral side of the EVN (**Figures 3C,E**, arrows), axon fibers bound for the ipsilateral and inner ear projected ventrolaterally, in the direction of the root of the eighth cranial (vestibulocochlear) nerve. However, axon fibers bound for the contralateral inner ear first projected rostrally before crossing the midline, and then returned caudally to rejoin the ventrolateral projecting fibers originating from the EVN on that side. Unexpectedly, yellow (red, and green overlap) labeling was found in two animals in a constrained area of the cerebellar vermis (**Figure 3B**, arrowhead, **Supplementary Figures 1A–C**).

In some cases where we needed to visualize finer structures, we used immunofluorescent labeling (GFP, RFP) to enhance virally expressed green and red fluorescent signals in labeled EVN neurons for better resolution of cytoarchitecture. EVN neurons and their projections were delineated in clear detail (**Figures 3F,I**), and in many cases, we were able to visualize dendritic spines (see **Figure 3F** inset). In addition, antibody labeling confirmed the simultaneous presence of ChAT and therefore the cholinergic identity of these neurons (**Figures 3F–K**). In all cases, where EVN neurons were virally tagged with eYFP or mCherry, they also labeled positive for ChAT (blue, **Figures 3G,J**)), further demonstrating the one-to-one labeling specificity (**Figures 3H,K**).

It should be noted that the EVN was always found close to a characteristic local blood vessel (bv, **Figures 3F–K**), which often impacted neuronal cytoarchitecture as fibers curved around the vessel (**Figure 3F**, arrowheads). In one case, the blood vessel separated EVN neurons.

EVN Contralateral Axons Cross the Midline Rostral to Their Cell Bodies

As described above, to view labeled processes, particularly the axonal fibers, we amplified the eYFP and mCherry signal using primary antibodies against GFP and RFP, respectively. We were able to visualize the axons originating from the EVN and identify the precise location where the axonal bundle crossed the midline of the brainstem and projected toward the contralateral vestibulocochlear nerve (**Figure 4**). The level of the crossing fibers (decussation) was rostral to the location of EVN cell bodies by approximately 100 μm (−5.6 mm from Bregma). Note, at this level (**Figures 4B,C**) there were only green and red distal dendrites of EVN neurons on the left side and right side, respectively (**Figure 4B**, left and right arrows).

A green axonal fiber bundle originating from the left side EVN (**Figure 4D**, arrowheads; **Figure 4F** arrows) and red fibers from the right side EVN (**Figures 4E,F**, arrowheads) crossed the midline of the brainstem at the same level. Two features can be observed from these contralaterally projecting axon bundles. (1) Following their decussation, the bundles travel ventral to the genu of the facial nerve (**Figure 4C**, arrowhead); and (2) the

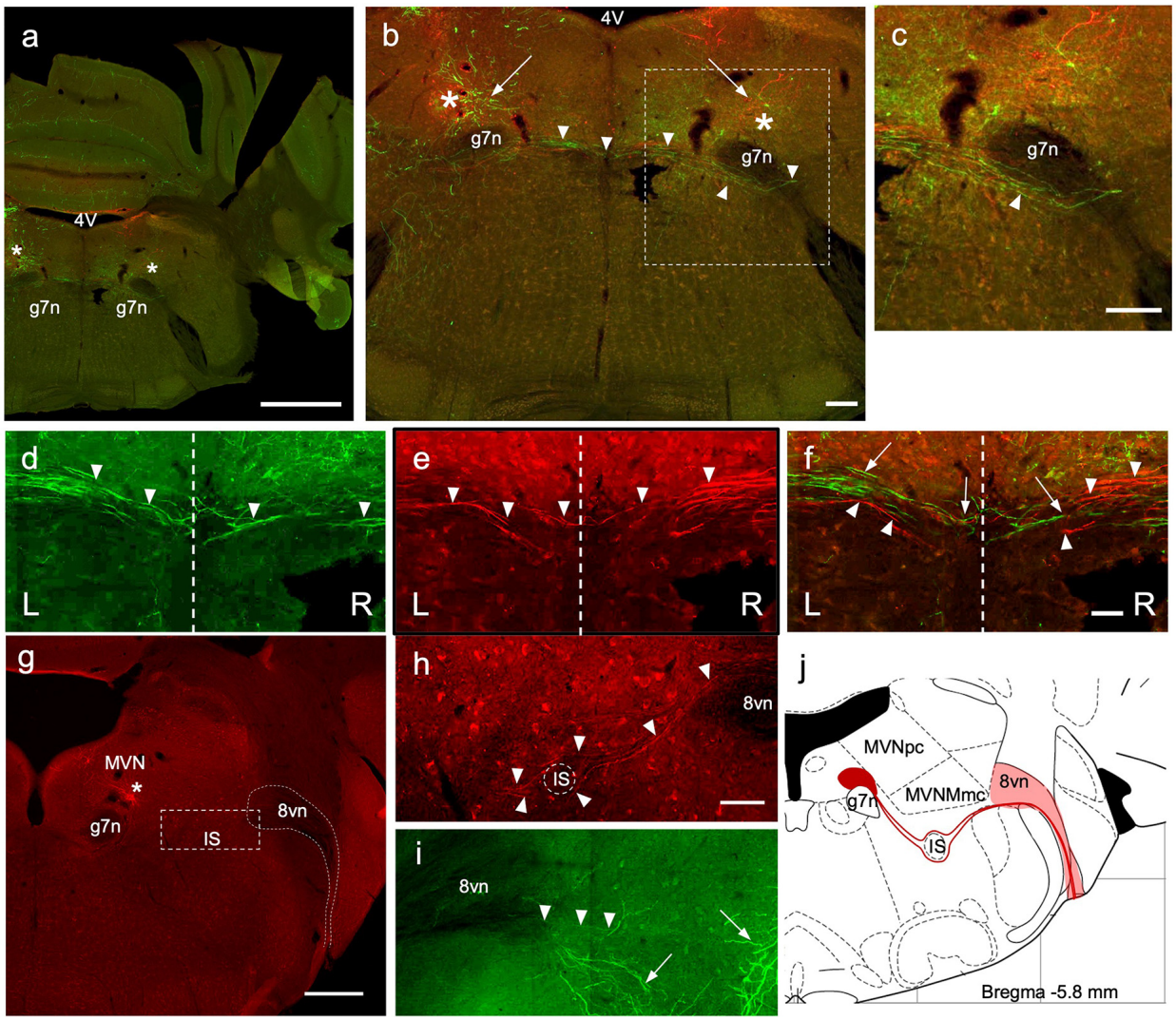

FIGURE 4 | Crossing EVN fibers. **(A)** Photo-merged image of a transverse brainstem section at the level of the crossing fibers. The right-side cerebellum was nicked before sectioning for orienting. 4V—4th ventricle, 7n—genu of the facial nerve. Asterisks represent a projected area where EVN cell bodies would be in more caudal slices. Scale bar: 1 mm. **(B)** Virally induced fluorescent efferent axons crossing the midline (arrowheads). 4V—4th ventricle, arrows—level of the EVN and fluorescent branches, 7n—genu of the facial nerve. Scale bar: 100 μm. **(C)** Higher magnification of "b" dashed box, showing the trajectory of contralateral efferent axons after crossing the midline, going underneath (arrowhead) the genu of the 7th nerve (g7n) and heading towards the eighth nerve exit. **(D–F)** Green and red efferent axonal fibers, originate from the left and right EVN, respectively, and cross the midline (dashed line) of the brainstem. Arrowheads point to crossing fibers. In composite panel **(F)**. Arrows—green (left) fibers; arrowheads—red (right) fibers. Scale bar **(D–F)**: 50 μm. L = Left, R = Right. Scale bar: 100 μm. **(G–J)** Low magnification **(G)** of the right side (red) showing labeled red fluorescent EVN cell bodies (below the asterisk) located near blood vessels. Since there are fewer ipsilateral axons, they were harder to trace than contralateral axons. Nevertheless, we saw ipsilateral axons descend ventrally (**I**; green) and then re-ascend, dorsally (**H**; red). As the ipsilateral axon bundle ascends it divides around the inferior salivary nucleus **(G,H)** on its way to the vestibular root of the vestibulocochlear nerve (8vn). This tortuous and winding trajectory of ipsilateral axons is summarized in schematic **(J)**. Scale bar for panel **(G)** is 500 μm; Scale bar 50 μm for panels **(H,I)**.

contralateral axonal bundle appeared to be larger relative to the number of ipsilateral axons.

EVN Ipsilateral Axons Stay at the Level of Their Cell Bodies

Although ipsilateral EVN axons exhibited endogenous fluorescence following injection of Cre-dependent AAVs, amplification *via* immunofluorescent labeling allowed for better visualization of finer structures (**Figures 4G–I**). EVN fibers projecting to the ipsilateral inner ear appeared fewer in number and less densely packed than those projecting to the contralateral inner ear. The trajectory of ipsilateral axons was more caudal to the level of the contralateral axons and could be observed in the same section as the EVN, at approximately −5.8 mm from Bregma (**Figure 4G**). We summarized the trajectory and the sparser density of ipsilaterally projecting EVN axons in a schematic drawing (**Figure 4J**). Starting from the EVN, ipsilaterally projecting fibers curved ventrally to avoid the genu

of the 7th nerve (g7n) located medially, and the magnocellular and parvocellular MVN (MVNmc, MVNpc) located superiorly. The fine axon fibers (**Figures 4H,I**, arrowheads) were easily distinguishable from EVN dendrites (**Figure 4I**, arrows), which had characteristically thicker and arborized morphology. The ipsilaterally-projecting fibers traveled both dorsal and ventral to the inferior salivatory nucleus (IS), thus helping to delineate it (**Figure 4H**). After passing by the IS, the ipsilateral fibers reconverged to form a single bundle where they joined with other afferent and efferent vestibular fibers entering the vestibular root of the vestibulocochlear nerve (**Figure 4**; 8vn).

The Peripheral Projections of the Efferent Vestibular System

To study the efferent innervation of the peripheral vestibular organs following intracranial injection of AAV, we used wholemounts of isolated, semi-intact, triad preparations comprising three conjoined vestibular organs: anterior crista (AC), horizontal crista (HC), and utricle (U; **Figures 5a4,b1**). We also used separate wholemounts of isolated posterior cristae (PC) and sacculus. This approach allowed us to preserve most of the vestibular neuroepithelium intact. However, due to the difficulty of isolation, saccular data remained incomplete. Nevertheless, data from the sacculus supported our general findings from the other vestibular organs.

In addition to being expressed in EVN cell bodies and dendrites, AAV-mediated and *ChAT-Cre*-dependent expression of eYFP and mCherry was observed in all peripheral vestibular organs (**Figure 5**). In most cases, endogenous expression was bright enough to observe efferent nerve fibers and bouton terminals within the peripheral vestibular organs, without immunolabeling enhancement (**Figures 5B,D**). Only the *septum cruciatum*, a characteristic non-sensory ridge in mouse vertical canals (AC and PC) was devoid of eYFP and mCherry fluorescence (AC: **Figures 5b1,d1**, arrows; PC: **Figures 5b3,d3**, arrows).

Vestibular organ wholemounts provided valuable information on the general presence of ipsi- and contralaterally-originating efferent projections. However, due to the curved surface of the vestibular cristae, capturing the detailed innervation patterns of efferent terminals is technically challenging. This is because observing a wholemounted cristae from above, for example, only provides a true indication of efferent terminal density where the surface of the crista is perpendicular to the line of sight. Viewing the remaining surface of the crista from above, particularly the sides of the crista, becomes increasingly problematic as the surface orientation, with respect to the line of sight, changes from perpendicular to parallel. Simply put, terminal density appears greater than it really is on the crista sides when viewed from above. This foreshortening effect is compounded in the cristae peripheral zones, where efferent terminals from both ipsi- and contralateral EVNs appeared to be more abundant when compared to central zones of the cristae (e.g., **Figures 5b1,b2,d1,d2**). This peripheral zone bias of crista efferent innervation was mirrored in the peripheral zones of the utricle (**Figures 5b1,b2,d1,d2**) and saccule (**Supplementary Figures 1D–G**). Therefore, for a more detailed examination, transverse sectioning of the vestibular organs was required (**Figures 5b2,d2**, dashed white lines). Immunofluorescent labeling was used to enhance eYFP and mCherry signal from fine terminal fields. As suggested by wholemounts, dense eYFP- and mCherry-positive efferent nerve fibers and boutons were found interspersed throughout the left and right AC (**Figures 5c1–c3,e1–e3**, arrowheads), however, peripheral regions were preferentially innervated (e.g., **Figure 5c3**). Similarly, eYFP- and mCherry-positive fibers and terminals were observed in the left and right HC along the whole length of the sections with a preferential peripheral distribution pattern (**Figures 5c4–c6,e4–e6**, arrowheads pointing at nerve end terminals). Similar interspersed distributions of ipsilateral and contralateral innervation were observed in the utricle (**Figures 5c7–c9,e7–e9**) and saccule (see **Supplementary Figures 1D–G**). Superimposing eYFP and mCherry images showed no differences in ipsilateral vs. contralateral efferent terminal fields within individual vestibular organs and although they were distributed throughout, in all vestibular organs: PC (**Figures 5b4,d4**), AC (**Figures 5c3,e3**), HC (**Figures 5c6,e6**), U (**Figures 5c9,e9**) there was a clear peripheral bias for both ipsi- and contralateral efferent innervation. All virally tagged fibers and terminals in the vestibular organs were positive for ChAT, and there were rarely ChAT-positive and eYFP- or mCherry-negative elements (data not shown). This confirmed our AAV labeling had captured the full complement of ChAT-positive efferent fibers and their associated terminal fields in the vestibular organs.

Retrograde Tracing and Cell Counts of EVN Neurons

Our anterograde tracing studies confirmed our viral injection studies that suggested a larger proportion of EVN axons crossed the midline to innervate the contralateral vestibular organs (**Figure 4**), compared to ipsilateral axons. However, using anterograde tracing alone, we could not determine what proportion of the total population this represented. We, therefore, used *retrograde* Fluoro-Gold (FG) labeling of EVN neurons originating from unilateral injections into vestibular organs in the *ChAT-GCaMP6$_f$* mouse strain to provide information on EVN laterality. This strain expressed the calcium indicator protein, GCaMP6$_f$, in all cholinergic cells including the EVN (confirmed by ChAT counterstaining—results not shown). Since GCaMP6$_f$ incorporates Green Fluorescent Protein (GFP) within its molecular structure, it can be visualized using standard GFP immunohistochemistry (**Figures 6D–F**). At the level of the EVN, this also included facial nerve genu (g7n), *abducens nucleus* (*abd*), and *facial nucleus* (*7n*; **Figure 6D**). Note, the EVN (**Figures 6E,F**), is clearly distinguished from the closest group of GFP-labeled cell bodies in the cholinergic abducens nucleus, located ventral to the facial nerve genu (**Figure 6D**).

Prior to the use of FG as a retrograde tracer, we injected Fast Green dye into the PC to confirm the spread from the PC to the rest of the vestibular portion of the membranous labyrinth (**Figure 6A**). Unilateral FG injections into the PC (**Figure 6A**, arrow) generated strong fluorescence in all ipsilateral vestibular neuroepithelia examined: AC, HC, U (**Figure 6B**), and the PC

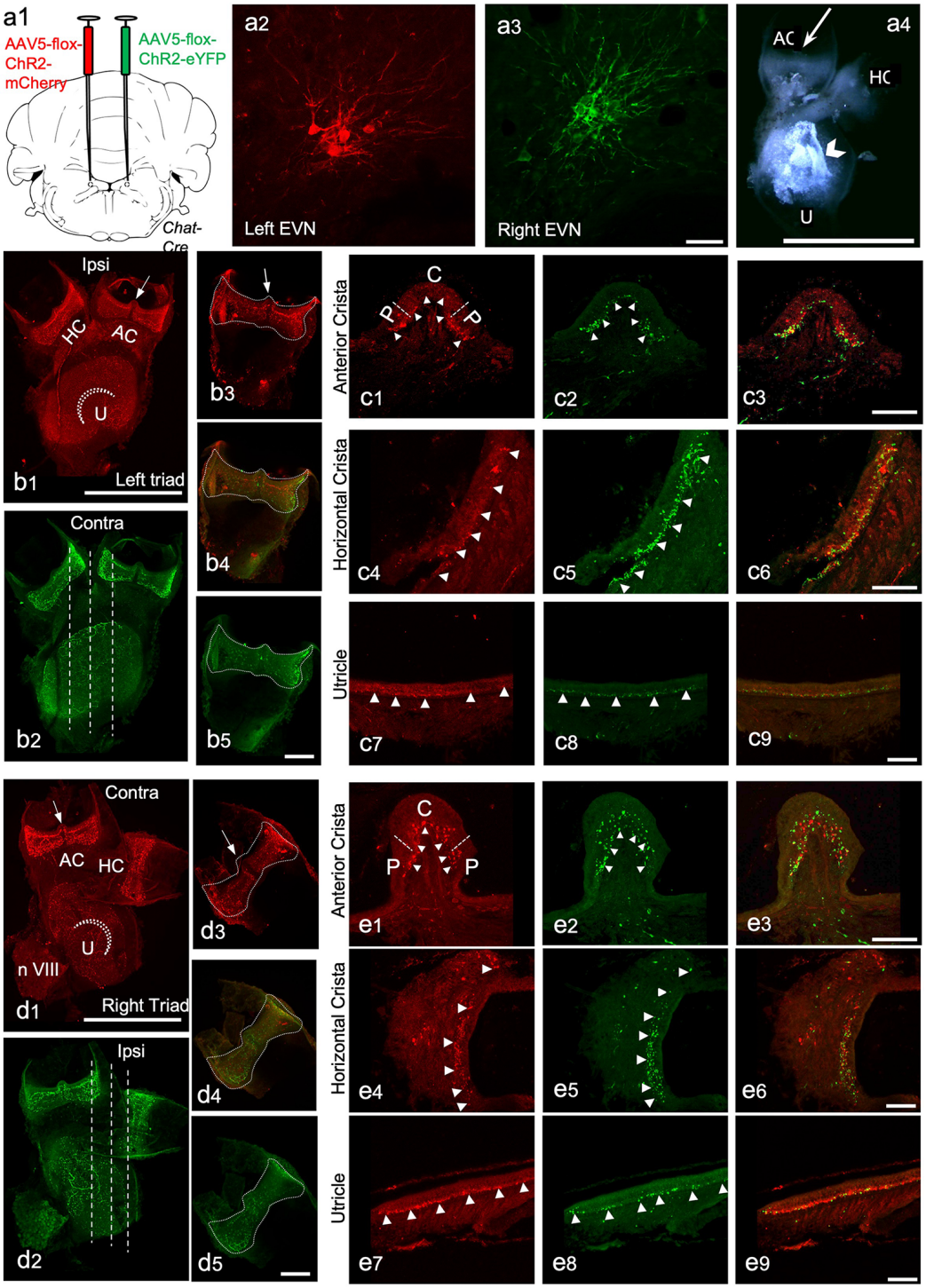

FIGURE 5 | The peripheral components of the Efferent Vestibular System. We used adeno-associated viruses (AAVs) to induce the expression of red and green fluorescent marker proteins in EVN neuronal cell bodies, their axons, and terminal fields in peripheral vestibular organs. Here we show the peripheral vestibular organs. **(A) a1**—the injection sites of AAV5-Chr2-mCherry (left) and AAV5-Chr2-EYFP (right) anterograde viruses in the brainstem; **a2,a3**—viral labeling of left EVN by mCherry red fluorescent protein and right EVN by EYFP fluorescent protein, Scale bar: 50 μm; **a4**—dissected vestibular organs, a semi-intact triad of anterior crista (AC), horizontal crista (HC) and utricle (U), arrowhead points at the otolith crystals, Scale bar: 1 mm. **(B) b1,b2**—maximum projection of z-stack from the left side triad visualized using red (mCherry) and green (EYFP) channels ∼3 weeks after virus injection in the brainstem. Arrow—eminentia cruciata; straight dashed line-showing the planes of sectioning; dashed curved line-striola in the utricle, HC—horizontal crista, AC—anterior crista, Scale bar: 500 μm; **b3–b5**—maximum projections of the

(*Continued*)

FIGURE 5 | Continued
left side posterior crista in red **(b3)** and green **(b5)** channels and the composite image **(b4)**, dashed line shows the outlines of the crista, arrow indicates eminentia cruciata, Scale bar: 100 μm. **(C)** Cross-sections of the left side anterior crista, horizontal crista, and utricle following immunohistochemistry against RFP (red) and GFP (green). **c1,c2**—anterior crista in red and green channels, dashed lines separate the central (C) and peripheral (P) parts of the crista, arrowheads point at the efferent nerve end terminals; **c3**—the composite image of the red and green channels; **c4–c6**—transverse section of the horizontal crista in red and green channels and the composite image, arrowheads point at efferent terminals; **c7–c9**—section of the utricle in red and green channels and the composite image, arrowheads point at nerve terminals. Scale bar: 50 μm. **(D)** **d1,d2**—Maximum projection from z-stacks of the right side triad in the red and green channel following virus injection in the brainstem, arrow—eminentia cruciata, straight dashed line-showing the planes of sectioning, dashed curved line—striola in the utricle, HC—horizontal crista, AC—anterior crista, Scale bar: 500 μm; **d3–d5**—maximum projections of the right side posterior crista in red **(d3)** and green **(d5)** channel and the composite image **(d4)**, dashed line outlines the crista, arrow—eminentia cruciata, Scale bar: 100 μm. **(E)** Cross sections of the right-side anterior crista, horizontal crista, and utricle after RFP (red) and GFP (green) immunohistochemistry. **e1,e2**—anterior crista in red and green channels, dashed lines separate the central (C) and peripheral (P) parts of the crista, arrowheads point at the efferent nerve end terminals; **e3**—composite image of the red and green channels; **e4–e6**—transverse section of the horizontal crista in red and green channels and the composite image, arrowheads point at nerve end terminals; **e7–e9**—section of the utricle in red and green channels and the composite image, arrowheads point at nerve terminals. Scale bar: 50 μm.

(**Figure 6C**). No FG label was observed in the ipsilateral cochlea, or contralateral labyrinth, or cochlear efferent neurons in the MOC and LOC of the superior olivary complex.

Immunofluorescent labeling was not required to amplify the FG label in peripheral or central tissue. However, GFP-immunolabeling was used to identify all GCaMP6/ChAT-positive EVN neurons. After a unilateral injection in the posterior canal, FG was retrogradely transported back to subsets of neurons in both left (ipsilateral) and right (contralateral) EVNs (**Figures 6G** arrows, **H,J**). While all FG-positive EVN neurons were double-labeled with GFP, not all GFP-positive EVN cells were double-labeled with FG (**Figures 6J,K**, arrows). **Table 1** summarizes the results from four retrograde FG experiments. In all cases, there was a significant difference in the number of double-labeled (FG+GFP) cells between ipsilateral and contralateral EVNs. Based on the proportion of GFP+FG and GFP-only in EVN cells, approximately one-third (32%) of ipsilateral EVN neurons were retrogradely labeled with FG, whereas over half of contralateral EVN neurons (55%) were FG-labeled. It should be noted that in none of the eight EVNs retrogradely labeled with FG did we see any evidence for additional clusters as reported in other rodents such as chinchilla (Marco et al., 1993) or gerbils (Perachio and Kevetter, 1989).

Antibody labeling for GFP also enabled us to count the total number of EVN neurons. **Table 1** summarizes the results. The average EVN cell number (± S.E.) was 53 ± 1.92 (ipsi EVN $n = 4$, average = 54.5 ± 2.1; contra EVN $n = 4$, average = 51.5 ± 3.5). There was no significant difference in the number of EVN neurons on opposite sides of the brainstem. The relatively small variation in the number of EVN neurons across the four animals and eight EVNs examined suggests a relatively stable cholinergic population. We also measured cell body cross-sectional areas, of all neurons in each of four EVNs, one EVN from each animal (**Table 2**). For a total of 210 EVN neurons measured, the average area (± S.D.) was 138.0 (± 38.2) μm^2, with the unimodal distribution. The average longest axis was 17.1 (± 3.0) μm and the shortest was 11.2 (± 1.9) μm, which gives a roundness index of 0.6 (4*Area / Pi*Maximum diameter^2), or oval appearance.

DISCUSSION

The Central Organization of EVN

The mammalian EVN was first described in kitten (Warr, 1975) using retrograde transport of horseradish peroxidase (HRP). Later tracing studies in rodent species, using additional labeling methods, identified the EVN in the guinea pig (Strutz, 1982), gerbil (Perachio and Kevetter, 1989), chinchilla (Marco et al., 1993; Lysakowski and Singer, 2000), and mouse (Leijon and Magnusson, 2014). Using transgenic mouse strains, we were able to anatomically target and characterize the mouse central and peripheral EVS to help fill important gaps in our understanding of this elusive sensory efferent circuit. Cre-dependent AAV-mediated expression of fluorescent reporters (Harris et al., 2012) provided highly specific labeling that allowed for visualization of neuronal cytoarchitecture and reliable tracing of axonal pathways to their terminal fields. Our retrograde FG data strongly supports a single EVN nucleus in mice with no other labeled clusters (cholinergic or non-cholinergic).

The clustering of EVN neurons suggests diversity among different mammalian species. In guinea pigs (Strutz, 1982) and gerbils (Perachio and Kevetter, 1989), two distinct clusters have been reported, and in chinchillas (Marco et al., 1993) and squirrel monkeys (Goldberg and Fernandez, 1980) there are putatively three. In mice, the EVN has been previously identified as comprising a single cluster of neurons, dorsolateral to the facial nerve genu (Leijon and Magnusson, 2014; Mathews et al., 2015), and is a location common to all mammalian species investigated to date, and often referred to as *group e*. Our results support these previous studies in mice. We found this single "central" cluster of densely packed multipolar cell bodies (see **Supplementary Video**), however, there were often examples of outlying or "peripheral" cell bodies, but still within 50 μm of the tightly packed core cluster. These outliers do not, in our opinion, constitute a separate EVN group, since there is no sharp delineation as seen in other larger mammals, which form two or more cell clusters. In addition, both core and outlying neurons were identified as cholinergic. This lack of extra clusters may be due to the smaller size of the mouse brain and fewer EVN neurons, when compared to their larger mammalian counterparts. However, it should be noted that in the much larger auditory efferent system, two different cell clusters, the lateral olivocochlear neurons (LOC) and the medial olivocochlear neurons (MOC; Guinan, 2006) have been retained in mice (see below, Anatomical comparison of the cochlear and vestibular efferent system).

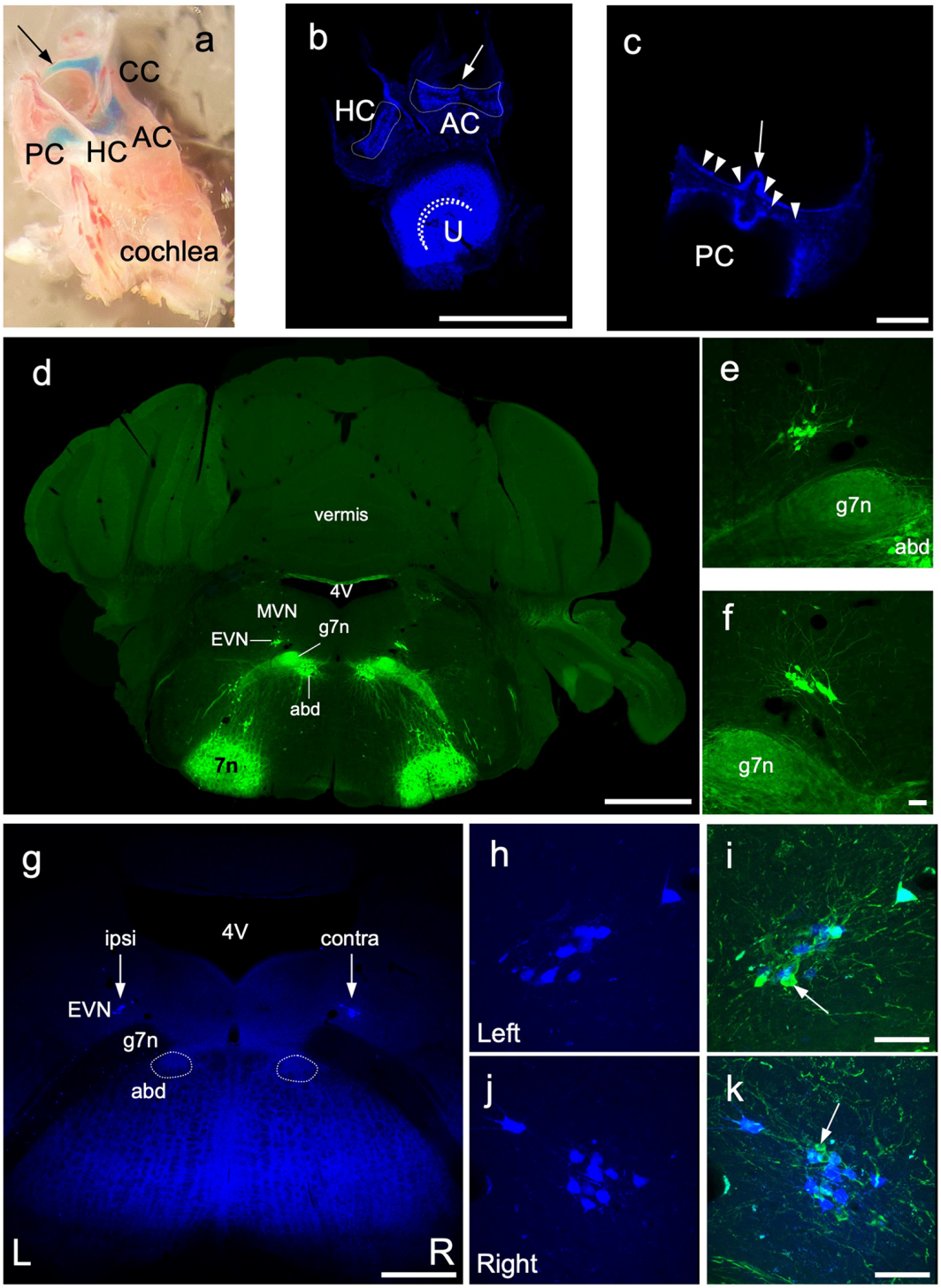

FIGURE 6 | Retrograde labeling of central EVN neurons. Fluoro Gold fluorescent retrograde tracer was injected unilaterally in the inner ear through the posterior semicircular canal and the efferent neurons were traced back retrogradely in the EVN on both sides. **(A)** Dissected bony inner ear following Fast Green dye injection through the posterior semicircular canal, arrow—injection site, PC, posterior semicircular canal, CC, common crus; AC, anterior crista; HC, horizontal crista. **(B,C)** Maximum projection image from z-stacks of the triad and posterior crista following dissections of a Fluoro Gold injected inner ear, dashed line outlines the vestibular cristae. curved dashed line—utricular striola, AC, anterior crista; HC, horizontal crista; U, utricle; arrow—eminentia cruciata; arrowheads—fluorescent neuroepithelium. Scale bar **(B)**: 500 μm, Scale bar **(C)**: 100 μm. **(D)** Photo-merged image of transgenic *Chat-gCaMP6f* mouse used for retrograde tracing and EVN cell counting. The ChAT dependent $GCaMP6_{fast}$expression was visualized by GFP immunolabeling in green. 4V—4th ventricle, MVN—medial vestibular nucleus,

(*Continued*)

FIGURE 6 | Continued
EVN—Efferent Vestibular Nucleus, abd—abducens nucleus, g7n—genu of the facial nerve, 7n—facial nucleus. Scale bar: 1 mm. **(E,F)** Left and Right side EVN nuclei under higher magnification. abd—abducens nucleus, 7n—genu of the facial nerve. Scale bar: 50 μm. **(G)** Fluoro Gold (FG) labeling of the EVN. 4V—4th ventricle, EVN—Efferent Vestibular Nucleus, arrows—position of the EVN, abd—abducens nucleus, 7n—genu of the facial nerve. Scale bar: 500 μm. **(H,I)** FG labeling in the left side EVN and the composite image of GFP and FG labeling. Arrow points to GFP but not FG-positive EVN neuron. Scale bar: 50 μm. **(J,K)** FG labeling in the right side EVN and the composite image of GFP and FG labeling. Arrow points to GFP-positive, FG-negative EVN neuron. Scale bar: 50 μm.

It is possible the mouse EVN may form two clusters of neurons but have remained physically close so that they appear as a central "core" and peripheral outliers, forming one EVN. But any differences between the core and outliers have yet to be determined.

To expand on the potential role of multiple EVN cell clusters in the species mentioned above, it may be worth considering their habitat type and their relative brain sizes. Chinchillas live in rocky mountain areas, while squirrel monkeys live in the canopy of tropical rainforest (Miller et al., 1983; Boinski, 1987). In contrast, the ancestors of the domesticated guinea pig and the gerbil lived on open grassy plains (Zhou and Zhong, 1989; Cassini and Galante, 1992). The two former species are extremely agile, which presumably requires a well-developed locomotor and balance system. Whereas guinea pigs and gerbils move about at ground level. Unsurprisingly, the brain size of the squirrel monkey is the biggest among these species, about 23 g (Hartwig et al., 2011). However, the chinchilla brain is only slightly larger, 5.25 g compared to the guinea pig, 4.28 g. The brain sizes of the gerbil and mouse are 0.9 g and 0.5 g, respectively (Wilber and Gilchrist, 1965; Sacher and Staffeldt, 1974; Goffinet and Rakic, 2012). It is plausible that differences in habitat and lifestyle may result in differently developed vestibular systems and the number of EVN cell clusters may reflect this; one or two EVN clusters in the less agile species (mouse, gerbil, guinea pig) and three clusters in more agile species (chinchilla, squirrel monkey).

In mice, the EVN was found clustered around a characteristic blood vessel, similar to that reported in gerbils (Perachio and Kevetter, 1989). This makes the nucleus potentially vulnerable to increased blood pressure. In addition, the proximity to the circulatory system also provides means for EVN neurons to secrete neuromodulators directly into the bloodstream. This could have clinical implications given that one of the neuropeptides found in EVN neurons is CGRP (Perachio and Kevetter, 1989; Luebke et al., 2014; Jones et al., 2018) a neuroactive substance known to be implicated in migraines (Goadsby et al., 2017). Therefore, EVN neurons may be involved in vestibular migraines.

Fluorescent labeling of the extensive dendritic architecture of the EVN allowed us to follow distal projections towards neighboring brain regions, especially the medial vestibular nucleus (MVN). This suggests a reciprocal influence of the vestibular nucleus complex (VNC) on the function of EVN neurons. A close association between VNC and EVN is consistent with a report that described polysynaptic inputs onto the EVN after rabies viral tracing, which identified the VNC as one of the major contributors (Metts et al., 2006).

Axonal Pathways From the EVN

In mice, individual EVN neurons project either to the ipsilateral or contralateral eighth nerve. We found no evidence for bilateral projections. We observed contralateral bound axons crossing the midline of the brainstem, approximately 100 μm more rostral to the level of the EVN neurons, suggesting a rostral-looping trajectory of the contralaterally projecting fibers before they turned back caudally to join ventrally projecting ipsilateral EVN fibers, as they exited towards the eighth nerve. Therefore, we did not observe any crossing axons in sections containing EVN neurons and this is the likely reason midline electrical stimulation of crossing efferent fibers was successful rostral to the known location of the EVN cell bodies (Schneider et al., 2021). This rostral decussation has also been reported in gerbils (Perachio and Kevetter, 1989) and is possibly the case in other mammalian species (Goldberg and Fernandez, 1980; Dechesne et al., 1984; Perachio and Kevetter, 1989). As they cross the midline, axons originating from left and right side EVN were intermingled and did not show any compartmentalization within the crossing "bundle".

Ipsilateral fibers join the genu of the 8th cranial nerve (g8n), at the level of the EVN, more caudal to the level of the contralateral fibers. The visualization of ipsilateral fibers is more difficult for two reasons: (1) there are fewer ipsilateral axons than contralateral axons; and (2) ipsilateral axons do not overlap or intermingle with other fibers, and their density is significantly lower making it harder to visualize them. Somewhat surprisingly, ipsilateral fibers project ventrally past the genu of the 7th cranial nerve avoiding the magno- and parvocellular MVN, despite the shortest route to the 8th cranial nerve would be straight across the MVN.

We hypothesize that the trajectories of the contralateral and ipsilateral efferent vestibular tracts are significantly impacted by other members of the vestibular nuclear complex during development. Thus, the contralateral fibers were pushed more rostrally from the EVN, while the ipsilateral fibers project more ventrally.

Our retrograde labeling results are similar to those reported previously in other mouse studies (Leijon and Magnusson, 2014; Mathews et al., 2015). A subset of $GCaMP6_f$ -positive EVN neurons, on both ipsi- and contralateral sides, were FG-labeled, the majority of which were found contralaterally. This is consistent with all previous mammalian studies and demonstrates significant contralateralization of the EVS. Based on the number of GFP/ChAT positive neurons that were either FG-positive or FG-negative on each side, we determined that, on average, EVN comprises over half (55.3%) contralaterally, and one third (32.1%), ipsilaterally projecting axons (**Table 1**). Our results were remarkably consistent despite the inherent variability of retrograde labeling. Indeed, Animal #1, which we consider as our best retrograde labeling example, a unilateral FG injection in the vestibular periphery accounted for 36.7% of ipsilateral EVN population and 62.0% contralateral EVN

TABLE 1 | Ipsilateral and contralateral EVN neuronal cell counts of retrogradely labeled with Fluoro-Gold (FG) and expressing Green Fluorescent Proteins (GFP).

Animal ID	Relative to FG-Injection	GFP + FG Positive (%)	GFP Only (%)	Total (EVN cells)	2 × 2 Table, Fisher *p* value
#1	Ipsi	18 (36.7)	31 (63.3)	49	0.0159
	Contra	31 (62.0)	19 (38.0)	50	
#2	Ipsi	17 (28.8)	42 (71.2)	59	0.0161
	Contra	31 (50.8)	30 (49.2)	61	
#3	Ipsi	19 (34.5)	36 (65.5)	55	0.0193
	Contra	29 (58.0)	21 (42.0)	50	
#4	Ipsi	16 (29.1)	39 (70.9)	55	0.0387
	Contra	23 (51.1)	22 (48.9)	45	
Average	**Ipsi**	**17.5** ± **0.6*** (32.1)	**37** ± **2.3** (67.9)	**54.5** ± **2.1***	**0.0200**
	Contra	**28.5** ± **1.9*** (55.3)	**23** ± **2.4** (44.7)	**51.5** ± **3.5***	

**Standard Error. Bold values represent averages.*

TABLE 2 | Average (± S.D.) cell body cross-sectional areas and their maximum and minimum diameters of EVN neurons labeled with GFP/ChAT.

Animal ID	n	$\bar{X}$ Area, μm²	Area, S.D.	$\bar{X}$ Max Dia, μm	Max Dia, S.D.	$\bar{X}$ Min Dia, μm	Min Dia, S.D.
# 1	50	141.8	44.3	17.6	3.2	11.1	2.1
# 2	60	145.4	34.0	17.5	3.1	11.6	1.7
# 3	55	121.9	27.6	15.8	2.3	10.7	1.7
# 4	45	142.8	42.1	17.5	2.7	11.2	2.0
Average	**210**	**138.0**	**38.2**	**17.1**	**3.0**	**11.2**	**1.9**

Bold values represent averages.

population. Taken together, these data account for 98.7% of a generic EVN nucleus, making bilateral projections from individual EVN neurons highly unlikely. While this finding is in agreement with other mammalian studies, including gerbil, it contrasts with a previous study in cat, that suggests up to 20% are bilaterally projecting (Dechesne et al., 1984). We attempted to confirm our result by injecting a second retrograde tracer, Fluoro Ruby (FR), into the contralateral posterior canal and look for double-labeled EVN neurons. However, we found transport from the inner ear using FR much less efficient and more variable when compared to FG, and therefore, FR results were not reported.

Peripheral Projections of the EVN

Peripheral EVN projections to the vestibular organs in mice have not been as widely studied. To date, there are no detailed reports of EVN peripheral projections in mouse vestibular organs. Our data show that the vestibular neuroepithelia receive innervation from both ipsilateral and contralateral EVN, as reported previously in other mammals. This observation is consistent with the only two anatomical studies to date describing the efferent innervation pattern of the vestibular periphery using anterograde biocytin tracing in the gerbil (Purcell and Perachio, 1997) and radioautography in the cat (Dechesne et al., 1984). The small number of EVN neurons in mice (n = 53), means efferent axons branch extensively to make many direct contacts with afferent fibers, afferent terminals (calyces), and type II vestibular hair cells within the vestibular peripheral organs (**Figure 7**). For recent reviews, see Mathews et al. (2017), Poppi et al. (2020), and Cullen and Wei (2021). Overall, our AAV tracing study presents evidence that both central and peripheral zones of the mouse vestibular cristae receive mixed innervation from both the ipsi- and contralateral EVN, although the majority of efferent contacts are from the contralateral EVN. In all mouse vestibular organs investigated, there appears to be no distinctive ipsilateral or contralateral innervation pattern as described previously in gerbil (Purcell and Perachio, 1997), where ipsilateral terminals innervate the central or apex zone of the crista, while contralateral terminals innervate the peripheral and planum zones. However, we did observe peripheral and planum regions of the cristae are favored both by a greater density of efferent terminals, and more efferent axons tend to pierce the neuroepithelial basement membrane in peripheral regions. This general mixed innervation pattern with a peripheral preference was also present in the utricle and saccule.

Factors to Consider

The most detailed study of efferent innervation of peripheral vestibular organs is in gerbils, and while our results in mice share many similarities, it is important to consider the differences. Gerbils and mice not only differ in size, but also in behavior, ecology, and taxonomy. It has been shown that habitat type, diet, zonation, and activity timing, all have an impact on brain size and development (Mace et al., 1981). In addition, molecular taxonomy suggests that although they are both rodents, the Gerbilinae family is more related to spiny mice (Acomys) than true mice (Murinae) (Chevret et al., 1993; Waiblinger, 2010), suggesting a different phylogenetic lineage. Perhaps the most obvious difference is the size of the gerbil brain, which is almost twice as big as the mouse, and this is reflected in our own results where the cross-sectional area of individual EVN neurons is almost twice as big in gerbils (259.8 ± 75.2 μm^2), when compared to mice (138.0 ± 38.2 μm^2). Gerbils have two recognized clusters of EVN cells, the bigger cell cluster of 200 neurons (*group e*, Purcell and Perachio, 1997) is thought to be equivalent to the single cluster mouse EVN of 53 neurons. In addition, there is a more ventral cell group which has no equivalent in mice. These differences suggest the function of

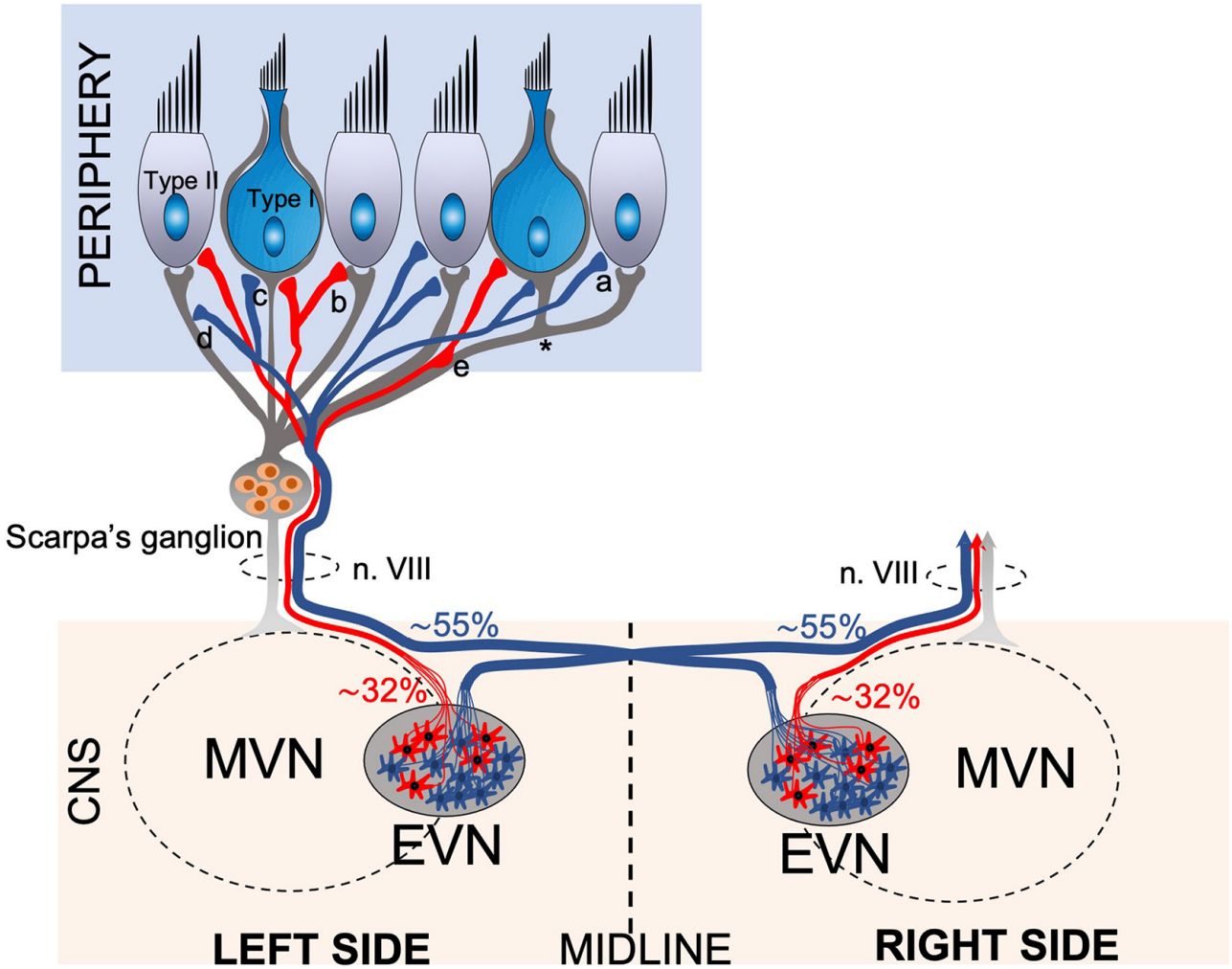

FIGURE 7 | Schematic drawing of the anatomical projections of the Efferent Vestibular System. Schematic of efferent (red, blue) and afferent (gray) innervation of the vestibular neuroepithelium, which consists of amphora shape Type I and cylindrical shape Type II hair cells. The afferent fibers originating from the bipolar neurons of Scarpa's ganglion transmit the vestibular sensory information from the labyrinths to the Vestibular Nuclei Complex (VNC) in the brainstem. The afferent fibers terminate in bouton terminals on Type II hair cells, calyx terminals on Type I hair cells, and dimorphic terminals comprising a bouton and a calyx (*). The efferent vestibular system originates from the Efferent Vestibular Nucleus (EVN) located in the brainstem. The EVN axons join the afferent fibers and travel in the vestibulocochlear nerve (n. VIII) to the neuroepithelium. Efferent fibers make synaptic contacts to the outer surface of type II hair cells **(a)**, afferent boutons **(b)**, calyx terminals **(c)**, afferent fibers **(d)**, and en-passant synapsis formed by axonal varicosities to afferent fibers **(e)**. Approximately 55% of EVN neurons provide contralateral (opposite side) projections, the axons cross the midline and join the opposite side vestibulocochlear nerve, while approx. 32% of neurons project ipsilaterally (same side).

the gerbil and mouse vestibular system may also differ due to interspecific behavioral and ecological differences and our morphological findings may reflect this.

Anatomical Comparison of the Cochlear and Vestibular Efferent Systems in Mice

There are critical similarities and differences between the two inner ear efferent systems in mice that are directly related to our findings. The mouse cochlea, with a total of ∼3,500 hair cells (765 IHCs and 2,625 OHCs; Ehret and Frankenreiter, 1977), receives efferent innervation from 475 superior olivary complex (SOC) neurons (Campbell and Henson, 1988). In mice, the five vestibular organs on one side, have a total of ∼10,500 hair cells (Lim and Brichta, 2012), and receive innervation from approximately 53 EVN neurons. As means of comparison, a very crude index of auditory efferent "branching" would suggest a ratio of approximately one central efferent neuron for every seven cochlear hair cells. In contrast, the vestibular efferent branching index has one efferent neuron for every 210 vestibular hair cells. This suggests a greater than an order of magnitude more exuberant vestibular efferent branching. In addition, the ratio of vestibular afferent to efferent neurons is lower in mice than for those typically reported for larger mammals. With approximately 3,500 vestibular afferents (Bäurle and Guldin, 1998) and 53 efferent neurons, the ratio is approximately 70:1, whereas it has been reported there is a ratio of 20:1 in guinea pigs, chinchilla, and squirrel monkeys (Lysakowski and Goldberg, 1997; Holt et al., 2011; Ryugo et al., 2011).

There are two efferent cell groups within the SOC: (1) the lateral olivary complex (LOC), which provide 65% of the total efferent innervation to the cochlea on the same side; and (2) the medial olivary complex (MOC), which provides the remaining 35% of the efferent innervation to the cochlea but coming mostly (75%) from the contralateral MOC (Campbell and Henson, 1988; Brown, 1993). In contrast, there is only one group of EVN neurons on each side. Therefore, EVN laterality more closely resembles the MOC than the LOC. Cochlear targets of LOC and MOC efferent neurons are different. LOC neurons innervate cochlear afferent fibers and inner hair cells, while MOC neurons innervate outer hair cells. EVN terminals are distributed throughout the vestibular organs although their axons are preferentially distributed in peripheral rather than the central zones of vestibular neuroepithelia. EVN terminals target vestibular primary afferent parent axons and their calyx terminals, and only innervate type II hair cells, since type I hair cells are typically isolated from direct efferent contact due to the intervening/surrounding calyx terminal. Centrally, MOC and maybe LOC axons form collaterals to the cochlear nucleus on their way to the periphery (Brown, 1993). We were unable to verify the presence of EVN collaterals projecting to any vestibular nucleus on their way to the periphery. Nor could we confirm the collateral EVN projection to the cerebellar flocculus, ventral paraflocculus, and interstitial nucleus of the vestibular nerve as seen in the gerbil (Perachio and Kevetter, 1989; Shinder et al., 2001). It should be noted, however, that in addition to the EVN nucleus, in two cases, we found doublelabeled (yellow) cells in a discrete region of the cerebellar vermis (see **Supplementary Figures 1A–C**). How these cells were double-labeled remains unknown.

Vestibulocochlear efferents originate from the same pool as facial branchial motor neurons in the brainstem (Fritzsch and Elliott, 2017). Given their common developmental origin, the principal fast neurotransmitter of both vestibular and auditory efferent systems is acetylcholine (ACh). In addition, LOC efferents have been reported to contain γ-aminobutyric acid (GABA), calcitonin-gene-related peptide (CGRP), and dopamine (Eybalin, 1993). MOC efferents have also been reported to also contain GABA and CGRP (Maison et al., 2003). In the EVS, ACh, and CGRP colocalize and are likely the dominant neurochemicals (Luebke et al., 2014; Jones et al., 2018), but there are also reports about the presence of enkephalins (Ryan et al., 1991) and μ-opioid receptors (Popper et al., 2004), but the presence of GABA and nitric oxide in efferent terminals has not been confirmed.

CONCLUSION

The function of the cochlear efferent system is far better understood than the efferent vestibular system. In the cochlea, the efferent system plays a role in unmasking the signal from noisy backgrounds, protection of acoustic trauma, interaural sensitivity by influencing the stiffness of the tectorial membrane and modulating cochlear sensitivity in response to visual or acoustic stimuli during selective attention (Délano Reyes and Elgoyhen, 2016). In contrast, the exact function of the efferent vestibular system is still unknown. Recent evidence in mice suggests there are both fast and slow excitation effects when the EVS is electrically activated (Cassini and Galante, 1992; Schneider et al., 2021). However, precisely when the EVS is naturally activated and under what conditions still remains to be determined. Two behavioral reports suggest the EVS is involved in longer term events such as adaptation and compensation of the vestibuloocular reflex (Hübner et al., 2015, 2017).

The anatomical data described in this study are in line with our physiological characterization of mouse vestibular afferent responses to efferent stimulation (Schneider et al., 2021) and also a study in chinchilla (Marlinski et al., 2004). First, midline stimulation, which only activates contralateral EVS neurons, excited most regularly- and irregularly discharging afferents consistent with deposition of contralateral efferent terminals throughout the vestibular neuroepithelia. Second, ipsilateral stimulation, which recruits both contralateral and ipsilateral EVS neurons, also excited most classes of afferents, but could be distinguished from contralateral stimulation in that the resulting excitation was significantly larger. Such excitation patterns reinforce the notion that ipsilateral efferent terminals are also broadly distributed across the neuroepithelia, and not representative of any discrete regional EVS innervation pattern as reported in gerbils (Purcell and Perachio, 1997).

In summary, our anatomical study contributes details about the central and peripheral organization of the mouse EVS and provides a context for comparison with the auditory efferent system. In addition, knowing the precise anatomical arrangement of the EVS allows us to better interpret existing studies examining the effects of electrical activation of the EVS in anesthetized mice. These anatomical data will also be important for developing future experiments in awake, behaving mice where the goal will be to record EVS activity in real-time. After more than 60 years since their discovery, results from the *in vivo* experiments described above will finally begin to reveal the role of the EVS in balance after a long and winding road of discovery.

DATA AVAILABILITY STATEMENT

The raw data supporting the conclusions of this article will be made available by the authors, without undue reservation.

ETHICS STATEMENT

The animal study was reviewed and approved by Animal Care and Ethics Committee, The University of Newcastle, Callaghan, NSW 2308, Australia.

AUTHOR CONTRIBUTIONS

DL, AB, and LP designed the study. DL, LP, and HD conducted the experiments. DL, AB, LP, and RL analyzed the data and made the figures. DL, AB, JH, and LP drafted the manuscript. DL, AB,

LP, RL, and JH edited the manuscript. All authors contributed to the article and approved the submitted version.

FUNDING

This work was supported by National Health and Medical Research Council of Australia, Ideas Grant APP1188181 to AB, RL, and LP; NIH Grant R01DC0016974 to JH; Vice Chancellor's HDR Academic Career Pathway Scholarship to DL.

SUPPLEMENTARY MATERIALS

The Supplementary Material for this article can be found online at: https://www.frontiersin.org/articles/10.3389/fncir.2021.751850/full#supplementary-material.

REFERENCES

Bäurle, J., and Guldin, W. (1998). Unbiased number of vestibular ganglion neurons in the mouse. *Neurosci. Lett.* 246, 89–92. doi: 10.1016/s0304-3940(98)00241-9

Boinski, S. (1987). Habitat use by squirrel monkeys (*Saimiri oerstedi*) in costa rica. *Folia Primatol. (Basel)* 49, 151–167. doi: 10.1159/000156319

Brown, M. C. (1993). Fiber pathways and branching patterns of biocytin-labeled olivocochlear neurons in the mouse brainstem. *J. Comp. Neurol.* 337, 600–613. doi: 10.1002/cne.903370406

Brown, M. C. (2011). "Anatomy of olivocochlear neurons," in *Auditory and Vestibular Efferents*, eds D. K. Ryugo, R. R. Fay, and A. N. Popper (New York: Springer), 17–37. doi: 10.1007/978-1-4419-7070-1_2

Campbell, J. P., and Henson, M. M. (1988). Olivocochlear neurons in the brainstem of the mouse. *Hear. Res.* 35, 271–274. doi: 10.1016/0378-5955(88)90124-4

Cassini, M. H., and Galante, M. L. (1992). Foraging under predation risk in the wild guinea pig: the effect of vegetation height on habitat utilization. *Annal. Zoologici Fennici* 4, 289–294.

Chevret, P., Denys, C., Jaeger, J.-J., Michaux, J., and Catzeflis, F. M. (1993). Molecular evidence that the spiny mouse (Acomys) is more closely related to gerbils (Gerbillinae) than to true mice (Murinae). *Proc. Natl. Acad. Sci. U S A* 90, 3433–3436. doi: 10.1073/pnas.90.8.3433

Cullen, K. E., and Wei, R.-H. (2021). Differences in the structure and function of the vestibular efferent system among vertebrates. *Front. Neurosci.* 15:684800. doi: 10.3389/fnins.2021.684800

Dechesne, C., Raymond, J., and Sans, A. (1984). The efferent vestibular system in the cat: a horseradish peroxidase and fluorescent retrograde tracers study. *Neuroscience* 11, 893–901. doi: 10.1016/0306-4522(84)90200-8

Délano Reyes, P., and Elgoyhen, A. B. (2016). Auditory efferent system: new insights from cortex to cochlea. *Front. Syst. Neurosci.* 10:50. doi: 10.3389/fnsys.2016.00050

Ehret, G., and Frankenreiter, M. (1977). Quantitative analysis of cochlear structures in the house mouse in relation to mechanisms of acoustical information processing. *J. Comp. Physiol.* 122, 65–85. doi: 10.1007/BF00611249

Eybalin, M. (1993). Neurotransmitters and neuromodulators of the mammalian cochlea. *Physiol. Rev.* 73, 309–373. doi: 10.1152/physrev.1993.73.2.309

Fritzsch, B., and Elliott, K. L. (2017). Evolution and development of the inner ear efferent system: transforming a motor neuron population to connect to the most unusual motor protein *via* ancient nicotinic receptors. *Front. Cell. Neurosci.* 11:114. doi: 10.3389/fncel.2017.00114

Goadsby, P. J., Holland, P. R., Martins-Oliveira, M., Hoffmann, J., Schankin, C., and Akerman, S. (2017). Pathophysiology of migraine: a disorder of sensory processing. *Physiol. Rev.* 97, 553–622. doi: 10.1152/physrev.00034.2015

Goffinet, A. M., and Rakic, P. (2012). *Mouse Brain Development.* Heidelberg: Springer Science & Business Media.

Goldberg, J. M., and Fernandez, C. (1980). Efferent vestibular system in the squirrel monkey: anatomical location and influence on afferent activity. *J. Neurophysiol.* 43, 986–1025. doi: 10.1152/jn.1980.43.4.986

Guinan, J. J., Jr. (2006). Olivocochlear efferents: anatomy, physiology, function and the measurement of efferent effects in humans. *Ear. Hear.* 27, 589–607. doi: 10.1097/01.aud.0000240507.83072.e7

Guo, J.-Y., He, L., Qu, T.-F., Liu, Y.-Y., Liu, K., Wang, G.-P., et al. (2018). Canalostomy as a surgical approach to local drug delivery into the inner ears of adult and neonatal mice. *J. Vis. Exp.* 135:57351 doi: 10.3791/57351

Harris, J. A., Wook Oh, S., and Zeng, H. (2012). Adeno-associated viral vectors for anterograde axonal tracing with fluorescent proteins in nontransgenic and cre driver mice. *Curr. Protoc. Neurosci.* 59, 1.20.1–1.20.18. doi: 10.1002/0471142301.ns0120s59

Hartwig, W., Rosenberger, A. L., Norconk, M. A., and Owl, M. Y. (2011). Relative brain size, gut size and evolution in new world monkeys. *Anat. Rec. (Hoboken)* 294, 2207–2221. doi: 10.1002/ar.21515

Hübner, P. P., Khan, S. I., and Migliaccio, A. A. (2015). The mammalian efferent vestibular system plays a crucial role in the high-frequency response and short-term adaptation of the vestibuloocular reflex. *J. Neurophysiol.* 114, 3154–3165. doi: 10.1152/jn.00307.2015

Hübner, P. P., Khan, S. I., and Migliaccio, A. A. (2017). The mammalian efferent vestibular system plays a crucial role in vestibulo-ocular reflex compensation after unilateral labyrinthectomy. *J. Neurophysiol.* 117, 1553–1568. doi: 10.1152/jn.01049.2015

Holt, J. C., Lysakowski, A., and Goldberg, J. M. (2011). "The efferent vestibular system," in *Auditory and Vestibular Efferents*, (New York: Springer), 135–186. doi: 10.1007/978-1-4419-7070-1_6

Jones, S. M., Vijayakumar, S., Dow, S. A., Holt, J. C., Jordan, P. M., and Luebke, A. E. (2018). Loss of α-calcitonin gene-related peptide (αCGRP) reduces otolith activation timing dynamics and impairs balance. *Front. Mol. Neurosci.* 11:289. doi: 10.3389/fnmol.2018.00289

Jordan, P. M., Fettis, M., and Holt, J. C. (2015). Efferent innervation of turtle semicircular canal cristae: comparisons with bird and mouse. *J. Comp. Neurol.* 523, 1258–1280. doi: 10.1002/cne.23738

Leijon, S., and Magnusson, A. K. (2014). Physiological characterization of vestibular efferent brainstem neurons using a transgenic mouse model. *PLoS One* 9:e98277. doi: 10.1371/journal.pone.0098277

Lim, R., and Brichta, A. M. (2012). "Vestibular system," in *The Mouse Nervous System*, (Amsterdam: Elsevier), 661–681. doi: 10.1016/B978-0-12-369497-3.10027-5

Luebke, A. E., Holt, J. C., Jordan, P. M., Wong, Y. S., Caldwell, J. S., and Cullen, K. E. (2014). Loss of α-calcitonin gene-related peptide (αCGRP) reduces the efficacy of the vestibulo-ocular reflex (VOR). *J. Neurosci.* 34, 10453–10458. doi: 10.1523/JNEUROSCI.3336-13.2014

Lysakowski, A., and Goldberg, J. M. (1997). A regional ultrastructural analysis of the cellular and synaptic architecture in the chinchilla cristae ampullares. *J. Comp. Neurol.* 389, 419–443. doi: 10.1002/(sici)1096-9861(19971222)389:3<419::aid-cne5>3.0.co;2-3

Lysakowski, A., and Singer, M. (2000). Nitric oxide synthase localized in a subpopulation of vestibular efferents with NADPH diaphorase histochemistry and nitric oxide synthase immunohistochemistry. *J. Comp. Neurol.* 427, 508–521. doi: 10.1002/1096-9861(20001127)427:4<508::aid-cne2>3.0.co;2-l

Mace, G. M., Harvey, P. H., and Clutton-Brock, T. (1981). Brain size and ecology in small mammals. *J. Zool.* 193, 333–354. doi: 10.1111/j.1469-7998.1981.tb03449.x

Maison, S. F., Adams, J. C., and Liberman, M. C. (2003). Olivocochlear innervation in the mouse: immunocytochemical maps, crossed versus uncrossed contributions and transmitter colocalization. *J. Comp. Neurol.* 455, 406–416. doi: 10.1002/cne.10490

Marco, J., Lee, W., Suaárez, C., Hoffman, L., and Honrubia, V. (1993). Morphologic and quantitative study of the efferent vestibular system in the chinchilla: 3-D reconstruction. *Acta Otolaryngol.* 113, 229–2234. doi: 10.3109/00016489309135798

Marlinski, V., Plotnik, M., and Goldberg, J. M. (2004). Efferent actions in the chinchilla vestibular labyrinth. *J. Assoc. Res. Otolaryngol.* 5, 126–143. doi: 10.1007/s10162-003-4029-7

Mathews, M. A., Camp, A. J., and Murray, A. J. (2017). Reviewing the role of the efferent vestibular system in motor and vestibular circuits. *Front. Physiol.* 8:552. doi: 10.3389/fphys.2017.00552

Mathews, M. A., Murray, A., Wijesinghe, R., Cullen, K., Tung, V. W., and Camp, A. J. (2015). Efferent vestibular neurons show homogenous discharge output but heterogeneous synaptic input profile *in vitro*. *PLoS One* 10:e0139548. doi: 10.1371/journal.pone.0139548

Metts, B. A., Kaufman, G. D., and Perachio, A. A. (2006). Polysynaptic inputs to vestibular efferent neurons as revealed by viral transneuronal tracing. *Exp. Brain Res.* 172, 261–274. doi: 10.1007/s00221-005-0328-z

Miller, S. D., Rottmann, J., Raedeke, K. J., and Taber, R. D. (1983). Endangered mammals of chile: status and conservation. *Biol. Conserv.* 25, 335–352. doi: 10.1016/0006-3207(83)90069-1

Paxinos, G., and Franklin, K. B. J. (2001). *The Mouse Brain in Stereotaxic Coordinates*. San Diego, CA: Academic Press.

Perachio, A. A., and Kevetter, G. A. (1989). Identification of vestibular efferent neurons in the gerbil: histochemical and retrograde labelling. *Exp. Brain Res.* 78, 315–326. doi: 10.1007/BF00228903

Popper, P., Cristobal, R., and Wackym, P. A. (2004). Expression and distribution of μ opioid receptors in the inner ear of the rat. *Neuroscience* 129, 225–233. doi: 10.1016/j.neuroscience.2004.08.008

Poppi, L. A., Holt, J. C., Lim, R., and Brichta, A. M. (2020). A review of efferent cholinergic synaptic transmission in the vestibular periphery and its functional implications. *J. Neurophysiol.* 123, 608–629. doi: 10.1152/jn.00053.2019

Purcell, I. M., and Perachio, A. A. (1997). Three-dimensional analysis of vestibular efferent neurons innervating semicircular canals of the gerbil. *J. Neurophysiol.* 78, 3224–3248. doi: 10.1152/jn.1997.78.6.3234

Ryan, A. F., Simmons, D. M., Watts, A. G., and Swanson, L. W. (1991). Enkephalin mRNA production by cochlear and vestibular efferent neurons in the gerbil brainstem. *Exp. Brain Res.* 87, 259–267. doi: 10.1007/BF00231843

Ryugo, D. K., Fay, R. R., and Popper, A. N. Eds. (2011). *Auditory And Vestibular Efferents*. New York: Springer.

Sacher, G. A., and Staffeldt, E. F. (1974). Relation of gestation time to brain weight for placental mammals: implications for the theory of vertebrate growth. *Am. Natural.* 108, 593–615. doi: 10.1086/282938

Schneider, G. T., Lee, C., Sinha, A. K., Jordan, P. M., and Holt, J. C. (2021). The mammalian efferent vestibular system utilizes cholinergic mechanisms to excite primary vestibular afferents. *Sci. Rep.* 11:1231. doi: 10.1038/s41598-020-80367-1

Shinder, M. E., Purcell, I. M., Kaufman, G. D., and Perachio, A. A. (2001). Vestibular efferent neurons project to the flocculus. *Brain Res.* 889, 288–294. doi: 10.1016/s0006-8993(00)03117-6

Sokal, R. R., and Rohlf, F. J. (1981). *Biometry: The Principles and Practice of Statistics in Biological Research*, 2nd Edn. San Francisco, CA: W. H. Freeman and Company.

Strutz, J. (1982). The origin of efferent vestibular fibres in the guinea pig. *Acta Otolaryngol.* 94, 299–305. doi: 10.3109/00016488209128917

Waiblinger, E. (2010). "The laboratory gerbil," in *UFAW Handbook on the Care and Management of Laboratory Animals*, 8th Edn, eds R. Hubrecht and J. Kirkwood (Oxford, UK: Wiley-Blackwell), 327–347.

Warr, W. B. (1975). Olivocochlear and vestibular efferent neurons of the feline brain stem: their location, morphology and number determined by retrograde axonal transport and acetylcholinesterase histochemistry. *J. Comp. Neurol.* 161, 159–181. doi: 10.1002/cne.901610203

Wilber, C. G., and Gilchrist, R. D. (1965). Organ weight: body weight ratios in the mongolian gerbil, meriones unguiculatus. *Chesapeake Sci.* 6, 109–114.

Zhou, Q., and Zhong, W. (1989). Ecology and social behaviour of Mongolian gerbils, meriones unguiculatus, at Xilinhot, inner Mongolia, China. *Animal Behav.* 37, 11–27. doi: 10.1016/0003-3472(89)90002-X

Conflict of Interest: The authors declare that the research was conducted in the absence of any commercial or financial relationships that could be construed as a potential conflict of interest.

Publisher's Note: All claims expressed in this article are solely those of the authors and do not necessarily represent those of their affiliated organizations, or those of the publisher, the editors and the reviewers. Any product that may be evaluated in this article, or claim that may be made by its manufacturer, is not guaranteed or endorsed by the publisher.

Advantages of publishing in Frontiers

OPEN ACCESS
Articles are free to read for greatest visibility and readership

FAST PUBLICATION
Around 90 days from submission to decision

HIGH QUALITY PEER-REVIEW
Rigorous, collaborative, and constructive peer-review

TRANSPARENT PEER-REVIEW
Editors and reviewers acknowledged by name on published articles

Frontiers
Avenue du Tribunal-Fédéral 34
1005 Lausanne | Switzerland

Visit us: www.frontiersin.org
Contact us: frontiersin.org/about/contact

REPRODUCIBILITY OF RESEARCH
Support open data and methods to enhance research reproducibility

DIGITAL PUBLISHING
Articles designed for optimal readership across devices

FOLLOW US
@frontiersin

IMPACT METRICS
Advanced article metrics track visibility across digital media

EXTENSIVE PROMOTION
Marketing and promotion of impactful research

LOOP RESEARCH NETWORK
Our network increases your article's readership